CHEMICAL REVIEWS

pubs.acs.org/CR Review

Electrocatalysis in Alkaline Media and Alkaline Membrane-Based Energy Technologies

Yao Yang, Cheyenne R. Peltier, Rui Zeng, Roberto Schimmenti, Qihao Li, Xin Huang, Zhifei Yan, Georgia Potsi, Ryan Selhorst, Xinyao Lu, Weixuan Xu, Mariel Tader, Alexander V. Soudackov, Hanguang Zhang, Mihail Krumov, Ellen Murray, Pengtao Xu, Jeremy Hitt, Linxi Xu, Hsin-Yu Ko, Brian G. Ernst, Colin Bundschu, Aileen Luo, Danielle Markovich, Meixue Hu, Cheng He, Hongsen Wang, Jiye Fang, Robert A. DiStasio, Jr., Lena F. Kourkoutis, Andrej Singer, Kevin J. T. Noonan, Li Xiao, Lin Zhuang, Bryan S. Pivovar, Piotr Zelenay, Enrique Herrero, Juan M. Feliu, Jin Suntivich, Emmanuel P. Giannelis, Sharon Hammes-Schiffer, Tomás Arias, Manos Mavrikakis, Thomas E. Mallouk, Joel D. Brock, David A. Muller, Francis J. DiSalvo, Geoffrey W. Coates, and Héctor D. Abruna*

Cite This: https://doi.org/10.1021/acs.chemrev.1c00331 Read Online

ACCESS | Metrics & More | Article Recommendations

ABSTRACT: Hydrogen energy-based electrochemical energy conversion technologies offer the promise of enabling a transition of the global energy landscape from fossil fuels to renewable energy. Here, we present a comprehensive review of the fundamentals of electrocatalysis in alkaline media and applications in alkaline-based energy technologies, particularly alkaline fuel cells and water electrolyzers. Anion exchange (alkaline) membrane fuel cells (AEMFCs) enable the use of nonprecious electrocatalysts for the sluggish oxygen reduction reaction (ORR), relative to proton exchange membrane fuel cells (PEMFCs), which require Pt-based electrocatalysts. However, the hydrogen oxidation reaction (HOR) kinetics is significantly slower in alkaline media than in acidic media. Understanding these phenomena requires applying theoretical and experimental methods to unravel molecular-level thermodynamics and kinetics of hydrogen and oxygen electrocatalysis and, particularly, the proton-coupled electron transfer (PCET) process that takes place in a proton-deficient alkaline media. Extensive electrochemical and spectroscopic studies, on single-crystal Pt and metal oxides, have contributed to the development of activity descriptors, as well as the identification of the nature of active sites, and the rate-determining steps of the HOR and ORR. Among these, the structure and reactivity of interfacial water serve as key potential and pH-dependent kinetic factors that are helping elucidate the origins of the HOR and ORR activity differences in acids and bases. Additionally, deliberately modulating and controlling catalyst−support interactions have provided valuable insights for enhancing catalyst accessibility and durability during operation. The design and synthesis of highly conductive and durable alkaline membranes/ionomers have enabled AEMFCs to reach initial performance metrics equal to or higher than those of PEMFCs. We emphasize the importance of using membrane electrode assemblies (MEAs) to integrate the often separately pursued/optimized electrocatalyst/support and membranes/ionomer components. *Operando/in situ* methods, at multiscales, and *ab initio* simulations provide a mechanistic understanding of electron, ion, and mass transport at catalyst/ionomer/membrane interfaces and the necessary guidance to achieve fuel cell operation in air over thousands of hours. We hope that this Review will serve as a roadmap for advancing the scientific understanding of the fundamental factors governing electrochemical energy conversion in alkaline media with the ultimate goal of achieving ultralow Pt or precious-metal-free high-performance and durable alkaline fuel cells and related technologies.

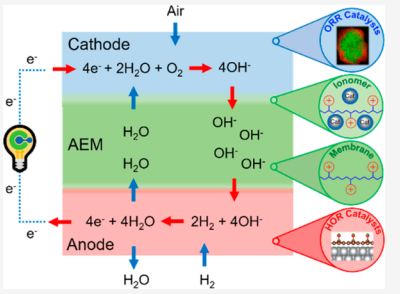

CONTENTS

Received: April 26, 2021

https://doi.org/10.1021/acs.chemrev.1c00331
Chem. Rev. XXXX, XXX, XXX−XXX

1. INTRODUCTION

One of the grand challenges of our time is how to meet the increasing global energy needs in a sustainable and environmentally responsible way. While the use of fossil fuels has greatly improved our standard of living, it has also caused detrimental environmental consequences associated with their extraction and combustion, causing pollution and carbon emission.[1] Shifting the energy landscape from fossil fuels to renewable energy technologies will play a key role in tackling complex environmental and economic challenges. One of the most promising approaches to lower carbon emission is to develop hydrogen energy based on hydrogen fuel cells and water electrolyzers ($H_2 + O_2 \Leftrightarrow H_2O$).[2] Hydrogen fuel cells can transform the chemical energy in hydrogen directly into electricity with an energy efficiency 2−3 times higher than that of internal combustion engines. Considering the high energy density (120 MJ/kg) and fast refill time (~5 min) of H_2 gas, hydrogen fuel cells have emerged as critical energy technologies for powering long-distance electric vehicles (EVs).[3] Water electrolyzers are cost-competitive technologies to produce H_2 at a large scale with potentially zero carbon emission if driven by renewable electricity.[4] Those two hydrogen-based technologies show the potential to balance the mismatch between intermittent solar/wind energy and the need for continuous power in existing electricity grids.[5]

Although fuel cells were first demonstrated by Sir William Grove in 1839, they were not practically useful until a century later when alkaline fuel cells (AFCs) were invented by Francis Thomas Bacon in 1932. A 5 kW AFC stack, using Ni to overcome electrode corrosion in concentrated KOH, was constructed in 1959 with an operating efficiency of 60%. Since then, AFCs have been used by NASA, in the mid-1960s, as power generators for Apollo missions and Space Shuttle programs, which used pure hydrogen and oxygen. However, when alkaline fuel cells are operated with air for daily automotive applications, KOH solutions react with CO_2 and produce carbonates, which can precipitate and block the porous electrodes and lower the ionic conductivity of the electrolyte, causing a detrimental performance drop. Proton exchange membrane fuel cells (PEMFCs) were developed later by William Grubb and Leonard Niedrach at General Electric in the 1960s and used briefly for the NASA Gemini program. However, water-management issues in PEMs made them less reliable and, therefore, less competitive than AFCs. AFCs were thus used by NASA as the primary power system through the 1990s. Several critical innovations, particularly Nafion membranes discovered by Walther Grot of DuPont, low Pt loadings in Pt-based alloys, and thin-film membrane electrode assemblies (MEAs), dramatically lowered the cost and improved the reliability of PEMFCs.[6] The compact configuration of PEMFCs enables a small cell volume and light weight, CO_2-tolerance, and the lack of a corrosive electrolyte, which offer PEMFCs great advantages over AFCs, especially for EV applications.

After more than 2 decades of development, PEMFCs have enabled a steadily growing global market for fuel cell EVs (FCEVs). However, PEMFCs inherently require a significant amount of scarce and expensive Pt-based electrocatalysts to facilitate the sluggish oxygen reduction reaction (ORR) while

https://doi.org/10.1021/acs.chemrev.1c00331
Chem. Rev. XXXX, XXX, XXX−XXX

only a minimal amount of Pt is required to catalyze the fast hydrogen oxidation reaction (HOR) in acid.[7,8] The Pt-based catalyst cost is projected to be the largest single component (up to 40%) of the total cost of a PEMFC.[9] As an alternative, anion exchange membrane fuel cells (AEMFCs) have drawn increasing attention since they enable the use of non-precious-group-metal (non-PGM) electrocatalysts, and AEMs can effectively mitigate the carbonate precipitation issue in KOH solutions. Nonprecious ORR electrocatalysts, such as 3d metals or metal oxides, perovskites, and metal-containing N-doped carbon, are attractive for their low cost, promising activity, and durability.[10,11] However, AEMFCs also face another challenge; the rate of the HOR on Pt is two orders of magnitude slower in alkaline media than in acidic media, leading to a significantly higher Pt loading required at the hydrogen anode. Thus, new low-Pt and eventually non-PGM HOR electrocatalysts must be developed in order to enable the implementation of high-performance alkaline fuel cell technologies at large scale and low cost.

Various naming schemes have been employed to describe alkaline fuel cell technologies, such as anion exchange membrane fuel cells (AEMFCs), alkaline anion exchange membrane fuel cells (AAEMFCs), alkaline membrane fuel cells (AMFCs), alkaline polymer electrolyte fuel cells (APEFCs), and hydroxide exchange membrane fuel cells (HEMFCs). In this Review, AEMFCs were chosen to be parallel to PEMFCs and convey the possibility to employ both hydroxide- and carbonate-conducting devices. Although the advantages of AEMFCs have been long recognized, early prototypes of AEMFCs still used Pt to catalyze both the ORR and HOR.[12] The first AEMFC with non-PGM electrocatalysts was reported to have a peak power density (PPD) of 50 mW/cm^2 by Zhuang et al. in 2008 using a Ag cathode, Ni−Cr anode, and a quaternary ammonium-functionalized poly(arylene ether sulfone)s (QAPS) membrane.[13] After 1 decade of extensive research efforts in AEMFCs,[14,15] MEA performances beyond 1 W/cm^2 have been recently achieved using a nonprecious Co−Mn spinel oxide cathode, a Pt−Ru anode, and a poly(*p*-terphenyl-piperidinium) (QAPPT) membrane.[16] The >20-fold performance enhancement arises, in part, from key advances in developing highly conductive and durable alkaline/anion exchange membranes (AEMs)/ionomers, nonprecious ORR/HOR electrocatalysts, and an optimization of MEA fabrication and testing protocols. AEMFCs can now achieve a comparable initial MEA performance to state-of-the-art PEMFCs. Practical FCEVs necessitate achieving not only a high initial performance but also long-term durability during MEA operation in air. While nonprecious electrocatalysts will bring new possibilities to fuel cell technologies, it is pivotal to deconvolve the degradation mechanisms of electrocatalysts from membranes and ionomers, in order to enable stable AEMFC operation over hundreds to thousands of hours. The strategies used to study alkaline fuel cells and water electrolyzers can be extended to investigate other alkaline-based energy technologies, such as flow batteries, CO_2 and N_2 electroreduction, and other electrochemical processes like coupling reactions used in biomass to extend chain lengths.

Here, we present a comprehensive review of fundamentals of electrocatalysis in alkaline media and applications for alkaline-based energy technologies, especially alkaline fuel cells and water electrolyzers. In this Review, we first establish a theoretical framework of the thermodynamics of one- and multiple-electron transfer processes in hydrogen and oxygen electrocatalysis and discuss the proton-coupled electron transfer (PCET) process in a proton-deficient alkaline environment. Those theoretical studies and concepts lay the foundation for the experimental investigations of hydrogen oxidation/evolution reactions (HOR/HER) and oxygen reduction/evolution reactions (OER/ORR) in alkaline media. Special attention has been paid to well-defined single crystals, especially Pt, with tunable facets and stepped structures, to provide an atomic and molecular-level understanding of the HOR and ORR mechanisms in alkaline media. We present electrochemical measurements to identify rate-determining steps (RDSs) of HOR/HER among Tafel, Heyrovsky, and Volmer steps. We then discuss spectroscopic and theoretical studies of various HOR/HER activity descriptors, including H-binding energy, electronic and oxophilic effects, alkali cation adsorption, and interfacial water structures. The sluggish HOR kinetics in alkaline media are proposed to arise from a more rigid water network since the applied potential is far away from the potential of zero free charge (pzfc), relative to that in acid. Selected examples of nanoparticle HOR electrocatalysts are presented, including Pt-based alloys, non-Pt PGM alloys (Pd, Ru, etc.), and nonprecious Ni-based architectures. In particular, Pt−Ru, supported on carbon, demonstrates a superior HOR activity compared to Pt in MEA measurements while Ni-based electrocatalysts exhibit the highest HOR activity and promising durability among all non-precious-metal-based catalysts. An early review on HOR kinetics in alkaline media and the roles of H-binding energy and electronic/oxophilic effects can be found elsewhere.[17]

A significant portion of this Review focuses on the understanding of complex ORR mechanisms and the design of non-PGM ORR electrocatalysts: a critical component at the heart of alkaline fuel cells. Based on extensive electrochemical, spectroscopic, and theoretical evidence, the general ORR mechanisms in acidic and alkaline media are presented, involving multiple reaction species of adsorbed HO_2, H_2O_2, and OH in acid and adsorbed O_2^-, HO_2^-, and OH in base. Adsorbed HO_2 in acid and O_2^- in base are recognized as key reaction intermediates preceding the bifurcation point towards the formation of water, by a 4e$^-$ process, or peroxide, by a 2e$^-$ process, which largely dictates the ORR activity and selectivity. Pt single crystals offer a model system to thoroughly investigate the effects of facets, stepped structures, pH, cation adsorption, and temperature on ORR kinetics. Special attention has been paid to spatially resolve interfacial water networks and their close interaction with coadsorbed OH by *operando/in situ* vibrational spectroscopy and theoretical simulations. The potential and pH-dependent interfacial water structures on stepped Pt are rigorously quantified by the potential of zero total/free charge (pztc/pzfc) and the potential of maximum entropy (pme).

The ORR mechanisms and the identification of activity descriptors of non-precious-metal oxides in alkaline media have also benefited tremendously from studies on well-defined atomically flat oxide thin films, such as perovskites (e.g., $LaMO_3$) and rutiles (e.g., RuO_2). Recently, despite their modest activity in rotating disk electrode (RDE) measurements, Co−Mn spinels outperformed their single-metal oxide counterparts and Pt/C as the oxygen cathode in MEA measurements, ascribed to the synergistic effects between Co and Mn.[16,18] To tackle the intrinsically low conductivity of oxides, 3d metal nitrides are being produced and demonstrate

https://doi.org/10.1021/acs.chemrev.1c00331
Chem. Rev. XXXX, XXX, XXX−XXX

enhanced ORR activities, although their long-term stability requires further investigation. Atomically dispersed metals in N-doped carbon (M−N−C) are emerging as a new promising family of non-PGM ORR electrocatalysts, due to their great structural and compositional tunability, high activity, and low cost. The chemical identity of ORR active sites, such as FeN_4 in Fe−N−C, and possible ORR pathways are discussed. Finally, the strategy to design non-Pt PGM catalysts, including Pd, Ru, and Ag, are presented, in an effort to diversify the catalyst candidates for AEMFC applications demanding very high current and power densities instead of solely relying on Pt-based ORR electrocatalysts as in PEMFCs. Interested readers are also encouraged to read other earlier reviews on ORR electrocatalysts in acidic media[3,6,9] and ORR electrocatalysts in alkaline media.[10,11]

Support materials are equally important to electrocatalysts since they provide not only stable loading/binding sites for catalytic nanoparticles but also pathways for electron, ion, and mass transfer by forming continuous porous channels. We review both carbon and noncarbon supports and discuss how the catalyst−support interactions modulate the catalyst activity, stability, and mass transport in AEMFCs. Carbon structures are the most widely used support material due to their high electrical conductivity, large surface area, electrochemical stability, and low price. Noncarbon supports, including oxide, nitride, and carbide, can have a much stronger interaction with catalyst nanoparticles, which can lead to increased activity and stability, whereas attaining as high of a surface area and conductivity as carbon is still a challenge.

Alkaline membranes and ionomers, when combined with supported electrocatalysts, compose the catalyst-coated membrane (CCM) layers, which are central components of MEAs. In this Review, we present a comprehensive summary of the design and synthesis of alkaline membranes and ionomers. The stabilities of cationic groups depend on temperature, hydroxide concentration, and types of reaction vessel. Thus, standard protocols for stability testing in alkaline solution are necessary to enable an objective comparison across the field. The alkaline stability of cations is summarized into three groups, quaternary ammoniums, imidazoliums, and phosphoniums in various solutions at elevated pH and temperature. The polymer backbones are designed to allow for sufficient cation incorporations to achieve high ionic conductivity (ion exchange capacity) and proper water uptake while maintaining mechanical integrity and long-term stability in alkaline media. The advantages and challenges of a variety of polymer backbones are reviewed, including polyarylenes, polyfluorenes, polystyrenes, polyethylenes, and polynorbornenes, in the context of polymer structure, morphology, ion exchange conductivity, stability, and processability. The dynamic formation of carbonate and the water distribution at the cathode and anode are investigated with various characterization techniques. Since ionomers are in close proximity to electrocatalysts, the effects of organic cation adsorption on catalysts are investigated in both RDE and MEA measurements.

The stability of the majority of AEMs is preliminarily examined in alkaline solution and indicates that a more realistic evaluation must be carried out in MEAs during fuel cell operation. Although many electrocatalysts exhibit impressive activity and stability in RDE measurements, few have translated into a comparable MEA performance in AEMFCs. The RDE−MEA discrepancy originates from the fundamental differences in the nature of their interfaces (solid−liquid vs solid−liquid−gas), mass transport, operating temperatures, and testing conditions. Thus, in an effort to integrate the above individual components of electrocatalysts, supports, and AEM/ionomers, we recommend that the development of electrode materials and membranes should include MEA device tests in early-stage development. We introduce standard MEA fabrication and testing protocols, in order to deconvolve the scientific challenges associated with kinetics and mass transport from device engineering. A comprehensive overview of the progress in initial AEMFC performances is introduced with emphasis on non-PGM oxygen cathodes and hydrogen anodes. The MEA stability of selected AEMs is reviewed, including polyarylene-, polyethylene-, and polynorbornene-based AEMs, which are affected by changes in mass transport, water distribution, and the degradation of catalysts and membranes/ionomers. The impact of CO_2 in air is discussed in great detail. The origin of performance degradation, due to carbonation, is associated with the CO_2 intake at the cathode and "self-purging" at the anode. Special attention is paid to understanding the ionic, gaseous, and electronic transport at both the nanoscale and mesoscale with the aid of numeric modeling.

Understanding the dynamic structural and compositional evolution of catalyst/support−polymer electrolyte interfaces is fundamental to the design of high-performance AEMFCs. In this Review, we provide a selective review of *operando*/*in situ* characterization techniques, in particular, the use of synchrotron-based X-ray techniques and scanning transmission electron microscopy (STEM) to resolve interfacial changes at macroscopic and microscopic levels. *Operando* X-ray absorption spectroscopy can track the dynamic changes of chemical and bonding information under electrochemical conditions, same as standard electrochemical measurements, while surface X-ray scattering provides atomic-scale structural changes at electrode−electrolyte interfaces.[18] *In situ* electrochemical liquid-cell STEM (EC-STEM) is capable of resolving real-time potential-dependent morphological, compositional, and structural changes of electrocatalysts with nm or better resolution and provides unique insights for enhancing catalyst activity and durability. Cryogenic TEM (cryo-TEM) can reliably characterize beam-sensitive soft materials at catalyst−ionomer−membrane interfaces and help deconvolve the degradation of electrocatalysts from that of alkaline polymers.

Finally, first-principles *ab initio* theories are instrumental to rationalize activity trends, guide the design of electrocatalysts, and ultimately unravel the real nature of reaction mechanisms at electrode−electrolyte interfaces. Here, we provide a selective review of *ab initio* theories for surface electrocatalysis in alkaline media and ion transport in liquid water, an *ab initio* joint DFT study of electrochemical environments in the presence of electrolyte, and degradation mechanisms of polymer membranes. The continuous advances in *ab initio* theory will provide more accurate and faster theoretical modeling of realistic electrocatalytic reactions at electrode−electrolyte interfaces.

In this illustrative Review, we present the dramatic progress and significant challenges in the fundamental understanding of electrocatalysis in alkaline media and the potential applications in alkaline-based energy technologies.

https://doi.org/10.1021/acs.chemrev.1c00331
Chem. Rev. XXXX, XXX, XXX−XXX

Scheme 1. Three Possible HOR Mechanisms in an Acid and Base[a]

Mechanism	Acid Media	Alkaline Media
Tafel step	$H_2 \leftrightarrow 2\,H_{ad}$	$H_2 \leftrightarrow 2\,H_{ad}$
Heyrovsky step	$H_2 \leftrightarrow H_{ad} + H^+ + e^-$	$H_2 + OH^- \leftrightarrow H_{ad} + e^- + H_2O$
Volmer step	$H_{ad} \leftrightarrow H^+ + e^-$	$H_{ad} + OH^- \leftrightarrow H_2O + e^-$

[a] H_{ad} represents the reactive intermediate adsorbed on the electrocatalytic surface. Each mechanism is composed of a sequence of two of the three steps shown. Depending on which is the rate-determining step (RDS), four possible reaction pathways are proposed: **Tafel**–Volmer, **Heyrovsky**–Volmer, Tafel–**Volmer**, and Heyrovsky–**Volmer** (bold indicates the RDS in each possible mechanism).

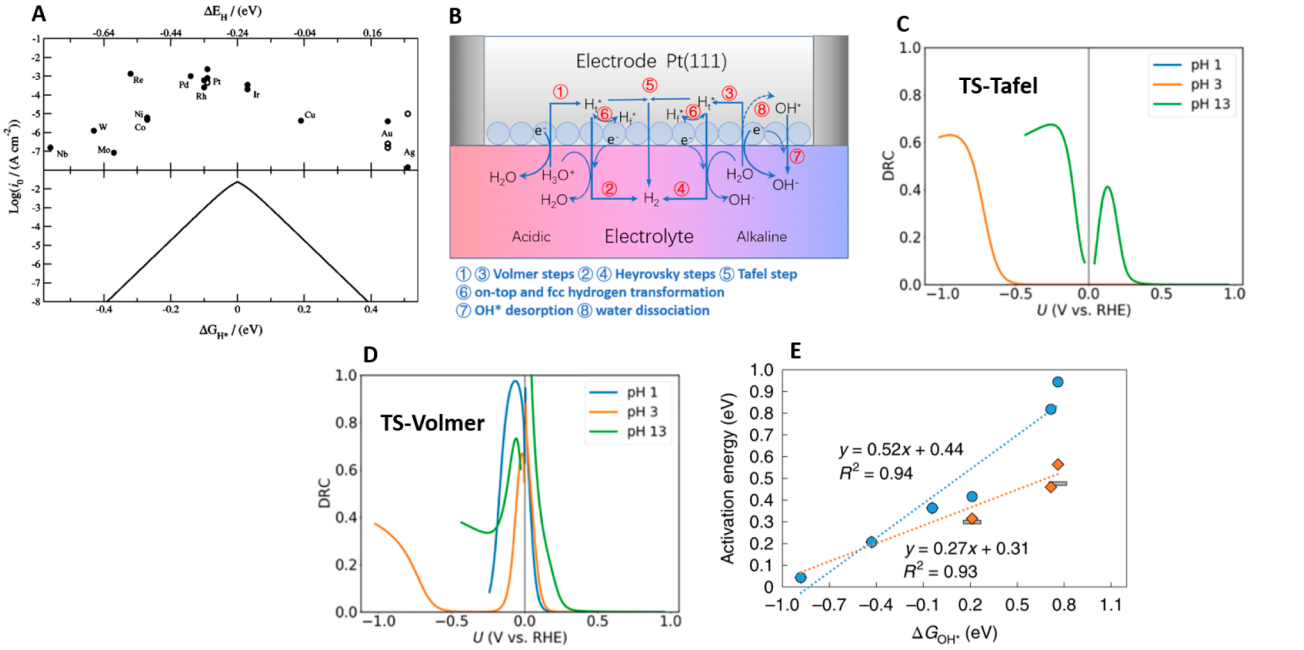

Figure 1. (A) HOR activity volcano plot as a function of the binding energy (upper panel) and the Gibbs free energy of adsorbed hydrogen (bottom panel), respectively. (B) Schematic of the HOR elementary steps on Pt(111) in an alkaline and acidic environment. (C) Degree of rate control for the transition state of the Tafel step on Pt(111) as a function of potential and pH. (D) Degree of rate control for the transition state of the Volmer step on Pt(111) as a function of potential and pH. (E) DFT-calculated activation energies for water dissociation on Pt(111), Pt(553), and Pt(553) decorated with 1 ML of Re, Ru, Rh, or Ag at the step edge, as a function of the Gibbs free adsorption energy of hydroxide. Blue circles and orange diamonds represent calculated activation energy barriers considering OH* and OH^- as products of water dissociation, respectively. The dashed lines are linear regressions according to the equations reported in the figure. Experimentally measured activation energies for hydrogen evolution (grey rectangles) on Pt(111)[82] and Pt(polycrystalline)[83] are given for comparison. Panel A is reprinted with permission from ref 20. Copyright 2010 The Electrochemical Society. Panels B–D are reprinted with permission from ref 33. Copyright 2020 American Chemical Society. Panel E is reprinted with permission from ref 34. Copyright 2020 Springer Nature.

2. THERMODYNAMICS AND KINETICS OF HYDROGEN AND OXYGEN ELECTROCATALYSIS

The chemistries of the ORR and HOR are among the most studied in the electrochemical literature. However, the identity of the reaction steps occurring at the electrocatalytic interfaces for these two reactions remains elusive. Combined experimental and theoretical approaches, resulting in the formulation of DFT-informed microkinetic models (MKMs), can provide information on the nature of the catalytic active site when the reaction is taking place and on the individual contribution of each reaction step to the overall reaction. For this reason, in this section, we present the key reaction steps for ORR and HOR and the main assumptions considered for the formulation of MKMs. In this context, particular attention will be devoted to the discussion of thermodynamic and kinetic aspects of the elementary steps.

2.1. Theory of the Hydrogen Oxidation Reaction (HOR)

The hydrogen oxidation and evolution reactions (HOR/HER) are of great importance for fuel cells and water electrolyzers. Although Pt is highly active for the HOR/HER in acid, it is significantly slower in alkaline media. Hence, it is essential to understand the reaction mechanisms and pathways that govern the electrocatalytic process. The overall HOR reaction can be written as $H_2 \leftrightarrow 2H^+ + 2e^-$ (acid); $H_2 + 2OH^- \leftrightarrow 2H_2O + 2e^-$ (base). Microscopically, the HOR proceeds through a two-step process, namely, H_2 chemical adsorption (Tafel step) or electrochemical adsorption (Heyrovsky step) followed by oxidative desorption of adsorbed H (Volmer step).

As illustrated in Scheme 1, the Tafel step is a chemical process of H_2 dissociation involving two active sites while only one site is required in the Heyrovsky step. For the Volmer step, H_{ad} is oxidatively removed from the active site, forming H^+ in

https://doi.org/10.1021/acs.chemrev.1c00331
Chem. Rev. XXXX, XXX, XXX–XXX

Scheme 2. General Mechanisms Proposed for the Oxygen Reduction Reaction (ORR) in an Acid and Base

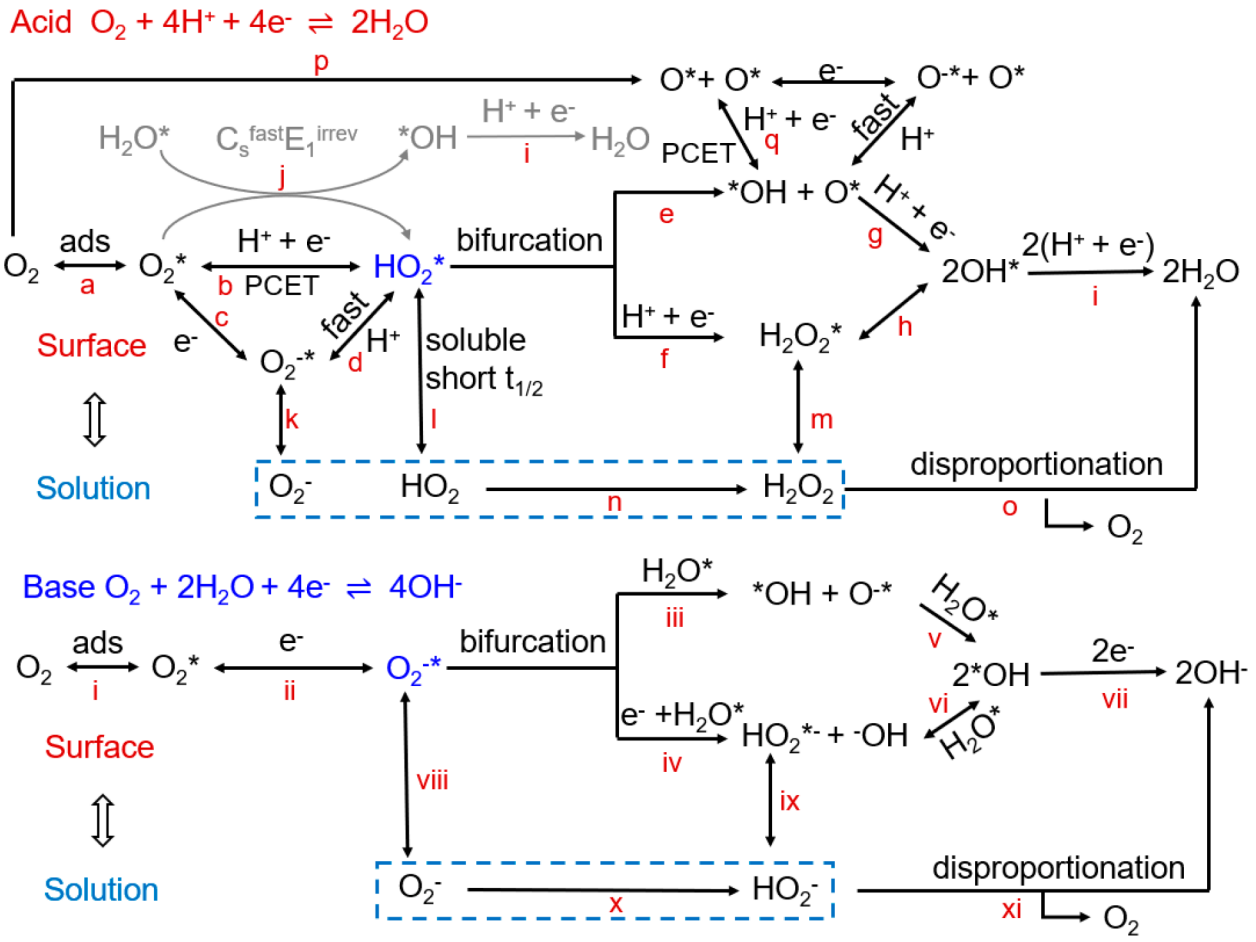

[a]Reaction pathways have been established based on extensive studies on Pt surfaces and may be applicable for other types of catalysts. A superscript * by an intermediate indicates a reaction intermediate adsorbed on the electrocatalytic surface. $C_s^{fast}E_1^{irrev}$ in acid represents a fast surface chemical reaction preceding an irreversible one-electron transfer process. PCET stands for proton-coupled electron transfer process. H_2O serves as the proton donor in alkaline media. Reaction pathways originating from steps "a" and "p" are the associative and dissociative pathways of the ORR, respectively.

acid or H_2O by reacting with OH^- in base. A detailed discussion of the RDSs will be covered in section 3.

Theoretical methods, such as DFT and microkinetic modeling, have provided critical insights into the reaction mechanism for the HOR and HER. In acidic media, the binding energy of hydrogen (HBE) has long been recognized as a descriptor for the HOR/HER.[19] DFT calculations yield a volcano-type relationship between the HBE and activity in acidic media, with the ideal catalyst binding hydrogen ~0.1 eV weaker than Pt(111) (Figure 1A).[20] Nonetheless, a similar correlation between HBE and activity is seen in alkaline media, with the largest difference being that the overall activity is far lower under alkaline conditions.[21] Because pH plays a key role in HOR/HER kinetics, several explanations and potential reactivity descriptors, based on experimental measurements, have been proposed: (1) The HBE shifts in alkaline conditions and the HBE serve as the key descriptor for the HOR/HER.[22,23] (2) The availability of OH* on the surface is critical for the overall reaction, and promoting OH adsorption increases HOR reaction rates; thus, the binding energy of OH* serves as a reactivity descriptor for the HOR/HER.[24,25] (3) Because interfacial electric fields are greater under alkaline versus acidic conditions, the water reorganization energy associated with proton transfer is pH dependent. Therefore, the potential of zero charge should be close to the onset potential of the HOR/HER.[26,27] Recently, theoretical methods have been utilized to further examine these proposals, particularly proposals 1 and 3, to determine why the HOR/HER is much slower in alkaline versus acidic media.

MKMs are a convenient theoretical tool constructed for bridging the gap between DFT-derived energetics and experimental data.[28,29] These models represent a series of elementary steps in a reaction and describe the rates of the elementary steps using a system of differential equations. For example, mean-field MKMs have been utilized to derive CV curves in acidic and alkaline media to further evaluate HOR/HER kinetics. Intikhab et al. developed an MKM for the HOR based on DFT-calculated binding energies to simulate CV profiles on Pt(110).[30] In particular, they considered whether OH_{ad} actively participates in the Volmer step of the HOR in the hydrogen underpotential deposition (H_{upd}) region [0−0.5 V vs reversible hydrogen electrode (RHE)]. They found the best agreement between their model and experiments when the HOR proceeded through a direct Volmer step (i.e., with OH^- as a reactant). They further determined that OH_{ad} decreased available surface sites, but the authors largely

https://doi.org/10.1021/acs.chemrev.1c00331
Chem. Rev. XXXX, XXX, XXX−XXX

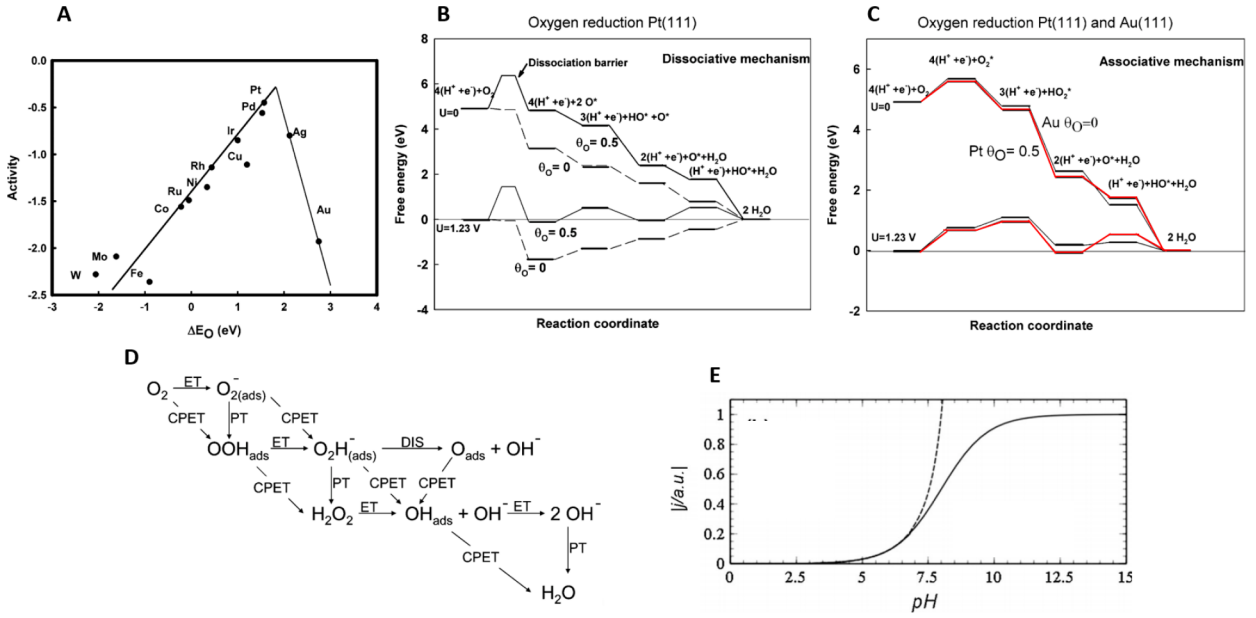

Figure 2. (A) DFT-derived activity of electrocatalysts for the ORR in an acidic environment as a function of the binding energy of oxygen. (B) Free-energy diagram (FED) for the ORR dissociative mechanism on Pt(111) at different potentials (U = 0 V and U = 1.23 V vs RHE) and different O* coverages (θ_O = 0, θ_O = 0.5). (C) Free-energy diagram (FED) for the ORR associative mechanism on Pt(111) (θ_O = 0.5, red lines) and Au(111) (θ_O = 0, black lines) at different potentials (U = 0 V and U = 1.23 V vs RHE). (D) Associative mechanism for the ORR on weakly binding electrocatalytic surfaces. The subscript "ads" indicates reaction intermediates adsorbed on the electrocatalytic surface. In the mechanism, tilted arrows indicate coupled proton−electron transfer steps (CPET), while straight arrows indicate consecutive decoupled proton (PT) and electron (ET) transfer steps. (E) Variation in current density as a function of pH obtained from the kinetic modeling of a generic decoupled proton and electron transfer step. Solid lines indicate H^+ as the proton donor, while for dashed lines water is assumed to be the proton donor. Panels A−C are reprinted and adapted with permission from ref 35. Copyright 2004 American Chemical Society. Panel D is reprinted with permission from ref 38. Copyright 2013 the Royal Society of Chemistry. Panel E is reprinted with permission from ref 44. Copyright 2015 the Author.

attributed the sluggish HOR activity under alkaline conditions to intrinsic kinetic barriers in the Volmer step (likely from pH-dependent interfacial water structures). Rebollar et al. expanded on this work by varying the adsorption strength of OH in their MKMs to demonstrate that increasing the adsorption strength of OH does not promote faster HOR/HER kinetics.[31]

Recently, Lamoureux et al. developed a MKM that not only included binding energies from DFT but also included DFT-derived reaction barriers for each step in the HOR/HER on Pt(111).[32] Much like the earlier MKM work on the HOR/HER, this work also found that experimental activity trends could be rationalized by differences in the barrier for the Volmer step as a function of pH. Specifically, the authors suggested that, as the pH increases, the proton donor for the Volmer step in the HER shifts from hydronium to water and that the barrier for donating a proton from water is higher than from hydronium. To date, the most detailed microkinetic modeling of the HOR/HER was performed by Liu et al.[33] In this work, the authors combined a mean-field MKM and a simplified diffusion model to calculate the polarization profiles for the HOR/HER on Pt(111) at a range of pH values. Furthermore, this model utilized potential- and coverage-dependent binding energies and reaction barriers that considered the role of an implicit solvent. Like the work from Intikhab et al.,[30] the authors found that the current near the HOR onset potential is mostly attributed to pathways involving OH^- rather than OH_{ad}. By analyzing the degree of rate control for the elementary steps in the HOR (Figure 1C,D), they found that the Tafel step largely controls the current in acidic media, but that the Tafel and Volmer steps both dictate the current in alkaline media due to the increasing barrier of the Volmer step increasing as the pH increases.

Overall, the body of work from MKMs based on DFT energetics reaches the conclusion that the Volmer step has a higher barrier as the pH increases, leading to sluggish HOR/HER kinetics under more alkaline conditions. Additionally, these models find that OH^-, rather than OH_{ad}, serves as the primary intermediate in the HOR/HER in alkaline media. While this might suggest that the binding energy of OH_{ad} would not be an appropriate descriptor for the HOR/HER in alkaline media, work from McCrum et al. utilized DFT calculations to show that the barrier for water dissociation in the HER correlates well with the binding energy of OH_{ad} (Figure 1E).[34] Therefore, even though OH_{ad} is not involved in the HOR/HER, the trends in HER kinetics could be rationalized using a volcano plot that utilizes both HBE and the binding energy of OH_{ad} as descriptors.

2.2. Theory of the Oxygen Reduction Reaction (ORR)

Among the most significant contributions to theoretical electrocatalysis of the ORR is that of Nørskov et al.[35] With the introduction of the so called "computational hydrogen electrode" (CHE) formalism, allowing the connection of DFT-derived energetics with experimental applied potentials, this work laid the foundations for the utilization of quantum chemical calculations for applications in electrocatalysis (more details are provided in section 9.1). Furthermore, for the first time, a computational approach was used to shed light on two different mechanistic propositions of the ORR: the "dissociative" and the "associative" mechanisms (Scheme 2). The latter was proposed on the basis of earlier electrochemical measurements, suggesting the presence of a *peroxy* (OOH)

https://doi.org/10.1021/acs.chemrev.1c00331
Chem. Rev. XXXX, XXX, XXX−XXX

intermediate.[36] Experimental evidence for the ORR mechanisms in Scheme 2 will be covered in section 4. Before discussing the thermodynamics and kinetics of the reaction, it is useful to review the elementary steps of the dissociative and associative ORR pathways.

In acidic environments, the dissociative pathway proceeds through O_2 dissociation (Scheme 2, step p), followed by consecutive proton-electron transfer steps (steps q−g−i). The mechanism proceeds through the exchange of 4e$^-$. The associative mechanism can proceed through either a 4e$^-$ pathway, through the formation of OOH* (step a) followed by protonation steps (steps b−e/f−g/h−i), or a 2e$^-$ pathway resulting in the formation of H_2O_2 (step f). Details of Scheme 2 will be covered in section 4.1. Using the CHE formalism in conjunction with thermodynamic scaling relations (section 9.1), the activity trends among different weakly and strongly binding electrocatalytic surfaces could be rationalized, as described by a Sabatier volcano plot, presented in Figure 2A. Under low oxygen coverages, and assuming that the activation barrier of each proton−electron transfer step is solely dependent on the Gibbs free-energy change associated to the step, Pt is the most active monometallic surface towards the ORR in acidic environments. The reaction proceeds through the 4e$^-$ pathway (Figure 2B). At oxygen coverages of ∼0.5 monolayer, the associative mechanism dominates (Figure 2C). The high tendency of Pt(111) to strongly bind oxygen is at the root of the experimentally observed overpotential;[37] hence, improved ORR electrocatalysts should be able to bind *OH ∼0.1 eV weaker than Pt.

The seminal work of Nørskov et al. on the mechanism of the ORR and electrocatalyst design principles relies on the following assumptions: (1) The proton−electron transfer steps occur in a concerted way [i.e., concerted proton−electron transfer (PCET)]. (2) The largest among the Gibbs free-energy differences associated to PCET steps in Scheme 2 defines the limiting potential of the reaction. (3) The effect of external electric fields is negligible. (4) The effect of applied bias on the stability of surface reaction intermediates is included by shifting the energy of a state by $-eU$ (for reduction steps), with U being the applied bias. (5) The effect of pH is included by accounting for the concentration dependence of the entropy. This is done by correcting the free energy of H^+ by kT ln10 × pH, where k is the Boltzmann constant, and T is the temperature. The vast majority of the previous literature relies on one or more of these assumptions. In this section, we discuss the assumptions made in previous studies, considering their relevance, applicability, and consequences, especially for the ORR and HOR in alkaline environments.

2.2.1. Concerted vs Decoupled Proton−Electron Transfer Steps. The concerted mechanism for the proton−electron transfer step is by far the most common assumption used in a wide variety of computational and experimental studies. In a 2013 perspective, Koper analyzed, in detail, the thermodynamic and kinetic consequences of considering consecutive PCET steps and decoupled proton−electron transfer in the context of the ORR.[38] A reaction scheme showing these two possibilities is presented in Figure 2D, where the diagonal reaction steps represent PCETs. While we direct the reader to section 2.3 for more details on the theoretical aspects of PCETs and decoupled electron transfer, we anticipate that the proton and electron transfers will decouple if the activation energy barrier associated to the PCET is higher than that of the decoupled processes. For reduction reactions, this condition is achieved when the proton and electron affinities of the reaction intermediates are sufficiently high. Combining scaling relations (described in section 9.1) with a thermodynamic analysis of the ORR, in the limit of PCETs, Koper derived an approximate expression for the minimum thermodynamic overpotential (η_T^{min}) required for the ORR. This is equal to $\eta_T^{min} = \frac{1}{2e_0}(\Delta G_{OH}^{OOH} - 2.46)$ where e_0 is the unit of charge, and $\Delta G_{OH}^{OOH} = G^{OOH} - G^{OH}$, i.e., the free-energy difference between adsorbed OOH* and OH*. Therefore, a consequence of considering fully PCET steps in the mechanism is the independence of the thermodynamic overpotential from pH, in the reversible hydrogen electrode (RHE) scale. This condition was later experimentally verified for the ORR on Pt.[39] Conversely, for weakly binding electrocatalysts (on the right side of the Sabatier volcano plot in Figure 2A), such as Au,[40,41] Ag,[42] and Hg,[43] the ORR occurs through consecutive decoupled proton−electron transfers. Koper analyzed the thermodynamic consequences of decoupled proton−electron transfer mechanisms,[38,44] focusing on the mathematical and physical relation of η_T^{min} with respect to pH. In light of this relation, it is, in principle, possible to achieve optimal conditions (minimum overpotential) by adjusting the pH. The optimal pH corresponds to the pK_a of the key surface intermediate. The variation of current produced during a decoupled electron ($A + e^- \rightleftharpoons A^-$) and proton transfer ($H_2O + A^- \rightarrow HA + OH^-$) of a generic reaction species A, as a function of pH, is presented in Figure 2E. These generic processes can be used as models for the first and second step of the ORR in alkaline environments (Figure 2D, Scheme 1), where H_2O acts as the proton donor. The plot shown in Figure 2E is obtained through kinetic modeling and shows an increase of the current produced with increasing pH, in agreement with experimental measurements of the ORR on Au-based electrocatalysts.[41] This observation corroborates mechanistic propositions identifying O_2^- (superoxide) as a key intermediate of the ORR in alkaline environments on weakly binding electrocatalysts[45−47] (section 4.2). Interestingly, the intrinsic pH-dependence, naturally arising from the thermodynamics and kinetics of decoupled proton−electron transfer, has been leveraged to optimize the OER performance of metal oxides and oxyhydroxides.[48−51] Despite these efforts, it is well-known that the electrocatalytic activity of several classes of materials is limited by linear scaling relationships correlated to the binding energy of different reaction intermediates, for example, OH* and OOH* for the ORR.[52,53] This important aspect will be reviewed in section 9.1.

2.2.2. Catalytic Consequences of Activation Barriers for PCET Steps. With the advent of more accurate and affordable quantum mechanical methods, MKM, originally developed in the 80s and 90s,[54] and in conjunction with reaction kinetics experiments, has become a powerful tool for elucidating catalytic reaction mechanisms in vapor-phase catalysis. Recent developments in MKM were reviewed by Mavrikakis and coworkers[55] and Dumesic and coworkers.[56,57] However, the application of DFT-informed MKMs to electrocatalytic processes remained largely unexplored until very recently. This stems from the intrinsic difficulty of calculating activation energy barriers for electrochemical steps through theoretical methods. Periodic DFT calculations are indeed usually performed under constant charge, rather than

https://doi.org/10.1021/acs.chemrev.1c00331
Chem. Rev. XXXX, XXX, XXX−XXX

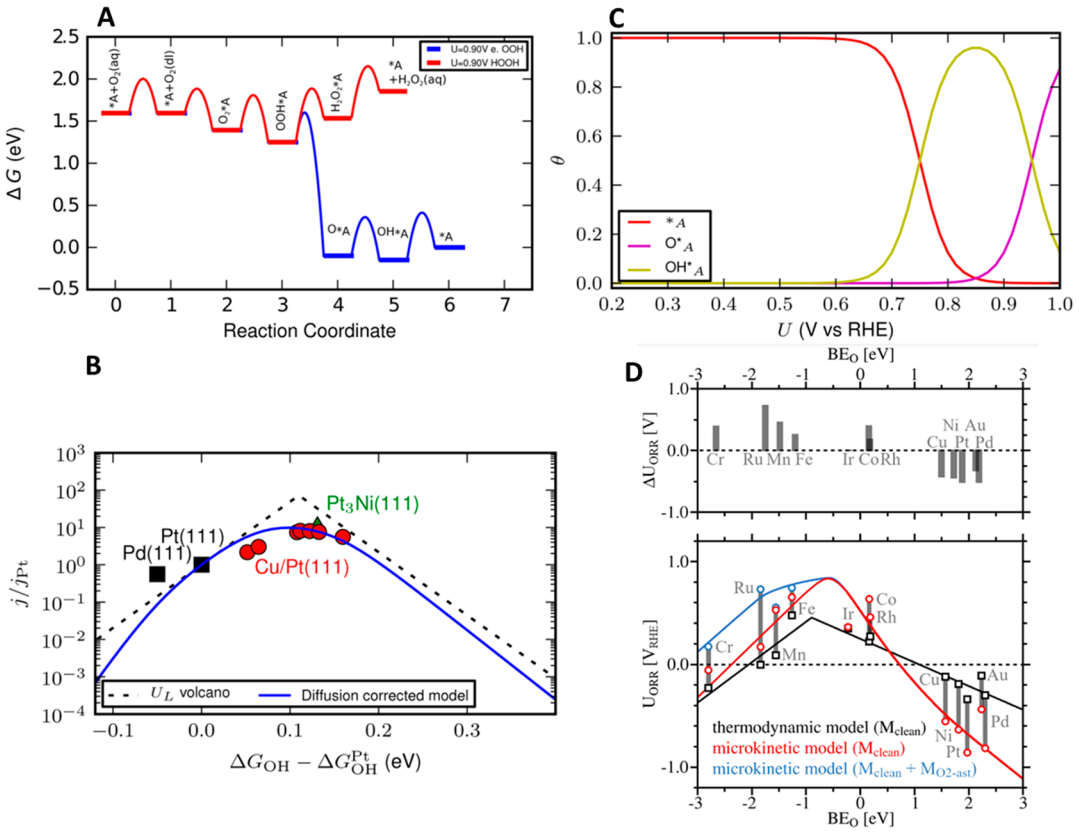

Figure 3. (A) Free-energy diagram (FED) for the ORR on Pt(111) in acidic conditions, following the $4e^-$ (blue lines) and $2e^-$ (red lines) pathway at 0.9 V vs RHE. (B) Simulated kinetic volcano at 0.9 V vs RHE (blue lines) compared to the potential limiting volcano (dashed lines). Filled red circles are experimental points (Pt overlayers on Cu/Pt near surface alloys) obtained from Stephens et al.[84] The experiments for Pt(111) (black square) and $Pt_3Ni(111)$ (green triangle) are taken from Markovic and co-workers[64] and Shao et al. for Pd(111) (black square).[65] (C) Coverage of surface reaction intermediates (O^*_A and OH^*_A) and surface vacant sites (*A) on Pt(111) as a function of potential, while the ORR is taking place. (D) ORR onset potentials in an acidic environment for different single-atom catalysts embedded in N-doped graphene. The black lines and points show results of a purely thermodynamic analysis. A full MKM analysis is reported as red and blue circles for a simple and a coverage-cognizant microkinetic modeling analysis, respectively. Differences in the onset potentials predicted from thermodynamic and microkinetic analysis (ΔU_{ORR}) are shown above: positive (negative) values correspond to an increase (decrease) in onset potential due to the microkinetic analysis. Panels A–C are reprinted with permission from ref 63. Copyright 2014 American Chemical Society. Panel D is reprinted with permission from ref 72. Copyright 2015 American Chemical Society.

under constant potential, the latter more realistically representing in electrochemical systems. To overcome this limitation, a variety of approaches, mostly based on the so-called "charge extrapolation" method, were previously proposed,[58] together with more computationally expensive methods based on molecular dynamics (MD) simulations.[59,60] We refer to the works of Chan and Nørskov[61] and to the earlier work of Tripković et al.[62] and to section 9.1 for more details. Here, we review mechanistic insights of full DFT-derived MKMs, encompassing thermal and electrochemical steps, in the context of the ORR.

The limitations of considering purely thermodynamic models have been identified by Hansen et al.[63] Thermodynamic models identify limiting potentials at which the free-energy diagram (FED) of the ORR in acidic or alkaline environments becomes downhill in energy. The FED of the ORR on Pt(111) obtained by Hansen et al. in an acidic environment following the associative $4e^-$ and $2e^-$ pathway is presented in Figure 3A. The activation energy barrier of each electrochemical step, 0.26 eV, was adapted by the work of Tripković et al.[62] A comparison between the "kinetic" volcano obtained through a combination of scaling relations and a full MKM model, with respect to a simple "thermodynamic" volcano (equivalent to the one reported in Figure 2A), is shown in Figure 3B. Experimental measurements on the (111) facets of Pt,[64] Pt_3Ni,[65] Pd,[66] and Cu overlayers on Pt[67] are in agreement with the kinetic volcano. Furthermore, the current density predicted by the MKM is approximately one order of magnitude lower than the one predicted by a simpler thermodynamic analysis. For strongly binding metals (Pt, Pd), the potential-limiting step—i.e., the most endothermic among the potential-dependent steps—is the removal of OH* from the surface. Instead, the rate-determining step, according to the degree of rate control analysis,[68,69] is the adsorption of O_2 on the surface from the double-layer region. On weakly binding metals, the potential-limiting step is OOH* formation, and similarly, the activation barrier for the formation of OOH* from O_2 limits the rate. In a more recent review, Exner and Over identified the source of the discrepancy between thermodynamic and kinetic volcanoes in the identity of the rate-determining step.[70] In particular, thermodynamic and kinetic models are in agreement only if the rate-determining step corresponds to the potential-determining one. Despite the fact that a quantitative agreement between experiments and models can be achieved only through a comprehensive MKM analysis, a simpler thermodynamic analysis is still able to

https://doi.org/10.1021/acs.chemrev.1c00331
Chem. Rev. XXXX, XXX, XXX−XXX

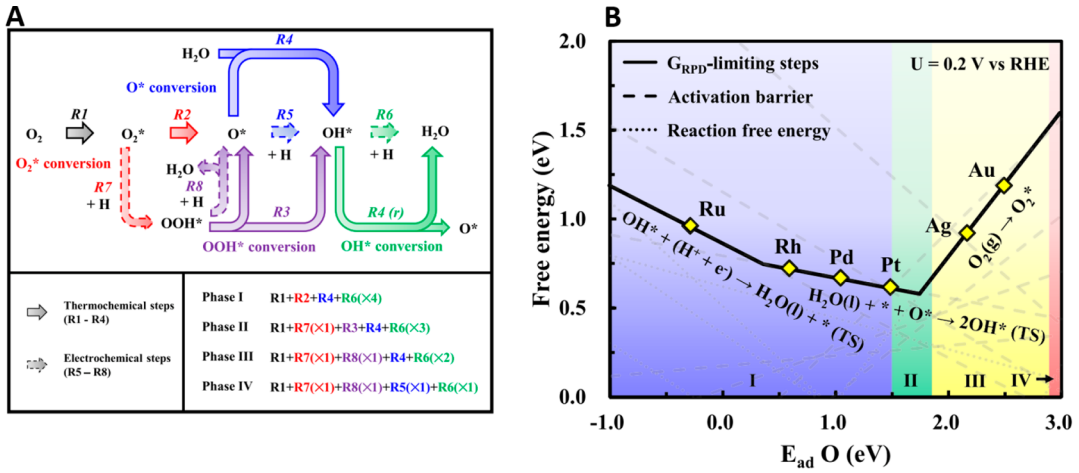

Figure 4. (A) Reaction mechanisms for the ORR in an acidic environment, considering a combination of electrochemical (dashed arrows) and pure thermochemical (solid arrows) steps. Phases I–IV represent different electrocatalyst conditions, in increasing order of binding energy of O* (see panel B). (B) Activity trend for different electrocatalysts for the ORR at 0.2 V, obtained from a DFT-derived "reaction phase diagram" (RPD) as a function of O* binding energy. Panels A and B are reprinted with permission from ref 73. Copyright 2020 American Chemical Society.

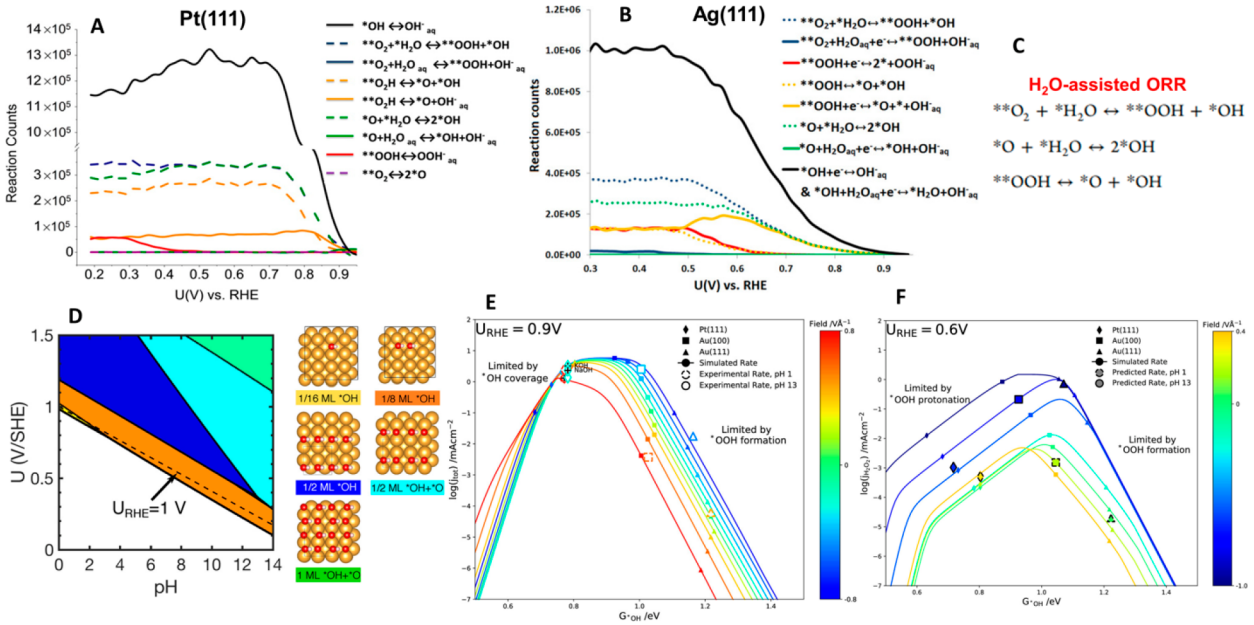

Figure 5. (A) Reaction counts with respect to applied potential from KMC simulations of the ORR on Pt(111) in 0.1 M KOH at room temperature. Solid and dashed lines represent potential-dependent and potential-independent steps, respectively. The ** superscripts indicate reaction intermediates adsorbed on the surface and occupying two vacant sites. (B) Reaction counts with respect to potential from KMC simulation of the ORR on Ag(111) in 0.1 M KOH at room temperature. (C) Reaction scheme for the first three steps of the H_2O-assisted mechanism of the ORR, in an alkaline environment. (D) DFT-derived Pourbaix phase diagram for Au(100), exploring different O* and OH* coverages. For conditions relevant to the ORR in alkaline environments the 1/8 ML OH* phase is the most stable. (E) Activity volcano for the overall ORR in an alkaline environment at 0.9 V vs RHE at varying fields. (F) Activity volcano for the $2e^-$ pathway of the ORR in an alkaline environment at 0.6 V vs RHE at varying fields. Panels A and C are reprinted and adapted with permission from ref 76. Copyright 2016 American Chemical Society. Panel B is reprinted with permission from ref 74. Copyright 2018 Wiley. Panel D is reprinted with permission from ref 77. Copyright 2019 American Chemical Society. Panels E and F are reprinted with permission from ref 78. Copyright 2020 American Chemical Society.

rationalize trends in catalytic activities. Furthermore, in the limit of very strongly or very weakly binding electrocatalysts (right and left sides of the volcano plot in Figure 3B), both approaches are in reasonable agreement.

One of the advantages of using a full MKM accounting for activation energy barriers for the PCET steps relies on the possibility of calculating the coverage of surface reaction intermediates at a given potential. For example, the coverage of O*, OH*, and empty surface sites (*) on Pt(111), while the ORR is taking place under acidic conditions, is shown in Figure 3C as a function of applied potential. Interestingly, Tripkovic and Vegge postulated that the presence of O* on the Pt(111) surface has important consequences for the ORR mechanism, because of the hydrophobic character of the O-covered surface, as opposed to the more hydrophilic OH-covered Pt(111).[71] Mavrikakis and coworkers have recently demonstrated the importance of using a coverage-cognizant MKM for accurately reproducing ORR onset potentials for

https://doi.org/10.1021/acs.chemrev.1c00331
Chem. Rev. XXXX, XXX, XXX−XXX

graphene-based single-atom catalysts.[72] In their case, purely thermodynamic models underestimate the onset potential of more oxophilic metals, such as Cr, Fe, Mn, and Ru, while overestimating the onset potential of Pt, Pd, Au, Ni, and Cu (Figure 3D).

Given the importance of including a proper description of the activation energy barriers of electrochemical steps for the correct reproduction of electrochemical features, it is interesting to comment on the competition between electrochemical and thermal barriers in the context of the ORR, the subject of a recent study by Guo et al.[73] In particular, the authors constructed a reaction phase diagram (RPD), a collective description of complete reaction pathways including reaction energies and activation energy barriers as a function of O* binding energy. On the basis of MKM and DFT calculations, they proposed a composite reaction mechanism for the ORR, consisting of a combination of electrochemical and purely thermal steps (Figure 4A,B). Surprisingly, the commonly known associative ORR reaction mechanism (Scheme 2) seems to be valid only for very weakly binding surfaces, while for all of the other surfaces, at least one of the hydrogenation steps occurs through a thermal hydrogen transfer, rather than a PCET step.

The studies mentioned so far mostly address the ORR in acidic environments. Studies reporting mechanistic insights on the ORR in alkaline environments, through the use of kinetic modeling and explicitly taking into account PCET barriers, are very limited. As mentioned earlier, the main approach utilized for taking into account the effect of pH is to shift the energy of H^+ by $kT \ln 10 \times$ pH and, in the case of alkaline environments, considering appropriate reaction steps where H_2O acts as the proton donor. This means that without taking into account the detailed nature of the active sites in alkaline environments, by considering the combined effect of applied potential and pH on the surface coverage, the only difference between thermodynamic or kinetic models in alkaline and acidic environments is a simple shift of the limiting potential, i.e., the maximum potential obtainable from the reduction reaction.

2.2.3. Kinetic Role of Single- and Multielectron Processes in Alkaline Environments. Understanding the mechanism of proton−electron transfer steps and their role in the kinetics of the ORR in alkaline environments, i.e., under extremely low concentrations of H^+, is a question of fundamental importance. The theory of proton−electron transfer steps will be reviewed in section 2.3. Here, we review the kinetic involvement of these steps in the ORR, in alkaline environments.

The critical role of water in the proton−electron transfer in alkaline environments has been highlighted in multiple studies[74−76] and will be later discussed with experiments in Figures 17−19 of section 4.1. The reaction scheme for the $4e^-$ and $2e^-$ ORR pathways, mediated by coadsorbed water molecules, is shown in Figure 3. Liu et al. used a combined DFT and Kinetic Monte Carlo (KMC) approach to study the ORR mechanism on Pt(111) in alkaline environments.[76] The methodology allows a "counting" of the occurrence of a given reaction step as a function of applied potential, similar to calculating the contribution of each electrochemical or thermal step to the overall reaction flux (see Figure 5A). The authors propose that under alkaline conditions the reaction follows mainly the $4e^-$ associative pathway and that the $*H_2O$-assisted pathway dominates (Figure 3C). The $2e^-$ pathway is only active at a potential lower than 0.4 vs RHE. Similar to the work of Guo et al. in acidic environments,[73] the authors claim that the ORR mechanism in alkaline media involves mostly potential-independent surface reactions and that water coadsorbed on the surface acts as the real O_2* and O* reducing agent. It is interesting to compare these results with those obtained for the ORR on Ag(111) (a more weakly binding metal with respect to Pt(111)) using the same DFT−KMC methodology.[74] The analysis of the "reaction counts" presented in Figure 5B suggests that the ORR on Ag(111) should also proceed via the $4e^-$ pathway, although the contribution of the water-mediated pathway is less dominant, compared to Pt(111). Furthermore, while on Pt(111) the ORR proceeds mostly through potential-independent steps, on Ag(111) both the OH* dissolution ($OH^* + e^- \rightarrow OH^-_{(aq)}$) and OOH* dissociation ($OOH^* + e^- \rightarrow O^* + OH^-_{(aq)}$) steps contribute to the current density.

The ORR on Au(100) in alkaline environments is an interesting case study, which exemplifies how the interplay between surface coverage, solvent, applied potential, and external electric fields is essential in determining the role of single and multiple electron transfer steps on the kinetics of the reaction. Au(100) is one of the most active electrocatalysts for the ORR in alkaline environments, although the $4e^-$ reduction pathway occurs just over a limited potential region (0.6−0.9 V vs RHE).[46,75] This particular behavior has not been completely understood so far, but the role of surface coverage and external electric fields has been explored further.

Starting with DFT calculations, Duan and Henkelman have constructed the Pourbaix phase diagram of Au(100) under electrochemical conditions relevant to the ORR (Figure 5D).[77] Their study highlights the importance of surface coverage for the accurate description of the active sites, responsible for the Au(100) activity towards the $4e^-$ pathway. In particular, they demonstrate that two vicinal adsorbed OH* (total 1/8 ML coverage) present on the surface over the potential window between 0.61 and 0.81 V vs RHE, at pH = 13, enhance the activity of Au(100). A similar explanation was also proposed by Lu et al.[75] By means of a combined experimental and theoretical approach, they propose that coadsorbed water molecules are able to stabilize OH*, hence catalyzing the $4e^-$ pathway as opposed to the formation and desorption of $OOH^-_{(aq)}$.

Recently, Kelly et al. have used a combination of DFT calculations and MKM to rationalize the pH-dependence of the ORR kinetics on Pt(111), Au(111), and Au(100).[78] Differently from previous studies that simply modeled the effect of pH by adjusting the free energy of H^+ (and consequently, of OH^-), the effect of pH was considered by examining the effects of the electric field on the activity and selectivity of electrocatalyst models. The thermal and electrochemical reaction steps considered in this study are presented in Scheme 2. In agreement with most studies on Pt(111), the ORR in alkaline environments is limited by the OH* removal step (step vii in Scheme 2), and the reaction proceeds through the $4e^-$ pathway. Instead, on Au(100), the identity of the rate-limiting step strongly depends on the pH: in acidic conditions, both the $4e^-$ and the $2e^-$ pathway are limited by the formation of OOH* (step iv in Scheme 2). However, the effect of the electric field (hence, of the pH) is much more pronounced on Au(100) than on Pt(111) because it directly affects the weakly binding species. As the pH increases (and the external electric field becomes more negative), Au(100) binds OOH* more strongly, and the formation of H_2O_2 (or OOH^- (aq), step ix in

https://doi.org/10.1021/acs.chemrev.1c00331
Chem. Rev. XXXX, XXX, XXX−XXX

Scheme 2) becomes the rate-limiting step for the $2e^-$ pathway, while the $4e^-$ pathway is facile. The activity/selectivity dependence of different electrocatalysts on the pH (or electric field) is captured well by the modeled volcano plots presented in Figure 5E,F, for the $4e^-$ and $2e^-$ reaction pathways, respectively.

The studies discussed so far in this section present important insights into the ORR in alkaline environments, albeit considering PCET steps as the only possible potential-dependent steps. However, different experimental studies suggest that the first step of the ORR in alkaline environments could actually be a single electron transfer step leading to the formation of O_2^- from O_2 in solution. Schmickler and coworkers have recently discussed several mechanistic propositions for the ORR in alkaline environments on Au- and Ag-based catalysts.[79−81] In particular, by performing a combination of DFT calculations and MD simulations based on a potential of mean force, the authors postulated that the ORR on Au(100) and Ag(100) should start with an outersphere electron transfer. Indeed, the negative binding energy of O_2 on Au(100) and Ag(100) cannot compensate for the loss of solvation, and as a consequence, the first step for the ORR occurs in the aqueous phase, rather than on the surface. As a result, they propose that the ORR in alkaline environments on Au(100) and Ag(100) likely proceeds through the solution-mediated mechanism described in Scheme 2.

2.3. Theoretical Modeling of Proton-Coupled Electron Transfer (PCET) in Alkaline Solutions

2.3.1. Volmer Reaction in Alkaline Solution. The most fundamental electrochemical proton-coupled electron transfer (PCET) reaction is the Volmer step of the hydrogen evolution reaction (HER), where a proton is transferred from a donor in solution to a metal electrode to accept an electron and form a covalent bond with a metal atom at the surface. This elementary reaction of proton discharge on the electrode surface has been studied extensively over the last few decades with a wide range of theoretical methods,[85−102] but its fundamental mechanism is still the subject of debate. Due to the quantum mechanical character of the transferring proton and the presence of a continuum of delocalized electronic states in the metal electrode, the reaction can exhibit a wide range of behaviors from adiabatic to nonadiabatic, depending on the nature of the interactions near the surface of the electrode. The electrochemical double layer (EDL) formed at the interface between the electrode and the electrolyte solution increases the complexity of electrochemical processes and has a profound effect on the mechanisms of reactions involving charged species at the interface.

Most of the theoretical modeling has been focused on the Volmer reaction in acidic aqueous solution, where the proton donor is typically presumed to be a partially solvated hydronium ion (H_3O^+) in the form of a cationic water cluster, such as the Zundel ($H_5O_2^+$) or Eigen ($H_9O_4^+$) cation. However, a few theoretical studies have examined the Volmer reaction in alkaline solution.[92,102−105,107−109] These particular studies include electronic structure calculations of the potential-dependent activation energies using local reaction center models[34,104,106,108,109] and various theoretical calculations based on model Hamiltonians and interfacial electron transfer theories.[102,103,105,110] The most notable feature of the HER in alkaline conditions is that it exhibits sluggish kinetics with an almost two orders of magnitude reduction in activity, relative to acidic media.[83] This phenomenon is still under active investigation and constitutes one of the unresolved puzzles in modern electrochemistry.[105,107] In contrast to acidic solutions, the proton donor for the Volmer reaction in basic solutions is expected to be the neutral water molecule, H_2O, which undergoes the cleavage of the very strong covalent H−OH bond to produce the hydroxide ion, OH^-, upon proton transfer to the metal electrode:

$$M + H_2O + e^- \rightarrow MH(ads) + OH^- \quad (1)$$

As a result, the elementary step involves a neutral reactant species and a negatively charged product species, and the Volmer reaction follows distinct pathways from those observed in acidic solution.

The mechanistic roles of the hydroxide ion produced in this reaction, as well as the supporting electrolyte ions, have been discussed in the literature,[25,34,111−115] although the detailed mechanism is still unknown. The recent experimental observation of the volcano-type relationship between the rate of the HER in alkaline solution and the hydroxide binding strength[34] suggests that the hydroxide could play an important role in the mechanism. Moreover, DFT calculations[34] have been interpreted as suggesting that the HER at surface sites that can strongly bind hydroxide might follow an alternative mechanism involving the homolytic dissociation of H_2O with a subsequent electrochemical reduction of the adsorbed hydroxide at the active site.[34,114] An additional indication of the importance of hydroxide adsorption is the rate enhancement observed for the Volmer reaction in alkaline solution upon modification of Pt electrodes with $Ni(OH)_2$, which is thought to play a catalytic role by enhancing the water dissociation step.[114] This mechanism, involving water dissociation, followed by adsorption of the hydroxide, illustrates the bifunctionality of the modified electrode surface for the HER in alkaline solutions.[105,112] More generally, the modification of electrode surfaces with transition metal oxides and oxide/metal nanocomposites has been shown to significantly enhance the HER in alkaline solutions.[25,110,112,116−118]

Hydroxide ions have also been found to coordinate to Au atoms on gold electrode surfaces even when the surface is negatively charged, at potentials more negative than the potential of zero charge (pzc).[115] The magnitudes of the calculated dipole moments associated with the adsorbed hydroxide ion indicate that the hydroxide ions form highly polar bonds with the Au atoms when the surface is negatively charged.[115] Recently, the mechanism illustrated in Figure 6 was proposed for the elementary step of the Volmer reaction at a gold electrode in alkaline solution.[102] This mechanism involves a water dimer as the proton donor to enable the hydroxide ion to coordinate to the surface concurrently with proton transfer, as suggested by the experimentally observed adsorption of hydroxide at potentials negative of the pzc.[115] In the proposed Grotthuss-like process, proton transfer to a Au atom on the electrode surface is accompanied by proton transfer between the two water molecules and coordination of the resulting hydroxide anion to an adjacent Au atom. This PCET mechanism can be expressed as

$$2Au + 2H_2O + e^- \rightarrow AuH(ads)\cdots H_2O\cdots AuOH^-(ads) \quad (2)$$

https://doi.org/10.1021/acs.chemrev.1c00331
Chem. Rev. XXXX, XXX, XXX−XXX

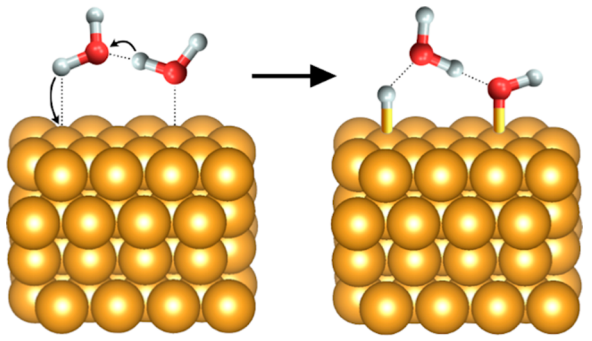

Figure 6. Schematic illustration of the mechanism for the elementary act of the Volmer reaction on a gold surface in alkaline solution. The Au atoms are depicted with gold spheres, and the oxygen and hydrogen atoms are depicted with red and gray spheres, respectively.

In a subsequent relatively fast step, the hydroxide is expected to desorb into the bulk solution because of electrostatic repulsion with the negatively charged surface. This desorption step does not impact the rate-limiting PCET step and thus will not influence the experimentally measured current densities or kinetic isotope effects (KIEs).

2.3.2. PCET Theory for the Volmer Reaction. Regardless of the specific mechanism, the rate constant for the Volmer reaction in alkaline solution can be calculated using a general PCET theory in the diabatic vibronic representation.[102,119−122] In this theory, the electrons and transferring proton(s) are treated quantum mechanically, and the PCET reaction is described in terms of nonradiative transitions between reactant and product diabatic electron−proton vibronic states. For the Volmer reaction, the reactant and product diabatic electronic states are depicted in Figure 7. In

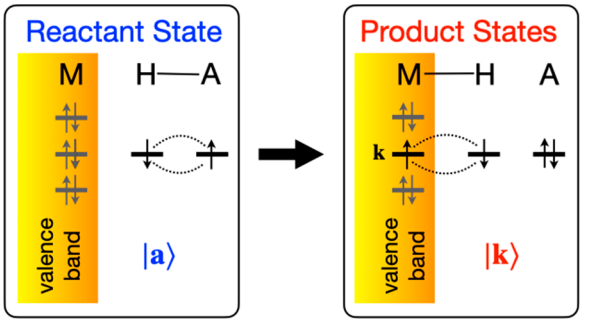

Figure 7. Schematic depiction of the reactant and product diabatic valence bond electronic states for the Volmer reaction, where a proton is transferred from a solvated acid, AH, to the gold surface to form a Au−H covalent bond and the conjugate base A. The dotted arcs denote a singlet two-electron chemical bond. Figure adapted from Figure 1 in ref 100. Copyright 2019 American Chemical Society.

the reactant state, the proton is bonded to the conjugate base, and in the product states, the proton is bonded to the metal electrode, forming a two-electron covalent bond involving a hydrogen orbital and one of the occupied states from the quasicontinuum of delocalized states in the metal electrode. Each diabatic reactant and product electronic state is associated with a set of proton vibrational states, and the reactant and product vibronic states correspond to the direct products of these electronic and proton vibrational states. The couplings between the reactant and product vibronic states defined above are very small due to the delocalized nature of the quasifree electronic states in the electrode, thus allowing the use of the Landau−Zener approximation for the transition probabilities. The overall PCET rate constant as a function of the distance of the proton donor to the electrode surface and the applied potential is then computed as the weighted sum of transition probabilities over all pairs of reactant and product electron−proton vibronic states.[102]

The expression for the total PCET rate constant is

$$k(E) = \frac{2\pi}{\hbar} \sum_{\mu} w_{\mu} \int_{-\infty}^{\infty} \kappa_{\mu}(\varepsilon)\, \bar{\Delta}_{\mu}(\varepsilon)\, W_{\mu}(\varepsilon, E)\, \mathrm{d}\varepsilon \tag{3}$$

where w_{μ} is the equilibrium population of the reactant vibronic state μ, $\kappa_{\mu}(\epsilon)$ is the analogue of the transmission factor that accounts for unreactive trajectories,

$$W_{\mu}(\varepsilon, E) = \sqrt{\frac{1}{4\pi\lambda k_{\mathrm{B}}T}} \exp\left[-\frac{\beta(\Delta G(E) + \lambda - \varepsilon_{\mu} - \varepsilon)^2}{4\lambda k_{\mathrm{B}}T}\right] \tag{4}$$

is the potential-dependent Marcus exponential describing the equilibrium probability of sampling the top of the barrier along the collective reaction coordinate, $\Delta G(E)$ is the potential-dependent reaction free energy referenced to the Fermi energy of the electrode, and λ is the solvent reorganizational energy. The key quantity characterizing the strength of the interaction between the reactant vibronic states and the manifold of product vibronic states is the so-called cumulative weighted densities of states (CWDOSs), which are represented by the density of occupied electronic states in the metal weighted by the squares of the individual vibronic couplings:

$$\bar{\Delta}_{\mu}(\varepsilon) = \sum_{\alpha} |S_{\mu\alpha}|^2 f(\varepsilon + \varepsilon_{\alpha})\, \Delta(\varepsilon + \varepsilon_{\alpha}) \tag{5}$$

Here, $S_{\mu\alpha}$ are the overlap integrals between the reactant and product proton vibrational wave functions, ε_{α} are the energies of the reactant proton vibrational states, $f(\epsilon)$ is the Fermi distribution function, and $\Delta(\epsilon)$ is the electronic broadening (i.e., chemisorption) function, which depends on the squares of the electronic couplings.[91]

This PCET rate constant expression is valid in both the adiabatic and nonadiabatic limits as well as the intermediate regime. The degree of adiabaticity is determined by the CWDOS, which is an intensive property of the system and depends on physical characteristics such as the distance between the proton donor and the electrode surface, the structure of the surface, and the electronic interactions between the proton donor and the metal electrode. Moreover, in the wide band approximation for the metal, it can be related to a coupling strength parameter V_0 that is associated with the nonadiabatic (i.e., golden rule) and adiabatic (i.e., transition state theory) limits of the rate constant expression for small and large values, respectively. Plots of the dependence of the PCET rate constant as a function of V_0 for model systems illustrate that this rate constant expression smoothly bridges the nonadiabatic and adiabatic limits.[102] To account for solvent dynamical effects,[123−125] an interpolation scheme has been used to extend this theoretical formulation to the solvent-controlled regime, where the reaction is controlled by the time scale of the solvent dynamics.[101,102]

2.3.3. Current Densities and Kinetic Isotope Effects for the Volmer Reaction. The PCET theory outlined above has been applied to the Volmer reaction at a gold electrode in

https://doi.org/10.1021/acs.chemrev.1c00331
Chem. Rev. XXXX, XXX, XXX−XXX

alkaline solution. The gold electrode states were modeled as a wide rectangular band extending over the Fermi energy representing the sp-band of bulk gold, and the proton donor was assumed to be a water dimer as depicted in Figure 6. The effects of the EDL were included using a multilayer dielectric continuum model used previously to describe a specific Volmer reaction in acetonitrile.[99] The linear drop of the electrostatic potential in the inner-Helmholtz layer as a function of the electrode potential was included in the calculation of the reaction free energy term in the rate constant expression. For this application, the electrostatic work term for the reactant state was assumed to be independent of the electrode potential because the water acting as the proton donor is neutral, whereas the work term for the product state depends on the electrode potential because the hydroxide is anionic. The rate constants were computed for a series of distances, R, between the proton donor and the electrode surface in both H_2O and D_2O. The corresponding current densities were computed by integrating the rate constant over all distances R, weighting each rate constant by the local proton donor concentration at R.

The apparent KIE was defined as the ratio of the current density $j^H(E)$ for 0.1 M OH^- in H_2O to the current density $j^D(E)$ for 0.1 M OD^- in D_2O at the same electrode potential E:

$$\mathrm{KIE}(E) = \frac{j^{\mathrm{H}}(E)}{j^{\mathrm{D}}(E)} \tag{6}$$

The results from these calculations were compared to the recent experimental measurements performed by Sakaushi[126,127] in alkaline purified solvents H_2O and D_2O, although the definition given in eq 6 differs from the one used in the experimental work. Specifically, the definition in eq 6 compares current densities at the same absolute electrode potential rather than the same overpotential, requiring a conversion from the overpotentials measured experimentally relative to the RHE or reversible deuterium electrode (RDeE) to the electrode potential relative to the standard hydrogen electrode (SHE). In addition, the H and D current densities were compared directly without adjusting for the difference in pH or pD because the proton donor was assumed to be pure H_2O or D_2O.

A comparison between the calculated and experimental KIEs is given in Figure 8. The calculated potential-dependent KIE is in qualitative agreement with the experimentally measured increase in the KIE from 66 to 98 over this electrode potential range. Related to this behavior, linear fits of the current densities for H_2O and D_2O plotted as a function of the electrode potential led to isotope-dependent apparent transfer coefficients. Specifically, the calculated apparent transfer coefficients for H_2O and D_2O were 0.59 and 0.57, respectively, compared to the experimental values of 0.56 and 0.50, respectively. An analysis of the vibronic state-to-state contributions to the PCET rate constant indicated that the different transfer coefficients for H and D are due to greater contributions from excited reactant proton vibrational states for D_2O compared to H_2O and also for less negative (i.e., less cathodic) potentials.

This model study highlights the importance of treating the transferring hydrogen nucleus quantum mechanically for a meaningful description of the Volmer reaction in alkaline solution. The relatively large observed KIEs and lower currents are indicative of hydrogen tunneling and vibrational non-

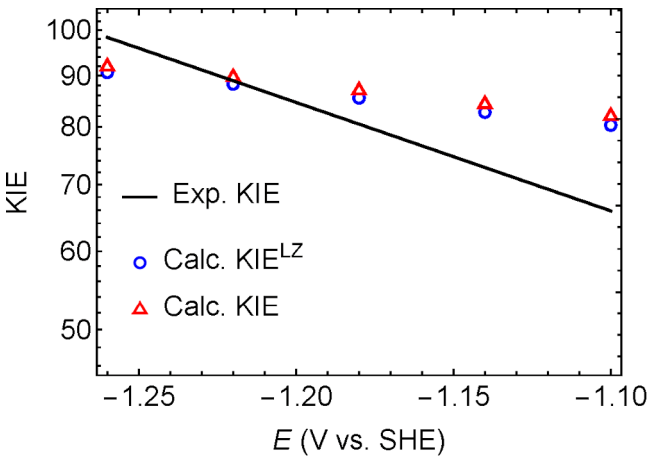

Figure 8. Experimentally measured[126] KIEs (solid black line) and KIEs calculated[100] using eq 3 (blue circles), and using an interpolation between the Landau−Zener regime and the solvent-controlled regime (red triangles) as functions of the electrode potential. Adapted with permission from Figure 1 in ref 102. Copyright 2020 American Chemical Society.

adiabaticity, which are described by the PCET theory discussed above. The potential-dependent KIE, or isotope-dependent transfer coefficients, can be explained in terms of contributions from excited reactant proton vibrational states. Similar qualitative behavior of the KIEs was observed both experimentally and theoretically for the Volmer reaction from triethylammonium acid to a gold electrode in acetonitrile.[99] For the Volmer reaction in alkaline solution, solvent dynamics were found to be important at shorter tunneling distances, but such distances did not contribute significantly to the total current densities; therefore, solvent dynamics exerted a negligible effect on the KIEs (Figure 8).

A remaining challenge in this field is to use first-principles computational methods describing the electrochemical interface with explicit solvent and ions to calculate the input quantities to the analytical PCET rate constant expression. This approach would provide atomic-level insights into the factors influencing the magnitude of the current densities of the Volmer reaction in alkaline solution.

2.4. Summary

In section 2, we have described successes and limitations associated with using simple DFT-derived descriptors for elucidating the catalytic activity of metal electrodes for the HOR and the ORR. We have examined the consequences of including activation energy barriers when characterizing the PCET steps of the ORR and the HOR, as opposed to using purely thermodynamic approaches. For the HOR, while simple DFT descriptors such as the hydrogen binding energy can be used to rationalize catalytic trends in an acidic environment, the explicit inclusion of activation energy barriers and their incorporation in MKMs is critical for developing a mechanistic understanding in an alkaline environment. The increasing activation energy barriers characterizing the Volmer step can be responsible for the slower kinetics of the HOR in alkaline conditions. Similarly, in the case of the ORR in an alkaline environment, purely thermodynamic approaches present several limitations but are useful for an initial fast catalyst screening. Quantitative agreement between experimental and predicted activity is often lacking, including the case of Au(100), a weakly binding metal. In this case, the latest

https://doi.org/10.1021/acs.chemrev.1c00331
Chem. Rev. XXXX, XXX, XXX−XXX

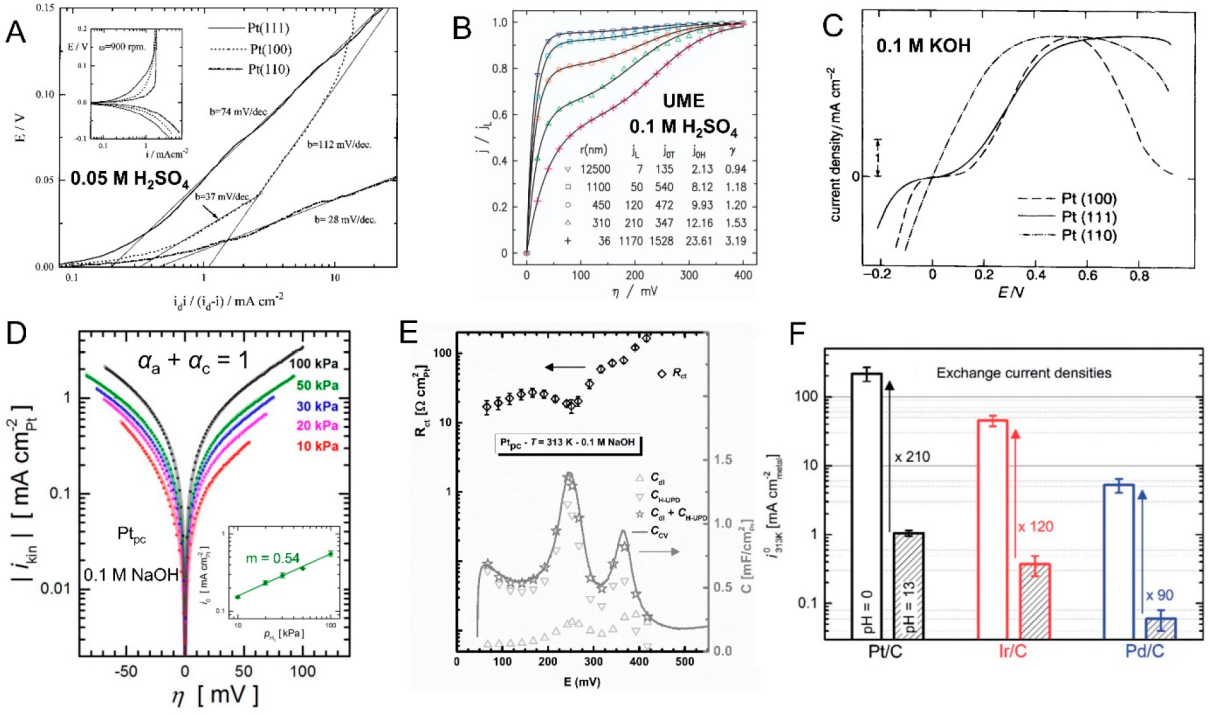

Figure 9. HOR/HER mechanistic and kinetic studies in an acid and base. (A) HOR Tafel plot on Pt(111), Pt(100), and Pt(110) surfaces in 0.05 M H_2SO_4 at 274 K. The inset shows the polarization curves for HOR/HER at low overpotentials at 900 rpm and 10 mV/s. From the Tafel slope, the HOR on Pt(110) proceeds through a **Tafel**−Volmer step while a **Heyrovsky**−Volmer step dictates the HOR on Pt(100). (B) HOR polarization curves at 5 mV/s obtained at an ultra-microelectrode with different radii (12 500, 1100, 450, 310, and 36 nm) and fitted by assuming a dual-pathway mechanism (**Tafel**−Volmer at η < 50 mV and Heyrovsky−Volmer at η < 50 mV). (C) HOR/HER polarization plots on Pt(100), Pt(111), and Pt(110) surfaces in 0.1 M KOH at 3600 rpm, 20 mV/s. **Tafel**−Volmer is assumed to be the reaction pathway. (D) Evolution of HOR/HER Tafel plot on polycrystalline Pt with different applied H_2 pressure in 0.1 M NaOH, 20 mV/s. Solid dots are measured values while line profiles are fitted from the Butler−Volmer equation. The inset indicates that the exchange current density is 1/2-order with respect to H_2 pressure. Tafel−**Volmer** is considered as the HOR/HER reaction sequence based on transfer coefficients ($\alpha_a + \alpha_c = 1$). (E) Charge transfer resistance and capacitance of hydrogen underpotential deposition on polycrystalline Pt measured by electrochemical impedance spectroscopy in 0.1 M NaOH at 313 K. The linear extrapolation of charge transfer resistance to η = 0 mV results in R_{ct} = 11 Ω cm^2_{Pt} ($i_{0,UPD}$ = 2.4 mA/cm^2_{Pt}), close to the experimentally measured HOR exchange current density ($i_{0,HOR}$ = 1.8 mA/cm^2_{Pt}), suggesting that the HOR kinetics is limited by the Volmer reaction (Tafel/Heyrovsky−**Volmer**). (F) Comparison of HOR/HER exchange current densities on Pt/C, Ir/C, and Pd/C in both an acid (pH = 0, H_2 pump method) and base (pH = 13, RDE method) at 313 K. The HOR/HER kinetics in alkaline media are about 2 orders of magnitude slower than in acid. Panel A is reprinted with permission from ref 130. Copyright 1997 American Chemical Society. Panel B is reprinted with permission from ref 134. Copyright 2006 The Electrochemical Society. Panel C is reprinted with permission from ref 139. Copyright 1996 Royal Society of Chemistry. Panel D is reprinted with permission from ref 140. Copyright 2014 The Electrochemical Society. Panel E is reprinted with permission from ref 129. Copyright 2014 The Electrochemical Society. Panel F is reprinted with permission from ref 22. Copyright 2014 Royal Society of Chemistry.

advanced theoretical methods, explicitly taking into account the effect of charge and external electric fields, are required to rationalize the ORR activity of Au electrodes. Given these latest developments, future mechanistic studies of electrochemical systems will take advantage of more accurate methods and improved models, where the complex interplay between charge, external electric fields, surface coverage, and solvent dynamics will be integrated in the formulation of mean-field MKMs or KMC methods.

In the last part of this section, we have described a PCET theory that treats the electrons and transferring protons quantum mechanically and includes the effects of excited electron−proton vibronic states. The PCET rate constant derived within this theoretical framework is valid in the adiabatic and nonadiabatic limits, as well as in the intermediate regime. The application of this theory to the Volmer reaction at a gold electrode in alkaline solution explains the experimental observation of relatively large, potential-dependent KIEs in terms of hydrogen tunneling, vibrational nonadiabaticity, and contributions from excited proton vibrational states. The combination of this PCET theory with the DFT methods, described in the first part of this section for computing the input quantities to the rate constant expression, enables the investigation of a wide range of electrochemical reactions.

3. HOR ELECTROCATALYSIS IN ALKALINE MEDIA

3.1. HOR Mechanisms

The activities of the HOR and its reverse, HER, of Pt in alkaline media are over two orders of magnitude lower than in acid.[22,83] In this part, we illustrate the HOR/HER mechanisms and possible origins for the sluggish kinetics in alkaline media. As shown in Scheme 1, four possible HOR reaction mechanisms have been proposed regarding the rate-determining step (RDS): Tafel(RDS)−Volmer, Tafel−Volmer(RDS), Heyrovsky(RDS)−Volmer, and Heyrovsky−Volmer(RDS).

3.1.1. HOR/HER Reaction Pathways (Tafel−Heyrovsky−Volmer Steps). Though the HOR reaction pathways

https://doi.org/10.1021/acs.chemrev.1c00331
Chem. Rev. XXXX, XXX, XXX−XXX

indeed seem relatively simple as they involve only one intermediate species, H_{ad}, tremendous efforts have been devoted to investigating the HOR kinetics.[128,129] Marković et al. pioneered the structure sensitivity of the HOR on Pt single crystals in acid and found that the HOR activity varied in the following order: Pt(111) < Pt(100) < Pt(110).[130] The Tafel slopes were used to deduce the RDS in the reaction. A Tafel slope of 28 mV/dec suggested that the HOR on Pt(110) might proceed via a Tafel−Volmer mechanism with the Tafel step as the RDS, while a Tafel slope changing from 37 to 112 mV/dec, under increasing overpotentials, indicated a Heyrovsky-(RDS)−Volmer mechanism on Pt(100) (Figure 9A). However, the HOR mechanism on Pt(111) was complicated by an intermediate Tafel slope of 74 mV/dec, which suggests that the determination of HOR mechanisms cannot be solely based on an analysis of Tafel slopes.[131] In fact, the Tafel slope of ∼30 mV/dec for the very fast HOR at Pt in acid suggests that the reaction might be mainly controlled by mass transport instead of kinetics.[132] To deconvolve kinetics from mass transport, Chen and Kucernak employed a Pt ultra-microelectrode (UME) to study the HOR kinetics in acid and observed two current plateaus in the HOR polarization profiles (Figure 9B).[133] They observed the anomalous presence of the first plateau, which they attributed to the limiting rate of the Tafel step. Based on fit results, the Tafel(RDS)−Volmer step was proposed to govern the HOR process. However, their fitting showed a noticeable deviation from the experimental values at high overpotentials. To solve this discrepancy, Adzic et al. proposed a dual-pathway mechanism model, where the Tafel(RDS)−Volmer step dominates at low overpotentials (η < 50 mV) while the Heyrovsky(RDS)−Volmer step takes over at overpotentials higher than 50 mV (Figure 9B).[134] Although the fittings matched the experimental results, over the entire overpotential region, the HOR kinetics information from the UME may be influenced by sulfate adsorption or other contaminants.[129] The HOR activity in acid could be sufficiently high such that the RDE may not be able to provide fast mass transport to reveal intrinsic electrochemical kinetics.[132,135−138] Scanning electrochemical microscopy (SECM),[135] the H_2 pump method,[136,132] and the floating vacuum carbon approach have been explored for a more in-depth analysis.[138] In comparison, the much slower HOR in alkaline media makes it feasible to reliably study the reaction kinetics with a conventional RDE.

The HOR on Pt single crystals in alkaline solution was first reported by the Marković group,[139] which showed the following activity order: Pt(111) ≈ Pt(100) ≪ Pt(110) (Figure 9C). A Tafel(RDS)−Volmer sequence was proposed as the reaction mechanism in alkaline media based on the underpotential of deposited H (H_{upd}) and OH_{ad} isotherms on Pt(111) and Pt(100), respectively, in which the H_{upd} and OH_{ad} could compete for adsorption sites. A linear relationship with a slope of 2 was observed in the plot of kinetically control current [log i_k) vs adsorption sites (log$(1 - \theta_{Hupd})$ or log$(1 - \theta_{OH_{ad}})$], suggesting an ideal dual-site interaction model that follows the Tafel(RDS)−Volmer reaction mechanism. Nevertheless, the distinction and/or interaction between H_{upd} and H_{ad} (from the dissociation of H_2) remains unresolved;[128] hence, the analysis of the HOR mechanism solely based on isotherms may not be reliable. A detailed analysis of the effects of H_{upd} and OH_{ad} on the HOR kinetics can be found in the book chapter by Marković and coworkers.[128] In contrast to that at room temperature, the activity difference between Pt(110) and Pt(111) decreased to less than a factor of two at an elevated temperature (333 K), ascribed to the 2 times higher activation energy barrier on Pt(111), relative to Pt(110).[82]

Herranz et al. investigated the HOR/HER kinetics as a function of H_2 pressure in 0.1 M NaOH on a polycrystalline Pt electrode and found that the reaction rate had a half-order dependence on H_2 pressure (Figure 9D).[140] They proposed that only the Tafel−Volmer reaction mechanism could account for the observed transfer coefficients, and the Volmer or Heyrovsky step as the RDS could yield kinetic expressions similar to the Butler−Volmer equation.[141] However, the half-order dependence on H_2 pressure could not be obtained from the microkinetic analysis based on the proposed Tafel−Volmer(RDS) mechanism. The Volmer step, as the RDS in alkaline media, was further reinforced by an electrochemical impedance spectroscopy (EIS) study.[129] Contrary to the earlier idea that H_{upd} and H_{ad} are different in nature,[142] Durst et al. claimed that H_{upd} and H_{ad} are indistinguishable, and the H_{upd} process is, therefore, actually equivalent to the Volmer step.[129] Hence, it is possible to use the charge transfer resistance, R_{ct}, measured from the EIS, in combination with the linearized Butler−Volmer equation (applicable at small η) to extract the exchange current density, i_0, for the Volmer step. In 0.1 M KOH, the calculated i_0 = 2.4 mA/cm^2 (R_{ct} = 11 Ω cm^2) at 313 K was close to i_0 (1.8 mA/cm^2) determined by the HOR polarization profiles (Figure 9E). This indicates that the Volmer step could be the RDS for the HOR in alkaline media, leading to the suggested HOR mechanism of Tafel−Volmer-(RDS) or Heyrovsky−Volmer(RDS). The i_0 of the Volmer step in acid was estimated from EIS to be (850−500 mA/cm^2 at 293 K), which is of the same order of magnitude to the i_0 of the HOR/HER measured by the H_2 pump method (200 mA/cm^2 at 313 K).[143,144] This finding suggested that the Volmer step could play a role in the HOR kinetics in acid, although a more precise determination of the Volmer step would be necessary to address this question.

In summary, these early studies have, thus far, pointed to the H_2 adsorption step on Pt (Tafel or Heyrovsky step) as the possible RDS in acidic media, although it is still unclear how much the Volmer step contributes to the overall reaction. The details of the Volmer contribution may depend on the orientation of the Pt crystal, which can be further convoluted by transport. These early studies also suggest the Volmer step as the RDS behind the HOR/HER in alkaline media.

3.1.2. Slowness of the HOR Kinetics in Alkaline Media. The slowness of the HOR in alkaline media has been well-known since the early HOR studies.[145] However, the activity gap between the acid and base has been largely underestimated since the traditional RDE method severely underestimated the exchange current density (i_0) of Pt in acid.[146] With the highly improved mass transport of the H_2 pump method,[132] the kinetic difference between the acid (pH = 0) and base (pH = 13) was reported to be about two orders of magnitude on Pt/C (Figure 9F).[146] A similar decrease in the HOR activity with pH was also observed for Ir/C and Pd/C. At 293 K, the i_0 of Pt/C is ∼60 mA/cm^2 at pH = 0 while it is only ∼0.6 mA/cm^2 at pH = 13.[129] The sluggish kinetics are also evident from the higher activation energies, from the Arrhenius plot, in base (30 kJ/mol) and in acid (20 kJ/mol).

Initially, Osetrova and Bagotzky attributed the sluggish kinetics in alkaline solutions to a different reaction mechanism,

https://doi.org/10.1021/acs.chemrev.1c00331
Chem. Rev. XXXX, XXX, XXX−XXX

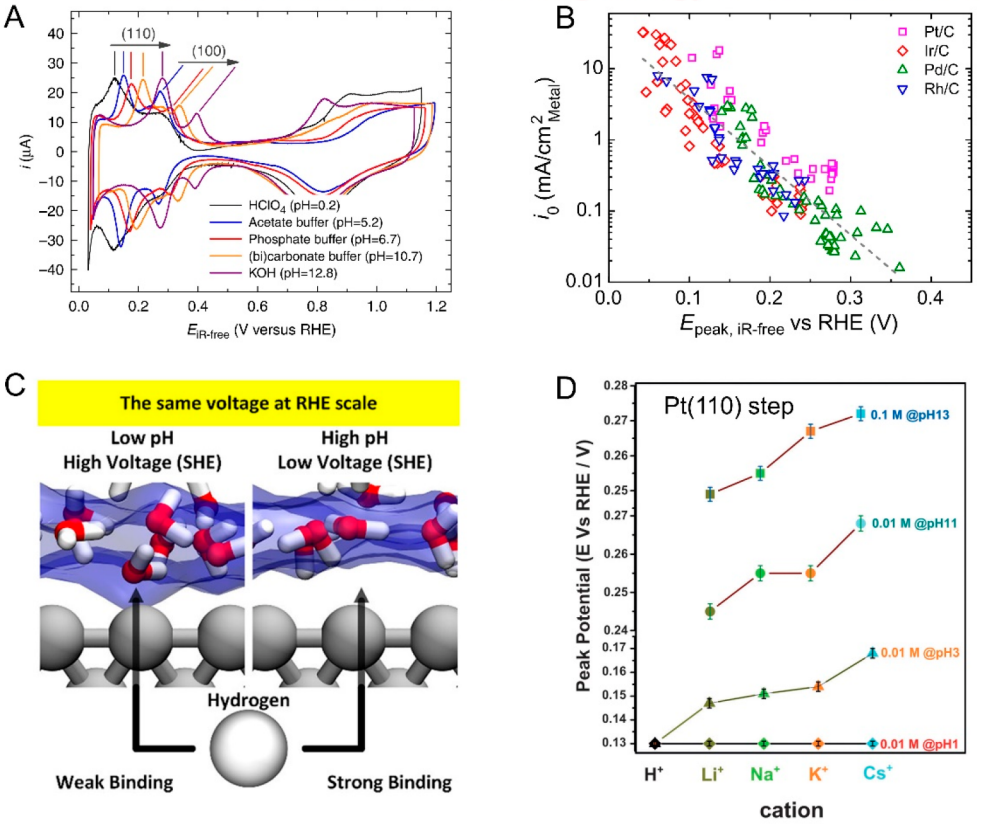

Figure 10. Hydrogen binding theory as a possible descriptor for the sluggish HOR kinetics in alkaline media. (A) Evolution of CV profiles on a polycrystalline Pt electrode with buffered solutions (pH: 0.2−12.8), 50 mV/s. H_{upd} peaks of Pt(110) and Pt(100) facets shift to higher potentials with increasing pHs. (B) Correlation of HOR/HER exchange current densities vs the lowest H_{upd} peak positions determined from CVs on Pt/C, Ir/C, Pd/C, and Rh/C. The dashed gray trendline indicates that the HOR/HER kinetics diminish with an increase in the H_{upd} peak positions. The peak position is assumed to be correlated with the hydrogen-binding energy. (C) Effect of water adsorption on hydrogen binding under different pHs by quantum mechanics molecular dynamics simulations. At high pH, water adsorption is weakened because of water repulsion, leading to observed stronger H-binding. (D) Effects of pH and cation identities on the potential shifts of step-related voltammetric peaks, which are related to the replacement of adsorbed H by OH. The positive shifts of peak potentials indicate that alkali cations weakening OH adsorption on the step sites is the main cause. Panel A is reprinted with permission from ref 23. Copyright 2015 Springer Nature. Panel B is reprinted with permission from ref 148. Copyright 2016 American Association for the Advancement of Science. Panel C is reprinted with permission from ref 151. Copyright 2018 American Chemical Society. Panel D is reprinted with permission from ref 113. Copyright 2017 Wiley-VCH.

in which H_2^+ was proposed to be the active intermediate instead of H_{ad}.[145] Later, Marković et al. ascribed the pH-dependent HOR kinetics to the pH-dependent adsorption of OH_{ad} in the H_{upd} region, where OH_{ad} may behave as an inhibitor.[82] However, the pH-dependent HOR kinetics, even at potentials as low as in the reversible hydrogen region, indicated that the effect of OH_{ad} on HOR kinetics is likely not the major contributor. Since the Volmer step is believed to be the RDS for the HOR/HER in alkaline media, the dramatic kinetic diminution from the acid to base can be attributed to the escalated energy barrier with pH in the Volmer reaction.[33] The sluggish HOR in alkaline media has been recently proposed to be related to the stronger H-binding energy[21] or more rigid interfacial water structure, due to a significant negative shift in the potential of zero free charge (pzfc), relative to acidic media.[26] In addition, the effect of OH_{ad} coadsorption has been proposed.[25] We now expand the discussion on these phenomena.

3.1.3. Hydrogen Binding Energy Effects. The H-binding energy (HBE) effect originates from the well-known volcano plot in acid media,[147,20] in which the H-binding should be neither too strong nor too weak in order to achieve the highest HOR/HER activity, also known as the Sabatier principle.[141] According to the volcano plot, Pt resides close to the peak point and, hence, yields the highest HOR/HER activity among all monometallic electrocatalysts. Thus, it has been speculated that the stronger HBE may lead to a sluggish HOR kinetics in alkaline media if the same hypothesis is still valid in alkaline media.[21] Yan et al. examined the HOR kinetics at a polycrystalline Pt electrode in various buffered solutions (pH = 0.2−12.8)[23] and ascribed the observed pH-dependent kinetics to the HBE effects. As shown in Figure 10A, the H_{upd} peaks from Pt(110) and Pt(100) progressively shifted to higher potentials as the pH increased, which was proposed to correlate to the increasing HBE. Consequently, the HBE was calculated to be 10 meV/pH for Pt(110) and 8 meV/pH for Pt(100). The HOR activity showed a linear decay as the HBE increased, suggesting that the HBE could be an effective descriptor for the pH-dependent HOR kinetics on Pt. Furthermore, the same group extended this concept to other precious-metal-based electrocatalysts, including Ir/C, Pd/C, and Rh/C (Figure 10B).[148] Based on the correlation of i_0 to more positive H_{upd} peak potentials (i.e., higher HBE values), they proposed that the HBE is a dominant descriptor for the HOR kinetics. However, those two studies require a further investigation of the effects of adsorbing anions (acetate,

https://doi.org/10.1021/acs.chemrev.1c00331
Chem. Rev. XXXX, XXX, XXX−XXX

phosphate, and carbonate) and the steps and defects of poly-Pt on the HOR kinetics.

The HBE framework that was proposed to be responsible for the slowness of the HOR kinetics of Pt in alkaline media predicted that Au should have enhanced HOR/HER reactivity in alkaline media, which goes in the opposite direction as Pt.[30] However, it was found that the HOR/HER kinetics of Au were slower in alkaline media.[149] This observation, along with why the HBE is strengthened at higher pH, given that it represents an intrinsic thermodynamic descriptor, has driven further investigations into the role of the interfacial environment. Recently, a modified HBE effect was proposed by taking account of both the intrinsic HBE and water adsorption on the electrode surface, suggesting that the pH-dependent HBE, derived from the H_{upd} peaks, should be referred to as apparent HBE (HBE_{app}).[150] Specifically, given that H_2O_{ad} and H_{upd} are competing for adsorption sites, the weakened water adsorption at higher pH would give rise to a stronger observed H-binding to the electrode surface, suggesting that the HBE_{app} should be used as a more appropriate descriptor for the HOR/HER kinetics. This hypothesis was further confirmed by a quantum mechanical molecular dynamics (QMMD) simulation by Goddard, which considered the adsorption of H and H_2O on a Pt(100) surface.[151] At higher pH, water tends to be repelled from the electrode surface at a low potential vs SHE, resulting in a reinforced H-binding (Figure 10C). This study predicted an increase in the HBE value by 10 meV/pH, consistent with the experimentally measured 8−12 meV/pH.[23] Recently, the HBE_{app} theory was adopted to rationalize the improved HER kinetics of Pd@Pt and PdH@Pt nanocrystals relative to Pt.[152]

Recently, the adsorption of cation and hydroxyl species has been proposed as an alternative to the HBE_{app} model. Koper et al. proposed that the peaks in the so-called H_{upd} region in Pt(110) and Pt(100) arise from the displacement of the H_{upd} by OH_{ad} instead of the direct oxidation of the H_{upd}.[153] These claims were supported by two anomalies on well-defined Pt(110) and Pt(100) surfaces: a shift of the H_{upd} peak by 50 mV/pH instead of 60 mV/pH; and that a well-defined OH_{ad} counterpart is missing in the hydrogen region, when compared to Pt(111). The sharp features of those voltammetric peaks indicate stronger attractive lateral interactions between H_{ad} and OH_{ad}.[153] To explain the unusual pH-dependence, they proposed that the replacement reaction proceeds via the following reaction:

$$H_{upd} + xH_2O \leftrightarrow xOH^{\delta+}{}_{ad} + [x+1]H^+ + [(1+\delta)x+1]e^- \quad (7)$$

Here, δ is known as the electrosorption valency while x is the ratio between the stoichiometric numbers of OH_{ad} and H_{upd}. This mechanism implies that the H_{upd} on step does not have full coverage and that the reaction involves more than one proton per electron, which can account for the observed non-Nernstian pH-dependence of 50 mV/pH. Furthermore, McCrum and Janik simulated the CV profiles on Pt basal planes with DFT calculations by taking into account cation and OH adsorption.[104] Their results suggested that the more favorable adsorption of K^+ can weaken the OH binding at higher pH and that cations may play a role in the adsorption. Koper et al. then investigated the effects of adsorption of Li^+, Na^+, K^+, and Cs^+ on the pH-induced voltammetric peak shift of stepped Pt surfaces (Figure 10D).[113] Specifically, the steplike voltammetric peaks exhibited positive shifts at higher cationic concentrations and with larger cationic radii at the same pH. All of the evidence pointed toward a situation in which the favorable adsorption of alkali cations near Pt steps weakened the OH adsorption on step sites, rendering a positive shift of steplike voltammetric peaks.

As discussed before, it remains unclear whether the H_{upd} is equivalent to the H_{ad} intermediate in the HER/HOR. Conway et al. claimed that only the overpotentially deposited hydrogen (H_{opd}), formed near or below the reversible hydrogen potential region, could be regarded as the H_{ad} intermediate in the Volmer step, while the H_{upd} served as a spectator,[142] competing for active sites or modifying the energy of the H_{ad}.[128,154] However, their physical nature remains unknown,[22,155] as only the H_{opd} was distinguishable from spectroscopic measurements.[156−159] Wang reported on an analysis of adsorption isotherms for two types of adsorbed H: H on atop sites (H_{Atop}) and in hollow/bridge sites ($H_{H/B}$), based on spectroscopic and electrochemical evidence.[160] According to the results of DFT calculations, they proposed that the H_{Atop} has a much lower energy barrier for the oxidative desorption than the $H_{H/B}$, despite the site-insensitive dissociative adsorption (Tafel step), suggesting that the H_{Atop} is likely the reaction intermediate for the HOR/HER. Although the majority of first-principles calculations overlooked the arrangement of adsorbed hydrogen,[20,95,161] recent studies on the configurations of the H_{ad} support that the calculation of the H-binding energy should be based on the H_{Atop}.[159,162,163]

In summary, the detailed nature of the hydrogen region of Pt is still an open question: whether the adsorption/desorption of H_{upd} occurs alone or with contributions from the replacement of the H_{upd} by OH_{ad} and the configuration of the adsorbed H. The correlation between the H_{upd} peak positions and the HBE has been proposed as an activity descriptor, albeit with limitations. For example, in the case of Pt(111) without an observable H_{upd} peak shift at different pH values, a similar pH-dependent HOR/HER activity trend still exists. Those studies all suggest that the HBE is unlikely to be the sole descriptor for the HOR kinetics in alkaline media.

3.1.4. Interfacial Water Structure. Growing evidence is pointing towards the role of interfacial water in the HOR/HER kinetics in alkaline media.[151,164,165] As will be discussed in detail in section 4.1.5, the value of applied potentials, relative to the pzfc, dictates the water orientation and H-bonding water network on the electrode surface (Figure 17C). In acid, the interfacial water network is relatively loose with an oxygen-down orientation at the HOR/HER potentials, which are slightly more negative than the pzfc. However, the interfacial water structure in alkaline media is much more rigid with the hydrogen-down orientation, as the interfacial electric field is strengthened at the HOR/HER potentials since the H region shifts negatively in the SHE scale and is significantly below the pzfc (0.28 V vs SHE for Pt(111)) in alkaline media.[166] The charge transfer of OH^- is hindered as it requires additional energy to break up the rigid water structure, which can help rationalize the pH-dependent HER/HOR kinetics.[26] In contrast to the conventional thermodynamic perspective based on the electronic or oxophilic effect, the interfacial water structure is rooted in its kinetic aspects, providing direct insights into the reaction kinetics.

Koper et al. first proposed the change of interfacial water structure to explain the promoting effect of $Ni(OH)_2$

https://doi.org/10.1021/acs.chemrev.1c00331
Chem. Rev. XXXX, XXX, XXX−XXX

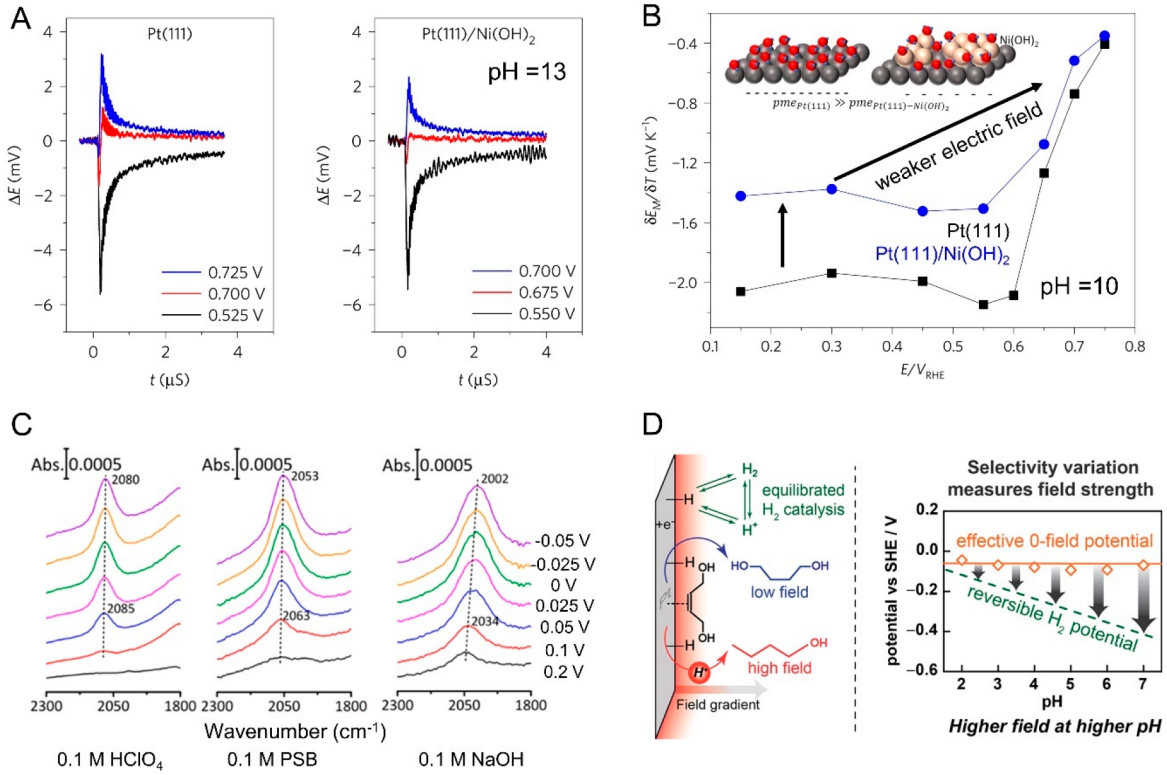

Figure 11. Interfacial water structure as a possible descriptor for the sluggish HOR/HER kinetics in alkaline media. (A) Coulostatic potential temporal response induced by the laser-temperature jump method on Pt(111) and $Ni(OH)_2$-decorated Pt(111) in 0.1 M NaOH. (B) Thermal coefficients calculated from the slopes of the potential decays on Pt(111) electrodes and $Ni(OH)_2$-modified electrodes by the laser jump method in solutions containing 0.05 M Na_2CO_3 + 0.05 M $NaHCO_3$. The decrease in the thermal coefficient on Pt(111)/$Ni(OH)_2$, compared to Pt(111), suggests a weakened interfacial electric field induced by a negative shift of the pzfc/pme (inset). (C) Surface-enhanced IR spectral evolution of Pt−H_{atop} vibration on a Pt polycrystalline film with applied potentials in 0.1 M $HClO_4$ (pH = 1), phosphate-buffered saline (pH = 7), and NaOH (pH = 13). The decreasing wavenumber of the Pt−H_{atop} denotes a weakened adsorption energy with increasing pH values. (D) Proposed scheme of Pt/C-catalyzed conversion of *cis*-2-butene-1,4-diol to *n*-butanol and 1,4-butanediol on the surface of an electrode as a protocol to probe the interfacial electric field (left). The measured interfacial potential drop (60 mV/pH) shows an increasing electric field strength with pH, changing from acid to neutral media (right). Panel A is reprinted with permission from ref 26. Copyright The Authors 2017 Springer Nature. Panel B is reprinted with permission from ref 168. Copyright 2019 American Chemical Society. Panel C is reprinted with permission from ref 159. Copyright 2015 American Chemical Society. Panel D is reprinted with permission from ref 27. Copyright 2019 American Chemical Society.

modification of Pt(111) on the HER kinetics in alkaline media.[26] The study was based on the shift of potential of maximum entropy (pme), at which the interfacial water is most disordered, which is closely related to the pzfc. As shown in Figure 11A, the potential transients of Pt(111) and Pt(111)/$Ni(OH)_2$ at a pH of 13 changed from negative to positive values at 0.700 and 0.675 V, respectively, indicating a shift of the pme of −25 mV after $Ni(OH)_2$ modification. Though the hydroxyl adsorption at a pH of 13 may influence the shift in the pme values,[167] the thermal coefficients ($\partial E\ \partial T$) measured at a pH of 10, with a smaller effect of OH adsorption, provided compelling evidence to support the change of the pme after the introduction of $Ni(OH)_2$ (Figure 11B). Both Pt(111) and Pt(111)/$Ni(OH)_2$ displayed a diminution of their thermal coefficients (absolute value) at more positive potentials, especially over the range 0.55−0.75 V vs RHE, denoting a weaker interfacial electric field at higher potentials. Consequently, the smaller thermal coefficients of Pt(111)/$Ni(OH)_2$, relative to Pt(111), suggested a weakened electric field, as evidenced by a more negative pme. Based on the proposed model, Feliu and coworkers investigated the effects of $Ni(OH)_2$ coverage. The positive pme at a higher coverage further supported the notion that $Ni(OH)_2$ induced a more disordered water structure (Figure 11B, inset).[168] Apart from the Pt−Ni system, the validity of this concept awaits to be verified in other bimetallic systems, such as Pt−Ru alloys, often used as the hydrogen anode in AEMFCs.[169] Although the interfacial water structure can rationalize the pH-dependent HER kinetics, additional studies are required to elucidate how the interfacial water interacts with alkali cations and other reaction intermediates during the HER and HOR in alkaline media.

Besides the sluggish HER/HOR kinetics in alkaline media, the reaction kinetics of the H_{upd} processes experience similar trends from an acid to base. Koper et al. found that the introduction of $Ni(OH)_2$ also helps lower the energy barrier for hydrogen adsorption/desorption processes on Pt(111), as indicated by the R_{ct} measured by the EIS, suggesting that the interfacial water structure also affects the reaction rates of the H_{upd}.[26] As discussed in section 3.1.3, the thermodynamic or kinetic information obtained from H_{upd} may not be directly translated to the H_{opd} or H_{ad}. On the other hand, it may not be necessary to distinguish H_{upd} from H_{opd} since both HER/HOR and H_{upd} processes are subject to the same restriction of interfacial water rigidity. Therefore, it is reasonable and valid to extract the information of interfacial water just from the study

https://doi.org/10.1021/acs.chemrev.1c00331
Chem. Rev. XXXX, XXX, XXX−XXX

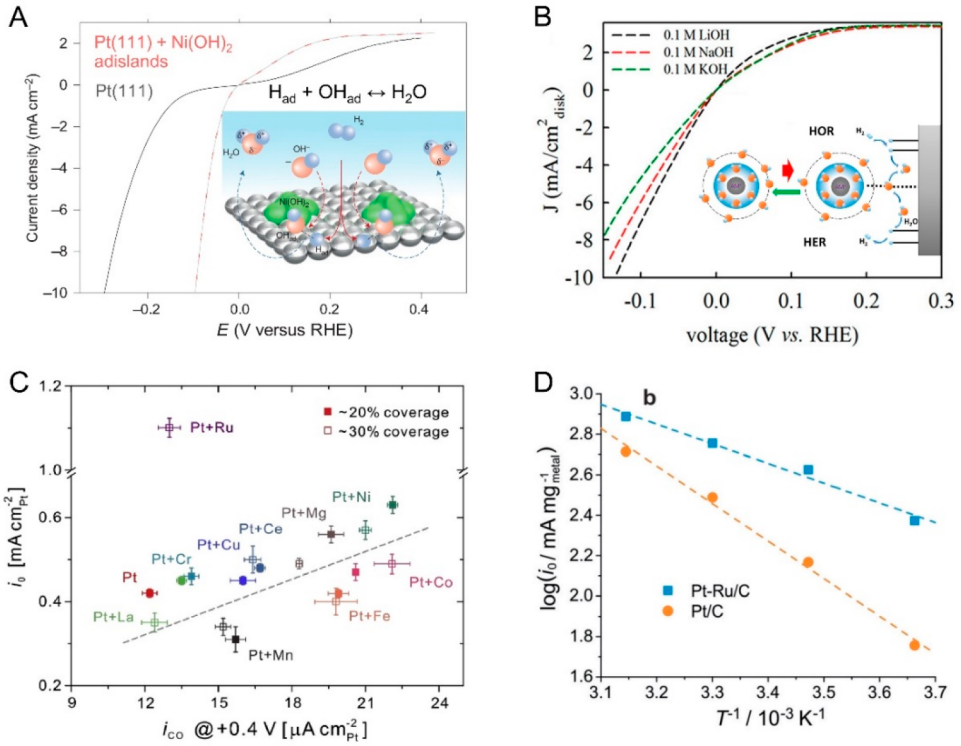

Figure 12. Bifunctional mechanism as a possible descriptor for the improvement of sluggish HOR kinetics in alkaline media. (A) HOR/HER polarization curves for Pt(111) and Pt(111) modified with $Ni(OH)_2$ adislands with 20% coverage in 0.1 M KOH, 1600 rpm, 50 mV/s. Inset scheme showing a proposed bifunctional mechanism, in which the introduction of $Ni(OH)_2$ promotes desorption of H_{ad} ($H_{ad} + OH_{ad} \leftrightarrow H_2O$) via the formation of reactive OH_{ad}. (B) HOR/HER polarization curves of the Pt polycrystalline electrode in 0.1 M LiOH, NaOH, and KOH, 2500 rpm, 10 mV/s. The inset scheme illustrates the role of $OH^--(H_2O)_x-AM^+$ adducts in determining HOR/HER kinetics. (C) HOR/HER exchange current densities (i_0) as a function of oxophilicity characterized by CO stripping current density at 0.4 V vs RHE (20 mV/s) on a Pt polycrystalline electrode modified by 10 metal hydroxides/oxides (Mg, Cr, Mn, Fe, Co, Ni, Cu, Ru, La, and Ce) in 0.1 M KOH. The dashed line indicates that the HOR/HER kinetics scale with the oxophilicity of the modified Pt electrode except for Ru-modified Pt. (D) Arrhenius plot of HOR/HER exchange current density and temperature of the Pt−Ru/C and Pt/C electrode in 0.1 M KOH. The steeper slope of Pt/C indicates that the HOR/HER kinetics of Pt/C become comparable to those of Pt−Ru/C at higher temperatures (fuel cell working temperatures) even though Pt−Ru/C has a much better HOR performance near room temperature. The calculated activation energies of Pt/C and Pt−Ru/C are 35.2 and 14.6 kJ/mol, respectively. Panel A is reprinted with permission from ref 25. Copyright 2013 Springer Nature. Panel B is reprinted with permission from ref 111. Copyright 2019 American Chemical Society. Panel C is reprinted with permission from ref 186. Copyright 2019 The Authors, Elsevier. Panel D is reprinted with permission from ref 187. Copyright 2019 The Authors, Wiley.

of the H_{upd} region to understand the HER/HOR kinetics. Recently, Yan et al. employed surface-enhanced infrared absorption spectroscopy (SEIRAS) to study the pH-dependence of the H_{upd} peak shifts and ascribed them to the interference of interfacial water,[170] rather than to the coadsorption of alkali metal cations, as proposed by Koper.[113] The SEIRAS study by Shao et al. indicated both weakened interfacial water and hydrogen adsorption as the pH increased.[159] As presented in Figure 11C, the H-band was assigned to the interactions between Pt and H adsorbed on top of Pt atoms (H_{atop}), which was proposed as the reaction intermediate for the HER and HOR, rather than H with multiple Pt coordinations ($H_{multiple}$), such as 4-fold sites on Pt(100) and 3-fold sites on Pt(111). At higher pH values, the band of $Pt-H_{atop}$ shifted to lower wave numbers, indicating a weakened H-binding. This weakening, which is in contrast to the HBE theory,[150,171] indicates that the hydrogen adsorption on Pt depends on multiple interfacial factors.[160,162] The much higher stark tuning rate in alkaline media than in acid suggested different degrees of polarization in the two environments, implying a pH-dependent interaction of the H_{atop} with the interfacial water structure.[172,173] Tang et al. reported a kinetic H/D isotope effect (KIE) of up to 3.4 for the HOR on Pt(111) in base, indicating a strong effect of the interfacial water structure in alkaline media.[172] This observation requires further study to elucidate the elemental step(s) of the HOR in alkaline media to break down the contributions to the observed KIE.

Since the interfacial water structure varies with the interfacial electric field, measurements of interfacial electric fields represent an important step toward understanding the HOR. Recently, Surendranath et al. probed the changing interfacial electric field based on a pH-sensitive H_2 addition reaction.[27] As shown in Figure 11D, the conversion of the probe molecule to 1,4-butanediol is preferred at low field, when the local H^+ concentration near the electrode surface is lower than the bulk concentration, while the formation of *n*-butanol dominates at high field. Based on the product selectivity, the calculated interfacial potential drops by 60 mV per pH. Nevertheless, since the investigated pH ranges from acidic to neutral media (pH = 2−7), an extrapolation of the trend to alkaline media needs further investigation. Additionally, the potential adsorption of organic molecules or products and their effects on the interfacial electric fields remain unknown, which may

https://doi.org/10.1021/acs.chemrev.1c00331
Chem. Rev. XXXX, XXX, XXX−XXX

undermine the interpretation of the calculated potential drops. Nonlinear spectroscopic methods such as second harmonic generation (SHG)[174] could offer an alternative tool to probe the interfacial electric field without using additional chemical agents.

3.1.5. Other Activity Descriptors for the HOR in Alkaline Media. We will briefly discuss other hypotheses beyond what was discussed above.[175,176] Chen et al. used a microscopic Hamiltonian model to encompass electronic interactions, bond breaking, solvent reorganization, and double-layer electrostatic effects and ascribed the large activation energy of the Volmer step to the large work term for moving OH^- to the negatively charged electrode surface.[107] Chan et al. examined the role of H-binding, proton donor, and water reorganization on the pH effects on the HOR/HER with first-principles DFT calculations and found that the water reorganization energy was too small to account for the much slower HER/HOR kinetics in alkaline media.[32] Alternatively, they proposed that the change of proton donor from hydronium in acid to water in base is the main reason for the sluggish HER in alkaline media since the water dissociation in alkaline media has a higher kinetic barrier relative to acidic media. However, the proton donor effect cannot explain why the HOR kinetics is also slower in base. In addition, Rossmeisl et al. proposed that a larger kinetic barrier for HER/HOR with rising pH is a consequence of a change of the configurational entropy of protons when approaching the surface.[173] The protons lose part of their entropy when crossing the outer Helmholtz region, giving rise to an entropic barrier, which increases with pH. This hypothesis also highlights that the pH effect is more pronounced for a good catalyst, with fast reaction kinetics, in agreement with the observation of Pt being strongly impacted by pH changes, relative to Pd or Ir, and the HOR being more pH-sensitive than the ORR.[22,83] While these studies have provided novel insights into the sluggish hydrogen reaction kinetics in base, it has not been straightforward for experimentalists to find evidence supporting the models. Recently, Feliu et al.[176] investigated the HER/HOR on three basal planes of Pt under nearly neutral pH conditions (pH = 3.0, 4.0, 5.4) without specifically adsorbing anions and found that the HER activity showed no pH-dependence on the three facets, while the HOR kinetics exhibited pronounced pH-sensitive features. The more negatively charged electrode, at a higher pH, favors the HER but suppresses the HOR, which was rationalized based on DFT results that proton solvation becomes more unfavorable on a more negatively charged electrode, leading to the drastic decrease of the HOR kinetics in alkaline media, relative to those in acid.

In summary, several reasons have been proposed to explain the HOR/HER activity in alkaline media. While the true nature of the mechanism is still a subject of debate, most explanations have so far pointed to the interfacial water structure and the interaction among intermediates (H*, OH*, H_2O*, etc.) in acid and base as likely possible. Further examination, from both experimental kinetic studies and more realistic theoretical simulations of the electrode/electrolyte interface, will further advance our understanding of the sluggish HOR in alkaline media.

3.1.6. Mechanisms for HOR Enhancement on Pt-Based Binary Catalysts. In an attempt to explain the improved alkaline HER kinetics on Ni-modified Pt surfaces, Marković et al. proposed a bifunctional effect, where the $Ni(OH)_2$ clusters can be added to Pt to facilitate the sluggish water dissociation into H_{ad} and OH_{ad}, followed by the recombination of the H_{ad} on Pt to form hydrogen and desorption of the OH_{ad} to OH^-.[34] Further, the $Ni(OH)_2$ modification on Pt(111) also enhanced the HOR kinetics in alkaline media (Figure 12A).[25] These insights support the view that alkaline HER/HOR electrocatalysis can be improved via the bifunctional effect, similar to the case of Pt−Ru for the methanol oxidation reaction.[177] The central idea is that the OH_{ad} becomes an important reaction intermediate in alkaline media, instead of the previously claimed inhibitor or spectator for the HOR reaction.[82] Notably, the sluggish HOR kinetics can be attributed to the difficulty of forming OH_{ad} and/or the competition between H_{ad} and OH_{ad} for active sites. As illustrated in the inset scheme in Figure 12A, the electrochemical removal of H_{ad} (the Volmer step: $H_{ad} + OH^- \leftrightarrow H_2O + e^-$) occurs via two processes, each involving OH_{ad}: the adsorption of hydroxyl species ($OH^- \leftrightarrow OH_{ad} + e^-$) and the recombination with H_{ad} ($OH_{ad} + H_{ad} \leftrightarrow H_2O$). The OH_{ad} sites from $Ni(OH)_2$ promote the desorption of the H_{ad} to form water. Consequently, the key to enhancing the HOR kinetics lies in improving the oxophilicity of the electrode surface, which can be enabled by combining Pt with more oxophilic metals (e.g., Ni, Ru) or using more oxophilic noble metals (e.g., Ir). Therefore, the HOR/HER activities depend not only on the H-binding energy but also on the binding strength of the OH_{ad} in alkaline media.[178,34]

The proposed bifunctional mechanism has faced some challenges.[22,30,31,179] Gasteiger et al. pointed out that Ir, in fact, has a lower HOR activity than Pt, and that the surface composition of Pt−Ru alloys is different from the bulk.[22] They further argued that the Volmer step in alkaline media may not involve the formation of OH_{ad} but rather the desorption of H_{ad} to protons, followed by a bulk reaction with OH^-. In other words, the microscopic details of the surface Volmer step do not change from acid to base. Similarly, Tang et al. argued that the Volmer step proceeds via a direct process ($H_{ad} + OH^- \leftrightarrow H_2O + e^-$), in which the OH_{ad} behaves as a spectator competing for active sites, based on the voltammetry and microkinetic analysis on Pt(110).[30]

The promoting role of the secondary metal in a Pt-based bimetallic system (e.g. Pt−Ni) has also been a subject of intense debates regarding whether the electronic effect (weakened HBE) or oxophilic effect (bifunctional mechanism) dominates. Different from the electronic effect, the oxophilic effect requires the secondary metal to be present on the surface. Therefore, Zhuang and coworkers attempted to isolate the effect of oxophilicity by investigating two surface-controlled model nanoparticles (NPs): Pt−Ni alloys with and without acid-leaching.[180] The acid treatment of Pt−Ni NPs led to the formation of a PtNi@Pt core−shell structure. Interestingly, the HOR activity of the Pt−Ni catalysts after acid treatment remained barely changed, indicating that the OH_{ad} (on Ni, which is absent in acid-leached samples) may play a minor role for the Pt−Ni model system, as opposed to the oxophilic effect proposed by Marković et al.[25] However, this argument was undermined by the fact that acid treatment likely did not render a complete removal of the surface Ni in Pt−Ni NPs.[111] Based on the effects of alkali cations on the HER/HOR kinetics of poly-Pt, Jia et al. proposed a modified bifunctional mechanism in combination with hard−soft/acid−base (HSAB) concepts.[111] The concept of $OH_{ad}-(H_2O)_x-AM^+$ (AM: alkali metals)[181] was introduced into the Volmer step, in which the interaction energy between $(H_2O)_x-AM^+$

https://doi.org/10.1021/acs.chemrev.1c00331
Chem. Rev. XXXX, XXX, XXX−XXX

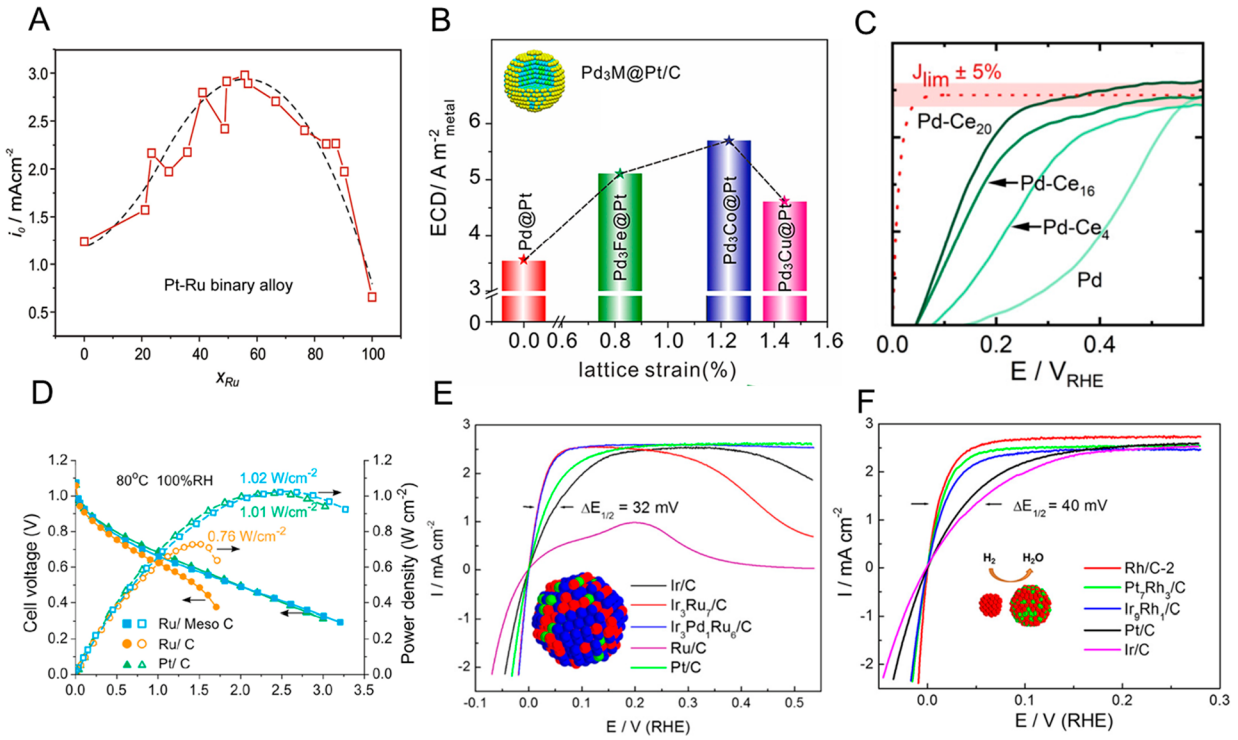

Figure 13. Recent advances of alkaline HOR catalysts based on precious metal catalysts. (A) Volcano shape relationship between HER/HOR exchange current densities and Ru atomic fraction analyzed by X-ray fluorescence in Pt−Ru binary alloy thin-film electrodes, prepared by magnetron sputtering. (B) HER/HOR exchange current density (ECD) of Pd@Pt/C and Pd_3M@Pt/C with different surface lattice strains. The increasing lattice strain corresponds to weakened hydrogen binding. (C) HOR activity evaluation of Pd−CeO_x samples with different CeO_x thicknesses in H_2-saturated 0.05 M NaOH aqueous solution at a scan rate of 20 mV/s; Ce_4 indicates that 4 ALD cycles were used to deposit the CeO_x layer. (D) MEA performance of an AEMFC using Ru/Meso C, Ru/C, and 20% Pt/C as the anode catalysts with a metal loading of 0.1 mg/cm^2 and 60% Pt/C as the cathode catalysts with a metal loading of 0.45 mg/cm^2 at a cell temperature of 80 °C and a backpressure of 0.1 MPa. (E) Alkaline HOR activities of Ir/C, Ir_3Ru_7/C, $Ir_3Pd_1Ru_6$/C, Ru/C, and Pt/C (loading: 3.5 $\mu g_{metal}/cm^2$) tested in H_2-saturated 0.1 M KOH at a scan rate of 5 mV/s and rotation rate of 1600 rpm. (F) Alkaline HOR activities of Rh/C-2, Pt_7Rh_3/C, Ir_9Rh_1/C, Pt/C, and Ir/C (loading: 3.5 $\mu g_{metal}/cm^2$) under the same test conditions as in panel E. Panel A is reprinted with permission from ref 189. Copyright 2019 The Authors, Elsevier. Panel B is reprinted with permission from ref 198. Copyright 2020 Elsevier. Panel C is reprinted with permission from ref 212. Copyright 2020 American Chemical Society. Panel D is reprinted with permission from ref 216. Copyright 2020 The Authors, Elsevier. Panel E is reprinted with permission from ref 224. Copyright 2017 American Chemical Society. Panel F is reprinted with permission from ref 230. Copyright 2019 American Chemical Society.

and OH_{ad} or OH^- was proposed to affect the HOR/HER kinetics.[111] According to this approach, the interaction of the $(H_2O)_x$−AM^+ with the OH_{ad} is weaker than that with the OH^- since the OH_{ad} is a soft base whereas the OH^- is a hard one. They observed that increasing the AM^+ concentration only promotes the HER, while varying the identity of AM^+ affects both the HER and HOR in alkaline media (Figure 12B). The hypothesis of the OH_{ad}−$(H_2O)_x$−AM^+ implies that the HER kinetics can be improved by increasing the AM^+ concentration, in agreement with experimental observations. The higher HER/HOR activity in LiOH was ascribed to the weaker Pt−OH_{ad} interaction, relative to NaOH or KOH. Recently, Li et al.[182] used *in situ* electrochemical surface-enhanced Raman spectroscopy (SERS) to support the presence of the OH_{ad} species on the surface of PtNi alloys during the HOR in alkaline media while the OH_{ad} was not observed on the pure Pt surface.

Similar to Pt−Ni, how the synergy between Pt and Ru takes effect in the HOR kinetics also remains debatable. Durst et al. argued that the Volmer step does not have to change from acidic media to alkaline media, suggesting that the change of the HBE rather than the oxophilic effect could be responsible for the HOR kinetic enhancement of Pt−Ru, relative to Pt.[22] Zhuang et al. proposed that the electronic effect played a major role as the voltammetric peaks of Pt−Ru in the H_{upd} region shifted to lower potentials compared to Pt, indicating a weakened Pt−H_{ad} binding.[183] Meanwhile, they proposed that the oxophilic effect might not explain the enhanced HOR activity since the reactive hydroxyl species on Pt sites can be generated even at lower potentials than Pt−Ru, as derived from the CO stripping voltammograms. Recently, Jia et al. suggested that the peak at lower potentials on Pt−Ru should be ascribed to the presence of Ru instead of the weakened hydrogen binding on Pt and that the CO stripping peak of Pt−Ru may not reflect the absence of the OH_{ad} at potentials below 0.4 V vs RHE, given that the CO_{ad} competes with the OH_{ad} for Ru sites.[112] Thus, they argued that the promoting effect of Ru in Pt−Ru alloys comes from the bifunctional mechanism, supported by the presence of OH_{ad} revealed by *in situ* X-ray absorption spectroscopy (XAS). Taking into account the double layer structure, Jia et al. proposed that Pt−Ru involves the quasispecifically adsorbed OH (−H_{upd}−$OH_{q\text{-}ad}$), which enhances the HOR kinetics by accelerating the bond formation to yield H_2O, while other bimetallic systems engage in only specifically adsorbed OH.[164] Schwämmlein et al. attempted to distinguish between the two effects by examining the HOR/

https://doi.org/10.1021/acs.chemrev.1c00331
Chem. Rev. XXXX, XXX, XXX−XXX

HER activity of a series of Ru@Pt core−shell NPs with different Pt thicknesses[184] and predicted that the optimal thickness of Pt, calculated from the bifunctional mechanism, should be less than one monolayer.[185] In contrast, the experimentally determined optimal thickness was 1.6 layers, supporting the electronic effect as the major contributor to the superior activity of Pt−Ru catalysts. However, it is challenging to know whether the observation is due to the changing structure of the Pt shell as a function of its thickness.[180,111] Recently, the Zhuang group reported on an alkaline HOR kinetic study based on poly-Pt electrodes modified by 10 different types of transition metal oxides or hydroxides (Pt−M, M = Mg, Cr, Mn, Fe, Co, Ni, Cu, Ru, La, and Ce).[186] A rising trend of the HOR activity with enhanced oxophilicity suggested that the oxophilic effect governs the HOR kinetics in those bimetallic systems except for Pt−Ru (Figure 12C). They observed Pt−Ru as an outlier, indicating that the improved HOR kinetics of the Pt−Ru system may be different from other Pt−M systems. Specifically, the electronic effects were proposed as the reason for the enhanced kinetics on the Pt−Ru while the oxophilic effect was proposed as the reason for the enhanced kinetics behind the other Pt−M systems. Furthermore, the same group recently reported that even though Pt−Ru/C exhibits a much higher HOR activity than Pt/C at room temperature, their HOR kinetics gap becomes less pronounced at higher temperatures, given the much larger activation energy of Pt/C (35 kJ/mol) compared to Pt−Ru/C (15 kJ/mol) (Figure 12D) and their comparable peak power densities in MEA tests at 80 °C.[187] Hence, the advantage of using Pt−Ru over Pt catalysts for the HOR in alkaline fuel cells is modest at elevated temperatures. Recently, we showed that Pt-based and Ir-based alloys with Ru, Rh, or Pd exhibited an enhanced HOR activity relative to pure metals, which was ascribed to a combination of oxophilic and electronic effects based on kinetic Monte Carlo simulations and differential electrochemical mass spectrometry (DEMS) of CO stripping.[188]

In summary, the electronic effects and/or the oxophilic effects, involving the OH_{ad} adsorption, play an important role in rationalizing the HOR/HER kinetics of Pt-based binary electrocatalysts in alkaline media either directly or indirectly. However, the molecular details of how the OH_{ad} participates in the electrocatalysis are still an open question.

3.2. Nanoscale HOR Electrocatalysts in Alkaline Media

AEMFCs require a significantly higher amount of Pt to catalyze the sluggish HOR at the anode, relative to PEMFCs. Thus, it is of great interest and importance to design and develop high-performance low-Pt and non-precious-metal-containing HOR electrocatalysts in alkaline media. This section reviews the recent progress on Pt-based, non-Pt precious- and non-precious-metal-containing HOR electrocatalysts.

3.2.1. Pt-Based HOR Catalysts. Pt−Ru-based catalysts are widely recognized as the most efficient HOR catalysts even though the explicit reason remains debatable, as thoroughly discussed in section 3.1. Zhuang et al.[189] prepared Pt−Ru binary alloy thin-film electrodes with 14 different compositions of Pt−Ru alloy via a high-throughput combinatorial approach to investigate the composition−activity relationships. The HOR exchange current density displayed a volcano shape vs Ru fraction (Figure 13A), with a maximum activity at 55 atom % Ru, which was ascribed to a lower electron charge density of Pt induced by Ru doping. The stability of Pt−Ru alloy NPs could be enhanced via a stronger interaction between NPs and the support.[190,191] Song et al.[190] demonstrated the use of N-doped carbon-supported Pt−Ru particles as stable HOR catalysts, prepared via an impregnation method followed by NH_3 etching. The significantly improved durability during potential cycling was attributed to the stabilizing effect of nitrogen dopants in the carbon support, relative to commercial Pt/C and PtRu/C. In addition to Pt−Ru alloy particles, Pt−Ru heterostructures have also provided some insights into activity improvements and minimizing Pt contents. Wang et al.[192] reported a 2-fold improvement in the HOR mass activity with Ru@Pt core−shell structure NPs with an optimal two-atomic-layer Pt shell, compared to random PtRu alloys. Further, Papandrew et al.[193] examined the HOR performance of Pt or Pd overlayers on unsupported Ru nanotubes, and the optimal $Ru_{0.9}Pt_{0.1}$ nanotubes displayed enhancements of 35 and 2.5 times specific activity, relative to pure Ru and Pt nanotubes, respectively. The improvement was ascribed to an increased Pt utilization efficiency and possible bifunctional, strain and/or ligand effects.

In addition to the Pt−Ru catalysts, Pt alloyed catalysts with other secondary metals have also been exploited to minimize the use of Pt while improving activity via tuning the electronic and/or strain effects. Wong et al.[194] investigated the HOR activity of a series of ultrathin Pt−M (M = Fe, Co, Ru, Cu, Au) alloy nanowires (NWs), among which Pt−Ru, Pt−Fe, and Pt−Co NWs achieved improved HOR exchange current densities while Pt−Au and Pt−Cu NWs exhibited a lower activity, relative to pure Pt. They claimed that the hydrogen binding energy played a key role in the observed activities since the trend was consistent with the hydrogen binding strength based on a volcano plot. Ohyama and colleagues[195] modified the surface of Pt particles with 15 metals (4th and 5th period elements) and found a similar "volcano plot" in the relationship between HOR and the standard oxidation potentials of the secondary metals. Consequently, they proposed that the enhanced activity could be ascribed to a change of the reactivity of surface oxidized species beyond a change in the HBE. An interesting observation was that while Pt−Cu alloyed NWs[194] and Cu-modified Pt/C[195] showed a decreased HOR activity, compared to their Pt counterparts, Cu-modified Pt electrodes displayed a slightly enhanced HOR.[186] Moreover, a study on Pt-coated Cu NWs generated by galvanic displacement by Yan et al.[196] suggested that the incorporation of Cu was actually beneficial to the HOR activity through a compressive strain on Pt and promotion of hydroxyl adsorption. Therefore, those seemingly contradictory results may arise from differences in chemical composition and surface coverages of Cu and should be examined carefully with surface characterization techniques.

Besides Pt-based binary catalysts, the potential of ternary catalysts has also been explored for low-Pt catalyst content design. For instance, Wang[197] reported a weakening of the HBE on Pt by forming a Pt skin surrounding an ordered PdFe intermetallic core. This electrocatalyst exhibited an enhanced HOR performance, when compared to a Pt skin on a disordered PdFe counterpart. The same group investigated the HOR kinetics with catalysts based on strain-engineered Pd_3M (M = Fe, Co, Cu) cores covered with a monolayer Pt skin (Figure 13B).[198] Their results suggested that the HOR activity enhancement was mainly governed by the oxophilicity of low-valence $M(OH)_x$ species, rather than by the change of HBE caused by surface lattice strain. Furthermore, they

https://doi.org/10.1021/acs.chemrev.1c00331
Chem. Rev. XXXX, XXX, XXX−XXX

developed a new class of Pt−Pd−Fe ordered intermetallics with an improved HOR activity and durability, arising from the widening and downshifting of d-band structure, induced by the formation of Pd hydrides (PdH_x) and/or ordered atomic arrangements.[199]

3.2.2. Non-Pt Precious-Metal-Based HOR Catalysts.

3.2.2.1. Pd-Based Catalysts. Pd represents a promising alternative to Pt given its comparable HOR activity. However, the quantification of the HOR kinetics on bulk Pd electrodes is complicated by the hydrogen absorption into the Pd lattice. Gasteiger et al.[200] circumvented this challenge by depositing a Pd adlayer onto a polycrystalline Au substrate. The measured exchange current density in alkaline media was observed to scale inversely with the palladium coverage on Au, pointing toward an excessive H-adsorption strength by the tensile strain induced by the Au substrate. Yan et al.[201] studied the size-dependent HOR kinetics of Pd/C and found that the exchange current density of Pd/C decreased in alkaline media as the particle size decreased from 19 to 3 nm, which was ascribed to the increased fraction of sites with stronger hydrogen binding energy.

Alloying has been proven an efficient strategy to boost the HOR performance of Pd. For example, PdIr/C alloyed NP catalysts were reported to exhibit HOR activities comparable to that of Pt/C.[202] Song et al.[203] revealed that $Pd_{0.33}Ir_{0.67}$ supported on N-doped carbon exhibited an optimal HOR activity, slightly higher than that of Pt/C, which was ascribed to its optimal H-binding strength and enhanced oxophilic properties. Shao et al.[204] examined the role of Ru in Pd_3Ru alloy nanocatalysts for the alkaline HER/HOR. Structural characterizations revealed that Ru was segregated on the alloy surface, forming adatoms and clusters, which led to a weakened HBE and enhanced OH adsorption. Li et al.[205] reported that Pd−Cu alloys, with a body centered cubic phase (bcc), displayed a 20-fold enhancement of HOR activity, relative to its face centered cubic (fcc) counterpart. The DFT calculations revealed that the bcc Pd−Cu surface possessed a much stronger OH binding, compared to the fcc Pd−Cu, despite a similar H-binding strength. This work underlined the importance of phase control during the synthesis of HOR electrocatalysts. In addition to alloying, the Pd layer surface coating or decoration provides another strategy for optimizing Pd atomic utilization.[206−208]

Dekel et al. established that the use of ceria (CeO_2) supports could enhance the HOR kinetics of Pd/C in alkaline electrolytes, possibly as a result of weakened Pd−H bonds and an improved supply of OH_{ad} sites from the oxophilic CeO_2, relative to carbon supports.[209] They reported that the preferably deposited Pd onto CeO_2/C led to significantly increased stability, compared to Pd/C, due to the strong Pd−CeO_2 catalyst−support interaction.[210,211] Furthermore, quasi-2D model catalyst systems with flat Pd and Pt surfaces covered by a thin layer of CeO_x prepared by atomic layer deposition (ALD) were developed in an effort to investigate the impact of CeO_x thickness on the HOR activity, and dissolution stability, in alkaline media (Figure 13C).[212] Although an improved dissolution stability was observed on both CeO_x-covered Pt and Pd, only CeO_x-covered Pd was found to exhibit enhanced HOR kinetics. Compared to pure Pd, the CeO_x−Pd interface exhibited not only a 15-fold increase in exchange current density but also a 10-fold reduction in Pd dissolution. This improvement was mainly attributed to the presence of semipermeable CeO_x films, which facilitated the OH^- supply directly to adsorbed H at the interface and also suppressed the mass transfer of Pd ions within the oxide layer.

3.2.2.2. Ru-Based Catalysts. Ru has received intense attention as an HOR catalyst since its cost is significantly lower than that of Pt. The size-dependence of the HOR kinetics of Ru/C NPs was investigated by Satsuma et al.[213] with particle sizes ranging from 2 to 7 nm. The HOR/HER exchange current density of Ru/C exhibited a volcano shape with a maximum activity (∼65 $\mu A/cm^2$) at 3 nm. They proposed unsaturated Ru surface atoms as highly active sites for the HOR, but too large a fraction of unsaturated atoms decrease the activity because of their high susceptibility to oxidation. Wang et al. reported that a metastable face centered cubic (fcc) Ru/C showed enhanced HOR kinetics, relative to the hexagonal closest packed (hcp) Ru/C.[214] Luo et al. reported that phosphorous-doped Ru/C exhibited a 5-fold higher HOR activity as compared to Ru/C.[215] DFT calculations suggested that the P could modify the electronic structure of Ru with the possible switching of the RDS from the water formation to the water desorption step. Recently, Zhuang et al. investigated the effects of carbon supports on the performance of Ru/C as the hydrogen anode in AEMFCs (Figure 13D).[216] Ru NPs, supported on mesoporous carbon, achieved a peak power density of 1.02 W/cm^2, which is significantly higher than Ru NPs supported on bulklike carbon (0.76 W/cm^2) and even comparable to a Pt/C anode (1.01 W/cm^2). They proposed that the holey microstructure is relatively hydrophobic, which mitigates possible water flooding and facilitates the H_2 transport, and the mesoporous channel can confine Ru NPs for oxidation.

Ru can be alloyed with other metals to further enhance the HOR activity.[217−219] Recently, Abruna et al. reported on a class of HOR catalysts based on Ru−M/C (M = Co, Ni, Fe) prepared by a simple impregnation method.[220] The HOR kinetics of Ru/C could be significantly improved with a very low content (5%) of Co, Ni, or Fe, with the half-wave potential shifting by ∼40 mV. In particular, $Ru_{0.95}Co_{0.05}$/C exhibited the highest HOR performance among the Ru alloys studied, with a mass activity even outperforming Pt/C. DFT calculations indicated that the d-band center was downshifted, due to alloying effect, leading to a weakened H adsorption. Zhuang Z. et al.[221] recently developed an HOR catalyst based on $Ru_{0.7}Ni_{0.3}$/C alloyed NPs, synthesized via a hydrothermal approach. The Ru−Ni/C alloy catalyst exhibited HOR activity with 3-fold mass activity and 5-fold specific activity increases, respectively, at an overpotential of 50 mV, compared to even PtRu/C, although the specific exchange current density was not available for comparing its intrinsic activity. Yan et al. recently reported that a $Ru_{0.7}Ni_{0.3}$/C anode delivered a PPD of 2.03 and 1.23 W/cm^2 in H_2/O_2 and H_2/air at 95 °C, respectively, in MEA measurements. The improved HOR activity of $Ru_{0.7}Ni_{0.3}$/C was ascribed to the weakened H-binding with Ni alloying and strengthened water adsorption by the presence of Ni oxide species at the surface. Though this catalyst seemed to be very promising in AEMFCs, its HOR polarization curves exhibited significant decay at potentials more positive than 0.1 V, indicating its rapid passivation and poor stability under higher polarization of the hydrogen anode when operating at high current densities. Wei et al.[222] recently used urchinlike TiO_2 to partially confine Ru clusters in the lattice (Ru@TiO_2) in an effort to mitigate the oxidation of Ru at positive HOR polarization potentials. The Ru@TiO_2 catalyst is active for catalyzing the HOR at potentials up to

https://doi.org/10.1021/acs.chemrev.1c00331
Chem. Rev. XXXX, XXX, XXX−XXX

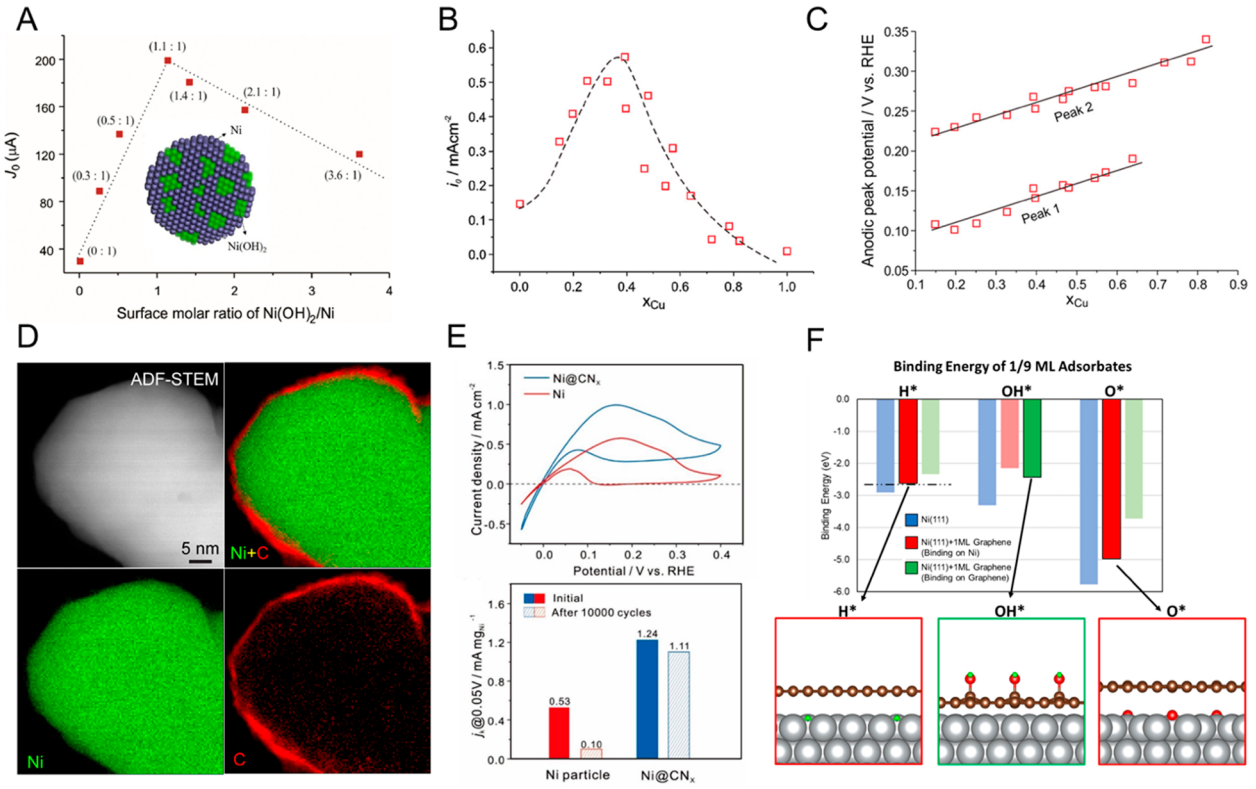

Figure 14. Recent progress on nonprecious HOR catalysts in alkaline media. (A) Relationship between HOR/HER exchange current (J_0) and surface coverage of $Ni(OH)_2$ over Ni of $Ni(OH)_2$/Ni/C catalysts, prepared by a three-step electrochemical treatment of Ni/C. A peak current can be found at a 1.1:1 ratio. The inset shows a model of a $Ni(OH)_2$-decorated Ni nanoparticle. (B) Relation between HER/HOR exchange current density (i_0) and Cu atomic ratio in Ni−Cu binary alloy thin-film electrodes, prepared by magnetron sputtering; the maximum can be observed at a Cu content of 40 atom %. (C) Anodic peak potentials with respect to Cu molar content in HOR polarization curves, indicating an increased tolerance toward oxidation; peak 1 corresponds to HOR and Ni−OH_{ad} formation while peak 2 indicates HOR and Ni−$(OH)_{2,ad}$ formation. (D) STEM-EELS analysis of a Ni@CN_x nanoparticle with an ADF-STEM image and Ni (green), C (red), and Ni + C composite mapping. The EELS mapping results indicate a uniform layer of carbon (~2 nm) coating a Ni core. (E) Comparison of HOR current density and stability between Ni@CN_x and Ni catalysts measured in H_2-saturated 0.1 M KOH solution at a rotation rate of 2500 rpm and scan rate of 5 mV/s; the Ni mass normalized HOR current density at lower positions was measured at 0.05 V after potential cycling between 0 and 0.5 V for 10 000 cycles at 100 mV/s. (F) Binding energy of HOR reaction intermediates (H*, OH*) and O* based on the Ni(111) and Ni(111)@graphene model. The blue, red, and green bars represent binding onto pristine Ni(111), Ni in Ni(111)@graphene, and graphene in Ni(111)@graphene, respectively. The bold colors describe the most stable state in the presence of the graphene layer over Ni(111). The dashed line indicates the optimal H binding energy. Green, red, and gold balls denote H, O, and C atoms in the three models below the chart, respectively. Panel A is reprinted with permission from ref 237. Copyright 2019 Elsevier. Panels B and C are reprinted with permission from ref 251. Copyright 2019 American Chemical Society. Panels D−F are reprinted with permission from ref 263. Copyright 2021 The Authors.

0.9 V vs RHE in both acid and base and showed strong anti-CO poisoning capabilities. The improved antioxidation and antipoisoning were claimed to be due to the formation of Ru−Ti bonds which facilitated electron transfer from electron-rich TiO_2 to the Ru metal, as indicated by XAS studies.

3.2.2.3. Ir and Rh-Based Catalysts. As shown in Figure 9F, Ir/C displayed the second highest HOR activity after Pt/C. The size effect of Ir/C NPs, ranging from 3 to 12 nm, was studied by Yan et al.[223] In this study, they deconvolved the H_{upd} regions in the CVs into different hydrogen binding sites and claimed that the HOR activity, normalized to the lowest hydrogen binding sites, showed little dependence on particle sizes, hypothesizing that these sites with low HBE are responsible for the HOR kinetics. Abruna et al. recently introduced a new family of Ir-based nanoparticles supported on carbon as HOR electrocatalysts in alkaline media.[224] A negative shift in the half-wave potential of more than 30 mV could be observed for Ir−Ru-based alloys compared to Ir/C and Ru/C (Figure 13E), indicating a synergy between Ir and Ru. Ir_3Ru_7/C and $Ir_3Pd_1Ru_6$/C exhibited the highest HOR activity but a much lower cost relative to Pt/C and Ir/C. Shao and Yi et al. designed IrNi@PdIr/C core−shell electrocatalysts by galvanic replacement reactions, which showed an enhanced HOR activity and stability relative to IrNi/C in alkaline media, owing to the PdIr overlayer lowering the hydrogen binding energy and mitigating Ni oxide formation.[225] By alloying with nonprecious secondary metals like Ni, Fe, and Co, Ir−Ni NPs displayed optimal HOR activities as a result of optimal interactions between the catalyst surface and hydrogen intermediates and an optimal oxophilic effect.[226,227] Even trace amounts of Ru or Fe, on the surface of Ir, could induce a modest adsorption of OH and result in improved HOR activity.[228] Recently, IrMo alloy nanocatalysts were shown to exhibit an HOR activity 5 times higher than that of Ir NPs and Pt/C,[229] which was ascribed to the bifunctional mechanism, in which the H_2O-adsorbed Mo sites on the IrMo surface could optimize the strength of H_2O_{ad} and OH_{ad}.

Wang and Abruna[230] have also developed a series of carbon-supported Rh and Rh−M alloy (M = Pt, Pd, Ir, Ru) NPs as efficient alkaline HOR catalysts (Figure 13F). The particle size

https://doi.org/10.1021/acs.chemrev.1c00331
Chem. Rev. XXXX, XXX, XXX−XXX

effect was first observed for Rh/C which exhibited enhanced HOR kinetics compared to the bulk Rh counterpart. In particular, Rh/C with a particle size of 2 nm (Rh/C-2) was identified as the most active among the studied catalysts in terms of mass activity. Alloying Rh with Ir and Pt was found to promote the HOR kinetics compared to Rh/C, Ir/C, and Pt/C, indicating that a synergistic effect exists in PtRh and IrRh alloy catalysts. The Pt_7Rh_3/C catalyst showed the optimal HOR activity in terms of specific activity and exchange current density (~1.2 mA/cm^2), even slightly higher than that of Pt_7Ru_3/C. In addition, Ir_9Rh_1/C exhibited the highest HOR activity among the studied Ir alloy particles. This study suggests that Rh and Rh-based alloy could be employed as active HOR catalysts in AEMFCs. Recently, Luo et al.[231] reported that rhodium phosphide (Rh_2P) with a P-terminated surface exhibited a high HOR activity, with an exchange current density (0.65 mA/cm^2) outperforming Rh/C (0.27 mA/cm^2) and Pt/C.

3.2.3. Nonprecious HOR Catalysts. The search for completely nonprecious HOR catalysts in alkaline media has been mainly focused on Ni-based materials, primarily because Ni represents the most active monometallic catalyst excluding PGM metals. However, the HOR kinetics on Ni remains low mainly due to its strong hydrogen adsorption.[232,233] Consequently, the Volmer step governs the reaction, and weakening the HBE of Ni represents the most important approach to enhance its HOR activity in alkaline media.

Partial oxidation was proven to be an effective strategy to improve the HOR kinetics of polycrystalline Ni.[234,235] A 10-fold enhancement in HOR/HER kinetics was reported after the formation of surface NiO upon air exposure.[234] The kinetic model indicated a shift of the reaction mechanisms from the Heyrovsky−Volmer on metallic Ni to Tafel−Volmer on an oxide-covered Ni surface. The partial coverage of Ni oxide on the electrode surface could lead to a decrease of the hydrogen binding strength, thus promoting the HOR activity with a diminution of the apparent activation energy from 30 to 26 kJ/mol.[235] Recently, Oshchepkov et al.[236] reported on the effect of NiO_x coverage on HOR kinetics on a polycrystalline Ni electrode by electrochemical oxidation. The HOR activity displayed a volcano shape with the maximum exchange current density (32.8 μA/cm^2) at 30% coverage, corresponding to a 14-fold enhancement, relative to metallic Ni. This observation was in agreement with a previous study on $Ni(OH)_2$/Ni/C from Zhuang and coworkers.[237] They also observed that the $Ni(OH)_2$-decorated Ni/C catalyst exhibited a "volcano plot" with an optimal surface $Ni(OH)_2$/Ni molar ratio of 1.1:1 and ~7-fold increase in the exchange current density relative to Ni/C (Figure 14A). Moreover, the stability of the catalysts was also enhanced with $Ni(OH)_2$ decoration. Consequently, Ni/C could be a promising HOR catalyst in alkaline electrolytes if the Ni NPs could achieve a high dispersion on the support with an optimal Ni/NiO_x ratio.[238,239] Hu et al.[240] reported that Ni/C, prepared by the pyrolysis of Ni-containing metal−organic frameworks, exhibited a mass-normalized exchange current density of 24.4 mA/mg. They proposed that the HOR activity enhancement originated from an optimal level of macro- and microstrains in the particles. Nevertheless, the calculated surface-area-specific activity was ~28.0 μA/cm^2, based on the estimation of the electrochemical surface area (ECSA), which was comparable to other studies,[239,241] indicating that the high mass activity observed in this study may be due to the small particle sizes (~5 nm). The improved HOR activity could also be achieved with stronger nickel−support interactions.[242,243]

Ni_3N was recently reported as a new type of Ni-based HOR catalyst.[244−246] Sun et al.[244] reported that the coating of Ni_3N on Ni NPs could boost both the HER and HOR performance. The superior performance was ascribed to the intimate contact between Ni_3N/Ni and a Ni foam substrate and facilitated mass transport resulting from the hierarchical structure. However, since the electrochemical measurements were conducted via linear sweep voltammetry, without rotation, rather than standard RDE measurements, it is difficult to make a comparison with other literature results. A similar Ni_3B/Ni catalyst was also reported to enhance the HOR kinetics, ascribed to the electron transfer from Ni_3B to Ni.[247] Hu et al.[245] reported the use of Ni_3N/C NPs with an average size of 4 nm as active HOR catalysts in alkaline media. The mass-normalized exchange current density reached 12 mA/mg even though the specific exchange current density was only 14 μA/cm^2. Meanwhile, Li et al.[246] also pointed out that the interstitial nitrogen doping in Ni_3N/C could weaken hydrogen adsorption and lower the activation barriers for the water formation step.

Another effective strategy to improve the intrinsic activity of Ni is through alloying with other metals. Copper is the most frequently employed metal to boost the HOR performance of Ni. Oshchepkov and Cherstiouk et al.[248,249] prepared a series of Ni−Cu bimetallic NPs supported on carbon and found an optimal content of Cu at 5 atom %. Similar observations were also reported by Atanassov et al.[250] However, achieving a higher level of Cu alloying was challenging given the phase separation at higher Cu contents.[248] In order to circumvent this challenge, Zhuang and coworkers[251] employed a high-throughput combinatorial magnetron sputtering method to prepare a series of Ni−Cu alloy thin films with uniform compositional distributions. This synthesis method also ruled out possible particle size effects, usually present in NPs, and enabled a comparison of samples with similar surface roughness. The XRD patterns together with XPS and XRF analysis confirmed a continuous change of Cu content from 0 to 100 atom % in Ni−Cu alloys. The Ni−Cu binary thin-film electrodes displayed a volcano-shaped HOR activity vs Cu content (Figure 14B). The maximum activity was found at 40 atom % Cu with a 4-fold enhancement in the exchange current density compared to pure Ni. Furthermore, the positive shift of the anodic peaks with Cu alloying indicated improved antioxidation properties of the Ni−Cu films (Figure 14C). This study suggested that the HOR activity of Ni−Cu-based NPs, with moderate Cu alloy content, could be further enhanced and provided a deeper understanding of the role of Cu on the HOR kinetics of Ni. The findings on Ni−Cu alloy film electrodes were supported by DFT calculations by Bonnefont et al.,[252] which predicted a significant reduction of hydrogen binding strength and a decreased activation barrier for the recombination process for a 50% Cu coverage on the surface. This may also help explain why 5% Cu was reported as the optimal content for Ni−Cu NPs[250] since Cu tended to surface segregate.[252] Additionally, Xu et al.[253] proposed that alloying Ni with Cu could modulate the electronic structure via ligand effects and downshift the d-band center, producing a variety of adsorption sites that could be close to the optimal HBE, although Ni−Cu in this work was intended for tuning the HER activity. Ni−Mo-based catalysts have also been explored with the purpose of weakening H adsorption.[254−256]

https://doi.org/10.1021/acs.chemrev.1c00331
Chem. Rev. XXXX, XXX, XXX−XXX

Yu et al.[257] reported the synthesis of Ni_4Mo and Ni_4W nanoalloys as efficient HOR catalysts in alkaline electrolytes. With higher loadings, the HOR performance of Ni_4Mo could outperform Pt/C in RDE polarization profiles; however, the real exchange current density was not available. The improved HOR reactivity was attributed to optimal H adsorption on Ni and OH adsorption on Mo or W. Ni supported on CeO_2 heterostructures was recently reported to exhibit an improved HOR performance in alkaline media.[258] DFT calculations suggested that the electron transfer between CeO_2 and Ni could lead to a thermoneutral free energy of hydrogen adsorption and facilitated hydroxyl adsorption through the oxygen-vacancy-rich CeO_2. With this heterostructure design, an exchange current density of 38 $\mu A/cm^2$ was achieved, corresponding to a 2.5-fold increase compared to Ni/C.

In addition to its low intrinsic HOR activity, another challenge of Ni-based catalysts arises from its susceptibility to oxidation at large overpotentials in hydrogen anodes in AEMFCs.[259] While a promising HOR activity can be observed in an RDE configuration, Ni catalysts easily undergo oxidation in MEA studies, leading to a rapid performance deterioration.[245,260] Though the stability could be possibly improved by partially covering the surface of Ni with $Ni(OH)_2$ species,[237] this electrochemical oxidation method is not practical for the large-scale production of hydrogen anode catalysts. One effective strategy is to weaken the interaction between Ni and surface oxygen species via Cr alloying[13] or W doping.[261] A core−shell architecture based on an h-BN shell was employed to protect the Ni core from oxidation, as reported by Bao and Zhuang et al.[259] According to DFT calculations, the interactions of H, O, and OH species with the subsurface Ni were weakened due to the presence of the h-BN shell. This structure not only suppressed Ni oxidation but also led to improved HOR activities with weakened hydrogen adsorption, to facilitate the Volmer step. In order to tackle the rapid surface passivation by the formation of Ni oxide(s) under HOR polarization conditions, we reported on a novel strategy to encapsulate metallic Ni nanocrystals with a 2 nm nitrogen-doped carbon shell ($Ni@CN_x$), as evidenced by atomic-scale STEM imaging and an EELS elemental mapping (Figure 14D).[262,263] The weakened O binding energy effectively mitigates the undesirable surface oxidation during HOR polarization, and the catalyst exhibited a significantly enhanced durability after 10 000 potential cycles (Figure 14E). The CN_x coating layer lowers the H-binding energy, close to the optimal value, as well as the O- and OH-binding energies, as supported by DFT simulations (Figure 14F). Moreover, the presence of N defects was believed to contribute to the enhanced electrocatalytic properties of $Ni@CN_x$ by anchoring Ni single atoms with pyridinic configurations. $Ni@CN_x$ exhibited a benchmark peak power density (PPD) of ~500 mW/cm^2, when paired with a Pt/C cathode, which represents the highest performance among non-precious-metal anodes in APEFCs reported to date (Figure 60I). In addition, $Ni@CN_x$ demonstrated a stable operation for over 20 h at 0.6 A/cm^2, superior to a Ni nanoparticle counterpart due to the enhanced oxidation resistance provided by the CN_x layer. Such durability represents a groundbreaking achievement for nonprecious HOR catalysts. Finally, $Ni@CN_x$ exhibited a dramatically enhanced tolerance to CO, relative to Pt/C, enabling the use of hydrogen gas with trace amounts of CO; critical for practical applications.

3.3. Summary

In this section, we have provided a detailed discussion regarding the Tafel−Heyrovsky−Volmer HOR/HER reaction mechanisms in acidic and alkaline media and possible activity descriptors, such as hydrogen binding energy and electronic and oxophilic effects. Interfacial water structures have been suggested to play an important role in the HOR/HER kinetics in alkaline media. We then presented an overview of nanoscale HOR electrocatalysts in alkaline media, including Pt-based, non-Pt PGM and nonprecious catalysts with several strategies to enhance the HOR activity and stability. In general, a promising HOR catalyst should exhibit high activity and durability and but also be low cost. Ru-based catalysts seem to be more promising than other PGM catalysts since they exhibit a superior HOR performance at a much lower cost. Nonprecious catalysts, especially Ni-based catalysts, have only a modest HOR activity, but their activity can be significantly enhanced by minimizing particle size and alloying with other metals or dopants. The durability of Ni-based catalysts has been effectively improved by surface coating strategies. One should also bear in mind that the HOR performances of the majority of studies were reported based on RDE measurements while very few reports have demonstrated MEA performance. For instance, when compared to Pt/C, PtRu/C shows a much higher HOR activity in room-temperature RDE measurements but only a minor performance enhancement in MEA studies when used as the hydrogen anode. We anticipate that advances in the fundamental understanding of HOR mechanisms will not only lead to high-performance nonprecious HOR electrocatalysts in AEMFCs but also contribute to the elucidation of the more complex multielectron ORR mechanisms (*vide infra*).

4. ORR ELECTROCATALYSIS IN ALKALINE MEDIA

4.1. Fundamentals of ORR Mechanisms in Acidic and Alkaline Media

The most significant challenge of fuel cell technologies is the development of electrocatalysts to accelerate the sluggish oxygen reduction reaction (ORR) at the cathode. Even Pt, the most active monometallic catalyst, still exhibits a large overpotential of 300−400 mV in order to achieve an appreciable current density (reaction rate) for the ORR. It is of fundamental importance to understand the reaction kinetics and mechanisms and establish design rules for ORR electrocatalysts with enhanced activity, selectivity, and durability. After more than 3 decades of extensive studies on ORR mechanisms,[155,264−266] while certain aspects are still being debated, a consensus has been reached on certain ORR pathways, key intermediates, and potential rate-determining steps (RDSs), which are deemed important. Here, we will review the general ORR mechanisms in both acid and base with an emphasis on well-defined single-crystal Pt electrodes. The use of single-crystal Pt surfaces greatly simplifies the complexity of the structure−activity relationship and has profoundly shaped and enhanced our fundamental understanding of the ORR mechanism.[267−269] The knowledge gained from single-crystal studies can be further extended to practical fuel cell catalysts in nanoparticle (NP) forms composed of terraces, steps, kinks, and/or random defects. Proposed mechanisms described here are supported by a variety of *in situ/operando* spectroscopic studies and further elucidated by detailed electrochemical kinetic studies, in

https://doi.org/10.1021/acs.chemrev.1c00331
Chem. Rev. XXXX, XXX, XXX−XXX

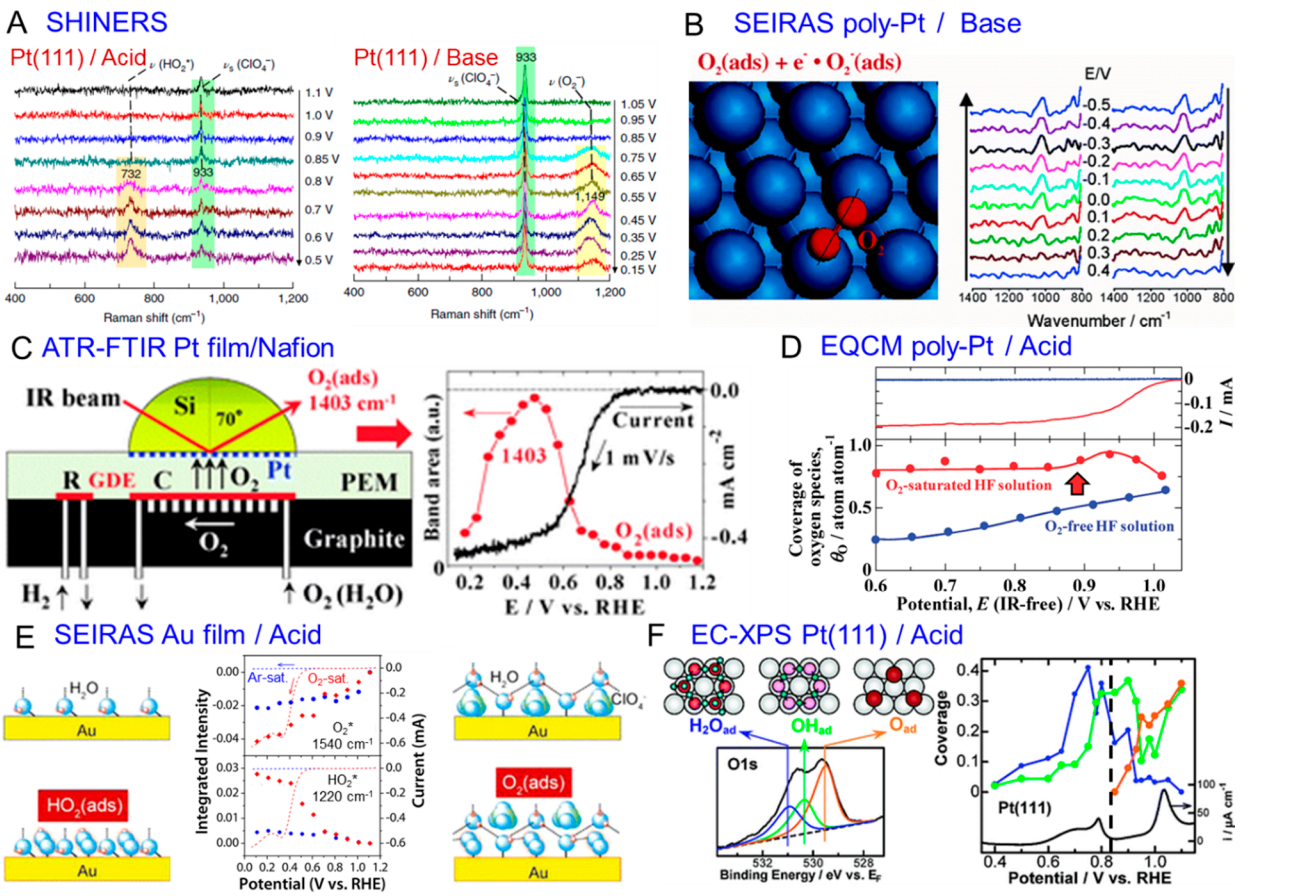

Figure 15. *In situ/operando* spectroscopic evidence of the ORR intermediates and reaction pathways. (A) *In situ* shell-isolated nanoparticle-enhanced Raman spectroscopy (SHINERS) of Pt(111) showing the key intermediates of HO_2* in acid and O_2^-* in base. (B) *In situ* attenuated total reflection surface-enhanced infrared reflection (IR) absorption spectroscopy (ATR-SEIRAS) of a Pt thin film in NaOH (pH = 11) showing the potential-dependent (vs Ag/AgCl) formation of O_2^-* in base (right) at ~1000 cm^{-1} and bridge-type adsorption geometry on Pt(111) based on DFT calculations (left). (C) *In situ* ATR Fourier-transform IR (ATR-FTIR) measurements at a Pt film/Nafion interface (left) and potential dependence of molecular O_2 adsorption on Pt surfaces (right). (D) Electrochemical quartz crystal microbalance (EQCM) measurements of the coverage of O-containing species (θ_O) in O_2-saturated and O_2-free HF solution. (E) *In situ* ATR-SEIRAS measurements of O_2 and HO_2 as well as ClO_4^- anion adsorption on Au(111) in O_2-saturated and Ar-saturated $HClO_4$. (F) Electrochemical X-ray photoelectron spectroscopy (EC-XPS) measurements of potential-dependent adsorption of H_2O, OH, and O on Pt(111). The left figure shows the structural models of adsorption on Pt(111) and the deconvolution of the O 1s spectra for a Pt(111) surface emersed from a N_2-saturated 0.1 M HF solution. The right figure shows the coverage of three types of O species and the CV profile of Pt(111) in 0.1 M HF (black). The dashed line indicates a 2/3 total coverage of H_2O and OH and nearly zero coverage of O at ~0.8 V vs RHE. Panel A is adapted with permission from ref 286. Copyright 2019 The Authors, Springer Nature. Panel B is adapted with permission from ref 289. Copyright 2006 American Chemical Society. Panel C is adapted with permission from ref 293. Copyright 2010 The Royal Society of Chemistry. Panel D is adapted with permission from ref 295. Copyright 2011 American Chemical Society. Panel E is adapted with permission from ref 291. Copyright 2012 American Chemical Society. Panel F is adapted with permission from ref 296. Copyright 2009 American Chemical Society.

particular, with rotating disk electrode (RDE) techniques.[270] With precisely controlled stepped Pt surfaces, we will systematically introduce the determining factors of ORR activity and fundamental properties of H and OH adsorption, including surface atomic arrangement, interfacial water structure, pH, temperature, and cations/anions in the electrolyte. Of particular interest is the newly emerged/realized importance of water structure at charged interfaces, which is nonetheless often neglected in traditional thermodynamic considerations of surface adsorptions due at least in part to great challenges in detecting the interfacial water as well as large-scale simulations of water on electrodes. Recent applications of surface-enhanced vibrational spectroscopy are providing a molecular picture of potential-dependent water orientation at charged interfaces. Finally, we will discuss efforts intended to accurately quantify the intrinsic properties of interfacial water with the potential of zero charge (pzc) and the potential of maximum entropy (pme) and correlate them to electrocatalytic activity.

General ORR mechanisms in acid and base are summarized in Scheme 2. Early studies of ORR mechanisms focused on acidic media, in part motivated by the development of PEMFCs. Early studies often used sulfuric or perchlorate acids since they are easier to purify than phosphoric acid. In acidic environments, O_2 can be reduced either completely to H_2O via a $4e^-$ process (E° = 1.229 V) or partially to H_2O_2 via a $2e^-$ process (E° = 0.695 V).[270−273] Both processes often occur concomitantly as competing reactions and determine the catalyst selectivity. The undesirably formed peroxide results in a lower energy density and can degrade the polymer membrane in fuel cells.[274,275] The first elemental step involves the adsorption of molecular O_2 (O_2*, Scheme 2, reaction a) on

https://doi.org/10.1021/acs.chemrev.1c00331
Chem. Rev. XXXX, XXX, XXX−XXX

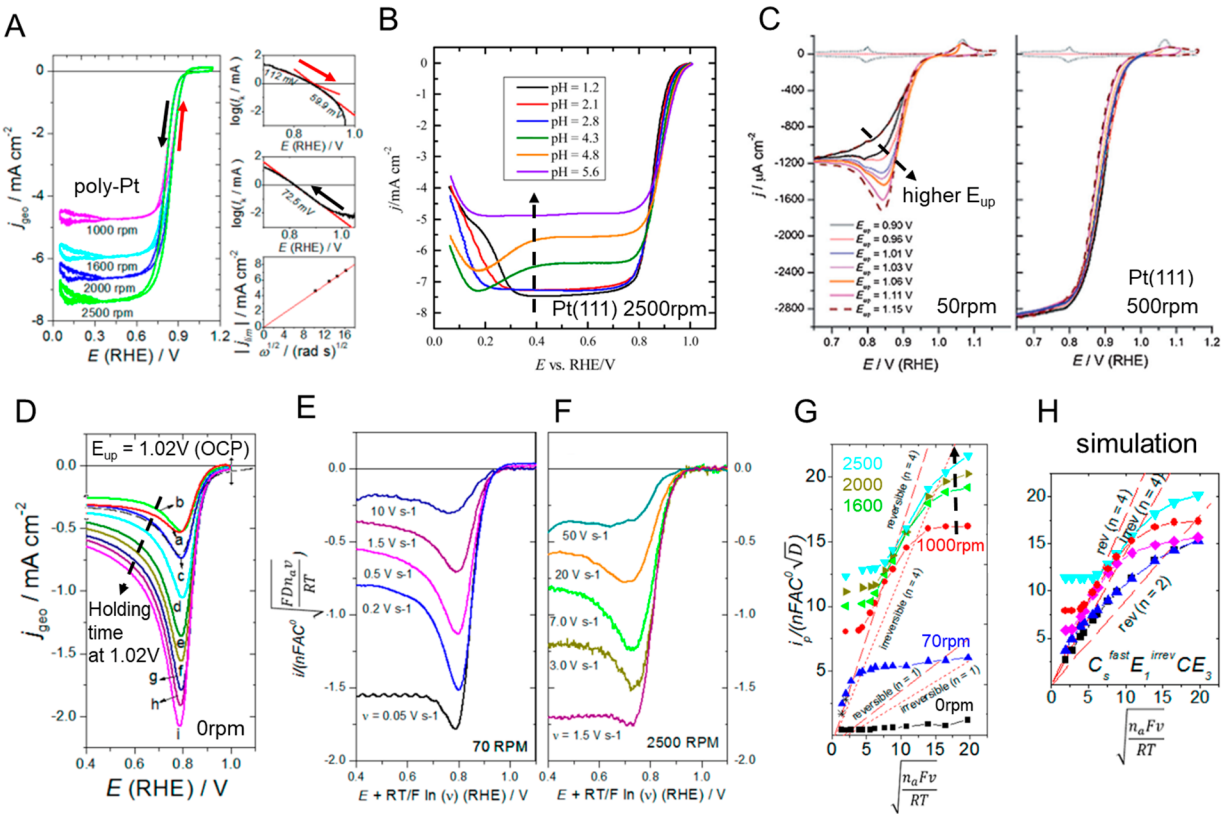

Figure 16. Electrochemical studies of ORR kinetics on Pt surfaces. The test solution is O_2-saturated 0.1 M $HClO_4$ for all following panels except B. (A) Rotating disk electrode (RDE) measurements of the ORR on a poly-Pt disk at 0.1 V/s and various rotation rates (left); corresponding Tafel plots in positive- and negative-going directions, respectively, and a Levich plot (j_{lim} vs $\omega^{1/2}$). (B) ORR polarization profiles of Pt(111) in O_2-saturated NaF/$HClO_4$ buffer solution at various pH values at 50 mV/s and 2500 rpm. (C) ORR profiles of Pt(111) with different upper potential limits (E_{up}) at 50 mV/s and 50 and 500 rpm, respectively. (D) Linear sweep voltammograms (LSVs) for the ORR on stationary poly-Pt after holding the potential at 1.02 V (OCP) for the various resting times from 0 to 120 s. (E, F) LSVs of normalized current, $j/(nFAC^{\circ}\sqrt{FDn\nu/RT})$, from background-subtracted negative-going scan profiles at 70 and 2500 rpm and various scan rates. (G) Normalized peak currents, $j_p/(nFAC^{\circ}\sqrt{D})$, against the square root of the normalized scan rate, $\sqrt{nF\nu/RT}$, for continuous LSVs during the ORR on poly-Pt at various scan rates and rotation rates from 0 to 2500 rpm. The potential was held at 1.02 V for 150 s before taking the LSVs. Theoretical linear curves for simple reversible (dashed) and irreversible (α = 0.5, dotted), charge transfers for n = 1 and 4. (H) COMSOL Multiphysics simulation of normalized peak current against the square root of the normalized scan rate for a $C_s^{fast}E_1^{irrev}CE_3$ mechanism. Symbols and dashed curves in panel H have the same meaning as in panels F and G. Panels A and E–H are adapted with permission from ref 276. Copyright 2019 American Chemical Society. Panel B is adapted with permission from ref 278. Copyright 2017 Elsevier. Panel C is adapted with permission from ref 301. Copyright 2013 Wiley. Panel D is adapted with permission from ref 277. Copyright 2018 American Chemical Society. All figures have Copyright by The Authors.

the metal surface. Traditionally, the adsorption energy of O_2 or O (ΔG_O) has been proposed as the preliminary descriptor to explain the volcano-type correlation of ORR activity for different metal surfaces (Figure 2A). An intermediate ΔG_O is expected to result in an optimal ORR activity, based on the Sabatier principle, and the scaling relationship between ΔG_O and ΔG_{OH}, since too weak of an oxygen adsorption impedes the kinetics of the first step, while too strong of an oxygen adsorption hinders the later removal of OH species. However, one should keep in mind that the volcano plots cannot predict the potential-dependent reaction rate, RDSs, or the significant effects of the electrolyte environment. In order to elucidate the complex nature of ORR mechanisms, it is highly desirable to couple spectroscopic and electrochemical studies.

Adsorbed O_2*, generated in step a, can convert into HO_2* (superoxide) through three different ways: (b) a concerted proton-coupled electron transfer process (PCET); (c, d) a decoupled electron transfer process forming O_2^{-}* (anion radical) followed by a fast protonation; (j, i) a fast surface chemical reaction with coadsorbed H_2O* generating another *OH followed by a fast irreversible electron transfer process ($C_s^{fast}E_1^{irrev}$),[276,277] which will be discussed in depth in kinetic studies in Figure 16. HO_2* is the central ORR intermediate in acidic media with a soluble nature and short lifetime. It has remained elusive until the very recent development of *in situ* surface-enhanced vibrational spectroscopy (Figure 15). The subsequent reactions of HO_2* split at a bifurcation point:[278,279] (e–g) a chemical process to *OH and O* followed by the conversion from O* to *OH; (f–h) a PCET process to H_2O_2 (peroxide) followed by the O–O breaking process to form two *OH. The final step is an irreversible PCET process of *OH and conversion to H_2O. Among those multiple O-containing species, O_2^{-}*, HO_2*, and H_2O_2* have the potential to diffuse into solution and establish an ad-/desorption equilibrium with the corresponding soluble species (k–m). In particular, HO_2 can disproportionate into H_2O_2 and O_2 (n), and H_2O_2 can go through a similar process to produce H_2O and O_2 (o). Neither process involves electron transfer and thus will cause a loss of Faradaic efficiency in the overall ORR. The electrogeneration of soluble H_2O_2 has been

https://doi.org/10.1021/acs.chemrev.1c00331
Chem. Rev. XXXX, XXX, XXX–XXX

extensively studied by rotating ring disk electrode (RRDE) and has been shown to be minimal on Pt[273] but dominant on Au in acidic media.[41]

Although the ORR mechanism in base is not as well understood as in acid, similar reaction pathways have been proposed and are summarized in Scheme 2 (lower part). In proton-deficient alkaline environments, O_2 is reduced to OH^- via a $4e^-$ process or to HO_2^- via a $2e^-$ process. It is important to note that H_2O, is the dominant proton donor for the PCET in base while H^+ (H_3O^+) is the dominant proton donor in acid.[280,281] Equally importantly, H_2O is a reactant in base while H_2O is a reaction product in acid, which leads to a fundamental difference in water management in AEMFCs vs PEMFCs, which will be discussed in detail in MEA studies in section 7). In contrast to acidic environments, O_2^{-}* (superoxide anion radical) and HO_2^- (superoxide anion) are the dominant species in base, considering that the pK_a values of HO_2 and H_2O_2 are 4.7 and 11.6, respectively.[282] In weak base (pH = 8−11), a significant amount of H_2O_2 will coexist with HO_2^-. O_2^- can go through a similar bifurcation process to form *OH by either chemical (iii, v) or electrochemical (iv, vi) processes. During the ORR, the interfacial pH can be dramatically different from the bulk pH in weak acid (pH = 3−6) or base (pH = 8−11) without buffer capability, since H^+ is constantly consumed, or OH^- is constantly produced. For instance, it has been reported that the ORR rate of Pt(111) is limited by the proton concentration in unbuffered $HClO_4$/$NaClO_4$ (pH = 2.5−4).[39,283] As the ORR rate increased and consumed protons more quickly, the interfacial pH gradually increased to be above 7, and the overall reaction transformed from $O_2 + 4H^+ + 4e^- \leftrightharpoons 2H_2O$ to $O_2 + 2H_2O + 4e^- \leftrightharpoons 4OH^-$. In contrast, the interfacial pH can also be well controlled to be close to the bulk pH value with buffer solutions with weak or no specific adsorption of anions such as NaF/$HClO_4$ and NaF/NaOH to reliably study the effect of pH on the ORR activity of Pt (Figure 16B).[278]

4.1.1. *Operando/in Situ* Spectroscopic Studies of ORR Mechanisms. Recent developments of *in situ/operando* spectroscopy have enabled the direct detection of surface-adsorbed reaction intermediates under electrochemical conditions. O-containing species during the ORR are generally challenging to study due to their low concentration, short lifetime, and similarity among coadsorbed species and surrounding water. Benefiting from greatly enhanced vibrational signals (by factors up to 10^8), due to localized surface plasmons on nanostructured metals,[284] surface-enhanced vibrational techniques, including surface-enhanced Raman spectroscopy (SERS) and surface-enhanced infrared absorption spectroscopy (SEIRAS), serve as powerful diagnostic tools to probe the identity of O-containing species at the electrode−electrolyte interface under operating conditions.

While the surface-enhanced effects have been known for decades, their application to the study of the ORR has been mainly on polycrystalline thin films of Au and Pt, in order to exploit the plasmonic excitation effect.[285] However, the recently developed shell-isolated nanoparticle-enhanced Raman spectroscopy (SHINERS) has expanded such studies to SERS-inactive electrodes, such as single-crystalline surfaces and alloy NPs.[286−288] Meanwhile, density-functional theory (DFT) simulations have often been employed to assist with the band assignment in vibrational spectroscopy and identification of specific adsorption sites and configurations. With well-defined surface structures and their compatibility for atomic-level modelling, Pt single crystals serve as a model platform to bridge the *in situ* vibrational spectroscopy and theoretical simulations.

In situ SERS showed compelling evidence for the existence of HO_2* in acid and O_2^{-}* in base on Pt single crystals. Li and coworkers recently employed SHINERS to probe various O-containing species during the ORR (Figure 15A).[286] In acidic media, Pt(111) exhibited a new Raman peak at 732 cm^{-1} below 0.85 V vs RHE, which was assigned to HO_2*, based on H/D isotopic experiments. H_2O_2 was ruled out since it would be immediately reduced to H_2O at such potentials. Similarly, HO_2* was identified by the same group on stepped Pt single crystals and Pt_3Co NPs.[287,288] In contrast, Pt(100) and Pt(110) showed no evidence of HO_2* but instead *OH, which was ascribed to the lower dissociation energy barrier of HO_2* on those surfaces compared to Pt(111). In alkaline media, Pt(111), as well as (100) and (110), only showed O_2^{-}* at ∼1150 cm^{-1} below E < 0.85 V, which was based on the absence of H/D but presence of ^{18}O isotopic effects. Similarly, an early *in situ* SEIRAS study by Adzic and coworkers identified the existence of O_2^{-}* on Pt thin films in base and its top−bridge−top configuration on Pt(111) based on DFT calculations (Figure 15B).[289] A very recent study by Feliu et al. detected the presence of O_2^- on Pt(111) in O_2-saturated NaF/$HClO_4$ solution (pH = 5.5) based on the observation of a O−O vibrational band at ∼1080 cm^{-1} using *in situ* external infrared reflection absorption spectroscopy (IRRAS).[290] *In situ* SEIRAS on Au(111) by Yagi and coworkers further identified HO_2* in acid at 1220 cm^{-1}, and its coverage continued to increase as the potential decreased from 1.0 to 0.1 V (Figure 15E),[291] which was consistent with a previous SERS study by Gewirth and coworkers.[292]

Adsorbed molecular O_2* was identified on Pt thin films with a proton exchange membrane, Nafion, by *in situ* attenuated total reflection Fourier-transform infrared spectroscopy (ATR-FTIR) (Figure 15C).[293,294] The IR peak at 1403 cm^{-1} achieved a maximum amplitude at ∼0.5 V vs RHE and was assigned to O_2*, given its absence in the N_2 environment, insensitivity to H/D isotopic experiments, and stability at potentials up to 1.1 V, which ruled out the possibility of O_2^{-}*. The presence of weakly adsorbed O_2* (1468 cm^{-1}) on commercial Pt/C catalysts under ORR conditions has also been reported.[294] Similarly, O_2* was detected on Au(111) in acids with the coadsorption of H_2O and ClO_4^- and showed a higher intensity in O_2-saturated solution, relative to a N_2 environment (Figure 15E).[291] In contrast to O_2* on Pt, its coverage on Au continued to decrease at lower potentials. It is worth pointing out that, for free O_2, as a mononuclear diatomic molecule, IR transitions are forbidden, but its adsorption on electrode surfaces may induce a dipole moment due to electron transfer and interfacial electric fields, allowing some transitions. Additional quantitative information about the surface has been revealed by an *in situ* electrochemical quartz crystal microbalance (EQCM) with nanogram-level sensitivity of mass changes at the surface (Figure 15D).[295] The coverage of O-containing species (θ_O) in O_2-saturated HF was much higher than that in He-saturated HF, which was similar to the difference in $HClO_4$. However, θ_O in O_2-saturated HF reached ∼0.8 at 0.6 V, much higher than that in O_2-saturated $HClO_4$ at 0.6 V (θ_O = ∼0.5), which was ascribed to the much lower $[H^+]$ in weak acid HF, hindering the consumption of O-containing species. To overcome the lack of chemical information in EQCM, Watanabe et al. employed electrochemical X-ray

https://doi.org/10.1021/acs.chemrev.1c00331
Chem. Rev. XXXX, XXX, XXX−XXX

photoelectron spectroscopy (EC-XPS) to identify and quantify each type of O-containing species at various potentials (Figure 15F).[296,297] One needs to be aware that the EC-XPS study described here involved the transfer of the electrode from solution to an ultrahigh vacuum (UHV) chamber under potential control and subsequent freeze-evacuation of bulk electrolyte in order to maintain the surface adsorbates. HF instead of $HClO_4$ was used to obtain O 1s spectra of reaction species without solution interference. The coverage of H_2O^* on Pt(111) increased as the potential rose from 0.4 to ~0.8 V and then decreased afterwards. θ_{OH} appeared at $E < 0.6$ V, consistent with the onset of OH formation in the "butterfly" region, while θ_O started to increase after 0.9 V, which coincided with the onset potential of Pt−O formation from Pt−OH oxidation. Remarkably, EC-XPS estimated that the total coverage of coadsorbed H_2O and OH achieved a maximum of ~2/3 as indicated by the dashed line (Figure 15F), which is a typical value for maximum coverage of O species from electrochemical measurements on Pt.[264] The structure of mixed OH/H_2O layers will be discussed in detail in Figure 18B. A nearly zero coverage of H_2O^* was found at 0.4 V in Figure 15F, which we believe underestimates the true coverage of H_2O. When E is close to the potential of zero free charge (pzfc) of Pt(111) (~0.28 V vs SHE), interfacial water adsorbs weakly on Pt and behaves more disordered like bulk water and may easily escape during freeze evacuation. In summary, *in situ/operando* spectroscopic studies, together with theoretical simulations and isotopic experiments, have unambiguously identified key reaction intermediates including O_2^*, H_2O^*, HO_2^* (acid), O_2^{-*} (base), *OH, etc., and investigated their potential-dependent coverages and interactions with other coadsorbed species. Such *in situ* studies support the ORR mechanisms in Scheme 2. Nonetheless, it is worthwhile to point out that the ORR is a complex electrochemical reaction which can follow different mechanisms at the molecular level, depending on the experimental conditions such as electrode surface structures, potentials, pH, electrolyte, etc.

4.1.2. Electrochemical Studies of ORR Kinetics at Rotating Disk Electrode (RDE). The ORR kinetics have been extensively investigated with electrochemical measurements using rotating disk electrode (RDE) techniques, and the most representative advances are presented here. Figure 16A shows the typical RDE polarization profiles of poly-Pt at various rotation rates.[276] Poly-Pt exhibits a kinetically controlled region with an onset potential (E_{onset}) at ~1.0 V and approaches a mass transport limit at $E < 0.75$ V. The diffusion-limited current (I_{lim}) follows the Levich Equation.

$$I_{lim} = 0.62nFAD^{2/3}\omega^{1/2}\upsilon^{-1/6}C^{o}_{O_2} \quad (8)$$

where n is the electron transfer number, F is Faraday's constant, A is the electrode area, D is the diffusion coefficient, ω is the rate of rotation, υ is the kinematic viscosity, and $C^{o}_{O_2}$ is the bulk O_2 concentration. On poly-Pt in 0.1M $HClO_4$, n was calculated to be ~4.0 from the slope of the diffusion-limited current density (j_{lim}) vs $\sqrt{\omega}$ plot (Figure 16A lower right), indicating a minimal amount of peroxide (H_2O_2 % < 1%). At $E < 0.3$ V, the current density drops below j_{lim} with a concomitant increase in the peroxide yield, initially indicating that H_{ads} may partially block the surface active sites, resulting in a larger contribution of the $2e^-$ process. However, a recent study of the H_2O_2 reduction reaction on Pt(111) suggested that the inhibition of H_2O_2 reduction, at more negative potentials, is not dependent on the hydrogen adsorption process but rather the interface water reorganization and the pzfc.[298] It is intriguing to observe a transition in the Tafel slope from 60 to ~120 mV/dec at ~0.9 V as the overpotential increases to drive a higher current density in the positive-going direction, but a constant Tafel slope at ~70 mV/dec in the negative-going direction (Figure 16A, right plots). The mechanisms responsible for the transition from 60 to ~120 mV/dec are still under debate. Damjanovic and coworkers initially proposed it as due to a change from a Temkin-type to a Langmuir-type adsorption mechanism since the O-containing species is gradually desorbed at larger overpotentials.[299,300] However, previous spectroscopic studies showed that a significant number of O-containing species still exist between 0.8 and 1.0 V vs RHE,[264,296] which questioned the validity of using a simplified Langmuir adsorption mechanism to explain the Tafel slope of 120 mV/dec at such potentials.

ORR polarization profiles for Pt(111) at various pH values were recorded at 2500 rpm in $HClO_4$/NaF buffer solution to maintain a stable pH at the interface (Figure 16B).[278] A significant diminution of the j_{lim} was observed as the pH increased from 1.2 to 5.6 ($[H^+]$ decreased from 63 mM to 2.5 μM). This seems to arise from a higher peroxide yield at higher pH, or the ORR simply being limited by the proton concentration. However, careful RRDE experiments clearly showed no increase in the peroxide yield despite the higher pH, and RDE experiments with different oxygen partial pressures suggested that the limiting factor was O_2 rather than H^+.[278] The electrochemical reduction from HO_2^* to $H_2O_2^*$ requires one proton and one electron (Scheme 2, reaction f), and thus, its kinetics would be slowed down at higher pH. Concomitantly, a larger portion of HO_2^* would go through chemical disproportionation (DISP) (Scheme 2, reaction n), which would lead to a loss of Faradaic efficiency and thus a diminution of the j_{lim} at higher pH. Therefore, the progressive decay of j_{lim} at higher pH supported the existence of the aforementioned bifurcation point with the transition from HO_2^* to peroxide in Scheme 2.[298,299] Further electrochemical evidence for the soluble nature of HO_2 was revealed by adjusting the upper limit potentials (E_{up}) from 0.9 to 1.15 V (Figure 16C).[301] At a slow rotation rate of 50 rpm, the peak reduction current density (j_p) in the negative-going scan noticeably increased at higher E_{up}. In contrast, no current overshoot was observed at a faster rotation rate of 500 rpm. These results suggested that a soluble intermediate was generated and accumulating above 1.0 V, which would go through electrochemical reaction at $E < 0.9$ V. Moreover, linear sweep voltammograms (LSVs) after holding at an E_{up} of 1.02 V [open circuit potential (OCP)] showed a sequential increase of j_p as the holding time increased from 0 to 1, 5, 15, 30, 45, 60, 90, and 120 s (labeled as a−h in Figure 16D, respectively).[277] In summary, those electrochemical measurements clearly suggest the existence of HO_2^* and its equilibrium with soluble HO_2 before participating in further electrochemical or chemical reactions.[302]

Feliu, Gómez-Marín, and coworkers recently reported an in-depth electrochemical analysis of the multielectron ORR mechanism by adjusting scan rates and rotation rates systematically with the RDE and digital simulations (Figure 16E−H).[277] Based on Randles−Ševčik equations, j_p in LSVs should be proportional to $\sqrt{\nu}$ for fast or slow 1e transfer or n-e transfer with a first electron transfer as the RDS.

https://doi.org/10.1021/acs.chemrev.1c00331
Chem. Rev. XXXX, XXX, XXX−XXX

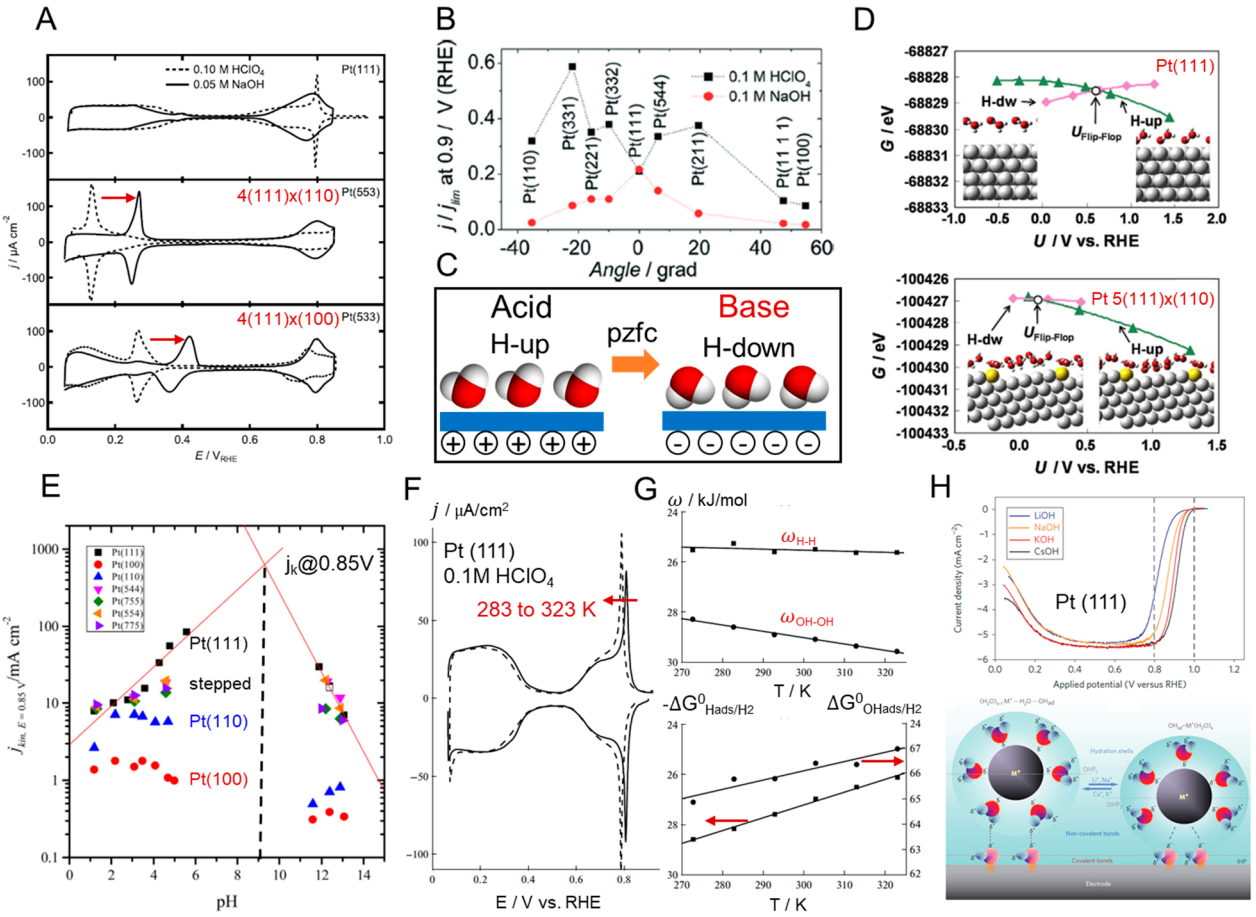

Figure 17. Effects of Pt surface structures and environments on H/OH adsorption and ORR activity. (A) CV profiles of Pt(111), Pt(553), and Pt(533) in acid and base at 50 mV/s. Red arrows indicates the positive shift of H peaks on (110) and (100) steps from acid to base. (B) Normalized ORR current, j/j_{lim} at 0.9 V during the positive-going scan on Pt single crystals in acid and base at 50 mV/s as a function of the angle of the surface normal to the (111) direction. (C) Simplified schematic of water orientation at a charged Pt(111) surface. Given the potential of zero free charge (pzfc) of Pt(111) at 0.28 V vs SHE, the Pt(111) surface contains positive charges in acid and negative ones in base, respectively, under typical fuel cell operation potentials (0.7−1.0 V vs RHE), which leads to preferential H-up and H-down water configurations in acid and base, respectively. (D) Free energies and structures of interfacial water on Pt(111) and Pt(332) [5(111) × (110)]. $U_{Flip\text{-}Flop}$ is defined as the potential at which water reorientates from H-down (H-dw) to H-up structures. (E) Activity plots of the kinetic current density, j_k, at 0.85 V vs RHE on Pt single crystals as a function of pH, which were measured by the RDE in O_2-saturated NaF/$HClO_4$ and NaF/NaOH buffer solution at 50 mV/s and 2500 rpm. The straight lines correspond to the pH-dependent activity of Pt, and the dashed line indicates that the optimal activity of Pt(111) occurs at a pH of ∼9. The open square corresponds to Pt(111) in a NaOH/NaF mixture. (F) CV profiles of Pt(111) in Ar-saturated 0.1 M $HClO_4$ at 283 K (solid line) and 323 K (dashed line) recorded in an isothermal cell at 50 mV/s. (G) Interaction energy parameter and standard Gibbs free energy of H_{ads} and OH_{ads} on Pt(111) in 0.1 M $HClO_4$. (H) CV profiles of Pt(111) in 0.1 M MOH where M is Li, Na, K, or Cs at 20 mV/s. Panel A is adapted with permission from ref 153. Copyright 2013 The Authors, Elsevier. Panel B is adapted with permission from ref 264. Copyright 2014 The Authors, The Royal Society of Chemistry. Panel C Copyright by the Author. Panel D is adapted with permission from ref 318. Copyright 2014 Elsevier. Panel E is adapted with permission from ref 278. Copyright 2017 The Authors, Elsevier. Panels F and G are adapted with permission from ref 323. Copyright 2012 The Authors, Springer. Panel H is adapted with permission from ref 320. Copyright 2009 Springer Nature.

$$j_p = 0.446nFAC^{\circ}_{O_2}\sqrt{\frac{nFD\nu}{RT}} \quad \text{(fast/reversible)} \tag{9}$$

$$j_p = 0.496nFAC^{\circ}_{O_2}\sqrt{\frac{\alpha nFD\nu}{RT}} \quad \text{(slow/irreversible)} \tag{10}$$

where n, F, $C^{\circ}_{O_2}$, and D are the same as in eq 8; R and T are the ideal gas constant and temperature; and α is the transfer coefficient for a slow irreversible process ($j_{p,slow}/j_{p,fast}$ = 0.78 for α = 0.5). However, Figure 16E,F shows that the normalization of current to $\sqrt{\nu}$, $j/(nFAC^{\circ}\sqrt{FDn\nu/RT})$, did not result in a constant but rather in a decrease as ν increased from 50 mV/s to 10 V/s. Moreover, a plot of $j/(nFAC^{\circ}\sqrt{D})$ against normalized scan rate, $\sqrt{nF\nu/RT}$, at 70 rpm (blue line in Figure 16G) exhibited a linear correlation for slow scan rates but a leveling of the reduction current as $\sqrt{nF\nu/RT}$ passed a threshold value of ∼5, corresponding to ν of ∼1 V/s. The initial linear correlation suggests a charge-transfer process as the RDS, while the later leveling of the reduction current at faster ν indicates that the reaction rate is limited by a chemical reaction instead of a charge transfer step. In other words, the chemical reaction rate can no longer keep up with the growing charge transfer rate at faster ν, which thus results in a maximum "kinetic current". During RDE experiments, a fast ν and slow ω, including a stationary electrode with no rotation, dictate a transient condition while a slow ν and fast ω (e.g., 50 mV/s, 1600 rpm) define a steady-state condition controlled by

https://doi.org/10.1021/acs.chemrev.1c00331
Chem. Rev. XXXX, XXX, XXX−XXX

convection. LSVs at 2500 rpm showed a significantly larger normalized j_p, relative to 70 rpm, at the same scan rates (Figure 16E,F). Figure 16G reveals that $j/(nFAC^{\circ}\sqrt{D})$ vs $\sqrt{nF\nu/RT}$ at ω > 1000 rpm shows a similar transition from a linear correlation to a leveling of the reduction current as 70 rpm, but the $\sqrt{nF\nu/RT}$ threshold increased from ∼10 to ∼20 as ω increases from 1000 to 2500 rpm. This ω-dependence of normalized j_p under transient conditions at fast ν can only be explained by the diffusion layer being controlled by a chemical reaction preceding a charge transfer step (i.e., a CE mechanism, *vide infra*) since a charge-transfer-controlled RDS would predict a linear $j_p - \sqrt{\nu}$-dependence and no ω-dependence. Additionally, a theoretical linear relation of normalized j_p vs $\sqrt{\nu}$ was calculated based on eqs 9 and 10 for both $4e^-$ and $1e^-$, fast reversible and slow irreversible processes assuming α = 0.5. Figure 16G clearly shows the deviation from the $4e^-$ process as ν increases, and LSVs at 70 rpm and stationary cases can even reach a $1e^-$ process or below; this requires higher ν to deviate LSVs at faster ω from the $4e^-$ process. The half-life time ($\tau_{1/2}$) of soluble HO_2* was estimated to be 1−2 ms based on the transition of normalized current from a linear relation to current plateau occurring at 10−20 V/s (Figure 16G), which corresponds to a diffusion distance of ∼3 μm before reacting, often too short to be detected by normal RRDE measurements.

On the basis of those observations, the COMSOL Multiphysics simulation package was used to study the normalized j_p vs $\sqrt{\nu}$ behavior for CE, ECE, and CECE mechanisms (C and E stand for chemical and electron transfer processes, respectively). The CECE mechanism in Figure 16H resembled the main features of the experimental observations in Figure 16G. In comparison, the CE mechanism failed to address the leveling of j_p at fast ν, and the ECE could not explain the ω-dependence. The proposed $C_s^{fast}E_1^{irrev}CE_3$ mechanism is a fast surface chemical reaction ($k_{forward}$ = 1 × 10^7 M^{-1} s^{-1}) preceding an irreversible one-electron transfer reaction followed by another first-order chemical reaction (k = 1 × 10^2 s^{-1}) and a second multistep $3e^-$ charge transfer reaction. The thermodynamic potential of the E_1 is more positive than that of the E_3 given that only one peak exists in the LSVs. The C_s^{fast} preceding E_1^{irrev} reactions were described in reactions j and i in Scheme 2, indicating the possibility of HO_2* formation without direct electron transfer. The following C and E_3 steps can be reactions e and reactions g and i, respectively. This CECE mechanism offers another explanation for the changes in Tafel slopes from 60 to 120 mV/dec in Figure 16A. The O−O bond breaking of HO_2* in reaction e will be the RDS at low overpotentials when free Pt sites limit the reaction rate. At high overpotentials, more Pt sites are available so that the RDS is no longer chemical step e but rather a previous charge transfer step E_1^{irrev} (i), which explains well the Tafel slope of 120 mV/dec, a characteristic value for the $1e^-$ RDS.[131,303] The exact nature of CE_3 is challenging to determine since those steps are likely after the RDS. Other possible CE_3 steps could also be the fast protonation of O_2^- (reaction d) followed by the PCET process of HO_2* to H_2O_2* and H_2O (reactions f, h, and i). It is important to notice the mismatch between experiments in Figure 16G and simulation results in Figure 16H, especially for slow ν or for the absence of rotation at faster ν (blue and black lines). This difference can be explained by a possible existence of parallel competing reactions in the diffusion layer, which can cause a faster current decay in experiments and loss of Faradaic efficiency as seen in the Levich plot.[304] It is likely that the competing processes are the disproportionation of HO_2 and/or H_2O_2 (reactions n and o in Scheme 2). In summary, comprehensive electrochemical measurements and digital simulations, for the first time, offer a clearer explanation of the complex CECE/DISP mechanisms for the ORR and point out the important, soluble, and short-lifetime nature of HO_2*. Again, the ORR is a complex reaction involving many steps, and the specific experiments described here illustrate the influence of different rate-controlling steps/intermediates.

4.1.3. ORR Activity of Pt Single Crystals and Effects of Steps, pH, Cation, and Temperature. With a fundamental understanding of the ORR kinetics and mechanisms, we now extend our discussions to the structural and environmental factors governing ORR activity, including the surface atomic arrangements (terraces and steps), pH and cation/anion adsorption, temperature effects, and, in particular, the interfacial water structure at charged interfaces. The CV profile of Pt(111) in 0.1 M $HClO_4$ shows characteristic H and OH ad-/desorption peaks separated by a double-layer region from 0.4 to 0.6 V vs RHE (Figure 17A).[153] OH_{ads} ad-/desorption in acid shows a broad prepeak from ∼0.6 to ∼0.75 V and a sharp reversible peak at ∼0.8 V, which are associated with the dissociation of bulk icelike water with repulsive H_2O/OH interactions and isolated solvation water surrounding anions with attractive interactions following the Frumkin isotherm.[305−307] In contrast, only a broad OH peak was observed in base, indicating larger repulsive lateral interactions. Single-crystal Pt(553) [4(111) × (110)] and Pt(533) [4(111) × (100)], with 4(111) terraces every (110) and (100) step, respectively, exhibit much sharper ad-/desorption peaks in the hydrogen regions (Figure 17A), relative to Pt(111). Those hydrogen peaks shifted to more positive values in base, which was ascribed not to H_{ads} but to the replacement of H_{ads} by OH_{ads} on steps as previously discussed in section 3.1.3.

Figure 17B presents a comprehensive summary of ORR activities of different stepped and low-index Pt surfaces.[264,308,309] Early RDE studies showed that the ORR activity of Pt decreased in the order (110) > (111) > (100) in 0.1 M $HClO_4$ and (111) ≫ (110) > (100) in 0.1 M NaOH and ascribed the lower activity of Pt(100) to the relatively stronger inhibitory effects of OH_{ads}, which block Pt sites available for O_2 adsorption.[310,311] In acid, it is well-established that the ORR activity increases with higher step density, and stepped Pt surfaces are much more active than the three low-index planes (black profile, Figure 17B). Those observations in model electrodes have stimulated extensive efforts to prepare Pt-based shape-controlled ORR NP electrocatalysts with high index facets.[312−314] Theoretical simulations ascribed the higher ORR activity on the stepped surface to the lower OH adsorption energy and smaller coordination number on (110) or (100) steps.[315,316] The (110) basal plane, despite having the highest step density as [2(111) × (111)], showed a lower activity than other stepped surfaces [n(111) × (111) or (n − 1)(111) × (110)] (n < 2), which was ascribed to too weak OH and O adsorption energies.[315,316] However, such thermodynamic approaches with $\Delta G_{OH_{ads}}$ failed to explain the significant difference in ORR activity trends between acid and base. Specifically, Pt(111) exhibits the highest ORR activity when compared to all stepped surfaces in base, and the addition of (110) or (100) steps next to (111) terraces only caused a

https://doi.org/10.1021/acs.chemrev.1c00331
Chem. Rev. XXXX, XXX, XXX−XXX

monotonic activity decay (red profile, Figure 17B). Structural factors, such as the coverage of O-containing species and pztc, have also not resulted in satisfying explanations for the differences between acid and base.[264,317] It is possible and likely that other significant changes in the near-surface environment must not have been considered yet. For example, on Pt(111), the interfacial water structure in acid and base can be fundamentally different (Figure 17C). The pzfc of Pt(111) is 0.28 V vs SHE and pH-independent, which is closely related to the water orientation on surfaces (an in-depth discussion of the pzfc will be covered in section 4.1.5). Under typical ORR conditions (0.7−1.0 V vs RHE), the ORR occurs over the range 0.64−0.94 V vs SHE in 0.1 M acid (e.g., $HClO_4$) but over −0.07 to 0.23 V vs SHE in 0.1 M base (e.g., NaOH). Thus, a Pt(111) surface will carry a positive net charge in acid and induce an H-up O-down water orientation while it will exhibit a negative net charge in base and form an H-down O-up water configuration. Similar changes in water dipole moments on Pt(111) and stepped Pt(332) [5(111) × (110)] surfaces were reported with DFT calculations with a modified Poisson−Boltzmann (MPB) theory by combining an explicit water adlayer and modeled continuum electrolyte (Figure 17D).[318] DFT-MPB simulation showed that the potential of water orientation ($U_{flip\text{-}flop}$) on a stepped Pt(332) surface was ∼0.4 V more negative than on Pt(111), which is consistent with the experimental difference in pzfc values (Figure 17B). Two structural effects of (110) steps have been proposed to explain the higher ORR activity of stepped Pt(332) in acid but lower activity in base: (1) (110) steps in Pt(332) can stabilize the H-up structure more strongly than Pt(111) in acid by forming an extended H-bonded network on the step and thus destabilizing the OH adsorption and facilitating the removal of OH from the surface. Such an effect does not exist in base since water has an H-down O-up orientation. (2) (110) steps can disrupt the overall H-bonded water network near the surface in acid and lead to a higher mobility of solution species through the water network compared to alkaline media. A similar argument is also applicable to explain the much lower HOR activity in base given the much more rigid water network in base, relative to acid (Figure 11A,B). In summary, besides traditional thermodynamic considerations of O species adsorption, the interfacial water−surface interaction and water−water H-bonded network offer another perspective to better rationalize the activity difference of stepped Pt surfaces in acid and base.

The pH effects of ORR activity on Pt have been thoroughly investigated on various stepped surfaces in acid and base with NaF as a buffer with little to no specific anion adsorption (Figure 17E).[278] The kinetic current density, j_k, at 0.85 V (surface-specific activity, SA) was extracted from ORR polarization profiles based on the Koutecký−Levich equation ($1/j_m = 1/j_k + 1/j_{lim}$ where j_m is the measured current density). The ORR activity of Pt(111) exhibits a linear correlation in both acid and base with a maximum activity predicted at a pH of ∼9 (dashed line in Figure 17E). It was proposed that the ORR activity of Pt(111) could achieve a maximum value when the onset potential of the ORR (∼1.0 V vs RHE), which is pH-independent vs RHE, is close to its pzfc value (0.28 V vs SHE) which is pH-independent vs SHE. When those two values are equal, the interfacial water layer has the highest degree of disorder when the ORR occurs, which allows solution species to repel water most easily and adsorb with the lowest energy barrier of reorientating water. This argument would predict an optimal pH of ∼11; the difference from experimental observation (optimal pH at ∼9) is likely because, in base, the pzfc of Pt(111) is within the OH_{ads} region, and the ORR kinetics are also influenced by the OH adsorption process.[264,309] In contrast to Pt(111), the ORR activities of Pt(100) and (110) are largely pH-insensitive (blue and red dots in Figure 17E). This was rationalized by the fact that Pt(111) has a relatively weak OH adsorption over the normal ORR potential window 0.7−1.0 V vs RHE, and OH_{ads} on Pt(111) tends to desorb completely at $E < 0.7$ V (Figure 17A). However, Pt(100) and (110) have a relatively stronger OH adsorption, and OH only begins to desorb at $E < 0.3$−0.5 V. Thus, the ORR activities of Pt(100) and Pt(110) are mainly dictated by OH adsorption processes and are much less influenced by the interfacial water structure. At pH <7, stepped Pt(544), (755) [$n = 9, 6, n(111) \times (100)$] has an ORR activity that lies in between Pt(111) and Pt(100), and Pt(554), (775) [$n = 9, 6, n(111) \times (110)$] showed activity in between Pt(111) and Pt(110). At pH >7, all stepped Pt surfaces followed the same trend as Pt(111) since Pt(111) is much more active than Pt(100) or (110) and largely determines the ORR activity. There is no data reported for a pH of 7−10 due to the strong anion-specific adsorption on Pt in that pH range, such as carbonate or phosphate, which complicates the interpretation of ORR profiles.[319]

ORR activities of Pt can be tuned by the nature of cations and anions in the electrolyte (Figure 17H). ORR activities of Pt(111) in 0.1 M MOH (M is the alkali cation) follow the order $Li^+ \ll Na^+ < K^+ < Cs^+$.[320] The addition of Li^+, with its high charge/radius ratio (Z/r), induces a strong polarization of its nearby solvation water and has strong noncovalent interactions with OH_{ads} through $(H_2O)_xM^+\cdots OH_{ads}$ or $(H_2O)_xM^+\cdots HOH\cdots OH_{ads}$ clusters as shown in Figure 17H. The interaction strength of $(H_2O)_xM^+\cdots OH_{ads}$ follows an opposite order of the ORR activity, which suggests that those clusters may inhibit the movement of reactants to the surface, block available Pt sites, and thus decrease the ORR rate. Koper and coworkers further studied the impact of alkali cations on stepped Pt surfaces and proposed that Li^+ could weaken the repulsive interactions between OH_{ads} in the OH adlayer, facilitate OH adsorption on both (111) terraces and (110) steps, and enhance CO oxidation kinetics.[321] The anions also have a significant impact on the ORR activity of Pt. In anion-adsorbing acids, e.g., H_2SO_4, the ORR activities increased in the opposite order, Pt(111) ≪ Pt(100) < Pt(110), which was ascribed to the strong adsorption of SO_4^{2-}/HSO_4^{2-} with a strong inhibiting effect on Pt(111).[322] Studies in H_2SO_4 can serve as a close proxy to sulfonic groups at the Pt/Nafion interfaces in PEMFCs.[294]

The investigation of temperature effects on the electrochemical behavior of Pt can provide fundamentally important thermodynamic and kinetic information of H and OH adsorption,[323−326] which are critical to a fundamental understanding of the HOR and ORR kinetics, especially at the elevated temperatures employed in most MEA measurements (Figure 12D). Figure 17F presents CV profiles of Pt(111) in 0.1 M $HClO_4$ at 283 K (solid line) and 323 K (dashed line) with a negative shift in the OH_{ads} peak, suggesting enhanced OH adsorption kinetics at a higher temperature.[323] The potential-dependent coverage of H or OH can be calculated by integrating the charge after subtracting the double-layer background. The formal molar Gibbs free energies, ΔG^f, can be calculated from eq 11, and the lateral interaction strength

https://doi.org/10.1021/acs.chemrev.1c00331
Chem. Rev. XXXX, XXX, XXX−XXX

Table 1. Thermodynamic and Kinetic Properties of H and OH Adsorption on Pt in Acid and Base[a]

	$\Delta G°$/(kJ/mol)	$\Delta H°$/(kJ/mol)	$\Delta S°$/(J/mol K)	ω/(kJ/mol)	$k°$/(S^{-1})	R_{ct}/(Ω cm^2)
H_{ads} on $Pt(111)^{acid}$	−27	−41	−48	28	$10^{4.5}$	$0.021-0.025^{a}_{T\text{-jump}}$; 0.031^{b}_{EIS}
H_{ads} on $Pt(100)^{acid}$	−36	−51	−56	9	$10^{3.4}$	$0.15-0.5^{a}_{T\text{-jump}}$; $0.3-0.4^{c}_{EIS}$
H_{ads} on $Pt(110)^{acid}$	−15	−36	−70	−4	$10^{4.8}$	N/A
H_{ads} on $Pt(111)^{base}$	−22	−41	−63	36	N/A	34^{d}_{EIS}
OH_{ads} on $Pt(111)^{acid}$	66	55	−37	13 ($\theta \leq 0.6$)	$10^{4.7}$	N/A
OH_{ads} on $Pt(100)^{acid}$	41	44	10	14	N/A	N/A

[a]Acid and base are 0.1 M $HClO_4$ and NaOH, respectively. ΔG, ΔH, ΔS, and the interaction parameter, ω, were calculated from CV measurements at different temperatures (Figure 17F,G) based on Frumkin isotherms. Reaction constants, $k°$, were calculated by fitting the potential transient in laser-pulsed T-jump experiments based on the Bulter−Volmer equation and Frumkin-type interactions. R_{ct} in a was estimated from laser-induced temperature jump (T-jump) measurements or electrochemical impedance spectroscopy (EIS). R_{ct} values in b−d were measured at 0.16 V in 0.5 M $HClO_4$, 0.125−0.35 V in 0.5 M H_2SO_4 and 0.05 M KOH, respectively. Table prepared by the authors with data reproduced with permission. ΔG, ΔH, ΔS, and ω from ref 323. Copyright 2012 The Authors, Springer. $k°$ and R_{ct} from T-jump from ref 371. Copyright 2020 The Authors, Elsevier. R_{ct} from EIS from ref 372, Copyright 2001 Elsevier; ref 373, Copyright 1996 Elsevier; and ref 374, Copyright 2010 The Royal Society of Chemistry.

among adsorbates, ω, can be estimated from the slope of the ΔG^{f} vs θ plot, assuming a Frumkin-type adsorption isotherm. $\Delta S°$ and $\Delta H°$ can be calculated from $\Delta G°$ at different temperatures.

$$\Delta G^{f} = -zFE - RT \ln\left(\frac{\theta}{1-\theta}\right) = \Delta G° + \omega\theta \tag{11}$$

where z is 1 or −1 for H or OH adsorption, respectively, E is the applied potential vs RHE, and θ is the adsorbate coverage. Positive and negative ω values indicate repulsive and attractive interactions, respectively. It should be stressed that $\Delta G^{f}_{H_{ads}/H_2}$ and $\Delta G^{f}_{OH_{ads}/H_2}$ represent the total reactions of $1/2H_2 = H_{ads}$ and $H_2O = OH_{ads} + 1/2H_2$, respectively, in the electrochemical cell, including the RHE reaction. Figure 17G shows the temperature effects on $\Delta G°$ and ω values for the H and OH adsorption.[323] The good linear correlations of $-\Delta G^{0}_{H_{ads}/H_2}$ and $\Delta G^{0}_{OH_{ads}/H_2}$ vs T validate the assumption of employing the Frumkin isotherm. ω_{H-H} is largely independent of temperature while ω_{OH-OH} steadily increases at higher temperatures, suggesting a larger repulsive interaction among OH_{ads}. The thermodynamic properties of Pt basal planes in acid and base are summarized in the first four columns in Table 1. H_{ads} on Pt(111), (100), and (110) all exhibit negative $\Delta S°$ values, indicating that hydrogen adatoms need a significant amount of energy to break the strongly adsorbed H-bonded water network. Compared to the ideal entropy loss of immobile H_{ads} (−61 J/(mol K)) on all three Pt surfaces in UHV,[324] it is important to realize that the $\Delta S°$ of Pt(111) in solution (−48 J/(mol K)) is less negative than that of Pt(100) (−56 J/(mol K)). Thus, Pt(111) exhibits a ΔS of ∼13 J/(mol K) when breaking the H-bonded water network, larger than that of Pt(100) (5 J/(mol K)), which was ascribed to a less ordered water structure on Pt(100) due to the larger mismatch between the hexagonal water network and the 4-fold symmetry of Pt(100) vs the 6-fold symmetry of Pt(111). Pt(110) has an even more negative $\Delta S°$ of −70 J/(mol K), which was rationalized as its H-bonded network being strongly disfavored on this stepped surface. H_{ads} on Pt(111) showed a much larger ω of 28 kJ/mol, as compared to Pt(100) (9 kJ/mol) or Pt(110) (−4 kJ/mol), indicating a much stronger repulsive interaction among H_{ads} on Pt(111) (Table 1).[324] Compared to that in acid, H_{ads} on Pt(111) in base shows a more negative entropy of −63 J/(mol K), indicating a larger energy barrier for H_{ads} to break a more rigid water network, which may explain, at least in part, the slower HOR kinetics in base.

OH_{ads} on Pt showed a much bigger difference in $\Delta S°$ between Pt(111) and Pt(100) (−37 vs 10 J/(mol K)) than H_{ads}.[325] Similar to the difference in $\Delta S°_{H_{ads}}$, hexagonal Pt(111) can interact much more strongly with the hexagonal H-bonded water network than the square Pt(100), so that OH_{ads} on Pt(111) experiences a much larger entropy loss in order to break the ordered water structure. However, there is a fundamental difference between H_{ads} and OH_{ads}: H_{ads} tends to lie deep in the threefold hollow sites of Pt and is not integrated into the H-bonded water network (i.e., hydrophobic Pt—H). However, OH_{ads} bonds to the Pt surface and interacts strongly with water to form a stable hexagonal OH_{ads}/H_2O_{ads} mixed layer (i.e., hydrophilic Pt—OH), which can enhance the H_2O—Pt interaction while undermining the Pt—OH interactions (a detailed discussion will be covered in Figure 18B). In contrast to H_{ads}, OH_{ads} on Pt exhibits positive $\Delta G°$ and $\Delta H°$ values, corresponding to their total reaction of $H_2O{=}OH_{ads} + 1/2H_2$. OH_{ads} on Pt(111) in solution shows a $\Delta H°$ of 55 kJ/mol and $\Delta S°$ of −37 J/(mol K), which can be converted to −265 kJ/mol and −200 J/(mol K), respectively, for the reaction of $OH(g){=}OH_{ads}$ and are consistent with −253 kJ/mol and −182 J/(mol K), respectively, measured by gas-phase OH adsorption.[325] Compared to the θ-independent thermodynamic values for H_{ads} on Pt(111), OH_{ads} on Pt(111) shows more positive $\Delta H°$ and $\Delta S°$ and a smaller ω at higher θ, which was ascribed to a higher OH mobility via H transfer/tunneling between neighboring OH and H_2O and/or a more disordered water structure at higher θ_{OH}.

In summary, surface structures (step symmetry and density), environment (pH, surface water, cation/anion), and temperature have significant impacts on H/OH adsorption and ORR/HOR activities. Interfacial water structures will be discussed further in the following two sections (*vide infra*).

4.1.4. Molecular Perspective of Interfacial Water Structures at Charged Surfaces. Solid−liquid interfaces, in particular electrode−electrolyte interfaces, play a central role in understanding not only electrocatalysis but also many other electrochemical reactions, such as corrosion and a majority of energy-related technologies.[327−330] We will review the recent progress of interfacial water structures at charged surfaces/interfaces with both *ex situ* atomic-scale imaging and modeling and *in situ* spectroscopic studies. We emphasize the complex structures of water and OH adlayers and their potential-dependent behaviors on well-defined Pt and Au single crystals. To separate interfacial water from bulk water, one strategy is to investigate water with X-rays or scanning tunneling microscopy

https://doi.org/10.1021/acs.chemrev.1c00331
Chem. Rev. XXXX, XXX, XXX−XXX

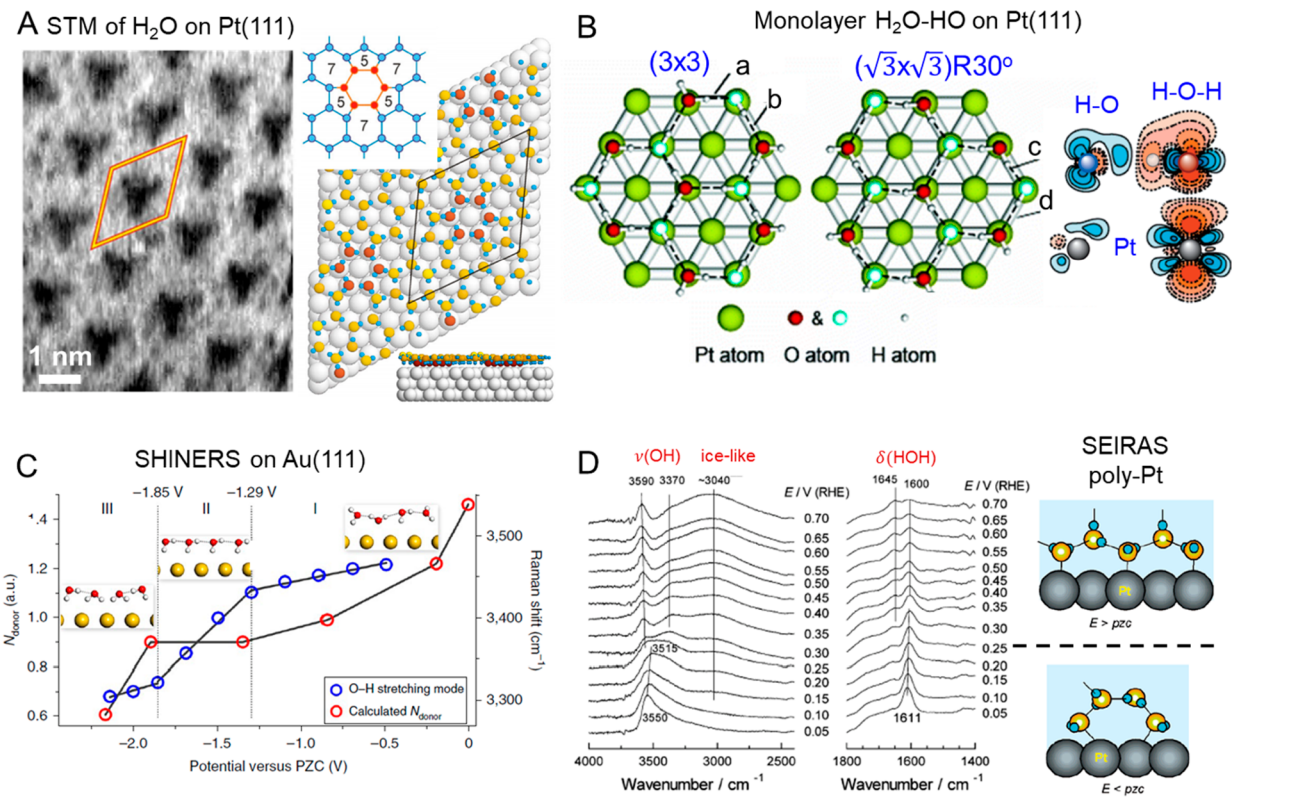

Figure 18. Molecular perspective of interfacial water structures at charged surfaces. (A) STM image of submonolayer water deposited on Pt(111) at 140 K showing an ordered structure (V_{tip} = 0.2 V, I_t = 1pA, left) and the corresponding schematic of a "575757" di-interstitial topological defect in a hexagonal lattice. The lower right figure suggests that the planar hexagonal water rings have the H-down configuration (brown) and are closer to the Pt(111) surface than the surrounding buckled pentagonal/heptagonal defect rings (yellow). (B) Two structural models of monolayer H_2O + OH (ratio of 1:1) coadsorbed on Pt(111) based on extensive XAS and XPS studies. Oxygen atoms belonging to H_2O and OH groups are indicated in red and green, respectively. The figure on the right panel shows the calculated charge density difference plot of the H−O···H−O−H bond on Pt(111) with H_2O as the proton donor (blue and red indicate gain and loss of charge, respectively). (C) *In situ* SHINERS measurements of the water structural transition on Au(111) from parallel to "one-H-down" and finally "two-H-down" at more negative potentials, as suggested by the progressive shift of Raman frequency ν(OH) (blue circle) and calculated number of H-bond donors (N_{donor}). (D) *In situ* ATR-SEIRAS measurements of H_2O at poly-Pt film in Ar-saturated 0.5 M $HClO_4$ at various potentials. ν(OH) and δ(HOH) represent the stretching vibration of OH and bending vibration of HOH. The right panel shows the transition from a weakly H-bonded H-down configuration at E < pzc (the dashed line) to a strongly H-bonded more flat orientation at E < pzc. Panel A is adapted with permission from ref 335. Copyright 2010 American Physical Society. Panel B is adapted with permission from ref 337. Copyright 2010 American Chemical Society. Panel C is adapted with permission from ref 341. Copyright 2019 Springer Nature. Panel D is adapted with permission from ref 346. Copyright 2008 American Chemical Society.

(STM) on an ultraclean single-crystal surface in a UHV environment in which only the topmost water layers will remain on the surface. Traditionally a "bilayer model" of water on a solid surface has been proposed,[331] which includes six water molecules forming a hexagonal ring with a puckered structure. The lower three water molecules interact strongly with the surface while the upper three water molecules are H-bonded to the lower part. However, later, a low-energy electron diffraction study (LEED) showed a coplanar configuration of O atoms. A recent theoretical study of H_2O on Ru(0001) predicted that H_2O could partially dissociate into OH^- and H^+, and the mixed layer of $^-$OH and H_2O could form a much more stable H-bonded coplanar hexagonal water network than the conventional bilayer model.[332,333] Advances of atomic-scale STM have enabled the direct visualization of water at interfaces and demonstrate a variety of water structures deviating from the traditional bilayer model, such as planar ice chains of water pentagons on Ni(110) but hexagons on Ag(110) as well as a coplanar H_2O/OH mixed layer on Cu(110).[334] Recent high-resolution STM images revealed the water structure on Pt(111) (Figure 18A).[335] The interplay between water−water and water−surface interactions drives the H-bonded water network to form a 26-H_2O 2D unit cell of a coplanar hexagonal water ring, surrounded by three pairs of water pentagons and heptagons, as evidenced by the topological defects in the STM image (darker contrast in Figure 18A). Water molecules in the central hexagon lie flat and interact strongly with the Pt surface. In order to optimize H-bonding among water, water molecules in pentagons and heptagons have dangling H bonds pointing down to the Pt surface and are buckled by ∼0.6 Å higher than the central flat-lying hexagons.

OH is an essential reaction intermediate for both the ORR and HOR. An extensive number of techniques have been employed by Nilsson and others to provide a clear molecular illustration of H_2O−HO mixed layer structures, including LEED, soft X-ray absorption spectrometry (XAS), X-ray photoelectron spectroscopy (XPS), Auger electron spectroscopy, and DFT simulations (Figure 18B).[336,337] H_2O−HO (1:1 ratio) on Pt(111) has two types of structural models: (3 × 3) and ($\sqrt{3} \times \sqrt{3}$)R30° with different symmetry, but the same hexagonal coplanar structure. Both models show a shorter O−

https://doi.org/10.1021/acs.chemrev.1c00331
Chem. Rev. XXXX, XXX, XXX−XXX

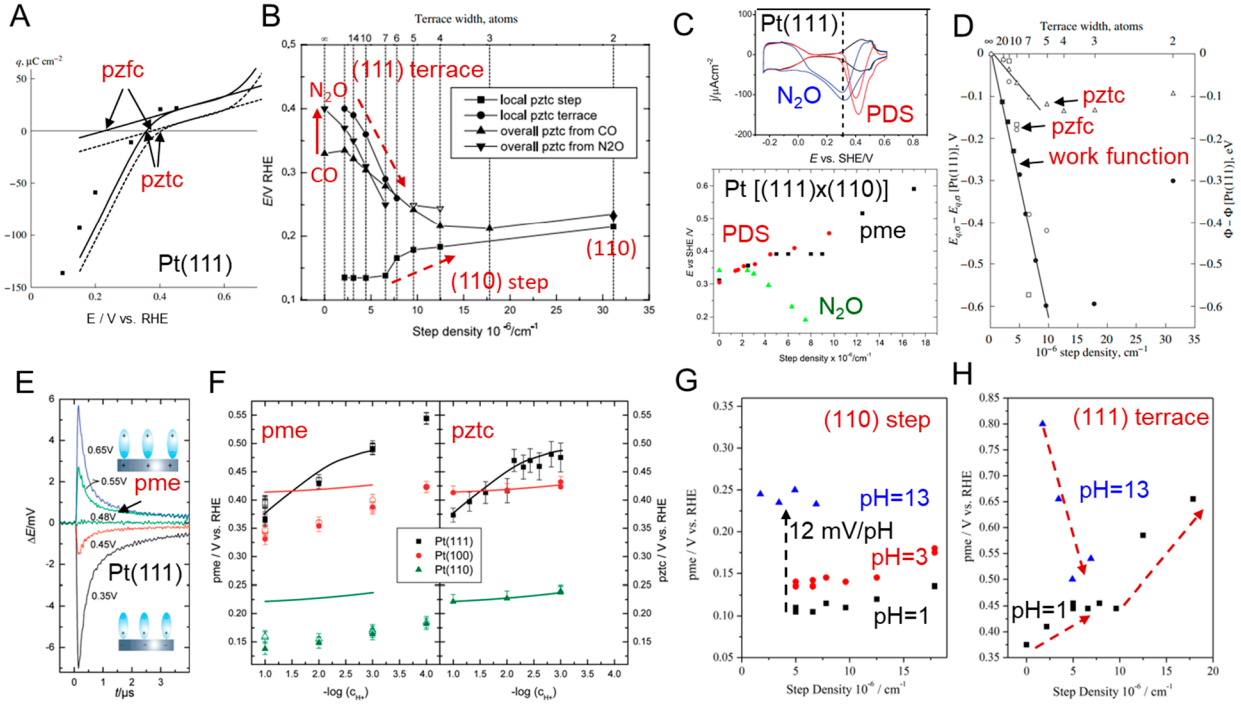

Figure 19. Quantitative descriptors of interfacial water structures: potential of zero charge (pzc) and potential of maximum entropy (pme). (A) Methods to measure potential of zero total charge (pztc) and potential of zero free charge (pzfc) in the charge-potential plot of Pt(111) in 0.1 M $HClO_4$. pzfc values can be extrapolated from the double-layer region to the H adsorption region. Solid and dashed lines show the uncorrected and corrected values of pzfc and pztc, respectively, to account for the residual charge on the CO-covered surface. Squares are the opposite of CO-displaced charges. (B) Local and overall pztc values extracted from both CO and N_2O charge displacement experiments as a function of step density of Pt[$(n - 1)(111) \times (110)$] since N_2O has weaker adsorption on the Pt surface than CO and can probe the local pztc on steps and terraces separately. Open symbols correspond to uncertainty in deconvolution of N_2O reduction peaks at high step density ($n < 6$). (C) Upper panel: CV profiles of Pt(111) at pH = 5 (blank in the black curve, peroxodisulfate (PDS) reduction in red and N_2O reduction in blue). Lower panel: comparison of local pzfc from PDS, local pztc from N_2O reduction, and local pme for (111) terraces of Pt[$(n - 1)(111) \times (110)$]. (D) Changes in pztc (open triangles) and pzfc with a charge constant of 0 (open squares) and 18 $\mu C/cm^2$ (open triangles) in 0.1 M $HClO_4$ and corresponding working function values tested in UHV (open and filled squares, respectively). Upper and lower *X*-axes are step width, *n*, and step density for Pt[$(n - 1)(111)) \times (110)$]. (E) Laser-induced temperature-jump (T-jump) measurements of coulostatic potential transients of Pt(111) at various potentials (vs RHE) in 1 mM $HClO_4$ + 0.1 M $KClO_4$ (pH = 3). The illustration shows the schematic of water dipole reorientation for H-down to H-up structures around pme. (F) pH-dependent pme and pztc values of Pt single crystals in $HClO_4/NaClO_4$ solution. Lines are drawn to indicate the tendencies of pztc values, and they are reproduced in the left for an easier comparison between pme and pztc values. (G, H) pme values of (110) step and (111) terrace of Pt[$(n - 1)(111)) \times (110)$] surfaces in 0.1 M $HClO_4$ (squares), 0.1 M $KClO_4$ + 1 mM $HClO_4$ (circles), and 0.1 M NaOH (triangles). Panels A and D are adapted with permission from ref 351. Copyright 2006 Springer. Panel B is adapted with permission from ref 354. Copyright 2002 Elsevier. Panel C is adapted with permission from refs 358 and 359. Copyright 2019 Elsevier. Panel E is adapted with permission from ref 364. Copyright 2008 American Chemical Society. Panel F is adapted with permission from ref 367. Copyright 2009 American Chemical Society. Panels G and H are adapted with permission from ref 371. Copyright 2020 Elsevier. All figures have Copyright by the authors.

O distance with OH as an H acceptor (2.66 and 2.73 Å, bonds a and c, respectively) and a longer O−O distance with OH as an H donor (3.16 and 3.02 Å, bonds b and d, respectively). This clearly shows that OH is a strong H-acceptor but a poor H-donor for forming H bonds, owing to its negatively charged O center. H_2O and OH exhibit a cooperativity effect between H-bonding and surface bonding. In order to optimize the H-bonding network, the coplanar structures enhance the H_2O−Pt interaction but weaken the HO−Pt interaction. Such an interplay can be clearly seen from the calculated charge density difference plots (Figure 18B, right). The loss of charge density between H_2O and Pt minimizes the Pauli repulsion and stabilizes H_2O_{ads} on Pt while the flat HO configuration is less favorable for HO−Pt interactions, which is compensated by forming a strong H bond with H_2O. This cooperativity effect through charge redistribution enhances the overall stability of the mixed H_2O/OH layered structure.

Although experiments and simulations in a vacuum provide an atomic-scale illustration of surface water structures, it is necessary to move beyond the first 1−2 layers and study the dynamic environment of liquid water near the surface *in situ*, under applied potential.[338−340] Tian et al. recently combined *in situ* Raman (SHINERS) and *ab initio* molecular dynamics (MD) to track the water reorientation on charged Au(111) surfaces (Figure 18C).[341,342] Owing to its electrochemically inert surface, Au can endure potentials as negative as −2.2 V vs the pzc of Au(111) (pzc value: 0.48 V vs SHE) before hydrogen evolution ensues in 0.1 M Na_2SO_4 (pH = 7). Figure 18C illustrates that, toward negative potentials, water evolves from an initially structurally "parallel" to a "one H-down" configuration beyond −1.29 V vs pzc and finally to beyond a "two H-down" arrangement after −1.85 V vs pzc. Concomitantly, the average number of H-bond donors (N_{donor}) decreases from 1.2 to only 0.7, indicating a significant increase of dangling unsaturated H bonds. A similar water configuration

https://doi.org/10.1021/acs.chemrev.1c00331
Chem. Rev. XXXX, XXX, XXX−XXX

of H pointing down with unsaturated H bonds on Au and Pt thin films was also reported by Salmeron and co-workers using *in situ* XAS in a surface-sensitive total electron yield mode.[343,344]

The dynamic water structures on Pt are more complex due to the coadsorption of H or OH below or above the double-layer regions.[337,345] Osawa et al. employed *in situ* SEIRAS to investigate the water structure on Pt thin films in 0.1 M H_2SO_4 (Figure 18D).[346] IR peaks at 3550−3590 cm^{-1} and 1600−1645 were assigned to the O−H stretching ν(OH) and HOH bending δ(HOH), respectively. In the H_{ads} region, as E increased from 0.05 to 0.4 V, both ν(OH) and δ(HOH) modes exhibited an intensity decay and were red shifted to lower wavenumbers (3550 to 3515 and 1611 to 1600 cm^{-1}, respectively). Such changes were ascribed to the formation of a more planar water orientation at higher potentials since the IR intensity is proportional to $\alpha \cos^2\varphi$ where α and φ are the IR absorption coefficient and the tilting angle of the water dipole from the surface normal, respectively. A new peak at 3040 cm^{-1} emerged beyond 0.25 V vs RHE, which is characteristic of strongly H-bonded water molecules as in ice (labeled as "icelike").[347] In the double-layer region (0.4−0.6 V vs RHE), new peaks emerged at 3590 cm^{-1} [ν(OH)] and 1645 cm^{-1} [δ(HOH)] which were assigned to the more vertical second layer of water in response to a planar orientation of the first-layer water (Figure 18D, upper scheme). The transition of the water structure is illustrated in the right scheme of Figure 18D: The water network near the Pt surface changes from a weakly H-bonded with H-down network at E < pzc to a strongly H-bonded icelike network, close to the planar configuration at E > pzc (pzc of poly-Pt is ∼0.25 V vs RHE). This icelike feature at ∼3000 cm^{-1} exists on Pt even when E is up to 1.2 V, well above the pzc, which is in contrast with Au with a similar feature only around the pzc,[347] which is probably due to the much stronger H_2O−Pt interaction, relative to H_2O−Au. The existence of the icelike water at ∼3000 cm^{-1} in the OH_{ads} region (0.7−1.2 V) would imply that the strongly H-bonded network among H_2O still exists. If a strong H bond between H_2O and HO occurs, the authors anticipated a peak shift from 3000 to 3200 cm^{-1}, which was not observed in their experiments. We believe such a contradiction may come from the unresolved interaction between H_2O−OH and H_2O−H_2O as well as their interaction with the Pt surface. If Nilsson's model is valid for the first layer of H_2O/OH in the OH_{ads} region on Pt in liquid (Figure 18B), given the planar nature of OH, it will not show up in the IR spectra. In this case, other techniques, such as Raman or X-ray methods,[348,349] may offer new opportunities to further elucidate the water structure on Pt. In summary, this section briefly summarized the current understanding of the surface water structure and its dependence on applied potentials. With the continuous development of *in situ* techniques and simulations capable of handling both surface interaction and bulk water, we anticipate more exciting breakthroughs in deciphering the water structure on metal (and more complex metal oxide) surfaces under applied potentials.

4.1.5. Potential- and pH-Dependent Interfacial Water Structures: Potential of Zero Charge and Potential of Maximum Entropy. Our understanding of interfacial properties of water at charged surfaces and interfaces has been greatly enhanced by the determination of the potential of zero charge (pzc) and potential of maximum entropy (pme).[350−352] Given that pseudocapacitive H and OH adsorption on Pt interferes with the determination of the pzc, two types of pzc have been defined: potential of zero total charge (pztc) and potential of zero free charge (pzfc). The pztc defines the potential at which the free charge in the double layer is exactly balanced by the "chemical charge" of chemisorbed species on an electrode surface. The pzfc represents the potential at which no extra cation or anion exists in the double layer and corresponds to the true charge determining the electric field at the interface. In other words, the pzfc is the analogue of the pzc of metal surfaces without the impact of H or OH adsorption and, thus, is closely related to the interfacial properties of water dipoles. The pme defines a potential at which surface water has the highest degree of disorder and reorients between H-up and H-down modes. Here, we will review the basic methodology to determine the pzc and pme of Pt and their dependence on step density, particle sizes, and solution pH as well as their correlation to H and OH adsorption.

The pztc can be determined from CV measurements and CO displacement experiments since CO is a neutral probe that does not induce charge transfer during adsorption. The integrated charge after subtracting the CO displacement charge is presented in Figure 19A.[351] The pztc of Pt(111) was measured as 0.33 V vs RHE in 0.1 M $HClO_4$ from the X-intercept of the q vs E plot (solid line). Since the double-layer region is free of H or OH adsorption on Pt(111), the charge is only related to the free charge in the EDL; the pztc and pzfc are equal in this case. Thus, assuming a constant double-layer capacitance, the free charge can be extrapolated from the double layer to H_{ads} region to obtain the pzfc of Pt(111) as 0.16 V vs RHE. However, the CO-covered surface still maintains a small residual charge of 10−15 $\mu C/cm^2$. After correcting for the residual charge, the pztc and pzfc of Pt(111) are 0.39 and 0.34 V vs RHE, respectively[353] (X-intercept with dashed lines, Figure 19A). The pztc of Pt(111) showed a pH-dependent behavior of 0.39 and 0.70 V vs RHE (i.e., 0.32 and −0.076 V vs SHE) at pH = 1 and 13, respectively. In contrast, it is remarkable that the pzfc of Pt(111) is pH-independent vs SHE and remains a nearly constant value of 0.28 V vs SHE, which is near the double-layer region without significant influence from H or OH adsorption. It represents an intrinsic property of the electrochemical double layer (EDL) and serves as a reference point for other systems. Pt(100) and Pt(110) exhibit pztc values of 0.42 and 0.22 V vs RHE in 0.1 M $HClO_4$, being higher and lower than that of Pt(111) (0.39 V), respectively. The pztc values of poly-Pt were reported to be ∼0.29 V vs RHE in 0.1 M $HClO_4$ as the average of the three basal planes.[358]

The impact of step density on the pztc of the stepped Pt [(n − 1)(111) × (110)] surface was investigated in 0.1 M $HClO_4$ with both CO displacement and N_2O reduction as molecular probes (Figure 19B).[354,355] Owing to its unique weak adsorption, N_2O molecules are able to show two distinct adsorption/reduction peaks on steps and terraces and are sensitive to the local pztc values. As step density increases (smaller terrace width, n), the local pztc values of (110) steps progressively increase from 0.14 V vs RHE and approach that of the Pt(110) basal plane (∼0.2 V) while the local pztc values of (111) terraces decrease from 0.4 V. This suggests a growing charge redistribution between steps and terraces at higher step densities. On Pt(111) (n = ∞), it is interesting to observe that the pztc from N_2O is 50 mV higher than that from CO. H_2O tends to naturally adsorb on Pt with a slightly H-up O-down configuration without applied potential due to the interaction

https://doi.org/10.1021/acs.chemrev.1c00331
Chem. Rev. XXXX, XXX, XXX−XXX

between O and Pt. Since N_2O is a weak probe and needs to repel water first before adsorption, it is reasonable to anticipate that more positive potentials will be required for N_2O to repel the site-blocking H-up H_2O dipole as compared to CO.[354]

In addition to the neutral probe of N_2O, peroxodisulfate ($S_2O_8^{2-}$, PDS) serves as a unique charged probe to resolve the local pzfc of terraces and steps.[356,357] The PDS reduction proceeds with significant current over a narrow potential range with the reduction current dropping to zero at more positive or negative potentials (Figure 19C, upper panel).[358] Since the PDS reduction requires a positive electrode charge and will be inhibited when the electrode charge becomes negative, the PDS reduction potential at zero current density can approximate the local pzfc value. The pzfc values of Pt(111) (~0.30 V vs SHE), based on PDS reduction at various pH values, are consistent with the pzfc values from the CO displacement method and pme values.[358] The pzfc of (111) terraces of $[Pt(n-1)(111)\times(110)]$, determined from PDS reduction at pH = 5, exhibit a similar trend of higher pzfc values at higher step density to the pme values but are opposite to the local pztc values from N_2O reduction (Figure 19C, lower panel).[359] The difference between PDS and N_2O reduction measurements possibly originates from the lack of sensitivity of the neutral N_2O molecule to follow the variation of free charge, relative to the sensitive PDS anion. Given that the local work function of the (111) terrace would remain constant, regardless of step density, the positive shift of the pzfc values from PDS reduction at higher step density is correlated to the effects of steps on the interfacial water network. PDS adsorbs more easily on Pt surfaces with a less organized water network caused by the increasing interruption at higher step density. In addition, PDS reduction points out a second pzfc of Pt(111) at a high potential of ~0.70 vs SHE, corresponding to the transition from positive to negative free charge caused by the oxidation of Pt, as initially proposed by Frumkin and Petrii.[350]

On stepped Pt surfaces, the correlation among the pztc, pzfc in solution, and work function measured in UHV sheds new insights on the fundamental properties of the Pt/solution interface (Figure 19D).[360] The pztc exhibits a decaying trend and then reaches a relatively stable value (open triangles in Figure 19D), while the work function exhibits a linear correlation with a slope of 0.6 D, which is directly related to the intrinsic dipole moment of the step, measured in UHV. From the previous discussion, we know that the pzfc is free of chemisorption and more relevant to the intrinsic properties of the surface. Thus, despite some uncertainty, the pzfc values of stepped Pt surfaces were estimated by extrapolating the q vs E plot from the double-layer region to a charge constant of 18 $\mu C/cm^2$ (open circles in Figure 19C) to mitigate the large uncertainty of extrapolating to the H adsorption region (open squares in Figure 19C). Remarkably, the pzfc values showed a trend with a slope similar to that of the work function values. This implies that a similar dipole effect is associated with the steps in both electrochemical and UHV measurements and, indirectly, validates the analysis of the pzfc of stepped Pt by the CO displacement method. With more accurate pzfc values, we anticipate that the differences between the pzfc and work function values may reveal additional information about the modification of the surface potential due to the interaction between water dipoles and the intrinsic dipole moment of the step. For instance, the water dipole may neutralize the excessive or deficient charge on steps, leading to a reduction in surface potential and a smaller slope of pzfc vs step density than that of the work function. The size and morphology of Pt nanoparticles (NPs) also have an impact on the pztc values, which, in turn, affects the catalytic activity.[361] Mayrhofer et al. reported that, as the Pt particle sizes decrease from 30 to 1 nm, the pztc values decrease by 35 mV, which corresponds to a progressive increase of OH coverage at 0.85 V vs RHE as well as an increase of OH binding strength.[362] This size-dependence significantly influences catalytic activity. 1 nm Pt NPs showed a much smaller specific ORR activity (0.8 mA/cm^2) than that of 30 nm (4 mA/cm^2) but a much higher CO oxidation activity, which was ascribed to the enhanced OH adsorption on smaller particles.

Besides the pztc and pzfc, the pme for the double-layer formation can be measured by the laser-induced temperature-jump (T-jump) method which provides new opportunities to investigate the potential-dependent water dipole and to deconvolve water from H/OH adsorption. The pme is closely related to the pzfc, and stepped Pt surfaces show a good correlation between the local pme and pztc from N_2O displacement experiments on steps and terraces. The T-jump method applies a nanosecond laser pulse to abruptly raise the temperature of the interface by 10−30 K. The coulostatic change of the potential transient, caused by the temperature perturbation, measures the thermal coefficient of the potential drop in the EDL, $\frac{\partial \Delta_S^M \phi}{\partial T}$, where $\Delta_S^M \phi$ is the potential drop at the interface, and T is the temperature. This thermal coefficient was related to the double-layer formation entropy with the following expression derived by Benderskii et al.:[363]

$$\left(\frac{\partial \Delta_S^M \phi}{\partial T}\right)_q = -\left(\frac{\partial \Delta S}{\partial q}\right) \tag{12}$$

When the thermal coefficient is equal to zero, $\frac{\partial \Delta S}{\partial q}$ is also zero, and the ΔS vs q plot achieves a maximum point, which corresponds to the pme for the double-layer formation at which water achieves a maximum level of disorder. Figure 19E shows a typical potential transient for Pt(111) in 1 mM $HClO_4$ + 0.1 M $NaClO_4$ (pH = 3).[364−366] Although the value of $\frac{\partial \Delta_S^M \phi}{\partial T}$ cannot be accurately measured, given the challenges of determining ΔT, the sign of the potential transient provides critical information. As the applied potential increases from 0.35 to 0.65 V vs RHE, ΔE changes from negative to positive values and becomes nearly zero at E = 0.48 V vs RHE (0.30 V vs SHE), which corresponds to the potential at which $\frac{\partial \Delta_S^M \phi}{\partial T} = 0$, i.e., the pme. At this point, the sign change of the potential transient corresponds to the change of water orientation and dipole moment, from H-down with a positive dipole near the surface to an H-up configuration with a negative dipole near the surface (scheme in Figure 19E). 1 mM $HClO_4$ was selected to lower the influence of H adsorption, and a pH close to 7 could lower the thermodiffusion potential of protons to a minimum level.[365,366] Figure 19F summarizes the impact of pH on the pme values of the three basal Pt planes and establishes the correlation with pztc values.[367,368] The trends of pztc values at different pH values were plotted (solid lines) with pme values for a better comparison between them. Pt(111) exhibits very similar trends in pme and pztc values at various pH values, suggesting that the free charge density is close to the total charge density. Both the pme and pztc of Pt(111)

https://doi.org/10.1021/acs.chemrev.1c00331
Chem. Rev. XXXX, XXX, XXX−XXX

show a pH-dependence of 60 mV/pH vs RHE. The pme of Pt(111) remains constant at 0.3 V vs SHE when the pH changes from 1 to 6,[369] suggesting that the pztc is mainly governed by the free charge density and remains close to the pzfc of Pt(111) (0.28 V vs SHE). When examining the data more carefully, the pme values of Pt(111) are always lower than the pztc values by ∼50 mV (black closed squares vs black line), which coincides with the 50 mV difference in pztc between CO and N_2O measurements (Figure 19B). This, again, suggests that water has a small net H-up orientation on Pt(111) in the absence of an electrical field. In sharp contrast, pztc values of Pt(100) and Pt(110) are largely pH-independent vs RHE (i.e., pH-dependent vs SHE) (Figure 19F, right), suggesting that their pztc values are mainly dictated by H adsorption in acidic media [recall the H peak positions of (110) and (100) in Figure 17A]. Both Pt(100) and Pt(110) exhibit higher pztc values than pme values, indicating that the total charges are composed by not only the free charges but also some excess charge corresponding to H_{ads}. The pme values of Pt(100) and Pt(110) exhibit a pH-dependence of 30 and 15 mV/pH, respectively, implying different effects from H adsorption. At pH = 3, the pme of Pt(111) is higher than those of Pt(100) and Pt(110), by ∼0.10 and ∼0.32 V, respectively, which are consistent with the differences in their work functions [Pt(111), Pt(100), and Pt(110): 5.93, 5.84, and 5.67 eV, respectively].[370] Similarly, a recent study of various adatoms on Pt(111) showed that Bi and Pb, with lower work function values than Pt(111), led to lower pme values, while S and Se, with a higher work function than Pt(111) led to higher pme values.[360] The close correlation among pme, pzfc, and work function provides new insights about the interactions between the water dipole and surface charge dipole.

In a recent report, the effects of step density on the pme, particularly in alkaline media, were investigated with Pt [$(n-1)(111)\times(110)$].[371] The potential transients on stepped Pt also showed two local maxima, corresponding to local pme for steps and terraces, respectively (Figure 17G), which is similar to the local pztc measured by N_2O. Overall, the pme values of (110) steps (0.1−0.3 V) are much lower than those of (111) terraces (0.4−0.7 V), which is consistent with the differences in the local pztc of steps and terraces from N_2O measurements as shown in Figure 17B. The pme values of (110) steps are largely unchanged with increasing step density in both acid and base and show a pH-dependence of 12 mV/pH vs RHE (∼50 mV/pH vs SHE), smaller than a typical Nernst shift of 59 mV/pH vs SHE. The non-Nernstian pH shift has been ascribed to the modification of the interfacial water network by the coadsorption of cations in solution (Figure 10D). In contrast to (110) steps, the pme of (111) terraces exhibits a strong pH-dependence vs RHE. In acidic media, the pme on Pt(111) terraces continues to increase at higher step densities. As previously discussed, the pme in acid is smaller than the pzfc due to the natural H-up configuration in the interfacial network. The introduction of steps can disrupt the H-bonded network and requires a less negative charge to turn over the H-up structure and, thus, displace the pme value closer to the pzfc. In alkaline media, the pme showed the opposite trend, decaying at a higher step density. Pt(111) terraces would show an H-down structure in base (Figure 17C), and the disruption of the water structure caused by steps would shift the pme to lower values. Another possibility is that OH_{ads} is more favored to adsorb on (110) steps than on (111) terraces and can induce a positive image charge on terraces, which would require a more negative potential to achieve the pme. The undesirable interference of H and OH adsorption on the pme can actually be used to investigate the H adsorption kinetic properties. The time-dependent potential transient profiles were used to extract thermodynamic properties in Table 1 by simulation based on the Bulter−Volmer equations and assuming the Frumkin-type interactions.[367] The reaction rate constant, k°, and charge-transfer resistance, R_{ct} can be calculated from this strategy (Table 1, right two columns). Pt(111) exhibits a k° of $10^{4.5}$ s^{-1} for H_{ads} in acid, which is one order of magnitude higher than that of Pt(100) ($10^{3.4}$ s^{-1}), suggesting a much faster H adsorption/desorption process on Pt(111) than on Pt(100). Concomitantly, Pt(111) shows an R_{ct} of 21−25 mΩ cm^2, less than 10% of that of Pt(100) (150−500 mΩ cm^2), which is consistent with the R_{ct} values measured by electrochemical impedance measurements (EIS).[372−374] It is interesting to note that the k° of OH_{ads} on Pt(111) in acid is $10^{4.7}$ s^{-1}, comparable to that of H_{ads} under the same conditions, which is consistent with the sharp reversible OH_{ads} feature observed on Pt(111) in acid (Figure 17A).

In summary, the interfacial water structure can be described well by the pztc, pzfc, and pme. The impacts of steps, pH, and particle sizes on those values reveal the interactions between water dipoles and the metal surface and how, on steps, H or OH adsorption may influence the H-bonded water network. This analysis highlights a fundamentally important aspect: the interfacial water structure often plays an instrumental role in determining the surface activity, and continuous efforts should be invested in this area to provide more rational guidance for regulating catalyst activity.

4.2. Nonprecious ORR Electrocatalysts

After 2 decades of extensive research and development, PEMFCs have achieved an initial stage of commercialization for electric vehicles. Nonetheless, even at a large scale, PEMFCs still require a significant amount of expensive Pt-based catalysts for the ORR in part because, thermodynamically, nonprecious catalysts such as 3d transition metals are not stable in acidic media. As an emerging alternative, AEMFCs have drawn increasing attention because they can enable the use of non-precious-metal electrocatalysts and effectively mitigate carbonate precipitation issues.[13] Nonprecious catalysts, such as 3d metals or metal oxides, perovskites, and metal-containing N-doped carbon (M−N−C), are attractive for their low cost, promising activity, and durability. The recent development of anion exchange membranes (AEMs) with high ionic conductivity and stability has advanced a variety of alkaline-based energy technologies, such as fuel cells, water electrolyzers, and CO_2 reduction.[375−378] AEMFCs are now able to demonstrate a comparable initial performance, using nonprecious ORR catalysts, to PEMFCs using Pt-based catalysts.[16] While the development of nonprecious ORR and HOR electrocatalysts shows promising progress, it is pivotal to assess the stability of nonprecious catalysts and AEMs in alkaline media during fuel cell operation. A preliminary assessment of non-precious-metal catalyst stability has been performed mainly in RDE measurements. More realistic durability tests require MEA testing.

In this section, we will outline the fundamental ORR mechanisms of non-precious-metal catalysts, especially metal oxides, nitrides, and M−N−C, and their catalytic mechanisms in alkaline media. We will discuss several structural descriptors

https://doi.org/10.1021/acs.chemrev.1c00331
Chem. Rev. XXXX, XXX, XXX−XXX

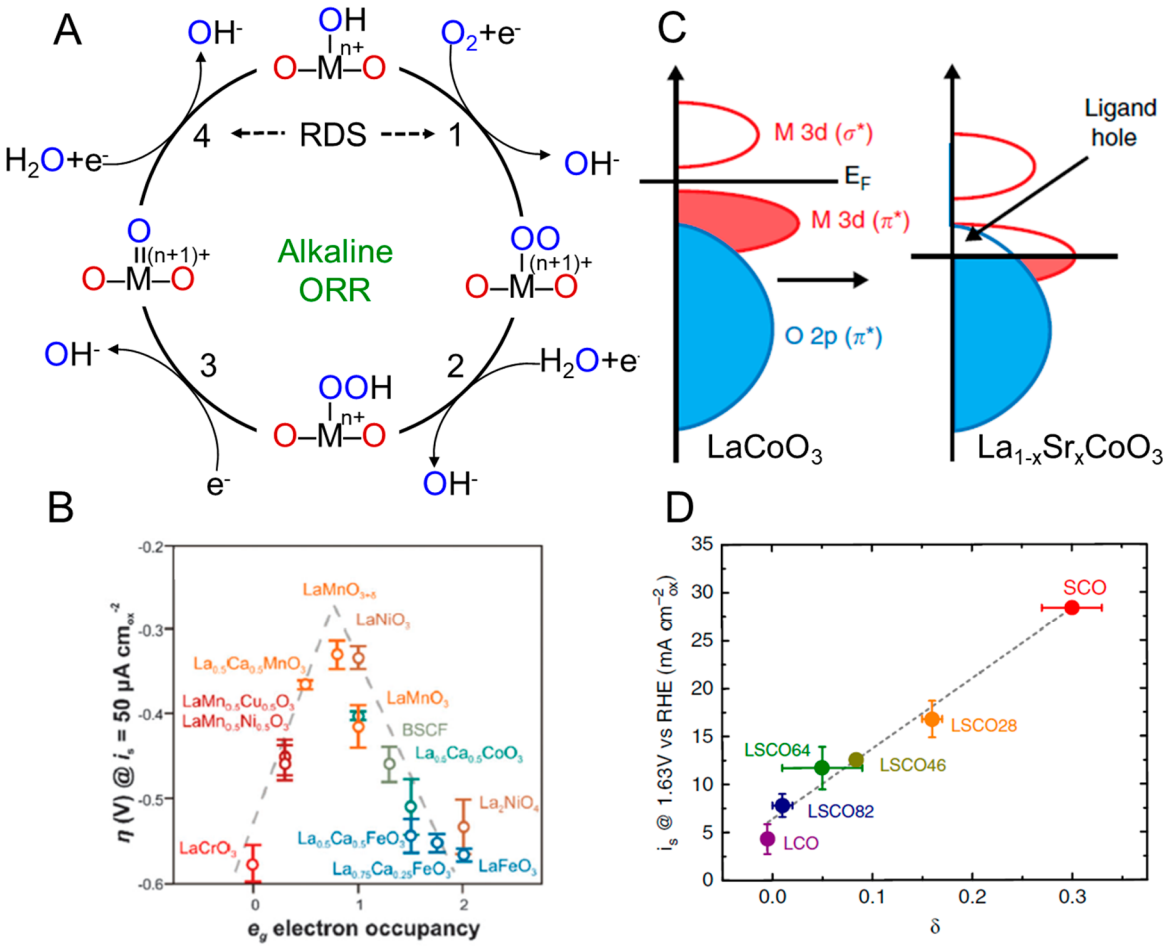

Figure 20. ORR mechanisms on oxide surfaces and proposed activity descriptors. (A) Possible ORR mechanism on metal oxide surfaces in alkaline media. Oxygens in blue and red represent species in solution and lattice oxygen, respectively. (B) Overpotentials for the ORR as a function of e_g electron occupancy on various perovskites. (C) Schematic of band structures of typical perovskites, $LaCoO_3$ and $La_{1-x}Sr_xCoO_3$, with the latter one having larger Co 3d/O 2p band overlap (i.e., larger M−O covalency). (D) Correlation of OER activity of $La_{1-x}Sr_xCoO_{3-\delta}$ with the oxygen vacancy parameter, δ. Panel A Copyright by the Author. Panel B is adapted with permission from ref 379. Copyright 2015 The Authors, Royal Society of Chemistry. Panels C and D are adapted with permission from ref 408. Copyright 2016 Springer Nature.

to rationalize the ORR activity trends and provide new design strategies for nonprecious catalysts, such as oxygen binding strength, e_g electron occupancy, M−O bond covalency, surface strain, and oxygen vacancies. We are particularly interested in using single-crystal metal oxides, with well-defined surface structures, to better understand the structure−(re)activity relationship(s) and potentially identify the ORR active site(s). Single-crystal oxides enable the use of *operando* X-ray diffraction and spectroscopy to correlate the activity to structural/compositional changes of oxide surfaces under operating conditions (details covered in section 9). Particular emphasis has been placed on the design and synthesis of 3d metal spinel nanocrystals as ORR electrocatalysts, in particular Co−Mn spinels, which have demonstrated MEA performances comparable to that of Pt/C. We will review the recent progress of metal nitrides and M−N−C and discuss their ORR activity and stability in alkaline media. Additionally, other non-Pt precious metal catalysts, such as Pd-, Ru-, and Ag-based alloys, have demonstrated an ORR activity close to Pt in alkaline media and can diversify options of ORR electrocatalysts for automotive applications that demand very high energy and power densities [in comparison, Pt remains as the sole element in Pt-group metals (PGMs) highly active for the ORR in acid]. We anticipate that these studies will provide a unified picture of ORR mechanisms of both precious and nonprecious electrocatalysts in alkaline media.

4.2.1. Nonprecious Oxide and Nitride Electrocatalysts for the ORR. The general ORR mechanisms on transition metal oxide surfaces can be simplified by a four-step PCET process in which water serves as the proton donor in alkaline media (Figure 20A). The reversed cycle can also be used to describe the oxygen evolution reaction (OER) with a certain level of similarity. Several other recent reviews have pointed out the parallel between the ORR and the OER on oxides.[38,379,380] It has been proposed that the competition between the O_2^{2-}/OH^- displacement in step 1 and OH^- regeneration in step 4 determines the overall ORR rate in alkaline media. Goodenough et al. first discussed the ORR mechanism on rutiles and pyrochlores via the exchange between OH^- and $O_2^{2-}/O_{2,ads}^-$ and suggested that the exchange rate depends on the M—OH binding strength and the protonation of surface OH species at different pH values.[380] In particular, an oxygen binding strength that is too weak can hinder the displacement of surface OH by O_2^{2-} species, while too strong of an oxygen binding strength would limit the surface OH generation. The O_2^{2-}/OH^- displacement

https://doi.org/10.1021/acs.chemrev.1c00331
Chem. Rev. XXXX, XXX, XXX−XXX

is followed by the protonation of M—OO with protons from water (step 2), and M—OOH transforms to M═O with the breaking of the O—O bond (step 3). Those four steps may involve the periodic changes of metal oxidation states, which can be probed by *operando* spectroscopic methods. In step 1, negative charged species, such as OH^-, from solution, can accumulate and adsorb on metal oxide surface sites such as unsaturated metal sites since the pH of the testing solution is often 13 or above, higher than the typical pH of zero charge (pH_{pzc}) of most oxides (7−11).[381−383] The ORR mechanisms on oxide surfaces are similar to the aforementioned ORR mechanisms on Pt surfaces in base (Scheme 2) since both involve the generation of O_2^- and/or O_2^{2-} species on surfaces and/or in solution. However, compared to Pt surfaces, it is much more challenging to distinguish the O-containing species formed during the ORR on oxide surfaces given that oxygen naturally exists in metal oxide lattices. Given that peroxide is commonly detected from oxide catalysts with the RRDE, it is reasonable to postulate that the O_2^- or O_2^{2-} species adsorbed on oxide surfaces can diffuse in solution and disproportionate into more stable forms of peroxide or water. The reaction intermediates and pathways on oxides are largely unexplored and remain as an active area for further investigation.

Figure 20A shows one possible simplified ORR mechanism on oxides in which all O species in the reactants, O_2 and H_2O, and products, OH^-, are from solution (marked in blue), and no lattice oxygen (marked in red) participates in the ORR process. However, the actual ORR mechanisms on oxide surfaces can be more complex and may vary depending on the coordination environment of the transition metal sites. Early differential electrochemical mass spectrometry (DEMS) studies on RuO_2 and IrO_2 particles reported lattice oxygen participating in the OER with ^{18}O isotope experiments.[384,385] Recent quantitative DEMS studies of Co_3O_4 NPs by Baltruschat and coworkers showed that 10−30% of the surface lattice oxygen participated in the OER via an oxygen exchange mechanism.[386] Another DEMS study showed the involvement of lattice oxygen in more covalent $SrCoO_{3-\delta}$ and $La_{0.5}Sr_{0.5}Co_{3-\delta}$ but not in less covalent $LaCoO_3$ particles.[50] It is worthwhile to point out that the detection sensitivity of DEMS largely depends on the cell geometry, and the recently developed dual thin-layer flow cell DEMS could provide enhanced collection efficiency to increase the reliability of the DEMS analysis.[387−391] Those studies suggest that the oxygen electrocatalysis can occur with the protonation of lattice oxygen and subsequent displacement by O_2^{2-} generated during the ORR, which may induce the formation of oxygen vacancies during the lattice oxygen exchange. $SrCoO_{3-\delta}$ and other perovskites have been reported to have pH-dependent OER activities vs RHE,[50] indicating that the RDSs of oxygen electrocatalysis are not a concerted PCET process and that the proton transfer can be decoupled from the electron transfer process.

To rationalize the ORR/OER activity trends, several activity descriptors of oxides have been proposed. Among those studied oxides, the crystal family of perovskites has gained particular attention due to their great structural tunability and promising activity since the initial discovery of $La_{0.8}Co_{0.2}Co_3$ as an active ORR catalyst in alkaline media in 1970.[392] Trasatti first correlated the OER activities of various perovskites, spinels, and rutiles to the enthalpy of the lower-to-higher oxidation state transition, which was used as an approximation of the M—O bond strength.[393] Bockris and Otagawa put together the molecular details by arguing that the OER activities should correlate with an increase of the d electron count, proposed as an approximation to the occupancy of the antibonding orbital of M—OH, which reflects a decrease of the M—O bond strength. They proposed a hypothetical volcano plot with $LaNiO_3$ having an optimum M—OH bond strength and OER activity and further suggested the possible RDS to be the electrochemical formation of peroxide-like species ($M—OH + {}^-OH = M\cdots H_2O_2 + e^-$).[381,394,395] Recognizing the crystal-field theory in the electronic structure of oxides, Matsumoto and coworkers established a correlation between the OER activity of perovskites and the overlap between the e_g-parentage band of transition metals and the sp_σ orbital of O or OH,[396−399] which indicated an RDS of the M—OH/M═O transition as shown in the reverse of step 4 in Figure 20A. Building on the work by Bockris and Matsumoto, Shao-Horn and coworkers reported the consideration of the e_g orbital occupancy through the picture of the localized metal−oxygen interaction. By investigating the ORR/OER activity trends on a series of ABO_3 perovskites, they established the correlation between the e_g occupancy of the octahedral B sites and ORR/OER activity and framed the mixing between the e_g-parentage and O 2p orbitals as the descriptor.[400−403] From a molecular orbital perspective, the hybridization of the metal d orbital and O 2p orbitals, in an octahedral coordination environment, leads to the crystal-field splitting of five degenerate d orbitals into two higher-energy e_g orbitals (d_{z^2}, $d_{x^2-y^2}$) and three lower-energy t_{2g} orbitals (d_{xy}, d_{xz}, d_{yz}).[404,405] The e_g occupancy model assumes that the e_g orbitals, which have σ-character, interact more strongly with the O $2p\sigma$ orbitals than the t_{2g}, which have π-characters.[400] The advantage of this approach is that the e_g electron occupancy of the B sites can be experimentally determined from the oxidation and spin states by bulk XAS and magnetic measurements. As shown in Figure 20B, perovskite oxides with a low e_g occupancy of B sites ($e_g < 1$, left branch) tend to bind oxygen too strongly, leading to a slower step 4, while oxides with a high e_g occupancy ($e_g > 1$, right branch) bind oxygen too weakly, hindering step 1. The presence of a single e_g electron can destabilize the B—OH bond and replace it with a more stable B—OO bond, leading to enhanced kinetics of the O_2^{2-}/OH^- displacement. However, the e_g occupancy alone cannot explain the ORR activity trends, for example, $LaNiO_3 > LaCoO_3 > LaMnO_3$, which share nearly the same e_g electron number. The M—O covalency was then proposed as a secondary descriptor: $LaNiO_3$ has a larger M—O covalency (i.e., stronger M d—O p hybridization), which can facilitate the electron transfer between M and O and benefit the O_2^{2-}/OH^- exchange on B sites.[387] Similar ORR activity trends of spinels were correlated to e_g occupancy in octahedral sites of AB_2O_4 normal spinels, where A and B, represent the tetrahedral and octahedral sites, respectively, estimated by extended X-ray absorption fine structure (EXAFS).[406] However, one needs to be cautious about the accuracy of quantifying metal valences and occupancy in different sites since XAS and magnetic measurements are average signals of bulk materials and cannot describe surface electronic structures or the existence of heterogeneity. Recently developed scanning transmission electron microscopy (STEM) imaging and electron energy loss spectroscopy (EELS) offer opportunities to explicitly characterize the surface structure and composition, at the atomic scale, and assess bulk/surface differences (section 8.2).[407]

https://doi.org/10.1021/acs.chemrev.1c00331
Chem. Rev. XXXX, XXX, XXX−XXX

Metal oxides can be either ionic, covalent, or in between. Depending on the overlap between electronic states, the extent of mixing can play a significant role on the physicochemical properties (Figure 20C).[408] At a zero-order approximation, since early transition metals in B sites of perovskites (e.g., V, Cr, and Mn) are less electronegative than oxygen, the mixing between the M 3d and O 2p is limited. As such, the corresponding perovskites are semiconducting with the "conduction" and "valence" band edges bearing predominantly d-character. Building on the same principle, late transition metals in B sites of perovskites (e.g., Co, Ni, Cu) are closer in their electronegativity to oxygen. This increases the extent of M−O hybridization, which results in an increased p-character of the "conduction" and "valence" band edges. This increased covalency results in the downshift of the Fermi level (E_F) and a reduced energy gap between metal 3d and O 2p states, to form delocalized bands. This mixture between O 2p and metal d bands can make oxides semiconducting (e.g., $LaCoO_3$) and even metallic (e.g., $LaNiO_3$), depending on the nature of the itinerant electron. Perovskites ABO_3 allow the partial substitution of A sites with various cations with valences from +1 to +3. This substitution can impact the B-site valences and/or oxygen stoichiometry. As shown in Figure 20C, partial substitution of La^{3+} with Sr^{2+} leads to the formation of $La_{1-x}Sr_xCo_{1-x}^{3+}Co_x^{4+}O_3$ with a larger overlap of Co 3d and O 2p bands (i.e., larger M−O covalency), which lowers the E_F into the Co 3d/O 2p π^* band and creates a ligand hole. Such an increase of the M−O covalency was correlated with the ability to facilitate the lattice oxygen oxidation and the enhanced OER activities of $SrCoO_{3-\delta}$ and $LaCo_{1-x}Fe_xO_3$, relative to $LaCoO_3$.[387,409] The increase in the M−O covalency, estimated via the gap between the Fermi level and the O p-band center, has been proposed to allow faster surface oxygen exchange kinetics and enhanced OER activity.[410] However, when the O p-band center is too close to the E_F, for instance, in the case of $Ba_{0.5}Sr_{0.5}Co_{0.8}Fe_{0.2}O_{3-\delta}$, the OER activity is compromised by poor stability with the leaching of A-site metals and rapid amorphization.[401] In other words, increasing the M−O covalency also increases the tendency of an oxide to release the lattice oxygen and form oxygen vacancies, which can potentially change the oxide structures from the designed/desired surface.

The growth of oxides and their postannealing play a crucial role in the formation of oxygen vacancies and related defects. Oxygen vacancies have a strong impact on lattice parameters, coordination environment, electrical conductivity, and catalytic activities. Oxygen stoichiometry can be measured through iodometric, cerimetric, and $Cu^{+/2+}$ coulometric titration methods;[411] gas volumetric analysis;[412] and structural refining based on neutron and X-ray diffraction[413] with a δ accuracy better than ±0.01. A recent study by Stevenson and coworkers highlighted the importance of oxygen vacancy content in rationalizing the OER activities of $La_{1-x}Sr_xCoO_{3-\delta}$ (Figure 20D).[408] The significantly enhanced OER activity of perovskites, in particular $SrCoO_{2.7}$, was correlated to the increase in oxygen vacancy and faster O^{2-} diffusion estimated from chronoamperometric methods. $La_{1-x}Sr_xCoO_{3-\delta}$ with $x > 0.4$ showed a noticeable increase in oxygen vacancies owing to the increasing M−O covalency and oxygen stoichiometry. They also proposed a vacancy-mediated OER mechanism through the participation of lattice oxygen through *ab initio* modelling to demonstrate an alternative pathway besides the mechanism presented in Figure 20A. A similar function of oxygen vacancies was reported for the OER catalysts, La-deficient $La_{1-x}FeO_{3-\delta}$.[414] The same group also investigated the impact of various N-doped carbon supports on perovskites using RRDE techniques and microkinetic modelling for the ORR. N-doped carbon was shown to be able to activate the initial ORR to O_2^- or HO_2^-, which was further reduced to OH^- on perovskite surfaces.[415] Schmidt and coworkers reported that acetylene black as a carbon support could reduce the Co valence in the supported perovskites, $Ba_{0.5}Sr_{0.5}Co_{0.8}Fe_{0.2}O_{3-\delta}$, which in turn improved the ORR/OER activities in alkaline media.[416] Those studies show the potential to understand the metal oxide catalyst−support interactions and design carbon and noncarbon supports that can not only stabilize oxide particles but also boost their ORR activities (section 5).

The structural descriptors for the stability of metal oxide catalysts under ORR conditions are not as well understood as their ORR activity. Preliminary experiments showed particle aggregation, dissolution, decomposition, and surface reconstruction of metal oxides during extended durability tests under negative applied potentials (cathodic conditions). Those changes can be monitored by TEM, X-ray spectroscopy, EQCM,[417] and inductively coupled plasma mass spectrometry (ICP-MS),[418] among other techniques. In contrast to the OER conditions where anodic potentials tend to induce an irreversible oxidation of metal sites and possible oxygen vacancies, ORR conditions can reduce metal oxides to lower valences or even metallic phases, which can induce irreversible structural changes of the oxides. Early studies reported that $LaNiO_3$ underwent heterogeneous reduction to $La(OH)_3$ and NiO during prolonged exposure to low potentials in alkaline media, causing rapid activity decay.[419−422] A recent study by Suntivich and coworkers showed a similar catalyst instability of $La/SrMnO_3$ single crystals at low potentials during the ORR in alkaline media.[423] A recent report shows that substituting Mn with Cu in B sites ($LaCu_{0.5}Mn_{0.5}O_3$) can maintain a stable structure down to 0.4 V vs RHE.[424] It remains a key challenge as to how to enhance the catalyst−support interactions while not blocking active sites and improve structural stability via stabilizing the $M^{3+/4+}$ in B sites while suppressing the leaching of metals in both A and B sites.

In summary, the ORR mechanisms on non-precious-metal oxide surfaces are rather complex, compared to precious metals, in part because the reaction pathways vary depending on the coordination environment of metal sites and structures of oxide surfaces. Several activity descriptors have been proposed from molecular orbital and band theories to correlate electronic structures and oxygen vacancies of metal oxides to their activity and stability. However, the proposed descriptors have forgone the molecular details and the complex nature of the oxygen electrocatalysis on oxide surfaces and thereby have limited applicability. For instance, the number of d-electrons or e_g electrons is of limited value when trying to explain the outstanding OER activities of other oxide families such as RuO_2, IrO_2, and Ni−Fe oxides. It is therefore inadequate to rely on the descriptor approach alone. Thus, molecular details of the interactions between oxides and reaction intermediates, at varying electrochemical potentials, are crucial to understand the unique role of extended H-bonded water networks, interacting with oxide surfaces, and how water serves as the proton donor for the PCET during the ORR in a proton-deficient alkaline environment.

4.2.2. Details of Electrocatalysis from Well-Defined Oxide Studies. The critical challenge with the ORR studies of

https://doi.org/10.1021/acs.chemrev.1c00331
Chem. Rev. XXXX, XXX, XXX−XXX

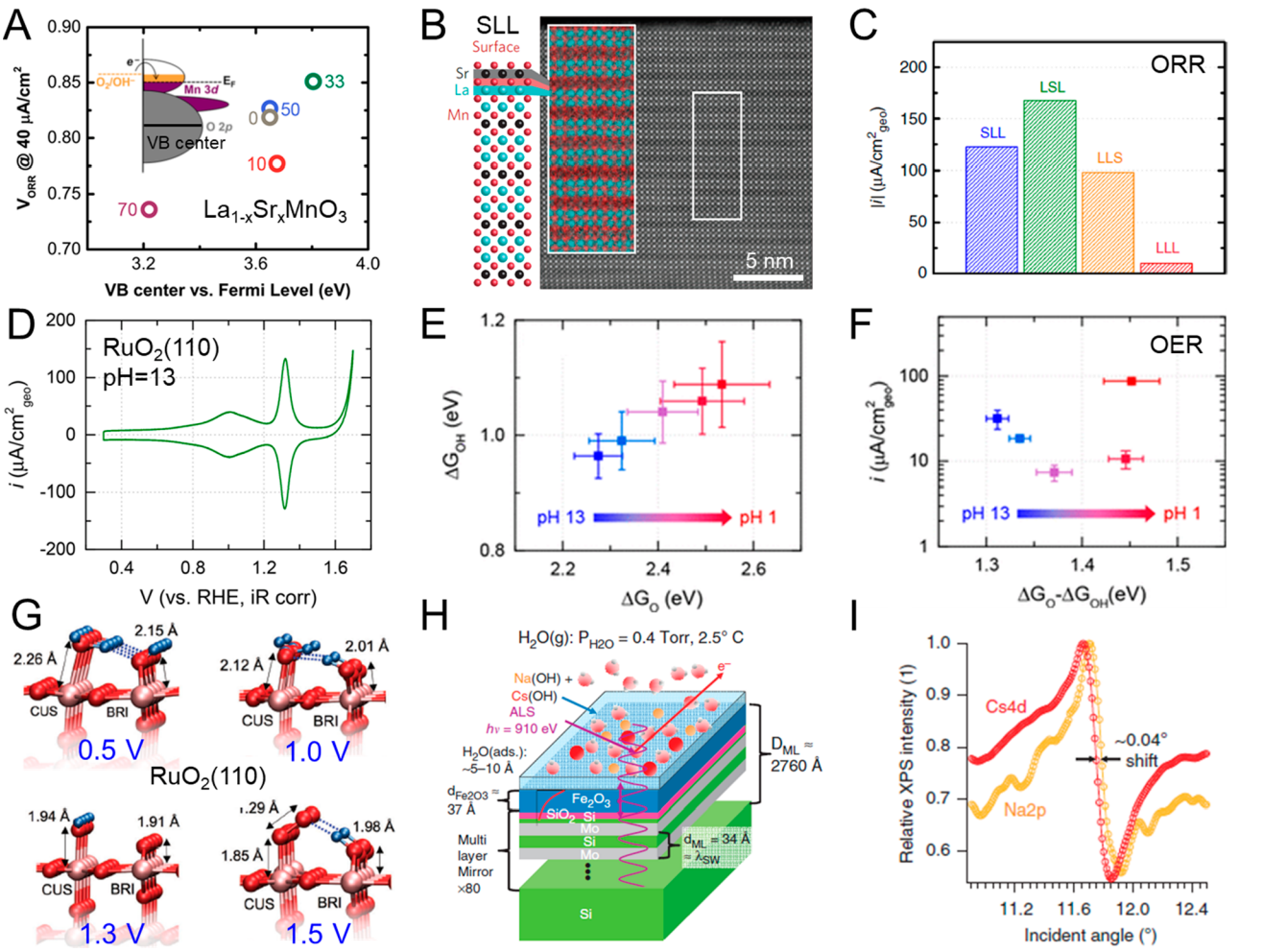

Figure 21. Oxygen electrocatalysis on well-defined oxide surfaces in alkaline media. (A) ORR activities (potentials for achieving 40 $\mu A/cm^2$) of a series of $La_{1-x}Sr_xMnO_3$ perovskite single-crystal films (numbers in different colors denote the percentage of Sr^{2+} in mixed A sites of La^{3+} and Sr^{2+}). (B) STEM images of $(LaMnO_3)_2/(SrMnO_3)$ layered superlattices (labeled as SLL), along with a schematic of the crystal structure with MnO_2 surface termination. Enlarged EELS maps (insets) show Mn in red and La in turquoise and demonstrate well-ordered films with a clear separation of Sr and La. (C) ORR activities of various $(LaMnO_3)_2/(SrMnO_3)$ [$(LMO)_2$/LSO] configurations (kinetic current density at 0.8 V vs RHE). SMO-LMO-LMO is denoted as "SLL", same as in panel B. (D) CV profile of $RuO_2(110)$ in 0.1 M KOH at 200 mV/s. (E) Experimentally measured adsorption energies of O_{ad} and OH_{ad} on $RuO_2(110)$ showing the scaling relation at different pH values. (F) Correlation of OER activity (current density at 1.63 V vs RHE) of $RuO_2(110)$ to the difference in adsorption energies of OH_{ad} and O_{ad}. (G) Most stable adsorbate configuration of surface O species on $RuO_2(110)$ obtained from X-ray diffraction CTR and a best fit from DFT calculations. Pink, red, and blue spheres represent Ru, O, and H atoms, respectively. CUS and BRI denote coordinatively unsaturated Ru sites and bridge sites, respectively. (H) Schematic of standing wave (SW) ambient-pressure XPS measurements on Fe_2O_3 polycrystalline thin films with synthetic Si/Mo layers serving as a built-in ruler for sub-nm spatial resolution. (I) Relative XPS intensity of Na and Cs as a function of the incident angle. Panel A is adapted with permission from ref 426. Copyright 2017 American Chemical Society. Panel B is adapted with permission from ref 430. Copyright 2012 The Authors, Springer Nature. Panel C is adapted with permission from ref 423. Copyright 2016 The Authors, Springer Nature. Panels D–F are adapted with permission from ref 431. Copyright 2018 American Chemical Society. Panel G is adapted with permission from ref 441. Copyright 2017 The Royal Society of Chemistry. Panels H and I are adapted with permission from ref 447. Copyright 2014 Springer Nature.

metal oxide nanoparticles is the convolution of synthesis methods, particle size (and its distribution), and morphology as well as crystal orientation, defects, and oxygen vacancies of the catalyst particles. Those factors present formidable challenges to simultaneously control, and likely complicate our understanding of, the intrinsic activity of metal oxide electrocatalysts. In comparison, single-crystal metal oxides provide a well-defined surface structure/composition. Thus, they have the potential to advance our understanding of oxygen electrocatalysis like single-crystal Pt studies have done for metals. Single-crystal metal oxides can be prepared through several methods; however, they often involve high-temperature syntheses. Recently, thin-film methods such as pulsed laser deposition (PLD) and molecular beam epitaxy (MBE), which enable a precise control of surface/bulk structure/composition with an atomically flat surface and minimal defects, have been demonstrated as an alternative approach to producing well-defined metal oxide surfaces. For simplicity, we will refer to these well-defined metal-oxide thin films as "single crystals" in the rest of this Review given their single-crystal-like surface behavior. As shown in Figure 21A, single-crystal $La_{1-x}Sr_xMnO_3(001)$ films were grown on Nb-doped $SrTiO_3$ by PLD and exhibited an optimal ORR activity at 33% Sr ($La_{2/3}Sr_{1/3}MnO_3$), which was first correlated to its apparent highest electronic conductivity and fast charge transfer kinetics.[425] Ambient pressure XPS (AP-XPS) further showed

https://doi.org/10.1021/acs.chemrev.1c00331
Chem. Rev. XXXX, XXX, XXX−XXX

that the valence band center had a positive correlation to the ORR activity (Figure 7A),[426] where it was rationalized that a lower valence band center, relative to E_F, could weaken the adsorption of OH species. This modified OH interaction facilitates the OH^-/O_2^{2-} exchange (step 1, Figure 20A) and consequently the ORR kinetics in alkaline media. $La_{0.8}Sr_{0.2}CoO_3$ single crystals grown by PLD exhibited an increasing ORR activity but also an increasing instability order: (110) > (111) > (001).[427] X-ray reflectivity measurements of $La_{0.8}Sr_{0.2}CoO_3$ showed a lattice expansion and formation of oxygen vacancies to compensate for the reduction of Co^{3+}, accompanied by the possible formation of La/Co hydroxides after sweeping to low potentials during the ORR in alkaline media. Placing oxides on different substrates, with compressive or tensile strains, offers another approach to tune the oxide surface structure similar to strategies used in designing Pt_3Co@Pt core−shell catalysts for PEMFCs. For instance, $LaCoO_3$ thin films with a moderate tensile strain (~1.8%) relative to the bulk phase, induced by substrates, showed faster charge transfer kinetics and enhanced ORR and OER activity, relative to $LaCoO_3$ films with a −0.5% compressive strain and a 2.6% tensile train.[428] The strain effect on the surface bonding of oxides is, however, not trivial. A recent study of $SrIrO_3$(100) grown on different substrates showed that water adsorption can counter the impact of strain on the surface oxygen binding strength, making the OER activity independent of strain.[429] This finding points to the nontrivial connection between surface oxygen binding in a vacuum and in electrochemical environments, where the interfacial water network, in the latter situation, can counter the intended impact of strain on the oxygen binding. Thus, even when using well-defined oxide surfaces, determining the interplay between atomic structure, electronic structure, and electrochemistry remains challenging.

The use of advanced deposition methods, to grow well-defined oxide electrocatalysts, opens a unique opportunity to realize a novel combination of atomic layers of chemically distinct metal oxides. Figure 21B presents an example of layered $(LaMnO_3)_2/SrMnO_3$ ($(LMO)_2$/SMO) superlattices grown layer-by-layer on $SrTiO_3$(001) by MBE.[430] STEM images and EELS elemental maps demonstrated the atomically abrupt LaO/MnO_2/SrO and SrO/MnO_2/LaO interfaces with a MnO_2 surface termination (labeled as SLL from the surface to subsurface), which shows a metallic behavior. Taking advantage of this capability, it is now possible to control the chemistry of the topmost surface layer down to the subsurface, e.g., stacking the compositions from the surface as either LMO-SMO-LMO (LSL) or LMO-LMO-SMO (LLS) and Sr-free LMO-LMO-LMO (LLL). These atomically precise materials were prepared with various surface and subsurface layers but with identical overall compositions and hence overall d-electron configurations (Figure 21C).[423] Although the SLL with $SrMnO_3$ as the topmost layer benefits the ORR with enhanced conductivity relative to the insulating LLL (pure $LaMnO_3$), $SrMnO_3$ can react with O_2 to form an undesirable insulating SrO layer. Engineering $SrMnO_3$ as the sublayer in the LSL maintains a stable $LaMnO_3$ surface while still benefiting from improved electronic effects from $SrMnO_3$, which results in the optimal ORR activity of the LSL.[423] Those studies illustrate the great tunability of oxide surface/subsurface structures and compositions with atomic-layer precision by thin-film deposition over conventional bulk crystal growth.

Single-crystal oxides have also enabled the examination of fundamental mechanistic concepts of the two most active OER electrocatalysts, RuO_2 and IrO_2, for the water electrolyzer industry. Figure 21D exhibits the well-defined CV profile in alkaline media of MBE-grown RuO_2(110) on a TiO_2 substrate.[431] The broad reversible peaks at ~1 V vs RHE were assigned to OH_{ad} electroadsorption ($H_2O_{ad} \rightarrow OH_{ad} + H^+ + e^-$) while the sharper peaks at ~1.3 V vs RHE represent the O_{ad} electroadsorption ($OH_{ad} \rightarrow O_{ad} + H^+ + e^-$), which correspond to the $Ru^{3+/4+}$ and $Ru^{4+/5+}$ redox couples, respectively.[380] An analysis based on the Frumkin isotherm (eq 11) suggests that OH and O adsorbates repel each other enthalpically (ΔH becomes more positive at higher coverage) but attract each other entropically (ΔS becomes more positive at higher coverage),[432] with OH adsorption showing a positive interaction parameter, ω (repulsive interaction), and O adsorption showing a negative value (attractive interaction). These observations indicate the critical role of the adsorbate−adsorbate interactions in understanding the electroadsorption process, an observation that was linked to the network of interfacial water molecules as a mediator to the interactions. Both OH and O adsorption peaks exhibited a non-Nernstian pH-dependence vs RHE (i.e., >59 mV/pH vs SHE), suggesting that the reaction may involve a partial charge transfer from Ru to O/OH, resulting in electron transfer numbers less than ideal ratios. To quantify the pH-dependence, OH and O adsorption peak positions, corresponding to 50% coverage, were used to estimate the adsorption free energy, ΔG_{OH} ($E_{OH_{ad}}$) and ΔG_O ($E_{OH_{ad}} + E_{O_{ad}}$) and the potential window at 90% coverage was used as error bars. As shown in Figure 21E, a linear scaling relationship was found between ΔG_{OH} and ΔG_O of RuO_2, which is similar to the well-established trends in Pt-based catalysts. One might anticipate a volcano-type relationship as commonly established in Pt-based catalysts. However, RuO_2 showed a minimum OER activity in neutral pH at an intermediate value of $\Delta G_O - \Delta G_{OH}$ (Figure 21F). Moreover, RuO_2 and IrO_2 single crystals exhibited a similar OER activity despite very different values of $\Delta G_O - \Delta G_{OH}$.[433] Such deviations from the conventional Sabatier principle suggest that the electroadsorption energy may lack the microkinetic details involving the proton and electron transfers in the presence of interfacial water. The activity trends in Figure 21F were rationalized as two possible different RDSs regarding the formation of OOH_{ad} in acidic and alkaline media (the reversal of step 3 in Figure 20A): acid, $O_{ad} + H_2O \rightarrow OOH_{ad} + H^+ + e^-$; alkaline, $O_{ad} + OH^- \rightarrow OOH_{ad} + e^-$. If the kinetics of OOH_{ad} formation are more favorable in acid than in alkaline media, increasing the pH can hinder the OOH_{ad} formation in acid but facilitate the OOH_{ad} formation and thus OER kinetics in alkaline media.

Recently developed surface-sensitive X-ray methods provide structural insights into interfacial water on oxide surfaces. For example, specular X-ray reflectivity of mica(001) (a layered aluminosilicate) showed that the first-layer water has a strong interaction with the oxide surface and an oxygen density twice as high as the bulk water.[434] The strong oscillation of the oxygen density within 10 Å of the surface in the direction normal to oxide surfaces indicates an interfacial ordering of water. AP-XPS studies on spinel Fe_3O_4(001) showed that water began to adsorb with progressively increasing dissociation into the surface OH species at a very low water pressure of 10^{-4} Torr and achieved a monolayer of OH at 10^{-2} Torr.[435,436]

https://doi.org/10.1021/acs.chemrev.1c00331
Chem. Rev. XXXX, XXX, XXX−XXX

Here, we focus on two selected catalysts (RuO_2 and Fe_2O_3) highlighting the recent progress on the elucidation of the interfacial water structure and O-containing intermediates on oxide catalyst surfaces under applied potentials. An early report on RuO_2(110) by Ertl and coworkers, with EELS and LEED, showed that O_2 gas molecules could adsorb and dissociate rapidly to form a stable Ru−O−Ru bridging configuration as well as Ru−O in the terminal position.[437,438] Lister and Nagy used an off-specular oxygen crystal truncation rod (CTR) to measure the potential-dependent water adsorption on RuO_2(110) and (100) in both acidic and alkaline media (details of CTR will be introduced in section 8.1.3).[439,440] They identified an OH adsorption layer on bulk RuO_2(110) in alkaline media, which could interact with interfacial water, forming an icelike bilayer structure under high potentials close to the OER. At low potentials, the bridging OH layer is converted to a layer of low-density commensurate water. Recent studies by Shao-Horn examined the surface structural changes of RuO_2 single crystals with various crystal orientations in acidic media with X-ray CTR measurements and DFT simulations.[441,442] It should be noted that the positions of H atoms are only speculated based on changes in the Ru−O bond lengths in CTR measurements since the X-ray scattering cross-section of H atoms is very small. Figure 21G illustrates the adsorption of reaction intermediates on RuO_2(110) with both coordinatively unsaturated (cus) Ru sites (Ru bound to 5 O atoms) and bridge Ru sites (Ru bound to 6 O atoms).[441] At low potentials (e.g., 0.5 V), H_2O adsorbs on Ru_{cus} sites, and OH forms on bridge sites through the protonation of oxygen species. At potentials close to the OH_{ad} peak (e.g., 1.0 V), every second water molecule on Ru_{CUS} sites dissociates while every OH_{ad} on bridge sites deprotonates. At potentials after the O_{ad} adsorption peak (e.g., 1.3 V), all Ru_{cus} sites are filled with OH while all bridge sites are deprotonated. At potentials close to the OER (e.g., 1.5 V), OO species on Ru_{cus} sites were identified and stabilized by OH_{ad} on neighboring bridge sites, and the deprotonation of the OH group and the following removal of OO were proposed as the possible RDS of RuO_2(110) in acid. The presence of OO species was later confirmed by *in situ* SEIRAS and H/D isotopic measurements.[442] RuO_2 single crystals exhibit an OER activity order in acid of (100) > (101) > (110) ≈ (111).[443] The highest OER activity of Ru(100) was ascribed to both the higher density of Ru_{cus} sites ($7/nm^2$), relative to that of (110) ($5/nm^2$), and reduced OO binding energy on Ru_{cus} sites. Despite having a high density of Ru_{cus} sites ($8/nm^2$), Ru(101) was shown to have an even weaker OO binding energy, and an alternative RDS was proposed as $Ru-O + H_2O \rightarrow Ru-OOH + H^+ + e^-$, which resulted in an intermediate OER activity. Finally, it is worthwhile to point out that practically used RuO_2 nanoparticles show an OER activity comparable to or even higher than the most active RuO_2(100).[444] A close examination of oxide nanoparticle surface steps, grain boundaries, and other structural defects can shed new light onto the observed high activity and help design other nonprecious OER catalysts.

Operando X-ray standing waves (XSWs) can resolve the electrode−electrolyte interface with atomic-scale depth resolution in the direction normal to the surface.[338] XSWs are generated by the interference between incident waves and strongly reflected waves at the Bragg reflection. The periods of XSWs can be tuned with high-*Z*/low-*Z* layered synthetic microstructures (LSM) from Å to nm to satisfy the length-scale requirement of experiments, such as charge distributions at interfaces over several tens of Ångströms. As the angle of the incident beam is advanced across the strong Bragg reflection, the XSWs can sample different atomic layers in the electrochemical double layer and further extend into the solution layer. The *d*-spacings normal to the surface, monitored by the incident angle of XSWs, serve as a "built-in ruler" which is capable of providing Å-level vertical resolution. Our early studies employed *operando* XSWs and X-ray fluorescence spectroscopy on Pt/C LSMs to provide the first unambiguous evidence of the displacement of an adsorbed iodide layer on Pt with electrodeposited Cu.[445,446] A recent study by Fadley et al. combined XSWs with AP-XPS to investigate the ionic distribution in NaOH/CsOH alkaline solution on polycrystalline Fe_2O_3 films (~6 Å surface roughness) deposited on Si/Mo LSMs (Figure 21H).[447] It provided direct evidence that Na^+ was ~4 Å closer to the oxide surface than Cs^+ given a 0.04° positive shift in the incident angle (Figure 21I). The further distance of Cs^+ from the oxide surface is similar to the weaker interactions of Cs^+ with Pt surfaces leading to a higher ORR activity (Figure 17H). It should be noted that the liquid layer in this *ex situ* study was limited to ~1 nm for AP-XPS with soft X-rays (~1 keV). *Operando* XSWs enable the use of polycrystalline oxide films deposited on LSMs, which clears the limitation of using single-crystal oxides and can have promising applications in resolving solid/liquid interfaces on nanoparticle oxide catalysts during realistic fuel cell reaction conditions. In addition to the aforementioned X-ray methods, optical vibration spectroscopy, in particular, surface-enhanced Raman and IR, have been widely employed to investigate the reaction intermediates at oxide−electrolyte interfaces.[448,449] Those surface-enhanced techniques often require a thin oxide film deposited on roughened (typically Au) metal substrates. Weaver and coworkers performed an early *in situ* SERS study with a 3-monolayer poly-Ru film electrodeposited on a roughened Au substrate to investigate the electrochemical oxidation of Ru and reduction of RuO_2 involving $Ru^{3+/4+}$ transitions in acid.[450,451] Bell and coworkers employed SERS to demonstrate the dynamic oxidation of Co_3O_4 and Ni−Fe hydroxides on Au substrates and captured the key reaction intermediates of CoOOH and NiOOH at potentials close to the OER.[452,453] It is worthwhile to mention that the oxide film thickness and the metal substrate have a significant impact on the electronic structures of oxides and, in turn, influence the catalytic activity.[452] One strategy is to coat metal substrates with a thin inert oxide layer to prevent charge transfer between the substrates and studied oxide catalysts. Recent work by Yang and coworkers employed SERS with Al_2O_3-coated Ag nanoparticle assemblies and identified OOH, O_2^{2-}, and OH intermediates on a TiO_2 surface during a photochemical water splitting process.[454] Future technical developments may enable the direct use of bulk oxide crystals in both single-crystal and polycrystalline forms. In summary, the use of *operando* X-ray and vibrational spectroscopies offers a rare glimpse at the dynamic structural changes at oxide surfaces. We anticipate that advances in spatially and temporally resolved spectroscopy will further our understanding of these complex oxide surfaces.

4.2.3. ORR Activity of Nanoscale Metal Oxides. Since alkaline fuel cells enable the use of nonprecious ORR catalysts, a variety of nanoparticle candidates have been reported to show promising ORR activity in alkaline media based on RDE tests, such as precious-metal-based alloys, N-doped carbons,

https://doi.org/10.1021/acs.chemrev.1c00331
Chem. Rev. XXXX, XXX, XXX−XXX

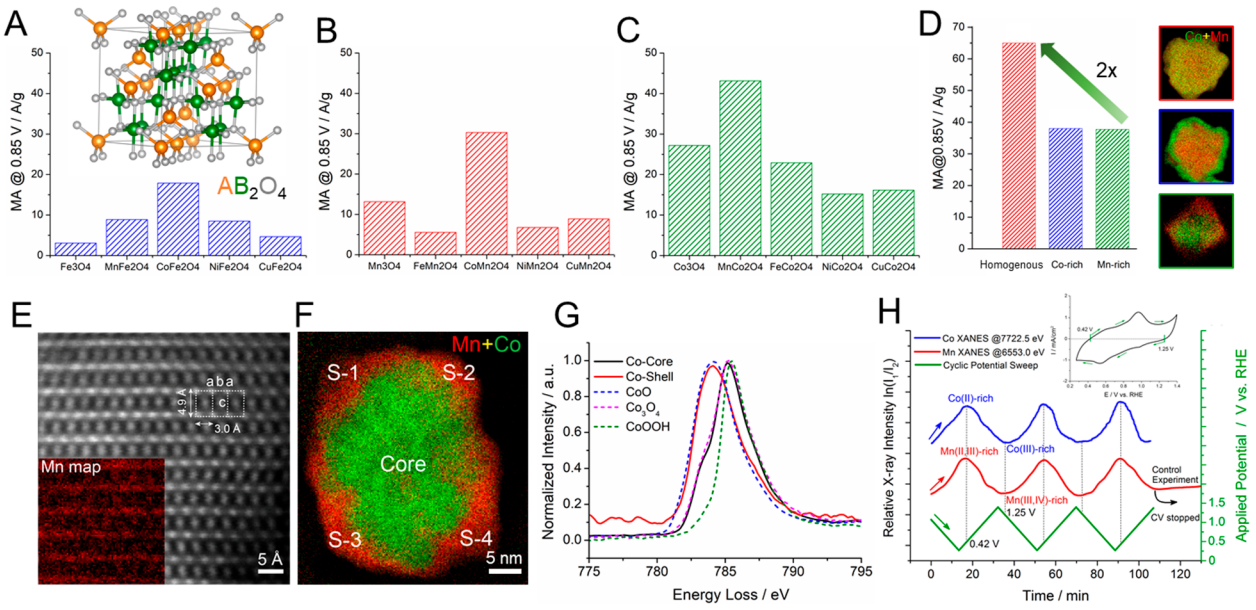

Figure 22. ORR activities of spinels in alkaline media and a correlation to their microstructures and compositions. (A–C) ORR activities (mass activity, MA at 0.85 V vs RHE) of a variety of spinels in an AB_2O_4 formula from RDE measurements in 1 M KOH at a loading of 0.1 mg_{oxide}/cm^2. The inset in panel A shows the crystal structure of cubic spinel with A in tetrahedral sites and B in octahedral sites. (D) ORR activities of $Co_{1.5}Mn_{1.5}O_4$ spinels as a function of surface compositions as shown in the EELS elemental maps of evenly distributed Co/Mn, Co-rich, and Mn-rich samples. Particle sizes are around 30 nm. (E) Atomic-scale STEM image of $CoMn_2O_4$ on the $[01\bar{1}]$ zone axis. (inset) Atomic-scale EELS elemental map of Mn showing the characteristic layered structure in spinels. (F) EELS elemental map of one $MnCo_2O_4$ nanoparticle with a Mn-rich shell (S-1, S-2, S-3, and S-4 represent four regions in the shell). (G). Comparison of average ELNES spectra of Co in the core and shell with standard Co oxide references. Co at the core clearly has a major contribution from Co_3O_4 (II, III) while Co at the shell is predominantly Co^{2+}, resembling the feature of the CoO (II) reference. (H) Periodic changes in the relative X-ray intensities ($\ln(I_1/I_2)$ at 7722.5 eV (Co K-edge) and 6553.0 eV (Mn K-edge), representing relative metal valence changes, as a function of the cyclic potential sweep. Intensity variations at 7722.5 and 6553.0 eV reflect the conversion between Co(II) and Co(III), and Mn(II, III) and Mn(IV), respectively. The upper inset shows the corresponding CV profile at 1 mV/s with oxidation and reduction currents divided by two boundary potentials, 0.42 and 1.25 V, respectively. Panels A–C and E–G are adapted with permission from ref 466. Copyright 2019 The Authors National Academy of Sciences. Panels D and H are adapted with permission from ref 469. Copyright 2019 American Chemical Society.

perovskites, and 3d transition metal oxides. However, only a few RDE results have translated into an encouraging MEA performance in AEMFCs. Although the previous two sections presented numerous perovskite candidates as active ORR catalysts, based on RDE tests, their present ORR activity is still very inferior compared to Pt/C in alkaline media, likely due to the small electrochemical surface area and/or poor electronic conductivity of μm-sized catalyst particles.[400,401] The large size arises from the fact that the majority of perovskite-based catalysts are prepared via solid-state synthesis, which often requires high-temperature calcination to achieve desirable single phases.[419−424] As previously discussed, the poor stability of many perovskite ORR catalysts at low reduction potentials (<0.6 V) is a great challenge facing this family of catalysts in realistic applications. The activity and stability of perovskites based on RDE tests are pending for examination in MEA tests. Considering that the typical cell voltage of MEA tests ranges from 1.0 to 0.3 V, it is important to design nonprecious ORR catalysts, which not only are highly active but also maintain stability at low reducing potentials for long time periods.

3d transition metal oxides with the spinel structure have emerged as a novel family of ORR electrocatalysts in alkaline fuel cells, due to their high activity, long-term durability, and low cost. Co and Mn oxides have been reported to be effective ORR electrocatalysts based on RDE tests in alkaline media.[455,456] Furthermore, Co−M (M is Mn, Fe, Ni, Cu, Zn, Mo, etc.)[457−465] and other bimetallic oxides have been reported to exhibit enhanced ORR activities in alkaline media, relative to their monometallic oxide counterparts. During the development of bimetallic oxides as ORR electrocatalysts, multivalence active sites and chemical interactions between two metal centers have often been proposed as possible structural/electronic factors correlating to the enhanced electrocatalytic activity.[379,406] Despite numerous studies of 3d metal oxide electrocatalysts, the electrocatalytic mechanism remains poorly understood. Recently, we reported a facile hydrothermal method to synthesize a family of 15 types of AB_2O_4 spinels (A: Mn, Fe, Co, Ni, and Cu; and B: Mn, Fe, and Co) as ORR electrocatalysts with a well-controlled octahedral morphology and small particle sizes (~30 nm) as shown in Figure 22A–C.[466] The Co-based spinel family, ACo_2O_4, has a regular cubic crystal structure in which the A atoms occupy the tetrahedral sites while the Co atoms occupy half of the octahedral sites (Figure 22A, inset). In contrast to Co_3O_4, the Mn-based spinel family (AMn_2O_4) had a tetragonal spinel structure with lower symmetry due to the Jahn−Teller distortion around the $Mn^{3+}[3d^4]$. Fe-based spinels, AFe_2O_4, often adopt a cubic inverse spinel structure, where all of the A atoms and half of the Fe atoms occupy octahedral sites, while the other half of the Fe atoms occupy tetrahedral sites. Preliminary RDE measurements showed $MnCo_2O_4$/C, $CoMn_2O_4$/C, and $CoFe_2O_4$/C as the three most active candidates among the 15 types of AB_2O_4 spinels in terms of mass activity at 0.85 V vs RHE (Figure 22A–C). In particular, $MnCo_2O_4$/C and $CoMn_2O_4$/C exhibited $E_{1/2}$ values above 0.85 V vs RHE and a significantly higher mass activity at 0.85 V

https://doi.org/10.1021/acs.chemrev.1c00331
Chem. Rev. XXXX, XXX, XXX−XXX

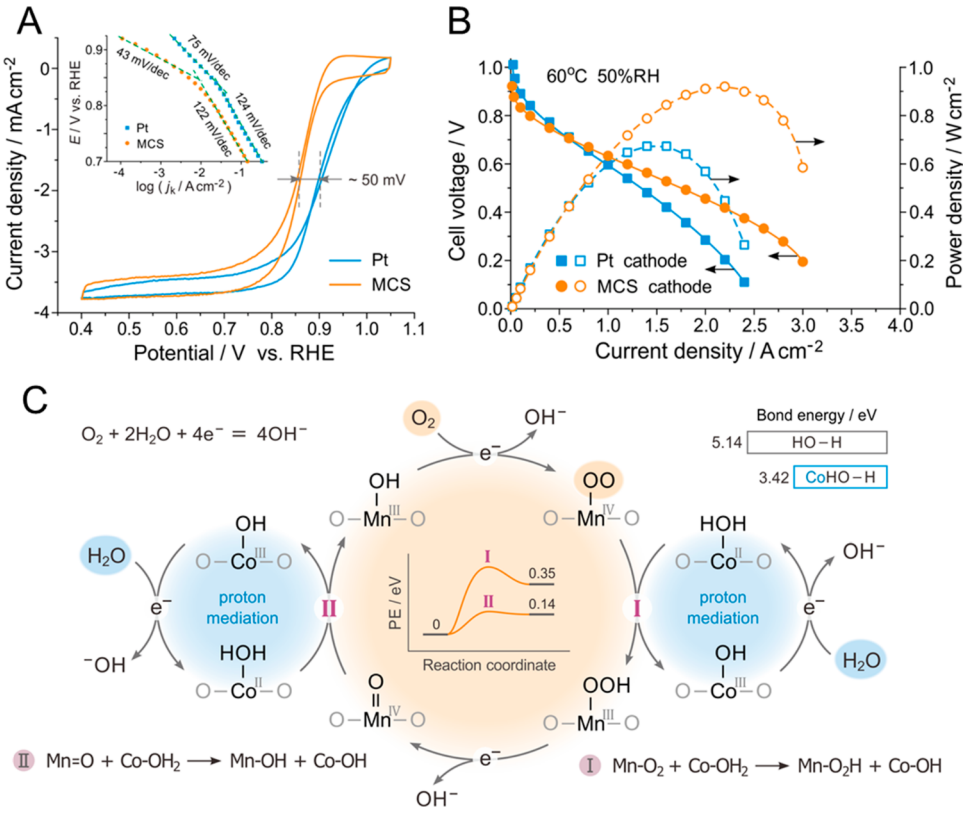

Figure 23. Comparisons of RDE and MEA performances of Mn−Co spinels (MCS) and proposed synergistic ORR mechanisms. (A) Rotating disk electrode (RDE) measurements in O_2-saturated 1 M KOH solution with 40 wt % Pt/C (50 $\mu g_{Pt}/cm^2$) and 40 wt % MCS/C (0.1 mg_{oxide}/cm^2), respectively, at 1600 rpm and 5 mV/s. Inset: Tafel plots. (B) practical membrane exchange membrane (MEA) tests in anion exchange membrane fuel cells (AEMFCs) with pure H_2 and O_2 at 60 °C and 50% RH with a back pressure of 0.1 MPa. Anode catalyst: 60 wt % Pt−Ru/C (0.4 mg_{metal}/cm^2). Cathode catalyst: 60 wt % Pt/C (0.4 mg_{Pt}/cm^2) or 40 wt % MCS/C (0.8 mg_{oxide}/cm^2) Alkaline polymer electrolyte: *a*QAPS-S_8 membrane and *a*QAPS-S_{14} ionomer. (C) Schematic illustration of the proposed mechanism of ORR on MCS, featuring the dissociative reduction of O_2 at the Mn site, the proton mediation by the Co site, and the surface proton transfer in between (reaction I and II). (central inset) DFT-calculated energy barriers for reactions I and II on MCS (100). (upper-right inset) DFT-calculated bond energies of O−H in H_2O and Co−OH_2. Panes A−C are adapted with permission from ref 16. Copyright 2019 The Authors, Springer Nature.

than previously reported oxide ORR catalysts,[400,401,419−424,455−465] benefiting from highly active surfaces and small particle sizes (~30 nm). Mn−Co spinels also demonstrated a comparable ORR selectivity to Pt/C with low peroxide yield and a remarkable durability during accelerated RDE stability tests. It is worth mentioning that simply putting Co and Mn together in bimetallic spinel phases is not sufficient; the surface chemical composition matters. By fine tuning synthetic methods, three types of spinels, with the same bulk composition $Co_{1.5}Mn_{1.5}O_4$, were synthesized with Co-rich, Mn-rich, and homogeneous surface elemental distributions, as evidenced by EELS elemental maps in Figure 22D.[16] The homogeneous Co−Mn spinel exhibited an ORR activity twice as high as that of either the Co-rich or Mn-rich spinels, suggesting that the precise control of the surface composition of electrocatalysts is crucial for designing highly active ORR electrocatalysts.

Atomic-scale STEM imaging and EELS spectroscopy were employed to investigate the structure and local chemical environment of Co−Mn spinels. As shown in Figure 22E, the high-angle annular dark-field (HAADF) STEM image of $CoMn_2O_4$ exhibits a characteristic layered structure of a tetragonal spinel along the $[01\bar{1}]$ direction.[466] Two *d*-spacings of 4.9 and 3.0 Å match well the ideal theoretical lattice planes of $CoMn_2O_4$(011) and (200), 4.88 and 3.04 Å, respectively. The EELS map (Figure 22E, inset) provides unambiguous evidence of the layered structure of $CoMn_2O_4$ along the $[01\bar{1}]$ direction. In contrast to $CoMn_2O_4$ with a homogeneous elemental distribution, $MnCo_2O_4$ exhibits a clear Co-rich core and Mn-rich shell (2−4 nm) structure (Figure 22F).[466] A detailed analysis of the local chemical environment of Mn, Co, and O in $MnCo_2O_4$/C requires fine structures in EELS spectra with both high energy and spatial resolutions, which is often referred to as the energy-loss near-edge structure (ELNES). The ELNES is very sensitive to changes in local electronic structure, such as valence states and the coordination environment, since it can directly probe the density of the unfilled density of states above the Fermi level.[467,468] Figure 22G exhibits the ELNES spectra of Co L_3 edges: the spectrum from the core resembles the features of Co_3O_4(II,III), indicating that Co is mainly cubic spinel in the core; i.e., Co^{2+} and Co^{3+} occupy tetrahedral and octahedral sites in the core and shell regions, respectively. However, Co in the shell shows a strikingly different ELNES very similar to CoO(II), with Co in octahedral sites in a rock salt (NaCl) structure. The ELNES spectra of the Mn L_3 edge suggest that Mn in the core also has a higher Mn valence than Mn in the shell. Mn L_3 edges, in both the core and shell regions, are much broader than the Mn oxide references, indicating a less-ordered nearest-neighbor oxygen distribution and a lower crystal symmetry

https://doi.org/10.1021/acs.chemrev.1c00331
Chem. Rev. XXXX, XXX, XXX−XXX

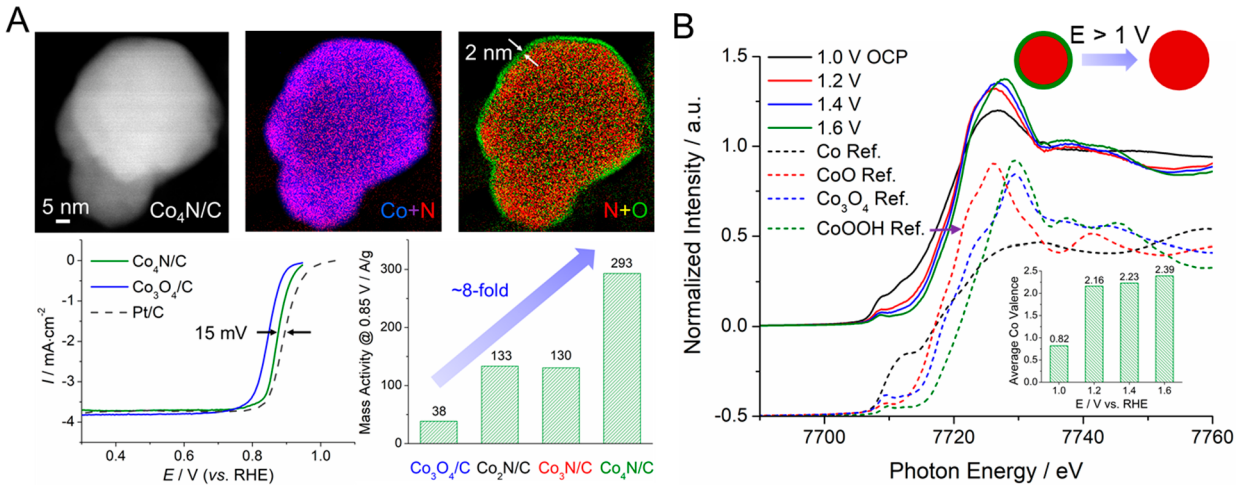

Figure 24. ORR activity and stability of metal nitrides in alkaline media. (A) Upper panel: HAADF-STEM images of one Co_4N nanoparticle and the corresponding EELS elemental maps and composite maps of Co vs N and O vs N with Co in green, N in red, and O in green. Lower panel: ORR polarization profiles of Co_4N/C, Co_3O_4/C, and Pt/C in O_2-saturated 1 M KOH at 5 mV/s and 1600 rpm and MA of Co_2N/C, Co_3N/C, Co_4N/C, and Co_3O_4/C at 0.85 V vs RHE (Co and Pt loadings are 50 and 25 $\mu g/cm^2$, respectively). (B) *Operando* XANES spectra of Co_3N/C under steady state at 1.0 V (open circuit potential, OCP) and followed by applying constant potentials at 1.2−1.6 V vs RHE, and the comparison with XANES reference spectra (a *Y*-offset of 0.5 was applied to better show the difference). Purple arrows show the progressive positive shift of the Co K-edge, indicating higher Co valences at higher potentials. The inset shows the average Co valences at 1.2−1.6 V based on a linear combination fitting analysis. (upper-right inset) Illustration of the irreversible conversion from pristine nitride-core oxide-shell catalysts completely to oxides upon oxidizing potentials above 1 V vs RHE in 1 M KOH. Panel A is adapted with permission from ref 477. Copyright 2019 American Chemical Society. Panel B is adapted with permission from ref 491. Copyright 2022 the Authors, American Association for the Advancement of Science.

likely due to the Jahn−Teller distortion of Mn^{3+}. The ELNES spectra of Co and Mn showed nearly the same features among the four different shell locations (S-1, S-2, S-3, and S-4), evidencing that all shell regions have a uniform chemical bonding environment. The superior ORR activity of Mn−Co spinel oxides, relative to Mn_3O_4/C and Co_3O_4/C, suggested underlying synergistic interactions between Mn and Co. *Operando* XAS, in a home-made electrochemical cell, enabled the tracking of Co and Mn electronic structures with a 3 mV potential resolution (Figure 22H, details can be found in section 8.1.1).[469,470] Both Mn and Co valences changed simultaneously and exhibited periodic patterns that tracked the cyclic potential sweeps, providing compelling evidence for synergistic interactions, i.e., Co and Mn serving as coactive sites for the ORR. The relative X-ray intensity, representing Co and Mn valences, reached peak values at 0.42 and 1.25 V, which are fully consistent with the boundary potentials (0.42 and 1.25 V) of oxidation and reduction currents in the CV profile (Figure 22H, inset). This unique synergistic catalytic mechanism may be the reason for the high activity of the Co−Mn oxide electrocatalyst. In summary, the combination of atomic-scale STEM-EELS and *operando* XAS characterizations, at multilength scales, has provided complementary pictures of the catalyst microstructures, chemical environments, and their dynamic changes under reaction conditions, at both microscopic and macroscopic levels.

In the development of PEMFCs and AEMFCs, the RDE technique has been widely used to preliminarily screen electrocatalysts and evaluate their activity/durability. For example, RDE measurements showed a rather good quantitative agreement with MEA tests for the benchmark activities of Pt/C in PEMFCs.[7] However, RDE measurements are often performed in an aqueous solution saturated with gas reactants at a mM level while the MEA is tested with high-flux humidified gases, which lead to distinct differences in water management, mass transport, and test conditions. For instance, although the spectacular ORR activity of shape-controlled Pt-based alloy catalysts, up to a factor of 20 relative to Pt/C, was reported from RDE measurements,[471,472] those reports have not translated into realistic MEA results in PEMFCs. After only 1 day of MEA testing, octahedral Pt—Ni catalysts exhibited a loss of their distinct shapes and leached out a significant amount of Ni, contaminating/poisoning the membrane.[473,474] Contrary to common observations, we previously showed that while Mn—Co spinels ($Mn_{1.5}Co_{1.5}O_4$) only exhibited a modest activity in RDE tests, they demonstrated an outstanding MEA performance (Figure 23A,B).[16] RDE profiles of Mn—Co spinels exhibited an $E_{1/2}$ of ~0.85 V vs RHE, 50 mV lower than the typical Pt/C (~0.90 V), indicating a noticeably lower ORR activity of Mn—Co spinels, and this difference remained at different potentials as shown in the Tafel plots (Figure 23A). The RDE tests would usually suggest that Mn—Co spinels would have a much lower performance in MEAs, relative to Pt/C. However, the Mn—Co spinel cathode exhibited a benchmark peak power density (PPD) of 1.1 W/cm^2, surpassing that of Pt/C at 1.0 W/cm^2 at 100% relative humidity (RH) and a cell temperature of 60 °C in H_2—O_2 mode. At a more realistic lower humidity (50% RH), the Mn—Co spinels maintained a high-level PPD of 0.92 W/cm^2 while that of Pt/C dropped drastically to 0.67 W/cm^2 (Figure 23B). The capability of working at low RH is vital for fuel cell engines operating in realistic H_2-air mode where water at the cathode is a reactant and is often depleted at high current densities. The RDE−MEA correlation/discrepancy shows that it is important to include MEA tests in early-stage catalyst development, in addition to RDE measurements for catalyst screening. A comprehensive survey of MEA studies will be introduced in section 7. With the additional comprehensive examination of Mn—Co catalysts with *in situ* FTIR, STEM-EELS and XPS

https://doi.org/10.1021/acs.chemrev.1c00331
Chem. Rev. XXXX, XXX, XXX−XXX

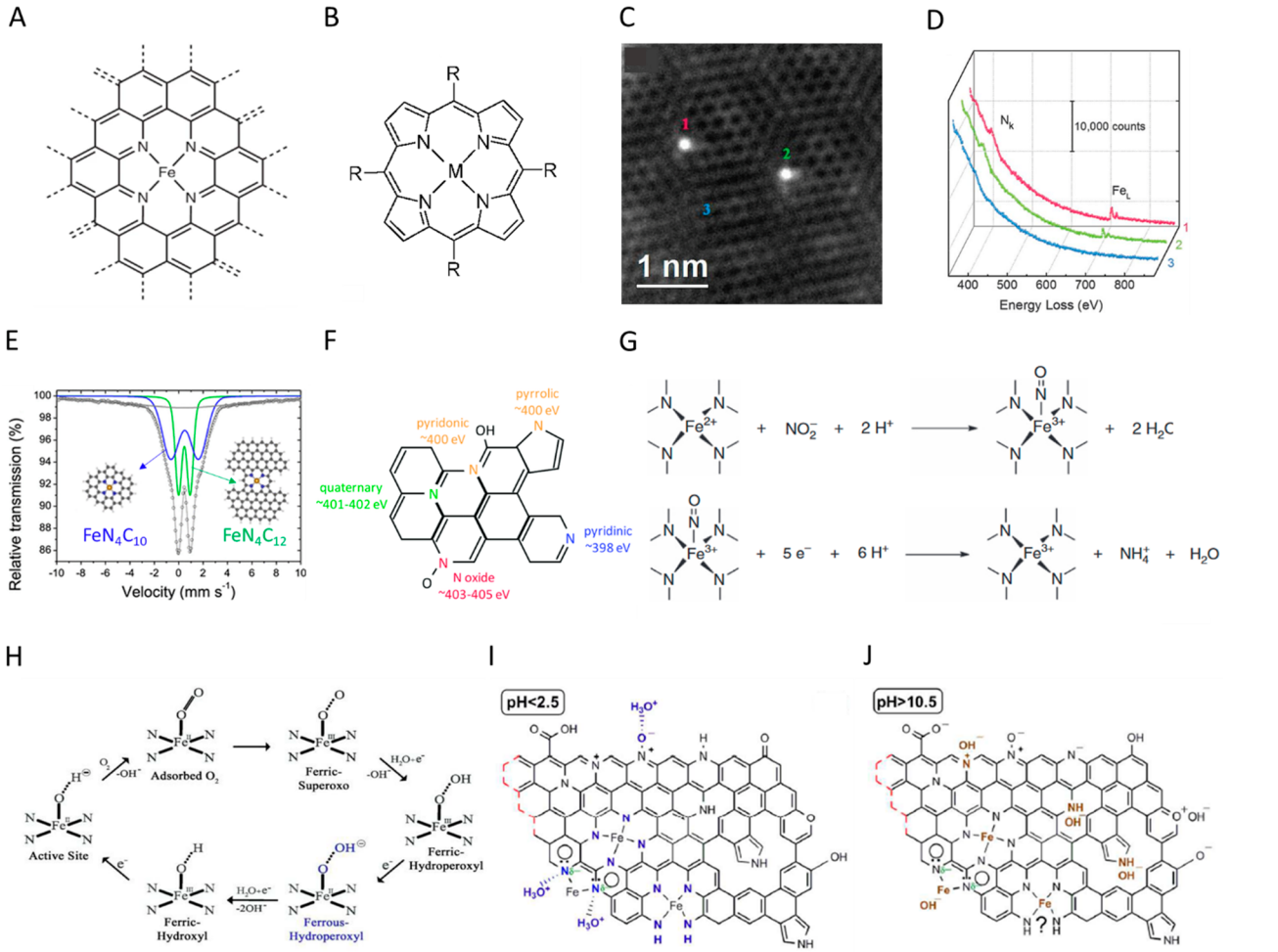

Figure 25. (A) Proposed chemical structure for Fe−N−C catalysts. (B) Chemical structure of the metal-porphyrin complex. (C, D) Direct observation of Fe−N−C sites by HAADF-STEM and ELLS. (E) Mössbauer spectra and proposed active sites for the Fe−N−C catalyst. (F) Schematic illustration of nitrogen-doped carbon with different types of N species and their XPS edge energy. (G) Proposed electrochemical reactions for nitrite poison and stripping on Fe−N_4 sites. (H) Proposed 4e$^-$ ORR pathway for Fe−N−C active sites in alkaline media. (I) Schematic illustration of protonation/deprotonation functional groups on the surface of Fe−N−C catalysts at pH < 2.5 and pH < 10.5. Panel A is adapted with permission from ref 515. Copyright 2020 Springer Nature. Panels C and D are adapted with permission from ref 502. Copyright 2017 The Authors, American Association for the Advancement of Science. Panel E is adapted with permission from ref 505. Copyright 2019 American Chemical Society. Panel F is adapted with permission from ref 518. Copyright 2018 Multidisciplinary Digital Publishing Institute. Panel G is adapted with permission from ref 528. Copyright 2016 Springer Nature. Panel H is adapted with permission from ref 529. Copyright 2012 Hindawi. Panels I and J are adapted with permission from ref 530. Copyright 2018 American Chemical Society.

analysis, and DFT and MD simulations, a synergistic reaction mechanism for spinels was proposed (Figure 23C).[16] Mn prefers to bind O_2 while Co prefers to bind and activate H_2O, so that proton transfer can occur from Co—OH_2 to neighboring Mn—O_2 (Reaction I), leading to the formation of Co—OH and Mn—OOH species. The reduction of Mn—OOH yields Mn═O, which can regenerate Mn—OH by taking the second proton from proximate Co—OH_2 (Reaction II). This mechanism highlights a synergistic mechanism with H_2O activation on Co sites and proton-transfer reduction of O_2 on Mn sites, which may explain why Mn—Co spinels outperform the Pt/C cathode in more realistic lower-RH conditions. The modest RDE performance was rationalized by the overwhelming H_2O adsorption on the hydrophilic Mn—Co spinel surface despite the preferable O_2 adsorption on Mn sites, as evidenced by MD simulations.[16] In comparison, O_2 adsorption on a relatively hydrophobic Pt surface is more feasible under water-flooding RDE conditions. The design of synergistic Mn—Co spinels highlights, besides the conventional wisdom of tuning electronic structures of catalysts, the paramount importance of activating interfacial water to facilitate the ORR kinetics in alkaline fuel cells.

4.2.4. ORR Activity of Nanoscale 3d Metal Nitrides. Moving beyond perovskite and spinel oxides, other types of metal oxides such as rutiles (e.g., MnO_2),[458] pyrochlores (e.g., $Pb_2Ru_2O_7$),[475] and rock-salt-type oxides (e.g., $MnCo_2O_3$)[476] have also shown promising ORR activities in alkaline media. However, metal oxides generally have low intrinsic conductivity due to their wide band gaps. To mitigate this issue and facilitate the electron transfer, metal nitrides and oxynitrides have emerged as a new family of ORR electrocatalysts in alkaline media owing to their intrinsically high conductivity and, often, metallic behaviors.[477] Previous reports include early 3d transition metal nitrides (TiN, VN, CrN),[478] Mn,[479] Fe,[480] Co,[481] Ni,[482,483] Cu_3N,[484] MoN, etc. However, their reported activities are, at best, modest ($E_{1/2}$ < 0.8 V vs RHE) and generally far lower than that of Pt/C. Cobalt-based nitrides, previously investigated mainly as magnetic materials,

https://doi.org/10.1021/acs.chemrev.1c00331
Chem. Rev. XXXX, XXX, XXX−XXX

have been reported to exhibit a promising performance in a wide range of energy-related applications, such as the OER[485−487] and metal−air batteries.[488,489] Recently, a novel family of cobalt nitrides (Co_2N/C, Co_3N/C and Co_4N/C) were synthesized via a facile nitridation process in NH_3 at controlled temperatures (Figure 24A).[477] The most active Co_4N/C exhibited an 8-fold improvement in mass activity at 0.85 V, when compared to Co_3O_4/C, and its $E_{1/2}$ was only 15 mV more negative than Pt/C at comparable Co and Pt loadings of 50 and 25 $\mu g/cm^2$, respectively, in 1 M KOH. Considering the larger particle size of Co_4N, relative to Pt (∼3 nm), the ORR activity of Co_4N/C is remarkably high. It should be noted that, based on the Levich equation, the I_d of the $4e^-$ reduction of oxygen in 0.1 M O_2-saturated KOH or $HClO_4$ should be −5.5 mA/cm^2 at 1600 rpm. Since the O_2 solubility (CO_2) in 1 M KOH at 25 °C and 1 atm is 8.42×10^{-4} mol/L, which is about 70% of the CO_2 in 0.1 M KOH (1.21×10^{-3} mol/L),[490] the I_d of the $4e^-$ ORR in 1 M KOH will be correspondingly lower with a value of −3.8 mA/cm^2 at 1600 rpm. The superior performance was ascribed to the formation of a conductive nitride core surrounded by a naturally formed thin oxide shell (∼2 nm). The conductive nitride core effectively mitigated the low conductivity of the metal oxide, and the thin oxide shell on the surface provided the active sites for the ORR. Co_4N exhibited a good stability with a modest $E_{1/2}$ decay of 14 mV, relative to that of Pt/C (17 mV) after 10 000 cycles between 0.6 and 0.95 V (U.S. DOE protocols[7,10]). Recently, the ORR activities of a broad range of metal nitrides were evaluated, including MN (M = Ti, V, Cr, and Mn) and M_3N (M = Fe, Co, and Ni) in alkaline media, and Co_3N showed the highest ORR activity.[491] Despite the fact that fuel cell voltage is often lower than 0.9 V when delivering appreciable current density during MEA tests, it is not uncommon to have large polarizations of oxygen cathodes during startup and shutdown procedures in automotive applications.[492] Thus, it is of great importance to investigate the catalyst stability at high oxidizing potentials. As shown in Figure 24B, the *operando* X-ray absorption near-edge structure (XANES) of the Co K-edge of Co_3N/C at 1.0 V (open circuit potential) resembled the feature of metallic Co and remained stable when potential decreased from 1.0 to potentials as low as 0.1 V.[491] However, as potentials increased from 1.0 to 1.6 V, the Co K-edge showed significant and irreversible shifts to higher energy values, and the Co average valences were estimated to increase from ∼0.8 to ∼2.4 based on a linear combination analysis. Simultaneously acquired *operando* EXAFS spectra clearly evidenced the complete transition from Co_3N to mixed phased Co_3O_4 and CoOOH. Those results demonstrate that oxidation potentials above a threshold of 1.2 V destroy the structure of metal nitrides and form new species of Co oxides, which also means that those types of catalysts cannot be used as stable electrocatalysts for the alkaline OER at high oxidizing potentials.[485−487]

4.3. Metal−Nitrogen−Carbon (M−N−C) ORR Catalysts

Metal−nitrogen−carbon (M−N−C) catalysts, a class of carbon materials containing a transition metal (e.g., Fe, Co, Mn, Ni, Cu), often in the form of metal atoms coordinated by nitrogen, have been studied for decades as low-cost alternatives to PGM-based ORR electrocatalysts for both acidic and alkaline media.[493−497] The M−N−C catalysts generally exhibit a higher ORR activity and better durability and have a lower propensity for carbon corrosion in alkaline media as compared to acidic media.[498] However, due to the maturity of PEMFC technology,[499] M−N−C catalyst studies to date have mostly focused on PEMFCs, especially in automotive applications.[500−503] Thanks to the recent progress in the AEMFC technology, there has been significant uptake in M−N−C electrocatalysis research in alkaline liquid electrolytes and in alkaline fuel cells. In this section, we focus on the development of M−N−C catalysts for oxygen reduction in alkaline media, as well as review the ongoing progress and assess the main challenges facing M−N−C electrocatalysts. The emphasis of this section is, in particular, on various concepts of the catalytic sites, different synthesis approaches, and structure−activity correlations.

4.3.1. Active Sites and Catalyst Structure. Atomically dispersed M−N−C catalysts originate from materials obtained via a high-temperature treatment of metal N-macrocycles,[493] often adding carbon as a support.[494] Very different from metal-nanoparticle catalysts, M−N−C materials contain nitrogen-coordinated metal atoms covalently bonded to carbon atoms in the carbon lattice (Figure 25A). The metal species are atomically dispersed in the catalysts. In some cases, metal-rich nanoparticles can also be found, especially in catalysts obtained using excessively high metal content in the precursors. The metal center is typically coordinated by either pyridinic or pyrrolic nitrogen atoms.[504,505] The unique structure of the metal sites makes M−N−C catalysts different from heteroatom-doped carbon materials, which share some similarities with metal N-macrocycles such as metal porphyrins (Figure 25B). While many metals, including Mn, Ni, Cu, and Zn,[495−497,506] have been used to synthesize M−N−C catalysts, the Fe- and Co-based catalysts, i.e., Fe−N−C and Co−N−C, have consistently shown the highest ORR activity and, consequently, have attracted the most attention.[500,501,507,508]

The M−N−C catalysts can host a variety of MN_x sites. While x can range from 1 to 5, the MN_4 sites are the most common.[509−511] Metallic metal species, such as Fe_3C and Fe NPs, are frequently detected in M−N−C catalysts due to a tendency of metals to cluster during high-temperature treatment.[501] XAS, electron microscopy, and ^{57}Fe Mössbauer spectroscopy (specifically in the studies involving Fe−N−C catalysts) have been widely used to identify metal sites in the M−N−C ORR catalysts. XAS, including XANES and EXAFS, have been used to identify the chemical state of the metal and determine the coordination number in MN_x structures.[507,512−514] For example, XAS was used to study the structural transformation of Fe−N−C sites in carbon-supported Fe meso-tetraphenylporphyrine chloride (Fe-TTP) as a function of the heat-treatment temperature.[512] XANES spectra showed that the Fe center in the planar FeN_4 center is pulled out of the N_4-plane as the pyrolysis temperature was increased. In turn, EXAFS revealed that the FeN_4 species in Fe-TPP is detached from macrocycles at temperatures above 800 °C, likely due to the conversion of the aromatic carbon atoms surrounding the FeN_4 to an amorphous form of carbon.[512]

HAADF-STEM coupled with EELS was shown to be especially useful in characterizing atomically dispersed metal sites in M−N−C catalysts. In work by Chung et al.,[502] the Fe sites in a highly ORR-active Fe−N−C catalyst were directly observed as two bright spots 1 and 2 in the hexagonal carbon matrix, represented by spot 3 in Figure 25C. The colocation of Fe and N at these two spots was confirmed by EELS (Figure 25D).

https://doi.org/10.1021/acs.chemrev.1c00331
Chem. Rev. XXXX, XXX, XXX−XXX

^{57}Fe Mössbauer spectroscopy is uniquely suitable for studying Fe−N−C catalysts, as it enables the determination of the coordination environment, as well as the oxidation and spin states of Fe species from the isomer shifts and quadrupole splitting in the ^{57}Fe spectra and referring them to known standards such as macrocycle compounds containing N-coordinated Fe, e.g., FeN_4.[504,505,513−515] For example, the D1 and D2 doublets in Figure 25E (the result of a fit to the experimental Mössbauer spectrum of an Fe−N−C catalyst) were assigned to a high-spin $Fe(III)N_4C_{12}$ porphyrinic structure (spin 5/2) and a low-spin $Fe(II)N_4C_{10}$ pyridinic site (spin 0), respectively.[505] It was also proposed that species responsible for doublet D1 were located on the catalyst surface and thus likely involved in the ORR, while D2 species were buried in the carbon matrix and thus unlikely to participate in the electrocatalytic process.[505]

Nitrogen-doped carbon (N−C) materials have been viewed as a metal-free alternative to M−N−C catalysts for the ORR in alkaline media, together with similar materials, in which nitrogen atoms are replaced by or used jointly with other heteroatomic dopants, e.g., B, S, P, or F.[516,517] In N−C catalysts, pyridinic, pyrrolic, quaternary/graphitic, or oxidized (NO_x) nitrogen substitutes carbon atoms in the carbon lattice (Figure 25F).[518] Metal impurities, even at levels undetectable by XPS or EDX, can significantly promote the ORR activity of N−C catalysts.[519−521] This presents a challenge, as metals are often involved in the synthesis of carbons typically used in the synthesis of N−C catalysts, and are very difficult to remove completely.[522−524,526] For example, this is the case for N−C catalysts consisting of nitrogen-doped CNTs.[522,523] In the synthesis of such carbon nanotubes, transition metal nanoparticles are used as nuclei for the nanotube growth,[523,525] becoming a source of metal contamination in the catalysts, often in the form of small metal particles entrapped in highly graphitic carbon shells.[524−526] Even trace amounts of transition metal impurities in N−C catalysts can result in noticeable improvements in the ORR activity,[519,520] through the formation of M−N−C sites.

Impurity concerns notwithstanding, model N−C catalysts based on nitrogen-doped highly oriented pyrolytic graphite (HOPG) were prepared to compare the ORR activity of pyridinic and graphitic nitrogen centers in acidic media.[516] A pyridinic N-rich catalyst was prepared by the heat treatment of edge-patterned HOPG at 700 °C in NH_3, while a graphitic N-rich HOPG was obtained via annealing at 800 °C in an ultrahigh vacuum. The HOPG containing 0.63 atom % of pyridinic N showed a higher ORR activity than the HOPG rich in graphitic N, in spite of the higher atomic content of nitrogen in the latter catalyst (0.73 atom %). The pyridinic-N was proposed to serve as an ORR active site, with carbon atoms next to it acting as the dioxygen binding site. One aspect not considered in this work was a possible effect of the high-temperature NH_3 treatment on the formation of additional active sites. Under the heat-treatment conditions employed, ammonia can act not only as a nitrogen-doping agent but also as an effective carbon etchant, capable of increasing the catalyst's surface area and creating potentially ORR-active functional groups in the carbon.[527]

While identification of the active sites is of fundamental importance to the understanding of the ORR mechanism at the M−N−C catalyst surfaces, their quantification is key to assessing the reaction kinetics. Malko et al. developed a quantitative approach for probing Fe−N−C sites electrochemically via adsorption and reductive stripping of the nitrite anion.[528] They treated Fe−N−C catalysts with sodium nitrite in a pH 5.2 buffer solution, which resulted in a 90 mV negative potential shift of the ORR polarization plot at a current density of 1.5 mA/cm^2. The ORR performance of the catalyst was fully recovered following the probe stripping. The authors assumed that nitrite anions specifically adsorb on FeN_4 sites, and their reductive stripping yields ammonia in a quantitative electrochemical process (Figure 25G), thus allowing for a precise determination of the number of active sites on the catalyst surface and consequently the turnover frequency (TOF) from the ORR kinetic current values determined at different electrode potentials. This approach to determining the surface concentration and activity of metal sites in M−N−C catalysts, while promising, still requires a proof of specificity to the metal center, and not to numerous functional groups present on the catalyst surface.

4.3.2. ORR Mechanisms. Ramaswany et al.[529] proposed different ORR mechanisms in alkaline and acidic media for an Fe-TPP/C catalyst derived from pyrolyzed Fe-macrocycle mixed with carbon as a support. The catalyst showed a much higher ORR activity in alkaline electrolyte (E_{onset} = 0.95 V vs RHE) than in acidic electrolyte (E_{onset} = 0.80 V vs RHE), with H_2O_2 generation not evident until 0.80 V vs RHE in both cases. The explanation of the observed difference in the onset potentials of the ORR and peroxide formation in alkaline media was given in terms of the formation of a stable Lewis acid−base adduct between the HO_2^- anion and Fe in $Fe−N_4$ sites ($Fe−HO_2^-$), claimed to favor the 4e$^-$ pathway in alkaline solution. Relatively low values of the ring current, in the disk potential range between 0.6 and 0.7 V in alkaline media, pointed to the suppression of the outersphere electron transfer, often proposed for the ORR in alkaline solutions. Instead, the authors proposed that the dominant 4e$^-$ ORR pathway in alkaline media involved the $Fe−HO_2^-$ adduct, following an innersphere mechanism with the replacement of a labile OH^- ligand at the FeN_4 site and adsorption of O_2 (Figure 25H).

Rojas-Carbonell et al.[530] investigated the effects of pH on the activity of an Fe—N—C catalyst obtained using a templated-synthesis approach. High-resolution XPS revealed the presence of various N and O functional groups on the catalyst surface (Figure 25I,J): pyridinic N/hydrogenated, graphitic N, FeN_x, pyrrolic N, quaternary N, NO_x groups; phenolic (—C—OH), lactone, pyrone (—C═O), and carboxylic (—COOH) groups. Based on their respective dissociation constants, all of these groups, with the exception of graphitic N, should be protonated at pH < 2.5 (Figure 25I) and undergo deprotonation at pH > 10.5 (Figure 25J). As the low H_2O_2 yields were observed at pH < 2.5, it was concluded that, in acidic media, the ORR at the Fe—N—C catalyst predominantly occurs via the 4e$^-$ ORR pathway (the PCET mechanism). The H_2O_2 yield increased at pH > 10.5 indicating an enhanced contribution from the 2e$^-$ ORR pathway. It was proposed that specific adsorption of OH^- on FeN_x sites at pH > 10.5 results in the reduced accessibility of these sites for the innersphere 4e$^-$ path, enhancing the contribution of the 2e$^-$ outersphere mechanism and peroxide formation. As carbon can also reduce O_2 to H_2O_2 at a high pH, more evidence is needed to confirm that specific adsorption of OH^- on FeN_x sites does indeed promote the outersphere reaction mechanism.

While the two latter studies offer valuable insights into the possible ORR mechanism at Fe−N−C catalysts in alkaline media, they heavily rely on H_2O_2 yields which tend to differ for

https://doi.org/10.1021/acs.chemrev.1c00331
Chem. Rev. XXXX, XXX, XXX−XXX

various Fe−N−C catalysts. Performing this or similar studies on Fe−N−C catalysts with a rigorously controlled composition and energetically homogeneous FeN_x sites would help validate these mechanistic findings and further enhance an understanding of the ORR mechanism as a function of pH.

4.3.3. Synthesis and ORR Activity of M−N−C Catalysts. As mentioned above, it was the first observation of the ORR activity of transition metal N-macrocyclic compounds that inspired the development of a wide range of PGM-free catalysts for the ORR.[493,494] M−N−C catalysts were initially obtained via a high-temperature treatment (pyrolysis, carbonization) of metal N-macrocycles mixed with high-surface-area carbons.[531] Subsequently, Gupta et al.[532] found that a high-temperature treatment of polyacrylonitrile, Fe or Co salts, and carbon can yield catalysts with an ORR activity similar to those of M−N−C materials prepared using macrocycles as precursors. The finding that active M−N−C catalysts could be synthesized from individual carbon, nitrogen, and metal precursors paved the way for the discovery of many M−N−C catalysts derived from various chemicals and ultimately to the realization of the importance of the MN_x sites for ORR activity. Among others, the synthesis involved nitrogen-rich small molecules, polymers, and metal complexes, as well as metal salts and a large variety of carbon supports.[500−502,527,533] Some of the M−N−C catalysts, prepared using the high-temperature approach exhibited ORR activities that approached that of PGM-based catalysts and allowed for performance metrics close to the DOE activity targets established for PEMFCs.[500−502]

One of the initial challenges facing the development of better performing heat-treated M−N−C catalysts was associated with the need for identifying the source of the ORR activity, specifically, whether it originated from atomically dispersed sites of the MN_x type or metal-rich nanoparticles embedded in graphitic-carbon shells. Initial observations of a correlation between the ORR activity and the content of atomically dispersed metal sites[502] resulted in M−N−C catalysts containing exclusively atomically dispersed Fe sites, typically derived from either individual precursors or N-macrocycles.[534,535] For example, a synthesis approach was developed to integrate graphitic C_3N_4 and $FeCl_3$ with a surfactant F127 (a symmetric triblock copolymer of ethylene oxide-propylene oxide, PEO−PPO−PEO) to obtain single-atom Fe catalysts (SA-Fe/NG) using a high-temperature treatment.[534] While Fe_3C species and graphitic carbon were detected in catalysts synthesized without the addition of the surfactant, only amorphous carbon was found to be present in catalysts obtained using the surfactant approach. It was suggested that the surfactant assists Fe ions in anchoring to graphitic C_3N_4 and preserves the atomic dispersion of the Fe sites during the heat treatment. HAADF-STEM imaging of SA-Fe/NG revealed atomically dispersed Fe sites within a graphene-like morphology, possibly inherited from the layered structure of C_3N_4. The EXAFS analysis of SA-Fe/NG pointed to the prevalence of the 1.5 Å Fe−N (Fe−O) bond, rather than the 2.5 Å Fe−Fe bond, also revealing a fourfold coordination of Fe by N (or O). The ^{57}Fe Mössbauer spectroscopy confirmed that SA-Fe/NG contained the D1, D2, and D3 species and the absence of any metallic phase. In RRDE experiments in 0.1 M KOH, the SA-Fe/NG catalysts exhibited excellent ORR activity ($E_{1/2}$ = 0.88 V) and very good selectivity for the 4e$^-$ ORR pathway, with an average number of transferred electrons of 3.9.[534]

Yi et al.[535] used an Fe-porphyrinic triazine-based porous framework as a precursor for atomically dispersed Fe catalysts obtained at 400−600 °C. A nitrile-functionalized Fe-porphyrin derivative (Fe-TPPCN) was first polymerized into Fe-porphyrinic triazine frameworks in the presence of $ZnCl_2$ and then partially carbonized to form atomically dispersed $Fe−N_x$ species under a vacuum for 40 h. In this approach, $ZnCl_2$ not only promoted the trimerization of nitrile groups into triazine rings but also served as a pore-forming agent. A strong IR absorption band at 1564 cm^{-1} confirmed the formation of triazine rings and partial carbonization of catalysts at 600 °C. Only atomically dispersed Fe was found in STEM images of the $Fe−N_x$ sites. EXAFS revealed a decrease in the Fe−N bond from 1.59 to 1.47 to 1.44 Å with an increase in the synthesis temperature from 400 to 500 to 600 °C. As expected based on STEM data, no EXAFS band, assignable to the Fe−Fe bond, was found. A similar reduction in the Fe−N bond length was observed by Zhang et al.[536] as a result of the conversion of the tetrahedral FeN_4 structure in zeolitic imidazolate framework (ZIF) precursors to FeN_4 sites in Fe−N−C catalysts during a high-temperature treatment.

4.3.4. MOF-Derived M−N−C Catalysts. Metal−organic frameworks (MOFs), a class of porous crystalline materials with a tunable composition and functionality,[537] have emerged as promising precursors for the synthesis of M−N−C ORR catalysts. MOFs consist of periodically bridged metal ions and organic linkers that form ordered porous crystals. Among many available MOFs, zeolitic imidazolate frameworks (ZIFs) have attracted special attention as precursors for the synthesis of highly active M−N−C catalysts thanks to their abundant nitrogen content and high volume of micropores.[503,508,537−539] In ZIFs, the imidazole-based ligands bridge transition-metal atoms into tetrahedral crystals, similar to the topologies of zeolites.[503,537−539] Metal, nitrogen, and carbon precursors can be integrated into the ordered porous crystal structure, allowing for a relatively high level of control over the composition and interactions within the ZIF precursors, which is not available in the traditional synthesis relying on the physical mixing of nitrogen and carbon precursors. This makes ZIF-derived M−N−C catalysts attractive model systems for studying the formation of M−N−C sites during high-temperature treatments.[513,514] Zn-based ZIFs can also be converted to nitrogen-doped microporous carbons without the addition of a separate carbon support. This helps to increase the mass activity of catalysts by removing an ORR-inactive carbon component.[503,539]

In an early study, Ma et al. used a cobalt ZIF to prepare Co−N−C catalysts via a single-step heat treatment.[508] An XAS study of the resulting Co−N−C catalyst revealed the presence of CoN_4 sites that allowed for reaching an $E_{1/2}$ of 0.68 V in an RDE study in acidic media. The catalyst had a large content of Co nanoparticles embedded in the carbon and a low Brunauer−Emmett−Teller (BET) surface area (305 m^2/g). One of the approaches used to prevent the agglomeration of metals in ZIF-derived catalysts has involved the addition of Zn as a second metal, acting as a "separator" for the atoms of the ORR-active metal, such as Co, during the high-temperature step in catalyst synthesis. Since Zn has a relatively low boiling point (907 °C), a Zn-containing ZIF precursor, e.g., ZIF-8, can be converted into a porous nitrogen-doped carbon during high-temperature treatment above 900 °C, resulting in BET surface area values as high as 1500 m^2/g.[540−542] When Fe and/or Co precursors are incorporated into ZIF-8 at moderate

https://doi.org/10.1021/acs.chemrev.1c00331
Chem. Rev. XXXX, XXX, XXX−XXX

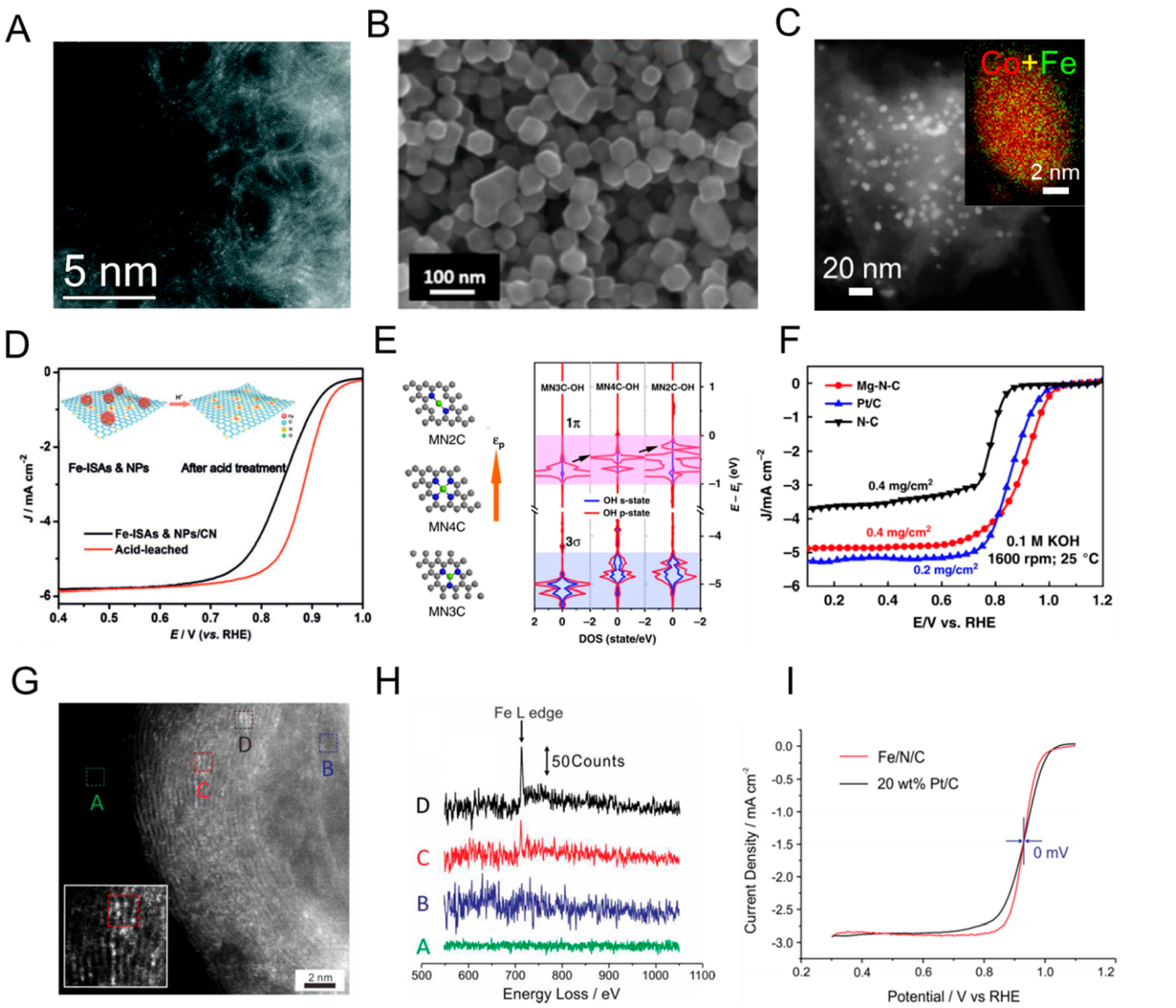

Figure 26. (A) STEM image of atomically dispersed Fe catalysts. (B) SEM image of an Fe-doped ZIF-8 precursor. (C) STEM image and EELS elemental maps of BMOF-derived Co−Fe alloy nanoparticles. (D) ORR polarization curves for Fe nanoparticles contained Fe−N−C catalysts with/without acid-leaching. (E) Mg cofactors' geometries in different N-coordinated environments which tune ε_p of Mg atoms, and the corresponding density of states changes of OH after interaction with p-state of Mg. (F) ORR polarization profiles for Mg−N−C in O_2-saturated 0.1 M KOH at 1600 rpm and 5 mV/s. (G) STEM images of adenosine-derived Fe−N−C catalysts at various points (A−D) of carbon nanotubes. Inset: enlarged point C. (H) ELLS analysis at regions A−D in panel G to detect the Fe L-edge. (K) RDE profiles of adenosine-derived Fe−N−C and 20% Pt/C with the same carbon loading in 1 M KOH at 1600 rpm and 5 mV/s. Panels A and B are adapted with permission from ref 543. Copyright 2019 The Royal Society of Chemistry. Panel C is adapted with permission from ref 461. Copyright 2019 American Chemical Society. Panel D is adapted with permission from ref 544. Copyright 2017 Wiley. Panels E and F are adapted with permission from ref 546. Copyright 2020 Springer Nature. Panels G−I are adapted with permission from ref 553. Copyright 2017 The Authors, American Chemical Society.

concentrations, catalysts free of metal-rich particles can be produced during the high-temperature treatment (Figure 26A).[543−545] The thus-obtained atomically dispersed M−N−C materials often tend to preserve the shape and morphology of their ZIF precursors (Figure 26B), indicating that the morphology of mostly carbon-based M−N−C catalysts can be controlled by tuning the size and shape of ZIF precursors. Thanks to the relative homogeneity of the active sites and control over the ZIF morphology, ZIF-derived M−N−C catalysts can serve as model systems in studies targeting an understanding of the role of metal sites and the ORR mechanism. Atomically dispersed Fe catalysts derived from ZIF precursors showed excellent ORR activity in alkaline media. In a study by Chen et al.,[544] $Fe(acac)_3$ was incorporated into the cavity of ZIF-8 via solution impregnation, followed by pyrolysis at 900 °C under Ar, which resulted in atomically dispersed Fe sites in an Fe−N−C catalyst. The individual carbon particles in this catalyst preserved the same rhombic dodecahedron shape as its Fe(acac)@ZIF-8 precursor. HAADF-STEM revealed an excellent dispersion of Fe atoms in the catalyst, without the presence of Fe-rich nanoparticles, in agreement with the XANES analysis. This MOF-derived catalyst exhibited a high ORR activity in 0.1 M KOH with an $E_{1/2}$ of 0.90 V achieved with a catalyst loading of 0.41 mg/cm^2 and H_2O_2 yield of <5%. Fe−N−C catalysts containing Fe nanoparticles were prepared using the same synthetic approach but with 6 times the amount of Fe in the precursor. As-received, the catalyst showed a relatively low ORR activity,

https://doi.org/10.1021/acs.chemrev.1c00331
Chem. Rev. XXXX, XXX, XXX−XXX

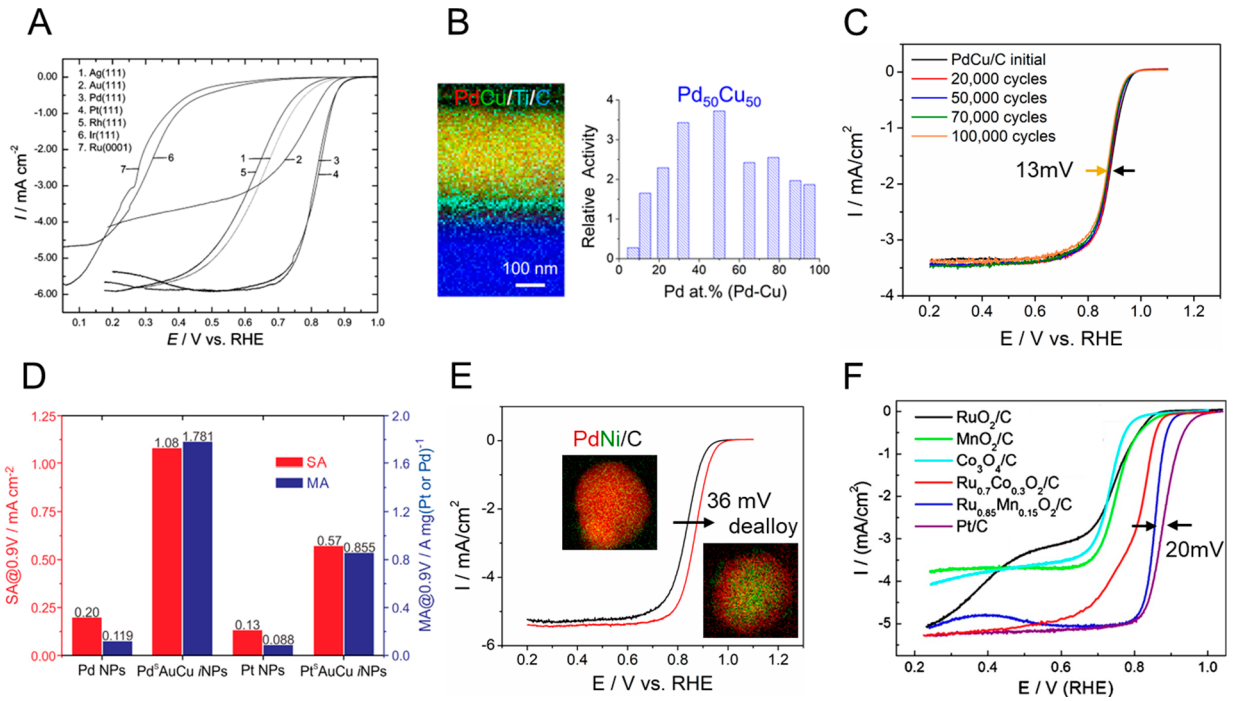

Figure 27. Activity and stability of non-Pt precious ORR catalysts. (A) ORR polarization on different metal single crystals in 0.1 M NaOH at 1600 rpm and 5 mV/s (B) Cross-section SEM-EDX maps of Pd−Cu alloy thin films deposited on a Ti adhesion layer on a glassy carbon electrode and the relative ORR activities as a function of Pd−Cu composition in alkaline media. (C) Extended long-term durability test of PdCu (1:1 ratio) nanoparticles on carbon after a certain number of potential cycles between 0.6 and 1.0 V at 100 mV/s. (D) Surface activity (SA) and mass activity (MA) of the Pd and Pt shell on AuCu intermetallic core materials, relative to Pd and Pt NPs, measured in 1 M KOH. (E) ORR polarization profiles of PdNi/C in 0.1 M NaOH at 1600 rpm and 5 mV/s before and after electrochemical dealloying in acid. (F) ORR polarization profiles of various metal oxides for the ORR in O_2-saturated 0.1 M NaOH at 1600 rpm and 5 mV/s. Panel A is adapted with permission from ref 559. Copyright 2019 American Chemical Society. Panels B and C are adapted with permission from ref 565. Copyright 2020 The Authors, American Chemical Society. Panel D is adapted with permission from ref 571. Copyright 2016 The Authors, Elsevier. Panel E is adapted with permission from ref 573. Copyright 2020 The Authors, American Chemical Society. Panel F is adapted with permission from ref 576. Copyright 2020 The Authors, Elsevier.

reflected by an $E_{1/2}$ of only 0.82 V. An acid leach helped to remove the majority of the Fe-rich nanoparticles, which resulted in an increase in the $E_{1/2}$ to 0.86 V (Figure 26D). This study confirmed that atomically dispersed Fe sites, rather than Fe nanoparticles, are responsible for the high ORR activity of the Fe−N−C catalysts. Liu et al. used DFT simulations to study the ORR activity of Mg, Al, and Ca, which was inspired by the optimum affinity of oxygenated species to Mg cofactors in enzymes (Figure 26E).[546] The results of that study showed that the transformation of O_2 to OOH* at Mg and Al sites is exothermic and that the adsorption of OH* is weaker at Mg sites than at Ca and Al sites, making Mg the most suitable of the three metals for catalyzing the ORR. Of several possible coordination environments, Mg coordination to two nitrogen atoms (Mg−N_2−C) results in a higher p-state location and thus in a nearly optimal adsorption strength of OH*, resembling that of d-band metals, and a promising higher ORR activity. In the follow-up to these calculations, a catalyst based on atomically dispersed Mg in a graphene framework (Mg−N−C) was synthesized by the heat treatment of a Mg-based MOF. A high $E_{1/2}$ of 0.91 V was measured with this catalyst in RDE testing in 0.1 M KOH (Figure 26F). An atomic-level modification of MOF-derived M−N−C catalysts was found necessary to maximize metal utilization. Li and coworkers designed an MOF-derived atomically dispersed Co catalyst containing a Co_1−N_3PS active moiety embedded in a hollow carbon polyhedron (Co_1−N_3PS/HC), which allowed the achievement of an $E_{1/2}$ of 0.92 V and a low Tafel slope of 31 mV/dec.[547] Atomically dispersed Fe catalysts were also derived from other MOF precursors.[548,549]

While it is generally recognized that the high ORR activity of M−N−C catalysts in acidic media originates from M−N−C sites rather than metal nanoparticles,[543,550] a superior ORR activity of some nanoparticle catalysts was demonstrated in alkaline media.[541,551−553] Abruna and coworkers designed bimetallic organic framework (BMOF) (ZIF-67 and ZIF-8)-derived Co−Fe alloys embedded in carbon nanocomposites, using a combination of a conventional self-assembly of MOFs and a guest−host strategy (Figure 26C).[465] $Co_{0.9}Fe_{0.1}$, derived from BMOF_Zn_6Co, exhibited promising electrocatalytic ORR activity in 0.1 M NaOH, with an $E_{1/2}$ of 0.89 V vs RHE, and robust durability during 30 000 CV cycles, which was ascribed to its structural and compositional integrity, confirmed by STEM and EDX measurements. Lou and coworkers studied a porous $Fe_{0.3}Co_{0.7}$ alloy supported on N-doped carbon cages by an "MOF-in-MOF hybrid" confined pyrolysis strategy,[552] which reached an $E_{1/2}$ of 0.88 V. A nitrogen-doped carbon-nanotube/Fe-nanoparticle composite, prepared by a high-temperature treatment of iron acetate, cyanamide, and carbon, showed a bamboolike morphology with iron particles encapsulated into graphene nanoshells.[551] This catalyst reached an $E_{1/2}$ of 0.93 V and a H_2O_2 yield below 2% and also showed excellent durability during 10 000 cycles. Jiang et al. reported BMOF-derived P-doped Co−N−C catalysts, which in addition to a superior ORR catalytic

https://doi.org/10.1021/acs.chemrev.1c00331
Chem. Rev. XXXX, XXX, XXX−XXX

activity exhibited better stability and tolerance to methanol than a reference Pt/C catalyst.[554]

Zhuang and coworkers used adenosine, $FeCl_3$, and $ZnCl_2$ as precursors in the solvothermal synthesis of Fe-containing N-doped carbon nanotubes (Fe−N−C).[553] The presence of atomically dispersed Fe atoms in the nanotube walls was confirmed with HAADF-STEM (Figure 26G) and atomic-scale EELS (Figure 26H). The existence of Fe−N−C sites was also corroborated by ^{57}Fe Mössbauer spectroscopy. The RDE performance in 0.1 M KOH of this Fe−N−C catalyst at a disk loading of 0.4 mg/cm^2 was very similar to that of a Pt/C catalyst at 0.08 mg_{Pt}/cm^2 (the same carbon loading in both cases and thus similar catalyst layer thickness), yielding an identical $E_{1/2}$ of 0.93 V (Figure 26I). The Fe−N−C catalyst displayed only a 15 mV loss in the $E_{1/2}$ after 10 000 cycles, compared to a 40 mV loss measured with a Pt/C catalyst. In fuel cell testing, the Fe−N−C at a cathode loading of 4.0 mg/cm^2 achieved a PPD of ∼500 mW/cm^2 at 60 °C.[553] Recently, atomically dispersed Fe−N−C catalysts, derived from MOF precursors, were reported to achieve a high MEA performance with an ethylene tetrafluoroethylene-based membrane and ionomer.[555] After an additional NH_3 treatment, the catalyst reached an $E_{1/2}$ of 0.82 V at 0.2 mg/cm^2 in RDE testing in 0.1 M KOH and a PPD of 1 W/cm^2 at 60 °C in MEAs with an Fe−N−C loading of 1.5 mg/cm^2 in the cathode and a high PtRu loading of 0.9 mg_{PtRu}/cm^2 in the anode.

In summary, M−N−C catalysts have achieved an ORR performance in alkaline media that matches, and in some cases exceeds, that of Pt/C catalysts in RDE testing. Further progress in the synthesis of M−N−C catalysts, especially those derived from highly porous MOF precursors, should lead to an increase in the active site density, promising further performance improvements in AEMFC cathodes.

4.4. Non-Pt PGM ORR Catalysts

Despite the high price and scarcity of Pt-group metals (PGMs), including Pt, Pd, Rh, Ir, Ru, and Os, Pt- and Pd-based catalysts have a high intrinsic ORR activity for high-current applications in electric vehicles.[556−558] While nonprecious ORR catalysts are promising regarding drastically lowering the cost of fuel cell technologies, the search for other Pt-alternative PGM candidates can greatly diversify the choice of ORR catalysts especially for AEMFC applications demanding very high current and power densities, instead of solely relying on Pt-based ORR catalysts as in PEMFCs. Here, we will emphasize the recent progress of Pd-based and Ru-based ORR catalysts in alkaline media and discuss several strategies to enhance their catalyst activity and durability.

Pd is the only transition metal with an ORR activity comparable to Pt in alkaline media, despite its much lower ORR activity in acidic media. Early single-crystal metal studies showed the following ORR activity order (mainly 4e$^-$) in alkaline media: Pt(111) ≈ Pd(111) ≫ Ag(111) < Rh(111) ≫ Ir(111) < Ru(0001) (Figure 27A).[559] Pd(100) single crystals exhibited a higher ORR activity than Pd(111) in acidic media, and similarly, Pd nanocubes with (100) facets showed an ORR activity three times higher than spherical Pd NPs in alkaline media.[560−562] Au(111) predominantly generates peroxide via the 2e$^-$ process. In comparison, Au(100) shows a high selectivity for the 4e$^-$ ORR at potentials above −0.2 V vs SHE and a transition to the 2e$^-$ ORR at potentials below −0.2 V vs SHE in alkaline media, which was ascribed to the existence of a negative charge density on the metal surface that inhibits further reduction of HO_2^-.[563,564] Adzic and coworkers established a volcano-type relation correlating the ORR activities of single-crystal PGMs in alkaline media to the d-band center, relative to the Fermi level, with Pt located at the peak point.[559] However, the traditional d-band center theory cannot explain the fact that Pd exhibits nearly the same activity as Pt despite their large differences in d-band center values. In-depth theoretical investigations are warranted to better understand the outstanding ORR activity of Pd in alkaline media. To further improve the ORR activity of Pd-based catalysts, a variety of strategies have been proposed, such as alloying with 3d meals, forming core−shell structures, doping with foreign elements, electrochemical dealloying, etc. Alloying Pd with 3d metals has been widely proposed to cause the contraction of the Pd lattice, weakening the surface oxygen adsorption energy and bringing it closer to the optimal value, which, in turn, enhances the ORR activity in alkaline media.[565,566] Abruna and coworkers developed a high-throughput combinatorial approach, using magnetron sputtering, to prepare 40 types of Pd−M (M = Fe, Co, Ni, and Cu) thin-film electrodes with well-defined structures and various compositions as a high-throughput method to assess the ORR activity of Pd-based alloys in alkaline media (Figure 27B).[565] The use of a replaceable disk electrode enabled the rapid and reliable evaluation of ORR activity using standard RDE measurements. PdCu with a 1:1 ratio was identified as the most promising candidate and showed an ORR activity twice as high as that of Pd films. Guided by thin-film studies, PdCu nanoparticles, supported on carbon, were synthesized with an ordered intermetallic phase and 2−3 atomic-layer Pd-rich shell. The PdCu/C not only validated the activity enhancement in thin-film studies but also achieved a remarkable durability with only 3 and 13 mV negative shifts in the $E_{1/2}$, which corresponds to 15% and 40% decay in mass activity after 20 000 and 100 000 potential cycles, respectively (Figure 27C). It was ascribed to the stable structure of ordered intermetallics and the generally enhanced stability of 3d metals in alkaline media. A recent MEA study, with a PdCu/C cathode (0.58 mg_{Pd}/cm^2) and a Pd/CeO_2 anode (0.42 mg_{Pd}/cm^2), demonstrated a promising PPD of ∼1.0 W/cm^2 at 70 °C and stable operation for 100 h at 0.5 A/cm^2.[567] However, the loading of Pd is clearly very high when compared to the typical Pt loading of ∼0.1 mg/cm^2 in the state-of-the-art PEMFCs. Additional efforts are required to minimize the Pd loading while maintaining a comparable MEA performance.

Placing a monolayer or several atomic layers of PGMs on less-expensive core materials is an attractive strategy to dramatically lower the loading of PGMs and fine tune the electronic structures of PGM surface layers by changing the compositions of the underlayers.[568−570] Common strategies involve the galvanic displacement of surface layers of core materials by controllable etching with noble metal cations or Cu underpotential deposition (UPD) followed by galvanic displacement. Figure 27D shows the ORR activity of 1−2 atomic-layer Pd or Pt shells (skins) on AuCu intermetallic cores (Pd^SAuCu) in alkaline media.[571,572] Pd^SAuCu showed a surface-specific activity (SA) 5 times as high as that of commercial Pd NPs while Pt^SAuCu exhibited a 4-fold SA enhancement, relative to Pt NPs. Previous DFT calculations showed that placing 1.5 monolayers of Pt on AuCu(111) caused the oxygen adsorption energy to weaken by ∼0.2 eV, relative to Pt(111), close to the optimal value predicted by the volcano plot of ORR activity in acid.[572] Thus, it seems

https://doi.org/10.1021/acs.chemrev.1c00331
Chem. Rev. XXXX, XXX, XXX−XXX

reasonable to ascribe the performance enhancement of Pd^{S}AuCu to the weakened oxygen adsorption energy induced by the AuCu underlayers. Besides galvanic displacement, electrochemical dealloying is another powerful method to intentionally etch 3d metals and form a Pd-rich shell. As shown in Figure 27E, after electrochemical dealloying in acid, PdNi/C formed a 1−2 nm Pd-rich shell and exhibited a mass activity twice as high as Pd/C in alkaline media.[573] In order to improve the long-term durability of Pt/Pd-based alloys, a small amount of foreign elements (e.g., Au, Rh) have been doped into PGM lattices.[566,574] Au incorporated into ordered PdZn/C (Au:Pd = 1:40) exhibited an enhanced durability [<10% loss in the mass-specific activity (MA) after 30 000 cycles], which was ascribed to the addition of Au effectively suppressing the loss of Zn and maintaining the structural integrity during long-term cycling.[566] It is interesting to observe that galvanic displacement of PdZn/C by Au resulted in the uniform distribution of Au through the entire lattice, in contrast to only surface Pt coating on Pd-based core materials.

Although Ru metal and oxides are known as superior OER catalysts, but inferior ORR catalysts, their alloys with 3d metals have shown significantly enhanced ORR activity in alkaline media.[575,576] Alloying Ru with only 5% Co ($Ru_{0.95}Co_{0.05}$) yielded the highest ORR activity among Ru−M alloys (M = Co, Ni, and Fe) and a 4-fold enhancement of MA and SA as well as a 40 mV positive shift of the $E_{1/2}$, relative to Ru/C.[220] Further increasing the Co contents to 10% and 30% did not increase the ORR activity. Preliminary DFT calculations ascribed such an activity enhancement to a negative shift of the d-band center, which often corresponds to a weakened oxygen adsorption energy. Nonetheless, even the most active $Ru_{0.95}Co_{0.05}$/C catalyst showed a much lower ORR activity with a more negative $E_{1/2}$ by ∼50 mV, relative to Pt/C. In a similar study, the formation of bimetallic Ru−M oxide (M = Co, Mn, Fe, Ni, and V) showed significantly enhanced ORR activities (Figure 27F).[576] Despite the poor ORR activity of RuO_2, rutile-phase $Ru_{0.7}Co_{0.3}O_2$ and $Ru_{0.85}Mn_{0.15}O_2$ showed a significantly enhanced ORR activity with an $E_{1/2}$ of 0.86 V vs RHE, which is only 20 mV away from that of Pt/C, and close to $4e^-$ selectivity in alkaline media. DFT calculations correlated the superior performance of Co- and Mn-doped RuO_2 to their optimal oxygen adsorption strength (i.e., weaker than RuO_2 but stronger than Fe- or Ni-doped RuO_2). The oxygen adsorption energy on Mn or Co in M-doped RuO_2 was also weakened, relative to pure MnO_2 and Co_3O_4. A possible synergistic mechanism was then proposed: the ORR mainly takes place at Mn or Co sites while Ru sites lower the oxygen adsorption energy on Mn or Co sites and also effectively enhance the overall conductivity of the semiconducting MnO_2 and Co_3O_4 nanoparticles. Besides Ru-based catalysts, Ag-based materials also have demonstrated a promising ORR activity in both RDE and MEA measurements in alkaline media. In fact, the first reported AEMFC employing a Ag cathode and Ni−Cr anode was reported in 2008.[13] Given its much lower price compared to Ru and Pt, one can afford to employ a high loading of Ag/C (∼1 mg/cm^2) on the cathode to achieve an MEA performance comparable to that of Pt/C.[577] However, based on phase diagrams, it is inherently challenging to form stable single-phase Ag-based alloys with most metals except the solid solutions of Ag−Au and Ag−Pd. Preliminary RDE results showed the higher activity of Pd−Ag alloys relative to Ag, which is likely mainly due to the very active Pd rather than Ag.[578] Another approach to circumvent the poor solubility of Ag with other metals is to form Ag-metal oxide hybrid catalysts. Hybrid catalysts of Ag−Co_3O_4/C showed much enhanced ORR activities, relative to Ag/C.[579,580] XPS studies showed the reduction of Co_3O_4 to $Co(OH)_2$ induced by the presence of Ag NPs, which was not observed in pure Co_3O_4. However, the chemical interactions between Ag NPs and Co_3O_4 NPs remain elusive and require *in situ* spectroscopic investigation.

4.5. Catalyst Durability

In order to implement realistic AEMFCs, ORR electrocatalysts need to not only achieve a high initial activity but also exhibit long-term durability. Extensive studies of PEMFCs have investigated the structural changes of Pt-based alloy catalysts related to performance degradation, such as Pt nanoparticle aggregation, Ostwald ripening, particle detachment, 3d metal leaching, corrosion of the carbon support, etc.[581] Those structural changes often cause the loss of active sites (Pt and/or 3d metals) as well as a decrease of the electrochemical surface area (ECSA), leading to smaller SA and/or MA. The catalyst durability is often evaluated with accelerated durability testing (ADT) protocols for RDE and MEA measurements.[7,10] One RDE protocol recommended by the DOE is triangular potential cycles between 0.6 and 1.0 V vs RHE at 100 mV/s in O_2-saturated electrolyte. Many ORR catalysts have shown promising durability with minimal activity decay after 10 000 or more cycles. While such preliminary RDE tests are helpful to identify which catalysts cannot survive after a short-time ADT test, they do not necessarily, and often fail to, predict a reasonably long-time stable operation in MEA measurements. Catalyst durability in MEAs can be performed in mainly three different modes: constant voltage, constant current density, or trapezoidal-wave cycle to simulate automotive operation conditions. One MEA protocol in PEMFCs recommended by the DOE is the trapezoidal voltage cycle between 0.6 and 0.95 V at 80 °C, 100% humidity, and ambient pressure.[582] The durability of catalysts needs to be deconvolved from that of membranes/ionomers in MEAs (details will be covered in section 7).

The common leaching problem of 3d metals in acid can be effectively suppressed in base due to the minimal solubility of their metal oxides or hydroxides based on their Pourbaix diagrams. However, structural changes of ORR catalysts in alkaline media have still been widely reported after ADT tests in RDE measurements. For instance, Mn−Co spinels supported on carbon exhibited a mild metal dissolution and particle aggregation after 10 000 cycles in 1 M KOH.[466] The stabilities of perovskites under low reduction potentials and nitrides under high oxidation potentials are topics under active investigation. Such structural or compositional changes can be examined by TEM, EDX, XPS, ICP-MS, and Raman among other techniques and will be instrumental to understanding the catalyst degradation mechanisms and the design of more durable electrocatalysts. Additionally, it is of paramount importance to explore how to enhance the chemical interactions between catalyst nanoparticles and catalyst supports in order to better stabilize nanoparticles on supports. Carbon supports are widely used owing to their excellent electronic conductivity, highly porous structures with enormous surface areas, chemical inertness, and low cost.[581] However, carbon corrosion often causes the detachment and aggregation of catalyst nanoparticles, leading to rapid performance degradation, especially under high potentials at the

https://doi.org/10.1021/acs.chemrev.1c00331
Chem. Rev. XXXX, XXX, XXX−XXX

cathode during startup/shutdown operations of fuel cells.[492] Some progress has been made to replace carbon with corrosion-resistant supports, such as oxides, nitrides, and carbides, which will be discussed in section 5.

4.6. Summary

In summary, this section reviews efforts to understand the complex ORR mechanisms in both acid and base and the recent progress of single-crystal and nanoparticle metal and oxide electrocatalysts for the ORR in alkaline media. We have introduced the fundamental differences of the ORR pathways and intermediates in acidic and alkaline media and discussed various elemental reaction pathways with the bifurcation point as the central step. In particular, we highlighted the *in situ* vibrational spectroscopic studies, as indispensable tools to identify the very challenging reaction intermediates during the ORR and their interactions with other solution species under electrochemical conditions. To understand the origin of larger ORR overpotentials, in-depth and systematic electrochemical studies on single-crystal Pt surfaces, based on RDE techniques, were employed to examine the proposed ORR pathways, quantify the lifetime of the short-lived intermediates, and, for the first time, narrow down the ORR mechanism on Pt surfaces to be CECE with potential-dependent RDSs. The activity trend differences on stepped Pt surfaces between acidic and alkaline media originated from the fundamental difference in interfacial water structures. Quantitative studies of the potential-dependent interfacial water structures and their impact on ORR activity were extensively discussed in terms of the pztc, pzfc, and pme.

The knowledge gained from Pt single-crystal studies lays down the essential framework to understand the ORR kinetics and is also instrumental to investigate the ORR of nonprecious catalysts, including oxides, nitrides, M−N−C, as well as non-Pt PGM metals. The ORR activities on well-defined metal oxides were correlated to electronic structures with various descriptors, such as the e_g electron, M−O bond covalency, and oxygen vacancies. We then introduced an important family of nanoparticle oxide catalysts, 3d spinel oxides, which outperformed Pt/C catalysts in alkaline fuel cells. The superior performance of Co−Mn spinels was ascribed to the synergistic effect of Co and Mn in which Mn prefers to bind O_2 while Co prefers to bind and activate H_2O. Metal nitrides and oxynitrides were designed to overcome the intrinsic low conductivity of metal oxide nanoparticles. We have discussed the identification of active sites, possible ORR mechanisms, and the correlation between M−N−C active sites and the activity/stability for M−N−C catalysts. Finally, we discussed the design rules for non-Pt PGM catalysts, particularly Pd-based and Ru-based alloys, aiming for diversifying PGM catalyst candidates for achieving high power densities in applications like electric vehicles. Overall, various nonprecious and non-Pt precious metal catalysts exhibit outstanding ORR activities based on preliminary RDE measurements. However, whether these highly active ORR electrocatalysts can show a similar enhancement in realistic MEA tests is still an open question. We encourage the fuel cell community to adapt MEA measurements, even in early-stage catalyst development, to perform evaluations under realistic fuel cell conditions.

5. ELECTROCATALYST SUPPORTS

A critical component of fuel cells that significantly affects their electrochemical performance, life cycle, and durability is the catalyst support material. In general, the support provides the surface upon which metal catalyst particles are deposited and can play a synergistic role in the catalytic and mass transfer processes that are interlinked in the electrochemistry of fuel cells.[583−586]

While catalyst supports are ubiquitous in heterogeneous catalysis and are found in a broad range of compositions, the choices of supports for fuel cell electrocatalysts are more limited and involve more constraints. In fuel cells, electrochemical half-cell reactions occur at three-phase interfaces/boundaries between the solid catalysts, polymer electrolyte, and gaseous reactants. The reactants are typically small molecules (e.g., hydrogen and oxygen) that are introduced to the cell in the vapor phase (often humidified) and transported through a gas diffusion electrode (GDE). Because the three-phase catalytic interface is connected to the electrical circuit of fuel cells, a basic requirement of the electrocatalyst support is high electronic conductivity. In addition, supports must also have a high surface area in order to achieve the desirable catalyst metal dispersion, porosity to facilitate gas flow, and good chemical and physical stability under fuel cell operating conditions.[583−586]

In this section, we describe the main categories of supports for alkaline fuel cells. In the first part, we focus on carbon catalyst supports, which have a long history of utilization in PEMFCs, AEMFCs, and other alkaline electrochemical systems. We review the broad variety of carbon materials, focusing on the parameters that can affect their performance, especially in alkaline media. In the second part, we describe conductive noncarbon supports that have been studied in both PEMFCs and alkaline fuel cell applications.

5.1. Carbon Catalysts Supports

Carbon utilization in electrochemical cells for energy generation dates back to the 19th century when Humphrey Davy used graphite as an electrode for the arc lamp, and William Jacques presented his carbon battery. One of the first reports regarding the use of carbon as a component of fuel cells was in 1937, when Baur and Preis used coke as an anode. It was in the 1950s, though, that Kordesch and Marco first used oxygen-depolarized carbon as an electrode for a carbon/potassium hydroxide/zinc cell,[587] paving the way for the use of hydrophobic porous carbons as catalyst supports in alkaline media.[588] During the same period, parameters that determine the performance of carbon supports during operation, including gas transport, electrolyte effects, resistance, and chemisorption of the catalyst on the carbon surface, were identified.[589]

Porous carbon materials continue to be widely used due to their morphology and properties that fulfill the prerequisites of an electrocatalyst support as articulated above. More specifically, structural characteristics such as high surface area and porosity, in combination with properties such as conductivity and the presence of active sites, justify their selection while their electrochemical stability and low cost make them very popular, relative to other support materials.[584,590−592]

5.1.1. Structures and Properties of Carbon Materials.

Carbon black (CB), which is the most commonly used material for fuel cell applications, is derived from the incomplete combustion of heavy petroleum products. Usually, CB has a paracrystalline structure[593] consisting of carbon particles of various sizes forming graphitic layers with a range

https://doi.org/10.1021/acs.chemrev.1c00331
Chem. Rev. XXXX, XXX, XXX−XXX

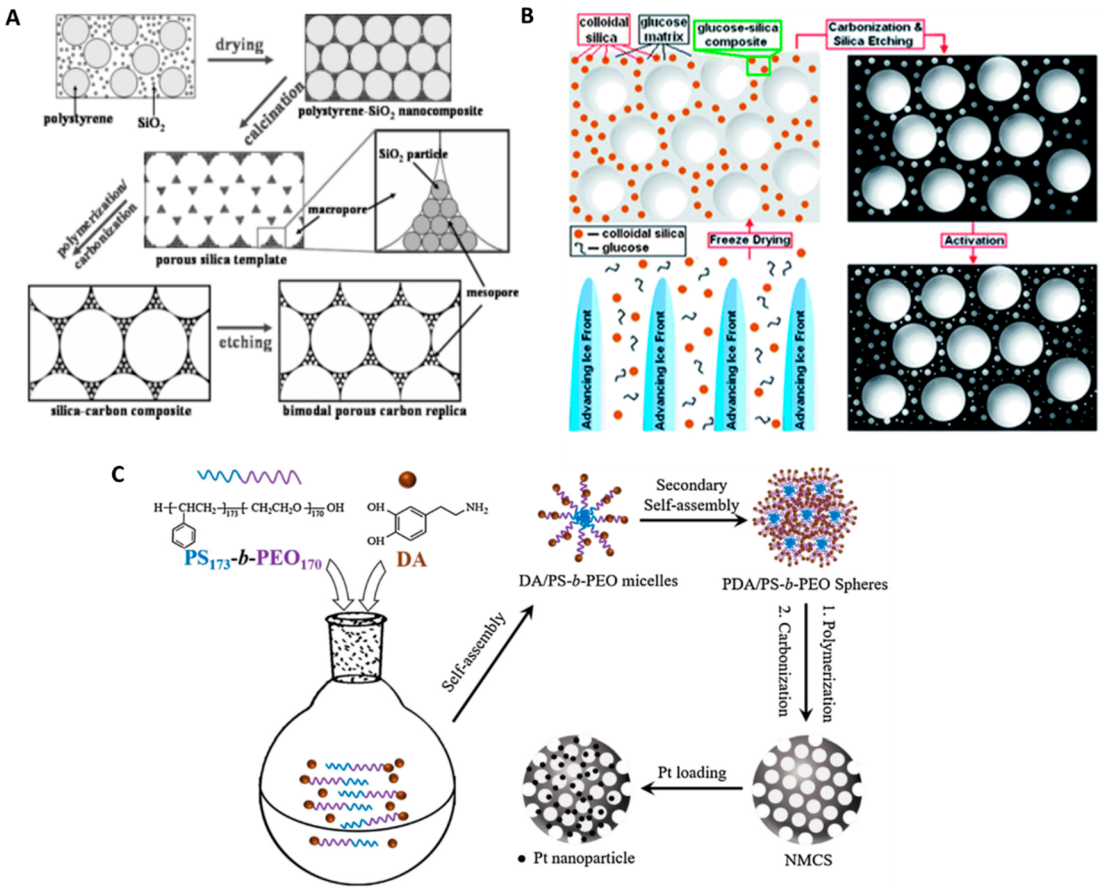

Figure 28. (A) Graphical representation of the synthesis of a periodically ordered macroporous carbon framework with mesoporous walls. (B) Hierarchical porous carbon of tuned macro-/meso- and microporosity by employing a modified hard template method. (c) Synthesis of Pt/mesoporous nitrogen-doped carbon spheres via a soft template method. Panel A is reproduced with permission from ref 609. Copyright 2004 Wiley. Panel B is reproduced with permission from ref 612. Copyright 2013 The Authors, Royal Society of Chemistry. Panel C is reproduced with permission from ref 615. Copyright 2017 Elsevier.

of surface area values starting from ~230 and reaching up to ~1600 m^2/g depending on their source.[584,594,595] Regarding porosity, CB typically consists of a high-volume percentage (around 50%) of micropores (i.e., pore sizes <1 nm).[596] Prior to use, CBs are further treated in order to remove impurities and obtain more active catalytic sites. The activation procedure is performed via either oxidative or thermal treatment at high temperature (~1100 °C) and results in an activated carbon with higher crystallinity and surface area. Vulcan XC 72 is the most widely used carbon black in the literature for PEMFCs and has an electrical conductivity of ~4.0 S/cm and a surface area of ~230−250 m^2/g.[584,595]

With the emergence of new carbon allotropes, various materials have been examined for their electrochemical performance and their potential as catalyst supports. One of the most frequently studied, mostly due to their high surface area, is carbon nanotubes (CNTs). CNTs, which are usually synthesized via chemical vapor deposition (CVD) from hydrocarbons, consist of hexagonal graphitic layers in a tubular structure. Depending on how many layers are rolled concentrically, they are distinguished as single-wall (SWCNTs) or multiwall carbon nanotubes (MWCNTs). The outer diameter of CNTs ranges from 10 to 50 nm while their inner diameter is 3−15 nm. Their typical length varies from 10 to 50 μm, and their BET surface area ranges from 400 to 900 m^2/g for single-wall and 200 to 400 m^2/g for multiwall nanotubes, respectively. While SWCNTs are microporous, MWCNTs possess two types of porosity: a fraction of pores with a small diameter of 3−6 nm and a fraction of larger pores of 20−40 nm diameters.[585,597] The conductivity of CNTs depends on the wrapping direction of the graphitic layers, rendering them metallic or semiconducting.[590]

Carbon nanofibers (CNFs) are imperfect cylindrical/tubular structures consisting of graphite layers and are derived from the decomposition of organic polymers such as polyacrylonitrile (PAN) or carbon-containing gases like methane. Even though their surface area of 90−210 m^2/g does not exceed that of CNTs, their very low levels of impurities, insignificant content of micropores (1%), high electrical conductivity, and resistance to corrosion are considered advantageous characteristics for fuel cell applications.[591,598]

Along with CNTs and CNFs, 2D graphene also exhibits promising properties that have led to its electrocatalytic evaluation as a catalyst support. Among these properties, the most beneficial for fuel cell applications are its high theoretical surface area (~2630 m^2/g) and high electrical and thermal conductivity.[599] Carbon nanodots (CNDs), nanohorns (CNHs), and nanocoils (CNCs) have also been studied as catalyst supports. In the case of CNDs, apart from their facile synthesis and low cost of production, their small size (10 nm) provides a high surface area suitable for the dispersion of metal NPs while their high oxygen content (~10%) is considered

https://doi.org/10.1021/acs.chemrev.1c00331
Chem. Rev. XXXX, XXX, XXX−XXX

advantageous since there is no need for further functionalization prior to the deposition of the metal catalyst.[600] Comparably, semiconducting carbon nanohorns (CNHs) that consist of horn-shaped aggregates of graphene with diameters of about 2−5 nm and lengths from 40 to 50 nm[601] also demonstrate a high surface area that can reach up to 1025 m^2/g.[602] Finally, CNCs, a category of CNFs that have a helical shape, a low content of micropores, and a high electrical conductivity have been examined as supports for catalytic NPs in DMFCs and PEMFCs exhibiting promising performances.[603,604]

One of the basic prerequisites of catalysts supports is the high surface area that facilitates and a promotes uniform dispersion of catalyst NPs. Compared to commonly used CB such as Vulcan, CNTs have a significantly higher surface area that permits a higher loading of catalyst NPs. Both the outer and the inner surface of CNTs, with a large diameter up to 200 nm, can be utilized for the deposition of electrocatalytic NPs.[605,606] Similarly, when graphene-based materials are used as supports, their structure and morphology affect catalyst utilization. For instance, their planar structure can facilitate the interaction of edge planes with the catalytic NPs. Nevertheless, graphene, due to van der Waals interactions, has a tendency to agglomerate, resulting in a blocking of the catalytic sites on the surface, thus inhibiting electrocatalytic activity.[586,607] Porosity is another parameter that affects the effectiveness of catalyst supports, since the size of the pores determines the accessibility of embedded catalysts to the electrolyte and affects the mass transport of reactants and the uniformity of the catalytic nanoparticle distribution on supports.

In general, the presence of macropores and mesopores allows easier gas flow and a higher accessibility of electrolyte to the electrocatalytically active sites. In order to achieve a sufficient transport of reactants, synthetic procedures that allow the creation of macropore−mesopore channels via hard template methods are used resulting in ordered porous structures. The most common way to obtain the desired structure is by nanocasting, usually achieved by using a silica hard template filled with carbon-containing materials. After calcination, the template is removed leaving an ordered graphitic network (Figure 28A,B).[596,608−612] As an alternative, the synthesis of the support can include the use of soft template precursors including polymeric surfactants (Figure 28C).[613−615] The supports synthesized by both methods allow a better dispersion of catalyst NPs due to the presence of macropores and mesopores resulting in an enhanced catalytic performance. However, the hydrothermal synthesis of carbon materials, e.g., reduced graphene oxide, can result in 3D hierarchical morphologies without the use of any template.[616] Micropores on the other hand are able to host a high density of metal active sites,[617] but their existence can often result in the deactivation of NPs used as the catalyst if gas flow is not also favored or if the electrolyte cannot permeate the micropores. More specifically, it has been found that, for CBs that consist of large amounts of micropores smaller than 1−2 nm, the supply of the gaseous fuel to the catalyst surface is not smooth/even, and pores are not easily accessible to the electrolyte resulting in tangled, nonactive catalyst NPs and a lower number of triple phase boundary active sites.[618,619]

Of note is the inverse correlation between porosity and electrical conductivity since an increased porosity of the support can lead to lower conductivity, such as in the study of doped porous CNFs[620] and CNTs.[621] Defects are also a crucial factor that can affect electrochemical performance. In carbon materials, it has been shown that edges and lattice defects with unpaired electrons or carbonyl groups create active sites that enhance electrocatalytic reactions occurring on the surface of the electrocatalyst, while at the same time they can induce hydrophilicity.[622] With that in mind, one can explain the high activity of CNTs, where edge sites promote catalyst nanoparticle anchoring.[584] Similarly, graphene edges possess a reactivity 2 times higher than that of atoms situated in the bulk, facilitating faster electron transfer.[623] Moreover, other topological defects, e.g., Stone Wales defects, have been reported to enhance the ORR by lowering the energy gap between the highest occupied and lowest unoccupied molecular orbital (HOMO and LUMO).[623] Additionally, it has been reported for certain carbon structures, e.g., carbon nanocages, that an increase of topological defects, like holes or broken fringes, leads to a higher ORR activity.[624,625]

The lateral size of the carbon support particles has also been suggested to have a significant impact on the electrochemical performance.[592] A study on N-doped graphene quantum dots showed that a larger particle size resulted in an improved ORR activity but did not provide a clear explanation for the size-dependence.[626] A less acknowledged, but important, factor that can affect the catalytic performance of carbon supports is the presence of impurities, such as trace amounts of metals inherited during the synthesis. Even if the amount of such species is very low, even at undetectable levels, they tend to have a profound effect and promote electrocatalytic activity towards the ORR, as previously discussed in the comparison of metal-free N−C and M−N−C catalysts (section 4.3).

Even if different carbon materials have distinct structural characteristics and properties, comparing them in terms of suitability as supports for fuel cells is not a simple task. For example, CNTs have emerged as promising catalyst supports, due to their high crystallinity, conductivity, and surface area and the anchoring effect of edge sites.[584,585] Their 1D nature could lead to the formation of long-range ordered channels for efficient ion transport in anion exchange membranes (AEMs).[627] In addition, Shao et al.[628] reported that SWCNTs, with a higher specific surface area, favor a better dispersion of Pt NPs, relative to double-wall and multiwall CNTs.

Generally, the comparison of carbon supports is challenging because one must consider various parameters. Apart from the initial structural features including porosity, surface area, crystallinity, and conductivity, other restrictions such as the production cost and complexity of preparation need to be considered. In terms of catalyst utilization, where surface area is a crucial factor, CNTs and graphene surpass most CBs while carbon nanohorns have also demonstrated promising results for the ORR to H_2O_2.[629] However, in terms of cost, CNTs are significantly more expensive than most commercial carbon supports, such as Vulcan, Ketjen Black, and graphene nanosheets.

5.1.2. Surface Reactions and Corrosion of Carbon Supports. Another critical parameter affecting the performance of catalyst supports is their stability during fuel cell operation. In general, PEMFCs only allow the use of Pt-based catalysts with a small fraction of 3d metals, while alkaline fuel cells enable the use of much lower-cost 3d metals and oxides. In addition, precious and nonprecious catalysts and supports also generally exhibit higher stability in alkaline media than in acidic media.[630,631] However, it is worth mentioning that some studies appear to contradict this trend. For example, Chatenet

https://doi.org/10.1021/acs.chemrev.1c00331
Chem. Rev. XXXX, XXX, XXX−XXX

reported that Pt NPs supported on Vulcan carbon experienced a loss of ECSA in alkaline media 3 times higher than in acid, which was attributed to the aggregation and detachment of Pt NPs due to changes of the support chemical properties, which caused weaker interaction with Pt NPs.[632] Whether this difference in stability measured in an aqueous electrolyte can be translated into MEA measurements remains to be seen in further investigations.

It is fair to note that, despite recent efforts, fewer studies focusing on the stability of carbon supports in alkaline media have been reported, relative to those in acid.[633−635] The most critical reaction regarding carbon supports that jeopardizes the efficiency of the electrocatalysts during fuel cell operation is the carbon corrosion that accompanies the ORR. Carbon corrosion is a primary degradation mechanism that not only affects the support structures, such as the porosity and consequently the transport of reactants, but also induces the detachment or agglomeration of catalyst NPs.[581,636]

The peroxide species produced during the ORR can react with the carbon surface forming carbon−oxygen groups, leading to a decrease of the initial hydrophobicity and formation of more defects and possibly CO_2 or CO formation, leaving inner carbon atoms subjected to further corrosion.[631] Tomantschger et al.[637] suggested that carbon corrosion during the ORR in alkaline media could cause increased wettability, which results in internal flooding and reduces the available density of pores for gas transport. They proposed that further modification of support surfaces such as heat activation or fluorination could enhance tolerance towards corrosion and consequently increase electrocatalyst stability. Similarly, Lafforgue et al. reported that metal catalysts such as Pt and Pd suffer extensive detachment in alkaline media and locally catalyze the corrosion of carbon supports by forming CO, which can poison Pt catalysts and then CO_2 at high potentials, which can combine with OH^- and form carbonates.[638] The formation of carbonates is additionally affected by the catalyst loading. In a study of Pt NPs supported on Vulcan, it was found that, at high Pt loading, the formation of carbonates occurs above 0.5 V vs RHE, whereas for lower loading the corresponding value was above 0.8 V, suggesting a catalytic effect of Pt towards carbon corrosion.[639]

As expected, the chemistry of the support plays a critical role in corrosion and degradation processes. For example, catalytic NPs follow different degradation mechanisms, when supported on different carbon materials. In particular, when Pd NPs were supported on Vulcan XC-72R, their degradation was attributed mainly to particle detachment, while in the case of graphene nanosheets, it was caused by dissolution and redeposition of isolated NPs followed by coalescence of agglomerates.[640] The structures of carbon supports can also affect stability. For instance, the corrosion of Vulcan carbon caused the collapse of the catalyst while, in the case of CNFs, this was suppressed even for severe carbon corrosion. The result was attributed to the 1D continuous shape and large diameter of CNF.[641] Recently, Muller and coworkers examined Pt and Pt−Co catalysts supported on carbons with different porosities in durability tests in MEAs and showed that, despite the fact that different carbon supports resulted in similar rates of Pt dissolution, high-surface-area Ketjen Black exhibited a much better ECSA retention than Vulcan carbon.[642]

5.1.3. Functionalization of Carbon Supports. The functionalization of carbon supports, resulting in oxygen-containing groups such as carboxylic acids and ketones, is mainly accomplished by acid treatment (e.g., HNO_3 or H_2SO_4). This treatment is typically required in order to transform the inactive surface of carbon through the generation of anchoring sites for the catalyst. Despite the necessity of functionalization, it can have undesired side effects including the creation of defects in the lattice or even changes to the surface area. It has been almost 40 years since McBreen and coworkers,[643] during their study using four types of commercial CBs as platinum supports for phosphoric acid fuel cells, reported that the surface chemistry of the support and, in particular, hydrophobicity and internal porosity affected their catalytic performance.

More recently, a study focusing on oxygen functionalization of CB supports and its effect on their activity and stability was presented by Kim et al.[644] The study described the development of Pt on carbon catalysts using commercial Vulcan XC-72R and compared it with its mildly oxygen-functionalized counterpart. As expected, the oxygen-functionalized support showed a higher ECSA and higher ORR activity, relative to the unfunctionalized one. However, the functionalized support was less stable, which was attributed to the oxidation of Pt particles triggered by the functional groups resulting in NP dissolution and leading to a decrease in their catalytic activity. Similarly to CB, functionalization of CNTs is usually performed by harsh oxidative methods,[645,646] resulting in the creation of functional groups, including −OH and −COOH on the initially inert surface, which can serve as anchoring sites for the catalytic metal NPs.

Despite its importance regarding the utilization of catalyst, functionalization can have a negative effect on the ECSA of the electrocatalyst. Molina et al. studied different carbon materials and, in particular, commercial CB, graphene oxide (GO), and MWCNTs. All supports had similar Pt catalyst loadings, but TEM revealed that the distribution and particle size of Pt electrocatalysts were different for each support.[647] Pt NPs on CB exhibited very good homogeneity with particle diameter ranging from 3−4 nm. Pt on MWCNTs retained high homogeneity, but the mean diameter of Pt particles increased to 4.5 nm, with some large particles reaching 7 nm while Pt on GO showed a mean diameter of 3.8 nm. The ECSA of Pt on GO and reduced GO supports was 1.8 and 3.5 m^2/g, respectively, considerably lower than those of Pt/CB and Pt/MWCNTs (20.6 and 15.3 m^2/g, respectively). These results were attributed to the higher content of oxygen in GO and rGO. Pt/rGO showed a slightly better performance than Pt/GO due to the lower content of carbonyl and carboxyl species on its edges, which hinder the ORR.

5.2. Metal Electrocatalysts Supported on Carbon

Pt and Pt-based alloys, due to their superior activity and stability, are the most widely used catalysts in both PEMFCs and AEMFCs. CB was among the earliest carbon supports for Pt, with its initial use dating back to the 1970s. In fact, deposition methods that were established at that time, such as the one that Jalan and Bushnell patented in order to reduce Pt migration during fuel cell operation, are still followed to date.[648,649] However, due to the susceptibility of CB to corrosion, its electrochemical instability, and low degree of catalyst utilization, research has recently turned to other carbon materials.[585] Exploiting the already mentioned characteristics of CNTs, a vast number of studies have reported their use to support Pt or Pd alloys in PEMFCs[619,646,650,651] and AEMFCs.[652] Pt NPs can be

https://doi.org/10.1021/acs.chemrev.1c00331
Chem. Rev. XXXX, XXX, XXX−XXX

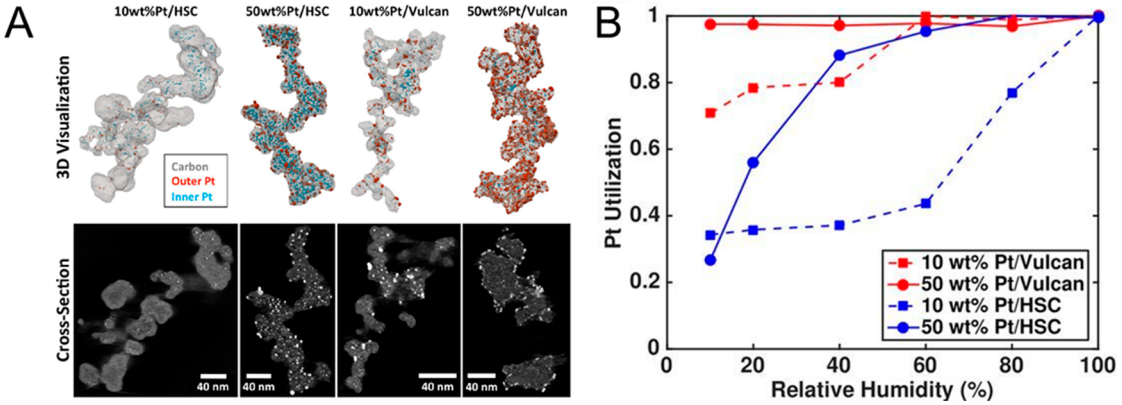

Figure 29. (A) Top: 3D STEM tomography of Pt NPs, with exterior Pt in red and interior Pt in blue on two types of carbon supports, Vulcan and high-surface-area Ketjen Black carbon (HSC KB). Bottom: cross-sections of 3D reconstructions perpendicular to the imaging axis. (B) Pt utilization with different types of carbon supports and metal loadings measured by CO stripping in MEAs with varied relative humidity (RH%). Panels A and B are reprinted with permission from ref 660. Copyright 2018 The Authors, The Electrochemical Society.

deposited on CNTs by a variety of methods including vapor deposition, electrodeposition, or via the reduction of metal salts.[653−655] For example, Shao-Horn and coworkers[650] reported that 31 wt % Pt/MWNTs catalyst exhibited an ORR MA of 0.48 A/mg_{Pt} at 0.9 V vs RHE, 3 times higher than that of 46 wt % Pt on a commercial carbon support. Similarly, Minett[656] reported using a microwave reduction technique to produce Pt/MWNT, which served as the oxygen cathode (0.1 mg_{Pt}/cm^2), with a Pt/C anode (0.2 mg_{Pt}/cm^2), to achieve a specific MA of 0.81 g_{Pt}/kW in PEMFCs.

Although graphene is considered as an ideal material against carbon corrosion due to its graphitic nature, other variables such as the lateral size and number of layers present can complicate its evaluation as a support.[657] Moreover, given its lack of oxygen-containing groups, the functionalization of its surface is a prerequisite step to enable a high dispersion of anchored catalytic NPs. On the other hand, the formation of such groups results in defects and decreases the conductivity of the carbon support. To tackle this challenge, Huang and coworkers used a soft chemical method to oxidize graphene nanoplates (GNPs). The material retained the intrinsic structure of graphene with a significantly lower density of framework defects.[658] In an effort to enhance the interactions between Pt-based alloys and carbon supports, Abruna and coworkers developed metal−organic framework (MOF)-derived Co−N−C with a BET surface area over 1000 m^2/g as carbon supports for Pt−Co electrocatalysts for the ORR.[659] Atomically dispersed Co−N−C can serve as the anchoring sites to stabilize the Pt−Co NPs on carbon supports through covalent Co−N bonds. Pt−Co/Co−N−C hybrid electrocatalysts exhibited an initial ORR MA of 0.46 mA/μg_{Pt} at 0.9 V vs RHE, surpassing the DOE 2020 target (0.44 mA/μg_{Pt}), and a minimal activity loss after 80 000 potential cycles.

In order to directly visualize the distribution of Pt NPs on porous carbon supports, we recently employed cryogenic STEM 3D tomography to study the distribution of Pt nanoparticles on both the outside and the inside of Vulcan and high-surface-area KB carbon (HSC) with different Pt loadings. The reconstruction 3D models clearly identify the inner Pt NPs marked in blue and outer Pt marked in red, as shown in Figure 29A.[660] The 3D segmented tomography of solid-carbon- and hollow-carbon-supported Pt NPs, with varied loading, was gained from the conventional cross-sectioned STEM images shown (Figure 29A, lower part). This enabled a determination of the correlation between the morphology of nanoparticle catalysts, internal pore region structure, and pore accessibility. It is clearly evident that the exterior Pt is dominant for Vulcan, whereas the majority of Pt is embedded inside of the pores of HSC KB, especially for the 50 wt % Pt loading. Coupled with automated quantitative analysis, the 3D tomography enables a calculation of the specific surface area and interior Pt fraction, which is consistent with electrochemical results.[660] The Pt utilization efficiency shown in Figure 29B at different relative humidity (RH) during MEA operation further reveals that essentially all Pt NPs are accessible to protons in liquid at 100% RH, whereas at RH < 50%, only exterior Pt NPs contribute to the surface catalytic reaction since the narrow pores preclude the infiltration of ionomers, which are crucial for proton transport in PEMFCs.

Among the alternatives to Pt catalysts, Pd shows ORR activities comparable to Pt in alkaline media, despite its much lower ORR activity in acidic media (section 4.4). Pd showed a higher stability than Pt, especially in direct ethanol fuel cells.[661,662] As expected, the type of carbon and its structural properties have a great influence on the activity of Pd. Zheng et al.[645] reported that Pd NPs supported on CNTs showed a uniform particle size distribution of 3−6 nm, smaller than that on activated carbon fibers (7−12 nm), which led to the enhanced activity of Pd/CNTs towards ethanol oxidation. A similar study[663] showed that the SWCNT support exposed a larger Pd surface area than MWCNTs, resulting in an enhanced ethanol oxidation activity. Similar to Pd, when Au NPs are supported on carbon supports, the catalyst formed exhibits an improved ORR activity in alkaline media.[664] When Au NPs with sizes smaller than 5 nm were supported on the edges and vertices of CNTs, Au/CNTs exhibited onset and half-wave potentials similar to those of Pt-based electrocatalysts for the ORR in alkaline media.[664] Similarly, rGO, which is rich in hydroxyl and carboxyl groups, has been used as a support to immobilize Ag NPs (<10 nm) at a high loading of 60 wt %. Ag/rGO showed a higher ECSA and enhanced ORR activity, relative to commercial Ag/C.[665]

Another approach towards the development of more inexpensive catalyst systems is the use of nonprecious transition metals in alkaline media. MnO_x and CoO_x supported on functionalized CNTs also showed a $4e^-$ ORR activity in alkaline media.[666,667] Recently, Abruna and coworkers reported

https://doi.org/10.1021/acs.chemrev.1c00331
Chem. Rev. XXXX, XXX, XXX−XXX

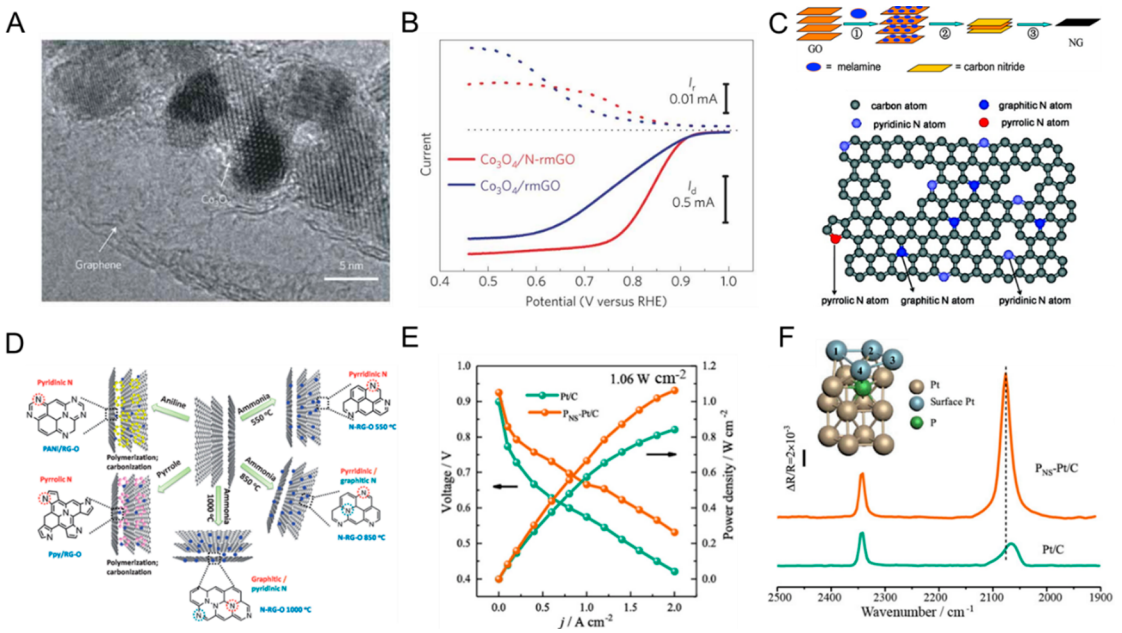

Figure 30. (A) High-resolution TEM (HR-TEM) image of Co_3O_4 NPs supported on N-doped reduced graphene oxide (Co_3O_4/N-rmGO) (B). RRDE profiles of Co_3O_4 NPs on rmGO with and without N-doping in 0.1 M KOH at 1600 rpm, 5 mV/s. (C) Graphical representation of the synthesis of nitrogen-doped graphene (NG) and the nitrogen configuration in NG. (D) Schematic illustration of the nitrogen doping of graphene resulting in different N states. (E) Voltage−current curves of Pt/C and near-surface P-doped Pt/C (P_{NS}−Pt/C) as the oxygen cathode (0.15 mg_{Pt}/cm^2) in PEMFCs in H_2-air mode at 80 °C. (F) *In situ* FTIR spectra of CO adsorbed on P_{NS}−Pt/C and Pt/C in 0.1 $MHClO_4$ at 0.10 V. Inset: near-surface P doping on Pt(111) model for DFT calculation. Panels A and B are reproduced with permission from ref 455. Copyright 2011 Springer Nature. Panel C is reproduced with permission from ref 673. Copyright 2011 American Chemical Society. Panel D is reproduced with permission from ref 677. Copyright 2012 Royal Society of Chemistry. Panels E and F are reproduced with permission from ref 682. Copyright 2021 American Chemical Society.

that $MnCo_2O_4$ spinel particles, grown on KB, exhibited a higher ORR activity and enhanced mass transport, relative to these grown on Vulcan XC-72, benefiting from the much higher surface area of KB.[466] Zhao et al. reported that Pd/MnO_2 hybrid catalysts on MWCNTs exhibited a 2-fold activity increase for the methanol oxidation reaction, relative to commercial Pd/C, which was ascribed to MnO_2 providing numerous nucleation sites that prevented the aggregation of Pd NPs.[668] Regarding other metal oxides, Hu described in detail the ORR behavior of iron oxides—GO catalysts showing their enhanced activity and stability in alkaline solutions.[669]

5.3. Heteroatom-Doped Carbon Supports

Another major strategy for lowering the cost of electrocatalysts is the use of metal-free supports and more specifically heteroatom-doped carbon structures. It is commonly accepted that doping causes electron modulation and defects in the carbon framework changing the electronic structure of electrocatalysts. For that reason, the effect of doping with elements like N, B, S, or P is of high interest in many catalytic systems including fuel cell applications. There is a plethora of reports showing that heteroatom-doped carbon supports present a similar or even enhanced catalytic activity compared to Pt-supported systems.[623] The effects of doping, however, depend on numerous factors such as functional edge sites or topological defects. In general, doping is performed either *in situ* during the synthesis of the carbon support or by post-treatment using a suitable precursor containing the dopant, with strategies such as heat treatment and carbonization, chemical vapor deposition, or hydrothermal methods.[592,670]

5.3.1. Nitrogen-Doped Carbon Supports. The most common heteroatom dopant is nitrogen. The promising ORR activity of N-doped carbons (N−C) and M−N−C was discussed in detail in section 4.4. It is believed that nitrogen dopants donate electrons to the π-orbital in carbon, which can then be transferred to the π^*-orbital of O_2, facilitating the splitting of oxygen bonds and increasing the ORR kinetics.[671,672] Dai and coworkers reported that Co_3O_4 NPs (4−8 nm) supported on mildly reduced GO (rmGO) exhibited a $4e^-$ reduction of oxygen with a high $E_{1/2}$ of ∼0.83 V vs RHE, close to that of Pt/C in alkaline media (Figure 30A).[455] N-doping in rmGO significantly increased the ORR activity and lowered peroxide formation (Figure 30B), which was ascribed to the intimate interaction between small Co_3O_4 NPs and N-doped rmGO through possible Co−O−C or Co−N−C bonds, as supported by soft XAS measurements.[455] They later reported on a similar promoting effect of N-doped rmGO on the ORR of $MnCo_2O_4$ in alkaline media.[456] To investigate the effects of N-doping levels, Sheng et al. synthesized nitrogen-doped graphene by annealing GO mixed with melamine (Figure 30C) at various temperatures.[673] They found that the nitrogen configuration and not the amount of nitrogen was the main factor affecting the ORR activity. They reported that pyridinic nitrogen, as the main nitrogen species based on XPS, is responsible for the ORR performance enhancement. Similarly, N-doping on CNTs and CNHs also showed a promising ORR activity.[674−676]

To explore the effects of different nitrogen species, Lai et al.[677] used a variety of nitrogen sources and a range of annealing temperatures to generate different nitrogen species during graphene doping (Figure 30D). They proposed that pyridinic nitrogens changed the $2e^-$ mechanism to a $4e^-$ pathway and improved the onset potential, while graphitic

https://doi.org/10.1021/acs.chemrev.1c00331
Chem. Rev. XXXX, XXX, XXX−XXX

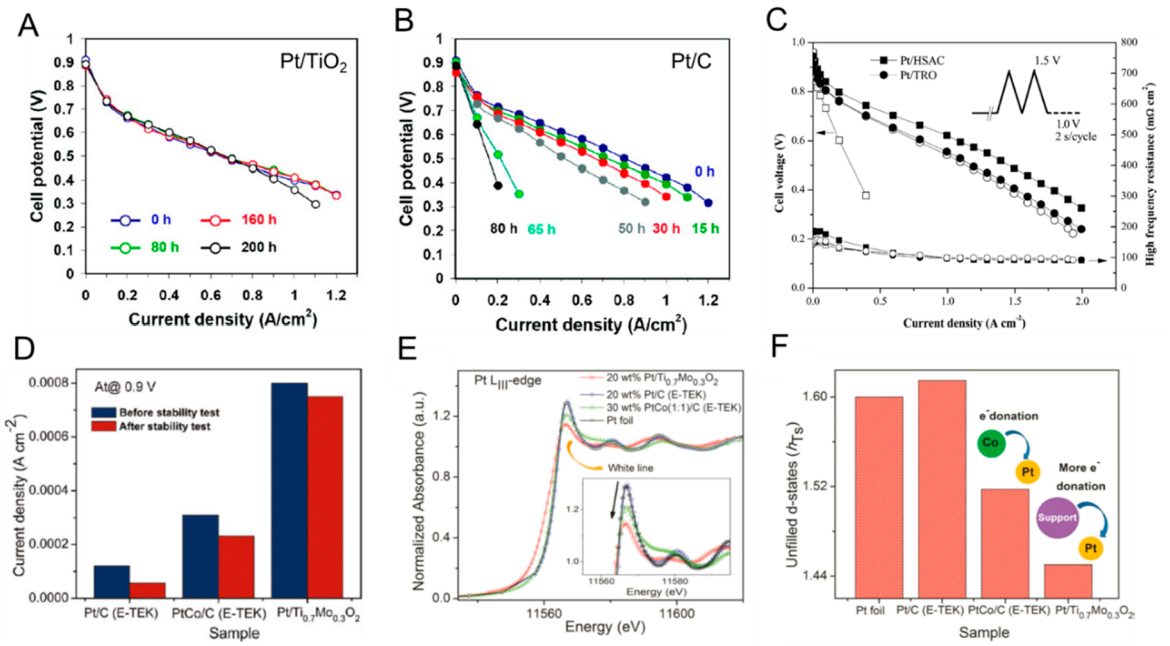

Figure 31. (A, B) Polarization curves in PEMFCs using Pt/TiO_2 and Pt/C after applying a potential as an accelerated stress test over several time ranges. A Pt loading of 0.5 mg/cm^2 was used on the anode and 0.4 mg/cm^2 on the cathode. (C) Voltage−current curves of Pt supported on high-surface-area carbon (HSAC) and Ti-RuO_2 (TRO) before and after 1000 oxidizing potential cycles at 80 °C and 40% RH. (D) ORR kinetic current density of $Pt/Ti_{0.7}Mo_{0.3}O_2$ at 0.9 V vs RHE before and after a stability test of 5000 potential cycles in 0.5 M H_2SO_4. (E) XANES spectra and (F) variations in unfilled d-states of the Pt L_{III}-edge showing a decrease in intensity as the metal−support interaction becomes stronger. Panels A and B are reprinted with permission from ref 698. Copyright 2009 American Chemical Society. Panel C is reprinted with permission from ref 713. Copyright 2014 National Academy of Sciences. Panels D−F are reprinted with permission from ref 711. Copyright 2011 American Chemical Society.

nitrogen determined the current density.[677] In contrast, in a later study, it was reported that isolated pyridinic or graphitic nitrogen species can improve the activity of doped carbons, but when those species interact, electron donation is not favored, which lowers the ORR activity.[678] In order to explain these somewhat contradictory results, one must consider that even though it is generally believed that both graphitic and pyridinic nitrogen serve as ORR active sites, the identification and quantification of nitrogen configurations are mainly based on XPS analysis. Different XPS peak fitting methods could lead to different interpretations of nitrogen spectra.[592]

5.3.2. Carbon Supports Doped with Other Heteroatoms. Like nitrogen, sulfur has also been considered as a possible heteroatom that can be doped into carbon supports in order to facilitate the ORR. Sulfur has a very similar electronegativity to carbon when incorporated into the carbon lattice and can induce strain and stress modulating changes of charge to adjacent carbon atoms.[592] For instance, Li et al.[679] showed that S-doped CNTs exhibited an enhanced ORR activity with a $4e^-$ process in alkaline media, owing to the formation of thiophenes after the doping process. Similarly, P-doped MWCNTs increased the electron transfer number from 2 to 3 in the ORR, owing to the change in charge density.[680] A P-doped graphite layer catalyst also showed an improved ORR activity.[681] Recently, Sun and coworkers reported that P introduced into the near surface of commercial Pt/C (P_{NS}−Pt/C) showed a 7-fold increase in the ORR activity in RDE measurements. Further MEA tests of P_{NS}−Pt/C in H_2-air PEMFCs achieved a higher PPD of 1.06 W/cm^2 with a Pt loading of 0.15 mg/cm^2 and a doubling of the current density to 1.54 A/cm^2 at 0.60 V, relative to Pt/C (Figure 30E).[682] The performance enhancement was ascribed to the P doping inducing Pt surface distortions, which led to the formation of concave Pt sites with an optimal OH binding energy for the ORR. *In situ* FTIR of P_{NS}−Pt/C exhibited a weaker CO chemisorption energy, which often corresponds to faster ORR kinetics for Pt-based electrocatalysts (Figure 30F). It should be noted that $NiSO_4$ was used to promote the decomposition of $NaH_2PO_2{\cdot}H_2O$ through the formation of NiP, favoring the P doping, which resulted in a P/Pt atomic ratio of ∼19% and less than 1% Ni. Although the author claimed that such low Ni contents could not induce lattice contraction as in traditional PtNi alloys, it is possible that a low coverage of Ni on the Pt surface can contribute to the ORR enhancement.

Finally, when carbons are doped with boron, the charge neutrality of carbon atoms is modulated due to the substitution of boron atoms in the sp^2 lattice. Doping is usually accomplished via pyrolysis with boron precursors such as boric acid. In general, there is a positive correlation between the amount of boron and the catalytic activity. Additionally, the pyrolysis temperature significantly affects the electrochemical performance since it determines the formation of the active B−C sites that can promote the ORR in alkaline media.[592,683]

5.4. Noncarbon Electrocatalyst Supports

Noncarbon electrocatalyst supports offer a number of potential advantages over carbon supports, although they face significant challenges as well. Graphitic carbon supports tend to interact weakly with polar metal catalyst NPs except at defect and edge sites. Noncarbon supports, including metal oxides, nitrides, chalcogenides, and carbides, can interact more strongly with metals through covalent bonding or polar noncovalent forces. Noncarbon supports can also provide enhanced catalyst

https://doi.org/10.1021/acs.chemrev.1c00331
Chem. Rev. XXXX, XXX, XXX−XXX

stability by eliminating the carbon corrosion that leads to catalyst degradation, but they typically cannot attain the very high surface area or conductivity of carbon supports. As carbon supports corrode, catalyst particles detach and coalesce, becoming less active and compromising fuel cell performance,[684,685] which was recently directly visualized by *in situ* liquid-cell TEM studies of Pt−Ni NPs weakly supported on carbon.[686]

Metal oxide supports are used extensively in heterogeneous catalysis because they can confer stability through strong covalent and polar interactions with catalyst NPs. Interfacial catalyst−support bonding inhibits catalyst ripening and agglomeration and, in some cases, also increases the activity by improving catalyst dispersion. Oxide supports can also exert synergistic effects that include nanoparticle encapsulation, participation in bifunctional reaction mechanisms, spillover effects, lattice strain, and molecular orbital mixing.[687−690] Early transition metal oxides that have unfilled d-orbitals interact strongly with d-electron-rich, catalytically active late transition metals,[691] a covalent bonding effect that is associated with the strong metal−support interaction (SMSI).[692] Despite these advantages, most metal oxides are electronically insulating, and even deliberately doping them may not sufficiently impact conductivity for them to be used as catalyst supports in alkaline fuel cells. In contrast, many metal nitrides and carbides are good electrical conductors while having the same advantages in catalyst stabilization as early transition metal oxides.

In addition to conductivity and the stabilizing effects of the metal−support interaction, the morphology, porosity, surface area, and degree of catalyst dispersion are also important features to optimize. This section describes relevant research on noncarbon electrocatalyst supports, grouped by composition, and highlights the strengths and weaknesses of each along with ideas for how they might be improved. Several reviews have been written about electrocatalyst supports, and some specifically cover noncarbon supports.[693−695] Here, we will focus specifically on noncarbon supports, the history of their use in PEMFCs, and potential applications in AEMFCs.

5.4.1. Metal Oxide Catalyst Supports. The most commonly studied metal oxide electrocatalyst support is TiO_2 which is due to its high surface area, its conductivity in doped forms, and its success as a heterogeneous catalyst support as well as its use in photocatalytic reactions. The metal−support interaction[692] has been well-characterized for TiO_2, but it is a wide band gap semiconductor (3.0 eV) and thus a very poor electronic conductor in the undoped form. Huang et al. studied Pt nanoparticles on mesoporous TiO_2 films for the acidic ORR and found that they were more active than Pt/C and more resistant to degradation upon cycling than unsupported Pt particles.[696,697] Pt/TiO_2 achieved a higher PPD (0.95 W/cm^2) than Pt/C (0.8 W/cm^2) (Figure 31A,B).[698] They measured the ECSA as a function of time under a constant current density of 0.5 A/cm^2 and found that the active surface area of Pt/TiO_2 decreased 3 times more slowly than that of Pt/C.[698,699] They postulated that the retention of the ECSA resulted in the higher activity of Pt/TiO_2 after aging. Several studies confirmed that titania-supported Pt catalysts are more stable than Pt/C.[698,700,701] It should be noted that conflicting results have been reported by other authors on TiO_2 as an electrocatalyst support, where they found a higher series resistance in the system and attributed it to the lower conductivity of titania.[702,703] Doping by introducing oxygen vacancies or other cations, such as Nb, has been shown to increase the conductivity,[704] and there have been many attempts to modify TiO_2 to improve its performance as an electrocatalyst support.[705] Bauer et al. found that TiO_2 reduced with H_2 was more stable electrochemically than when calcined in air but not as stable as Nb-doped titania.[700,706] Many types of TiO_2 and its derivatives have been shown to suppress the degradation/poisoning of catalysts compared with carbon supports.[707,708]

Mallouk et al. studied Ti_4O_7 and mixed Ti_nO_{2n-1} phases (Ebonex) supported Pt−Ru−Ir catalysts for the ORR and OER in acidic media. The enhanced activity and stability were ascribed to strong electronic interactions between the catalyst and support. They found that Ti tends to be oxidized at very positive potentials (1.6 V vs RHE) during the OER, which decreases its conductivity and leads to poorer catalyst utilization.[702,703,709] Experimental proof of stability is often obtained either by comparing the ECSA or activity before and after an accelerated degradation test (ADT) or by comparing the catalyst/support morphology before and after aging. Dang et al. observed that Au NPs on TiO_2 showed minimal thermal sintering after treatment at 500 °C for 4 h, whereas Au particles on carbon grew 5−10× larger under the same conditions.[710]

Most of the work on metal oxide electrocatalyst supports has been done by mixing titania precursors with another transition metal in order to achieve n-type doping. Siracusano et al. studied Nb-doped TiO_2 as a catalyst support for the acidic ORR. They were able to make TiO_2 with a relatively high surface area of 279 m^2/g and a series resistance lower than that of KB.[707] Several different tests of Nb-TiO_2 supports report lower corrosion currents than Pt/C.[706−708] Pt supported on $Ti_{0.7}Mo_{0.3}O_2$ showed a significantly better stability than PtCo/C and Pt/C during the ORR in acidic media (Figure 31D).[711] This was ascribed to the noticeable electron transfer from oxide to Pt as evidenced by the relative density of unfilled d-states extracted from XANES (Figure 31E,F).[711] Park et al. also reported a decrease in the XANES edge intensity of the Pt L_{III}-edge with a Nb-TiO_2 support, indicating an electron transfer from the oxide support to Pt, which might explain the superior ORR activity of Pt/Nb-TiO_2, relative to Pt/C.[712] Ramani and coworkers recently reported that Ti-RuO_2, with a good conductivity of 21 S/cm, showed significantly enhanced durability for supported Pt NPs as the oxygen cathode in PEMFCs, with an 18% loss in MA after 10 000 voltage cycles in MEAs, compared to a 52% loss in the case of Pt/C (Figure 31C).[713] Pt on TiRuO_2 also showed much less corrosion under oxidizing voltage cycles between 1.0 and 1.5 V, which are often triggered by fuel cell startup and shutdown, relative to the severe carbon corrosion of Pt/C under the same conditions.

Doped tin oxides and indium tin oxide (ITO) are well-known conducting metal oxides that have widespread use in touchscreens and transparent glass electrodes. This makes them interesting candidates to study as electrocatalyst supports. Several studies have found success with these materials in various electrochemical environments, but the stability of SnO_2 and its derivatives in alkaline media is in question since SnO_2 is amphoteric and can dissolve in both strongly acidic and alkaline environments.[714−716] It is possible that conductive SnO_2 supports could be stabilized by surface passivation, e.g., with TiO_2 or other stable oxides, in order to remain active over long periods of operation in alkaline fuel cells. Cerium oxides have been successfully used as catalyst supports in high-temperature electrolyzers and heterogeneous

https://doi.org/10.1021/acs.chemrev.1c00331
Chem. Rev. XXXX, XXX, XXX−XXX

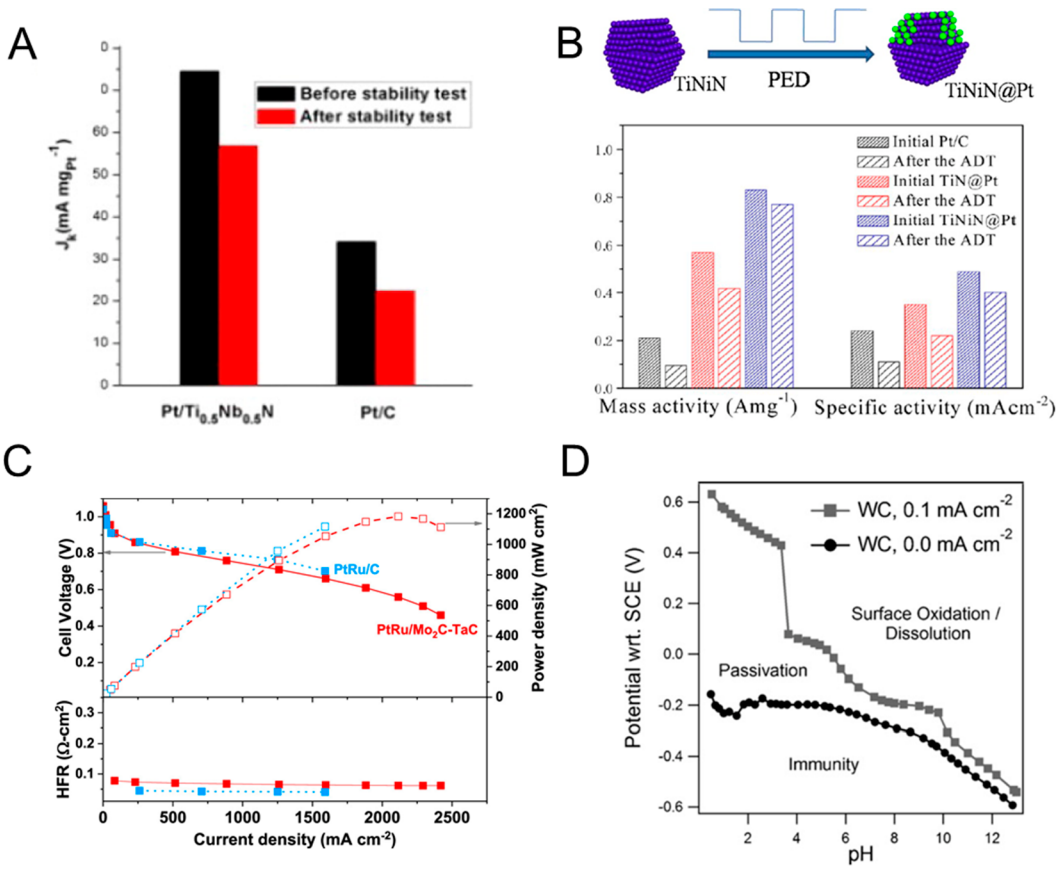

Figure 32. (A) ORR kinetic current density at 0.9 V vs RHE measured in 0.1 M KOH before and after stability tests of 5000 potential cycles. (B) Schematic of placing few-atomic-layer Pt on Ti−Ni nitride through pulse electrodeposition (PED) and mass and specific activities of Pt/C, TiN@Pt, and TiNiN@Pt catalysts before and after the durability test of 10 000 potential cycles. (C). Voltage−current density curve of AEMFC in H_2−O_2 mode of $PtRu/Mo_2C$−TaC and PtRu/C at 70 °C. (D) Chronopotentiometric titration experiments for stability mapping of WC with titration currents held at 0.0 and 0.1 mA/cm^2 to outline the regions of immunity, passivation, and surface oxidation/dissolution. Panels A and B are reprinted with permission from refs 723, 724. Copyright 2013, 2016 American Chemical Society, respectively. Panel C is reprinted with permission from ref 727. Copyright 2021 American Chemical Society. Panel D is reprinted with permission from ref 728. Copyright 2012 Elsevier.

catalysis because they stabilize the catalyst particles, are good oxide ion conductors, and can maintain catalyst morphology and activity at high temperatures.[717] The problem with using ceria as a support in low-temperature applications is its low conductivity in the undoped form. To address this problem, Wu and coworkers mixed ceria with molybdenum oxide to enhance its conductivity and showed promising activity towards methanol oxidation.[718] Some work has been done on using other transition metal oxides as electrocatalyst supports with promising results. Atanassov and coworkers made Pt/NiO and Pt/MnO_2 and compared their performance to Pt/C for ammonia electrooxidation in alkaline media. They found that Pt/NiO had a peak current about 2 times higher and a better durability as compared to Pt/C.[719] XPS of Pt/NiO and Pt/MnO_2 showed a shift in the Pt 4f peaks towards higher binding energies, relative to Pt/C, indicating electron donation from the oxide support to Pt, but it could not be determined if the effect arose from the metal−support interaction or from the smaller size of the Pt particles.

5.4.2. Metal Nitrides and Carbides as Electrocatalyst Supports. In addition to the 3d metal nitride ORR electrocatalysts discussed in section 4.2.4, the most commonly studied metal nitride support is TiN, which shows exceptional stability and corrosion resistance along with good electronic conductivity in PEMFCs and direct methanol and ethanol fuel cells. Sampath and coworkers reported that Pt supported on TiN showed better stability for methanol oxidation than PtRu/C.[720] *In situ* IR spectroscopy showed a prominent band around 3250 cm^{-1}, indicating the presence of Ti−OH groups formed upon oxidative cycling, which could facilitate methanol oxidation by removing the intermediate species. Pt supported on TiC and TiCN also showed promising activity for the methanol oxidation reaction.[721] Chen and coworkers designed a three-dimensionally porous titanium oxynitride decorated with ultrafine Co metal particles.[722] The composite exploited an oxygen vacancy-induced strong metal support interaction to stabilize the Co NPs, which had an ORR activity comparable to that of Pt/C in alkaline media and extended cycling stability in an alkaline Zn−air battery.

Nitrides of the early transition metals are typically good electronic conductors, and a number of studies have explored their properties as catalyst supports in fuel cells. DiSalvo and coworkers synthesized a mesoporous and highly conductive ternary nitride $Ti_{0.5}Nb_{0.5}N$ by coprecipitation followed by ammonolysis.[723] $Pt/Ti_{0.5}Nb_{0.5}N$ exhibited a good catalytic activity for the ORR, with a higher SA (0.53 mA/cm^2) at 0.9 V for the ORR in acid, relative to Pt/C (0.25 mA/cm^2), and slower activity decay by 19% after 5000 cycles as compared to that of Pt/C (29%). In alkaline media, $Pt/Ti_{0.5}Nb_{0.5}N$ also showed a kinetic current 2.2 times higher than Pt/C and a

https://doi.org/10.1021/acs.chemrev.1c00331
Chem. Rev. XXXX, XXX, XXX−XXX

smaller activity decay of ~23%, relative to Pt/C (~34%) (Figure 32A). Recently, Adzic et al. employed pulse electrodeposition (PED) to place 2−3 atomic layers of Pt on a TiNiN support, which achieved a 4-fold and 2-fold increase in MA and SA, respectively, for the ORR in acid, relative to Pt (Figure 32B). Moreover, such a thin-layer Pt on TiNiN exhibited only a slight loss of activity after 10 000 potential cycles in RDE measurements, which was ascribed to the strong interaction between the Pt and the nitride substrate.[724] Wei and coworkers reported that Pt supported on $Ti_{0.9}Co_{0.1}N$ showed a 2-fold increase in mass activity at 0.9 V vs RHE, relative to Pt/C, and enhanced durability for the ORR in acid, which correlated to the stabilizing effect against Pt oxidation/dissolution induced by electron transfer from the nitride support to Pt.[725] CrN was also reported to serve as a support for Pt NPs, and a Pt/CrN catalyst showed a higher ECSA of 82 m^2/g as compared to Pt/C (75 m^2/g), which led to a higher methanol oxidation activity and enhanced stability owing to the strong interaction between Pt and CrN.[726]

In addition to titanium nitrides and titanium carbonitrides, titanium carbides have also been reported as catalyst supports with high conductivity, high corrosion resistance, and robust electronic interactions with noble metal catalysts.[191] Recently, Dekel and coworkers prepared mixed carbides with Mo, Ta, and W to support PtRu for the HOR in alkaline media. *In situ* XANES spectra under HOR conditions (0.05 V vs RHE in 0.1 M KOH) showed a pronounced decrease in adsorption edge intensity for all carbide-supported PtRu with the most significant decay for PtRu/Mo_2C−TaC, relative to PtRu/C.[727] This indicates that TaC induces a larger degree of electron transfer from carbides to fill the Pt d-states than W_2C and Mo_2C and is consistent with the superior HOR activity of PtRu/Mo_2C−W_2C over three carbides in RDE measurements. To validate the feasibility of using carbide supports in AEMFCs, MEA measurements of a PtRu/Mo_2C−TaC anode, with a Pt/C cathode, showed a promising PPD of 1.2 W/cm^2 at 70 °C in H_2−O_2 mode (Figure 32C). However, it should be noted that both the anode and cathode had a very high PGM loading of 0.7 mg/cm^2. Whether the carbide will hinder the mass transport of reactants at lower Pt loading requires further investigation. PtRu/carbides demonstrated an enhanced durability relative to Pt/C in RDE measurements after 5000 potential cycles, which correlated to lower PtRu loss/detachment from supports relative to Pt/C. It remains an open question as to the durability of PtRu/carbides as the hydrogen anode in MEAs over long time periods. Carbide supports may also be sufficiently stable to serve as the oxygen cathode at oxidizing potentials in MEAs.

Another type of carbide that has been recently studied as a catalyst support for the alkaline ORR is tungsten carbide (WC).[728,729] Chen and coworkers used chronopotentiometric (CP) titrations to determine the electrochemical stability of the carbide electrocatalyst supports, WC, W_2C, and Mo_2C. The titration curves were conducted at current densities of 0 and 0.1 mA/cm^2, and the region in between those two current densities was defined as the passivation region, where the material could function without much risk of surface oxidation or dissolution. All three carbides have large regions of passivation at low pH values and narrow passivation regions in neutral and alkaline solutions, which indicates that the surface oxides of these three carbides are increasingly unstable at higher pH (Figure 32D).[728] WC exhibits enhanced resistance to surface oxidation in acidic solution and comparable stability in neutral/alkaline solution to Mo_2C and W_2C. The authors suggested that WC could stably operate in the potential range for the HOR while being unstable at oxidizing potentials during the ORR. The stability of Pt supported on WC for the ORR in alkaline media requires examination in RDE and MEA measurements.

Other electrocatalyst supports have ranged from simple materials such as pure metals to more complicated structures and stoichiometries. Liu and coworkers studied a Ag-modified nickel foam as a substrate for providing high conductivity and stability, reaching over 96% of its original activity after 10 h and improving the charge transfer rate of $Ru(OH)_x$/Ag/NF in alkaline water electrolyzers. The authors proposed that Ag doping contributed to the oxidation of Ru(III) to Ru(IV), which benefited the HER in alkaline media.[730] Duan et al. used CoAl layered double hydroxides as supports to stabilize Pd NPs for the alkaline ethanol oxidation, which was stabilized by the formation of Pd−OH bonds.[731] In a related study, hydroxyapatite (HAP), a calcium phosphate that is rich in surface hydroxyl groups, was studied as a catalyst support for Pd NPs for alkaline ethanol electrooxidation.[732] Layered metal oxides can serve as a high-surface-area oxidation-resistance support for fuel cell electrocatalysts.[733]

5.5. Summary

In summary, the basic requirements for a fuel cell catalyst support are high surface area, which promotes catalyst dispersion, porosity that facilitates gas flow and polymer electrolyte penetration, and high electrical conductivity and stability during operation. Carbon materials combine many of these properties. Their high surface area and porosity, conductivity, and the presence of active sites combined with their availability and cost make them very attractive among other support materials. Carbon black is the most commonly used material as a support for fuel cell applications. With the emergence of various carbon allotropes, new materials, such as carbon nanotubes and nanofibers, graphene, and carbon dots, have been studied for their electrochemical performance and their potential as catalysts supports. Their performance is also affected by structural properties, including the surface area and porosity, while the chemistry of their surfaces significantly affects their stability, since it modulates the degree of corrosion that takes place during fuel cell operation. Functionalization of carbon supports leads to the creation of oxygen-containing groups that transform the surface of carbon into a reactive form that allows the catalytic NPs to be immobilized on the active sites. In the quest of lowering the cost, researchers have turned their attention to the use of nonprecious electrocatalysts or the development of metal-free supports via heteroatom doping.

Beyond carbon, a broad family of materials, including conductive oxides, nitrides, and carbides, can provide improved catalyst stabilization and often higher activity for electrocatalytic reactions in both acidic and alkaline media. These materials also provide synergistic effects such as modulation of d-band filling and direct participation in bifunctional catalytic cycles. With metal oxides, the principal challenge is low electrical conductivity, relative to carbons. The best studied early transition metal oxides and nitrides (e.g., Ti oxides, nitrides, and oxynitrides) are susceptible to oxidation and loss of conductivity, especially in alkaline media where oxidation and dedoping occur at less positive potentials. However, the potential parameter space of conductive oxides,

https://doi.org/10.1021/acs.chemrev.1c00331
Chem. Rev. XXXX, XXX, XXX−XXX

Scheme 3. Observed Degradation Pathways for Quaternary Ammonium Cations: (A) S_N2 Attack at the Benzylic Position, (B) S_N2 Attack at the α-Position, (C) β-Hydrogen (Hofmann) Elimination, (D) S_N2 Attack at the α-Position of the Ring Causing Ring Opening, and (E) β-Hydrogen (Hofmann) Elimination on the Ring Causing Ring Opening

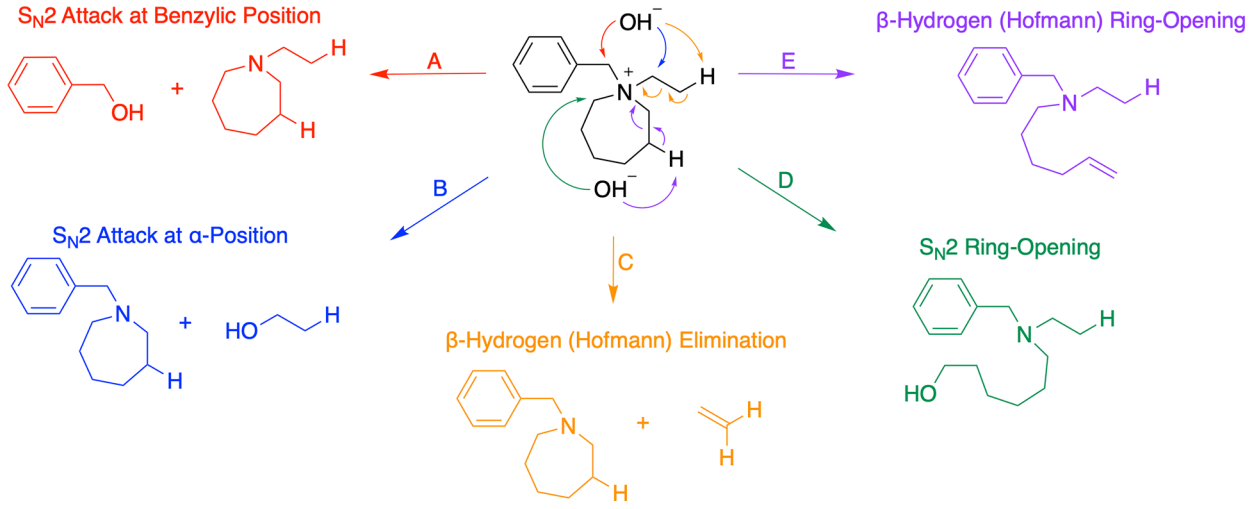

carbides, nitrides, and other materials is broad and still relatively unexplored and thus continues to hold promise for enhancing catalyst durability in alkaline fuel cells.

6. ALKALINE MEMBRANE/IONOMER DESIGN AND SYNTHESIS

Anion exchange membranes (AEMs) facilitate the flow of ions (OH^-) in alkaline/anion exchange membrane fuel cells (AEMFCs). Polymers bearing either pendant or main-chain cations can serve as the membrane in AEMFCs. The identity and concentration of cationic functionality and the polymer backbone itself impact initial performance, long-term durability, mechanical properties, and processability. Numerous studies on cation and backbone stability have improved the field's understanding of the degradation pathways that hinder successful AEM implementation in membrane electrode assemblies (MEAs) and have led to the development of more stable and mechanically robust AEMs. Here, we highlight recent innovations in hydrocarbon-based AEM materials with specific attention to cation and backbone stability. There are a number of literature reviews that focus on the cation stability and/or synthetic methodologies to achieve AEMs.[14,734−740] This section is meant to be a comprehensive look at cation stability and degradation mechanisms and present the best-in-class results from polymer membranes as a part of an even more comprehensive overview of the field. Below, the subsections are divided by choice of cation and backbone for the membrane. The cation stability subsection is focused on quaternary ammoniums, imidazoliums, and phosphoniums which have all shown promise as stable pendant cations in AEMs.[741−745] The membrane discussion highlights the design and synthesis of hydrocarbon-based AEMs that paved the way for achieving high-performance and durable AEMs under MEA operating conditions.

6.1. Cation Stability

The stability of the cation is critical for continuous hydroxide transport and needs to be addressed in parallel with backbone stability. Numerous cationic functionalities have been studied for use in AEMs that vary in both the charge carrying atom and type of substituents to enhance the interactive steric/electronic environment and promote charge delocalization. These primarily functionalities include, but are not limited to, imidazolium, phosphonium, ammonium, sulfonium, and metal-based cations. The main cationic degradation mechanisms that have been observed, nucleophilic substitution, β-hydrogen (Hofmann) elimination, nucleophilic addition, phosphine oxidation, and α-hydrogen abstraction, are depicted in Schemes 3−7.

A wide variety of experimental methodologies have been employed to study cation stability and degradation. Temperature, hydroxide concentration, solvent, and reaction vessel can all influence the cation degradation rate and mechanism; thus, varying these conditions from study to study makes for inconsistent results. For example, model compound studies on benzyltrimethylammonium (BTMA) conducted under a variety of conditions have shown conflicting outcomes. Many literature accounts show a low stability of BTMA in alkaline media[745] owing to the facile S_N2 attack at the benzylic position[746−748] (Scheme 3A), while other accounts claim that BTMA, in fact, is stable in alkaline media.[746,749] Discrepancies between literature reports are most likely due to the numerous experimental parameters making it challenging to objectively compare the stabilities of cations for AEMs across the field; thus, standardized conditions for cation stability experiments have been proposed.[745,749] Further details on the parameters of these studies and specific factors that influence cation stability are discussed in greater detail in section 6.1.5 with BTMA as a case study, but a brief summary of the effects of some of the parameters are given below.

6.1.1. Temperature. 60−100 °C is the target operating temperature range for AEMFCs for optimal reaction kinetics and CO_2 removal. Higher temperatures up to 160 °C[748] have been used to accelerate the degradation of cations. However, at higher temperatures, the predominant mechanism of degradation may change[748] rather than simply accelerating the degradation rate. This temperature-dependent behavior contributes to the range in degradation mechanisms reported for a particular cation. Potential changes in degradation mechanism as a function of temperature warrant more study to understand the exact effect of temperature on the degradation reactions observed for cations in alkaline solution.

https://doi.org/10.1021/acs.chemrev.1c00331
Chem. Rev. XXXX, XXX, XXX−XXX

Table 2. Quaternary Ammonium Stability Study Conditions and Results; Counteranions Omitted for Clarity

Entry	Name	Model Compound	Time (h)	Solvent	[OH] (M)	Temp (°C)	Cation Remaining (%)	Ref.
1	BTMA	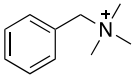	96	D_2O	2 M	80	100%	756
				CD_3OD/D_2O 3:1	2 M	80	85%	
				CD_3OD	2 M	80	49%	
2	BTMA	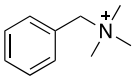	2000	H_2O	2 M	80	96%	749
3	BTMA	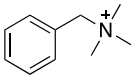	672	D_2O	0.24 M	60	100%	746
						120	87%	
4	QA5	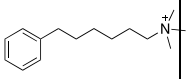	672	CD_3OD	0.24 M	90	66%	746
5	BTMA	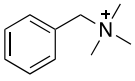	720	CD_3OH	1 M	80	11%	745, 747
					2 M	80	1%	
6	QA9	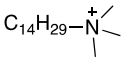	720	CD_3OH	1 M	80	94%	745, 747
					2M	80	89%	
7	BTMA	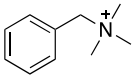	3	CD_3OD/D_2O 3:1	0.6 M (20 eqiv)	120	80%	760
8	QA4	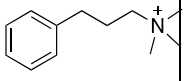	3	CD_3OD/D_2O 3:1	0.6 M (20 eqiv)	120	88%	760
9	QA11	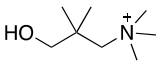	167	D_2O	1 M	88	95%	761
			~1000	D_2O	1 M	88	50%	
10	QA1	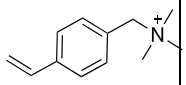	400	D_2O	1 M	80	50%	761
11	BTMA	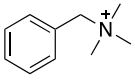	180	70 wt% CD_3OD/D_2O	3 M	80	50%	742
12	QA10	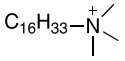	1420	70 wt% CD_3OD/D_2O	3 M	80	50%	742
13	QA6		2069	70 wt% CD_3OD/D_2O	3 M	80	50%	742
14	QA6		62	H_2O	6 M	160	50%	748
15	BTMA	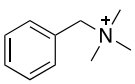	4	H_2O	6 M	160	50%	748

https://doi.org/10.1021/acs.chemrev.1c00331
Chem. Rev. XXXX, XXX, XXX−XXX

Table 2. continued

Entry	Name	Model Compound	Time (h)	Solvent	[OH] (M)	Temp (°C)	Cation Remaining (%)	Ref.
16	QA7		3	H_2O	6 M	160	50%	748
17	QA8	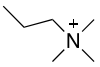	33	H_2O	6 M	160	50%	748
18	QA13	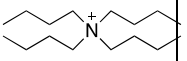	720	CD_3OH	2 M	80	94%	745, 747
19	QA12	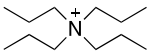	7	H_2O	6 M	160	50%	748
20	QA10	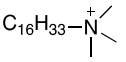	2	H_2O	6 M	160	50%	748
21	QA3	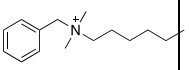	672	D_2O	0.24 M	120	78%	746
22	QA2	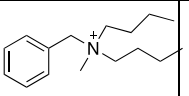	672	D_2O	0.24 M	120	91%	746
23	QA14		37	H_2O	6 M	160	50%	748
24	QA23	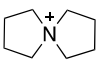	28	H_2O	6 M	160	50%	748
25	QA15		96	D_2O	2 M	80	100%	756
				CD_3OD	2 M	80	77%	
26	QA15		720	CD_3OH	1 M	80	32%	745, 747
27	QA24	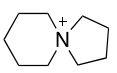	720	CD_3OH	1 M	80	73%	747
28	QA17	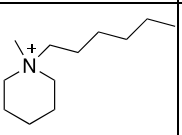	720	CD_3OH	1 M	80	97%	745, 747
29	QA16	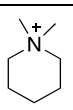	87	H_2O	6 M	160	50%	748
30	QA25	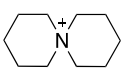	720	CD_3OH	1 M	80	98%	747
31	QA25	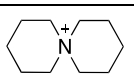	110	H_2O	6 M	160	50%	748
32	QA27	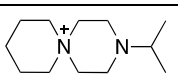	720	CD_3OH	1 M	80	92%	747
33	QA26	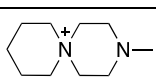	720	CD_3OH	1 M	80	83%	747

https://doi.org/10.1021/acs.chemrev.1c00331
Chem. Rev. XXXX, XXX, XXX−XXX

Table 2. continued

Entry	Name	Model Compound	Time (h)	Solvent	[OH] (M)	Temp (°C)	Cation Remaining (%)	Ref.
34	QA28	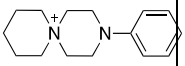	720	CD_3OH	1 M	80	29%	747
35	QA19	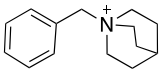	720	CD_3OH	1 M	80	67%	745, 747
36	QA20	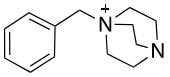	720	CD_3OH	1 M	80	5%	745, 747
37	QA20	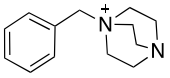	1	H_2O	6 M	160	50%	748
38	QA21	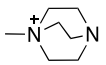	14	H_2O	6 M	160	50%	748
39	QA20	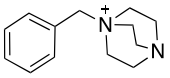	672	D_2O	0.24 M	60	100%	746
						120	91%	
40	QA18	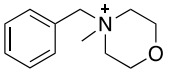	720	CD_3OH	1 M	80	<1%	745, 747

However, when considering cation degradation in AEMFCs, the temperature for the study should be within the operating range for AEMFCs to ensure that the study is an accurate representation of the system.

6.1.2. Hydroxide Concentration. Hydroxide concentrations ranging from 0.25 to 6 M have been used to examine the stability of organic cations at fuel cell operating temperatures (Tables 2−5). The concentration of hydroxide in solution can influence cation solubility, degradation rate, and degradation mechanism. In some systems, a lower hydroxide concentration is favorable for the solubility of organic cations,[746] while higher hydroxide concentrations can lead to insolubility and impact both the observed degradation rate and mechanism. A higher hydroxide concentration can accelerate the rate of degradation of the cations affording a reduced time for experiments. However, degradation reactions that are second order or higher in hydroxide may be favored at an increased hydroxide concentration, thus altering the degradation mechanism. Coates and coworkers demonstrated this in imidazolium-based cations where switching from 2 to 5 M KOH changed the observed degradation products[750] due to a change in degradation mechanism.

6.1.3. Solvent. Solvent−cation compatibility is pertinent to both the observed degradation mechanism and rate. Different chemical environments arise from partial solubility or insolubility which significantly impacts the observed degradation rate and potentially the mechanism of degradation. Methanol is primarily used to ensure organic cation solubility due to its compatibility with a variety of cationic systems.[745] However, methanol produces harsher alkaline conditions because of its lower dielectric constant (ε) compared to water (ε = 33 and 80, respectively). A lower dielectric constant lessens the solvation of the ions and leads to higher reactivity between the methoxide/hydroxide ions and the cationic functionality, thus influencing the observed cation degradation rate. Additionally, the methoxide anion is more nucleophilic than the hydroxide present in aqueous alkaline conditions which further contributes to differences in observed degradation rates. If deuterated solvents with labile protons such as D_2O and CD_3OD are used, then deuterium exchange with the cation can convolute the quantification of degradation.[745,749] The use of CD_3OH can mitigate this issue[745] but does not resolve the difference in observed degradation rate and mechanism associated with using methanol as a solvent for these experiments.

6.1.4. Reaction Vessel. The vessel used to perform the stability study can interfere with the observed degradation rate and mechanism from the cation interacting with the vessel itself, uneven heating, and escape of volatile degradation products. When a glass vessel is used, hydroxide can etch the glass, thus lowering the pH of the solution and yielding an artificially higher stability.[749] Teflon, fluorinated ethylene-propylene (FEP), and polypropylene containers and liners can be used to avoid etching, but absorption of the degradation products has been observed in FEP liners, which can convolute the analysis of the degradation mechanism.[751] Uneven heating can lead to the sample temperature being lower than intended and influence the degradation rate.[749] Volatile degradation products can be lost if the container used for the stability study is not sealed or if the solution is transferred between containers before characterization, resulting in misleading analyses. Using sealed nuclear magnetic resonance (NMR) tubes can ensure that all degradation products are retained.[745]

It is important to keep these factors in mind when comparing results across studies. Herein, we summarize the alkaline stabilities of the most commonly studied classes of cations, quaternary ammoniums, imidazoliums, and phosphoniums, in various media at elevated pH and temperature, and

https://doi.org/10.1021/acs.chemrev.1c00331
Chem. Rev. XXXX, XXX, XXX−XXX

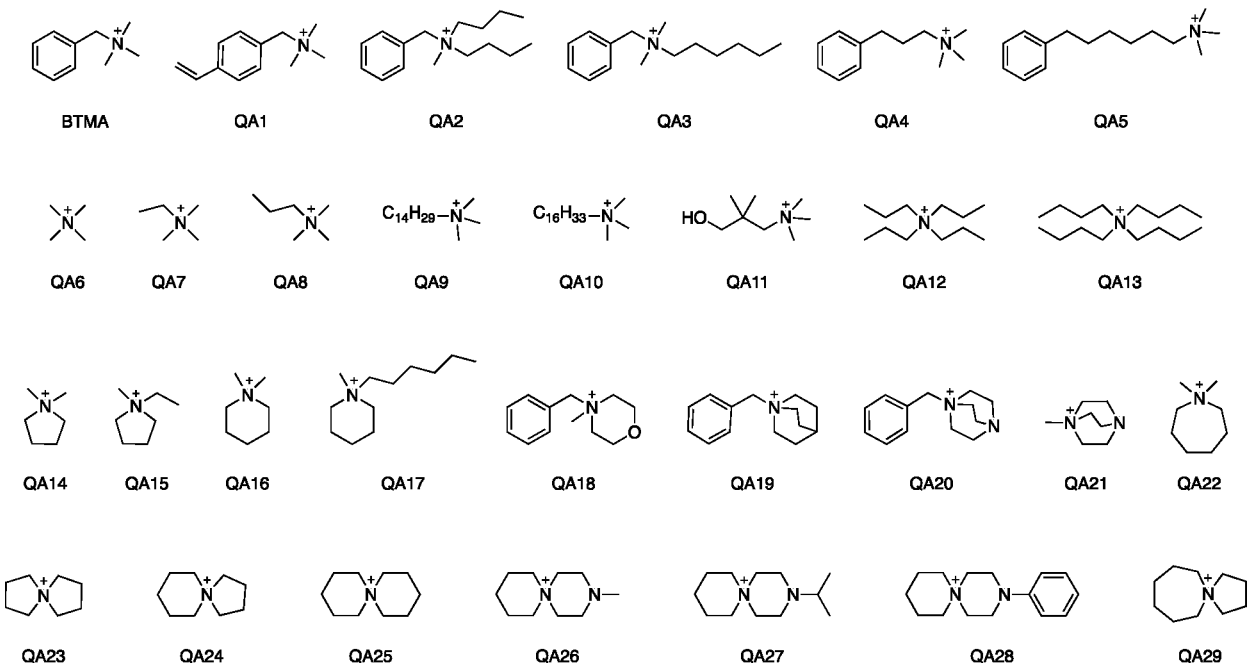

Figure 33. Naming scheme for quaternary ammoniums (QAs) discussed herein, counteranions omitted for clarity.

highlight the predominant mechanisms leading to their degradation.

6.1.5. Quaternary Ammonium Cations. Quaternary ammoniums (see Figure 33) are the most commonly implemented cations in AEMs as they are easily appended to membranes either through postpolymerization functionalization or via the direct polymerization of quaternary ammonium-functionalized monomers. However, ammoniums are susceptible to several degradation mechanisms with the favored pathway depending on the substituents. For example, membranes with trimethylammonium (TMA) cations appended using an alkyl linker predominantly degrade by S_N2 demethylation (Scheme 3B) whereas the primary degradation mechanism for trimethylammonium cations appended in a benzylic position (e.g., BTMA) is S_N2 attack at the benzylic carbon (Scheme 3A).[746−749] Additionally, quaternary ammonium cations with substituents containing hydrogens beta to the nitrogen are susceptible to Hofmann elimination (Scheme 3C) which competes with S_N2 attack on the alkyl substituent (Scheme 3B).[746−748] Similarly, cyclic ammoniums can undergo S_N2 attack at the α-carbon with respect to the nitrogen atom or Hofmann elimination, both leading to ring opening (Scheme 3D,E, respectively).[747,752−755] There have been numerous studies directed at understanding and improving the stability of quaternary ammoniums by identifying and mitigating the effects of these degradation pathways, many of which are discussed herein.

6.1.5.1. Benzyl Substituent Stability. BTMA is the stability standard to which most cations are compared.[741−743,745−748,750,756−759] However, studies of BTMA alkaline stability have been reported utilizing an array of conditions which, in turn, produces vast variability in the reported BTMA stabilities. Solvent choice influences the degradation rate and thus is one of the main contributing factors to varying results. Yan and coworkers demonstrated the effect of differing CD_3OD:D_2O ratios on the percent degradation of cations in alkaline media.[756] For example, in their study of BTMA in 2 M KOH/D_2O, no degradation was observed after 96 h at 80 °C, but when 3:1 CD_3OD:D_2O or CD_3OD was used as the solvents, BTMA had 85% and 49% cation remaining, respectively (Table 2, entry 1), indicating that CD_3OD facilitates the degradation of BTMA more than D_2O, as the basic species and cation solvation have changed.

In an attempt to standardize the conditions under which BTMA stability is studied, Pivovar and coworkers established a procedure to obtain reliable stability data for BTMA in alkaline media.[749] The procedure employs Teflon-lined Parr reactors placed in an oven and the use of an internal standard sealed in a capillary when acquiring NMR spectra of the resulting solutions. The use of Teflon liners prevents hydroxide etching of glass containers, as the production of silicates can lower the pH of the solution. The Parr reactors were placed in the oven to avoid reflux in the headspace of the reaction vessel. The sealed capillary with the internal standard prevents the hydroxide from degrading the internal standard. Low concentrations of BTMA (0.1 M) ensure solubility in 2 M aqueous KOH. This was necessary to prevent deuterium exchange and retain a similar solvent polarity present in AEM operating conditions. With these potential sources of error eliminated, BTMA showed great stability with 96% cation remaining after 2000 h at 80 °C in 2 M KOH (Table 2, entry 2).

Mohanty and Bae compared the alkaline stability of 11 ammonium cations against BTMA, all but one of them having a benzylic connection. Using Ag_2O in D_2O, the halide counterion was exchanged with OD^- so that cation degradation could be monitored by ^1H NMR.[746] The study was performed in D_2O to maintain solvent polarity and mimic the conditions present during AEM operation, similar to Pivovar's use of H_2O.[749] Instead of using a low cation concentration, quantitative exchange to the hydroxide form was used to retain the solubility of BTMA in water, as the cations were not soluble in highly concentrated hydroxide solutions. After heating at 60 °C or 120 °C in D_2O for 672 h, the degradation products were extracted into $CDCl_3$ and analyzed by NMR and gas chromatography−mass spectrom-

https://doi.org/10.1021/acs.chemrev.1c00331
Chem. Rev. XXXX, XXX, XXX−XXX

etry (GC−MS) to determine the degradation pathways. The investigation revealed that 87% of the BTMA cation remained (Table 2, entry 3) with nucleophilic attack at the benzylic position (Scheme 3A) as the only observed degradation pathway.

While these studies imply that BTMA has sufficient stability for implementation in AEMs, Mohanty and Bae showed that there are more stable ammonium alternatives.[746] The model ammonium compound without benzylic substituents (QA2) was the most stable, requiring harsher conditions to detect any degradation byproducts. QA2 showed 66% cation retention in 2 M NaOD/CD_3OD at 90 °C (Table 2, entry 4) with degradation occurring primarily by Hofmann elimination (Scheme 3C).

The increased stability of alkyl-substituted ammonium cations was further supported by alkaline stability studies performed by the Coates group using a standardized protocol that they proposed could be used to obtain comparable cation stability results across the field.[745] The percent cation remaining was quantified for a variety of cations after 720 h in 1 and 2 M KOH/CD_3OH at 80 °C in sealed NMR tubes. The use of excess hydroxide in CD_3OH ensures no interference in determining cation stability by hydrogen−deuterium exchange, and the sealed NMR tube ensures that volatile degradation products are not lost. Using these conditions, only 11% of the BTMA cation remained (Table 2, entry 5), with nucleophilic substitution at the benzylic position (Scheme 3A) as the major degradation pathway (67%), and nucleophilic substitution at the methyl position (Scheme 3B) as the minor degradation pathway (22%).[747] Replacing the benzylic substituent with an aliphatic group (QA9) boosted cation retention to 94% (Table 2, entry 6). The improved stability is attributed to the elimination of nucleophilic displacement of the benzylic substituent (Scheme 3A) as it is a far more facile reaction than demethylation (Scheme 3B) or Hofmann elimination (Scheme 3C), which are the potential degradation pathways for the alkyl-TMAs.

Many studies report that all alkyl ammoniums show higher stability than BTMA, but the extent to which the stability improves depends greatly on the conditions used for the study. Hickner and coworkers report 80% of BTMA remaining in 0.6 M NaOD/(3:1 CD_3OD:D_2O) at 120 °C after 3 h[760] (Table 2, entry 7). With the addition of a three-carbon spacer between the ammonium and the benzyl group (QA4), the percent cation remaining increased to 88% under the same conditions (Table 2, entry 8). S_N2 at the benzylic position (Scheme 3A) and at the alkyl substituents (Scheme 3B) were the predominant degradation pathways observed. Beyer and coworkers found alkyl-substituted ammoniums (QA11) to be more stable than those with benzylic substituents (QA1) when in 1 M NaOD/D_2O at 80 °C (88 °C for QA11), resulting in half-lives of ∼1000 and ∼400 h, respectively[761] (Table 2, entries 9 and 10). Holdcroft and coworkers also found increased stability in alkyl-substituted ammoniums when studied in 3 M NaOD in 70 wt % CD_3OD/D_2O at 80 °C; half-lives of BTMA, QA10, and QA6 were measured to be 180, 1420, and 2069 h, respectively[742] (Table 2, entries 11−13). Additionally, Marino and Kreuer implemented a high hydroxide concentration (6 M NaOH/H_2O) and temperature (160 °C) to measure the half-lives of 26 ammonium cations.[748] In agreement with Holdcroft, methyl substituents were found to have greater stability than benzylic substituents, with half-lives of 62 and 4 h measured for QA6 and BTMA, respectively (Table 2, entries 14 and 15). While there is disagreement on the stability of BTMA, it has been shown that, for longer-term stability, benzylic connections should be avoided to prevent S_N2 attack at the benzylic position (Scheme 3A).

6.1.5.2. Linear-Alkyl Substituent Stability. Implementing linear-alkyl-substituted ammoniums eliminates the benzylic position that is susceptible to S_N2 attack (Scheme 3A), leaving S_N2 attack at the α-carbon (Scheme 3B) and β-hydrogen (Hofmann) elimination (Scheme 3C) as the major degradation pathways for tetraalkylammoniums. The *N*-alkyl substituent chain length determines the ammonium's major degradation pathway. While the α-position of longer *N*-alkyl chains can potentially undergo nucleophilic attack, this degradation pathway is less common due to increased steric hindrance. For longer *N*-alkyl-substituted ammoniums, Hofmann elimination (Scheme 3C) becomes the major degradation pathway. Ethyl and isopropyl groups are especially prone to Hofmann elimination[746−748] because they have three and six β-hydrogens, respectively, that are able to freely rotate into an antiperiplanar position relative to the nitrogen. Furthermore, these groups have no steric protection from hydroxide ions, and Hofmann elimination (Scheme 3C) can occur readily.[747,748,762] The preference for Hofmann elimination (Scheme 3C) on ethyl groups as compared to *n*-propyl groups was demonstrated in a stability study on QA7 and QA8 by Marino and Kreuer, yielding half-lives of 3 and 33 h, respectively, in 6 M NaOH(aq) at 160 °C[748] (Table 2, entries 16 and 17, respectively). The additional methylene unit on QA8 reduces the extent of Hofmann elimination (Scheme 3C), thus showing that ethyl and isopropyl groups should be avoided when choosing substituents for ammonium cations.

For *N*-methyl substituents, S_N2 attack on the α-carbon (Scheme 3B) is the sole degradation pathway and is more favorable than in longer alkyl chains as the methyl is easily accessible to nucleophilic attack by hydroxide ions. When Coates and coworkers studied the stability of QA9 in 1 and 2 M KOH/CD_3OH at 80 °C, 94% and 89% cation remained,[745,747] respectively (Table 2, entry 6); after 720 h of the 11% cation degradation observed using the 2 M KOH conditions, 9% was attributed to demethylation (Scheme 3B), and 2% was attributed to Hofmann elimination (Scheme 3C) on the long alkyl chains.

Exchanging the methyl groups and long alkyl chains for *n*-butyl groups (QA13) results in improved ammonium stability with 96% and 94% cation remaining after 720 h in 1 and 2 M KOH/CD_3OH at 80 °C,[747] respectively (Table 2, entry 18). This suggests that alkaline stability increased because nucleophilic attack (Scheme 3B) is blocked by the butyl substituents. Hofmann elimination (Scheme 3C) on the butyl groups was the only observed degradation pathway. Conversely, Marino and Kreuer observed decreased cation stability with an increasing number of *n*-propyl substituents.[748] The half-lives of QA6, QA8, and QA12 were 62, 33, and 7 h, respectively, when degradation experiments were performed in 6 M NaOH(aq) at 160 °C (Table 2, entries 14, 16, and 19, respectively). Although these results suggest a trend opposite to the Coates study where they compared QA9 to QA13, a long-chain TMA should be compared to QA12 to ensure a fair comparison of results. QA10 exhibited a half-life of 2 h in 6 M NaOH(aq) at 160 °C (Table 2, entry 20), lower than the 7 h half-life observed for QA12, suggesting that QA12 is more stable than QA10. This finding aligns with trends observed in the Coates study, both showing that all medium-length alkyl

https://doi.org/10.1021/acs.chemrev.1c00331
Chem. Rev. XXXX, XXX, XXX−XXX

substituents produce higher stabilities than long-chain alkyl-TMAs. It is thought that these long-chain TMAs can form micelles in alkaline solution and thus reduce the stability of the ammonium by affecting local hydroxide concentrations and reaction rates.[748] The half-lives of alkyl-TMAs as a function of chain length from the Marino and Kreuer study are depicted in Figure 34, demonstrating the nonlinear relationship between alkyl chain length and ammonium cation stability.

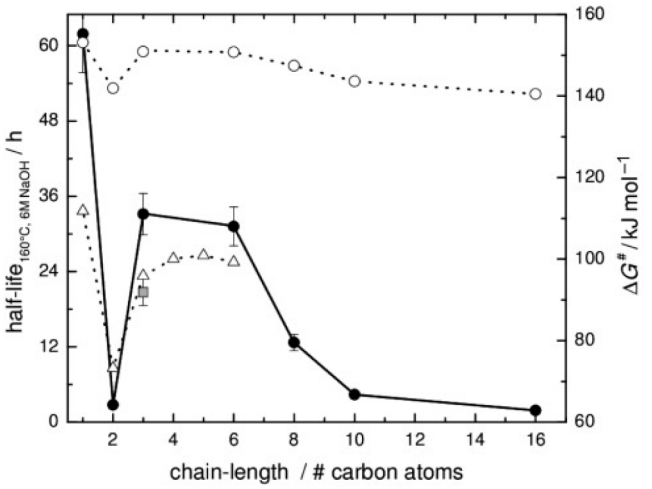

Figure 34. Half-life of alkyl-TMA cations of varying alkyl chain length in 6 M NaOH at 160 °C (●) and a neopentyl chain under the same conditions (■). Corresponding reaction free-energy barrier $\Delta G^{\#}$ data (○) was calculated using the Eyring equation.[748] DFT data by Long et al.[763] (△) follows the same qualitative trend, but absolute values differ by about 50 kJ/mol. Adapted with permission from ref 748. Copyright 2015 Wiley.

Mohanty and Bae have also demonstrated the trend that a long-chain substituent (hexyl group, QA3) lowers the stability of the ammonium compared to multiple butyl substituents (QA2) or methyl substituents (BTMA) with 78%, 91%, and 87% cation remaining, respectively, after 672 h in stoichiometric OD^-/D_2O at 120 °C (Table 2, entries 21, 22, and 3).[746] They found that butyl-substituted ammoniums were slightly more stable than ammoniums substituted with methyl groups, opposing the findings by Marino and Kreuer.[748] However, Mohanty and Bae studied ammoniums with a benzyl substituent, which degrade primarily by benzylic substitution (Scheme 3A), meaning that their study mostly informed on the effects of methyl, butyl, and hexyl groups on the rate of benzylic substitution (Scheme 3A). Marino and Kreuer studied alkyl substituents that degrade solely via nucleophilic substitution on the α-carbon (Scheme 3B) and Hofmann elimination (Scheme 3C).[748] From this, we can conclude that it is important to consider all substituents when analyzing ammonium cation stability as substituents influence the major degradation pathway and can play a major role in the discrepancies between the degradation studies.

Overall, it has been found that ammonium cation stability decreases as follows: tetramethylammonium (QA6) > tetraalkylammoniums with medium-length alkyl chain substituents > TMAs with long alkyl chain substituents. However, long alkyl chain substituents likely simulate TMA's local environment when tethered to a polymer better than free tetramethylammonium. Based on this, a tributylammonium tethered to a polymer may be more stable than TMA on a polymer, though the butyl chains can still degrade by Hofmann elimination (Scheme 3C).

6.1.5.3. Cyclic Substituent Stability. As Hofmann elimination requires an antiperiplanar configuration between the nitrogen and a β-hydrogen, the extent of Hofmann elimination can be reduced by implementing cyclic ammonium functionalities. A cyclic structure can restrict the formation of an antiperiplanar configuration between the nitrogen and β-hydrogen. The bond angles produced in the transition state required for elimination can further induce significant ring strain (Figure 35) and, thus, disfavor degradation by ring-opening elimination (Scheme 3E).[748] While Hofmann elimination can be reduced or eliminated as a degradation pathway in cyclic ammonium cations, the increased strain in some rings, such as in bridged bicyclic structures, increases degradation via nucleophilic ring opening. (Scheme 3D).[746−748]

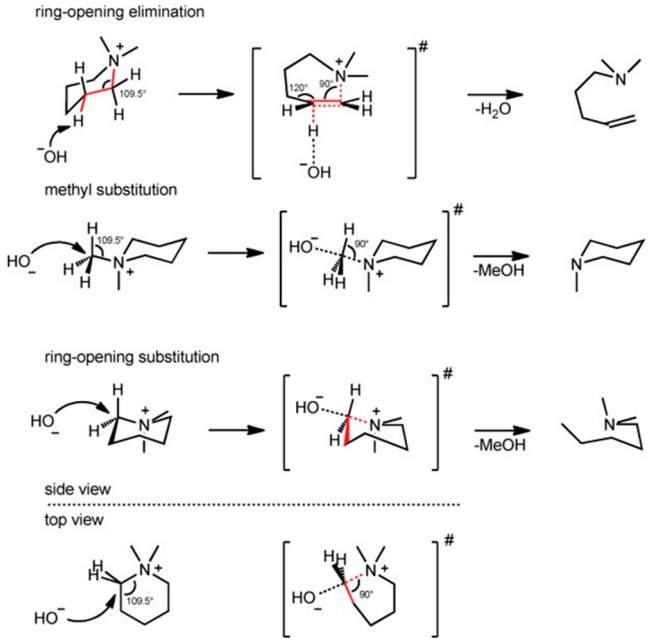

Figure 35. Depiction of preferred bond angles for ring-opening elimination and nucleophilic substitution of QA16.[748] Adapted with permission from ref 748. Copyright 2015 Wiley.

Five-Membered Rings. Pyrrolidinium cations (QA14 and QA15) and spirocyclic ammoniums containing five-membered rings such as QA23 and QA24 degrade by ring-opening substitution at the α-position[747,748,764] (Scheme 3D), as it is thermodynamically favorable to relieve ring strain. However, ring opening by Hofmann elimination (Scheme 3E) is blocked due to the inability of the β-hydrogens to form an antiperiplanar configuration.[748] In a study by Marino and Kreuer, QA14 (Table 2, entry 23) and QA23 (Table 2, entry 24) displayed half-lives of 37 and 28 h, respectively, when subjected to 6 M NaOH(aq) at 160 °C:[748] a marked reduction in stability compared to the QA6 analogue with a half-life of 62 h. The increased degradation rates can be attributed to the replacement of methyl groups with five-membered rings, which are more prone to decomposition by nucleophilic attack than methyl groups. Conversely, Jannasch and coworkers observed a greater degree of cation degradation in polyelectrolytes containing QA14 than those with QA23 with NMR results

https://doi.org/10.1021/acs.chemrev.1c00331
Chem. Rev. XXXX, XXX, XXX−XXX

suggesting that demethylation (Scheme 3B) occurs at a higher rate than nucleophilic ring opening (Scheme 3D).[764]

When comparing the degradation rates of QA15 in a range of solvents, Yan and coworkers found that 100% cation was remaining after 96 h in 2 M KOH/D_2O at 80 °C, yet only 77% cation was remaining when CD_3OD was used (Table 2, entry 25), demonstrating the effects of solvent on degradation rate.[756] In studies by Coates and coworkers, 32% of QA15 remained after 720 h in 1 M KOH/CD_3OH at 80 °C[745,747] (Table 2, entry 26). Although it was expected that Hofmann elimination would be the major degradation product, it was observed that 37% of the degradation occurred by S_N2 ring opening (Scheme 3D) with 31% by Hofmann elimination on the ethyl group (Scheme 3C). The nearly equal contribution of ring-opening substitution (Scheme 3D) and Hofmann elimination on the ethyl group (Scheme 3C) may be partly due to the nucleophilicity of methoxide, but it emphasizes the vulnerability of five-membered rings to ring-opening substitution (Scheme 3D) and lends credit to the exploration of other cyclic systems. Under the same conditions, QA24 (Table 2, entry 27) had 73% cation remaining after 720 h with all of the observed degradation due to ring-opening substitution (Scheme 3D) on the pyrrolidinium ring, leaving the six-membered piperidinium ring intact,[747] suggesting that piperidiniums are a far more stable cyclic cation.

Six-Membered Rings. Six-membered rings, such as piperidiniums (QA16 and QA17), have lower ring strains making nucleophilic ring opening unfavorable and are rigid enough to lessen the extent to which the ring can achieve the bond angles required for Hofmann elimination.[748] Thus, piperidiniums show greater stability under accelerated degradation conditions as compared to pyrrolidiniums; after 720 h at 80 °C in 1 and 2 M KOH/CD_3OH, QA17 had 97% and 94% cation remaining,[745,747] respectively (Table 2, entry 28). Marino and Kreuer also observed an enhanced stability when employing piperidinium functionalities; they found that QA16 had a half-life of 87 h in 160 °C, 6 M NaOH(aq) (Table 2, entry 29), an improvement over QA6 which has a half-life of 62 h[748] (Table 2, entry 14). In both cases, the primary degradation mechanism was demethylation (Scheme 3B), although Hofmann elimination (Scheme 3E) was also observed as a minor contributor to the overall degradation of QA16.[747,748]

To further incorporate cyclic structures into ammonium cations, the alkyl groups on the piperidinium can be replaced with another six-membered ring, giving QA25. This substitution further improves stability, affording 98% and 96% cation remaining after 720 h in 1 and 2 M KOH/CD_3OH at 80 °C, respectively (Table 2, entry 30), with Hofmann elimination on the ring as the exclusive degradation product[747] (Scheme 3E). Marino and Kreuer also observed an improved stability in QA25 compared to QA16 with half-lives of 110 and 87 h, respectively, at 160 °C in 6 M NaOH(aq)[748] (Table 2, entries 31 and 29, respectively). Under these conditions, QA25 was found to degrade by ring opening at the α-position (Scheme 3D). Substitution at the α-position occurred at a slower rate than the demethylation of QA16, indicating that the extents of elimination and substitution are both greatly reduced in piperidiniums as compared to linear-alkyl substituents. They propose that the unfavorable bond angles and lengths required for elimination or substitution on six-membered rings (demonstrated in Figure 35) give rise to the enhanced stability despite the presence of hydrogens antiperiplanar to the nitrogen in the piperidinium and spirocyclic compounds.[748]

While the model compound studies suggest that QA25 is more stable than QA16, Jannasch and coworkers showed that the trend reverses when the cations are appended to a poly(terphenylene alkylene) backbone.[753] While QA25 still showed good stability, they observed 10% and 27% cation loss after 720 and 2900 h, respectively, when the membrane was allowed to soak in 2 M NaOH(aq) at 90 °C. They attributed the cation loss to Hofmann elimination on the rings (Scheme 3E). They also studied the stability of a poly(terphenylene alkylene) backbone substituted with QA16 instead of QA25, which showed less than 5% and 13% cation degradation after 720 and 2900 h, respectively, when subjected to the same conditions. It was reported that Hofmann elimination (Scheme 3E) was responsible for 7% of the QA16 degradation after 2900 h, while the remaining 6% degradation is thought to be due to demethylation (Scheme 3B). They attribute this trend to the increased degree of bond angle distortion within QA25 as compared to QA16 when attached to a rigid polymer backbone. When QA25 and QA16 are tethered to PS with a triazole linker, QA25 exhibits a higher stability with no degradation detected after 3000 h in 1 M NaOH CD_3OD/D_2O at 80 °C while the QA16 equivalent showed signs of demethylation after 144 h under the same conditions,[765] thus supporting that direct attachment of the ammonium cation to the rigid backbone caused the destabilization of QA25. However, when an isopropylidene spacer was implemented to link QA16 or QA25 to a PS backbone, QA16 had a slightly higher stability than QA25, yet the overall stability of both cations was greater than when the cations were linked directly to the rigid poly(terphenylene alkylene) backbones.[752] Overall, it can be determined that while model cation stabilities are helpful in determining promising cation candidates, such as QA16 and QA25, the polymer backbone and method of linking can further complicate the stability trends.

Introducing additional heteroatoms into the six-membered ring was thought to improve conductivity and stability due to the increased hydrophilicity of the ammonium cation. However, piperazine-based spirocycles demonstrated a lower stability than QA25 (Table 2, entry 30) with the degree of degradation depending on the substituent of the tertiary amine. QA25 and all three spiropiperaziniums (QA26, QA27, and QA28) degrade via Hofmann elimination (Scheme 3E),[747] as the additional nitrogen in the ring promoted elimination of the adjacent β-hydrogens. However, the increased steric bulk of *i*-Pr-spiropiperazinium (QA27) suppressed cation degradation relative to Me-spiropiperizinium (QA26) or Ph-spiropiperizinium (QA28) (Table 2, entries 32−34).

A similar decrease in stability is also observed when additional heteroatoms are implemented in bridged bicyclic ammoniums. Quinuclidinium, a bridged bicyclic ammonium, is quite stable even with a benzyl substituent as 67% QA19 remained after 720 h in 1 M KOH/CD_3OH at 80 °C[745,747] (Table 2, entry 35). For comparison, only 11% BTMA remained under the same conditions. The major degradation pathways observed for QA19 were nucleophilic ring opening (Scheme 3D) (18%) and nucleophilic attack at the benzylic position (Scheme 3A) (14%). An additional nitrogen group in the bridged bicyclic system gives the DABCO-based cation: QA20, which only had 5% cation remaining (Table 2, entry 36) due to a drastic increase in nucleophilic ring opening (Scheme 3D) (64%) and nucleophilic attack at the benzylic

https://doi.org/10.1021/acs.chemrev.1c00331
Chem. Rev. XXXX, XXX, XXX−XXX

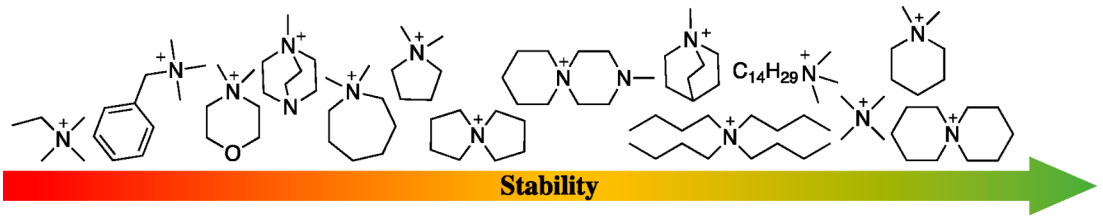

Figure 36. Approximate ranking of quaternary ammonium stability in alkaline conditions from low (red) to high (green). Results vary depending on test conditions used; counteranions omitted for clarity.

position (Scheme 3A) (31%).[745,747] Marino and Kreuer also found low alkaline stabilities for QA20 and QA21 with half-lives of 1 and 14 h, respectively, in 6 M NaOH(aq) at 160 °C (Table 2, entries 37 and 38), as compared to 4 h for BTMA and 62 h for QA6 under the same conditions[748] (Table 2, entries 14 and 15). Conversely, Mohanty and Bae found that QA20 has stability comparable to BTMA with both having 100% and >85% cation remaining after 672 h in quantitative OD^-/D_2O at 60 °C and 120 °C, respectively (Table 2, entry 39).[746] These studies demonstrate that the 1,4-diazabicyclo[2.2.2]octane (DABCO) functionality lowers the alkaline stability when compared to their trimethylammonium counterparts.

The inductive effects of oxygen in the morpholine ring make morpholinium cations more prone to nucleophilic ring-opening (Scheme 3D) and Hofmann elimination on the ring (Scheme 3E).[747,755,764] Benzyl-substituted morpholinium (QA18) was less stable than BTMA, with <1% QA18 and 11% BTMA remaining after 720 h in 1 M KOH/CD_3OH at 80 °C[745,747] (Table 2, entry 40). In studies by Jannasch, morpholinium-functionalized AEMs demonstrated the highest extents of cation degradation,[755,764] with nucleophilic ring opening (Scheme 3D) and Hofmann ring-opening (Scheme 3E) occurring at similar rates.[764] In their study, the AEM substituted with azepaniums demonstrated a similar degree of Hofmann ring opening (Scheme 3E) as the morpholiniums but a higher overall stability.[764] Cations derived from seven-membered rings such as azepaniums (QA22 and QA29) are more flexible than six-membered rings and can orient into a more favorable position for Hofmann elimination[755] (Scheme 3E) without inducing as much ring strain as in the pyrrolidinium and piperidinium cases.

6.1.5.4. Conclusion—Quaternary Ammonium Cations. Overall, it is very challenging to definitively rank the stabilities of quaternary ammonium cations based upon differences in substitution on the quaternary ammonium, as reaction conditions used to study them can influence the results of the stability studies. Therefore, an approximate ranking of the different classes of quaternary ammoniums is shown in Figure 36. Ethyl substitution leads to low alkaline stability as the freely rotating β-hydrogens are particularly susceptible to degradation by Hofmann elimination (Scheme 3C). Benzyl substituents are more prone to cleavage by S_N2 attack (Scheme 3A) than alkyl substituents (Scheme 3B) and should therefore be avoided for long-term stability. Rings with high ring strain such as in pyrrolidinium, DABCO, and quinuclidinium can be susceptible to nucleophilic ring opening (Scheme 3D), while highly flexible rings such as azepanium are susceptible to Hofmann ring opening (Scheme 3E). Additional heteroatoms in the rings (morpholinium, DABCO, spiropiperazines) reduce the stability of the cation by promoting nucleophilic and Hofmann ring opening (Scheme 3D,E, respectively). Tetramethylammonium and alkyl-trimethylammoniums have relatively high stability with demethylation (Scheme 3B) and, if β-hydrogens are present, Hofmann elimination (Scheme 3C) as possible degradation pathways. Medium−long alkyl chains, piperidinium, and QA25 show a higher alkaline stability with minimal Hofmann elimination as the main degradation product (Scheme 3C,E). Systematic studies where substituents are varied one by one and the conditions are held constant are incredibly important for determining which cations are best suited for use in AEMs.

6.1.6. Imidazolium Cations. Unsubstituted imidazolium cations have been shown to be unstable when employed in AEMs[757,766−768] due to their tendency to degrade via S_N2 attack at the C2 position leading to ring-opening with subsequent enamine and amide hydrolysis resulting in carboxylic acid and amine products[747,751] (Scheme 4A).

Scheme 4. Observed Degradation Pathways for Imidazolium Cations: (A) Nucleophilic at the C2-Position, (B) S_N2 Attack at the *N*-Benzyl Position, and (C) S_N2 Attack at the α-Position of *N*-Alkyl Substituents

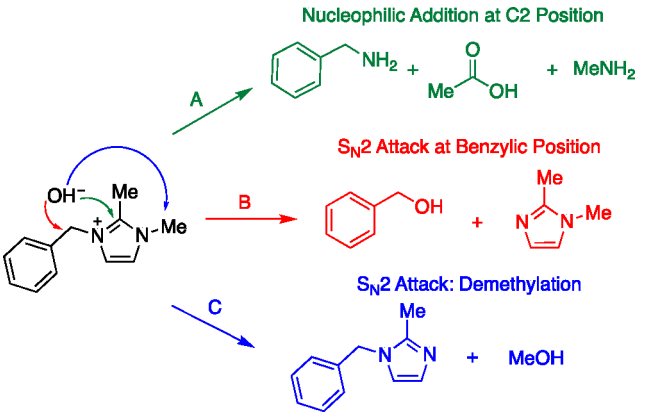

Another prominent degradation mechanism is the attack of N1/N3 substituents to yield neutral imidazoles (Scheme 4B,C). In addition, the multiple acidic hydrogens on the imidazolium ring are subject to reversible deprotonation (Scheme 5). This has been shown through rapid deuterium exchange observed for hydrogens at the C2 position (Scheme 5A), at the α-position of C2 (Scheme 5B), N1/N3 substituents (Scheme 5C), and the C4/C5 positions[745,750,761,766,767,769−771] (Scheme 5D). These reversible deprotonations can lead to stabilization of the imidazolium ring,[761] while also leading to degradation by rearrangement and subsequent reactions.[750] Degradation by these pathways can be mitigated with substitution at the C2, N1/N3, and C4/C5 positions, and as such, systematic studies of substituent effects on stability have transformed imidazoliums from one of the least to one of the

https://doi.org/10.1021/acs.chemrev.1c00331
Chem. Rev. XXXX, XXX, XXX−XXX

Scheme 5. Observed Deprotonations of Acidic Hydrogens on Imidazolium Cations, Where Rearrangements or Subsequent Reactions Can Result in Cation Degradation: (A, B) Deprotonation at the C2-Position, (C) Deprotonation of the α-Position of *N*-Substituents, and (D) Deprotonation at the C4/C5-Positions

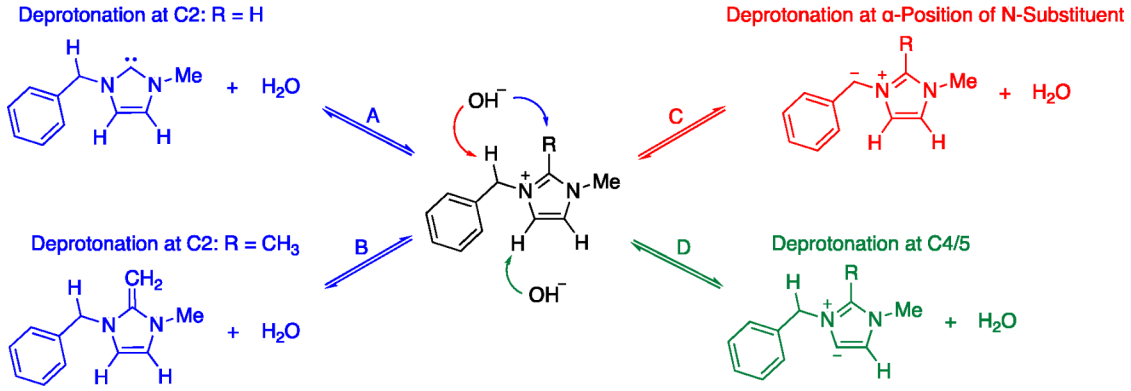

most stable classes of cations in AEMs (Figure 37).[741,742,744,772]

6.1.6.1. C2 Substitution. In a study by Yan and coworkers, Im3 and Im8 were subjected to 2 M KOH in D_2O, CD_3OD and several combinations of the two solvents at 80 °C for 96 h[756] (Table 3, entries 1 and 2). As the proportion of CD_3OD to D_2O increased, the degree of degradation increased likely due to the lower dielectric constant and more nucleophilic nature of methanol compared to water. They found that, in all of the solvent systems, the imidazolium with the C2-methyl had a significantly lower degree of degradation. Many other studies conducted under a variety of conditions agree that employing a methyl at the C2-position produces higher alkaline stability (Table 3, entries 3−10).[745,747,750,751,767,771]

Additionally, Yan and coworkers found that an *n*-butyl substituent at the C2-position demonstrated the lowest degree of ring-opening degradation[769] (Scheme 4A; Table 3, entry 13), followed by methyl, isopropyl, and phenyl substituents (Table 3, entries 10−12).[767] Yan reported a higher stability for C2-methylated Im7 relative to C2-phenylated Im18 and attributed this stability to a higher lowest unoccupied molecular orbital (LUMO) energy.[767] For the C2-substituted imidazoliums, it was observed that the higher LUMO energy of the imidazolium, the less susceptible it is to ring-opening nucleophilic attack (Scheme 4A). Their calculated LUMO energies gave Im15 > Im7 > Im14 > Im18, matching the observed alkaline stability trend. Interestingly, Im18 had a lower LUMO energy than Im2 yet had a higher stability, likely owing to protection of the C2-position with steric hindrance. Im15 may have the highest stability due to the C2-*n*-butyl group combining both steric hindrance and hyperconjugation between the C−H σ bond and the π-conjugation on the ring. However, unlike the phenyl group on Im18, the *n*-butyl can provide the steric bulk to protect the C2 on Im15 from attack (Scheme 4A), without delocalizing the electron density.

Overall, under a wide array of conditions, C2 substitution has been shown to improve alkaline stability; however, one substituent can lead to an increased degradation rate. Beyer and coworkers reported a stability trend of C2 substitution where methyl > phenyl > hydrogen > *tert*-butyl when comparing Im6, Im17, Im1, and Im16 with half-lives of ~1000, 107, 15, and 3 h, respectively, in 1 M NaOD/D_2O at 80 °C (88 °C for Im6)[761] (Table 3, entries 15−18). Similarly to Yan, Beyer reported that the methyl-substituted Im6 is more resistant to ring-opening degradation (Scheme 4A) than the phenyl-substituted Im17. They attribute this finding not to LUMO energies but to acidic proton stabilization that results from the reversible deprotonation of the protons on the C2-methyl substituent (Scheme 5B), which outweighs the stabilization from the steric hindrance induced by a C2-phenyl. Further evidence of proton stabilization effects (Scheme 5A) is shown by comparing Im1 to its C2-*t*-butyl analogue, Im16, with half-lives of 15 and 3 h, respectively (Table 3, entries 17 and 18). In all other cases, having any C2 substituent induces higher stability than having a hydrogen at the C2-position. The surprisingly low stability of Im16 was attributed to destabilization from 1,3-allylic strain between the hydrogens on the *tert*-butyl and the *N*-methyl groups. While reversible deprotonation (Scheme 5A,B) reduced the extent of degradation by nucleophilic addition at the C2-position (Scheme 4A), there are irreversible degradation reactions on the deprotonated species that can still degrade the imidazolium. With all potential degradation mechanisms in mind, C2 substituents with α-protons can yield lower imidazolium stabilities as seen in studies by Coates.[745,747,750]

When Coates and coworkers compared the stabilities of Im22, Im26, Im21, and Im20 in 1 M KOH/CD_3OH at 80 °C, a different stability trend appeared, where substitution at the C2-position with phenyl ≈ 2,6-dimethylphenyl > isopropyl ≈ methyl groups.[750] For these imidazoliums, 91%, 87%, 82%, and 80% cation remained, respectively (Table 3, entries 19−22), after 720 h. Instead of degrading by ring opening (Scheme 4A), the imidazoliums with alkyl substituents at the C2-position (Im21 and Im20) likely degraded via C2 substituent deprotonation followed by rearrangement (Scheme 5B), while those with aryl substituents (Im22 and Im26) degraded by S_N2 attack at the N1/N3 substituents, with more degradation from attack at the benzyl groups (Scheme 4B) than the methyl groups (Scheme 4C).

The disagreement between the stability trends observed by Yan/Beyer and Coates is likely due to the differing degradation mechanisms observed for each series of compounds. Yan quantified the degree of ring-opening degradation at the C2-position[767] (Scheme 4A); however, Coates did not observe ring-opening degradation (Scheme 4A) as the major degradation pathway in the series of imidazoliums used to study C2 substituent effects.[750] Thus, the stability trend observed by Yan where C2-methyl > C2-isopropyl > C2-phenyl relates to the rate of nucleophilic attack at the C2-position[767] (Scheme 4A), while the stability trend observed by

https://doi.org/10.1021/acs.chemrev.1c00331
Chem. Rev. XXXX, XXX, XXX−XXX

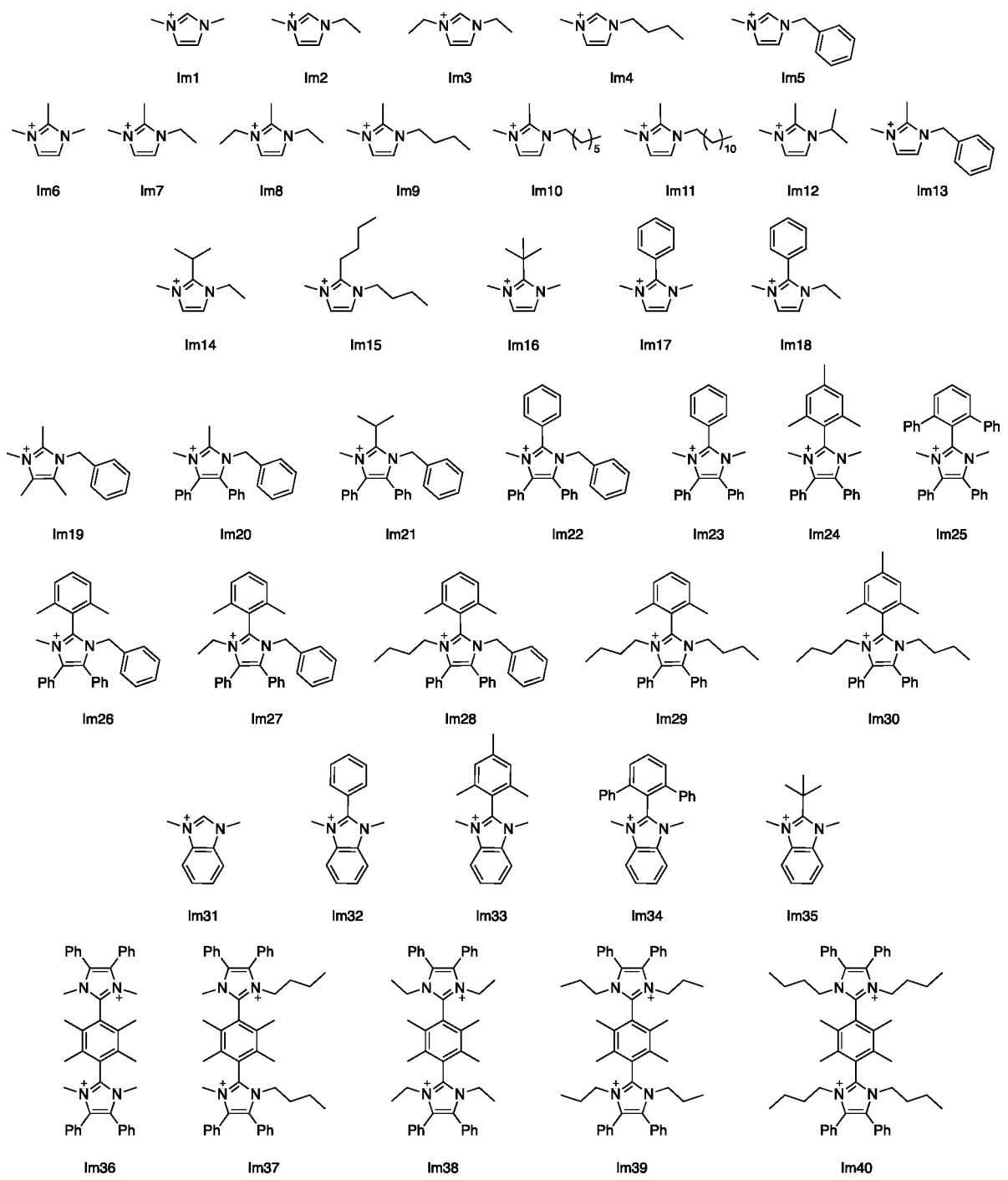

Figure 37. Naming scheme for imidazoliums (Im) discussed herein; counteranions omitted for clarity.

Coates et al., C2-phenyl ≈ C2-2,6-dimethylphenyl > C2-isopropyl ≈ C2-methyl, likely results from a combination of C2 substituent deprotonation (Scheme 5B) and attack at the N1 and N3 substituents[750] (Scheme 4B,C).

The difference in observed degradation mechanism is likely due to differing N1/N3 and C4/C5 substituents on the imidazoliums studied by Yan and Coates. Bulkier *N*-benzyl substituents may protect the C2-position from attack more readily than the *N*-methyl groups,[773] which may also contribute to why Coates does not observe ring-opening degradation (Scheme 4A) as a major degradation pathway.[750] Additionally, *N*-benzyl substituents are more prone to attack by hydroxide (Schemes 4B and 5C) than methyl groups, which may give rise to S_N2 at the benzylic position (Scheme 4B) as the observed major degradation pathway in the Coates study, while the imidazoliums studied by Yan and Beyer did not have a benzylic position to be attacked.

Additionally, when Coates investigated the degradation mechanism of an imidazolium with a C2-methyl and without substitution at the C4/C5-positions (Im13; Table 3, entry 4), they observed nucleophilic addition to the C2-position[750] (Scheme 4A) as the degradation pathway similarly to Yan and Beyer. This finding suggests that substitution at the C4/C5-position influences the favored degradation pathway, which, in turn, affects the trend observed when varying the C2 substituent. However, when Webb investigated the degrada-

https://doi.org/10.1021/acs.chemrev.1c00331
Chem. Rev. XXXX, XXX, XXX−XXX

Table 3. Imidazolium Stability Study Conditions and Results; Counteranions Omitted for Clarity

Entry	Name	Model Compound	Time (h)	Solvent	[OH] (M)	Temp (°C)	Cation Remaining (%)	Ref
1	Im3	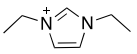	96	D_2O	2 M	80	35%	756
				CD_3OD/D_2O 3:1	2 M	80	4%	
				CD_3OD	2 M	80	2%	
2	Im8	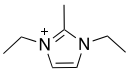	96	D_2O	2 M	80	>99%	756
				CD_3OD/D_2O 3:1	2 M	80	95%	
				CD_3OD	2 M	80	93%	
3	Im4	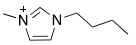	168	D_2O	7.16 M (50 equiv)	30	12%	771
4	Im9	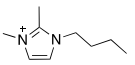	168	D_2O	6.63 M (50 equiv)	30	86%	771
5	Im5	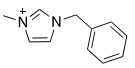	240	CD_3OH	1 M	80	<1%	745, 747, 750
6	Im13	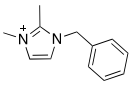	720	CD_3OH	1 M	80	36%	745, 747, 750
					2 M	80	<1%	
7	Im5	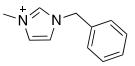	120	H_2O	1 M	80	0%	751
8	Im13	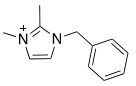	480	H_2O	1 M	80	62%	751
9	Im2	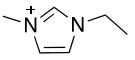	60	D_2O	1 M	80	52%	767
10	Im7	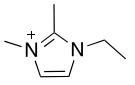	168	D_2O	1 M	80	>99%	767
					2 M	80	>99%	
11	Im14	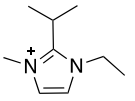	168	D_2O	1 M	80	>99%	767
					2 M	80	90%	
12	Im18	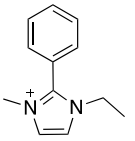	168	D_2O	1 M	80	>99%	767
					2 M	80	74%	
13	Im15	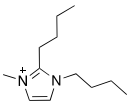	240	D_2O	4 M	80	84%	769
14	Im9	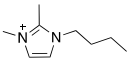	192	D_2O	4 M	80	76%	769

https://doi.org/10.1021/acs.chemrev.1c00331
Chem. Rev. XXXX, XXX, XXX−XXX

Table 3. continued

Entry	Name	Model Compound	Time (h)	Solvent	[OH] (M)	Temp (°C)	Cation Remaining (%)	Ref
15	Im6	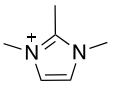	167	D_2O	1 M	88	82%	761
			~1000	D_2O	1 M	88	50%	
16	Im17	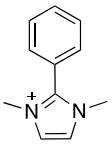	107	D_2O	1 M	80	50%	761
17	Im1	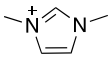	15	D_2O	1 M	80	50%	761
18	Im16	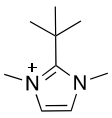	3	D_2O	1 M	80	50%	761
19	Im26	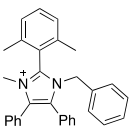	720	CD_3OH	1 M	80	87%	750
					2 M	80	66%	
					5 M	80	18%	
20	Im22	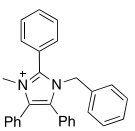	720	CD_3OH	1 M	80	91%	750
					2 M	80	69%	
					5 M	80	<1%	
21	Im21	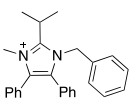	720	CD_3OH	1 M	80	82%	750
22	Im20	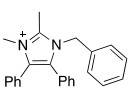	720	CD_3OH	1 M	80	80%	750
23	Im19	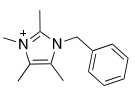	1536	H_2O	4.25 M	80	60%	751
24	Im24	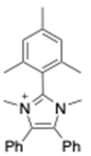	240	70 wt% CD_3OD/D_2O	3 M	80	98%	741, 742
			7790	70 wt% CD_3OD/D_2O	3 M	80	50%	
			19	DMSO/crown ether	0.5 M	22		
25	Im25	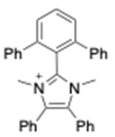	240	70 wt% CD_3OD/D_2O	3 M	80	93%	741, 742
			2075	70 wt% CD_3OD/D_2O	3 M	80	50%	
26	Im23	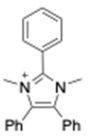	240	70 wt% CD_3OD/D_2O	3 M	80	88%	742
			1370	70 wt% CD_3OD/D_2O	3 M	80	50%	

https://doi.org/10.1021/acs.chemrev.1c00331
Chem. Rev. XXXX, XXX, XXX−XXX

Table 3. continued

Entry	Name	Model Compound	Time (h)	Solvent	[OH] (M)	Temp (°C)	Cation Remaining (%)	Ref
27	Im36	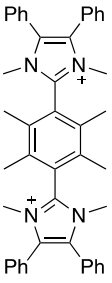	240	70 wt% CD_3OD/D_2O	3 M	80	94%	741
			2330	70 wt% CD_3OD/D_2O	3 M	80	50%	
			60	DMSO/crown ether	0.5 M	22		
28	Im32	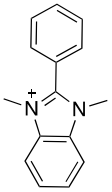	n.d.[a]	70 wt% CD_3OD/D_2O	3 M	80	0%	742, 774
29	Im33	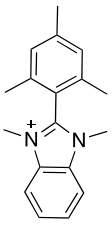	240	70 wt% CD_3OD/D_2O	3 M	80	69%	742, 774
			436	70 wt% CD_3OD/D_2O	3 M	80	50%	
30	Im34	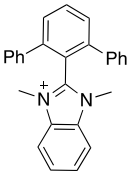	240	70 wt% CD_3OD/D_2O	3 M	80	95%	742, 774
			3240	70 wt% CD_3OD/D_2O	3 M	80	50%	
31	Im19	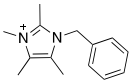	720	CD_3OH	1 M	80	87%	750
32	Im33	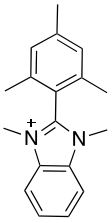	720	CD_3OH	1 M	80	91%	750
					2 M	80	73%	
33	Im35	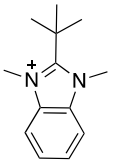	n.d.[a]	D_2O	0.5 M	22	0%	761
34	Im31	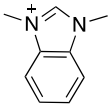	0.7	D_2O	1 M	80	50%	761

https://doi.org/10.1021/acs.chemrev.1c00331
Chem. Rev. XXXX, XXX, XXX−XXX

Table 3. continued

Entry	Name	Model Compound	Time (h)	Solvent	[OH] (M)	Temp (°C)	Cation Remaining (%)	Ref
35	Im12	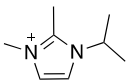	432	D_2O	2 M	80	97%	758
					4 M	80	98%	
36	Im9	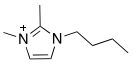	432	D_2O	2 M	80	97%	758
					4 M	80	84%	
37	Im10	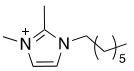	432	D_2O	2 M	80	96%	758
					4 M	80	73%	
38	Im6	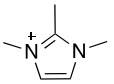	432	D_2O	2 M	80	64%	758
39	Im11	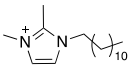	72	D_2O	2 M	80	52%	758
40	Im27	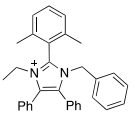	720	CD_3OH	1 M	80	91%	750
					2 M	80	84%	
41	Im28	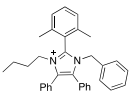	720	CD_3OH	1 M	80	95%	750
					2 M	80	86%	
42	Im29	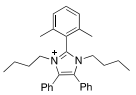	720	CD_3OH	1 M	80	>99%	750
					2 M	80	>99%	
					5 M	80	>99%	
43	Im9	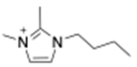	189	D_2O	3 M	80	92%	757
44	Im13	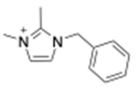	73	D_2O	3 M	80	71%	757
45	Im30	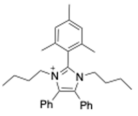	240	70 wt% CD_3OD/D_2O	3 M	80	>99%	741
			>10,000[b]	70 wt% CD_3OD/D_2O	3 M	80	50%	
			40	DMSO/crown ether	0.5 M	22		
46	Im37	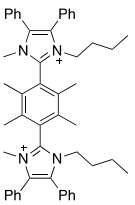	240	70 wt% CD_3OD/D_2O	3 M	80	97%	741
			5830	70 wt% CD_3OD/D_2O	3 M	80	50%	
			40	DMSO/crown ether	0.5 M	22		
47	Im40		240	70 wt% CD_3OD/D_2O	3 M	80	>99%	741
			>10,000[b]	70 wt% CD_3OD/D_2O	3 M	80	50%	

https://doi.org/10.1021/acs.chemrev.1c00331
Chem. Rev. XXXX, XXX, XXX−XXX

Table 3. continued

Entry	Name	Model Compound	Time (h)	Solvent	[OH] (M)	Temp (°C)	Cation Remaining (%)	Ref
		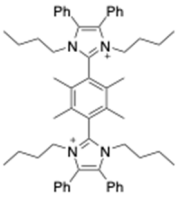	83	DMSO/crown ether	0.5 M	22		
48	Im38	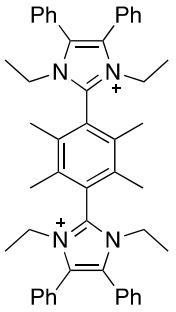	240	70 wt% CD_3OD/D_2O	3 M	80	>99%	741
			>10,000[b]	70 wt% CD_3OD/D_2O	3 M	80	50%	
			50	DMSO/crown ether	0.5 M	22		
49	Im39	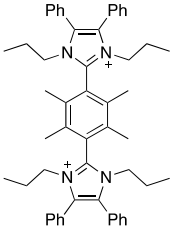	240	70 wt% CD_3OD/D_2O	3 M	80	99%	741
			>10,000[b]	70 wt% CD_3OD/D_2O	3 M	80	50%	
			120	DMSO/crown ether	0.5 M	22		

[a]Too fast to measure. [b]Determined from >99% cation remaining after 240 h.

tion pathway for Im19 (Table 3, entry 23), an imidazolium with C4/C5-methyl substituents, they found that the imidazolium degraded by nucleophilic addition[751] (Scheme 4A), which implies that the C4/C5-methyl substitution is not impacting the degradation mechanism. However, in order to induce degradation, the base concentration was increased to 4.25 M, which can influence the primary degradation mechanism.

It is thought that attack at the C2-position (Scheme 4A) is higher order in base and therefore is favored at high base concentrations. This can explain why Webb observed nucleophilic addition at the C2-position (Scheme 4A) in their study of Im19 in 4.25 M KOH(aq) (Table 3, entry 23). A change in degradation mechanism as a function of hydroxide concentration is further evidenced by Im26 possessing a higher stability than Im22 at 5 M KOH/CD_3OH when they possess similar stabilities at 1 and 2 M KOH/CD_3OH (Table 3, entries 19 and 20).[750] The steric bulk of 2,6-dimethylphenyl provides better protection of the C2-position than a phenyl substituent against nucleophilic addition at the C2-position (Scheme 4A), which becomes the major degradation pathway at higher hydroxide concentrations.

This finding is supported by a study from Holdcroft and coworkers where the stabilities of Im24, Im25, and Im23 are compared in 3 M NaOD in 70 wt % CD_3OD/D_2O at 80 °C, and a percent cation remaining of 98%, 93%, and 88% was observed, respectively, after 240 h[742] (Table 3, entries 24−26). Im24 and Im25 degraded via demethylation (Scheme 4C), while Im23 degraded primarily by attack at the C2-position (Scheme 4A), showing that 2,6-substitution on C2-aryl substituents better guards the C2-position from ring-opening degradation (Scheme 4A), with a more electron-donating group (methyl) inducing a higher stability than the bulkier phenyl group. Additionally, Holdcroft found that when two imidazoliums are fused through the C2-position, cation stability decreases from 98% cation remaining for Im24 to 94% for the bis-imidazolium, Im36, with a similar substitution pattern[741] (Table 3, entries 24 and 27). They attribute this loss in stability to a higher electrostatic potential in Im36 indicating a greater electrostatic attraction between the imidazolium and hydroxide, possibly leading to the faster degradation.

When the same substitution pattern is investigated on benzimidazoliums, which have a phenyl ring fused to the C4/C5-positions, the stability of the imidazolium correlates more to steric bulk. A C2 substitution of 2,6-diphenyl gave rise to the highest stability followed by mesityl and phenyl substituents (Im34, Im33, Im32). After 240 h in 3 M NaOD in 70 wt % CD_3OD/D_2O at 80 °C, Im34 and Im33 showed 95% and 69% cation remaining, respectively, while Im32 had 0% cation remaining within 1 min[774] (Table 3, entries 28−30). The difference in trends between the two sets of imidazoliums, pentasubstituted (Im23, Im24, and Im25) and benzimidazo-

https://doi.org/10.1021/acs.chemrev.1c00331
Chem. Rev. XXXX, XXX, XXX−XXX

liums (Im32, Im33, and Im34), further demonstrates how all of the imidazolium substituents contribute to stability trends even if they are not explicitly being varied for structure−stability relationship determination.

6.1.6.2. C4/C5 Substitution. Imidazoliums with hydrogens at the C4/C5-position are susceptible to degradation via deprotonation followed by rearrangement at the C4/C5-position (Scheme 5D). Substitution at the C4- and C5-positions blocks this deprotonation and other degradation pathways giving rise to higher alkaline stability.[745] Webb and coworkers studied the influence of methyl substitution at the C4/C5-positions by comparing the degradation rate and mechanism of Im13 and Im19.[751] They observed 62% cation remaining for Im13 after 480 h in 1 M KOH(aq) at 80 °C (Table 3, entry 8), while Im19 required a higher hydroxide concentration of 4.25 M KOH(aq) to evoke any degradation. Even under harsher conditions, Im19 showed 60% cation remaining after 1536 h (Table 3, entry 23).

Coates and coworkers demonstrated a similar trend showing 36% Im13 remaining after 720 h in 1 M KOH/CD_3OH at 80 °C[745,747,750] (Table 3, entry 6), degrading by nucleophilic addition at the C2-position[747,750] (Scheme 4A). Substituting the C4- and C5-position with phenyl groups (Im20) afforded a significantly higher stability with 80% cation remaining under the same conditions[745,747,750] (Table 3, entry 22). Exchanging the C4/C5 phenyl groups for methyl groups produces Im19, further improved stability with 87% cation remaining (Table 3, entry 31).

When the C4/C5-positions were fused with a phenyl ring to give a benzimidazolium, Im33, there was 91% and 73% cation remaining in 1 and 2 M KOH, respectively, at 80 °C for 720 h[745,747] (Table 3, entry 32). There was degradation from attack at the C2-position (Scheme 4A) as well as demethylation (Scheme 4C).[747] While this may suggest that benzimidazoliums achieve higher stability than imidazoliums with methyls or phenyls at the C4/C5-positions, the substituents at other positions on the imidazolium may be playing a role. Im33 has N1/N3-methyl and C2-mesityl substituents while Im13, Im20, and Im19 have *N*-benzyl and C2-methyl substituents. Due to these differences in substitution, the effect of the C4/C5 substitution cannot be directly observed. However, when Im29, a cation with substitution patterns more similar to those of Im33, has >99% cation remaining when subjected to the same conditions[745,747,750] (Table 3, entry 42), which shows that pentasubstituted imidazoliums can be more stable than benzimidazoliums depending on the substitution of the other sites. In order to obtain a true idea of how the imidazoliums compare, substituents should be altered one at a time.

Holdcroft compared three benzimidazoliums (Im32, Im33, and Im34) and three C4/C5-phenyl-substituted imidazoliums (Im23, Im24, and Im25), which all had *N*-methyl substituents and varied C2 functionality.[742] When comparing the stabilities of Im23 and Im32, both with C2-phenyl substitutions, in 3 M NaOD in 70 wt % CD_3OD/D_2O at 80 °C, C4/C5-phenyl-substituted Im23 with 88% cation remaining after 240 h showed a much higher stability than its benzimidazolium counterpart Im32, which degraded entirely in less than 1 min (Table 3, entries 26 and 28). Im24 and Im33 both with C2-mesityl substitutions demonstrated the same trend with 98% and 69% cation remaining after 240 h, respectively (Table 3, entries 24 and 29). Conversely, when the C2-position is substituted with 2,6-diphenyl, the opposite trend is observed, and the benzimidazolium (Im34) achieves a higher stability with 93% and 95% cation remaining for Im25 and Im34, respectively (Table 3, entries 25 and 30). Beyer found benzimidazoliums to be less stable than C4/C5-hydrogen-substituted imidazoliums when compared in 1 M NaOH(aq) at 80 °C.[761] With C2-*t*-butyl substitution, Im35 had a half-life too short to measure while Im16 had a half-life of 170 min (Table 3, entries 33 and 18), and for Im31 and Im1, the half-lives were 46 and 880 min, respectively (Table 3, entries 34 and 17), demonstrating that, irrespective of C2 substitution, benzimidazoliums have even lower stabilities than imidazoliums that are not substituted at the C4/C5-position. While the C2 and nitrogen substituents can affect the relative stabilities between benzimidazoliums and imidazoliums, overall, it has been found that methyl or phenyl substituents at the C4/C5-position produce a higher alkaline stability than unsubstituted imidazoliums or benzimidazoliums.

6.1.6.3. N1/N3 Substitution. Substitution of the N atoms was found to significantly modulate the alkaline stability of imidazolium compounds. The substituents at the N1- and N3-positions can influence the rate of nucleophilic attack at the C2-position[757,758,769,773] (Scheme 4A) in addition to any degradation that may occur on the N1 and N3 substituents themselves[741,747,750] (Scheme 4B,C).

Yan and coworkers studied imidazoliums with a methyl group at the N1-position while varying substituents at the N3-position in 2 M NaOH/D_2O at 80 °C.[758,769] It was observed that installing an isopropyl (Im12), *n*-butyl (Im9), or *n*-heptyl group (Im10) at the nitrogen position produced more stable imidazoliums than those with a methyl group (Im6) at that position (Table 3, entries 35−38).[758] After 432 h, 97% cation remained for the Im12 and Im9 (Table 3, entries 35 and 36), while Im10 had 96% cation remaining (Table 3, entry 37), and Im6 had 64% cation remaining (Table 3, entry 38). They attribute the improved stability to the steric bulk of alkyl groups that block nucleophilic addition at the C2-position (Scheme 4A).

The relative stabilities of Im12, Im9, and Im10 were differentiated in 4 M NaOH/D_2O at 80 °C, and after 50 h, 98%, 84%, and 73% cation remained,[758] respectively (Table 3, entries 35−37). Under these harsher conditions, the longer alkyl chains Im9 and Im10 displayed a lower stability than Im12 with its shorter, but bulkier, isopropyl substituent. An imidazolium with an even longer linear alkyl chain substituent, Im11, only had 52% cation remaining after a mere 72 h in 2 M NaOH/D_2O at 80 °C (Table 3, entry 39). This trend of imidazoliums substituted with long alkyl substituents displaying a lower stability than the isopropyl-substituted imidazolium was attributed to a lower LUMO energy of the imidazoliums caused by alkyl tail aggregation.

Coates and coworkers compared the stability of N1/N3 substituents by keeping the N3 constant with a benzyl group and varying the N1-position with methyl, ethyl, and *n*-butyl substituents.[750] After 720 h in 2 M KOH/CD_3OH at 80 °C, Im26, Im27, and Im28 displayed 66%, 84%, and 86% cation remaining, respectively (Table 3, entries 19, 40, and 41). This trend of increasing stability with increasing chain length can be attributed to the observed decrease in the degree of S_N2 attack at the α-positions (Scheme 4C). Additionally, no alkene products formed, suggesting that, even with the presence of β-hydrogens, Hofmann elimination (Scheme 3B) is not a prominent degradation pathway for these imidazoliums.

Replacing the N3-benzyl group in Im28 with an *N*-*n*-butyl group gives Im29 and increases the percent cation remaining

https://doi.org/10.1021/acs.chemrev.1c00331
Chem. Rev. XXXX, XXX, XXX−XXX

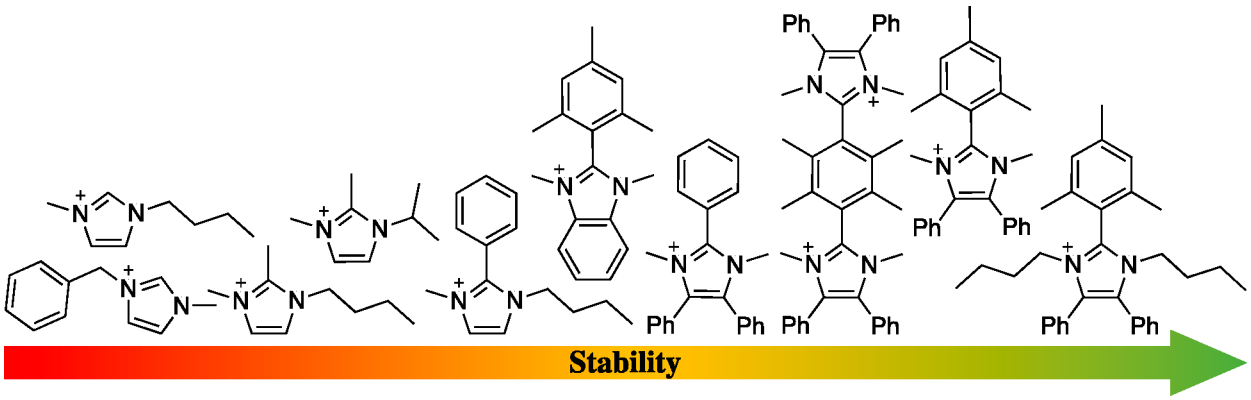

Figure 38. Approximate ranking of imidazolium stability in alkaline conditions from low (red) to high (green). Results vary depending on test conditions used; counteranions omitted for clarity.

from 86% to >99% after 720 h in 2 M KOH/CD_3OH at 80 °C[750] (Table 3, entry 42). Even with an increase in hydroxide concentration to 5 M KOH, there is still >99% Im29 remaining after 720 h, demonstrating the high alkaline stability of this imidazolium. *N*-*n*-butyl groups promote higher stability because they remove the possibility of S_N2 attack or deprotonation that would occur at the benzylic position (Scheme 4B,C), and they shield the C2-position (Scheme 4A) from nucleophilic addition. This finding was further supported by Yang et al., where they quantified the extent of ring-opening degradation of imidazoliums with either *N*-*n*-butyl or *N*-benzyl substituents.[757] When subjected to 3 M KOH/D_2O at 80 °C, *N*-*n*-butyl-substituted imidazolium (Im9) had 8% degradation by ring opening after 189 h compared to 29% for the *N*-benzyl-substituted imidazolium (Im13) after only 73 h (Table 3, entries 43 and 44), indicating that *N*-*n*-butyl groups are more effective at blocking attack at the C2-position than benzyl groups.

Holdcroft also demonstrated the improved alkaline stability of *N*-*n*-butyl groups. The *N*-methyl-substituted imidazolium, Im24, degrades solely by demethylation (Scheme 4C); thus, exchanging the *N*-methyl groups for *N*-*n*-butyl groups (Im30) increased the percent cation remaining from 98% to >99% after 240 h in 3 M NaOD in 70 wt % CD_3OD/D_2O at 80 °C[741] (Table 3, entries 24 and 45). The benefit of *N*-*n*-butyl groups is further supported by the comparison of Im36, Im37, and Im40, where *N*-methyl groups are gradually replaced with *N*-*n*-butyl groups on bis-imidazoliums, with each replacement resulting in higher stability (Table 3, entries 27, 46, and 47). Im36, with all *N*-methyl substitutions, demonstrated 94% cation remaining after 240 h in 3 M NaOD in 70 wt % CD_3OD/D_2O at 80 °C (Table 3, entry 27). By exchanging half of the *N*-methyl groups for *N*-*n*-butyl groups (Im37), the stability improved to 97% cation remaining (Table 3, entry 46), and by exchanging all of the *N*-methyl groups for *N*-*n*-butyl groups (Im40), the stability improved further to >99% cation remaining (Table 3, entry 47) under the same conditions. These results indicate that *N*-*n*-butyl groups are one of the best choices for nitrogen substitution in imidazoliums as they effectively prevent nucleophilic addition (Scheme 4A) as well as dealkylation (Scheme 4C) without inducing Hofmann elimination. Furthermore, Holdcroft found that *N*-ethyl and *N*-*n*-propyl groups also induce the same level of stability, as Im38 and Im39 had >99% and 99% cation remaining, respectively, under the same conditions (Table 3, entries 48 and 49). This aligns with Coates' finding that *N*-ethyl and *N*-*n*-butyl substituents result in imidazoliums with similar stabilities (Table 3, entries 40 and 41).

In order to elucidate the relative stabilities of the imidazoliums with half-lives >10 000 h, Holdcroft implemented harsher conditions through the use of 0.5 M ultradry KOH/DMSO/crown ether at 22 °C.[741] Under these conditions, Hofmann elimination (Scheme 3B) becomes the major degradation pathway instead of demethylation (Scheme 4A). Despite the change in dominant degradation pathway, Im24 still had a shorter half-life than Im30 of 19 and 40 h, respectively (Table 3, entries 24 and 45). However, the bis-imidazoliums (Im36−Im40) demonstrated interesting behavior in the new low hydration conditions as the half-lives no longer correlated with the number of butyl substituents. Im36 had a higher half-life than Im37 of 60 and 40 h, respectively (Table 3, entries 27 and 46), suggesting that butyl groups are lowering the cation stability, but Im40 had a half-life of 83 h (Table 3, entry 47), higher than Im36 and Im37. Additionally, one might expect the *N*-ethyl-substituted imidazolium to have the lowest stability under these conditions due to the emergence of Hofmann elimination (Scheme 3B) as a degradation pathway, but Im38 had a half-life of 50 h (Table 3, entry 48)—higher than Im37. Im39 demonstrated the highest half-life of 120 h (Table 3, entry 49). These results would imply that *N*-*n*-propyl substitutions provide the highest alkaline stability. Overall, this study shows how solvent choice can influence both the degradation rate and mechanism. While it is important to be able to differentiate highly alkaline-stable cations, the results may not accurately reflect the processes occurring under MEA operating conditions, an issue present in all model compound studies that can be exacerbated by solvent choice.

6.1.6.4. Conclusion—Imidazolium Cations. Imidazoliums are very modular cations, and changes to the C2-, N1/N3-, and C4/C5-positions have been shown to influence the alkaline stability of these compounds. The many factors influencing imidazolium stability and the opposing trends that arise from differing testing conditions make it difficult to determine the exact stability trends for this class of cation; therefore, an approximate ranking of imidazolium stability is shown in Figure 38. Overall, C2 substituents improve the alkaline stability of imidazoliums through both protection of the C2-position from nucleophilic addition (Scheme 4A) and deprotonation (Scheme 5A), as well as protecting the N1/N3 substituents from S_N2 attack (Scheme 4B,C). Aryl groups, especially those with 2,6-substitution, seem to provide the best

https://doi.org/10.1021/acs.chemrev.1c00331
Chem. Rev. XXXX, XXX, XXX−XXX

protection against degradation as C2 substituents with an α-hydrogen such as methyl groups can undergo deprotonation (Scheme 5B), potentially leading to further degradation, especially under fuel cell operating conditions.[761] Substitution of the C4/C5-position with methyl groups or phenyl groups drastically increases the stability of the imidazolium irrespective of the substitution of other positions, and thus, all future imidazoliums studied should have C4/C5 substitution to better provide information about the effects of substitution at the other positions on overall stability. Lastly, N1/N3-positions should be substituted with *n*-butyl or isopropyl groups to deliver the highest stability as benzyl and methyl substituents are prone to S_N2 attack (Scheme 4B,C) and deprotonation (Scheme 5C). Pentasubstituted imidazoliums adhering to the above recommendations should provide excellent cation stability when implemented in AEMs, some examples of these materials are discussed in section 6.2.

6.1.7. Phosphonium Cations. Some studies show that phosphonium cations may be a more stable alternative to quaternary ammonium cations (Figure 39). Yan and coworkers observed that, in 2 M KOH/CD_3OD at 80 °C, P1 had 97% cation remaining (Table 4, entry 1) after 96 h while BTMA and QA15 had 49% and 77% cation remaining, respectively[756] (Table 2, entries 1 and 25). However, in a study by Coates and coworkers, P2 had a much lower stability than its quaternary ammonium analogue BTMA, degrading completely after 120 h in 1 M KOH/CD_3OH at 80 °C (Table 4, entry 2) via phosphine oxidation, also known as the Cahours−Hofmann reaction[747] (Scheme 6A). Yan and coworkers performed studies on the stability of P3,[759,775] a phosphonium with aromatic groups instead of methyl substituents, which largely degraded via phosphine oxidation (Scheme 6A) rapidly at 20 °C in 1 M KOD in CD_3OD/D_2O (5/1 v/v) (Table 4, entry 3).[759] Yan showed that replacement of phenyl groups on the phosphonium with *para*-tolyl groups, giving P4, improves the stability of the phosphonium, as the time until complete degradation increased from several minutes to 6 h (Table 4, entry 4). The addition of electron-donating groups to the para position of the aromatic rings resulted in increased stability of P4 relative to P3. Thus, exchanging the methyl groups for methoxy groups, an even more electron-donating species, should induce an even higher cationic stability. Consistent with the predicted trend, P5 showed an extended stability up to 87 h at 20 °C in 1 M KOD in CD_3OD/D_2O (5/1 v/v) (Table 4, entry 5). While the stability of the phosphonium improved with the addition of electron-donating groups at the para positions of the aryl substituents, the degradation was still rapid at elevated temperatures. P6, a phosphonium very similar to P5, only showed 1% cation remaining after 4 h in 1 M KOD in CD_3OD/D_2O (5/1 v/v) at 80 °C[775] (Table 4, entry 6).

An addition of electron-donating groups to the ortho position of the aryl groups P7, instead of the para position, resulted in a slightly higher alkaline stability in 1 M KOD in CD_3OD/D_2O (5/1 v/v) at 80 °C,[775] taking 8 h to reach 13% cation remaining (Table 4, entry 7), degrading solely via phosphine oxidation (Scheme 6A). The di-ortho methoxy-substituted phosphonium, P8, showed improved stability from the P7, taking 960 h to reach 13% cation remaining (Table 4, entry 8). A 120-fold increase in degradation time shows that *o*-methoxy substitution on aryl groups induces higher stabilities in phosphonium cations. However, a new degradation mechanism was observed for P8, as it degrades by both phosphine oxidation (Scheme 6A) and ether hydrolysis (Scheme 6B) resulting from the attack of the methoxy groups on the ring followed by subsequent ketone rearrangement.[775] Despite the appearance of this new degradation pathway, a higher stability is achieved, proven by the decrease in phosphine oxidation with the addition of electron-donating groups.

Trimethoxy-substituted aryl rings yield even higher alkaline stabilities as P9 showed 28% cation remaining after 960 h in 1 M KOD in CD_3OD/D_2O (5/1 v/v) at 80 °C[759,775] (Table 4, entry 9), more than twice the percent cation retained for the di-substituted phosphonium P8. Replacing the P-methyl with a P-benzyl (P10) demonstrated a similar stability of 21% cation remaining after 960 h in 1 M KOD in CD_3OD/D_2O (5/1 v/v) at 80 °C[759,775] (Table 4, entry 10). However, while P9 degraded by a mix of phosphine oxidation (Scheme 6A) and ether hydrolysis (Scheme 6B), P10 only degraded by ether hydrolysis (Scheme 6B). This finding is consistent with a study by Coates and coworkers where P10 exhibited 67% cation remaining after 720 h in 1 M KOH/CD_3OH at 80 °C[745,747] (Table 4, entry 11), with ether hydrolysis (Scheme 6B) as the only observed degradation pathway.[747] These findings indicate that a benzyl substituent on the phosphonium completely prevents phosphine oxidation (Scheme 6A). However, P9 experienced less degradation despite having two possible degradation pathways.[759,775] This indicates that the benzyl

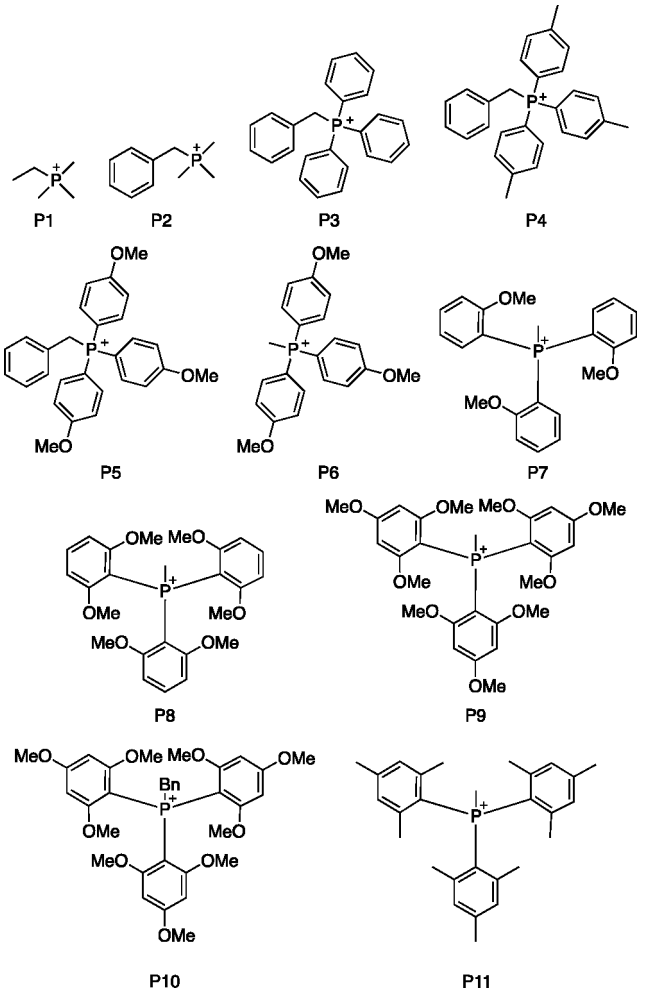

Figure 39. Naming scheme for phosphoniums (P) discussed herein; counteranions omitted for clarity.

https://doi.org/10.1021/acs.chemrev.1c00331
Chem. Rev. XXXX, XXX, XXX−XXX

Table 4. Phosphonium Stability Study Conditions and Results; Counteranions Omitted for Clarity

Entry	Name	Model Compound	Time (h)	Solvent	[OH] (M)	Temp (°C)	Cation Remaining (%)	Ref
1	P1		96	D_2O	2 M	80	100%	756
				CD_3OD	2 M	80	97%	
2	P2	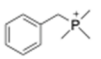	120	CD_3OH	1 M	80	<1%	747
3	P3	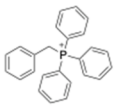	<1	CD_3OD:D_2O (5:1 v/v)	1 M	20	0%	759
4	P4	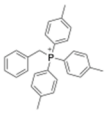	6	CD_3OD/D_2O (5/1 v/v)	1 M	20	0%	759
5	P5	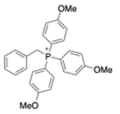	87	CD_3OD/D_2O (5/1 v/v)	1 M	20	<5%	759
6	P6	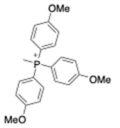	4	CD_3OD/D_2O (5/1 v/v)	1 M	80	1%	775
7	P7	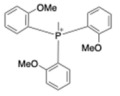	8	CD_3OD/D_2O (5/1 v/v)	1 M	80	13%	775
8	P8	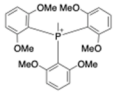	960	CD_3OD/D_2O (5/1 v/v)	1 M	80	13%	775
9	P9	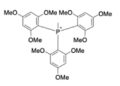	960	CD_3OD/D_2O (5/1 v/v)	1 M	80	28%	775
10	P10	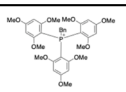	960	CD_3OD/D_2O (5/1 v/v)	1 M	80	21%	775
11	P10	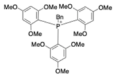	720	CD_3OH	1 M	80	67%	745, 747
					2 M	80	38%	
12	P11	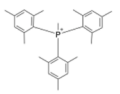	960	CD_3OD/D_2O (5/1 v/v)	1 M	80	93%	775
			5000	CD_3OD/D_2O (5/1 v/v)	1 M	80	82%	

Scheme 6. Observed Degradation Pathways for Phosphonium Cations

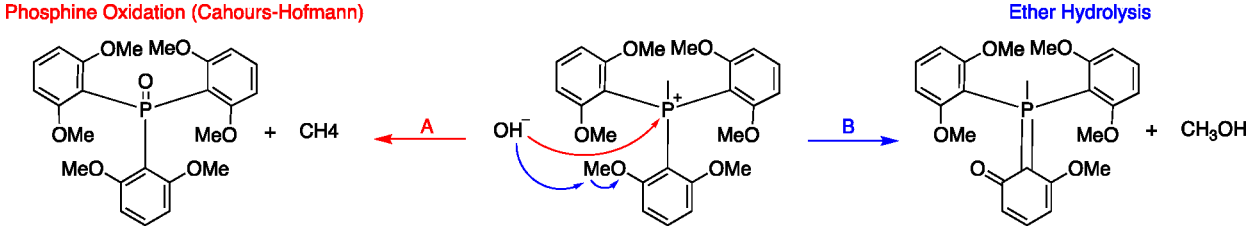

https://doi.org/10.1021/acs.chemrev.1c00331
Chem. Rev. XXXX, XXX, XXX−XXX

substituent in P10 leads to a higher rate of ether hydrolysis (Scheme 6B).

To avoid ether hydrolysis (Scheme 6B) as a potential degradation pathway, Yan replaced the methoxy groups on P9 with methyl groups,[759,775] which still provide enough electron donation to prevent phosphine oxidation (Scheme 6A), without the possibility of ether hydrolysis (Scheme 6B). The resulting P11 demonstrated a substantial increase in the alkaline stability from 28% cation remaining for P9 to 93% cation remaining for P11 after 960 h in 1 M KOD in CD_3OD/D_2O (5/1 v/v) (Table 4, entries 9 and 12). Even after 5000 h, 82% of the P11 cation remained. The implementation of methyl groups on the aryl substituents successfully prevented ether hydrolysis (Scheme 6B). Phosphine oxidation (Scheme 6A) was the only observed degradation pathway, and its effects were also greatly reduced. Replacing the methyl substituent on the phosphonium with a benzyl substituent may produce an even more stable phosphonium, as the benzyl substituent better prevents phosphine oxidation, and ether hydrolysis is not possible with methyl groups on the aryl substituents. Unfortunately this phosphonium was unable to be synthesized.[759]

Studies by both Yan and Coates indicate that implementing electron-rich, bulky aromatic rings reduces the effects of phosphine oxidation (Scheme 6A).[747,759,775] Methoxy groups can enhance the electron density on the aromatic rings, but they can also permit degradation by ether hydrolysis (Scheme 6B). To mitigate the effects of both degradation mechanisms, substitution with methyl groups on the aromatic substituents is the optimal compromise providing the highest stability.

6.1.7.1. Tetrakisaminophosphonium Cations. Tetrakisaminophosphonium cations provide a viable option for increased stability of phosphonium cations as the positive charge is delocalized between the phosphonium and amino substituents (Figure 40). There was no observed degradation of TP1 (Table 5, entry 1) or TP2 (Table 5, entry 2) when subjected to 2 M KOH/CD_3OH at 80 °C for 720 h.[747] P10, however, subjected to the same conditions resulted in only 38% cation retention (Table 4, entry 11), thus strongly suggesting that amino substituents effectively stabilize phosphonium cations. In order evaluate the relative stabilities of tetrakisaminophosphoniums, harsher conditions are needed, as the above conditions were not sufficient to induce any observable degradation.

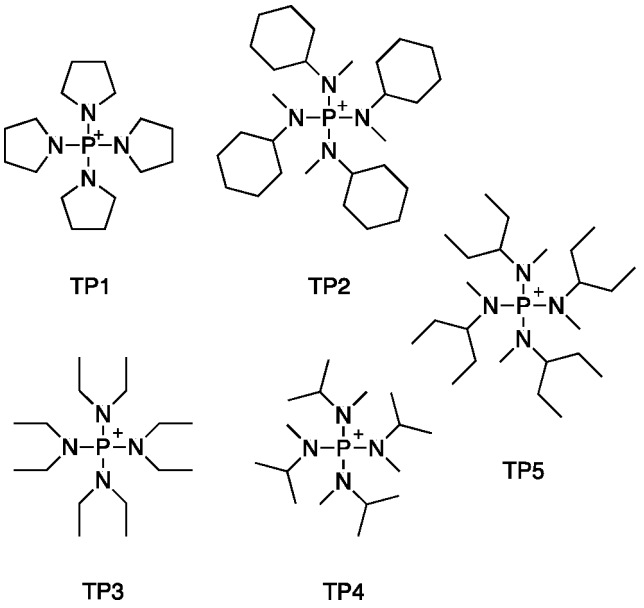

Figure 40. Naming scheme for tetrakisaminophosphoniums (TPs) discussed herein; counteranions omitted for clarity.

Elevated temperatures and solvents with lower dielectric constants can facilitate faster degradation in alkaline media. To this end, Noonan and coworkers employed methyl Carbitol as a solvent, combined with KOH, at high temperature to bring about rapid decomposition of these highly stable tetrakisaminophosphoniums.[776] The authors noted that increasing steric congestion around the phosphorus center, as well as protection of β-hydrogens, results in improved stability for these cations in this medium. For example, the smallest cation (TP1) degraded completely after 4 h in 2 M KOH/methyl Carbitol at 120 °C (Table 5, entry 3). A phosphine oxide was the only degradation product observed, suggesting decomposition by direct attack at the P atom. TP3, with pendant diethylamino groups rather than pyrrolidino groups, exhibited improved stability and required higher temperatures for rapid decomposition, likely from increased steric protection of the P center. TP3 still almost completely degraded (12% cation remaining) after 4 h in 2 M KOH/methyl Carbitol at 160 °C (Table 5, entry 4), with 66% of the degradation due to Hofmann elimination (Scheme 7B) and 21% due to phosphine oxidation (Scheme 7A).

TP3 and TP4 have the same number of atoms but differ in atomic arrangement with a branched alkyl group for TP4. TP4 was more stable than TP3, with 37% cation remaining under identical testing conditions (Table 5, entry 5).[776] For TP4, Hofmann elimination (Scheme 7B) slightly decreased, from 66% to 57%, while the degree of phosphine oxidation (Scheme 7A) significantly decreased from 21% to 5%. This was attributed to the branched alkyl group increasing the steric protection at the P atom. TP5, with longer branched alkyl substituents, showed an even higher stability in 2 M KOH/methyl Carbitol at 160 °C, reducing the propensity for Hofmann elimination (Scheme 7B) by steric blocking of the β-H sites. Approximately, 57% of TP5 was remaining after 4 h (Table 5, entry 6). Finally, TP2 displayed the highest stability under these accelerated degradation conditions with 76% cation remaining after 4 h at 160 °C (Table 5, entry 7). In addition to the steric protection imposed by the cyclohexyl group, the higher stability observed can be attributed to the amino group being locked into an equatorial position on the cyclohexane ring, making the antiperiplanar configuration required for Hofmann elimination (Scheme 7B) unfavorable.

6.1.7.2. Conclusion—Phosphonium Cations. Overall, it has been shown that altering the steric and electronic properties of the phosphonium substituents impacts the alkaline stability, and an approximate ranking of phosphonium stability is shown in Figure 41. The incorporation of electron-donating groups on the aryl substituents reduces the effects of phosphine oxidation (Scheme 6A). While methoxy substituents are the best electron-donating groups for reducing phosphine oxidation, they are susceptible to degradation by ether hydrolysis (Scheme 6B). Tetrakisaminophosphoniums have extremely high alkaline stabilities such that degradation is only observed in extremely harsh alkaline conditions. Under these conditions, the phosphorus can undergo phosphine oxidation (Scheme 7A) if there is not sufficient steric protection of the phosphorus center. If there are readily

https://doi.org/10.1021/acs.chemrev.1c00331
Chem. Rev. XXXX, XXX, XXX−XXX

Table 5. Tetrakisaminophosphonium Stability Study Conditions and Results; Counteranions Omitted for Clarity

Entry	Name	Model Compound	Time (h)	Solvent	[OH] (M)	Temperature (°C)	Percent Cation Remaining	Reference
1	TP1	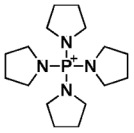	720	CD_3OH	2 M	80	>99%	747
2	TP2	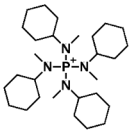	720	CD_3OH	2 M	80	>99%	745, 747
3	TP1	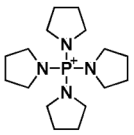	4	Methyl carbitol 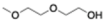	2 M	120	0%	776
4	TP3	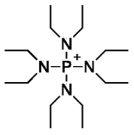	4	Methyl carbitol 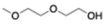	2 M	160	12%	776
5	TP4	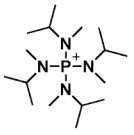	4	Methyl carbitol 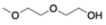	2 M	160	37%	776
6	TP5	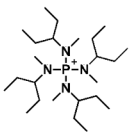	4	Methyl carbitol 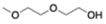	2 M	160	57%	776
7	TP2	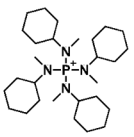	4	Methyl carbitol 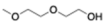	2 M	160	76%	776

accessible β-hydrogens, then Hofmann elimination (Scheme 7B) can occur on the amine substituents. When both of those degradation mechanisms are sufficiently blocked, as in the case of TP2, α-hydrogen abstraction can arise as a degradation mechanism (Scheme 7C). Although there are not many examples of tetrakisaminophosphonium-based AEMs,[743,777] they are excellent cation candidates for stable membranes, and more investigation is warranted.

6.1.8. Conclusion—Cations. Throughout this section, many organic cations and their respective stabilities in a range of conditions have been discussed, and though there is no general consensus on the best cation, there are some candidates that should be considered for further study and implementation in AEMs. Of the quaternary ammoniums, piperidinium, especially spirocyclic piperidinium structures such as QA25, is the most promising yet far more challenging to incorporate into polymer than TMA. In the case of imidazoliums, 2,6-dimethylphenyl or mesityl substitution at the C2-position paired with methyl or phenyl substitution at the C4/C5-positions and butyl groups at the N1/N3-positions, Im29, Im30, and Im40, should induce the highest stability. The incorporation of such compounds into polymers for AEMs may be challenging without compromising the polymer properties, especially with how much cation incorporation would be necessary to achieve reasonable ion exchange capacities. Tetrakisaminophosphoniums, such as TP2, are also highly stable but bulky cations that, if well incorporated into a polymer, should produce alkaline-stable AEMs.

For future model compound stability studies, it is important to alter one substituent at a time so clear structure−stability

https://doi.org/10.1021/acs.chemrev.1c00331
Chem. Rev. XXXX, XXX, XXX−XXX

Scheme 7. Observed Degradation Pathways for Tetrakisaminophosphoniums

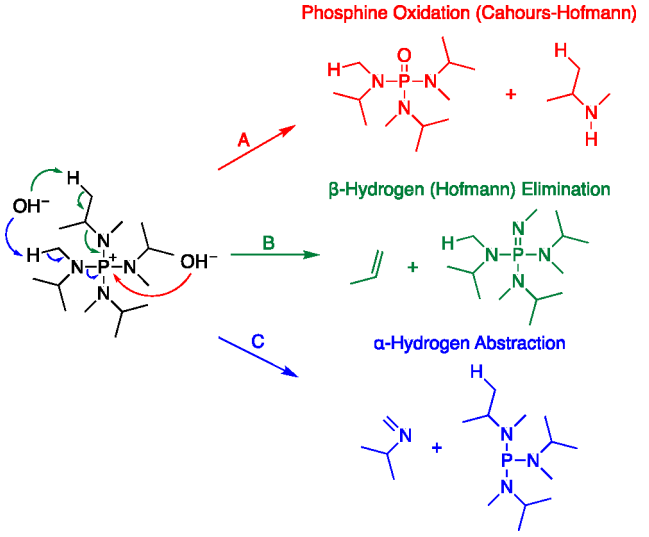

relationships can be determined. It is also crucial that the field use a standard protocol so that results can be compared across different research groups. This can be challenging as cation solubility and stability can make one set of conditions infeasible. We propose that each set of cations is studied in multiple sets of conditions to obtain a complete picture of the cation stability in a range of conditions, and then, at least one of the sets of conditions will match other studies in the field, making cation studies more comparable across groups. Of the protocols available, 0.05 M cation dissolved in 2 M KOH at 80 °C should be used for aqueous conditions as long as the cation is soluble.[751] 0.05 M cation dissolved in 2 M KOH/CD_3OH at 80 °C should be used as a slightly accelerated condition as more organic cations will be soluble in methanol than water, and methanol is a potential fuel for AEMFCs.[745] For extremely accelerated conditions, 0.05 M cation dissolved in 2 M KOH/methyl Carbitol at 80 °C should be used, as the solvent has a low dielectric constant and is still a protic solvent, to better mimic aqueous conditions than nonprotic solvents.[776] To determine degradation mechanisms while retaining the hydroxide anion under dehydrated conditions, a two-phase method[776] such as 0.05 M cation, 50 wt % NaOH/H_2O, and chlorobenzene at 80 °C can be implemented. The favored degradation mechanism may change as a function of solvent, which must be taken into consideration when determining what substitutions should improve cation stability, but testing the cations in multiple solvent systems should make those trends more clear.

The temperature should be held constant so as to not change more factors that can alter the degradation mechanism or skew away from realistic AEMFC conditions. Any NMR studies should be performed in sealed tubes as to prevent the loss of volatile degradation products that may be useful in determining degradation pathways.[745] Internal standards should be used to quantify degradation as opposed to "nonlabile" hydrogens on the cation as even hydrogens not directly involved in degradation can shift. The internal standard can be sealed in a capillary tube before being added to the NMR tube to ensure that it is not degraded.[749] Only nonlabile protons should be deuterated in solvents, paired with the use of solvent suppression in the NMR so that any signals from cation degradation are not lost to deuterium exchange.[745]

While not every model cation study can accommodate these experimental parameters, if possible, multiple degradation conditions should be studied and reported to determine relative cation stability and, therefore, good candidates for incorporation into AEMs. Furthermore, model studies can only predict how stable the cations will be when incorporated into polymer backbones, and the only way to truly compare is through the study of AEMs directly (sections 6.2 and 7).

6.2. Membrane Properties and Performance

In the synthesis of novel polymers for AEMs, one must consider the choice of backbone, cation, and tethering group. AEMs are typically copolymers, with insulating segments to provide mechanical integrity and ionic groups to promote anion movement through the material. Polymer morphology will be impacted by the choice of synthesized polymer (statistical, block, cross-linked network), which impacts membrane properties [e.g., mechanical stability, alkaline stability, ion exchange capacity (IEC), and water uptake (WU)]. All of these features are critically important when integrating the membrane/ionomer with electrocatalysts in MEAs as later discussed in section 7.

Generally, there is an inherent trade-off between the ionic content of a membrane and its WU which has propagating effects on mechanical durability and conductivity; as ion content increases, the membrane has an increased affinity for

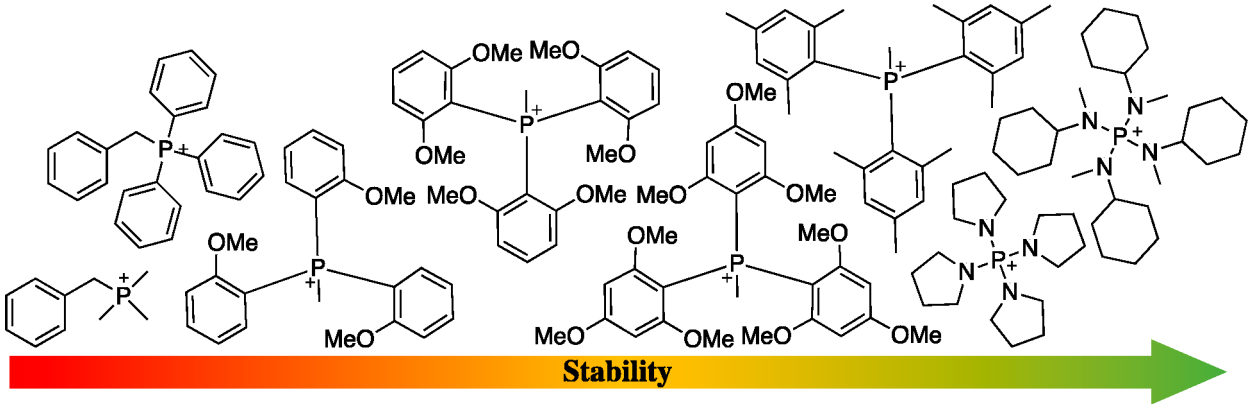

Figure 41. Approximate ranking of phosphonium stability in alkaline conditions from low (red) to high (green). Results vary depending on testing conditions used; counteranions omitted for clarity.

https://doi.org/10.1021/acs.chemrev.1c00331
Chem. Rev. XXXX, XXX, XXX−XXX

water. Excess water content may dilute the effective concentration of ions leading to a membrane with reduced ion conductivity. Furthermore, excess water can result in mechanical destabilization. Conversely, too little water has the potential to inhibit hydroxide transport throughout the membrane and result in reduced ion conductivity. This challenge of water management and hydroxide transport is further discussed in sections 7.5 and 7.6, respectively.

When trying to optimize the WU and IEC, there are a number of methods that can be used to manipulate the properties of a polymer membrane. These include choice of the comonomers, cationic monomer, and relative concentration of the two. Cross-linking polymer membranes is another effective method which works to rigidify polymer segments and lower the mesh size (distance between two polymer chains) so as to exclude water and enhance the mechanical properties. While the deleterious effects of WU vary polymer-to-polymer, a balance in mechanical integrity and performance tends to be found in membranes with less than 100 wt % WU and should be critically considered in the design of novel AEMs.

Studies of the properties and performance of polymer backbones have been crucial to determining optimal materials for use as AEMs. Factors such as backbone flexibility, glass transition temperature, stereo-/regioregularity, and constitutional isomerism dictate the properties important for operation in AEMFCs. These backbone properties significantly influence processing parameters such as film formation, thermomechanical behavior, and morphology, which in turn impact hydroxide conductivity and membrane swelling in water. A variety of polymer backbones have been employed, including poly(arylene ether)s (PAEs), poly(arylene ether sulfone)s (PAESs), polyphenylenes (PPs), polyfluorenes (FLNs), polystyrene (PS), polyethylene (PE), and polynorbornene (PNB). The presence of heteroatom linkages in PAEs and PAESs has been shown to lower the alkaline stability as these polymers are susceptible to nucleophilic attack at the ether linkages.[765,778−780] For this reason, we will primarily focus on the properties and performance of AEMs that are composed of hydrocarbon backbones, both aromatic and aliphatic, and highlight the specific advantages and disadvantages in the context of polymer structure, stability, and processability. A recent review highlights specifically the synthetic methodologies employed for the preparation of AEMs using a variety of functional precursors.[740] Before discussing the specific literature examples of AEMs, it is useful to introduce several concepts that are integral to the design of polymers for AEMFCs.

6.2.1. Film Formation. The most basic property required of a polymer membrane for AEMs is to form a mechanically robust film. Film formation is dependent on the inherent properties of the polymer such as type of backbone, molecular weight (MW), glass transition temperature (T_g), crystallinity, and presence of cross-linkers or plasticizers as well as processing conditions. For example, the film-forming properties and mechanical integrity of low-MW polymers tend to be poor resulting from the lack of chain entanglement necessary to resist deformation. While crystalline domains in polymers typically improve mechanical properties, though there has not been extensive investigation into the direct impact of crystallinity on AEM performance. One report by Treichel et al. has posited that crystallinity in a series of phosphonium-based ROMP norbornene polymers can impact WU.[777] However, pre- and postprocessing steps (cross-linking, annealing, and mechanical deformation) will affect the final polymer membrane, and therefore, it is difficult to examine the impacts of crystallinity on both film formation and membrane properties.

Solvent casting requires the polymer system to be soluble, preferably in a wide array of solvents to yield the best chance of film formation. Choosing solvents that evaporate too quickly can result in nonhomogeneous film formation due to the kinetics of mass transport at the solvent interface.[781] Therefore, medium- to high-vapor-pressure solvents (e.g., chlorobenzene, tetrachloroethane, DMSO[753]) are used to better control this phenomenon in cationic AEMs. Some methods to produce cationic membranes utilize postpolymerization functionalization (PPF) on already cast films. In this case, a broader array of solvents may be used to cast polymers, as cationic polymers tend to be less soluble than their unfunctionalized precursors. Solution viscosity is another parameter used to control the thickness and homogeneity of a polymer film—important qualities for obtaining reproducible results. Other more sophisticated techniques such as tape casting, dip-coating, slot-die coating, and spin-coating may also be used to generate large-area and homogeneous membranes. However, each technique has its own challenges and set of parameters to optimize but can be useful with proper knowledge of polymer solution properties.

Cross-linking will increase the mechanical strength (e.g., modulus, elongation at break, stress at break) of a polymer by the formation of rigid networks. Furthermore, cross-linking will prevent the swelling of polymers and is a straightforward way to reduce deleterious effects of water in AEMs. However, too much cross-linking may lead to mechanical failure and materials unfit for AEMFC implementation. There are many chemistries that can be utilized to synthesize cross-linked materials such as Diels−Alder, radical-based thiol−ene click chemistry, or UV-promoted cross-linking with a UV-sensitive molecule appended to the polymer scaffold or added to initiate cross-linking postpolymerization. However, each method of functionalization also necessitates the investigation of alkaline stability to ensure that the cross-linking moieties do not degrade or undergo further reaction at long periods of time at high pH. Another popular method in the AEM field is cross-linking using a difunctional molecule or polymer that will react at pendant groups along the polymer chain to form a cross-linked network. The judicious choice of cross-linking moieties can even aid in hydroxide transport by selecting a functionality that will produce cationic groups and cross-link simultaneously. Kohl and coworkers have used this technique frequently[782,783] by reacting *N*,*N*,*N*,*N*-tetramethylhexamethylenediamine (TMHDA) with pendent alkyl halides in a postpolymerization casting method to produce a cross-linked polymer membrane and further add cation content to increase the IEC of the resultant material.

Reactive casting incorporates a cross-linker or modifier during polymerization to create robust films. Cross-linked AEMs are typically fabricated in a two-step process: (1) casting the polymer membrane containing a cross-linking moiety either tethered to the polymer or added as a small molecule additive and (2) using some external stimuli (e.g., heat, light, pH) to induce cross-linking of the polymer membrane. Coates and coworkers routinely use this technique in the synthesis of cross-linked polyolefin-based AEMs by ring-opening metathesis polymerization (ROMP).[772,784,785] For example, the

https://doi.org/10.1021/acs.chemrev.1c00331
Chem. Rev. XXXX, XXX, XXX−XXX

addition of dicyclopentadiene to a mixture of functional norbornene monomers allows for cross-linking to take place during polymerization and can be carried out in a casting dish to yield mechanically rugged membranes in one step.[785] While this method is useful for the rapid fabrication of homogeneous cross-linked membranes, this method only allows for one attempt at making a film due to the irreversible cross-linking reaction. Further batch-to-batch variation can arise due to incomplete mixing or diffusion-limited mass transport during the polymerization/cross-linking reaction. Conversely, plasticizers will promote polymer processability by effectively decreasing the T_g of the polymer membrane.[786] This will allow easier handling when using processing techniques such as melt processing which necessitates a lower T_g to fabricate films. Therefore, much consideration must be taken into the synthetic design of polymers to promote the many aspects that contribute to film formation and other polymer properties.

Lastly, melt pressing is a common technique to fabricate films that are generally insoluble. This technique applies pressure to a polymer sample using two heated plates. Polymers processed in this way are required to have a lower melting transition temperature (T_m) and T_g to induce segmental motion when pressure is applied. PE-based polymers tend to be insoluble and can be processed in this manner, but melt pressing can be utilized in a wide array of systems that have amenable thermal properties.

6.2.2. Thermomechanical Properties. Favorable thermal properties of AEMs are important for processing into films, mechanical integrity, and potentially hydroxide transport. While there have not been any studies that directly show the link between T_g, crystallinity, or mechanical behavior on hydroxide transport, these factors should be considered in tandem with transport characteristics. Many methods exist to characterize thermal and thermomechanical properties of AEMs, such as differential scanning calorimetry (DSC), thermogravimetric analysis (TGA), dynamic mechanical analysis (DMA), rheology, and tensile testing. DSC is typically used to elucidate thermal transitions of polymers [i.e., T_g, T_m, and crystallization temperature (T_c)], and characterize crystallinity in polymers. However, Kohl and coworkers have demonstrated the use of DSC to further characterize swelling properties by running experiments on a hydrated sample, lowering the temperature below the freezing point of water, and measuring the enthalpy arising from unbound water in the membrane.[787] Using DSC, "unproductive" free water (water not bound to a cation) can be quantified and help describe ion transport phenomena in terms of swelling behavior. TGA is used to quantify the thermal stability of polymers by measuring the mass loss as a function of temperature. Most reports use the temperature at which 5% of the polymer mass is lost as the metric to report thermal stability. DMA, rheology, and tensile testing are primarily used to understand the mechanical integrity of dry and, more importantly, hydrated films to consider the viability of AEMs during fuel cell operation.

6.2.3. Morphology. One aspect of AEMs that should be further investigated is the effect of microphase separation and the resulting morphology of the polymer on conductivity. A few reports have shown that multiblock copolymers are advantageous for hydroxide transport, due to the formation of ordered phases that facilitate ion transport. It is difficult to systematically study morphological effects on hydroxide transport, although it is thought that a bicontinuous morphology will greatly enhance transport. Small-angle X-ray scattering (SAXS) and scanning transmission electron microscopy (STEM) (section 8) analyses of polymers currently used as AEMs have shown the presence of ionic aggregates. Polymer morphology offers a way to tune polymer properties and ion transport behavior, and its effects on AEM performances must be studied further. Lin and coworkers recently reviewed the effects of microphase separation in AEMs and provide further insight into the work and specific challenges associated with the implementation of block copolymer AEMs.[788]

6.2.4. Poly(arylene) (PA) Backbones. Poly(arylene) (PA) backbones such as poly(terphenylenes) (PTPs), poly(biphenylenes) (PBPs), poly(arylene imidazoliums), poly(benzimidazoles) (PBIs), and poly(fluorenes) (FLNs) have been of interest for use in AEMs as they are great film-formers and can be easily synthesized through polycondensation[742,753,754] or metal-catalyzed couplings[774] followed by PPF to incorporate cations. Many studies on arylene backbones have investigated the impact of polymer backbone structure, cross-linking, and cation linker length on membrane properties such as microphase separation and ion conductivity. Understanding the relationships between polymer architecture, morphology, and membrane properties will be critically important in making advancements in AEM performance.

6.2.4.1. Poly(phenylenes) (PPs). In a study of *m*-PP1, *p*-PP1, and PP2-65, depicted in Figure 42, Bae and coworkers explored the influence of polymer backbone structure on the morphology and conductivity of polyphenylene membranes substituted with trimethylammonium via alkyl linkers.[789] All three membranes demonstrated significant alkaline stability

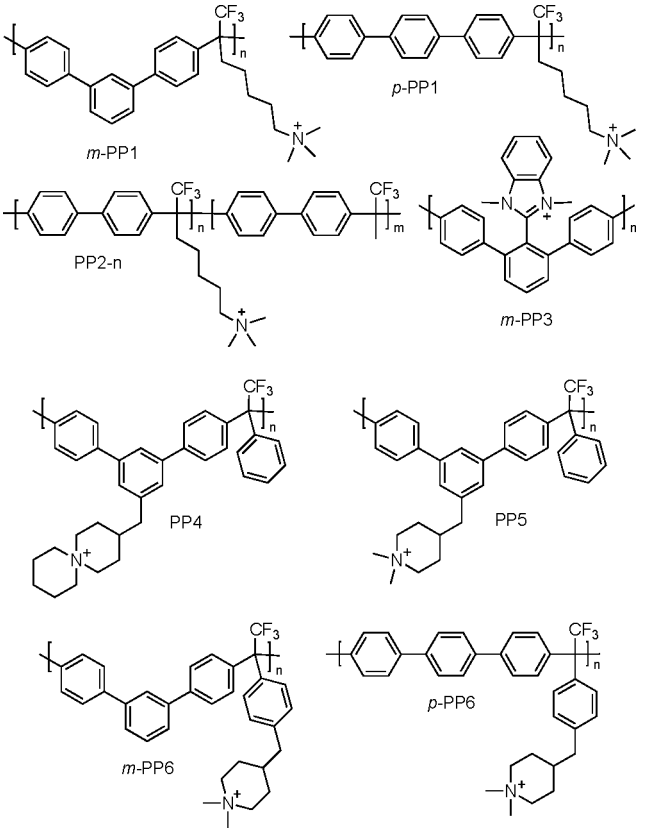

Figure 42. Naming scheme for poly(phenylene)s; counteranions omitted for clarity.

https://doi.org/10.1021/acs.chemrev.1c00331
Chem. Rev. XXXX, XXX, XXX−XXX

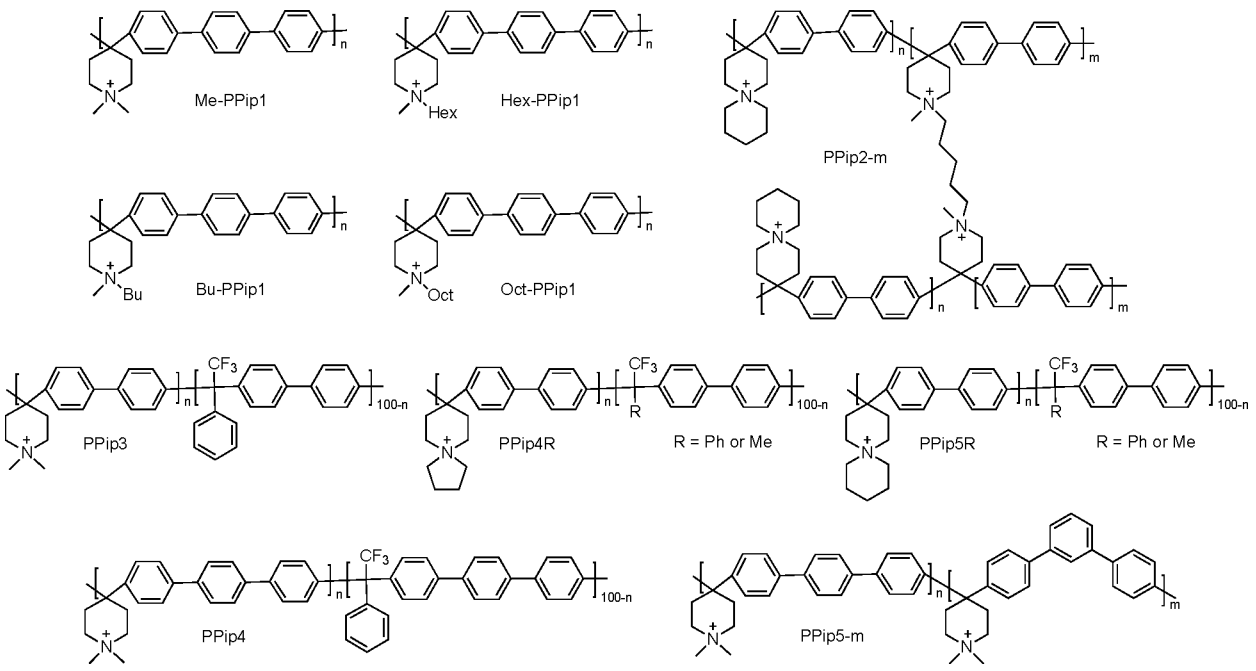

Figure 43. Naming scheme for poly(*p*-terphenyl-piperidinium)s and poly(biphenyl-piperidinium)s; counteranions omitted for clarity.

with negligible signs of degradation after 720 h in 1 M NaOH at 95 °C. Despite having similar IECs, *m*-PP1, *p*-PP1, and PP2-65 displayed conductivities of 112, 81, and 88 mS/cm at 80 °C, respectively. However, there was only a slight difference between *m*-PP1, *p*-PP1, and PP2-65 when compared in MEAs with relatively low peak power densities (PPDs) of 0.20, 0.15, and 0.16 W/cm^2,[790] respectively, which may be due to the need for MEA optimization. General MEA fabrication and optimization are further discussed in section 7.1. The higher conductivity and PPD for *m*-PP1 may be attributed to the microphase separation and polymer self-assembly that was observed by SAXS, wide-angle X-ray scattering (WAXS), and transmission electron microscopy (TEM), which was not observed for *p*-PP1 or PP2-65.[789]

Jannasch and coworkers further investigated the effects of backbone structure and cation placement through a series of spirocyclic and piperidinium-substituted poly(terphenyl alkylene)s.[753] While monomers that are able to form spirocycles are typically challenging to obtain, the monomers in this report were synthesized in three steps. Polycondensation of the monomers followed by quaternization of the resulting polymers produced PP4, PP5, *m*-PP6, and *p*-PP6 shown in Figure 42. The conductivity of PP5 was twice as high as that of PP4 with 107 and 51 mS/cm at 80 °C, respectively, demonstrating that piperidiniums give rise to higher conductivity through a combination of higher IEC and clustering of the cations observed by SAXS. *m*-PP6, with the cation placed on the trifluoroacetophenone unit, demonstrated the highest hydroxide conductivity of the membranes with 146 mS/cm at 80 °C, showing that the placement of the cation on the polymer backbone can make a substantial difference in performance. The comparison of *m*-PP6 to *p*-PP6 demonstrates how backbone rigidity influences conductivity, as *p*-PTP backbones are more rigid than *m*-PTPs, which lead to a drop in conductivity to 103 mS/cm at 80 °C, in the same way Bae observed a drop in conductivity from *m*-PP1 to *p*-PP1.[789] Flexibility is important for promoting ion mobility and can be induced through choice of cation, backbone placement, and backbone structure.

Additionally, incorporating the piperidinium into the rigid polyarylene backbone, giving poly(*p*-terphenyl-piperidinium)s, resulted in generally lower hydroxide conductivities despite higher IECs.[791] Of the piperidinium substitutions, two *N*-methyl groups (Me-PPip1), a *N*-methyl and a *N*-butyl (Bu-PPip1), *N*-hexyl (Hex-PPip1), or *N*-octyl (Oct-PPip1) (Figure 43), Hex-PPip1 demonstrated the highest conductivity, outperforming the pendant cation analogue (*p*-PP6) with 47.9 and 38 mS/cm, respectively, at 20 °C. The higher conductivity observed may be in part due to the change in morphology observed for the polymers substituted with long alkyl chains. While Me-PPip1 did not have the highest conductivity with 36.9 mS/cm at 20 °C and 89 mS/cm at 80 °C, it did display the highest stability, with less than 10% cation degradation after 720 h in 2 M NaOH at 90 °C. These materials largely degraded by ring-opening elimination, likely owing to the rigid polymer backbone destabilizing the piperidinium by locking it into unstable conformations.

Me-PPip1 was also synthesized by Zhuang and coworkers (Figure 43) giving hydroxide conductivities of 49 and 137 mS/cm at 30 and 80 °C, respectively.[792] The higher observed conductivity may be in part due to the method of measurement, as Jannasch measured the conductivity with the membrane immersed in degassed water that was under nitrogen before the measurement,[791] while Zhuang measured the membrane in a realistic fuel cell test fixture with a feed of humidified N_2 to avoid any interference from CO_2 on the measurement.[792] A higher alkaline stability was also observed with only 4% and 16% cation degradation observed after 5040 h in 1 and 3 M NaOH at 80 °C, respectively. A high performance and stability were achieved when Me-PPip1 was employed in an MEA with a PPD of 1.45 W/cm^2 at 3.0 A/cm^2 with H_2/O_2 and 125 h of stable operation at 0.62 V with H_2/CO_2-free air at 80 °C.

Similar polymer structures were synthesized by Yan and coworkers via polycondensation of trifluoroacetophenone and

https://doi.org/10.1021/acs.chemrev.1c00331
Chem. Rev. XXXX, XXX, XXX−XXX

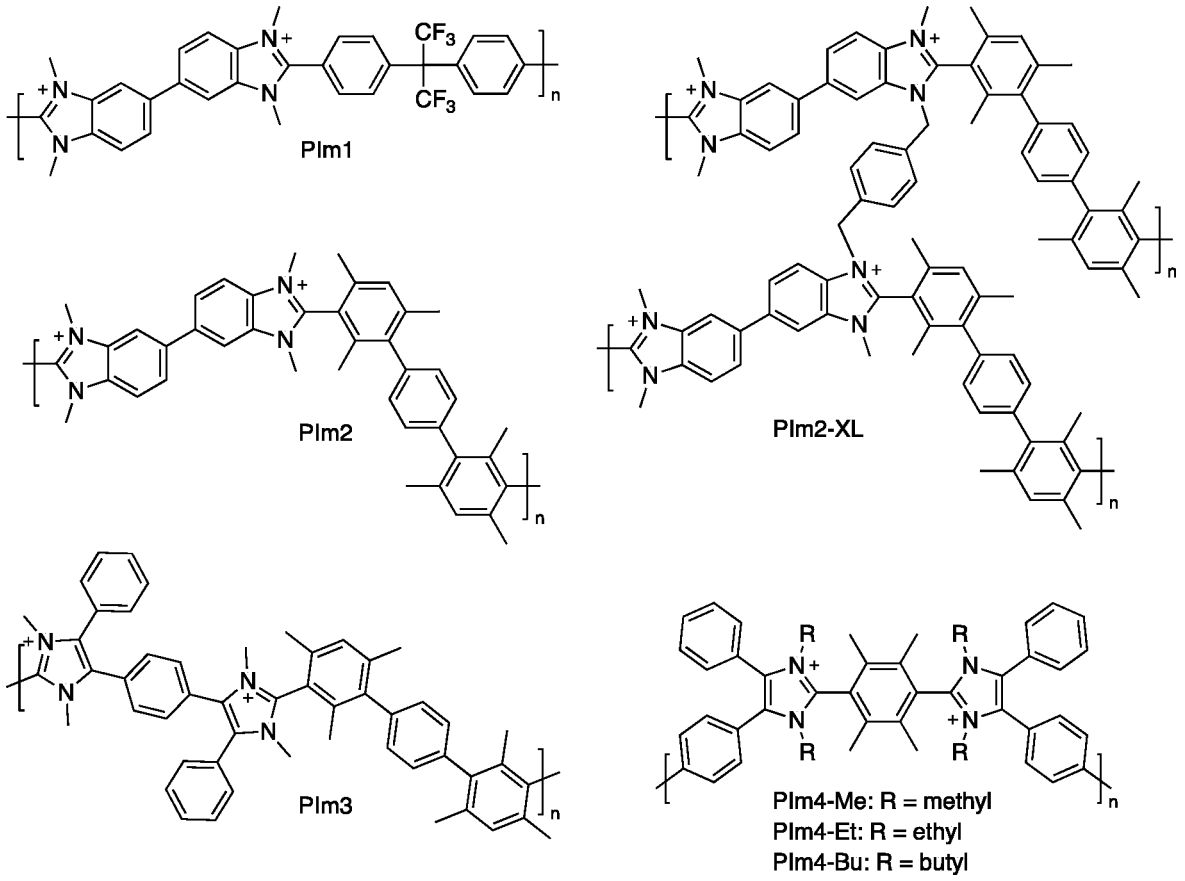

Figure 44. Naming scheme for poly(arylene benzimidazoliums) and poly(arylene imidazoliums); counteranions omitted for clarity.

N-methyl-4-piperidone with biphenyl or *p*-terphenyl to produce a series of PPip3-*n* and PPip4-*n* copolymers,[793] where *n* is the number of cationic units (Figure 43). The introduction of trifluoroacetophenone allows for higher molecular weights and tunable IECs by varying the comonomer feed ratio. PPip4-85 achieved the highest conductivities of the polymers studied in the series with 78 mS/cm at 20 °C and 193 mS/cm at 95 °C, despite having a similar IEC to PPip3-70. Additionally, there was no observed conductivity loss for PPip4-85 after 2000 h in 1 M KOH at 100 °C, demonstrating that this material is not only highly conductive but also highly alkaline-stable. An MEA was assembled with MPBP-100-BP as the ionomer, due to its solubility in IPA/H_2O solutions, and with PPip4-85 as the membrane. The resulting MEA achieved a PPD of 0.92 W/cm^2 at 95 °C in H_2/CO_2-free air mode. When subjected to 0.5 A/cm^2 at 95 °C, the MEA had a voltage loss of 11.5% after 250 h of operation.

A series of *N*-spirocyclic poly(biphenyl-piperidinium)s were synthesized by Jannasch and coworkers using the same polycondensation method with trifluoroacetophenone or trifluoroacetone.[754] All of the membranes with IECs of 1.81−2.00 demonstrated similar conductivities at 80 °C between 94 and 102 mS/cm despite PPip4Ph and PPip5Ph having WUs twice those of PPip4Me and PPip5Me. The spirocyclic piperidinium incorporated into PPip5Ph and PPip5Me has demonstrated excellent stability in model compound studies, but incorporation into the rigid biphenylene backbone promoted Hofmann elimination, as evidenced by the significant degree of degradation after 720 h in 2 M NaOH at 90 °C, which was favored at the ring directly attached to the polymer opposed to the pendant ring of the spirocyclic ammonium.

Conversely, when Zhu et al. made a series of *N*-spirocyclic poly(biphenyl-piperidinium)s, it was found that there was only 5−9% cation degradation after 2000 h in 3 M NaOH at 80 °C, with attack occurring at the pendant and backbone rings.[794] In this system, the cross-link density was varied without changing the IEC by implementing a cationic cross-linking architecture, PPip2-*m* in Figure 43 where *m* is the percent cross-linking. Membranes were synthesized with 0%, 4.2%, 8.4%, and 15% cross-linking. They found that WU and degree of swelling decreased as a function of increasing cross-link density, where the non-cross-linked membrane fractured during the measurements, and the cross-linked membranes remained intact. Interestingly, the PPip2-8.4 membranes demonstrated the highest conductivity with 116.1 mS/cm at 80 °C. The authors attributed this finding to the distinct microphase separation detected by TEM and atomic force microscopy (AFM) for PPip2-8.4, while they propose that conductivity was lower in PPip2-15 due to the extreme surface-phase separation observed by AFM. The low MEA performance observed for PPip2-8.4, with a PPD of 0.087 W/cm^2, was attributed to a high ohmic resistance for the membrane, indicating that further membrane optimization is necessary, but the membrane demonstrated promising conductivity and stability.

Mayadevi et al. synthesized a series of poly(terphenylpiperidinium)s with varying ratios of *para*-terphenyl and *meta*-terphenyl units in the backbone (PPip5-m).[795] With equal *para*-terphenyl and *meta*-terphenyl incorporation, PPip5-50

https://doi.org/10.1021/acs.chemrev.1c00331
Chem. Rev. XXXX, XXX, XXX−XXX

demonstrated a hydroxide conductivity of 53.5 mS/cm at 20 °C and 130 mS/cm at 80 °C, which was higher than the conductivities exhibited by PPip5-20 and PPip5-60 despite having similar experimental IECs. PPip5-50 also had the most pronounced SAXS diffraction patterns attributed to a long-range-ordered morphology and continuous ionic channels which may have given rise to the enhanced conductivity. AFM showed that the size of the ionic domains in the membranes increased with increasing *meta*-terphenyl unit incorporation because the kinked structure of the *meta*-terphenyl induced more free volume in the membrane than the *para*-terphenyl units. The finding that equal incorporation of *meta*-terphenyl and *para*-terphenyl units gave the best membrane is interesting as Bae[789] and Jannasch[764] both found that poly(*m*-terphenylene)-based membranes gave the highest conductivity in their respective systems. Given these findings, a study comparing the performance of poly(*m*-terphenylene-piperidinium) and combinations of *meta*-terphenyl and *para*-terphenyl in other systems would be beneficial.

6.2.1.2. Poly(arylene imidazoliums). In order to append benzimidazoliums to a poly(*m*-terphenylene) backbone (*m*-PP3), Holdcroft and coworkers synthesized a monomer through the cross coupling of a C2-2,6-dibromophenyl-substituted benzimidazole with (4-chlorophenyl)boronic acid.[774] The monomer was polymerized via Yamamoto coupling, and the resulting polymer was methylated to produce an extremely strong cationic membrane with a tensile strength of 72 MPa and IEC of 2.56 mequiv/g that exhibits a modest hydroxide conductivity of 13.2 mS/cm. There was only 5% degradation observed after the membrane was soaked in 2 M KOH at 80 °C for 168 h. This membrane was synthesized in six steps to produce benzimidazolium-substituted AEMs with modest conductivity and reasonable stability.

While cations are often tethered to the polymer backbone, they can also be incorporated into the backbone. Holdcroft also synthesized a series of poly(arylene benzimidazoliums) depicted in Figure 44, where PIm2 with a degree of quaternization (dq) of 92% gave a hydroxide conductivity of 9.7 mS/cm,[796] and with 95% dq, a chloride conductivity of 15 mS/cm was observed.[773] Chloride conductivity was measured to avoid any bicarbonate formation that can interfere with hydroxide conductivity measurements. However, if the 95% dq membrane was heated above 22 °C or if 100% of the nitrogen atoms were methylated, the membrane became water-soluble at 22 °C, demonstrating the need for a balance between maximizing IEC and retaining mechanical integrity. Cross-linking was used to enhance the mechanical integrity of the higher IEC membranes giving PIm2-XL. With 15% cross-linking and a total dq of 95% and 100%, the chloride conductivities achieved at 80 °C were 30 and 35 mS/cm, respectively. While the membranes were mechanically robust, they lost 85−95% of their conductivity after exposure to 3 M KOH at 80 °C, demonstrating the need for a more alkaline-stable alternative.

Pentasubstituted imidazolium cations show higher stabilities than benzimidazoliums in model compound studies and were chosen for incorporation into poly(arylene) scaffolds. A poly(arylene imidazolium) (PIm3) film was synthesized by Holdcroft through microwave polycondensation of bisbenzil, a dialdehyde monomer, and an excess ammonium acetate followed by methylation of the resulting imidazole groups.[742] The PIm3 film was insoluble in water at 25 °C, but at 80 °C, the membrane slowly dissolved. In basic aqueous solutions (10 M KOH), the film was not soluble up to 100 °C, and no degradation was observed after 168 h. When PIm3 was applied in an MEA, the 20 μm thick membrane achieved a PPD of 0.82 W/cm^2 at 1.8 A/cm^2, and the hydroxide conductivity was estimated to be 280 mS/cm from the high frequency resistance (HFR). After 10 h of operation, excess swelling and partial dissolution of the membrane caused a decreased performance.

Holdcroft then implemented bis-imidazoliums in the poly(arylene imidazolium) backbone and found that the *N*-methyl-substituted imidazolium (PIm4-Me) membranes gave the highest chloride conductivity of 32.7 mS/cm.[741] This is likely due to a high IEC of 2.86 mequiv/g, but only 66% cation remained after 240 h at 80 °C in 10 M NaOH. This membrane also had the highest tensile strength (75 MPa) of the membranes synthesized for the study. PIm4-Bu gave a chloride conductivity of 8.5 mS/cm but had 98% cation remaining under the same conditions and achieved a PPD of 0.25 W/cm^2 at 70 °C. X-ray scattering of PIm4-Me revealed ∼4, 8, and 16 nm^{-1} peaks corresponding to monomer−monomer spacing, anion−anion spacings, and anion−imidazolium spacings, respectively. It was observed from the X-ray scattering that as *N*-alkyl chain length increased the distance between the imidazolium and the counteranion decreased which was consistent with their X-ray diffraction (XRD) results for the imidazolium model compounds.

6.2.4.3. Poly(benzimidazoles). Ding and coworkers were unable to form films from PIm1, a polymer similar in structure to PIm2, but incorporating long-chain linkers to imidazolium cations led to better film formation and higher conductivities than PIm2.[797] AFM was used to study the morphology of membranes composed of PBI backbones with either an *n*-propyl (PBI1) or hexyl (PBI2) linker to an imidazolium. It was observed that longer alkyl chains separating the backbone from the cation better promoted phase-separated morphologies allowing for larger ionic clusters. This finding was confirmed by SAXS where interdomain Bragg spacings of 2.91 and 5.51 nm were observed for (PBI1) and (PBI2), respectively. The larger ionic clusters likely aided in hydroxide transport as PBI2 demonstrated a higher conductivity and PPD than PBI1 despite having a slightly lower IEC. Both membranes lost ∼12% conductivity after 240 h in 2 M KOH likely due to degradation of the imidazolium cation. When exposed to Fenton's reagent at 60 °C for 120 h there was ∼15% weight loss observed, indicating that the polymer is susceptible to degradation by oxidation, which has been shown to induce a loss of performance in MEAs.[798]

Ding and coworkers went on to prepare nanocomposite AEMs composed of PBI with imidazolium-functionalized graphene oxide.[799] Moving the cation from the polymer backbone to dispersed nanoparticles (NPs) resulted in higher conductivity with ∼50 mS/cm at 20 °C compared to the ∼17 mS/cm observed for PBI1. The composite membrane lost ∼15% of its conductivity after 200 h in 2 M KOH at 60 °C, which is a higher conductivity loss in less time compared to PBI1. PBI backbones with cobaltocenium cations embedded synthesized by Chen et al. achieved moderate hydroxide conductivities and stabilities.[800] Of the various backbone modifications studied, PBI3, depicted in Figure 45, demonstrated the highest conductivity with 33 mS/cm at 80 °C which is around half that of PBI2. PBI3 exhibited a conductivity loss of 15−20% after 672 h in 1 M KOH at 60 °C, with degradation observed on the cobaltocenium ring and on the benzimidazolium ring.

https://doi.org/10.1021/acs.chemrev.1c00331
Chem. Rev. XXXX, XXX, XXX−XXX

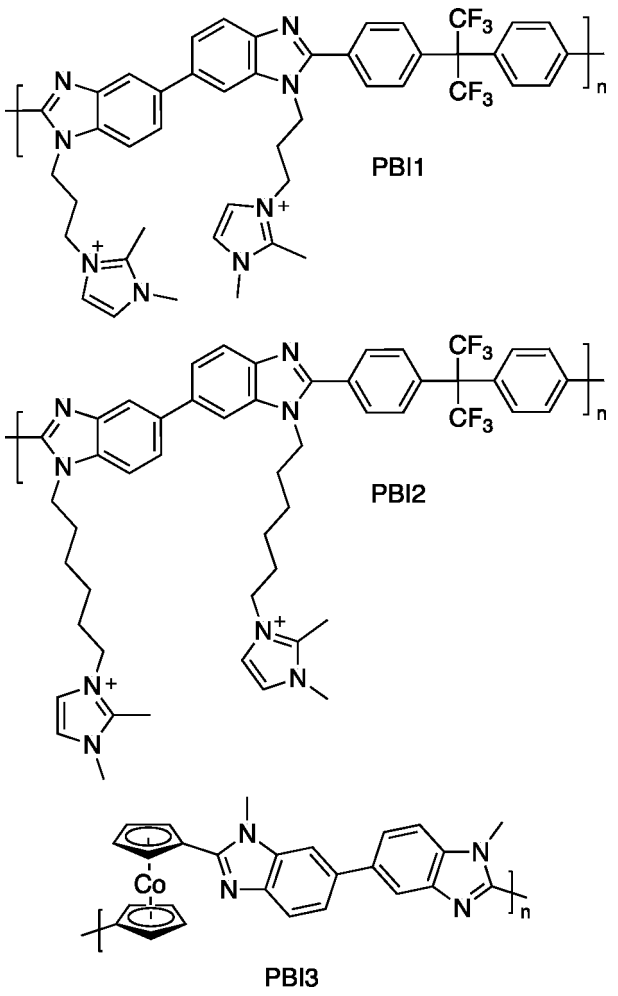

Figure 45. Naming scheme for poly(benzimidazoles); counteranions omitted for clarity.

6.2.4.4. Poly(fluorenes). Poly(fluorenes) (FLNs) are another promising polymer backbone structure for AEMs as they are easily synthesized, solvent processable, and alkaline-stable and have lower deleterious catalyst interactions compared to poly(phenylenes). Kim and coworkers demonstrated that FLN polymer structures reduce the effects of phenyl group adsorption on the surface of electrocatalysts compared to poly(phenylenes) due to the nonrotatable nature of the FLN backbone.[801] As an ionomer, FLN1 induced higher MEA performances than PBP with PPDs of 1.0 and 0.37 W/cm^2, respectively, when paired with an *m*-PTP membrane despite the ionomers having similar IECs and hydroxide conductivities. They found that the MEA performances correlated well with the calculated adsorption energies for each of the backbone structures, indicating that adsorption is a likely cause of the loss of performance.

Bae and coworkers employed a palladium-catalyzed Suzuki coupling to synthesize FLN4, FLN2, and FLN3[802] depicted in Figure 46. These AEMs demonstrated low swelling ratios, moderate water WUs, and good hydroxide conductivities and stabilities. FLN4 demonstrated the highest conductivity with 124 mS/cm at 80 °C with a high IEC of 3.56 mequiv/g. The aggregation of ions resulting from the high IEC likely caused the FLN4 membrane to become fragile after 168 h in 1 M NaOH at 80 °C despite there being no observable chemical degradation even after 720 h.

In order to access higher molecular weights, Miyanishi and Yamaguchi used polymerization via palladium-catalyzed C−H activation to synthesize a series of polymers similar to FLN4 with tetrafluorophenyl groups in the backbone and a variety in the size of linker to the trimethylammonium group.[803] FLN5-Hex achieved a hydroxide conductivity of 156 mS/cm at 70 °C, 32 mS/cm higher than FLN4 despite having a lower IEC and being measured at a lower temperature. This finding indicates that fluorination of the phenyl component of the backbone promotes hydroxide conductivity. There was 14% conductivity loss after 168 h in 8 M NaOH at 80 °C, and it was found by NMR that the quaternary ammonium signals did not change. Instead, backbone degradation from fluoride displacement by hydroxide was observed with possible subsequent cross-linking from aryl-ether formation. While others have found that longer alkyl chain linkers can lead to higher conductivity,[797] FLN5-Hex, with the shortest alkyl linker, had the highest conductivity likely owing to the higher IEC.[803] The differences in conductivity with linkers of 6−10 carbons may also just differ less than linkers varying between 1−6 carbons.

Ono et al. also synthesized FLNs with a fluorinated comonomer; in this case, a dimethylamine-functionalized fluorene was copolymerized with (perfluorohexane-1,6-diyl)-dibenzene as the perfluorinated alkylene units can provide greater membrane flexibility and solubility.[804] After quaternization of the amines with iodomethane, the polymer was solvent cast to produce FLN6 as a very flexible film, especially for those composed of aromatic backbones, as exemplified by the origami bird folded from it.[804] More quantitatively, FLN6 with an IEC of 0.75 mequiv/g was able to achieve an elongation at break of 414%. The highest maximum stress was achieved by the membrane with an IEC of 1.47 mequiv/g with 22.7 MPa. This membrane also demonstrated the highest hydroxide conductivity with 47.8 mS/cm at 30 °C and 86.2 mS/cm at 80 °C, despite not having the highest IEC of the series. This finding demonstrates the need to balance membrane properties with cation density; it is predicted that the excessive WU observed for the membrane with a higher IEC caused the decrease in conductivity. The FLN6 membranes demonstrated excellent stability as there was no conductivity loss after 1000 h in 1 M KOH at 80 °C, where the polyphenylene analogue lost all conductivity. In an MEA test, FLN6 with an IEC of 1.84 mequiv/g was able to reach a PPD of 0.515 W/cm^2 and only had a potential loss of 0.26 V after 1067 h of operation at 0.02 A/cm^2. While the MEA demonstrated great stability, higher current densities are typically required for stability studies (>0.2 A/cm^2) which should be taken into account when comparing MEA stability results.

Yang et al. synthesized a series of polymers with biphenyl and fluorene segments through the polycondensation of 9,9-bis(5-bromopentyl)-fluorene with biphenyl and trifluoroacetone.[779] The resulting polymers were then substituted with trimethylammonium (FLN7-TMA) or bulky imidazoliums (FLN7-Im4Me and FLN7-Im4Ph). FLN7-TMA demonstrated the highest conductivity with 78 mS/cm at 30 °C compared to 50 and 7 mS/cm for FLN7-Im4Me and FLN7-Im4Ph, respectively. This conductivity trend is likely due to the difference in IEC for the membranes, but the IECs of FLN7-Im4Me and FLN7-Im4Ph are quite similar, 1.49 and 1.36, respectively. However, there is a drastic difference in conductivity, suggesting that more than just IEC is playing a role. FLN7-Im4Me had a WU of 100%, while FLN7-Im4Ph had a WU of 28% and was very brittle, and the higher WU in

https://doi.org/10.1021/acs.chemrev.1c00331
Chem. Rev. XXXX, XXX, XXX−XXX

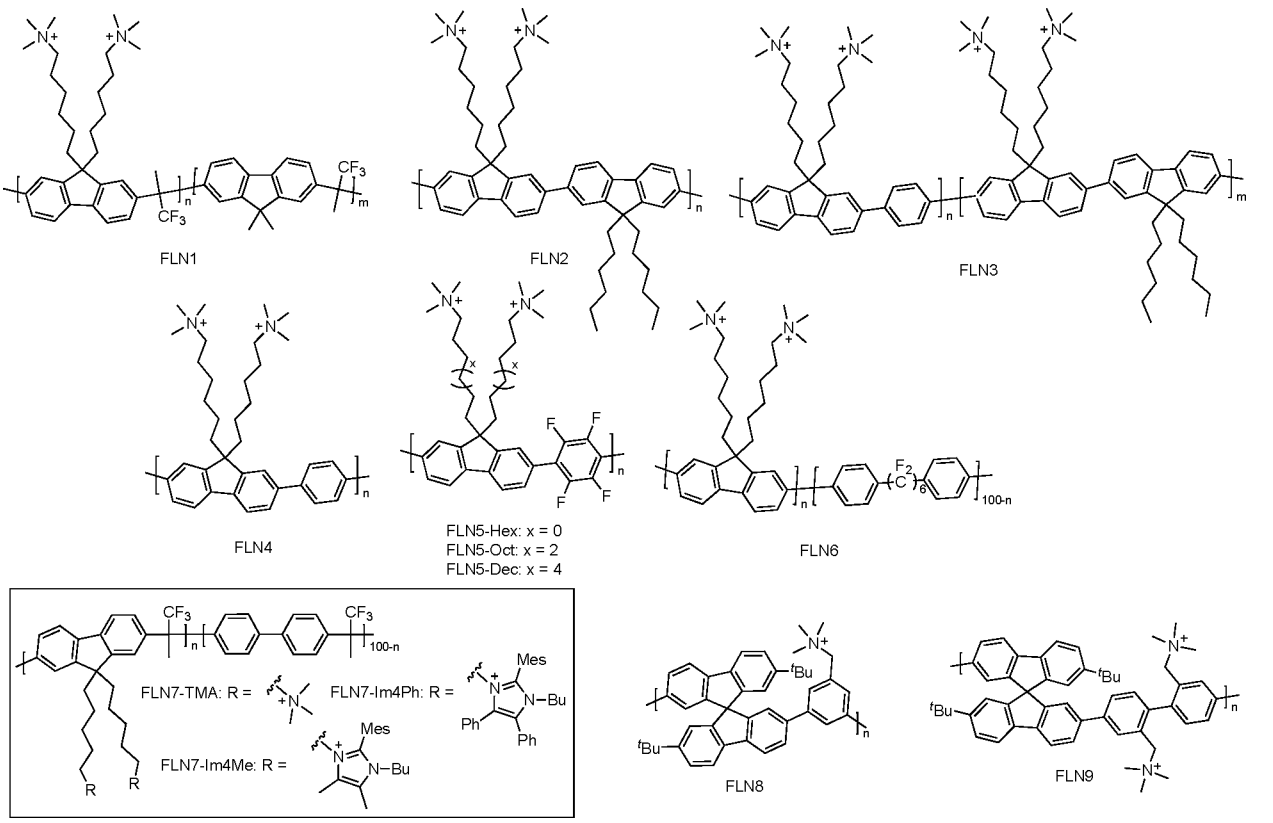

Figure 46. Naming scheme for poly(fluorenes); counteranions omitted for clarity.

FLN7-Im4Me may have allowed for better hydroxide transport. All three membranes retained their conductivity after 720 h in 2 M NaOH at 80 °C, demonstrating excellent stability. When implemented in an MEA, FLN7-TMA and FLN7-Im4Me produced PPDs of 0.610 and 0.032 W/cm^2, respectively. While FLN7-TMA demonstrated a moderately high PPD, it was unstable when held at a constant current density of 0.2 A/cm^2 at 60 °C, after 71 h, the PPD dropped to 0.235 W/cm^2, and degradation of the ammonium by ylide formation and Hofmann elimination was detected. If the FLN7-Im4Me MEA can be optimized to produce higher PPDs, it may be a promising candidate in AEMs given its stability.

Spirobifluorene-based AEMs, FLN8 and FLN9, were synthesized by Miyanishi and Yamaguchi through a Suzuki−Miyaura coupling reaction followed by Wohl−Ziegler and Menshutkin reactions.[805] While polyaromatics can suffer from poor solubility, the resulting twisted structure disrupts polymer chain stacking, thus improving the polymer solubility and processability. Furthermore, this twisted structure can also promote chain entanglement which can lead to better film formation. Both membranes showed very low WUs likely due to the hydrophobicity of the polymer backbone. Despite the low WU, FLN9 demonstrated a moderately high hydroxide conductivity of 82.6 mS/cm at 70 °C. Moreover, the hydroxide conductivity of FLN8 and FLN9 is much lower than those of other fluorene AEMs with similar IECs.

6.2.4.5. Conclusion—Poly(arylene)s. Poly(arylene)-based membranes can be high-performance AEMs with hydroxide conductivities upwards of 100 mS/cm and PPDs up to 1.45 W/cm^2 (Table 6). However, this class of membranes can be quite brittle due to the rigid aromatic segments composing the backbone. Various strategies have been used to manipulate the mechanical properties such as varying the backbone structure through bonding (*meta* vs *para*), cross-linking, and the use of flexible comonomers. Additionally, aromatic backbones are prone to oxidation at the cathode[798], and phenyl group adsorption is the major limiting factor for MEAs employing polyaromatic-based membranes.[806] As such, polymer structures with less aromatic moieties should be investigated as they are more promising for producing membranes that will have long-term stability and performance when implemented in AEMFCs.

6.2.5. Polystyrene (PS) Backbones. Polystyrene (PS) is an attractive candidate for scalable AEM production. Commercially available PS can be easily substituted with cations in two steps using chloromethylation followed by a Menshutkin reaction. However, the rigidity of PS results in poor mechanical properties that may inhibit its utility. Cross-linking, copolymerization with softer comonomers, and polymer blending strategies can help to improve the mechanical properties and mitigate WU and swelling of PS-based membranes. Additionally, these strategies can be used to invoke advantageous changes in microphase separation, which can influence hydroxide transport.

Yang et al. have reported two PS membranes: one (PS1-BTMA) functionalized with BTMA and the other with 1,2-dimethylimidazolium (PS1-MeIm) (Figure 47).[757] To control swelling, the membranes were cross-linked with 10 mol % dichloro-*p*-xylene. Both membranes demonstrated a relatively low tensile strength <15 MPa and elongation at break <7%, demonstrating the need for a material with greater strength and flexibility. The membranes also displayed very low WUs (2−3%), causing the membranes to exhibit low conductivity. Even so, PS1-BTMA showed higher conductivity than PS1-

https://doi.org/10.1021/acs.chemrev.1c00331
Chem. Rev. XXXX, XXX, XXX−XXX

Table 6. Poly(arylene) Membrane Properties and Performances

entry	name	IEC, theoretical (experimental) (mequiv/g)	WU[a] (wt %)	dimensional change[a] (Δ*L*%)	hydroxide conductivity (mS/cm)	PPD (W/cm^2) [current density (A/cm^2)]	ref
1	*m*-PP1	(2.15)	70	NA[b]	54 at 30 °C; 112 at 80 °C	0.20 (0.36)	789
2	*p*-PP1	(2.12)	65	NA	43 at 30 °C; 81 at 80 °C	0.15 (0.31)	789
3	PP2-65	1.94	85	NA	41 at 30 °C; 88 at 80 °C	0.16	789, 790
4	PP2-100	2.70	124	NA	62 at 30 °C; 122 at 80 °C	NA	789
5	PP4	1.58 (1.57)	54 at 80 °C	NA	19 at 30 °C; 51 at 80 °C	NA	753
6	PP5	1.69 (1.71)	99 at 80 °C	NA	44 at 22 °C; 107 at 80 °C	NA	753
7	*m*-PP6	1.69 (1.73)	103 at 80 °C	NA	66 at 22 °C; 146 at 80 °C	NA	753
8	*p*-PP6	1.69 (1.82)	73 at 80 °C	NA	38 at 22 °C; 103 at 80 °C	NA	753
9	Me-PPip1	2.38 (2.42)	145	NA	36.9 at 22 °C; 89 at 80 °C	NA	791
10	Me-PPip1	2.49	145	10 at 80 °C	49 at 22 °C; 137 at 80 °C	1.45 (3.0)	792
11	Bu-PPip1	2.16 (2.21)	109	NA	32.9 at 22 °C; 84 at 80 °C	NA	791
12	Hex-PPip1	2.04 (2.08)	44	NA	47.9 at 22 °C; 111 at 80 °C	NA	791
13	Oct-PPip1	1.93 (1.98)	33	NA	29.3 at 22 °C; 61 at 80 °C	NA	791
14	PPip4-85	2.37	NA	NA	78 at 22 °C; (193) at 95 °C	0.92[d]	793
15	PPip4Me	2.00	90 at 22 °C; 187 at 80 °C	39 at 80 °C	102 at 80 °C	NA	754
16	PPip5Ph	1.94	100 at 22 °C; 220 at 80 °C	49 at 80 °C	94 at 80 °C	NA	754
17	PPip4Me	1.94	55 at 22 °C; 96 at 80 °C	25 at 80 °C	95 at 80 °C	NA	754
18	PPip5Ph	1.81	50 at 22 °C; 97 at 80 °C	21 at 80 °C	102 at 80 °C;	NA	754
19	PPip2	2.92 (2.34)	133	30	82 at 80 °C	NA	794
20	Ppip2-8.4	2.94 (2.39)	95	22	116 at 80 °C	0.09	794
21	PPip5-50	2.80 (2.49)	49	19	53.5 at 22 °C; 130 at 80 °C	0.17 (.41)	795
22	*m*-PP3	2.56	81	NA	13.2 at 22 °C	NA	774
23	PIm2	2.7	180	NA	9.7 at 22 °C	NA	796
24	PIm2	2.71	NA	NA	15[c] at 22 °C	NA	773
25	PIm2-XL	2.87	NA	NA	35[c] at 80 °C	NA	773
26	PIm3	2.61	82	NA	280 at 80 °C	0.82 (1.8)	742
27	PIm4-Me	2.86	48	45	32.7[c] at 22 °C	NA	741
28	PIm4-Et	2.65	28	26	21.3[c] at 22 °C	NA	741
29	PIm4-Bu	2.30	12	14	8.5[c] at 22 °C	0.25	741
30	PBI1	2.29	30	11	~17 at 22 °C	0.34	797
31	PBI2	2.09	37	16	20.1 at 22 °C; 63.4 at 80 °C	0.45	797
32	PBI-GO	2.27	40	10	~50 at 22 °C; ~70 at 80 °C	NA	799
33	PBI3	(1.92)	40	27	13 at 22 °C; 33 at 80 °C	NA	800
34	FLN1	2.5 (2.5)	180	60	110 at 30 °C; 120 at 80 °C	NA	801
35	*m*-PP1[e]	2.15	70 at 80 °C	NA	100 at 80 °C	1.46	801
36	FLN4	3.56 (3.61)	71	10	50 at 30 °C; 124 at 80 °C	NA	802
37	FLN2	2.44 (2.34)	25	5	21 at 30 °C; 48 at 80 °C	NA	802
38	FLN3	2.90 (2.89)	40	7	24 at 30 °C; 85 at 80 °C	NA	802
39	FLN5-Hex	3.0	41	30	90.2 at 40 °C; 156 at 70 °C	NA	803

https://doi.org/10.1021/acs.chemrev.1c00331
Chem. Rev. XXXX, XXX, XXX−XXX

Table 6. continued

entry	name	IEC, theoretical (experimental) (mequiv/g)	WU[a] (wt %)	dimensional change[a] (ΔL%)	hydroxide conductivity (mS/cm)	PPD (W/cm^2) [current density (A/cm^2)]	ref
40	FLN5-Oct	2.8	40	18	68.3 at 40 °C; 117 at 70 °C	NA	803
41	FLN5-Dec	2.6	34	10	58.7 at 40 °C; 101 at 70 °C	NA	803
42	FLN7-TMA	2.17 (2.15)	48 at 30 °C	26 at 30 °C	78 at 30 °C	0.61	779
43	FLN7-Im4Me	1.49 (1.51)	100 at 30 °C	26 at 30 °C	50 at 30 °C	0.03	779
44	FLN7-Im4Ph	1.36 (1.35)	28	NA	7 at 30 °C	NA	779
45	FLN6	1.47	105 at 30 °C	NA	47.8 at 30 °C; 86.2 at 80 °C	NA	804
46	FLN6	1.84	~190 at 30 °C	NA	~45 at 30 °C; ~80 at 80 °C	0.52 (0.93)	804
47	FLN8	(1.2)	11	12	23.1 at 70 °C;	NA	805
48	FLN9	(2.3)	25	26	86.2 at 70 °C	NA	805

[a]Measured at room temperature unless otherwise specified. [b]NA: not applicable. [c]Chloride conductivity. [d]Conducted with H_2/CO_2-free air. [e]MEA assembled with an *m*-PP1 membrane and an FLN1 ionomer.

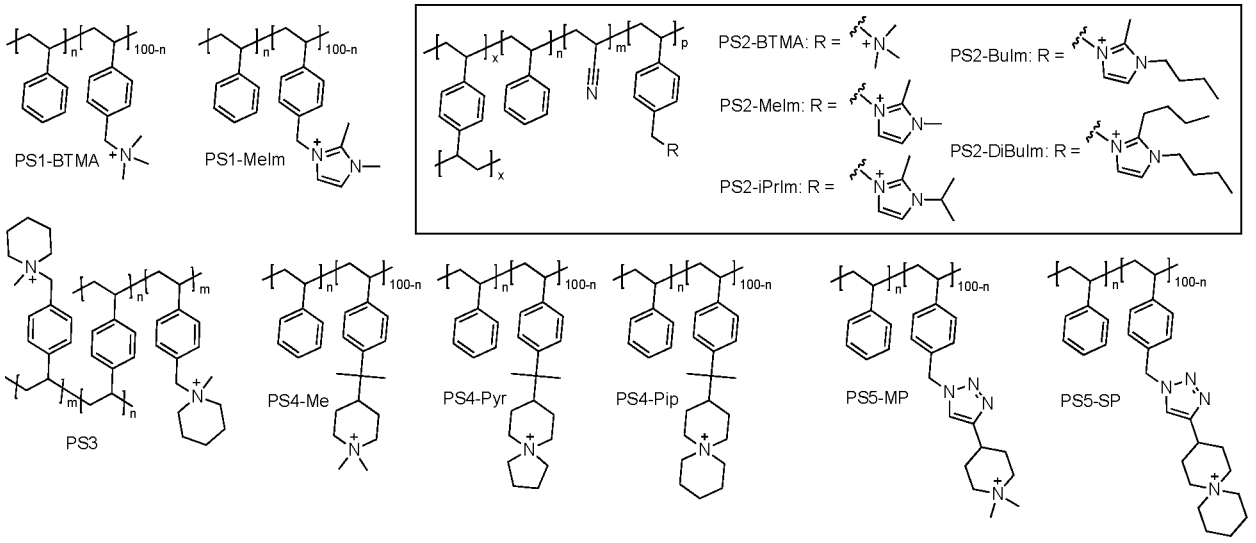

Figure 47. Naming scheme for polystyrenes; counteranions omitted for clarity.

MeIm with 18.9 and 11.6 mS/cm at 30 °C. When implemented in a direct methanol fuel cell, PS1-BTMA displayed a low PPD of 0.022 W/cm^2, and PS1-MeIm gave a negligible PPD of <0.001 W/cm^2. Some of the differences in performance may be due to the lower initial IEC of PS1-MeIm compared to PS1-BTMA (0.48 and 1.34 mequiv/g, respectively). When subjected to 1 M KOH at 60 °C, PS1-BTMA retained all of its conductivity and IEC after 800 h, while PS1-MeIm lost nearly half of its conductivity and 0.035 mequiv/g of its IEC after 90 h in the same conditions. Conversely, some studies by Yan and coworkers suggest that membranes functionalized with imidazoliums retain their conductivity, regardless of nitrogen substitution, better than membranes functionalized with BTMA.[758]

A series of cross-linked polystyrene/polyacrylonitrile AEMs were synthesized by Yan and coworkers via a photoinitiated copolymerization of styrene, acrylonitrile, cationic monomer, and divinylbenzene cross-linker.[758] Membranes using 2-dimethyl-3-butylimidazolium (PS2-BuIm), 2-dimethyl-3-isopropylimidazolium (PS2-iPrIm), and BTMA cations (PS2-BTMA) were synthesized in order to compare membrane performances. All three membranes have very similar properties: IEC values of 0.93−0.97 mequiv/g, WU values from 64% to 68%, dimensional swelling of 21−24%, and initial conductivities of 10.2−10.9 mS/cm at 30 °C and 15.3−15.8 mS/cm at 60 °C. This shows that if the IECs of the membranes are more similar, then there is no difference in conductivity between the BTMA and imidazolium-substituted membranes. After 600 h in 1 M NaOH at 80 °C, both imidazolium-based membranes retained 94% of the initial conductivity at 30 °C while the BTMA-substituted membrane only retained 59% conductivity. PS2-MeIm has an IEC value of 1.52 mequiv/g, and the membrane achieved a modest conductivity of 14.1 mS/cm at 30 °C.[767] The membrane retained its conductivity for 96 h in 1 M KOH at 80 °C. Exchanging the 1,2-dimethylimidazolium for a 1,2-dibutylimidazolium (PS2-DiBuIm) did not make any significant change in the conductivity or stability, but it showed an increase in the WU from 50% to 82%.[769]

As piperidinium-based model compounds showed high stability, Jannasch and coworkers employed a Friedel−Crafts alkylation to functionalize PS with dimethylpiperidinium (PS4-

https://doi.org/10.1021/acs.chemrev.1c00331
Chem. Rev. XXXX, XXX, XXX−XXX

Me) and two different spirocyclic ammoniums (PS4-Pyr and PS4-Pip).[752] There was little degradation observed for PS4-Me and PS4-Pip after 720 h in 2 M NaOH at 90 °C and only 13−25% cation loss after 240 h at 120 °C, demonstrating the excellent stability of these membranes. PS4-Pyr and PS4-Pip were functionalized to an IEC of 1.3 mequiv/g, and PS4-Me was synthesized with a range of IECs from 1.3 to 1.6 mequiv/g. While a higher IEC normally leads to a higher conductivity, in this case, PS4-Me (IEC = 1.4 mequiv/g) achieved the highest conductivity with 106 mS/cm at 80 °C. Increasing to an IEC of 1.6 mequiv/g leads to a drop in conductivity to 79 mS/cm at 80 °C, likely due to the excessive WU of 268% at this charge density. This demonstrates the need to balance maximizing IEC with retaining mechanical durability. At nearly identical IECs, PS4-Me demonstrated the highest conductivity followed by PS4-Pyr and then PS4-Pip, which trends with the WU of each membrane, again showing how WU greatly influences hydroxide transport in these systems. When PS4-Me was blended with PBI to mitigate the WU and provide additional mechanical integrity to the weak membranes, a 28−64% drop in WU was observed, as expected, which came with a 10−30% drop in conductivity.

Piperidinium can also be incorporated into PS via copolymerization of functionalized monomers. Wei and coworkers synthesized piperidinium-functionalized cross-linked PS through the direct copolymerization of piperidinium-functionalized styrene monomer with 1,4-divinylbenzene.[807] This was done in the presence of poly(vinyl alcohol) (PVA) that was subsequently cross-linked to make an interpenetrating poly network (IPN) membrane. This process yielded a membrane with good mechanical properties, when compared to the incredibly fragile membrane without PVA. PS3 demonstrated excellent hydroxide conductivity with 89.3 mS/cm at 20 °C and 202.8 mS/cm at 80 °C with an IEC of 1.62. When applied in an MEA, a PPD of 1.2 W/cm^2 was achieved with a nonprecious FeN_x-CNT cathode and PtRu/C anode at 60 °C. The high performance of the membrane is likely related to the restriction of cations to the PS network within the IPN, causing the formation of distinct ion-conducting channels, which can be seen by TEM. This membrane demonstrated great hydroxide stability with a conductivity loss of 19% after 1248 h in 6 M NaOH at 80 °C. Nucleophilic hydroxide attack at the benzylic attachment to the ammonium was identified as the main degradation pathway.

A novel AEM architecture was explored by Ge et al. with the synthesis of a series of hyperbranched poly(vinylbenzyl chloride) (HB-PVBC)-based membranes.[808] A hydroxide conductivity of 123 mS/cm at 80 °C was observed, which is quite high in comparison to similar materials and is attributed to the formation of microphase separation in the hyperbranched polymer as observed by AFM and TEM. In a follow-up report, the HB-PVBC system was cross-linked with a diamine linker with either a 2, 6, or 10 carbon spacer to give HB-PVBC-XL-*x*,[809] where *x* is the number of carbons in the spacer. For HB-PVBC-XL-2, microphase separation was not detected by TEM, while HB-PVBC-XL-6 displayed 3 nm wide hydrophilic domains. HB-PVBC-XL-10 demonstrated less defined domains (7.5 nm wide). These results demonstrate how polymer morphology can be tuned to induce the desired level of microphase separation. HB-PVBC-XL-10 demonstrated the highest conductivity, likely owing to its high WU of 109%. This high WU rendered HB-PVBC-XL-10 unfit for use in MEAs, although HB-PVBC-XL-6 gave a modest PPD of 0.097 W/cm^2. All of the HB-PVBC-based AEMs demonstrated good alkaline stability, and of all of the variants, the non-cross-linked membrane achieved the highest conductivity.

6.2.5.1. Poly(styrene-ethylene-co-butylene-styrene) (SEBS). Poly(styrene-ethylene-*co*-butylene-styrene) (SEBS), a commercially available thermoplastic elastomer with a high elongation at break (461%), can be used as a polymer backbone for AEMs or as an additive to improve the mechanical properties of PS membranes.

Wang et al. used an azide "click" reaction to substitute commercial PS with dimethylpiperidinium (DMP) and spirocyclic piperidinium (SP) via a triazole linker.[765] The resulting polymers were too brittle to form films with mechanical properties suitable for AEMs. For this reason, the PS polymers were blended with SEBS, which allowed for solvent casting of AEMs: PS5-MP and PS5-SP. Despite blending with SEBS, the membranes still demonstrated relatively low tensile strengths and elongations at break. Surprisingly, the spirocyclic-functionalized membrane, PS5-SP, gave a higher conductivity than PS5-MP despite having similar IECs with 25.8 and 31.6 mS/cm at 20 °C, respectively. PS5-SP also demonstrated a higher hydroxide stability than PS5-MP with 83% and 59% conductivity remaining after 1800 h in 5 M NaOH at 80 °C. While PS5-SP demonstrated an excellent alkaline stability and moderate hydroxide conductivity, only a modest PPD of 0.130 W/cm^2 was achieved.

Mohanty et al. functionalized the SEBS polymer with a series of quaternary ammoniums using metal-catalyzed aromatic C−H borylation followed by Suzuki coupling.[810] Of the six membranes synthesized, SEBS1-BTMA demonstrated the highest conductivity with 45 mS/cm at 30 °C and 102 mS/cm at 80 °C, likely owing in part to having the highest IEC of 2.19 mequiv/g. When implemented in an MEA, SEBS1-BTMA gave a PPD of 0.223 W/cm^2 with some voltage loss but no sign of membrane degradation after 110 h at 60 °C. A comparison of the conductivity values of SEBS1-TMHA (59 mS/cm) and SEBS1-BDMHA (34 mS/cm) at 60 °C demonstrates the benefit of alkyl spacers on hydroxide transport. SAXS peaks suggest that nonfunctionalized SEBS has a cylindrical morphology resulting from the incompatibility of the different blocks within the polymer. These peaks were absent in SAXS of SEBS1-BTMA, SEBS1-TMHA, and SEBS1-BDMHA, indicating a loss of the nanoscale structure previously observed in SEBS. Additionally, most of the membranes demonstrated high WUs near or above 200%, which may make water management difficult for these membranes.

With the goal of achieving higher conductivities, Yang et al. synthesized a SEBS membrane grafted with poly(ethylene glycol) (PEG) and functionalized with trimethylammonium cations.[811] The membranes with (SEBS4-PEG) or without PEG chains (SEBS4) demonstrated incredibly low WUs for SEBS-based materials: <10% as compared to the 150−250% typically observed for these materials. This may be due to the low IEC of these membranes, though it is still an exceptionally low WU. Using TEM, the authors observed that the size of the hydrophilic phases increased with increasing PEG, feasibly giving rise to larger ion-conducting channels. The degree of PEG incorporation varied from 0% to 22% and did not correlate linearly with conductivity. Membranes incorporating only 10% PEG gave lower conductivity than those with 0% incorporation. Moreover, membranes with 15% PEG incorporation gave the highest conductivity. This finding may indicate

https://doi.org/10.1021/acs.chemrev.1c00331
Chem. Rev. XXXX, XXX, XXX−XXX

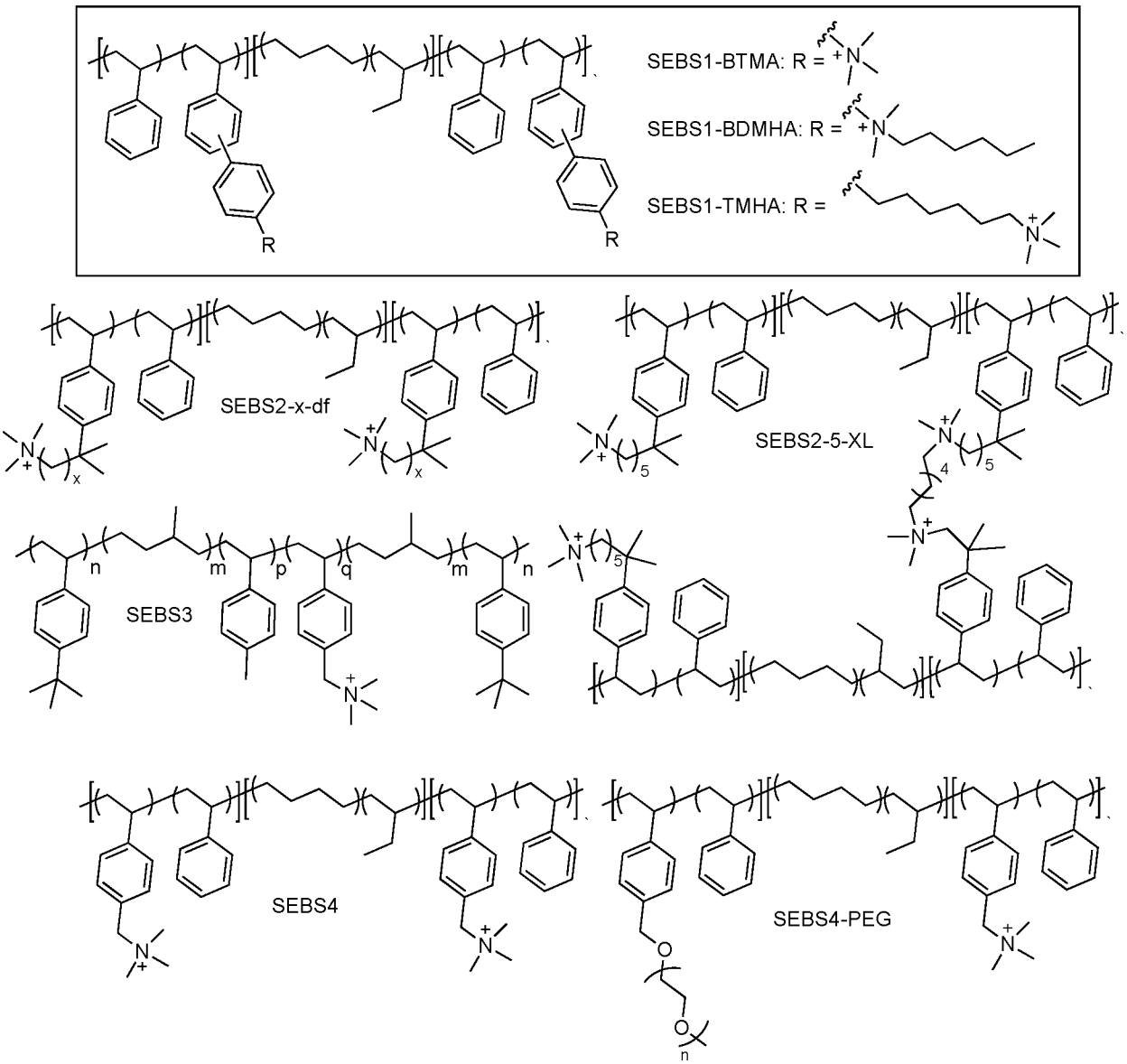

Figure 48. Naming scheme for poly(styrene-ethylene-*co*-butylene-styrene); counteranions omitted for clarity.

that a bigger hydrophilic channel size does not necessarily mean a better conductivity. Based on the channel size observed for the membrane with the highest conductivity, the optimal channel size may be ∼11 nm for this system. In addition to higher conductivity, the grafted PEG chains also made the membranes more mechanically robust by increasing the elongation at break from 250% to the limit of the instrument (∼500%). The membranes demonstrated excellent stability in 2.5 M KOH at 60 °C for 3000 h, though some swelling was observed.

Jeon et al. used Friedel−Crafts bromoalkylation followed by a Menshutkin reaction with trimethylamine to synthesize SEBS functionalized with trimethylammonium with a range in linker lengths.[762] Membranes with a 3, 4, or 5 carbon linker to the cationic group (SEBS2-3-0.5, SEBS2-4-0.5, and SEBS2-5-0.5, respectively) with IECs 1.09−1.12 exhibited nearly identical WUs, degrees of swelling, and conductivities regardless of linker length, with the exception that, at 80 °C, SEBS2-5-0.5 experienced mechanical failure. The higher IEC variants, SEBS2-3-0.8, SEBS2-4-0.8, and SEBS2-5-0.8, demonstrated similar WUs and degrees of swelling, but the hydroxide conductivity decreased as a function of increasing linker length. Other reports have suggested that longer linker length should induce higher microphase separation and thus provide higher conductivity, but this improved ordering was not observed in these materials. SAXS patterns showed that unfunctionalized SEBS exhibited a hexagonally packed cylinder morphology. Upon functionalization, the morphology changed, and SEBS2-5-0.8 displayed a lamellar structure that is less well-defined. The authors used cross-linking strategies to compensate for the poor mechanical properties of the SEBS membranes and found that, with increasing cross-link density, there was a decrease in the interdomain spacing of the membranes. These cross-linked membranes demonstrated much lower WUs but retained the hydroxide conductivity of the linear version. Additionally, the membrane was now mechanically stable enough to measure hydroxide conductivity at 80 °C. An MEA using SEBS2-5-XL, the membrane with the highest cross-link density, achieved a PPD of 0.52 W/cm^2, which is a great MEA performance for these materials.

https://doi.org/10.1021/acs.chemrev.1c00331
Chem. Rev. XXXX, XXX, XXX−XXX

Table 7. Polystyrene Membrane Properties and Performances

entry	name	IEC, theoretical (experimental) (mequiv/g)	WU[a] (wt %)	dimensional change[a] (ΔL%)	hydroxide conductivity (mS/cm)	PPD (W/cm^2) [current density (A/cm^2)]	ref
1	PS1-BTMA	1.34	2	6	18.9 at 22 °C	0.02 (0.082)	757
2	PS1-MeIm	0.48	3	< 1	11.6 at 22 °C	0.003	757
3	PS2-BuIm	1.02 (0.93)	64	21	10.3 at 30 °C; 15.3 at 60 °C	NA	758
4	PS2-iPrIm	1.02 (0.97)	68	24	10.9 at 30 °C; 15.8 at 60 °C	NA	758
5	PS2-BTMA	1.02 (0.94)	65	23	10.2 at 30 °C; 15.5 at 60 °C	NA	758
6	PS2-MeIm	1.52 (1.61)	63	32	14.1 at 30 °C; 25.9 at 60 °C	NA	767
7	PS2-MeIm	1.15 (1.22)	50	28	13.0 at 30 °C; 19.9 at 60 °C	NA	767
8	PS2-DiBuIm	1.39 (1.22)	82	35	16.6 at 30 °C; 23.1 at 60 °C	NA	769
9	PS-DiBuIm	0.93 (0.87)	54	25	15.4 at 30 °C; 21.9 at 60 °C	NA	769
10	PS4-Me	1.26	85	NA	64 at 80 °C	NA	752
11	PS4-Pyr	1.23	70	NA	52 at 80 °C	NA	752
12	PS4-Pip	1.22	53	NA	37 at 80 °C	NA	752
13	PS3	1.62	79	18	89.3 at 22 °C; 202.8 at 80 °C	1.20	807
14	HB-PVBC	2.36	<45	<16	39.6 (123.0)	NA	808
15	HB-PVBC-XL-2	~2.70	16	6	20.1 at 30 °C; 41.2 at 80 °C	0.08	809
16	HB-PVBC-XL-6	~2.70	40	5	27.2 at 30 °C; 47.9 at 80 °C	0.01 (0.19)	809
17	HB-PVBC-XL-10	~2.70	109	11	41.8 at 30 °C; 61.8 at 80 °C	NA	809
18	PS5-MP	1.92 (1.52)	72	19	25.8 at 22 °C	NA	765
19	PS5-SP	1.50 (1.35)	46	18	23.5 at 22 °C	0.13 (0.21)	765
20	PS5-SP	1.76 (1.75)	88	22	31.6 at 22 °C	NA	765
21	SEBS1-BTMA	2.41 (2.19)	211	NA	45 at 30 °C; 102 at 80 °C	0.22	810
22	SEBS1-BDMHA	2.01 (1.91)	236	NA	28 at 30 °C; 34 at 60 °C	NA	810
23	SEBS1-TMHA	2.01 (1.95)	194	NA	39 at 30 °C; 59 at 60 °C	NA	810
24	SEBS2-5-0.8	1.55	155	26	23 at 30 °C; 41 at 60 °C	NA	762
25	SEBS2-5-XL	1.50	28	10	29 at 30 °C; 41 at 60 °C	0.52	762
26	SEBS4	0.75	6	10	29.2 at 80 °C	NA	811
27	SEBS4-PEG	0.42	4	4	51.9 at 80 °C	NA	811
28	SEBS3	1.7 (0.94)	22	NA	31[b] at 60 °C	NA	812

[a]Measured at room temperature unless otherwise specified. [b]Bromide conductivity.

A pentablock copolymer very similar in structure to SEBS was brominated and subsequently quaternized with trimethylamine by Liberatore and coworkers to produce SEBS3,[812] which is shown in Figure 48. TEM revealed an ordered microphase-separated morphology, and SAXS peaks suggest that there is a well-ordered hexagonally packed cylinder structure, similar to the observed morphology for SEBS. The observed morphology was credited with allowing for a bromide conductivity of 31 mS/cm at 60 °C and 57 mS/cm at 90 °C, which is comparable to hydroxide conductivities achieved by some other SEBS membranes. As bromide conductivity should theoretically translate to even higher hydroxide conductivities, this study demonstrates how multiblock copolymer architectures can induce the phase separation needed to boost conductivity.

6.2.5.2. Conclusion—Polystyrene. PS-based membranes have largely demonstrated moderate conductivities and low PPDs, but synthetic strategies such as the formation of IPNs and hyperbranched polymers have produced some high-performance materials (Table 7). Simply substituting commercial PS without incorporating other polymer architectures through blending or copolymerization typically leads to membranes with poor mechanical properties and thus nullifies some of the benefits of PS as a polymer backbone. Commercially available SEBS-based membranes have, for the most part, outperformed PS membranes in terms of mechanical durability as well as conductivity, likely owing to the microphase separation that is more efficiently induced by the multiblock copolymer architecture present in SEBS. Overall, it has been shown that there are a variety of strategies that can be used to make PS viable for use in AEMs, but other, more flexible polymer motifs should be pursued. Additionally, PS still contains phenyl groups that can adsorb onto electrocatalysts in MEAs which can lead to a loss of performance, making aromatic-free polymer backbones an attractive alternative.[798]

6.2.6. Polyethylene (PE) Backbones. Polyethylene (PE) backbones are a common choice in the AEM community due

https://doi.org/10.1021/acs.chemrev.1c00331
Chem. Rev. XXXX, XXX, XXX−XXX

to their all-aliphatic hydrocarbon structure, mechanical versatility, and ease of synthesis. Unfunctionalized PE is a semicrystalline polymer with a T_g of −78 °C and a T_m of approximately 110−140 °C. These thermal transitions in PE, coupled with its high thermal stability, enable processing via commercial methods such as melt pressing making it an attractive candidate for AEM industrialization.

6.2.6.1. Alkene Insertion Polymerization. A variety of functional PE monomers have been synthesized to fabricate AEMs with alkaline-stable cations suitable for implementation into MEAs (Figure 49). Alkene insertion polymerization is a common methodology to synthesize functional PE scaffolds and is amenable to a range of olefins that allow for postpolymerization modification. Hickner and coworkers demonstrated the utility of this methodology to produce AEMs that contain single or multiple cations in a single pendent group.[813] Using a monomer bearing long-chain alkyl bromides and a phenyl-substituted comonomer, polymers were formed in a single step and were subsequently solution cast into membranes. Functionalization by postpolymerization Menshutkin reactions on the alkyl bromide was carried out with the appropriate tertiary amine to afford AEMs (PE1). Polymers with up to 30 mol % of cationic side chain were produced where the higher incorporations of cation led to significant swelling in water (237 wt %) and higher hydroxide conductivities (~34 mS/cm at 22 °C). Therefore, the authors chose to continue studies on polymers containing 20 mol % of cation which possessed lower swelling (127 wt %), slightly lower hydroxide conductivity (25 mS/cm at 22 °C), and a modest performance (PPD = 0.14 W/cm^2). In a follow-up, replacement of the methyl group on the phenyl substituent with a fluorine atom afforded PE3 with decreased WU (109 wt %), similar hydroxide conductivities (23 mS/cm at 22 °C), and an enhanced MEA performance (1.01 W/cm^2) at the same IEC.[814]

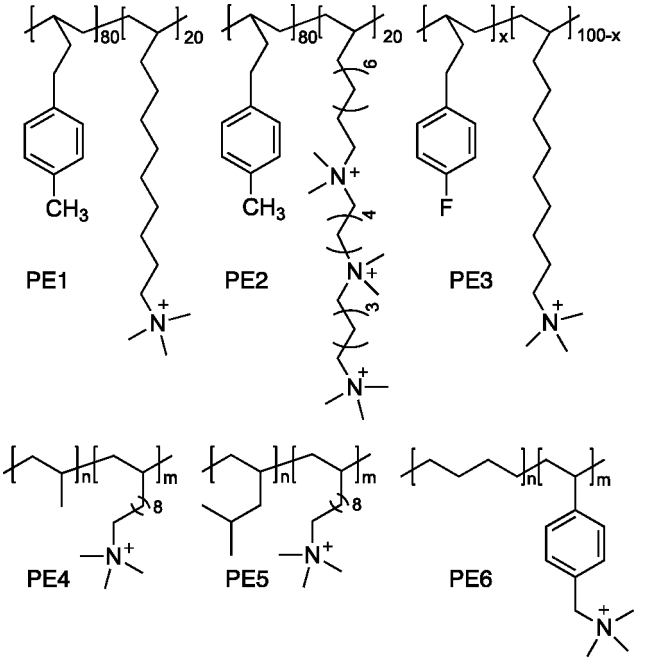

Figure 49. Naming scheme and structures for polyethylene-based AEMs prepared by alkene insertion polymerization and anionic polymerization (PE6). The counterions are omitted for clarity.

In an effort to increase the ionic content, polymers were synthesized bearing three cations on a single side chain. PE2 containing 20 mol % of a triple cation side chain with more than double the IEC of the single cation analogue possessed a high hydroxide conductivity (66 mS/cm at 22 °C and 201 mS/cm at 80 °C) with a large increase in swelling (WU = 193 wt %). However, polymers with three cation side chains performed well in MEA tests with a PPD of 0.94 W/cm^2 due primarily to the enhanced hydroxide transport enabled by increasing the cation density in the polymer membrane.

Li and coworkers utilized insertion polymerization to prepare polypropylene and functionalized polyethylene copolymers (PE4).[815] In PE4, the cation was spaced away from the polymer backbone which can help mitigate excessive WU and provide accessibility of the cation for hydroxide transport. PE4 showed a modest conductivity of 17 mS/cm at 22 °C with

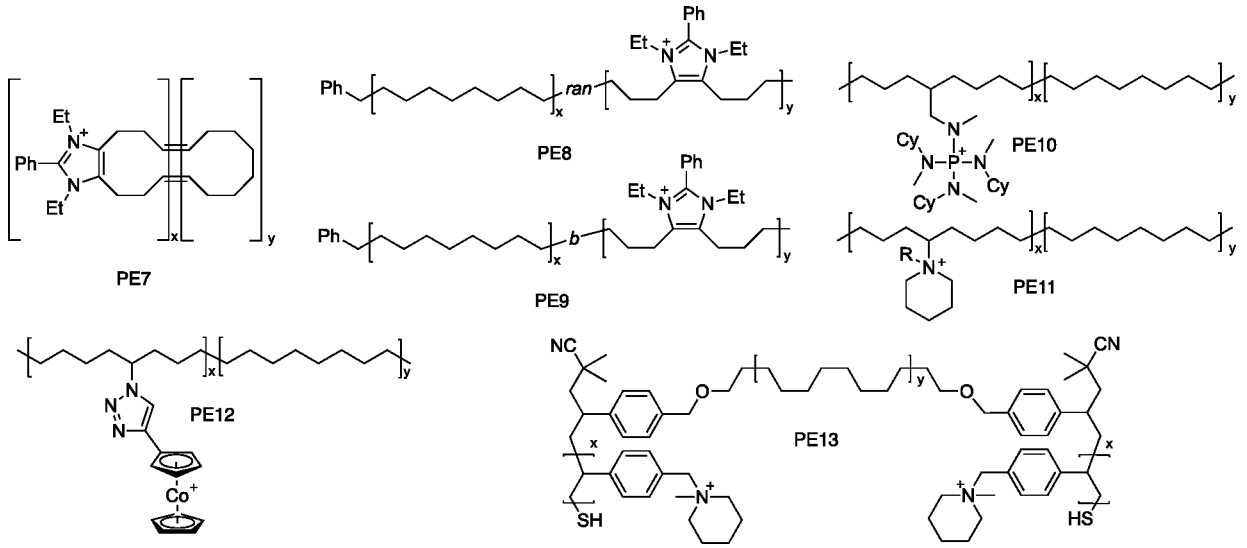

Figure 50. Naming scheme and structures for polyethylene-based AEMs prepared by ring-opening metathesis polymerization (ROMP). The counterions are omitted for clarity.

https://doi.org/10.1021/acs.chemrev.1c00331
Chem. Rev. XXXX, XXX, XXX−XXX

Scheme 8. Ring-Opening Metathesis Polymerization to Form (A) Functionalized PE Statistical Copolymers and (B) Functionalized PE Block Copolymers

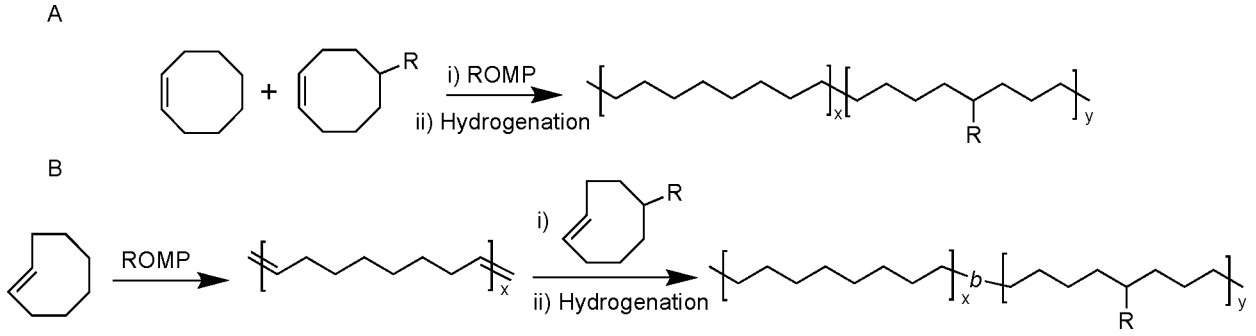

low swelling and high alkaline stability over 700 h. Polymers with similar cation content were also synthesized with a tethered cross-linker to enhance the mechanical properties. However, the best candidate chosen for fuel cell testing was the un-cross-linked derivative containing 20 mol % cation in the polymer structure. This AEM demonstrated a PPD of 0.122 W/cm^2 demonstrating a high performance at the time of publication over other systems.

In a follow-up report, Li utilized a similar system but replaced the methyl group on the comonomer with an isopropyl group to facilitate lower swelling without the need for cross-linking (PE5).[816] PE5 demonstrated low WU and dimensional swelling as well as high thermal and alkaline stability. Hydroxide conductivity was relatively high with 43 mS/cm at 22 °C; however, these *ex situ* properties did not carry over in fuel cell performance with their best candidate only showing a PPD of 0.037 W/cm^2. In both of these systems, there is a large discrepancy in the measured and theoretical IECs which could be an indication of incomplete hydroxide exchange. This is a function of the hydration of the polymer, and it is important to note that lower swelling does not necessarily correlate to higher conductivity or better performance.

6.2.6.2. Ring-Opening Metathesis Polymerization. While insertion polymerization is an attractive method to produce PE-based AEMs, functional PE derivatives can also be readily prepared by ring-opening metathesis polymerization (ROMP; Figure 50). Typically, *cis*- or *trans*-cyclooctene (COE) derivatives are polymerized followed by catalytic hydrogenation to yield cation-functionalized PE (Scheme 8). ROMP of COE derivatives is advantageous due to the exceptional functional group tolerance of this method, allowing for direct polymerization of cations and fast polymerization kinetics. ROMP of certain monomers is living which further enables tuning of the resulting polymer morphologically which can lead to enhanced performance due to the formation of phase-separated domains that can facilitate hydroxide transport. The resulting unsaturation in the backbone after ROMP is also a useful handle for postpolymerization cross-linking reactions to increase the mechanical stability and mitigate excessive swelling and WU leading to better membrane performance.

The synthesis of PE AEMs by ROMP necessitates the derivatization of COE. This can be accomplished by building the functionality into the ring structure, affording cationic moieties in the polymer backbone, or appending the cation functionality to the ring structure and, therefore, to the polymer backbone. Coates and coworkers demonstrated both of these functionalization methodologies in the investigation of imidazolium-based cations for AEMs.[772] Two generations of COE monomers were developed, one with the imidazolium functionality pendent (Generation 1) and one where the imidazolium was built onto the cyclooctene ring structure (Generation 2) as shown in Figure 51.

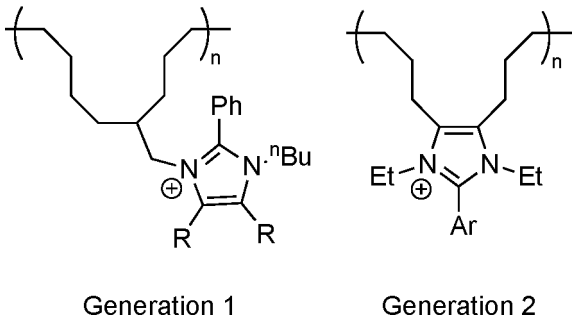

Figure 51. Structure of Generation 1 (pendent) and Generation 2 (backbone) imidazolium-based polymers as outlined in ref 772. Copyright 2015 American Chemical Society.

Imidazoliums were synthesized by a one-pot, proline-catalyzed, cycloaddition reaction of an aldehyde (C2-position), a diketone (C4- and C5-positions), and an amine. COE-methylamine was used to synthesize the Generation 1 COE monomer, placing the imidazolium group pendent to the backbone, whereas the Generation 2 COE monomer was synthesized from COE dione to fuse the imidazolium to the COE unit. The COE imidazole monomers were further converted to the imidazolium cations by simple alkylation with either ethyl or butyl iodide. ROMP of the Generation 1 monomers proceeded smoothly but resulted in polymers lacking sufficient WU to produce hydroxide-conducting films after hydrogenation. To reduce the hydrophobicity of the polymer, Generation 2 monomers were implemented and surprisingly afforded oligomeric macrocycles (PE7) instead of linear polymers due to the moderate ring strain and planar structure of the second-generation monomers (Table 8, entry 6). However, upon cross-linking PE7 via a reactive casting process followed by hydrogenation, membranes with WUs of 94% with low dimensional swelling were obtained (Table 8, entry 7). The in-plane hydroxide conductivities of cross-linked PE7 were 37 and 59 mS/cm at 22 and 80 °C, respectively.

In a follow-up to this report, linear polymer analogues of the Generation 2 monomers were synthesized through the living ROMP of *trans*-COE derivatives forming random (PE8) and diblock (PE9) copolymer PE-based membranes (Table 8,

https://doi.org/10.1021/acs.chemrev.1c00331
Chem. Rev. XXXX, XXX, XXX−XXX

Table 8. Polyethylene Membrane Properties and Performances

entry	name	IEC, theoretical (experimental) (mequiv/g)	WU[a] (wt %)	dimensional change[a] (ΔL%)	hydroxide conductivity (mS/cm)	PPD (W/cm^2) [current density (A/cm^2)]	ref
1	PE1	1.23 (1.15)	129	32	25 at 22 °C; ~70 at 80 °C	0.14	813
2	PE2	2.76 (2.41)	193	41	70 at 22 °C; 201 at 80 °C	0.94	813
3	PE3	1.21 (1.12)	109	26	23 at 22 °C; 91 at 80 °C	1.01	814
4	PE4	2.57 (1.56)	34	8	17 at 22 °C	0.122	815
5	PE5	2.84 (1.92)	29	9	43.2 at 22 °C	0.037	816
6	PE7	1.32	70	17	29 at 22 °C; 43 at 50 °C	NA	772
7	PE7 (XL)[b]	1.37	94	17	37 at 22 °C; 59 at 50 °C	NA	772
8	PE8	1.88 (1.87)	257	46	28 at 22 °C; 83 at 80 °C	NA	744
9	PE9	1.10 (1.03)	28	10	5 at 22 °C; 11 at 80 °C	NA	744
10	PE8 (XL)[b]	1.69 (1.60)	115	17	49 at 22 °C; 134 at 80 °C	NA	744
11	PE10	0.69	52	NA	22 at 22 °C	NA	743
12	PE12	2.02 (1.86)	38 at 22 °C; 175 at 80 °C	6	20 at 22 °C; 90 at 90 °C	NA	817
13	PE11	1.31	26	7	35 at 22 °C	NA	818
14	PE14 (LDPE)	(2.54)	149	27[c]	100 at 22 °C; 208 at 80 °C	2.01	819
15	PE14 (HDPE)	(2.44)	155	38[c]	121 at 22 °C; 214 at 22 °C	2.55	819
16	PE15	(2.01)	53	28[c]	60[d] at 22 °C	1.16	577,820
17	PE16	1.15 (0.95)	42	NA	56 at 22 °C; 97 at 60 °C	0.080[e]	822
18	PE16	2.30 (1.92)	37	NA	73 at 60 °C	NA	823
19	PE13	2.1 (1.66)	94	16.5	179 at 80 °C	NA	824

[a]Measured at room temperature unless otherwise specified. [b]XL = cross-linked. [c]Through-plane swelling. [d]Chloride conductivity. [e]Hydrazine hydrate fuel cell.

entries 8−10).[744] At lower ion exchange capacities (~1.0 mequiv/g), PE8 possessed a high hydroxide conductivity of 83 mS/cm at 80 °C and a WU of 67% with low dimensional swelling. The conductivity of PE9 was markedly lower (28 mS/cm at 80 °C) which is most likely the result of a low WU of 28%. Upon increasing the cationic content of PE8 (IEC ~1.6−1.9 mequiv/g), the polymer lost mechanical integrity at 80 °C due to excessive swelling. However, when cross-linking was used to mediate WU and strengthen the polymer, a hydroxide conductivity of 134 mS/cm was achieved at 80 °C. TEM revealed the presence of disordered ionic aggregates in PE9 while PE8 had a relatively homogeneous morphology. Ionic aggregation could, in part, lead to reduced hydroxide conductivity by the formation of local hydroxide traps that would impede transport through the membrane. Other reports from the Coates group have demonstrated other cation choices for AEMs on polyethylene backbones enabled by the synthesis of functionalized cyclooctene. For example, tetrakisamino-phosphonium-functionalized cyclooctene was prepared by a Staudinger reaction on azido cyclooctene followed by a reaction of the iminophosphorane with cyclohexylmethyl-amine.[743] The phosphonium-functionalized monomer was subsequently polymerized by ROMP with cyclooctene as a comonomer. The resulting polymer, PE10, showed a relatively low hydroxide conductivity of 21 mS/cm at 80 °C with a WU of 52% and IEC of only 0.67 mmol/g. However, the phosphonium moiety showed excellent alkaline stability with almost no loss in conductivity over 140 days in 15 M KOH carving a path forward for novel cations for AEMFCs.

Another example of ROMP-based PE scaffolds was shown by Zhu et al. where PE AEMs were produced by ROMP copolymerization of COE with a cobaltocenium-functionalized COE enabled by Cu-catalyzed click chemistry followed by chemical hydrogenation with tosyl hydrazide (PE12).[817] PE12 incorporating 40 and 50 mol % of ionic monomer was produced, and PE12 with 50 mol % cation showed the highest conductivity and WU at both 22 and 80 °C (20 mS/cm at 22 °C and 90 mS/cm at 80 °C). The increased WU led to poorer mechanical properties (EaB = 120% vs 153% for 40 mol %). Nonetheless, polymer conductivity held stable in 1 M NaOH at 80 °C over 35 days showing the stability of novel metallocene-based AEMs.

While high hydroxide conductivities and stabilities have been achieved, the synthesis for these COE-derivative monomers can range from five to eight steps with low overall yields. However, there are some recent examples of improved syntheses of COE derivatives ideal for implementation in AEMs. Piperidinium-functionalized COE monomers with a range of alkyl substituents were synthesized by hydroamination followed by alkylation in a one-pot, two-step synthesis.[818] All of the membranes synthesized from the ROMP and subsequent hydrogenation of these monomers (PE11) demonstrated low degrees of swelling (<10%), moderate conductivities between 15 and 53 mS/cm at 22 °C, and a range of WUs 22−92%, depending on the alkyl substituent and

https://doi.org/10.1021/acs.chemrev.1c00331
Chem. Rev. XXXX, XXX, XXX−XXX

cation incorporation. The membrane with the highest stability retained 80% of its conductivity after 720 h in 1 M KOH, despite model compound cation studies showing that the cationic moiety has high alkaline stability. In model oligomer NMR studies, Hofmann elimination was observed on the β-hydrogens in the polymer backbone. This finding explains the discrepancy between model compound membrane stability and further demonstrates the effects of backbone-tethered cations on membrane performance.

6.2.6.3. Radiation Grafting. Commercially available PE homopolymers [e.g., low- or high-density PE (LDPE or HDPE)] and copolymers can be functionalized postpolymerization to form robust membranes for use in AEMs. Varcoe and coworkers utilized a radiation grafting method to produce functional PE bearing cationic moieties as AEMs (Figure 52).[819] Radiation grafting with an electron beam in air produced peroxy groups on the polyethylene backbone, which could then be used to initiate radical polymerization of vinylbenzyl chloride. The grafted PS chains were then converted to the trimethylammonium cations by immersion in trimethylamine to afford PE14. Varcoe's reports highlight the utility of this approach and how both the polymer backbone and pendant cation influence MEA performance. In an effort to recreate the chemical motif found in Nafion, ethylene-tetrafluoroethylene copolymers were functionalized with poly(vinylbenzyl trimethylammonium) units to produce PE15 with chloride conductivities approaching 70 mS/cm with moderate WU values between 50% and 70% at an IEC ~2.0.[820] While the mechanical properties suffered due to cation functionalization, the performance in MEAs showed PPD values upwards of 1.2 W/cm^2.[577,820] Replacing the grafted benzyltrimethylammonium units with benzylmethylpyrrolidinium cations produced similar results.[821] However, the authors found that enhanced alkaline stability is obtained with longer alkyl spacers, as the attachment of the cation at the benzylic position led to 27% loss in IEC, and attachment through a butyl group gave a 13% loss after 28 days in 1 M KOH at 80 °C. Interestingly, removing the fluorinated portion of the polymer produced enhanced membrane properties and performance. Radiation-grafted LDPE and HDPE showed an increase in WU versus radiation-grafted poly(ethylene-*co*-tetrafluoroethylene) (ETFE) due to the lack of the fluorinated backbone. However, the PPD drastically increased to 2.55 W/cm^2. LDPE displayed a lower lifetime stability than HDPE in an MEA configuration with failure of the LDPE scaffold observed after 100 h, whereas HDPE remained stable over 450 h.

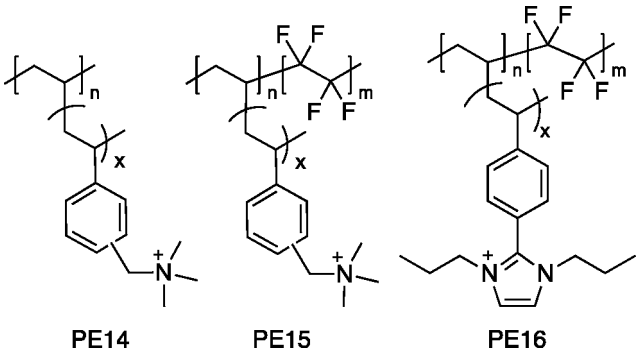

Figure 52. Naming scheme and structures for polyethylene-based AEMs prepared by radiation grafting. The counterions are omitted for clarity.

Utilizing a similar synthesis to Varcoe, Maekawa and coworkers used radiation grafting on ETFE to append di-*n*-propylimidazolium-functionalized polystyrene to afford PE16.[822] These polymers showed very promising *ex situ* properties with their best performing polymer showing a conductivity of 181 mS/cm at 60 °C with 80% WU largely owing to the hydrophobic ETFE backbone. They thoroughly investigated PE16 using small-angle neutron scattering (SANS) and found two IEC-dependent morphological regimes. At lower IECs (<0.8 mmol/g), "reverse-micelle" structures composed of hydrated hydrophilic domains in a matrix of hydrophobic polymer are prevalent. At higher IECs (>0.8 mmol/g), the opposite phenomenon is observed with hydrophobic domains suspended in a matrix of a hydrophilic majority phase. SANS depicted that the micellar structures were well-connected and formed a percolating network throughout the polymer membrane. These features correlate well with observations that at lower IECs the polymer remains alkaline-stable, but when the morphology inverts (at higher IECs), rapid degradation of the ionic moieties is observed owing to the higher hydroxide concentrations when the cationic group is exposed. Therefore, a polymer with lower IEC was chosen for incorporation into a hydrazine hydrate fuel cell that resulted in a peak power density of 0.08 W/cm^2 with a non-Pt-group metal (PGM) Ni-based anode and Co−Fe cathode.

6.2.6.4. Other Methods. Other methods to incorporate polyethylene into functional copolymers have been utilized to obtain AEMs with a distinct emphasis on morphology. Knauss and coworkers carried out anionic polymerization of butadiene and 4-methylstyrene followed by postfunctionalization to afford BTMA block copolymers (PE6).[823] These block copolymers showed bicontinuous structures due to phase segregation of the hydrophilic and hydrophobic domains which is thought to aid in hydroxide transport. The best performing polymer showed a hydroxide conductivity of 73 mS/cm at 60 °C and a low WU of 37%. All polymers synthesized showed a high elongation at break and mechanical rigidity.

Recently Herring and coworkers demonstrated an ABA triblock copolymer with poly(chloromethylstyrene) as the flanking blocks and a polyethylene midblock with the polyolefin midblock providing enhanced mechanical properties.[824] The flanking blocks were substituted with either *N*-methylpiperidine or trimethylamine to afford PE13. SAXS and TEM analysis showed a cylindrical morphology for many of the synthesized membranes with domain spacings ranging from 18 to 29 nm. The best performing membrane, a piperidinium-functionalized polymer, showed a high hydroxide conductivity of 179 mS/cm at 80 °C with a WU of 94% and relatively low dimensional swelling (~17%). PE13 showed excellent mechanical properties with a stress at break of 26 MPa and Young's modulus of 21 MPa for the hydrated membranes. However, the alkaline stability of these membranes was quite low with only 50% of the original IEC remaining after 1 week in 9 M KOH at 22 °C. Nonetheless, this report highlights the importance of morphology and choice of cation when designing materials for AEMFCs.

6.2.6.5. Conclusion—Polyethylene. AEMs with PE backbones are currently at the forefront of performance AEMs due to rapid, efficient, and precise polymerization and the resulting

https://doi.org/10.1021/acs.chemrev.1c00331
Chem. Rev. XXXX, XXX, XXX−XXX

robust mechanical properties. However, there are critical design strategies that should be considered for future development. While the Coates group has made strides in the derivatization of COE to form functional PE AEMs, more efficient and high-yielding synthetic strategies to anchor a diverse set of cations are necessary to fully realize the potential of PE backbones. Varcoe demonstrated that graft copolymers on commercially available PE provide highly conductive membranes with outstanding efficiency in MEAs. As such, other polymer architectures such as branched, bottlebrush, stars, as well as multiblock variants should be investigated to understand the role of polymer architecture in ion conductivity. Finally, solution processability has always plagued functional PE membranes but is crucial for the high-throughput fabrication of membranes for AEMFCs.

6.2.7. Polynorbornene (PNB) Backbones. PNB backbones have gained interest in the AEM community due to the availability of various functional derivatives and the ease of polymer preparation. Norbornene possesses a high ring strain because of its bicyclic structure which facilitates straightforward, fast, and efficient polymerization by ROMP (Figure 53A). PNB prepared by ROMP (rPNB) has a low T_g range

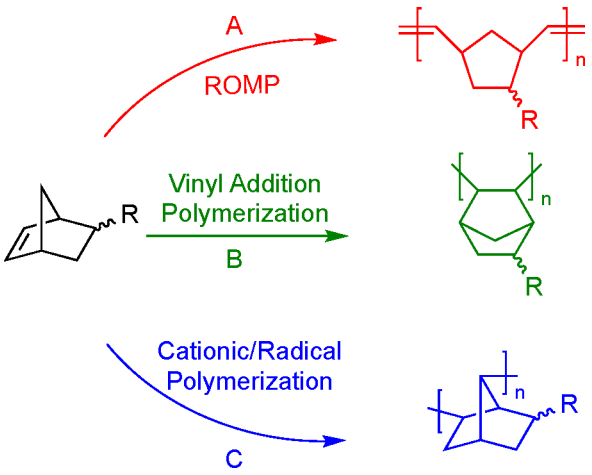

Figure 53. Polymerization methodologies for norbornene monomers by (A) ROMP, (B) vinyl addition polymerization, and (C) cationic or radical polymerization.

(30−70 °C) and is soluble in a wide array of hydrocarbon solvents. Once hydrogenated, rPNB is semicrystalline and possesses higher operating temperatures allowing for applications in AEMs.

Norbornene has alternatively been polymerized via metal-catalyzed vinyl addition polymerization (vaPNB) to afford polymers maintaining the bicyclic structure in the purely hydrocarbon backbone (Figure 53B). This structural motif yields amorphous polymers with enhanced thermal properties (T_g >300 °C) while retaining solution processability in conventional organic solvents. Recent progress in vinyl addition polymerization of norbornene has led to the ability to form well-defined polymers by living polymerization using a palladium catalyst.[825−827] Furthermore, vaPNB forms high-quality, flexible, and transparent membranes ideal for implementation in fuel cells. Other methods such as radical or cationic polymerization have been used to synthesize PNB (Figure 53C) but give polymers with poor yield, residual olefins, and inconsistent structure resulting in a mixture of backbone identity and have not been thoroughly investigated in the context of functional derivatives.[828]

6.2.7.1. ROMP Polynorbornene (rPNB) Backbones. Cationic ROMP polynorbornene (rPNB)-based AEMs have rapidly developed due to their ease of synthesis and functionalization (Figure 54). Coates and coworkers demonstrated a straightforward synthesis of poly(norbornenes) bearing trimethylammonium moieties with a methyl group in the β-position to prevent degradation by Hofmann elimination.[785] Polymer films were prepared by reactive casting with dicyclopentadiene to afford cross-linked and mechanically robust rPNB1 membranes. At relatively low measured IECs (1.0−1.1), the hydroxide conductivity was modest at 18 mS/cm at 22 °C and 28 mS/cm at 50 °C. A discrepancy in theoretical and measured IEC is potentially a product of low swelling in water or methanol leading to inefficient hydroxide exchange. Nonetheless, rPNB1 resulted in reasonably high in-plane conductivity, low swelling, and favorable mechanical properties with only 7% strain at 16 MPa of applied stress.

More recently, Wang et al. developed novel norbornene-based monomers that contain both a cyclic pyrrolidinium and a trimethylammonium cation in the same unit.[829] Furthermore, a difunctional norbornene cross-linker containing two ammonium groups was incorporated to improve mechanical properties and contribute to the overall ion content to increase conductivity. rPNB2 was prepared by reactive casting to afford cross-linked polymer films with high IECs (2.46−2.89). With such high ion content, membranes with an IEC of 2.89 achieved hydroxide conductivities of 65 mS/cm at 22 °C and 140 mS/cm at 85 °C. With approximately 26% cross-linker content, rPNB2 membranes demonstrated low swelling in water (~31% at 25 °C and 43% at 60 °C) while maintaining high hydroxide conductivities. The tensile modulus for the best performing membrane approached 15 MPa—roughly half the value observed for Nafion 117. When applied in a single-cell fuel cell, a peak power density of 0.15 W/cm^2 was achieved at a current density of 350 mA/cm^2.

Beyer and coworkers synthesized a trimethylammonium norbornene derivative in an attempt to address the primary design motifs for AEMFC polymers.[830] These motifs include the following: (1) a semicrystalline hydrogenated rPNB backbone to enhance mechanical integrity vs the amorphous unsaturated polymer, (2) ether linkages pendent to the polymer backbone to facilitate WU, and (3) two methyl groups at the β-position relative to the trimethylammonium moiety to prevent Hofmann elimination. Two different compositions of rPNB3 were synthesized with theoretical IECs of 1.0 and 1.25. The polymer with the higher IEC demonstrated outstanding transport properties with hydroxide conductivity reaching 177 mS/cm while curbing excessive swelling (WU = 82%). SAXS of the polymers showed a disordered but phase-separated morphology on the scale of 10−20 nm suggesting the presence of ionomeric aggregates that tend to be found in hydrocarbon-based AEMs. Despite beneficial conductivity and WU, rPNB3 suffered from low mechanical properties (tensile modulus = 5.5 MPa) and alkaline degradation. They ascribed the loss of mechanical properties to the lack of crystallinity which is potentially due to long pendent groups suppressing crystalline domain formation. Additionally, a roughly 50% loss in conductivity was observed over 239 h in 0.1 M NaOH at 90 °C despite designing a monomer to prevent Hofmann degradation. The authors speculated that the primary cause of degradation was the

https://doi.org/10.1021/acs.chemrev.1c00331
Chem. Rev. XXXX, XXX, XXX−XXX

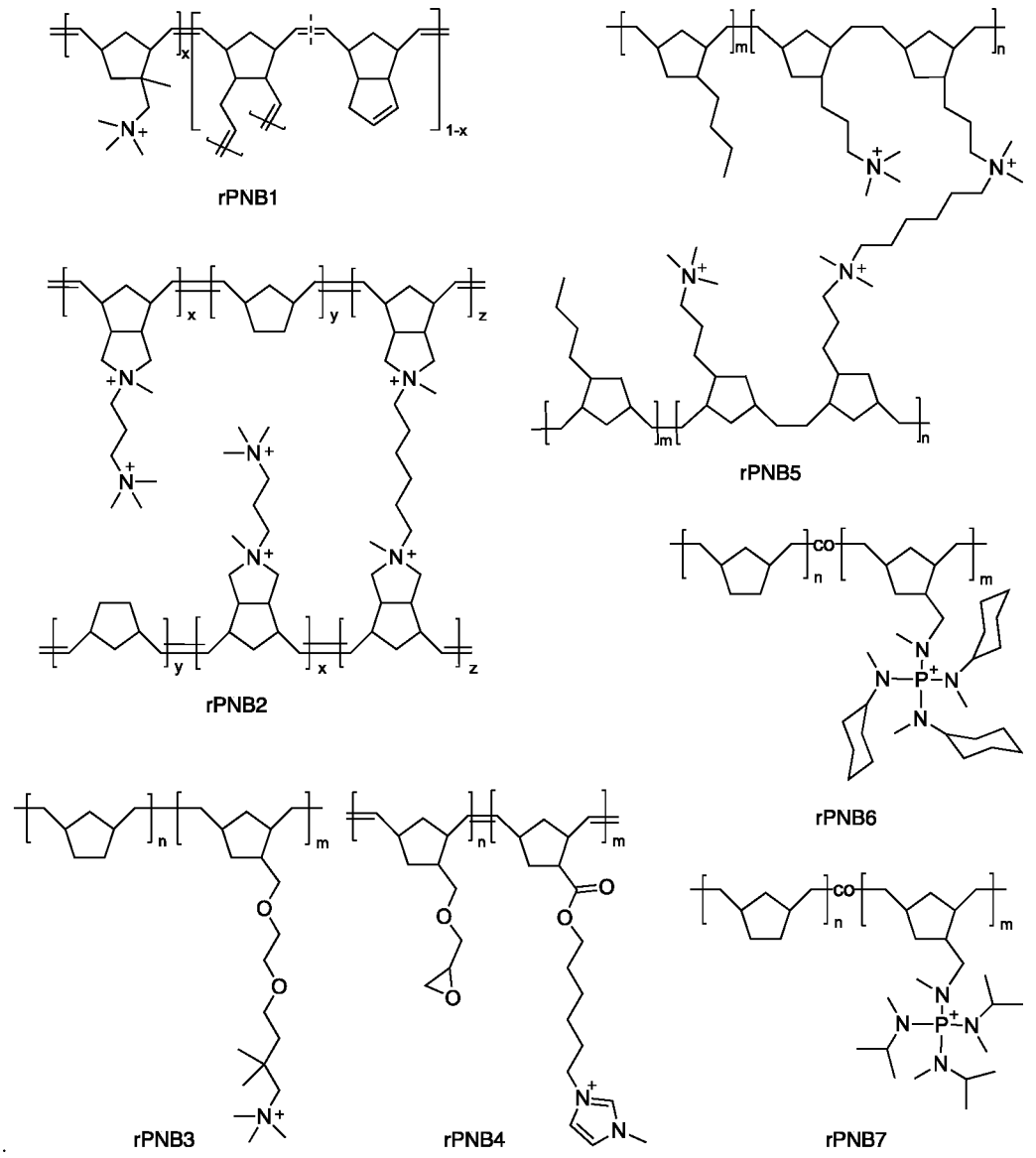

Figure 54. Naming scheme and structures for polynorbornene-based AEMs prepared by ROMP (rPNB). The counterions are omitted for clarity.

difference in hydroxide concentration when measuring a polymer film versus a small molecule. They rationalized that, in a polymer membrane, the lack of swelling and capacity to solvate ions leads to an increase in effective hydroxide concentration leading to an increase in the reactivity of the hydroxide ion.

Chen and coworkers also utilized ROMP to directly prepare copolymers with imidazolium moieties as the cation and a glycidyl ether functionality to cross-link.[831] The resulting rPNB4 membranes presented with high thermal stability, relatively high hydroxide conductivities (90 mS/cm at 80 °C), and ideal WU (61 % at 60 °C). As described in the previous sections, imidazolium cations can undergo degradation in base and, as a result, the authors saw a 25% decrease in hydroxide conductivity over 10 days suggesting lower alkaline stability for these polymers. Moreover, the single cell performance was lacking, only reaching a PPD of 0.12 W/cm^2 using Pt/C catalysts.

Postpolymerization functionalization is an alternative way to fabricate membranes and circumvents issues associated with solubility and film formation which can be a challenge for cationic polymers. Kohl and coworkers adopted this strategy for norbornene polymers formed by ROMP.[782] Diblock copolymers of bromopropyl norbornene and butylnorbornene and a homopolymer of bromopropyl norbornene were synthesized by ROMP. The resulting polymers were cross-linked by postpolymerization reactive casting using TMHDA followed by immersion of the films in aqueous trimethylamine to further transform any unreacted bromide to ammonium groups. The resulting rPNB5 membranes possessed very high IECs ranging from 2.31 to 4.73 and retained mechanical integrity in water. However, it was noted that the cationic homopolymers were brittle, and they were unable to obtain swelling ratios. A number of cross-linker compositions were tested from 10% to 45% to elucidate the optimal membrane properties in terms of swelling and conductivity. It was reported that, for all of the polymers studied, there is an optimal cross-linker concentration (~20 mol %). Higher concentrations result in lower hydroxide conductivities. Swelling in water ranged from 57% to 224% with hydroxide conductivities reaching up to 99 mS/cm at 25 °C and 195 mS/cm at 80 °C, one of the highest hydroxide conductivities to

https://doi.org/10.1021/acs.chemrev.1c00331
Chem. Rev. XXXX, XXX, XXX−XXX

Table 9. Polynorbornene Membrane Properties and Performances

entry	name	IEC, theoretical (experimental) (mequiv/g)	WU[a] (wt %)	dimensional change[a] (ΔL%)	hydroxide conductivity (mS/cm)	PPD (W/cm^2) [current density (A/cm^2)]	ref
1	rPNB1	2.28 (1.4)	<10[b]	NA	18 at 22 °C; 28 at 50 °C	NA	785
2	rPNB2	(2.89)	32 at 25 °C; 43 at 60 °C	12 at 25 °C; 18 at 60 °C	65 at 22 °C; 140 at 80 °C	0.15 (0.35)	829
3	rPNB3	1.25 (1.05)	82	NA	~60 at 22 °C; 177 at 80 °C	NA	830
4	rPNB4	1.19 (1.01)	46 at 22 °C; 61 at 60 °C	42 at 22 °C; 56 at 60 °C	22 at 22 °C; 90 at 80 °C	0.12 (0.25)	831
5	rPNB5	(2.2)	100	28	53 at 22 °C; 109 at 80 °C	0.17 (0.40)	782
6	rPNB6	1.0 (0.99)	82	NA	19 at 22 °C	NA	777
7	rPNB7	1.1 (0.78)	86	NA	27 at 22 °C; 43 at 80 °C	NA	777
8	vaPNB1	(2.21)	71	NA	50.9 at 22 °C; 101.9 at 80 °C	0.54 (1.26)	787
9	vaPNB2	(3.43)	69	NA	95.2 at 22 °C; 198 at 80 °C	0.51 (0.95)	783

[a]Measured at 22 °C unless otherwise specified. [b]Measured in MeOH(aq).

date. All rPNB5 polymers were thermally stable up to 200 °C and displayed alkaline stability over 500 h as indicated by conductivity and Fourier-transform infrared spectroscopy (FTIR) experiments. Three polymers were selected to be incorporated into MEAs based on conductivity, WU, and mechanical properties, with the diblock copolymer containing 40 mol % cation and 35 mol % cross-linker demonstrating the best performance of 0.17 W/cm^2 at a current density of 0.4 mA/cm^2. While more optimization is necessary in this system to achieve a better performance, this study pushed the limits of polymer composition for AEMFCs and highlighted the potential for chemical crosslinking to synthesize high-performance membranes.

Much of the literature has been dominated by the use of tetraalkylammonium-based polymers for AEMFCs due to their high hydroxide conductivity and synthetic ease. However, as shown earlier in this Review, ammonium stability is convoluted, and while some studies show alkaline stability, others show significant decomposition. Other cations such as phosphoniums have shown great promise in terms of alkaline stability but have yet to yield conductivities that rival those of ammonium functionalities. A few studies have begun to investigate phosphonium incorporation into polymer scaffolds to address alkaline stability and attempt to increase the hydroxide conductivity. Noonan and coworkers recently described the incorporation of the alkaline-stable tetrakisdialkylaminophosphonium cations in a ROMP polynorbornene scaffold.[777] Using a two-step, one-pot synthesis, variants of the phosphonium cation were prepared by the choice of secondary amine, namely, isopropylmethyl (IPrMe) and cyclohexylmethyl (CyMe) phosphonium. These precursors were easily converted to norbornene monomers by simple SN_2 substitution to afford monomers amenable to ROMP (Table 9, entries 6 and 7). Initially, random copolymers and diblock copolymers were synthesized by direct polymerization of the phosphonium-functionalized monomers to afford rPNB6 and rPNB7 with a high molecular weight (~80−100 kDa) and low dispersity. While the random copolymers of both CyMe (rPNB6) and IPrMe (rPNB7) were easily cast into ductile membranes, diblock copolymers were found to be brittle and fell apart upon hydration. In an effort to utilize the living nature of ROMP, ABA triblock copolymers were synthesized, but these too mechanically failed upon casting membranes. The polymers displayed little-to-no crystallinity which seems to originate from the identity of the phosphonium with the CyMe cation completely suppressing crystallinity and IPrMe showing very little crystallinity versus a homopolymer of polynorbornene. IPrMe-based polymers displayed the best membrane properties with hydroxide conductivities of 27 mS/cm at 25 °C and 43 mS/cm at 80 °C with a WU of 86%. These polymers demonstrate a first step into non-ammonium-based AEMFCs that are alkaline-stable. With further study of polymer backbone structure, morphology, and other phosphonium derivatives, a competitive phosphonium AEMFC can be realized.

Other metal-based cationic polymers have been used as AEMs that are amenable to direct polymerization by ROMP. Tew and coworkers synthesized cross-linked AEMs bearing bisterpyridine-ligated metal cations by reactive casting of a difunctional metal-based monomer with norbornene, dicyclopentadiene, and a bis(oligo-ethylene glycol)norbornene.[832] The identity of the metal cation was varied (Ru, Ni, and Co), and the resultant membranes showed quite low conductivity, which is most likely a product of the immense swelling in water (ranging from 152% to 193%). However, they proposed another viable reason for the low conductivity based on the thermodynamics of counterion release. Using isothermal titration calorimetry (ITC), they characterized the thermodynamics of counterion release of both metal-based cations and more conventional ammonium cations to fundamentally differentiate the transport behavior of cations based on their structure. By titrating model cations with $NaHCO_3$ to exchange the counter ion from the chloride form and measure the enthalpy released during the exchange, a correlation between the cation identity and energy required to release the counterion was established. Their findings show the low enthalpy of exchange for ammonium cations (~200−350 cal/mol) while the metal-based cations showed enthalpies ranging from 586 to 1120 cal/mol suggesting that ion transport is intrinsically limited based on the identity of the cation, which is relatively consistent with observed experimental data in the literature. Nonetheless, many factors should be considered beyond cation identity such as swelling, mechanical behavior,

https://doi.org/10.1021/acs.chemrev.1c00331
Chem. Rev. XXXX, XXX, XXX−XXX

and synthetic ease to prepare the AEM practical for implementation into AEMFCs.

6.2.7.2. Vinyl Addition Polynorbornene (vaPNB) Backbones. An alternative to ROMP norbornene is the metal-catalyzed vinyl addition polymerization of norbornene (Figure 53B). This is typically accomplished with *in situ* generated cationic palladium or neutral nickel catalysts. Vinyl addition polymerization retains the bicyclic norbornene structure as the backbone of the polymer and, as a result, affords amorphous polymers with much higher glass transition temperatures (>300 °C) and excellent film-forming properties. Register and coworkers have shown that polymerizations with palladium catalysts are living whereas nickel catalysts are highly active and afford high-molecular-weight polymers but lack living characteristics.[825] Very few examples of vinyl addition norbornene polymers have been shown in the context of AEMs, but recent studies have demonstrated their viability in this field (Figure 55).

Kohl and coworkers developed high-performance AEMs from vinyl addition polynorbornene functionalized with trimethylammonium (vaPNB1; Table 9, entry 8). In a similar postpolymerization functionalization strategy used in a prior report on ROMP norbornene systems, tetrablock copolymers of bromopropyl norbornene and butyl norbornene were prepared by living Pd-catalyzed vinyl addition polymerization followed by quaternization in trimethylamine (Scheme 9).[787] The authors chose to use tetrablock copolymers to create phase separated domains to facilitate hydroxide transport. Different compositions were synthesized to vary the IEC of the resulting membrane from 1.55 to 2.60. Owing to the mechanical properties of vinyl addition polynorbornenes, membranes were easily cast to form flexible films. The hydroxide conductivity of the best performing membrane containing 38 mol % cation content was 51 mS/cm at 25 °C and 102 mS/cm at 80 °C with moderate swelling in water of 78%. Furthermore, all membranes in the study were found to be stable in 1 M NaOH at 80 °C over 1000 h. Using the same MEA conditions as the previously reported ROMP system, the best performing membrane demonstrated a marked increase in PPD with 0.54 W/cm^2. It is useful to note that a high Pt loading of 2.1 mg/cm^2 was used, which is 5 times the amount (0.4 mg/cm^2) typically used in present AEMFC applications.

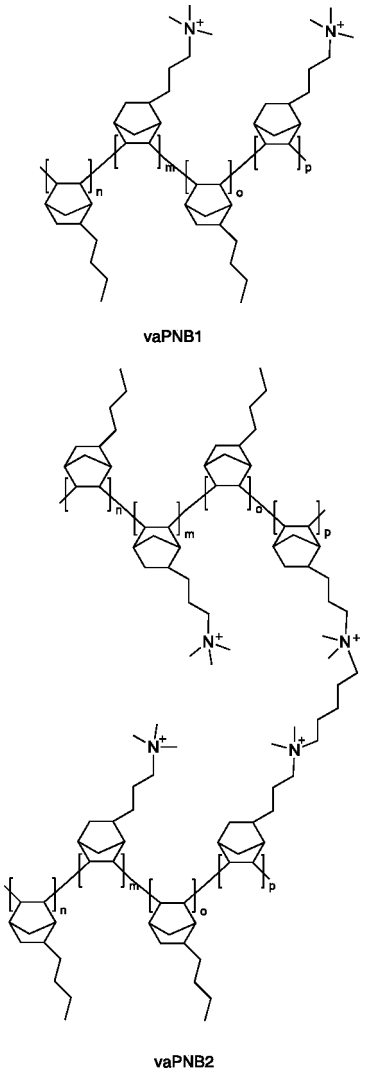

Figure 55. Naming scheme and structures for poly(nobornene)-based AEMs prepared by vinyl-addition polymerization (vaPNB). The counterions are omitted for clarity.

In a follow-up report to the tetrablock ammonium-functionalized vaPNB, Kohl investigated the effects of cross-linking a selected composition (66 mol % cation) with a diamine by reactive casting (vaPNB2; Table 9, entry 9).[783] They found that increasing the cross-linker concentration had deleterious effects on hydroxide conductivity, potentially due to the exclusion of conductive pathways at high cross-linker compositions. Nonetheless, at 5 mol % cross-linker concentration, a mechanically stable vaPNB2 membrane was formed with a hydroxide conductivity of 95 mS/cm at 25 °C and 198 mS/cm at 80 °C with an optimal WU of 69%. The membrane demonstrated a PPD of 0.51 W/cm^2 in the same MEA setup. The MEA performance of vaPNB2 was further improved by manipulating ionomer properties and optimizing electrode design, which is discussed in detail in section 7, Figure 59G.

6.2.7.3. Conclusion—Polynorbornenes. PNB scaffolds have shown promise for use as AEMs due to their advantageous properties such as facile film formation, high T_g, and ease of polymer synthesis. Despite the high performance of PNB AEMs, more work is needed to further improve monomer derivatization and synthetic yields. Furthermore, vinyl addition polymerization is not functional group tolerant making for a limited monomer scope. More investigation into more robust catalysts that can maintain its living nature should be carried out.

6.2.8. Conclusion—Membranes. Great advancements have been made in the synthesis of polymers for use as AEMs with MEAs exceeding PPDs of 1 W/cm^2 and some that can operate stably for hundreds of hours at low or medium current density. The studies discussed herein have demonstrated the importance of polymer morphology, structure, microphase separation, and water management for the promotion of hydroxide transport. Many design strategies have been implemented in order to induce favorable membrane properties including cross-linking, polymer blends, IPNs, and composite membranes. A variety of characterization techniques, such as S/TEM, SAXS, and AFM, have served as useful tools to investigate the relationship between polymer morphology/structure and ordering on the resulting hydroxide transport. Overall, it has been shown that microphase separation into favorable structures can promote the formation of ionic channels that better facilitate hydroxide transport.

https://doi.org/10.1021/acs.chemrev.1c00331
Chem. Rev. XXXX, XXX, XXX−XXX

Scheme 9. Synthesis of Trimethylammonium-Functionalized Tetrablock Copolymer AEMs by Vinyl Addition Polymerization of Norbornene Followed by Postpolymerization Modification[a]

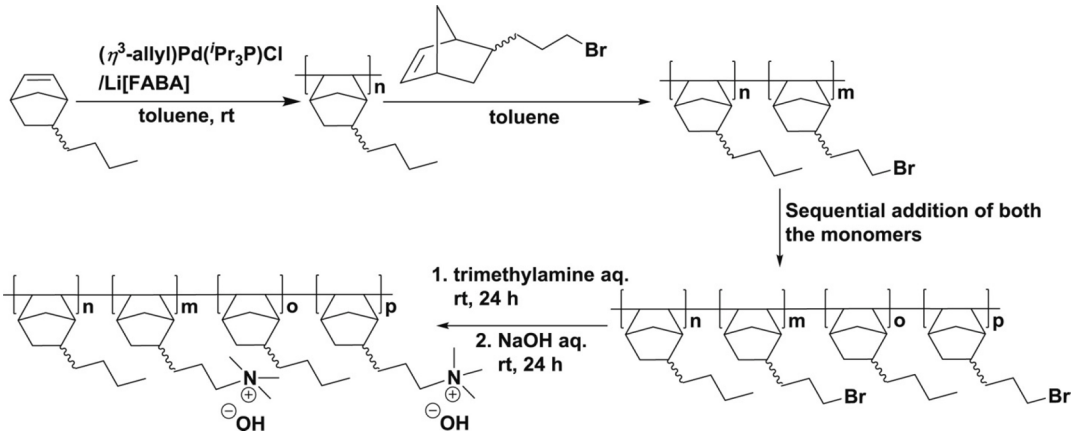

[a]Reproduced with permission from ref 787. Copyright 2019 Elsevier.

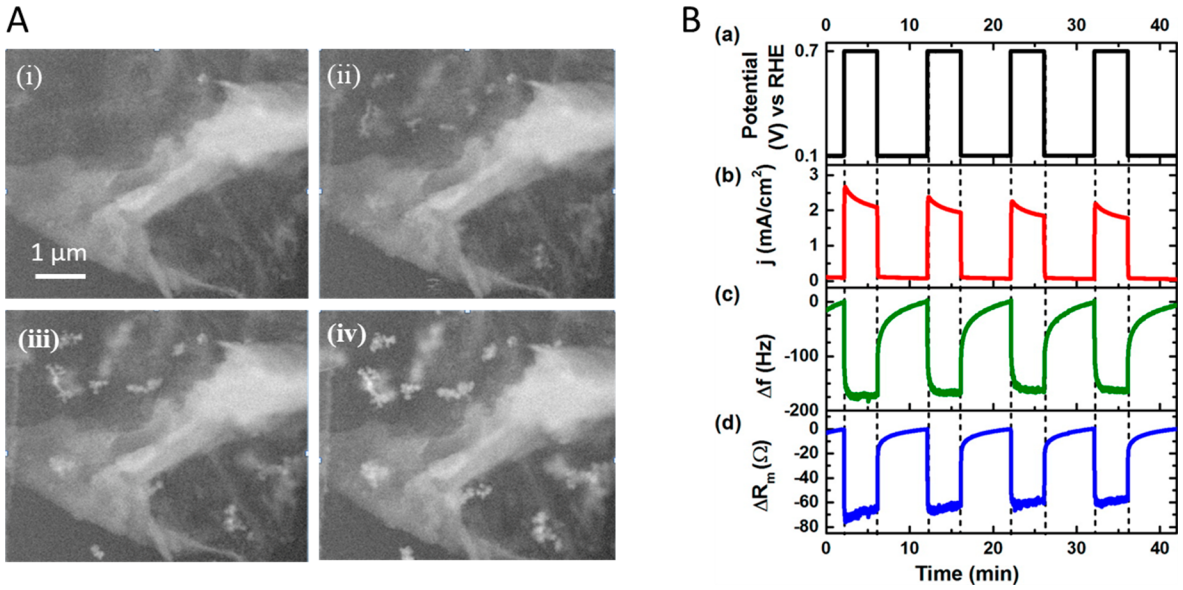

Figure 56. (A) *In situ* liquid-cell STEM images captured after (i) 0, (ii) 30, (iii) 60, and (iv) 90 s while conducting methanol oxidation in 0.1 M CH_3OH/0.1 M NaOH on a microchip modified by phosphonium-based ionomer and Pt nanoparticles. (B) Series of potential steps with the corresponding current density obtained and the simultaneous frequency (Δf) and motional resistance (ΔR_m) changes measured at the ionomer-film modified Pt QCM electrode in 0.1 M CH_3OH/0.1 M NaOH. Panel A is reprinted with permission from ref 834. Copyright 2015 American Microscopy Society. Panel B is reprinted with permission from ref 839. American Chemical Society.

To promote mechanically durable and stable membranes, aromatic groups should be avoided, as they tend to produce brittle films. Despite polyaromatic membranes showing stability under alkaline conditions, phenyl groups are susceptible to degradation through oxidation[798] and can adsorb onto metal-based electrocatalysts, both of which cause performance loss.[806] All-aliphatic polymers such as polyethylene and polynorbornenes are attractive alternatives for use in AEMs as they can produce mechanically tough membranes that are alkaline-stable and more resistant to oxidation. Ultimately, a balance of high conductivity, mitigation of WU, mechanical durability, and functionalities that avoid unfavorable interactions with catalysts is needed. While we have shown many successful systems implemented in AEMFCs, more systematic studies that probe the effects underlying intrinsic conductivity and the dependence of polymer structure, morphology, and architecture on the *ex situ* and *in situ* membrane characteristics must be carried out to further the understanding of AEMs during MEA operating conditions (*vide infra*).

6.3. Challenges for Membranes and Ionomers in an Electrochemical Environment

As the alkaline membrane and ionomer are polymer electrolytes for hydroxyl ions and water molecule transport, their conductivity and stability are usually of major concern. Protocols have been developed on measuring the true OH^- conductivity[833] and quantitatively assessing the chemical stability[745] of the membrane materials. However, the anion transport and the stability would be greatly influenced by the potential, carbonate formation, humidity, etc., during the operation of AEMFCs. The interaction between catalysts and ionomers also impacts the fuel cell performance. To resolve these challenges, fundamental studies on membrane/ionomer

https://doi.org/10.1021/acs.chemrev.1c00331
Chem. Rev. XXXX, XXX, XXX−XXX

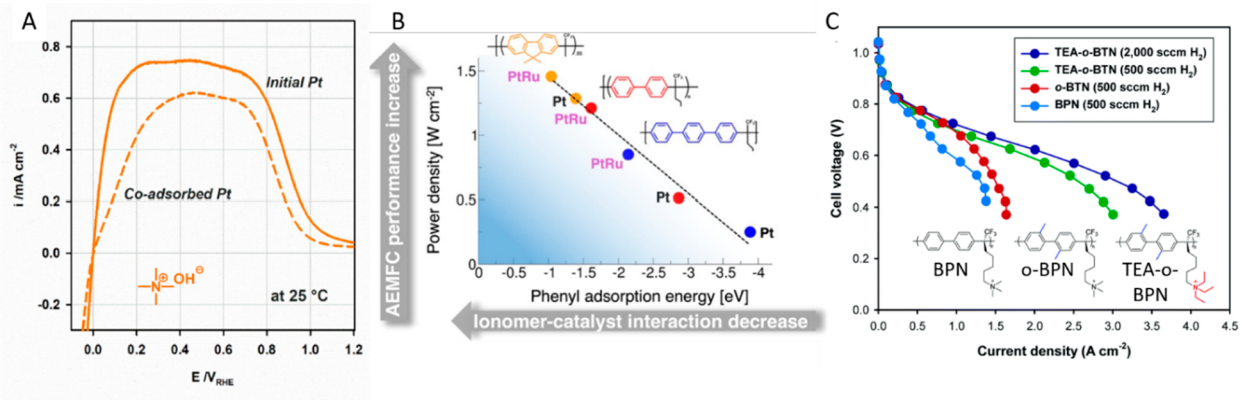

Figure 57. (A) HOR voltammograms of Pt at 25 °C in 0.1 M TMAOH before and after applying 0.1 V RHE for 15 min; rotating speed, 900 rpm; scan rate, 5 mV s^{-1}. (B) Correlation between phenyl adsorption energy of the ionomer backbone fragments on the Pt or PtRu surface and peak power density of MEAs using the corresponding ionomer and catalyst at the anode. (C) Impact of anode ionomer structure on AMFC performance. Performance measured at 80 °C under H_2/O_2 (500/300 sccm, 2000/1000 sccm) at 285 kPa backpressure. Panel A is reprinted with permission from ref 845. Copyright 2018 Elsevier. Panel B is reprinted with permission from ref 847. Copyright 2018 American Chemical Society. Panel C is reprinted with permission from ref 849. Copyright 2019 Royal Society of Chemistry.

behaviors in an electrochemical environment have been conducted. In particular, *operando/in situ* studies on anion/molecule dynamics and membrane degradation in electrochemical environments are germinating.

6.3.1. Dynamic Carbonate Formation in Alkaline Media. One of the main incentives of AEM development, as a substitute to the alkaline solution electrolyte, is to mitigate the carbonate precipitation in alkaline fuel cells. However, it has been shown that carbonate is still generated in the membranes with the presence of CO_2 and greatly impacts performance. Figure 56A shows the *in situ* liquid-cell STEM images of a phosphonium-based AEM deposited with Pt NPs during the methanol oxidation reaction (technical details can be found in section 8.2).[834] The formation of carbonate particles in the AEM over the entire electrode was observed for the first time with locally generated CO_2. Since the mobilities of formed CO_3^{2-} and HCO_3^- are lower than that of OH^-, the conductivity of AEM decreases with the increase of CO_2 uptake.[835−837] The fuel cell performance is also significantly compromised by the absorbed CO_2 in the AEM. For instance, the peak power density obtained with ambient air was less than half that obtained with clean air (< 0.1 ppm of CO_2) as the oxidizing gas.[838]

Nevertheless, despite the negative effect of carbonate on fuel cell performance, the incorporation of carbonate and bicarbonate species is found to be reversible. The anion exchange dynamics in a prospective AEM were studied via electrochemical quartz crystal microbalance (EQCM) with CO_2 locally generated from methanol oxidation.[839] The incorporation of CO_3^{2-} and $HCOO^-$ into the AEM and the simultaneous deswelling of the AEM film were observed from a sharp drop in oscillation frequency and motional resistance on the AEM-modified Pt quartz crystal electrode, when stepping the potential from 0.1 to 0.7 V vs the reversible hydrogen electrode (RHE), where the methanol oxidation takes place (Figure 56B). After stepping the potential back to 0.1 V where no oxidation is happening, the frequency and motional resistance slowly recovered to the original values, which indicates the film swelling and mass decrease resulting from the exchange of CO_3^{2-} and $HCOO^-$ in the film with OH^- in the solution. The fuel cell performance degradation resulting from the presence of CO_2 was also found to be reversible.[838,840,841] Inaba reported that the cell resistance increased, and the performance decreased with an increase in the CO_2 concentration in the inlet gas.[840] However, the gradual restoration of the performance after switching the cathode gas into pure oxygen suggests that the carbonate in AEMs is able to be self-purged with CO_2-free inlet gas, instead of forming precipitates as in the alkaline solution electrolyte.

6.3.2. Impact of Ionomer Adsorption on Electrocatalysts. The adsorption of ionomers to the catalysts significantly impacts the fuel cell performance and durability. Analogous to the more extensively studied proton exchange membrane fuel cell (PEMFC) system, ionomers provide anions to the catalysts while impeding the diffusion of reactant molecules (i.e., O_2 or H_2) to the catalyst surfaces.[473,842] Thick ionomer layers on the catalysts, caused by an inhomogeneous distribution of ionomers, lead to a lower reaction activity and fuel cell performance.[843] Strategies, such as employing carbon supports with accessible mesopores,[842] modifying support−ionomer interaction with N doping,[843] and treating ionomers under supercritical conditions,[844] have been developed for improving the performance or durability of PEMFCs with a more homogeneous ionomer distribution.

In alkaline media, the adsorption of ionomers on hydrogen oxidation reaction (HOR) catalysts and its influence on the catalytic activity have been mainly interrogated by Kim and his coworkers.[845] Cation−hydroxide−water coadsorption and phenyl group adsorption are the two specific adsorptions that they have proposed on the surface of platinum group metal HOR catalysts. A reduced HOR activity was observed after applying 0.1 V vs RHE to the Pt electrode in TMAOH for 15 min, compared with the initial Pt (Figure 57A), indicating specific adsorption of TMA^+ under potential polarization.[846] The H_2 diffusion barrier resulting from the coadsorbed layer was responsible for the decreased activity, which was proven by combining impedance analysis with the rotating disk electrode (RDE) to distinguish the diffusion-controlled process from the kinetic-controlled process. To investigate the phenyl group adsorption, the fuel cell performances of polyaromatic ionomers with different backbone structures at the anode, which have a different DFT-calculated adsorption energy on catalysts (Pt or PtRu), were evaluated and compared.[847] The

https://doi.org/10.1021/acs.chemrev.1c00331
Chem. Rev. XXXX, XXX, XXX−XXX

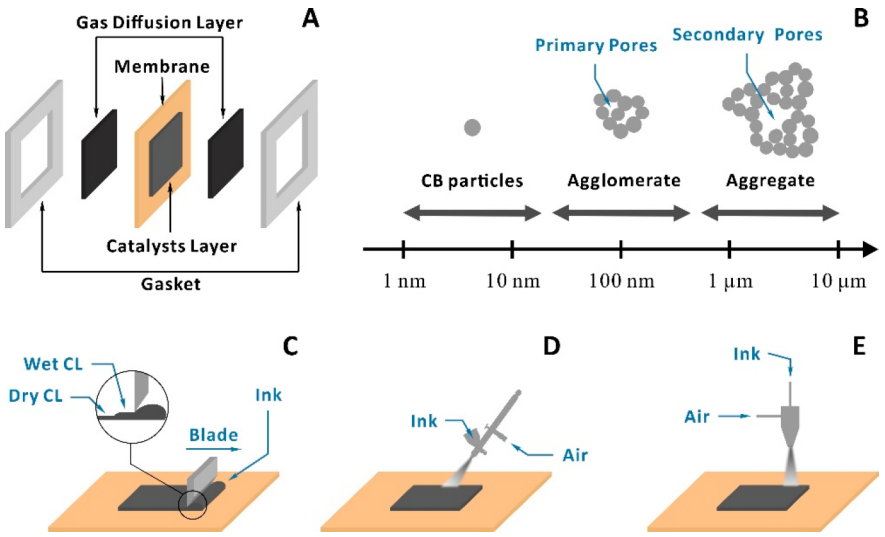

Figure 58. Diagrammatical illustration of the MEA structure and MEA fabrication methods. (A) AEMFC MEA components and their relative position. (B) AEMFC CL structure forming illustration, schematically showing the aggregates forming and stacking process in CL fabrication. (C–E) AEMFC MEA fabrication methods: blade coating, air-brush spray, and ultrasonic spray, respectively.

results manifest that weaker phenyl adsorption would result in higher peak power density exhibited by Figure 57B.

The ionomer–catalyst interactions and gas permeability can be tuned by the structure and conformation of both the aromatic ionomer backbone and the tethered cations.[848−850] Figure 56C shows a significant enhancement of fuel cell performance by slightly altering the ionomer structure.[849] The symmetric methyl groups on the phenyl backbone increase the fractional free volume in the ionomer so that the hydrogen permeability increased. The triethylammonium group ameliorated the interaction between catalyst and ionomer with steric hindrance compared with the trimethylammonium group. Both modifications on the structure led to a higher performance, which suggests that ionomers, with a higher fractional free volume and weaker adsorption on catalysts, are expected to deliver a higher fuel cell performance.

6.4. Summary

There are numerous factors that can impact membrane performance and stability. The cation incorporated into the AEM will influence the rate of performance decay. Of the cations discussed in this section, piperidiniums, pentasubstituted imidazoliums, and tetrakisaminophosphoniums are the most promising cationic structures for long-term stability in an alkaline environment. The AEM's polymer backbone will determine the mechanical properties of the membrane, which in turn influences the durability, water uptake, and conductivity of the AEM. Hydrocarbon-based polymers yield the highest backbone stability under alkaline conditions. Furthermore, aliphatic backbones can avoid the adsorption of the backbone on the electrocatalysts which causes performance degradation. Even for the most stable AEMs, reversible carbonation can still cause a loss of performance, presenting a major challenge for the implementation of AEMs. The conditions used to test an AEM, when in an MEA, also drastically influence the resulting performance, which is discussed in detail in section 7.

7. MEMBRANE ELECTRODE ASSEMBLY (MEA) STUDIES

The early stages of anion exchange membrane fuel cell (AEMFC) research have mainly focused on the development of the alkaline polymer electrolytes (APEs), which include anion exchange membranes (AEMs) and ionomers. With many high-performance APEs developed in recent years, tremendous advancements have been made in AEMFCs. Performance metrics comparable to or even exceeding those of proton exchange membrane fuel cell (PEMFC) benchmarks have been achieved.[851,852] Key progress has also been made in AEMFC stability.[3,853] Non-Pt-group metal (PGM) catalysts have been successfully incorporated into AEMFCs enabling reduced cost.[16] The unique concern of carbonation has also been studied in detail.[854] In this section of the Review, we discuss the fabrication and performance tests of MEAs with both PGM-based and non-PGM-based electrocatalysts and emphasize the important effects of carbonation, water management, and mass transport in MEAs.

7.1. Introduction to AEMFC and MEA Fabrication

The core component of a fuel cell is the membrane electrode assembly (MEA) where the electrochemical reactions take place. The MEA has a sandwich structure; from the center out, it consists of a polymer membrane, a catalyst layer (CL), gas diffusion layer (GDL), and gasket as shown in Figure 58A. The term MEA can refer to all, or just the central, components. The number of layers is specified for clarity as needed. A 3-layer MEA refers to a membrane sandwiched by a CL on both sides. The membrane is crucial yet very challenging to design, because it serves as both a separator and an electrolyte. In other words, it must separate the gas-phase reactions at the cathode from those at the anode and permit ionic transport between the two electrodes while being electronically insulating. In AEMFCs, the membrane is an OH^- transporting AEM. The CL is an electron- and ion-conducting porous layer consisting of ionomer and carbon-supported catalysts. Where the ion conductor (ionomer) and electron conductor (carbon support) intimately mix within porous voids, a solid–liquid–gas triple phase boundary (TPB) is formed. The TPB provides the simultaneous ion, electron, and mass transport pathways necessary for electrochemical reactions to take place. The construction of the TPB is one of the most important aspects in CL fabrication. Ionic and electron conductivity and porosity

https://doi.org/10.1021/acs.chemrev.1c00331
Chem. Rev. XXXX, XXX, XXX−XXX

must be well balanced to maximize the utilization of the electrocatalysts.

A 5-layer MEA, additionally, has a GDL atop both CLs. The GDL provides mechanical support for the CL and membrane and collects electric current. There is usually a microporous layer (MPL) on the GDL side facing the CL to better distribute gas and maintain appropriate levels of water in the CL and membrane. The MPL is made of high-surface-area carbon and polytetrafluoroethylene (PTFE) to obtain a high gas diffusion rate and optimal hydrophobicity. With a gasket on both sides of a 5-layer MEA, a 7-layer MEA is formed. The thickness of the gasket is very crucial; a too thin or too thick gasket will result in gas leakage or insufficient electron conductivity, respectively. Compressing the GDL by roughly 20% is normally appropriate to achieve good electron conductivity and maintain the structural integrity of the MEA. The compression ratio of the gasket itself should also be considered while selecting the gasket thickness. A 7-layer MEA sandwiched between flow field plates constitutes a complete single fuel cell.

Fabrication of the CL is the primary part of the MEA preparation. The CL is formed by applying catalyst ink onto the membrane or GDL using various methods. The first step in all methods is the preparation of the catalyst ink. This is done by stirring and ultrasonication to disperse the carbon-supported catalyst powder and ionomer into a solvent. Isopropanol is a common solvent owing to its good carbon dispersion quality and appropriate boiling point. The porous structure of the CL is mainly constructed by the carbon support. Carbon particles will spontaneously form agglomerates of several hundred nanometers in the catalyst ink as schematically shown in Figure 58B. Primary pores form naturally as a consequence of agglomeration. During the CL fabrication process, the solvent is removed, and agglomerates further stack together to form micrometer-scale aggregates. This leads to the formation of larger secondary pores.

Depending on where the catalyst ink is applied during the fabrication process, CL fabrication methods can be divided into gas diffusion electrode (GDE) methods and catalyst-coated membrane (CCM) methods. The catalyst ink is applied onto the GDL in GDE methods and directly onto the membrane in CCM methods. CCM methods are now more widely used due to the better membrane/CL interface, often leading to a better performance and stability. The GDE method lends itself to hot pressing. This enables good membrane/CL interphase formation if the membrane and ionomer have appropriate glass transition temperatures.

How the catalyst ink is applied defines the MEA fabrication methods, such as airbrush spray, ultrasonic spray, blade coating, slot-die, and microgravure roll-to-roll coating. Blade coating-based methods are highly efficient and often used in high-volume production processes but require more catalyst for a single batch. The catalyst slurry/ink is applied onto a substrate (GDL or membrane) evenly using a moving blade as schematically shown in Figure 58C. The substrate is then heated to evaporate the solvent from the ink, forming the CL. Catalyst loading on the MEA can be controlled by adjusting the blade height, ink concentration/composition, ink supply speed, blade moving speed, etc. The blade coating catalyst slurry/ink requires a higher concentration (higher solid content) to obtain proper rheological properties. Airbrush spray (Figure 58D) and ultrasonic spray (Figure 58E) are more suitable for small MEAs and are often used in laboratory MEA fabrication. In the airbrush method, the catalyst ink is directly loaded in a gravity-fed airbrush and sprayed onto the substrate manually or with the aid of an *XY* table. Again, the substrate is heated to accelerate solvent evaporation ensuring that a uniform CL is produced. In the ultrasonic spray method, the catalyst ink is atomized by the ultrasonic nozzle and carried down by a small air flow. The ultrasonic nozzle is mounted on a robotic gantry and moves to spray the catalyst ink onto the heated substrate. In spray-based methods, catalyst loading is controlled by varying the volume of catalyst ink sprayed. Ultrasonic spray creates smaller and more uniform droplets (usually <50 μm) than airbrush (usually >100 μm), resulting in a better CL structure. In all MEA fabrication methods, the substrate (GDL or membrane) is placed on a vacuum hot plate, and a plastic mask is used to define the region (size and shape) the CL occupies on the substrate.

The optimal MEA fabrication method depends on the properties of catalyst and ionomer used and on the production scale. Typically, the ink is sprayed onto the membrane (CCM method). The GDE method is used in polyethylene (PE)-backbone-based MEA fabrication[819,851] mainly because PE-backbone-based APE membranes are often resistant to catalyst ink adhesion, resulting in exfoliation of the CL.

To fully exploit the potential of AEMFCs, the MEA fabrication process must be optimized for the specific catalyst and APE pair. This requires careful consideration of several process variables including solvent selection, ink deposition method, etc. Catalyst ink solvents should facilitate a good dispersion of both catalyst powder and ionomer. The solvent's boiling point must also be in a suitable temperature range to produce a uniform CL upon deposition. Dispersing processes (stirring and ultrasonic) should be long enough to ensure a homogeneous and relatively stable catalyst dispersion. Spray-based methods are more suitable for small-batch laboratory MEA fabrication, and airbrush spraying is often used considering availability. Future AEMFC development and MEA fabrication will focus on applying non-PGM catalysts, and fabrication process optimization should take non-PGM catalyst properties into consideration. As such, blade coating methods may be more suitable in thick (high-loading) non-PGM CL fabrication.

Prior to assembling the fuel cell, an ion exchange bath is usually required because most APEs and ionomers are synthesized in halide rather than OH^- form. Ion exchanging is often accomplished by soaking the CCM or GDE and membrane in an alkaline solution at elevated temperatures (usually 1 M KOH at 60−80 °C). Thorough ion exchange is crucial for achieving a high AEMFC performance. Any remaining anion (usually halides) will hinder OH^- transportation and sometimes adsorb onto catalysts, poisoning them. Close attention should also be paid to residual surfactants remaining from the catalyst synthesis process. Even minor contamination will result in severe poisoning of the fuel cell catalysts.

7.2. AEMFC Performances

Although the concept of an AEMFC was proposed in the early 2000s,[855,856] and numerous studies have been conducted since, it was not until the mid-2010s that AEMFC performances were widely reported in the literature. After decades of development, AEMFC performance has improved dramatically. This is intimately linked to the recent advances of APEs that exhibit both facile OH^- transport and good mechanical properties.

https://doi.org/10.1021/acs.chemrev.1c00331
Chem. Rev. XXXX, XXX, XXX−XXX

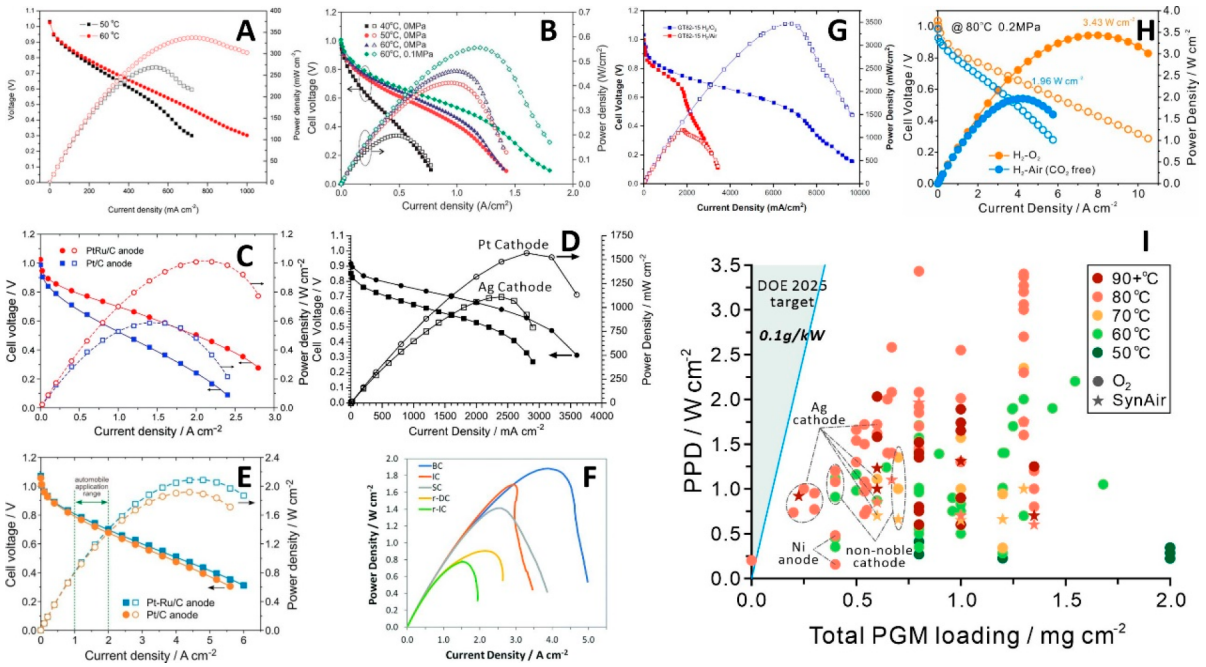

Figure 59. AEMFC performances and comparison with respect to MEA PGM loading. The AEMFC performances using PGM catalysts, pure H_2 in the anode, and O_2 in the cathode if not otherwise specified. (A, B) With 0.4 mg_{Pt}/cm^2 in both the anode and cathode. (C) With a PtRu (red line) or Pt (blue line) anode and Pt cathode, both 0.4 mg_{PGM}/cm^2. (D) With a PtRu anode (0.6 mg/cm^2) and Pt (0.4 mg/cm^2) or Ag (1.0 mg/cm^2) cathode. Cell tested at 70 °C. (E) With a PtRu anode or Pt anode and Pt cathode, all 0.4 mg/cm^2. Cell tested at 80 °C with 0.2 MPa backpressure. (F, G) With a PtRu anode and Pt cathode with a total loading of about 1.2−1.6 mg_{PGM}/cm^2. Cell tested at 80 °C. (H) With a PtRu anode and Pt cathode, all 0.4 mg/cm^2. Cell tested at 80 °C with 0.2 MPa backpressure. AEMFC performance advanced dramatically with high-performance APE development, cell fabrication, and testing protocol optimization. (I). The AEMFC performance comparison with respect to total PGM catalyst loading on both the anode and cathode, including Pt, Ru, Pd, Ir, and Rh. The light green area on the left side of the blue line represents the DOE 2025 target[873] for PGM loading (0.1 g/kW). Different colors represent different cell operating temperatures; the circle and pentagram represent the usage of pure oxygen or air (CO_2-free) as the cathode oxidant, respectively. AEMFCs using Ag-based or non-PGM catalysts are noted in the graph. All panels are reproduced with permission. Panel A is reproduced from ref 859. Copyright 2013 Elsevier. Panel B is reproduced from ref 860. Copyright 2013 The Authors, Royal Society of Chemistry. Panel C is reproduced from ref 861. Copyright 2015 The Authors, Royal Society of Chemistry. Panel D is reproduced from ref 577. Copyright 2017 Royal Society of Chemistry. Panel E is reproduced from ref 862. Copyright 2018 The Authors, Wiley. Panel F is reproduced from ref 865. Copyright 2018 Royal Society of Chemistry. Panel G is reproduced from ref 866. Copyright 2019 The Electrochemical Society. Panel H is reproduced from ref 852. Copyright 2021 The Authors.

With proper MEA fabrication and testing protocol optimization, initial performance is no longer a deficiency for AEMFCs, relative to the stat-of-the-art PEMFCs. Utilization of non-PGM catalysts is another important milestone that has been achieved. Non-PGM oxygen reduction reaction (ORR) catalysts have shown very promising results in AEMFCs (sections 3.2 and 4.2). Several oxide-based ORR catalysts have achieved peak power densities (PPDs) of over 1 W/cm^2.[16,871,872] However, AEMFCs with a non-PGM hydrogen oxidation reaction (HOR) catalyst are largely unexplored. In this section, we will review the AEMFC performance advancements and discuss key factors that have led to this progress. The potential for further progress will be discussed, including CL optimization, AEMFC testing and operating conditions, and corresponding requirements for the APE.

7.2.1. PGM-Based Catalysts. In the early history of AEMFCs, the lack of suitable APEs has limited their performance. To guide APE development, an accurate evaluation of APE performance is required. Although many types of APEs have been studied, few of those have been tested in an actual fuel cell. To exclude variability associated with the electrocatalyst, commercially available fuel cell catalysts (e.g., from Johnson-Matthey) are commonly used when assembling an AEMFC to evaluate APE performance (Figure 59). Pt/C is usually used as the cathode ORR catalyst. At the anode, PtRu/C is a more favorable HOR catalyst (section 3). Although air is the oxidant in practical fuel cell applications, pure oxygen is still used in most research tests to exclude the impact of CO_2.

The lower diffusion rate of OH^- compared to H^+ has been a major challenge in synthesizing APEs with sufficiently high ionic conductivities. Many strategies have been adopted, such as increasing the IEC, constructing microphase separation, etc. (see section 6.2 for more details). Due to the low ionic conductivity of APEs developed in early stages, AEMFCs reported very low PPDs (usually <200 mW/cm^2).[857,858] As APEs with superior ionic conductivity emerged, AEMFC performance gradually improved. Yi and coworkers achieved a PPD of 350 mW/cm^2 with a maximum current density of 1000 mA/cm^2 (Figure 59A).[859] They employed a cross-linked composite APE with a high ion exchange compacity (IEC) (>2 mequiv/g). Pan et al. further reduced APE ionic resistance using a thin composite membrane (25 μm), reaching a PPD of 550 mW/cm^2 and a maximum current density of 1800 mA/cm^2 (Figure 59B).[860] It proved that lowering the ionic resistance can increase AEMFC performance, but there was still a substantial gap between AEMFC and PEMFC performance.

Researchers then realized that the slow HOR kinetics in alkaline conditions are an important limiting factor in AEMFCs. It was found that a PtRu alloy is better at catalyzing

https://doi.org/10.1021/acs.chemrev.1c00331
Chem. Rev. XXXX, XXX, XXX−XXX

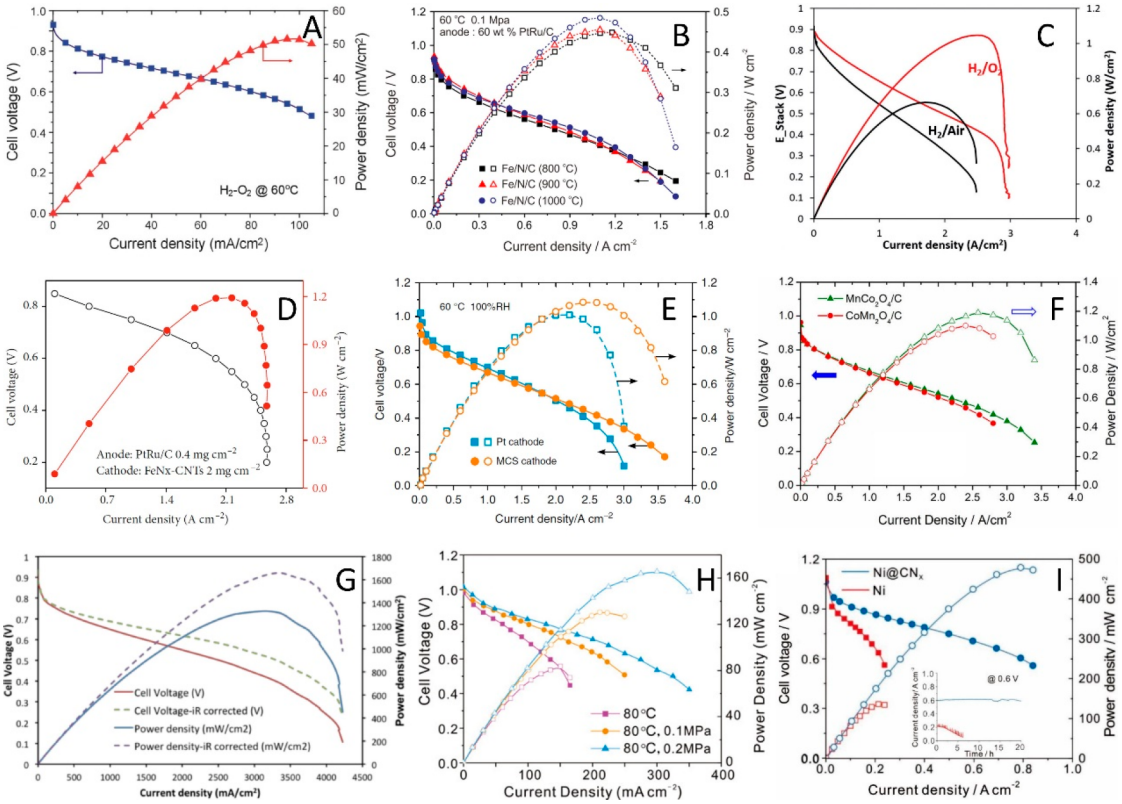

Figure 60. AEMFC performances using non-PGM catalysts. (A) Ni-based anode catalysts and Ag cathode catalysts. (B–D) Metal-containing nitrogen-doped carbon (M–N–C)-based cathode catalysts and composite M–N–C-oxide cathode catalysts and PtRu anode catalysts. (B) Fe–N–C cathode with a catalyst loading of 2 mg/cm^2 and PtRu/C anode (0.4 mg_{PtRu}/cm^2). (C) N-doped carbon-supported CoO_x cathode with a metal loading of 2.4 mg/cm^2 and PtRu/C anode (0.7 mg_{PtRu}/cm^2). (D) FeN_x-carbon nanotube (CNT) cathode with a metal loading of 2 mg/cm^2 and PtRu/C anode (0.7 $m4_{PtRu}$/cm^2). (E–G) Transition metal oxide-based cathode catalysts. (E) $Co_{1.5}Mn_{1.5}O_4$/C cathode (40 wt %) with an oxide loading of 0.8 mg/cm^2 and PtRu/C anode (0.4 mg_{PtRu}/cm^2). (F) $MnCo_2O_4$/C and $CoMn_2O_4$/C (80 wt %) cathode with same oxide and PtRu/C anode with the same loading as in panel E. (G) $CoFe_2O_4$/C cathode (50 wt %) with an oxide loading of 2.4 mg/cm^2 and PtRu/C anode (0.7 mg_{PtRu}/cm^2). (H) Ni anode coated with a carbon shell. (I) Ni anode coated with a N-doped carbon shell (CN_x). Pure H_2 in the anode and O_2 in the cathode if not otherwise specified. All panels are reproduced with permission. Panel A is reproduced from ref 13. Copyright 2008 The Authors, National Academy of Sciences. Panel B is reproduced from ref 553. Copyright 2017 The Authors, American Chemical Society. Panel C is reproduced from ref 870. Copyright 2019 Wiley. Panel D is reproduced from ref 807. Copyright 2020 AAAS. Panel E is reproduced from ref 16. Copyright 2019 Springer Nature. Panel F is reproduced from ref 871. Copyright 2019 The Authors, American Chemical Society. Panel G is reproduced from ref 872. Copyright 2018 Multidisciplinary Digital Publishing Institute. Panel H is reproduced from ref 262. Copyright 2020 American Chemical Society. Panel I is reproduced from ref 263. Copyright 2021 The Authors.

the HOR in alkaline conditions compared to pure Pt (section 3).[183,187,189] Commercial PtRu/C catalysts were applied to the AEMFC anode and demonstrated the first AEMFC to achieve a PPD of 1.0 W/cm^2 along with a maximum current density of 2.8 A/cm^2 (Figure 59C).[861] This leap in progress validated the potential of AEMFCs and inspired more researchers to tackle the many remaining challenges. During this period of development, APEs were usually made based on engineering plastics, such as polysulfone, polyether ether ketone, and poly(phenylene oxide).[14,15] However, the mechanical strength of these APEs was not enough to withstand harsh fuel cell operating conditions (high temperature and high back pressure), so AEMFCs were often tested at low temperatures (≤60 °C) and small back pressure (≤0.1 MPa), which limited further performance advancement.

In pursuit of a better AEMFC performance, higher cell operating temperatures are needed to facilitate ion transport and accelerate electrode kinetics, especially for the sluggish ORR. Varcoe and coworkers increased the fuel cell testing temperature to 70 °C using a PE-backbone-based APE.[577] The cell performance was improved significantly, reaching a PPD of 1.6 W/cm^2 with a maximum current density of 2.9 A/cm^2 (Figure 59D). Zhuang and coworkers further elevated the testing temperature and back pressure (80 °C, 0.2 MPa) by employing more robust poly(aryl piperidinium)-based APEs,[862] which led to a huge performance boost. A PPD of 2.1 W/cm^2, which is comparable to PEMFC performance, was achieved along with a maximum current density of 6 A/cm^2 (Figure 59E). This attested to the potential of AEMFCs for high-power applications such as fuel cell electric vehicles (FCEVs). They also discovered that, under an elevated temperature, the performance difference between Pt and PtRu anode catalysts diminished as the HOR activity of both increased, but Pt shows a larger activation energy than PtRu/C (Figure 12D).[862] Many researchers subsequently adopted the aforementioned testing conditions with PtRu/C as the anode and also achieved a high AEMFC performance with a wide variety of APEs developed, such as poly(aromatics) (PA)-based (section 6.2.4), poly(olefin)-based (section 6.2.6), and poly(norbornene) (PNB)-based (section 6.2.7). PPDs of 1.5 W/cm^2 or above have now been reported by several groups.[792,813,863,864]

https://doi.org/10.1021/acs.chemrev.1c00331
Chem. Rev. XXXX, XXX, XXX–XXX

These advancements in HOR catalysts and APEs demonstrated that AEMFC performance was no longer limited solely by the reaction rate or membrane conductivity. As such, water management and mass transport began to play important roles in further advancing AEMFC performance. Water is consumed at the cathode and generated at the anode, which may result in severe drought at the cathode and flooding at the anode. Proper water management in AEMFCs is important to further improve their performance. Mustain et al. alleviated anode flooding by manipulating anode ionomer and carbon content and achieved a PPD of 1.9 W/cm^2 (Figure 59F) with a PE-based APE.[865] Kohl et al. further boosted AEMFC performance to a PPD of 3.5 W/cm^2 (Figure 59G) using a PNB-based APE with a very high IEC (>3.7 mequiv/g) to facilitate water transport.[866] However, they used high catalyst loadings of 0.7 mg_{PtRu}/cm^2 (anode) and 0.6 mg_{Pt}/cm^2 (cathode). Zhuang and coworkers examined AEMFC water transport using an ultrathin (<15 μm) poly(aryl piperidine)-based APE, achieving a PPD of 3.43 W/cm^2 with a record maximum current density of 10.5 A/cm^2 (Figure 59H) with a lower PGM catalyst loading of 0.4 mg_{PtRu}/cm^2 (anode) and 0.4 mg_{Pt}/cm^2 (cathode).[852] It should be noted that researchers often employed a very high gas feeding flow rate (from 500 up to 2000 sccm) to alleviate flooding and facilitate mass transport in order to improve performance. However, the amount of gas fuel at such a high flow rate is 1−2 orders of magnitude higher than that consumed by AEMFCs, leading to low fuel utilization. A better understanding of water management is required in order to lower the gas flow rate to a level similar to PEMFCs. AEMFCs without anode humidification and H_2 emission can be achieved with proper adjustment of the hydrophilicity/hydrophobicity of the ionomer resulting in good water management.[867] By utilizing all of the aforementioned strategies, many researchers have now achieved AEMFC performances that rival or even exceed PEMFCs,[819,851,868−872] demonstrating that the initial performance is no longer a shortcoming for AEMFCs.

However, there are still many demands to be met in order to achieve performance metrics relevant for the application of AEMFCs. Thus far, good power densities have only been achieved with very high PGM catalyst loading as summarized in Figure 59I. Clearly, most examples reported are far from reaching the DOE 2025 target[873,874] (0.1 g_{PGM}/kW, drawn with a blue line on the left side of Figure 59I). Lowering the PGM catalyst loading to a level similar to PEMFCs should be the major task in the next stage of developing AEMFC with the use of non-PGM catalysts as the ultimate goal. In addition, most AEMFCs have been tested using pure oxygen (Figure 59I), but any practical application will most certainly require air. Only a small fraction of AEMFCs have been tested using CO_2-free air (denoted with a star), and the performances were much lower, due to the lower oxygen concentration.[792,793] The highest performance achieved using CO_2-free air as the cathode oxidant is 1.96 W/cm^2 (Figure 59H).[852] Future AEMFC research should shift to air as the cathode oxidant and investigate the influence of CO_2 in air on AEMFC performance.

7.2.2. Non-Pt and Non-PGM Catalysts. A big advantage of AEMFCs is the alkaline environment, which enables the use of non-PGM catalysts, thus lowering the cost significantly, at both the cathode and the anode. Achieving an all-non-PGM catalyst-based AEMFC has been the ultimate goal for researchers since the initial period of development. Zhuang and coworkers first reported an AEMFC completely free from noble metal catalysts, using Cr-decorated Ni as the anode and Ag as the cathode, which achieved a PPD of 50 mW/cm^2 (Figure 60A).[13] Replacing Ag with Co-polypyrrole (PPy)/C at the cathode yielded a PPD of 40 mW/cm.[261] Though exhibiting only modest activity, these works glimpse at the possibility of a low-cost, high-performance alkaline fuel cell.

There has been more success in removing PGMs from the cathode side of the MEA compared to the anode. This is because, unlike for the HOR, there are many examples of PGM-free materials that show ORR activity and are stable in the fuel cell environment (sections 4.2 and 4.3). By far the most extensively studied non-PGM ORR electrocatalysts are metal-containing N-doped carbons (M−N−C) due to their excellent rotating disk electrode (RDE) performances—some exhibiting a higher half-wave potential than Pt/C (Figures 25 and 26). However, Zhuang and coworkers showed that the spectacular ORR activity of Fe−N−C in RDE experiments does not translate into a comparable MEA performance. Although their Fe−N−C catalyst's RDE activity was equal to 20 wt % Pt/C (Figure 26I), a PPD of only 500 mW/cm^2 (Figure 60B) could be achieved in MEAs.[553] The low MEA performance is likely due to the low density of active sites and small micropores (<10 nm) that hinder access to many active sites, since the ionomer cannot penetrate into those micropores. Additionally, the stability of M−N−Cs also requires further investigation.

Mustain and coworkers adopted a composite nitrogen-doped carbon−CoO_x (N−C−CoO_x) catalyst in AEMFC cathodes and achieved a PPD of 1.05 W/cm^2 (Figure 60C).[870] They proposed both Co oxides and nitrogen-doped carbon as possible active sites for the ORR. Full utilization of active sites is necessary for M−N−C-based ORR catalysts to achieve a high performance in AEMFCs. Wei and coworkers synthesized an FeN_x-CNT catalyst using an Fe-ZIF@PPy precursor, which likely resulted in active sites on the surface instead of micropores. A higher PPD of 1.2 W/cm^2 was achieved (Figure 60D),[807] indicating that the structure of the active sites is also important to achieve a high performance.

Transition metal oxides (TMOs) are also capable of catalyzing the ORR and are exclusive to AEMFCs because of their instability in acid. Mn−Co spinel composite oxides were applied in the cathode, achieving a PPD of 1.1 W/cm^2 (Figure 60E)[16] at 100% relative humidity (RH) and a significantly better PPD than the Pt/C cathode at 50% RH (Figure 23B). This study also demonstrated how important water activation, on Co sites in this case, is for the ORR in alkaline media, especially at low RH conditions. Recently, Abruna and coworkers systematically explored the compositions of Co−Mn oxides and the ratio of oxide to carbon supports (40−80%) at the cathode, among which $MnCo_2O_4$ with 80% mass fraction supported on carbon achieved an optimal benchmark PPD of 1.2 W/cm^2 at 2.5 A/cm^2 at an oxide loading of 0.8 mg/cm^2 (Figure 60F).[871] A Co−Fe composite oxide ORR catalyst, explored by Mustain and coworkers, reached a PPD of 1.35 W/cm^2 at a very high oxide loading of 2.4 mg/cm^2 (Figure 60G).[872] These results exemplify the potential of metal oxide-based ORR catalysts despite their modest RDE performance. The next step for metal oxide-based catalyst studies is to focus on improving their intrinsic activity and, more importantly, long-term stability necessary for practical applications.

The development of non-PGM catalysts for the HOR now remains the biggest challenge for AEMFCs. Many works have

https://doi.org/10.1021/acs.chemrev.1c00331
Chem. Rev. XXXX, XXX, XXX−XXX

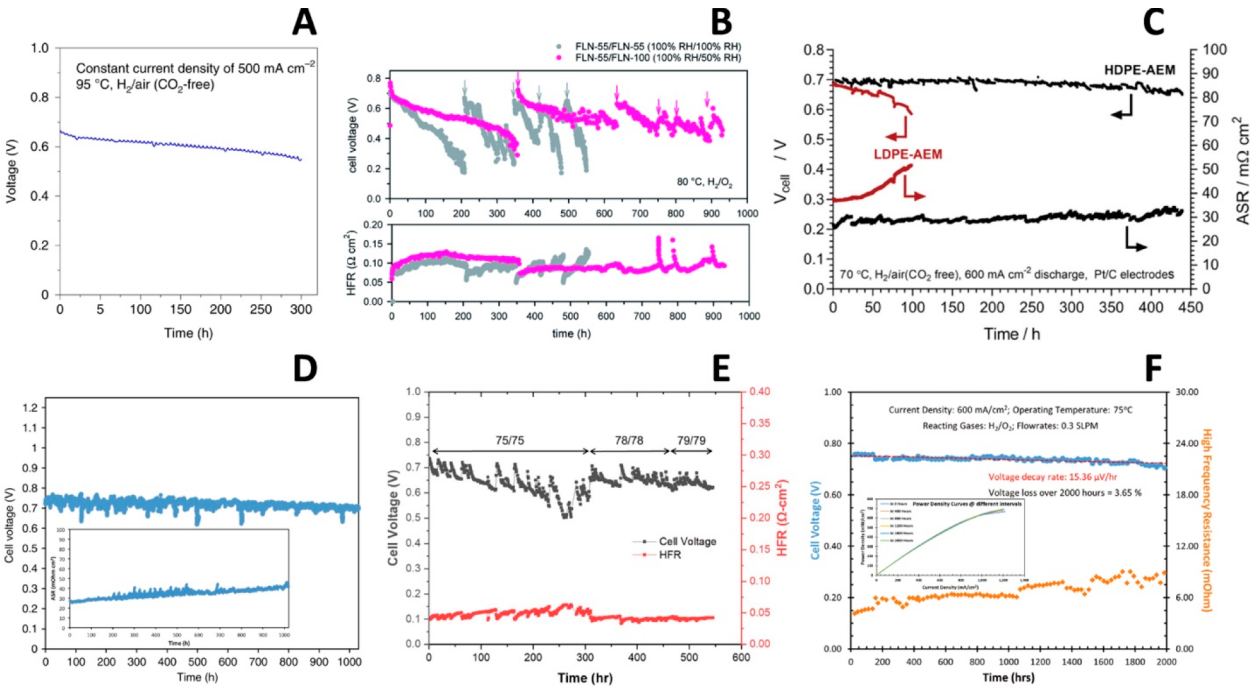

Figure 61. Constant current AEMFC stability test of most studied APEs. (A, B) Stability of AEMFC using poly(aromatics)-based APE. (C, D) Stability of AEMFC using poly(ethylene)-based APE. (E, F) Stability of AEMFC using poly(norbornene)-based APE. PGM-based catalysts and air (CO_2-free) are used in these stability tests. A Pt/C cathode and PtRu/C anode were used in those studies. All panels are reproduced with permission. Panel A is reproduced from ref 793. Copyright 2019 Springer Nature. Panel B is reproduced from ref 877. Copyright 2020 Royal Society of Chemistry. Panel C is reproduced from ref 819. Copyright 2019 Royal Society of Chemistry. Panel D is reproduced from ref 904. Copyright 2020 Springer Nature. Panel E is reproduced from ref 851. Copyright 2019 The Electrochemical Society. Panel F is reproduced from ref 853. Copyright 2020 Wiley.

been done in exploring non-PGM catalysts, but nearly all researchers were evaluating the catalyst HOR activity using RDE testing without further AEMFCs integration.[241,244,245,257,875,876] Only Ni has a shown marginal HOR activity among non-PGM catalysts.[233−263] However, Ni is prone to surface passivation due to the formation of an oxide under anodic polarization at large current densities. Zhuang and coworkers increased the antioxidation ability of Ni catalysts by a carbon shell coating formed during vacuum pyrolysis, and as a result, a PPD of 160 mW/cm^2 was achieved (Figure 60H).[262] Recently, a nitrogen-doped carbon shell was used to prevent Ni (Ni@CN_x) catalysts from oxidation and further improved the HOR activity (Figure 14D−F). A PPD of 480 mW/cm^2 was then achieved with a maximum current density of 0.85 A/cm^2 (Figure 60I).[263] In this study, a completely noble-metal-free AEMFC was realized, for the first time, and achieved a record PPD of 200 mW/cm^2 using a Ni@CN_x anode and $MnCo_2O_4$/C cathode.[263] These works demonstrated the ability of Ni to catalyze the HOR at the anode. A further improvement of the performance of Ni-based HOR electrocatalysts is required to achieve the use of completely precious-metal-free anodes in realistic high-performance AEMFCs. We also, again, emphasize the importance of testing catalysts in MEA, even at early stages of catalyst development, as we previously discussed in section 4.2.3 (Figure 23A,B). As has been shown numerous times, an excellent RDE performance does not imply the same in an MEA, as illustrated in Figure 26H,I, whereas a modest RDE performance may mask the potential of a highly active catalyst that would otherwise be highly active in an MEA, such as shown in Figure 23.

We include a discussion of Ag-based catalysts because of the significantly lower cost of Ag compared to PGMs (Ag, $0.9/g vs Pt, $36/g) and high ORR activity in alkaline media.[13,577−580] Many high-performance AEMFCs have been achieved using Ag-based catalysts in the cathode, and these points are indicated in Figure 59I.[13,577] These showed performances much closer to the DOE 2025 target.[873] The only AEMFC performance that achieved the DOE 2025 target is the aforementioned completely noble-metal-free AEMFC achieved using the Ni@CN_x catalyst in the anode and Mn−Co composite oxide catalysts in the cathode[263] (see the bottom left side of Figure 59I). These results indicate that developing non-PGM catalysts is crucial for achieving the DOE noble metal loading target, i.e., developing a high performance fuel cell with low cost, and should be one of the main tasks in subsequent AEMFC research.

In conclusion, very high AEMFC performances have been achieved, enabled by the development of high-performance APEs and advances in MEA fabrication techniques. It is foreseeable to achieve the DOE preliminary AEMFC milestones:[874] (1) By 2022, initial performance, 0.65 V at 1000 mA/cm^2 on H_2/O_2; $T \geq 80$ °C; $P \leq 150$ kPa; total PGM loading, ≤0.2 mg/cm^2; durability, ≤10% voltage degradation over 1000 h; $T \geq 80$ °C; $P \leq 150$ kPa; total PGM loading, ≤0.2 mg/cm^2; (2) by 2030, initial performance, ≥600 mW/cm^2 under H_2/air (maximum pressure of 1.5 atm) in a PGM-free MEA.

7.3. AEMFC Stability

AEMFC stability is crucial for achieving realistic fuel cell applications. In the early ages of AEMFC research, the cell stability was not studied because the performance was too poor

https://doi.org/10.1021/acs.chemrev.1c00331
Chem. Rev. XXXX, XXX, XXX−XXX

to begin with. As power density is now reaching target values, AEMFC stability is receiving more attention. Single cell stability has been mainly studied with commercially available noble metal catalysts (PtRu/C and Pt/C) to reveal the stability of APEs, and the stability test is usually conducted at constant current or constant voltage mode. CO_2-free air has been adopted as the cathode oxidant instead of pure O_2 in most APEFC stability tests, which is closer to realistic application conditions.

The fuel cell stability of poly(aromatic)-based APEs, discussed in section 6.2.4, was the first to be studied. Zhuang and coworkers reported that a continuous operating time of more than 100 h was achieved for a poly(*p*-terphenyl-piperidinium) (QAPPT) membrane at 80 °C with a current density of 0.2 A/cm^2 (H_2 and CO_2-free air fed in the anode and cathode, respectively).[792] The cell potential decreased from 0.7 to 0.6 V, with a degradation rate of ∼1 mV/h. A recent report on a similar type of polypiperidium, by Park and coworkers, showed a higher initial power density but a faster degradation rate (from 0.75 to 0.55 V within 100 h).[869] Yan and coworkers further increased the fuel cell working temperature to 95 °C and achieved 300 h of working life at a current density of 0.5 A/cm^2 using H_2 and CO_2-free air.[793] The cell potential dropped ∼19% from 0.67 to 0.54 V (Figure 61A) at a decreasing rate of 0.43 mV/h. Kim and coworkers optimized the PA-based ionomer used at the anode and cathode, improving lifetime to more than 900 h at a current density of 0.6 A/cm^2 at 80 °C using H_2 and O_2. The cell potential decreased from 0.78 to 0.4 V, with a potential loss of ∼0.4 mV/h (Figure 61B).[877] However, it should be noted that a replenishment process with NaOH solution was done several times to recover cell performance during the stability test, which reduced the high frequency resistance (HFR) significantly. This is by far the longest operating time reported using PA-based APEs.

PE-based APEs have also been widely studied due to their high stability (section 6.2.6), and thus, their fuel cell stability has also been reported. Mustain and coworkers reported a radiation-grafted ETFE with a lifetime of ∼400 h at 600 mA/cm^2 and a performance decay of ∼40%, but there was a significant voltage drop during the first 50 h.[865] Varcoe and coworkers then employed a high-density PE-based APE to further extended the working life to 450 h at 70 °C. Using H_2 and CO_2-free air,[819] the rate of cell voltage loss was only ∼0.14 mV/h from 0.7 to 0.64 V (Figure 61C), but the degradation rate increased in the final hours of operation. The HFR remained nearly unchanged at ∼30 mΩ cm^2 except in the initial and final stages. Mustain et al. further improved water management with hydrophobic PTFE in both GDL and catalyst layers and achieved a lifetime of more than 1000 h at a current density of 0.6 A/cm^2 at 65 °C (H_2 and CO_2-free air used).[853] The cell voltage decay rate was only ∼0.04 mV/h, ∼5.5% voltage loss from about 0.72 to 0.68 V (Figure 61D). The fuel cell HFR gradually increased from 26 to 43 mΩ cm^2 (Figure 61D, inset). This outstanding result shows the importance of good water management for AEMFC stability. It also exemplifies the challenges facing APEs to achieve long operation times at high temperature.

PNB-based APEs are another class of high-performance materials that have been studied widely in recent years, as previously discussed in section 6.2.7. Mustain and coworkers achieved an initial peak power density of 3.5 W/cm^2 and a stability of over 100 h at 600 mA/cm^2.[866] Kohl and coworkers achieved a working life of 550 h with a lightly cross-linked composite PNB-based APE with a current density of 600 mA/cm^2 at 80 °C using H_2 and CO_2-free air.[851] The cell voltage decreased by ∼17% from 0.72 to 0.6 V, at a rate of ∼0.22 mV/s (Figure 61E). The cell voltage was somewhat unstable, fluctuating over a large range of about 100 mV, and the feed gas humidity was changed several times to extend the working life of the device. These results show the necessity of proper water management for long AEMFC lifetimes. Mustain and coworkers then optimized the electrodes' hydrophobic/hydrophilic properties by manipulating ionomer properties. As a result, an outstanding working life of 2000 h was achieved at 75 °C with a current density of 0.6 A/cm^2 using H_2 and CO_2-free air (Figure 61F).[853] The average cell voltage loss rate was only about 0.015 mV/h (from ∼0.75 V initially to 0.7 V at the end), and the cell performances remained almost unchanged (Figure 61F, inset). The cell HFR gradually increased from 26.4 to 44.6 mΩ cm^2 in a 2000 h test. This groundbreaking result shows the potential of AEMFCs for practical applications.

Other than the aforementioned results which use Pt-based catalysts, some Pt-free and PGM-free AEMFC stability results have also been reported. Both Pd and Ag catalyst-based AEMFCs have demonstrated a working life of 100 h.[793,878] In terms of non-PGM catalysts, a 100 h life has also been achieved with nitrogen-doped carbon−CoO_x ORR catalysts.[870] These results show the potential of non-Pt and non-PGM catalysts for long-duration operation.

Up to now, AEMFC stability tests have been conducted primarily to evaluate the stability of APEs developed. The stabilities of different types of APEs are quite different as discussed above; PNB-based APEs showed the best stability, and PE-based APEs also showed good stability performances, while PA-based APEs had trouble in achieving long-term stability. This showed that APEs with fewer aromatic groups tend to have better stability performances. This is likely due to aryl adsorption on catalysts and oxidation to phenol as reported. More work is needed to study the stability of the aryl groups during fuel cell operation to further guide the development of APEs. The fuel cell operation temperature is still restricted due to APE stability concerns, mainly the stability of cations, which is discussed at length in section 6.1. More stable cations are needed to achieve a longer AEMFC working life at higher temperatures and larger current densities.

7.4. AEMFC Carbonation

Different from an alkaline fuel cell (AFC) which employs an alkaline solution as the electrolyte, carbonate precipitation is effectively suppressed in AEMFCs since the cationic groups are tethered to polymers, and there is no free-floating OH^- as in alkaline solution.[13] However, when hydroxide is generated at the cathode in AEMFCs (eq 13), it will quickly turn into carbonate (eq 14) with continuous CO_2 feeding in the cathode when air (often containing 400 ppm of CO_2) is used:

$$\frac{1}{2}O_2 + 2e^- + H_2O \rightarrow 2OH^- \quad (13)$$

$$2OH^- + CO_2 \rightarrow H_2O + CO_3^{2-} \quad (14)$$

The generated carbonate then migrates through the membrane towards the anode, where the carbonate participates in a hydrogen oxidation reaction to reform CO_2 which is purged from the anode in the product gas stream (eq 15). This is the "self-purging" process of carbonation in AEMFCs.[854,879]

https://doi.org/10.1021/acs.chemrev.1c00331
Chem. Rev. XXXX, XXX, XXX−XXX

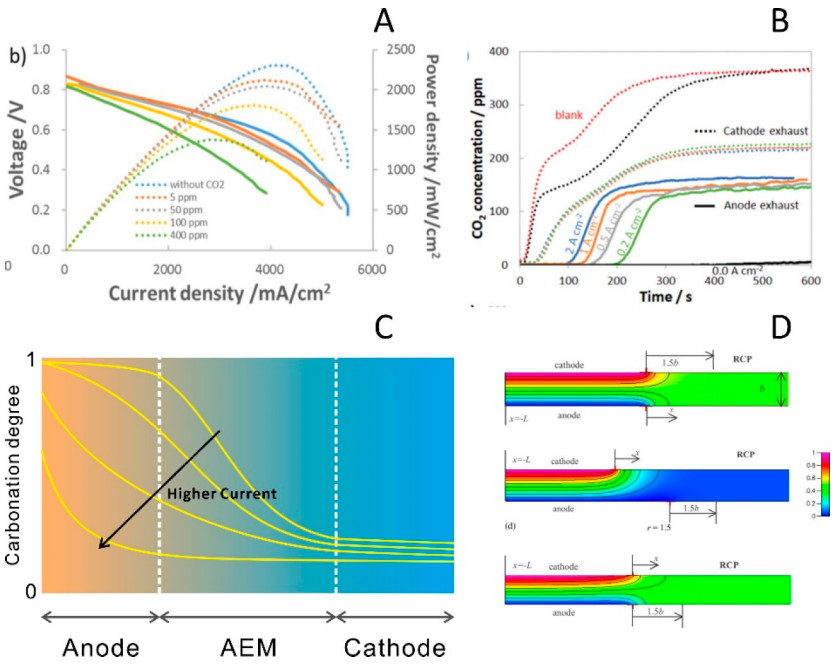

Figure 62. CO_2 influence on AEMFC performance and illustration of potential deviations in a thin electrolyte reference electrode measurement. (A) Influence of carbonation on AEMFC performance with different CO_2 concentrations. (B) Anode and cathode emission CO_2 concentration when CO_2 is purged to the cathode; the CO_2 purging process at the AEMFC anode is called "self-purging". (C) Schematic illustration of the carbonate distribution in an AEMFC; yellow and blue represent higher and lower carbonation degrees, respectively. The yellow line depicts the carbonation degree across the anode, AEM, and cathode. (D) Influence of electrode symmetry and electrode kinetics on potential distribution in thin electrolyte system; b is the thickness of the electrolyte. Different potentials are presented in different colors (see scale bar on the right). All panels are reproduced with permission. Panel A is reproduced from ref 879. Copyright 2020 Elsevier. Panel B is reproduced from ref 854. Copyright 2019 Royal Society of Chemistry. Panel D is reproduced from ref 889. Copyright 2004 Elsevier.

$$H_2 + CO_3^{2-} - 2e^- \rightarrow H_2O + CO_2\uparrow \quad (15)$$

The CO_2 intake at the cathode, carbonate transporting in the AEM, and carbonate "self-purging" at the anode compose the carbonate balance in AEMFCs.

7.4.1. Effects of Carbonation on AEMFC Performance. The existence of CO_2 lowers the AEMFC performances significantly. There is a noticeable influence on performance even with only 5 ppm of CO_2 in the cathode inlet.[879] Performance further degrades when the CO_2 concentration increases and is nearly reduced to half with 400 ppm of CO_2 (Figure 62A).[879] When ~350 ppm of CO_2 is introduced to the cathode, the anode emission has a CO_2 concentration of ~150 ppm at a cell current <0.2 A/cm^2 at the same gas feed rate at the anode and cathode. This means that nearly half of the CO_2 will migrate from the cathode to anode before being purged out. No CO_2 is purged when the cell is held at the open circuit voltage (OCV) (Figure 62B).[854] However, the CO_2 concentration in the anode product stream increases slightly when the cell discharging current density increases. The anode CO_2 emission rate also changes with different gas feeding flow rates; it increases with a higher cathode feeding rate, but an increasing anode gas flow rate will not change the amount of CO_2 transferred from the cathode to anode. This indicates that the CO_2 absorption rate in the cathode is controlled by mass transfer due to the fast reaction rate of CO_2 with OH^- and the large amount of OH^- generated at the cathode (compared to CO_2). The anode CO_2 emission rate, however, is controlled by the reaction rate (eq 15). Lower air flow rates at the cathode can reduce the carbonation degree and alleviate its influence on the AEMFC performance. The carbonate distribution in the membrane and catalyst layers has been proposed based on experimental results and is schematically shown in Figure 62C.[854,879] The anode carbonation degree is the highest because of the slow CO_2 purging reaction rate at the anode, while the carbonation degree at the cathode is much lower because of rapid carbonate transfer to the anode. The AEMFC carbonation degree decreases at higher discharge currents (Figure 62 C).

The AEMFC carbonation usually causes a potential drop of >200 mV.[854,879] The most obvious influence of carbonation is the decrease in ionic conductivity due to slower diffusion rate of carbonate compared to hydroxide. The resulting increase in ionic resistance has been analyzed using HFR, which shows that the ohmic potential drop due to carbonation is often below 50 mV, and a large portion of the potential drop is caused by other factors.[854,879] Some researchers have used a reference electrode in AEMFCs to decouple anode and cathode overpotentials.[880−882] It was found that anode overpotentials increase significantly during carbonation while cathode overpotentials remain largely unchanged. This indicates that the carbonation has a significant influence on the HOR. However, one should pay close attention to reports on reference electrodes in thin electrolyte systems, because electrode alignment and electrode reaction rate difference can cause large edge effects.[883−888] A potential distribution at the edge with exactly aligned electrodes and the same kinetics is shown in Figure 62D (top).[889] It shows a symmetrical but highly nonuniform potential distribution near the electrodes' edge due to the ohmic drop effect. The potential distributions are highly nonlinear in the region ~1.5b (b is the thickness of the membrane) outside the electrode edge. Beyond this is a region of constant potential (RCP). The measured potential is

https://doi.org/10.1021/acs.chemrev.1c00331
Chem. Rev. XXXX, XXX, XXX−XXX

in the center of the membrane when a reference electrode is positioned within the RCP. A small asymmetry can shift the measured potential position significantly (Figure 62D, middle).[889] When one electrode is 1.5*b* larger than the another, the measured potential position moves substantially toward the larger electrode. This degree of alignment requirement is unreachable in laboratory MEA fabrication, which indicates that the measured potential position will deviate from one electrode to another. The difference in electrode kinetics will also influence the potential distribution (Figure 62D, bottom),[889] as the potential within the RCP shifts toward the electrode with faster kinetics. Therefore, the MEA results based on reference electrodes may not correctly reveal the influence of carbonation on AEMFC electrode reactions. More research is needed to further illustrate the impact of carbonation on AEMFC performance degradation.

7.4.2. Nernst Potential Drops Due to Carbonation. A Nernst potential drop (pH-potential) is expected in AEMFCs due to the uneven carbonate distribution between the anode and cathode,[854,879] which results in a pH difference. This can be expressed as follows:

$$\Delta\varphi_{\text{Nernst}} = -\frac{RT}{F}\ln\left(\frac{[\text{H}^+]_{\text{cathode}}}{[\text{H}^+]_{\text{anode}}}\right) = 0.059(\text{pH}_{\text{cathode}} - \text{pH}_{\text{anode}}) \quad (16)$$

However, this analysis does not take all potential contributions into account. Different from a pure electrolyte solution, the existence of a nondialyzing AEM will lead to the formation of a membrane potential according to Donnan equilibrium.[890] To theoretically analyze the potential difference resulting from carbonation, a model that consists of two RHE separated by an AEM is proposed by the authors (Figure 63).[891] The two RHEs are in different alkaline solution concentrations corresponding to the difference in carbonation degree between the anode and cathode. The potential difference between the two RHEs represents the thermodynamic voltage drop brought by carbonation in AEMFCs. A Nernst potential forms as expected due to the pH difference between the RHEs as sketched in Figure 63 (upper part). Further, a double layer forms at the AEM/electrolyte interfaces on either side of the membrane due to the nondialyzing properties of the AEM (Figure 63, lower part). Both interfaces have a characteristic potential. The net potential difference between the two RHEs is the sum of the Nernst potential and two membrane potentials.

The Nernst potential can be expressed as follows:

$$\Delta\varphi_{\text{Nernst}} = \varphi^1_{\text{RHE}} - \varphi^2_{\text{RHE}} = \frac{RT}{F}\ln\left(\frac{[\text{H}^+]_1}{[\text{H}^+]_2}\right) = \frac{RT}{F}\ln\left(\frac{C_2}{C_1}\right) \quad (17)$$

When an equilibrium forms in the electrolyte/AEM interface, the electrochemical potential of ions is equal on both sides, so the membrane potential can be expressed as follows:

$$\varphi^1_{\text{Mem}} = \frac{RT}{F}\ln\left(\frac{[\text{H}^+]_{\text{AEM}}}{[\text{H}^+]_1}\right) = \frac{RT}{F}\ln\left(\frac{C_1}{C_0}\right) \quad (18)$$

$$\varphi^2_{\text{Mem}} = \frac{RT}{F}\ln\left(\frac{[\text{H}^+]_2}{[\text{H}^+]_{\text{AEM}}}\right) = \frac{RT}{F}\ln\left(\frac{C_0}{C_2}\right) \quad (19)$$

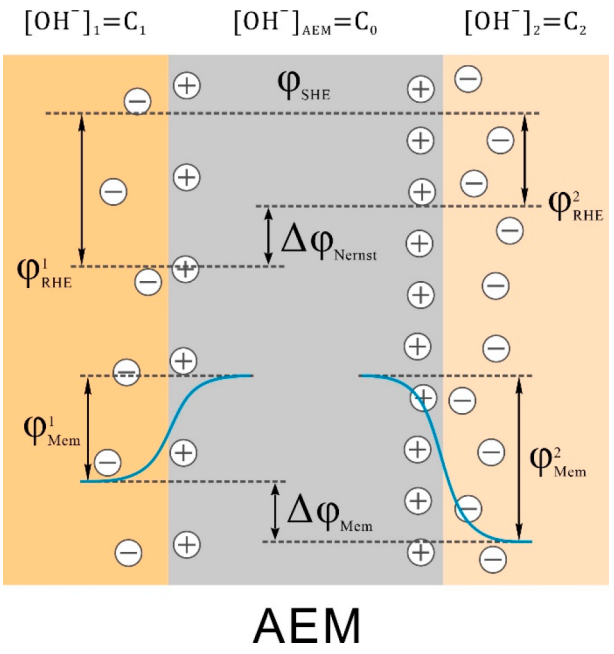

Figure 63. Theoretical analysis diagram of the thermodynamic potential difference in AEMFC carbonation. Yellow parts on two sides represent alkaline solution with different [OH⁻] concentration (C_1 and C_2); the gray part represents nondialyzing AEM (with an OH⁻ concentration of C_0). A Nernstian potential forms due to the pH difference between the two alkaline solutions (depicted in the upper part). Two membrane potential forms in both sides of the solution/AEM interface due to Donnan equilibrium. The membrane potentials and the membrane potential difference are depicted in the lower part.

$$\Delta\varphi_{\text{Mem}} = \varphi^1_{\text{Mem}} + \varphi^2_{\text{Mem}} = \frac{RT}{F}\ln\left(\frac{C_1}{C_2}\right) \quad (20)$$

The total potential difference is the sum of the Nernst potential and membrane potential:

$$\Delta\varphi = \Delta\varphi_{\text{Nernst}} + \Delta\varphi_{\text{Mem}} = 0 \quad (21)$$

This analysis shows that, due to the nondialyzing property of AEMs, the Nernst potential is canceled out by the membrane potential, which means that thermodynamic potential differences due to carbonation will not occur in AEMFCs. Based on the reviewed experimental results and theoretical analysis, carbonation will cause a significant performance drop to AEMFCs. Ionic transport resistance increases are responsible for a part of the voltage losses, but an uneven carbonate distribution will not cause a thermodynamic potential drop. This analysis suggests that a large part of the potential drop caused by carbonation is due to larger electrochemical overpotential rather than a difference in pH.[891] More work is needed to elucidate the influence of carbonation on the HOR and ORR in AEMFCs.

Besides a fundamental understanding of carbonation, practical methods to eliminate or reduce the influence of CO_2 in air are also important for realistic applications. Removing the CO_2 out of air in advance to avoid AEMFC carbonation is one possible way. Recyclable CO_2 removing is feasible via both thermochemical and electrochemical methods.[892] Yan and coworkers have proposed an electrochemically driven CO_2 separator (a CO_2 scrubbing device) that is able to remove 98% of CO_2 from the air.[893] CO_2

https://doi.org/10.1021/acs.chemrev.1c00331
Chem. Rev. XXXX, XXX, XXX−XXX

elimination in a fuel cell stack is expected in future AEMFC applications.

In AEMFC carbonation research, further study is required to understand the influence of carbonate on electrochemical reactions. CO_2 removal to eliminate the performance loss is also possible in the foreseeable future.

7.5. Water Management in MEAs

In PEMFCs, the impact of water has been widely investigated, and most of the efforts have been dedicated to mitigating the "water flooding" phenomenon at the cathode, to enhance the fuel cell performance.[894] In contrast to PEMFCs, water in AEMFCs is produced in the anode and consumed as one of the reactants in the cathode side during MEA operation (Figure 64A). There are two ways for water to flow between those two electrodes: one is a water gradient caused by the back-diffusion of water from the anode to cathode, and the other is electro-osmotic drag, resulting in water transport from the cathode to anode.[895] Additionally, cationic groups in the AEMs have a lower degree of dissociation than in PEMs at low water contents, leading to anion transfer resistance being more sensitive to the hydration level in the electrode and membrane.[896,897] Thus, the intrinsic water imbalance will simply lead to the anode flooding and cathode dry-out under AEMFC operation.

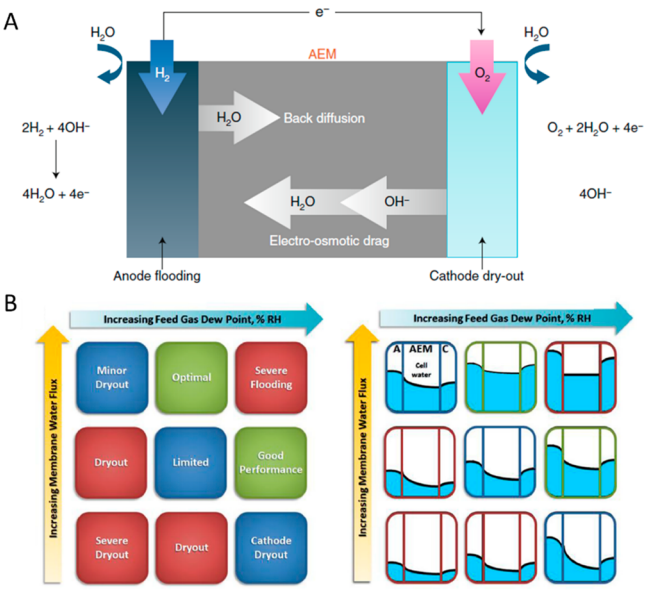

Figure 64. (A) Water imbalance in an AEMFC. (B) Illustration showing the balance between the degree of water transport and reacting gas dew points. Panel A is reprinted with permission from ref 895. Copyright 2020 Springer Nature. Panel B is reprinted with permission from 868. Copyright 2018 Elsevier.

Cell operation conditions, such as cell temperature, backpressure, and inlet gas dew point, have been widely tuned to optimize the water balance to achieve a better fuel cell performance. A higher cell temperature enhances the catalytic kinetics and the membrane conductivity and thus a higher MEA performance, while it also plays an important role on the water management in the device.[898] Recent experimental results revealed that the water diffusion coefficient in the membrane is positively correlated to the cell temperature.[362,899] The higher water permeability will help to mitigate the anode flooding issue and provide sufficient hydration to both the membrane and cathode. Additionally, in the gas diffusion layer, a higher cell temperature can accelerate the water transport by shear force and water evaporation removal process at a higher water vapor pressure gradient and effective diffusivity.[900,901] Backpressure of inlet gas is another parameter that contributes to the water management in the cell. Equal backpressure should always be applied in the cathode and anode to avoid physical damage to the membrane. However, a pressure gradient between the anode and cathode brings about a larger liquid water permeation rate leading a higher fuel cell performance.[902,903] However, the anode under a higher inlet gas pressure will cause a flooding issue by retarding the water evaporation due to a higher boiling point of water at a higher gas pressure.[864] Changing the electrodes' inlet gas dew point can directly affect the water accumulation in both the cathode and anode. As shown in Figure 64B, reducing the dew point of the hydrogen gas in the anode can increase the water evaporation rate and mitigate the flooding issue.[864] In the cathode, maintaining a sufficient dew point of inlet gas provides enough humidity to avoid membrane and electrode

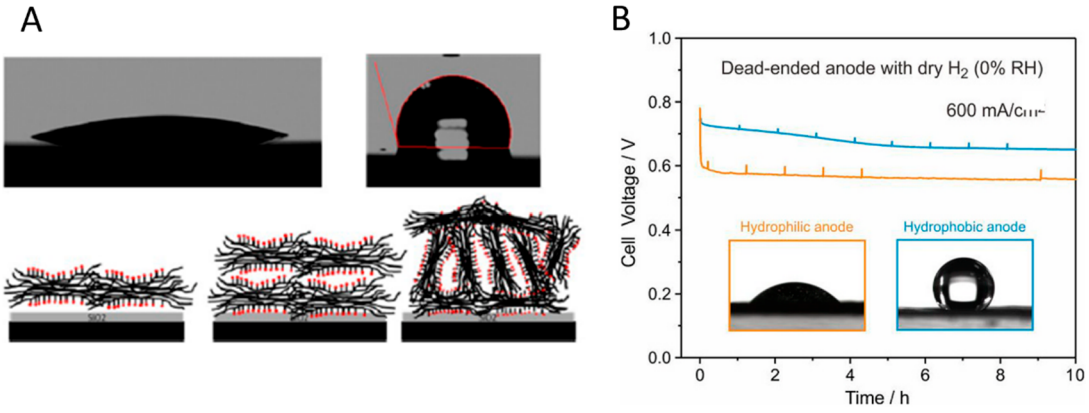

Figure 65. (A) (Top) Water droplet contact angle on ultrathin (100 nm) Nafion films (right) and Nafion membrane (left). (Bottom) Illustration of the evolution from a hydrophilic to hydrophobic surface with increasing thickness, based on bundles of ionomer chains. (B) Stability test of APEFCs using a different anode ionomer and operated under a dead-end anode mode. Dry H_2 was fed into the cells, and the gas outlet of the anode was sealed. The inset presents the contact angle of water droplets on the surface of the anode side of the CCM (blue, QAPAF; orange, QAPPT). Panel A is reprinted with permission from ref 917. Copyright 2013 American Chemical Society. Panel B is reprinted with permission from 912. Copyright 2020 The Authors, Elsevier.

https://doi.org/10.1021/acs.chemrev.1c00331
Chem. Rev. XXXX, XXX, XXX−XXX

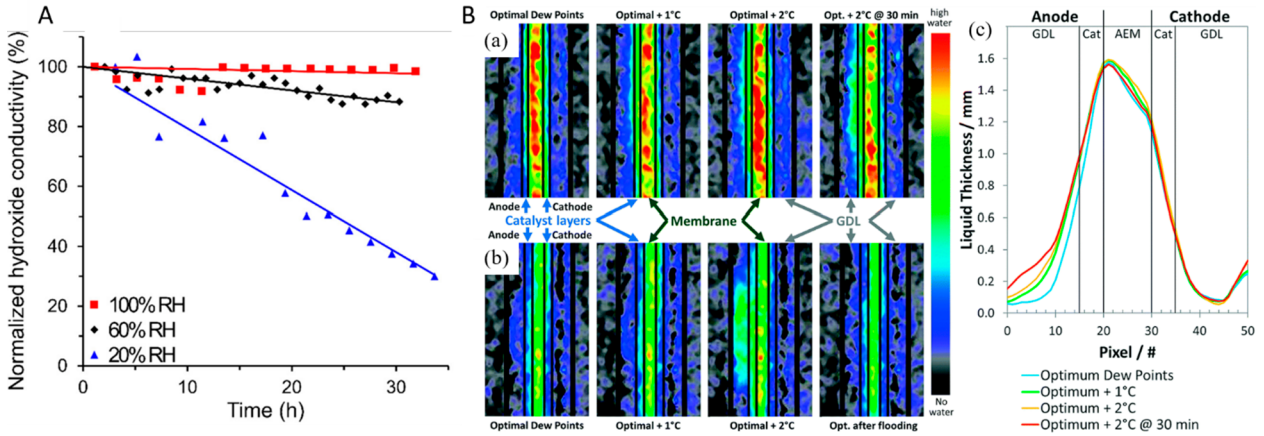

Figure 66. (A) Normalized true OH^- conductivity of a BTMA-LDPE AEM as a function of test time (80 °C, 100 μA, and a nitrogen flow of 500 sccm/min) at different RH levels. (B, a) *Operando* in-plane neutron radiographic images of water in the gas diffusion layers, catalyst layers, and the radiation-grafted ETFE–BTMA AEM in an AEMFC operating at 1.5 A cm^2, 60 °C, 1.0 L min^{-1} H_2 and O_2, after equilibration at the following symmetric dew points: optimized (anode/cathode: 50 °C/50 °C), optimized +1 °C, the first 30 min at optimized +2 °C, and the performance "crashed condition" seen after 30 min at optimized +2 °C. (B, b) *Operando* in-plane neutron radiographic images of a PFAEM-based AEMFC after equilibration at the following symmetric dew points: optimized (anode/cathode: 54 °C/51 °C), optimized +1 °C, optimized +2 °C, and a recovered cell at optimized dew points and 1.0 A cm^2 current density. (B, c) Qualitative through-plane water distribution plots extracted from the data in panel B, a. Panel A is reprinted with permission from ref 922. Copyright 2020 American Chemical Society. Panel B is reprinted with permission from ref 865. Copyright 2018 Royal Society of Chemistry.

dry-out. While under high current density, reducing the dew point of the inlet gas in the cathode is necessary to avoid possible flooding issues caused by the excess water back-diffused from the anode.[866]

Studies on point-by-point polarization curves already have demonstrated that the optimized operating conditions are current-dependent and not applicable to the real cell operation.[904] In MEAs, a water transfer event occur in both the membrane and catalyst layer where the catalyst–ionomer and ionomer–membrane interfaces play an important role on the water transport across different cell components.[895,868] In addition to the membrane structure reviewed in section 6.2, the thickness of the membrane also affects the fuel cell performance and durability.[905] A thinner membrane not only reduces the membrane ionic resistance but also influences the water dynamics of the cell.[906] With a constant membrane water diffusion coefficient, a thinner membrane will benefit the water flux from the anode to the cathode, lowering the mass transport losses under high current density conditions.[866,906] However, a study by Holdcroft and coworkers reported that the water diffusion resistance at the vapor/membrane interface did not correlate to the thickness of the membrane. The calculated interfacial water permeation coefficient of the membrane was magnitudes lower than through the bulk membrane, suggesting that the membrane interface plays a crucial role in the permeation of water through the membrane.[907]

In AEMFCs, the ionomer often has the same polymer structure as the membrane to ensure the membrane/ionomer compatibility.[908] However, studies on PEMFCs have exhibited different performances between the ionomer thin film and membrane film, based on the orientation of the polymer chains. As shown in Figure 65A, the drop in the contact angle decreased from more than 100° on a Nafion thin film to only 20° on a Nafion membrane.[908] Grazing incident small-angle X-ray scattering (GISAXS) was used to study different thin film polymer chain arrangements with different polymer film thicknesses.[909] Recently, researchers found that the polymer chains in the thin film of ionomer were parallel to the Si substrate, which blocked water and ion transfer.[910] Thus, it is not appropriate to speculate on the water properties of the ionomer based on the membrane directly. The modeling study of the saturation jump effect in AEMFCs exhibited a lower contact angle in the cathode catalyst layer, which improved the fuel cell performance by maintaining an interfacial hydration layer and helping the water injection into the cathode.[911] Because of the high coverage of the ionomer on the catalyst particle, the contact angle of the catalyst layer can partially reflect the water properties of the ionomer and could serve as one of the measurable parameters for further studies of water and its management. Zhuang and coworkers applied different ionomers in the anode and recorded the contact angle to study the impact of hydrophilicity of the catalyst layer on fuel cell performance (Figure 65B).[867] They showed that a hydrophobic, fluorine-containing ionomer in the anode can benefit water management and enhance the cell performance. Kim and coworkers applied asymmetric electrode ionomers to the cathode and anode and investigated how the different water properties of the ionomers affected the water balance in the cell. Their study claimed that a more hygroscopic ionomer with a higher IEC is preferred in the anode, and a less hygroscopic ionomer with a lower IEC is preferred in the cathode.[877] However, an opposite configuration was employed in studies by Mustain and coworkers where a high fuel cell performance was achieved with a higher IEC in the anode and a lower IEC in the cathode. Those conflicting results can be explained by the differences in water permeability of the membranes.[853]

Most of the AEMFC papers have been focused on the development of AEMs with the use of commercial catalysts to optimize fuel cell performance. However, few of them have investigated how the water properties of the catalyst layer affects the water balance in AEMFCs. Early studies on PEMFCs explored the impact of the catalyst layer on the water management and can provide some preliminary guidance for selecting the proper catalysts for AEMFCs.[912] When the

https://doi.org/10.1021/acs.chemrev.1c00331
Chem. Rev. XXXX, XXX, XXX–XXX

carbon supports for PGM catalysts are corroded under the high potential during the start−stop process, the carbon surface will form oxidized functional groups (section 5), converting the catalyst layer from being hydrophobic to hydrophilic, leading to flooding issues in the cathode in PEMFCs.[913] Furthermore, when hydrophilic catalyst supports, such as metal oxides, were applied in PEMFCs, the optimized performance could only be achieved under lower RH so as to minimize the flooding in the cathode.[914,915] A significant performance difference between PEMFCs and AEMFCs was observed when non-PGM catalysts were used in the cathode. This suggests that the hydrophilic catalyst and/or support leads to cathode flooding in PEMFCs but helps maintain water in the cathode to avoid the dry-out processes in AEMFCs (Figure 23).[608,872,916,917]

Under applied potential, the less hydrated conditions in the cathode of AEMFCs would make the hydroxyl ions more reactive towards the cation functional groups, leading to a shorter lifetime of the membranes. The degradation of quaternary ammonium (QA) salts (discussed in section 6.1.5) with less hydrated OH^- has been investigated and further applied to AEMs by Dekel and coworkers.[918−921] To quantify the extent of hydration, λ, the mole fraction of water molecules to hydroxide ions, is often used as a characterizing parameter. Faster degradation rates, indicated by NMR measurements, were observed with lower λ values.[918] Figure 66A presents an *ex situ* study of OH^- conductivity change over time, as an indicator for AEM stability, at conditions simulating the real fuel cell environment.[922] Higher RH was found to be helpful in maintaining the conductivity and IEC of the AEMs. The influence of water content on the stability of membrane materials was also demonstrated by QCM studies of ionomers exposed to gas with varied humidity and elevated temperature.[837,923] The change in viscoelasticity of the ionomer films, before and after the rise in operating temperature, indicates a higher level of film degradation at a lower RH.

On the other hand, the fuel cell performance and stability can be optimized by water management.[920,924,925] Light cross-linked AEMs with high IECs and small thicknesses were found to be optimal for water transport, which supports high power densities.[866] The water tolerance at the anode, which can be controlled by the ionomer/carbon supports/catalyst ratio, also assists in improving the fuel cell performance.[865,926,927] The water distribution with an increase in the RH throughout the MEAs, with two different AEMs, was visualized by *operando* neutron imaging (Figure 66B).[865] Water accumulation at the anode, which resulted in cell voltage diminution of the fuel cell, was observed from the through-plane water distribution plot from pixel 0 to 10 (Figure 66B,c) extracted from the neutron radiographic images (Figure 66B,a,b). Nevertheless, the amount of water remained the same at the cathode (pixels 30−50). This indicates that the water that back-diffused from the anode maintains the hydration level at the cathode, suggesting that fast water transport is indispensable for AEMFCs.

Further studies on the water distribution at the interfaces and the mechanisms of water transport in AEMs are gaining increased attention.[928−931] The humidity-dependent surface structure of a quaternary ammonium AEM was mapped by a phase-contrast tapping mode and conductive-probe atomic force microscopy.[929] Water distribution profiles in AEMs coated on SiO_2 and Pt substrates under various RH conditions have been analyzed by neutron reflectometry.[931] Given more studies with *in situ/operando* measurements that combine the state-of-art analytical techniques with electrochemical environments, the water diffusion and balancing in AEMs will be better interpreted, and valuable insights will be provided in the rational design of AEMs.

7.6. Mass Transport in MEAs

In addition to the interfacial charge transfer kinetics, species transport represents an important and complex challenge at the system level. Figure 67 shows the various transport processes

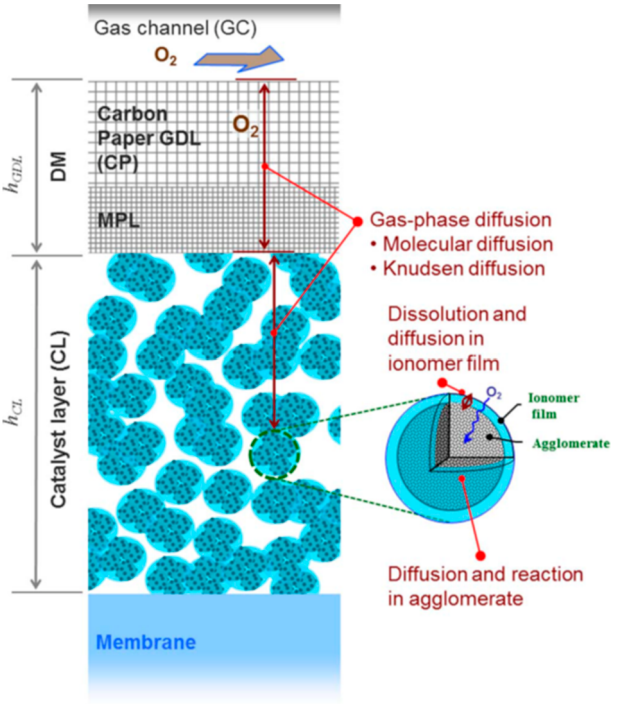

Figure 67. Overview of transport phenomena at the cathode ORR of a typical PEM fuel cell. For the electrochemical reaction to proceed in the catalyst layer, supplies of oxygen gas, electrons, and ions are required. The green dashed circle represents an agglomerate of supported catalyst and ionomer. Reprinted with permission from ref 932. Copyright 2011 The Electrochemical Society.

of a cathode electrode in a typical MEA configuration.[932] For the alkaline cathodic ORR to proceed, the simultaneous presence of oxygen and water as reactants, electrons, and pathways for dissipating the generated OH^- is needed. Electrons can be transported to the reactive sites through the catalyst itself and the conductive supports, such as high-surface-area carbon. Resistance, due to electronic transport, can be dominant at low cell current densities where the supply of other species is sufficient. Transporting ions to and away from the catalyst layer is carried out mainly by the ionomer, which is added to the catalyst suspension before coating it onto the membrane. However, it is possible to operate fuel cells with ionomer-free catalyst layers, such as the 3M nanostructured thin film (NSTF) design.[933] Without an ionomer conducting the ions, the primary transport pathway has been speculated to be through water in the pores or via surface diffusion. The gaseous reactant can be delivered very rapidly through molecular diffusion in the large pores in the GDL. Diffusion in pores smaller than the mean free path of oxygen (~100 nm) will be slower according to the Knudsen diffusion mechanism where the gaseous molecules collide more frequently with the

https://doi.org/10.1021/acs.chemrev.1c00331
Chem. Rev. XXXX, XXX, XXX−XXX

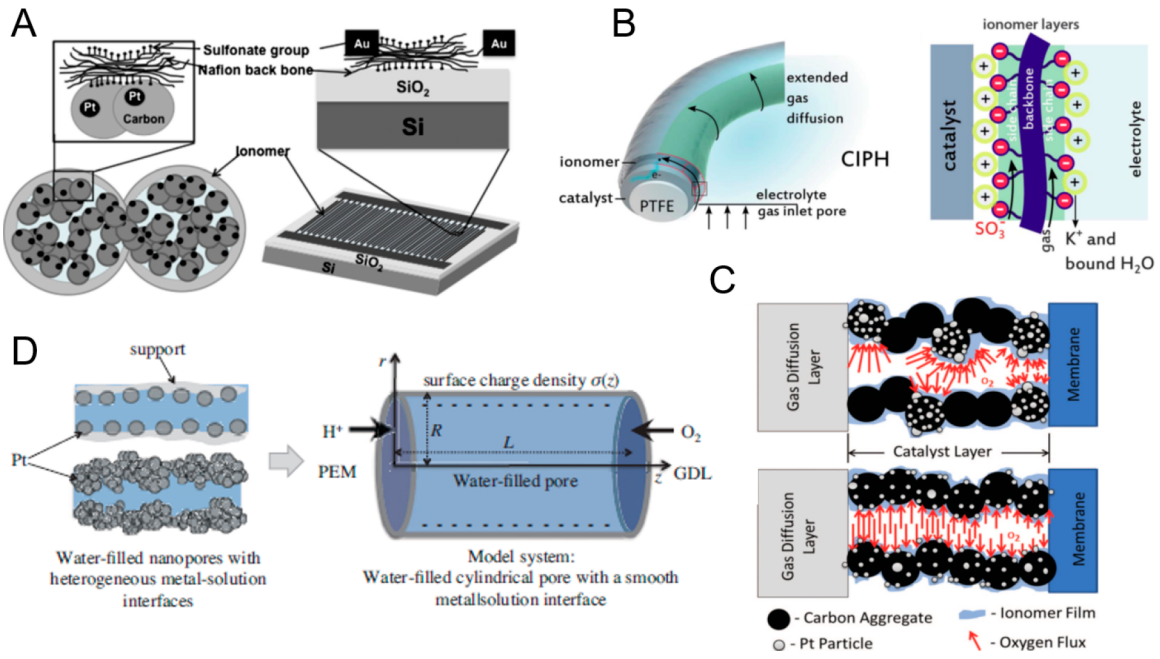

Figure 68. (A) Proton conductivity measurements of a Nafion film adsorbed onto a SiO_2 surface (right); the left part shows the agglomerate structure in the PEM catalyst layer. The structure and properties of the ionomer film were found to be different from those of the bulk Nafion film (10s of microns). (B) Schematic of a thin ionomer film on a Pt catalyst layer wrapped around a PTFE fiber (left); a Nafion ionomer extends the hydrophilic SO_3^- domain over the catalyst layer, and the backbone provides fast transport pathways for nonpolar gases such as CO_2 (right). (C) The presence of ionomer may impede gaseous transport. The effect is more severe at low catalyst loading and low dispersity. The catalyst layer with diluted Pt/C shows much higher O_2 transport resistance because the effective ionomer surface area is reduced (top), compared to the sample with a uniform Pt distribution (bottom). Note that the two samples have the same Pt loading. (D) Water-filled pore scale model to account for the transport of protons in water. Proton transport is also assisted by the surface charge of the Pt wall under certain conditions. Panel A is reprinted with permission from ref 936. Copyright 2011 Elsevier. Panel B is reprinted with permission from ref 941. Copyright 2020 American Association for the Advancement of Science. Panel C is reprinted with permission from ref 946. Copyright 2013 The Electrochemical Society. Panel D is reprinted with permission from ref 953. Copyright 2010 The Electrochemical Society.

wall than between the molecules. The presence of ionomer and water can introduce extra resistance to gas transport due to the lower diffusion coefficients in the liquid and solid phases.

Transport within the catalyst layer is a complex problem because not only are the transport media not totally independent of one another, but the transported species are also sometimes correlated. For example, filling of the pores with ionomers will facilitate the transport of ions but diminish the available space for gas diffusion. In addition to being one of the reactants, water assists in the transport of ions but retards that of gases. This section reviews the current understanding of transport of gases and ions in the catalyst layer with MEA configurations that mostly pertain to PEM fuel cells, which are the most well-studied system. Much of this knowledge is expected to be transferable to AEMFCs. Water-related transport has been discussed above and so will not be covered in this section.

Compared to the transport of ions in bulk membranes on length scales of tens of micrometers, much thinner ionomer films (<50 nm) with drastically different structures and properties are expected to exist in the catalyst layer. Generally, thinner Nafion films tend to form a lamellar structure with less phase segregation and fewer water channels.[934−937] The ionic transport is mainly through surface diffusion rather than by a fast hopping process, resulting in a lower ionic conductivity. Studies with thin Nafion films formed on SiO_2 particles have shown a higher activation energy than the bulk membranes when the film thicknesses are below 50 nm (Figure 68A).[936] The hydrophobic domains of perfluorocarbon-based ionomers, such as Nafion, have a higher affinity for nonpolar gases (including oxygen) than their hydrocarbon counterpart. The net result is improved permeability in perfluorocarbon-based ionomers as compared to other types.[35,938−940] This property of Nafion has recently been explored in an alkaline CO_2 electrolyzers (Figure 68B).[941] When the Nafion ionomer, dissolved in a polar solvent such as methanol, is coated onto a Pt catalyst surface, the hydrophilic $-SO_3^-$ domains preferentially attach to the Pt, and the hydrophobic $-CF_2$ domains form continuous percolating channels. The latter hydrophobic channels promote the fast transport of gaseous reactants. This new design enables a deeper penetration of CO_2 along the catalyst/ionomer interface, resulting in a CO_2 electrolyzer that reaches over 1.5 A/cm^2 as its limiting current density.

When the thin ionomer film covers the entire surface of the supported catalyst particle, it can dramatically increase the gaseous transport resistance,[942−944] particularly in systems with low catalyst loading and low dispersity.[945,946] As shown in Figure 68C, catalyst layers with the same catalyst loading but lower dispersity, by doping with innocent carbon support, result in a much higher gas transport resistance. Regions with denser catalyst particles have a larger oxygen flux at the catalyst/ionomer interface than bare carbon surfaces, which essentially decreases the effective ionomer surface area.[945−947] The origin of the resistance might be the sluggish diffusion across the thin film itself, which leads to a lower partial pressure of the gases at the catalyst surface. Alternatively, it can result from the slow chemical adsorption of the gas at the ionomer/pore or ionomer/catalyst interfaces.[945] Quantifica-

https://doi.org/10.1021/acs.chemrev.1c00331
Chem. Rev. XXXX, XXX, XXX−XXX

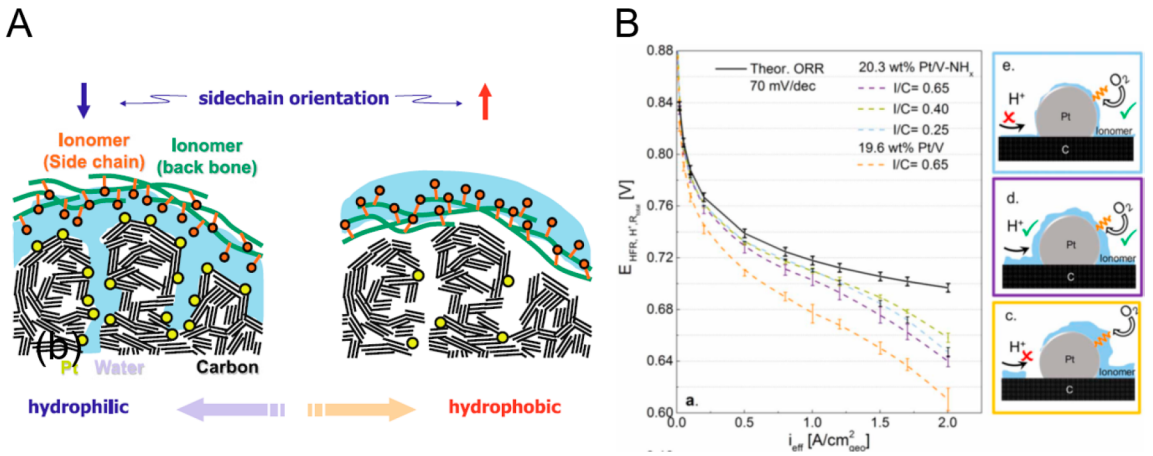

Figure 69. (A) Proposed structure of Nafion ionomer with (left) and without (right) Pt on the exterior surface of the carbon support. The aggregate with Pt on the surface is more hydrophilic. (B) Fuel cell performance of Pt/C and Pt/C-NH_x, where the C−NH_x represents a carbon sample with N doping. The positively charged NH_x center allows for a more uniform Nafion coverage (middle right). Panel A is reprinted with permission from ref 957. Copyright 2011 Springer. Panel B is reprinted with permission from ref 960. Copyright 2017 The Electrochemical Society.

tion of the ionomer-induced transport resistance can be done through temperature- and pressure-dependent limiting current measurements. The rate of molecular diffusion in the GDL has a small dependence on temperature but larger dependence on pressure, whereas the extra resistance from the ionomer film is largely independent of pressure in the gas channel.[932,948] Assuming an ideal uniform ionomer coverage, a balance between gas and ion transport has to be considered as the ionomer generally facilitates ionic conduction but slows down gas transport.[942] Strategies to improve the transport properties of ionomers include adding spacers between backbone chains[473] and modulating the side chain length.[949]

The effect of water on the transport of ions and gas can be similar to that of ionomers. The water film impedes the transport of gaseous reactants but facilitates ionic transport either by itself or by connecting the discontinuous ionomer network. Water can be absorbed by the added ionomers or condensed on the surface of the support, and the effect of water thus depends on the structure of the support and the amount of ionomer. For example, the abundant micropores in the Ketjen Black (KB) carbon serve to condense water from the vapor phase.[950,951] As a result, it shows a larger performance loss with low ionomer loading at lower RH, because it relies more on the densified water inside the micropores to conduct protons. By comparison, Vulcan carbon has a more solid structure with fewer micropores, leading to a smaller dependence on RH, although Pt NPs on solid Vulcan are subjected to more severe particle aggregation/coalescence, relative to KB. Utilizing water to conduct ions can be essential for achieving high-performance fuel cells with low catalyst loadings.[842] The deposition of Pt nanoparticle (NP) catalysts inside the micropores (<4 nm) has been confirmed, but the role of these catalysts is not clear. The narrow pores in KB prevent the penetration of ionomers from reaching the catalyst surface, leading to inaccessible catalyst regions during operation due to the lack of ionic species (Figure 29).[617,660] However, it has also been shown that the absence of direct contact between ionomer and the catalyst surface is beneficial because of the poisoning effect of adsorbed sulfonate groups on the reaction kinetics.[842] Pt catalyst particles, deposited inside but close to the openings of the micropores, might be even more active as long as the transport of ions and gases can be ensured. In this scenario, the transport of ions could be achieved by the condensed water film on the support. A similar mechanism has been invoked to explain ionic transport in the catalyst layers without ionomers, such as in the 3M NSTF electrode.[933] Ions are thought to be conducted through diffusion either along the catalyst surface or within a thin water film. The conductivity of protons in the water film can be orders of magnitude larger than that of pure water, which can be explained by surface charge-assisted transport.[952] Water-filled pore scale models are often used to simulate the microscopic transport processes (Figure 68D).[953] The models consist of a Pt cylindrical pore and hollow center filled with water. One end of the pore connects to the proton exchange membrane that supplies the proton source which then enters the pore. The transport of the positively charged proton is significantly enhanced if the Pt wall is negatively charged. The surface charge of the Pt surface depends on the applied potential as well as the potential of zero charge (pzc), as discussed in section 4. Whether or not a similar transport mechanism exists on the carbon support is an open question as the carbon surface is more hydrophobic and may have a different charging behavior than the Pt surface.

Beyond the working principles of each individual component at the microscopic scale, the efficient operation of the catalyst layer also depends on the appropriate arrangement of different components. Both the ionomer and the catalyst/support form secondary aggregates in the catalyst ink, the structure of which is at least partially preserved in the catalyst layer. Most of the methods to control the catalyst layer structure thus far have focused on tuning the compositions and conditions in preparing the ink.[954−956] For example, a study using different ratios of water and either 1-propanol or 2-propanol showed that much better fuel cell performance can be achieved if the cathode catalyst layer is deposited from the ink suspended in 16 wt % water plus 1-propanol.[954] Replacing 1-propanol with 2-propanol leads to much larger aggregates in the suspension and results in nonuniform microsized patches of ionomer distribution. The higher performance was mainly ascribed to facilitated gas transport due to the uniform ionomer coverage since the proton conductivity does not change appreciably with different solvents. The smaller ionomer aggregates in the water/1-propanol mixture tend to occupy the micropores in

https://doi.org/10.1021/acs.chemrev.1c00331
Chem. Rev. XXXX, XXX, XXX−XXX

the catalyst/support aggregates. It is possible to adjust the ionomer aggregation size using the different affinity of solvents for the Nafion perfluorinated backbone. By increasing the amount of dipropylene glycol in the solvent mixture with water, the hydrodynamic radius of the ionomer aggregates shrinks to the nanometer regime because of the higher affinity of dipropylene glycol for the ionomer.[956] Interestingly, an optimal aggregate size was found because even though small ionomer aggregates help to establish a uniform coverage, they can also clog the micropores if their size passes a certain threshold. For achieving the best fuel cell performance, the size of the ionomer aggregates needs to match well with that of the catalyst/support. In addition to the use of isopropanol under conventional conditions, supercritical fluids made from isopropyl alcohol with water as a cosolvent were also used to prepare ionomer solutions that contain small colloidal particle sizes. The resulting catalyst layer showed improved proton conductivity and durability under accelerated stress testing, which could be explained by the effective proton transport pathways and the high crystallinity of the ionomers deposited under supercritical conditions.[844]

In addition to the various physical processing conditions, the organization of ionomers and the catalyst/support in the catalyst layer also depend on the surface chemistry of the support. The interactions among Pt, carbon, and ionomers have been studied using simulation tools.[957,958] Molecular dynamics simulations of the catalyst layer suggest that the presence of Pt catalysts on the carbon support disrupts the ionomer network and thus affects proton transport (Figure 69A).[957] Pt/C aggregates are more hydrophilic than the pristine carbon surface, inducing more SO_3^- groups and water molecules to orient towards the aggregated particles. In comparison, carbon surfaces without Pt interact mainly with the hydrophobic domains of the Nafion ionomer. Similar effects have been found for carbon supports with functional groups. A simulation study indicated that surfaces with hydroxyl groups enhance the adhesion of the Nafion film while epoxidation leads to partial film delamination.[958] The amount of surface oxygen in the carbon support also changes its interactions with the ionomers. For example, carbon surfaces with minimal oxygen content preferably interact with the hydrophobic domain of the Nafion ionomer.[959] The best fuel cell performance was observed with supports of intermediate surface oxygen content because both proton and oxygen transport are ensured by having both the hydrophobic and hydrophilic domains attached to the support. Incorporating NH_x groups into the carbon support through oxidation and amination processes allows for a more uniform ionomer coverage because of the Coulombic interaction between the positively charged NH_x centers and negatively charged $-SO_3$ domains in the ionomer (Figure 69B).[960] The NH_x-functionalized carbon support showed decreased pressure-independent O_2 transport resistance due to the thinner and more uniform ionomer film, which also provides continuous ionic pathways to the catalytic sites.[843,960]

Agglomerates consisting of Pt, carbon, and ionomers have been proposed to explain the mass transport resistance at high current densities.[961,962] The agglomerates are usually thought to be aggregates of supported catalysts with ionomers or water filling the voids, and sometimes the aggregates are covered by a thin layer of ionomer. The model assumes a first-order reaction of oxygen gas in the ORR and couples it to a diffusion process. Analytical solutions to the coupled equations are possible if the ionic transport is ignored, leading to an effective factor that depends on the radii of the agglomerates and the ratio between the ORR kinetics and the effective diffusion coefficients. These extra parameters could allow for better fitting between the simulated and experimental data.[963] A more comprehensive numerical model suggested that there are significant variations in overpotential and reaction rates inside the agglomerates, with the distribution depending on the proton conductivity, oxygen dissolution kinetics, and the oxygen reaction order.[942] The connectivity of the agglomerates in the catalyst layer is also an important factor in transporting ions and gaseous reactants. A bottom-up particle packing approach based on a random walk method was used to study the connectivity of carbon black aggregates in the catalyst layer.[964,965] The model predicted a fourth power dependence of the effective oxygen diffusion coefficient on the porosity, due to the combined effect of the surface morphology of the reconstructed carbon particle and Knudsen diffusion. The importance of connectivity is also experimentally confirmed by the different oxygen transport resistance in two agglomerates with the same volume and ionomer but different aspect ratios.[966] The one with a smaller aspect ratio, i.e., the more spherical shape, showed lower local O_2 transport resistance due to the shorter average diffusion distance for catalysts in the core region.

When integrated into the fuel cell, the catalyst layers on the membrane are interfaced with the GDL that, under compressive pressure, partially registers the structure of the flow fields. As a result, there are variations in the conductivity, reactant supply, and the reaction rate, along the directions both into and perpendicular to the catalyst layer. For example, with a serpentine flow channel, the maximum current density shifts from under the wall at lower overpotentials to under the channel at higher overpotentials because the transport of oxygen gas becomes rate-limiting at high overpotentials, and the catalyst closer to the channel has easier access to it.[967,968] For a similar reason, maximum reaction rates are found to be near the catalyst layer/membrane and catalyst layer/GDL interface at low and high current densities, respectively.[969] Due to the variations in current densities, strategies to create a distribution of compositions in the catalyst layer have been found to improve the fuel cell performance under certain conditions. Generally, structures with more ionomer at the catalyst layer/membrane interface allow for facilitated transport of protons, while at the catalyst layer/GDL interface, less ionomer results in more pore space that is beneficial for oxygen transport.[970−973] The local performance at the catalyst layer/membrane and catalyst layer/GDL interfaces worsens due to the decreased *oxygen* and *proton* sources. However, a net increase in the overall fuel cell performance can be obtained when the gain is in the center of the catalyst layer due to improved supply of both protons and oxygen, and it surpasses the losses at the edges of the catalyst layer.

7.7. Summary

In conclusion, AEMFC performances have advanced enormously in recent years; significant progress has also been made to improve the initial performance of stability of AEMFCs. Developing non-PGM ORR and HOR electrocatalysts and highly conductive and stable membranes/ionomers remains as the primary challenge in AEMFCs. CO_2 removal and optimal water management are required to eliminate AEMFC performance losses in realistic CO_2-containing and low-RH operating conditions, and understanding the water management and

https://doi.org/10.1021/acs.chemrev.1c00331
Chem. Rev. XXXX, XXX, XXX−XXX

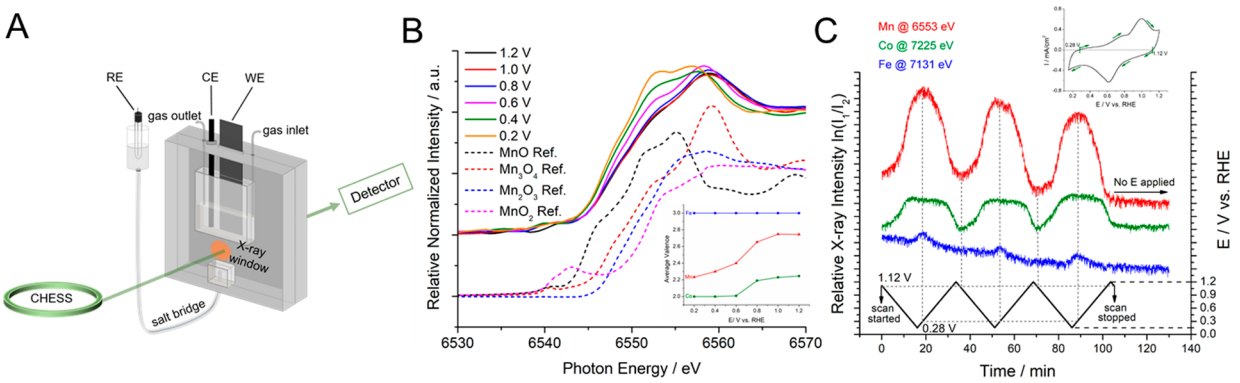

Figure 70. (A) Schematic of an *operando* XAS electrochemical cell with a working electrode (WE, catalyst on carbon paper) and counter electrode (CE, carbon rod) immersed in 1 M KOH. (B) *Operando* XANES spectra at the Mn K-edge of the Mn−Co−Fe trimetallic spinel oxides (solid lines) and the reference manganese oxides (dashed lines). The inset shows the calculated average metal valence as a function of potential. (C) Periodic changes of the relative X-ray intensities $[\ln(I_1/I_2)]$ at 6553 eV (Mn K-edge), 7225 eV (Co K-edge), and 7131 eV (Fe K-edge) as a function of the cyclic potential. The upper inset shows the corresponding CV at 1 mV/s from 0.15 to 1.2 V vs RHE. Panels A−C are reprinted with permission from refs 469 and 470. Copyright 2019 The Authors, American Chemical Society.

mass transport at catalyst/ionomer/membrane interfaces is instrumental to maintain an optimal performance at a large current density. Future AEMFC development should employ more practical testing conditions, including lower gas flow rates (especially hydrogen fuel), the use of air in the cathode, and a larger active area. Achieving low-PGM and ideally non-PGM AEMFCs with stable operation in air for thousands of hours will be the ultimate goal in AEMFC development.

8. *OPERANDO* AND *IN SITU* CHARACTERIZATIONS

In this section, we review *operando*/*in situ* characterization techniques, specifically the use of synchrotron-based X-ray techniques and scanning transmission electron microscopy (STEM) to resolve interfacial changes at macroscopic and microscopic levels. We define the terms "*in situ*" and "*operando*" as follows: *In situ* (Latin, on site/in position) refers to the real-time measurement of an (electro)catalytic process under relevant reaction conditions, versus the conventional *ex situ* (Latin, off site) measurements performed before and after reactions. *In situ* methods need to take into account the operating conditions of instruments (e.g., low temperature, high vacuum), which often deviate from the optimal (electro)catalytic reaction conditions (e.g., elevated temperatures and pressures under a gas/liquid environment). *Operando* (Latin, operating/working) refers to the measurement of a working (electro)catalyst under the same reaction conditions as those inside a catalytic reactor or an actual operating device. *Operando* methods minimize the experimental gap in measurement conditions between instrumental requirements and realistic (electro)catalytic reactions. The term "*operando* spectroscopy" was first proposed by Banares, Weckhuysen, and others in 2002 as an alternative for "*in situ* spectroscopy" to emphasize the importance of maintaining working conditions of (electro)catalysts in a regular reactor/device.[971,972] The term *in situ* has been widely used by many researchers for the past several decades since the real *operando* measurements often required considerably more complexity in device design and are just emerging in the literature. This section serves as an overview of the development of *in situ*/*operando* techniques in electrocatalysis and highlights the revolutionary transition towards *operando* approaches. For detailed reviews on *operando*/*in situ* X-ray and TEM techniques, interested readers are also encouraged to read recent comprehensive reviews by Toney et al.[973,974] as well as our reviews.[18,446]

8.1. *Operando* Synchrotron-Based X-ray Methods under Electrochemical Conditions

X-rays have three characteristics that make them ideal probes for *in situ*/*operando* studies of electrocatalysts in aqueous and gaseous environments: (1) large penetration depths (tens of micrometers to several millimeters), (2) low interference with a material's functionality, and (3) structure sensitivity over a wide range of length scales. Modern synchrotron X-ray facilities deliver exceptionally high flux, fine collimation, small spot sizes, and continuously tunable X-ray energies. There are a wide variety of synchrotron-based X-ray techniques which are well-matched to studying electrocatalysis. Here, we have chosen three techniques to illustrate how synchrotron X-ray techniques can be used to advance our understanding of electrocatalysis: (1) X-ray absorption spectroscopy (XAS) in conventional mode and high-energy resolution fluorescence detection (HERFD) mode, (2) crystal truncation rod (CTR), and (3) resonant inelastic X-ray scattering (RIXS).

8.1.1. X-ray Absorption Spectroscopy (XAS). X-ray absorption spectroscopy (XAS) measures the changes in X-ray absorption or fluorescence as a function of X-ray photon energy. The synchrotron-based X-ray energy is sufficiently high to excite core-level electrons to higher-level unoccupied states, and the X-ray absorption process follows the Beer−Lambert law. An XAS is composed of three regions: the pre-edge region, the X-ray absorption near-edge structure (XANES), as well as the extended X-ray absorption fine structure (EXAFS). The XANES region covers a range from the adsorption edge/near-edge to ~50 eV above the edge, which contains rich information in atomic positions, occupancy of orbitals, site symmetry, and electronic configuration. Located further away above the edge, the EXAFS region extends from around 50 up to 1000 eV. Oscillations in the absorption coefficient dominate the EXAFS region and originate from the interference between the outgoing and backscattered electron waves ejected from the absorbing atoms. The amplitude and frequency of the EXAFS oscillations can offer valuable information about near-neighbor distances, coordination numbers, and elemental identities. The EXAFS signal is dominated by single electron,

https://doi.org/10.1021/acs.chemrev.1c00331
Chem. Rev. XXXX, XXX, XXX−XXX

single scattering events in which the plane wave approximation is valid. The EXAFS, with appropriate phase correction and fitting procedures, can lead to the determination of interatomic distances and coordination numbers with an accuracy as good as ±0.02 Å and ±20%, respectively.[18,974] In contrast, the XANES signal is dominated by multiple scattering events near the absorption edge and adapts a spherical photoelectron wave approximation, which requires rather sophisticated theoretical modeling. An in-depth analysis of the XANES and EXAFS spectra can be found in two early reviews.[446,975]

Synchrotron-based XAS studies can provide valuable insights for the reaction mechanisms of metal-based electrocatalysts. The success of implementing an *operando* XAS experiment relies on the customized electrochemical cells designed for the target electrocatalytic reactions.[975] XAS measurements are often performed in a transmission mode as shown in Figure 70A.[469,470] The sample thickness needs to be optimized to yield the maximum change in the absorbance while not being too thick as to minimize background absorption. A typical X-ray absorbance is in the range 0.3−1.0, depending on the elements of interest and sample thickness, and can be estimated if given the X-ray absorption cross-sections. In an electrochemical cell, the total thickness of the electrolyte and catalyst support needs to be sufficiently thin to minimize background absorption and scattering while not being too thin to cause undesirable iR-drops in the electrochemical measurements, which is critical for high-quality XANES/EXAFS signals. For instance, the total thickness in the customized cell in Figure 70A was designed to be below 200 μm, with a catalyst layer of less than 50 μm. The reference electrode (RE) was connected through a salt bridge to minimize the iR-drop (Figure 70A).[469] It is critical to realize that X-rays can cause radiation damage to the catalysts, electrolytes, and other parts of the cell. Strategies have been reported to effectively mitigate such radiation damage to ensure rigorous electrochemical measurements, such as lowering the incident intensity, constantly flowing fresh electrolyte, and translating the X-ray illuminated area. For thick samples, or low elemental concentrations in thick catalyst supports, XAS measurements should be performed in a fluorescence mode, in which the fluorescence detector is placed perpendicular to the incident beam direction, to minimize the effects of Compton scattering.[976]

Operando XAS has been extensively used to study changes in precious-metal-based electrocatalysts for the ORR,[977−982] non-precious-metal oxides for water oxidation,[983−985] and CO oxidation[986] among many other electrocatalytic reactions. Recently, it has also been used to study M−N−C electrocatalysts for the ORR in alkaline media.[541,987] Early *operando* XAS studies of MEAs by Smotkin, Mukerjee, and others have provided valuable insights into the structural changes of catalysts during fuel cell operation, when compared to the widely used half-cell design.[988−990] The high penetration depth of high-energy X-ray beams enables XAS as a unique technique to perform time-resolved studies on reaction kinetics of Pt-based ORR electrocatalysts in realistic MEA devices.[991,992] Abruna and coworkers recently employed *operando* XAS to investigate the ORR mechanisms of the aforementioned Co−Mn bimetallic spinel oxide catalysts in alkaline media (Figures 22 and 23). *Operando* XANES was used to monitor the oxidation state changes of Co and Mn not only under steady-state conditions (constant applied potential) but also under non-steady-state conditions (potentiodynamic, CV).[469] Rapid X-ray data acquisition, combined with a slow sweep rate in CV, enabled a 3 mV potential resolution, approaching a nonsteady state. Changes in the Co and Mn valence states were synchronized and exhibited periodic patterns that tracked the cyclic potential sweeps. The non-steady-state study suggested possible synergistic effects between Co and Mn, which may explain the superior ORR activity of the bimetallic Co−Mn spinel electrocatalyst over the monometallic oxide counterparts. *Operando* XANES and EXAFS were employed to investigate the structural roles of a more durable Mn−Co−Fe trimetallic oxide under electrochemical conditions.[470] As shown in Figure 70B, the XANES spectra of the Mn K-edge of Mn−Co−Fe spinel oxides exhibited progressive changes in local electronic structures under various applied potentials (vs RHE). The main absorption Mn K-edge at around 6560 eV corresponds to the excitation of Mn 1s core electrons to unoccupied 4p orbitals. The shoulder peak at ∼6553 eV exhibits a higher intensity and a progressive shift to lower energies and when the applied potential decreased from 1.2 to 0.2 V, indicating the reduction of Mn at more negative potentials. The linear combination fitting analysis of Mn XANES spectra with pure Mn oxide references quantitatively showed that the average Mn valences continued to decrease from 2.58 to 2.23 when the potential decreased from 1.2 to 0.2 V (Figure 70B, inset). In comparison, the Co valences decreased from 2.25 to 2.00, suggesting that Co is fully reduced to CoO(II), when the potential decreased from 1.2 to 0.6 V, and remained at 2.00 as the potential was further lowered to 0.2 V. The average Fe valence remained virtually unchanged at 3.00 over the entire potential range, indicating that Fe was chemically stable, even under a strong reducing environment in alkaline media. The changes in relative X-ray absorption intensity at characteristic energy values of Mn, Co, and Fe were used to represent the relative changes in metal valences (Figure 70C). Mn and Co valences changed synchronously under applied potentials with intensity increases and decreases in a periodic fashion, corresponding to reduction and oxidation of those two elements, respectively. The highest and lowest X-ray intensities are marked by two boundary potentials of 0.28 and 1.12 V, respectively, which are fully consistent with the potentials separating oxidation and reduction currents at 0.28 and 1.12 V, respectively (Figure 70C, inset). In sharp contrast to Mn and Co, the oxidation state of Fe remained virtually constant during the potential cycles. This shows that the fast-tracking strategy, described here, is capable of accurately monitoring dynamic changes with a mV-level potential resolution. The authors thus proposed a collaborative effort among Mn, Co, and Fe, in which Mn and Co serve as the synergistic coactive sites and result in the observed high ORR activity in alkaline media, while Fe works to maintain the structural integrity of the spinel oxides, likely contributing to the remarkable durability of the Mn−Co−Fe catalyst. Additionally, *operando* EXAFS showed the changes in Mn−O interatomic distances under applied potentials. The Mn−O atomic distance (no phase correction) increased from 2.23 to 2.58 Å as the potential decreased from 1.2 to 0.2 V. The longer Mn−O interatomic distance is consistent with a gradual decrease in the Mn valence at more reducing potentials. Similar changes in the Co−O distances occurred while Fe−O showed no appreciable changes across all potentials, again confirming that Fe serves as the stabilizing element to help maintain the structural integrity of the spinel structure and enhance long-term durability in alkaline media.

https://doi.org/10.1021/acs.chemrev.1c00331
Chem. Rev. XXXX, XXX, XXX−XXX

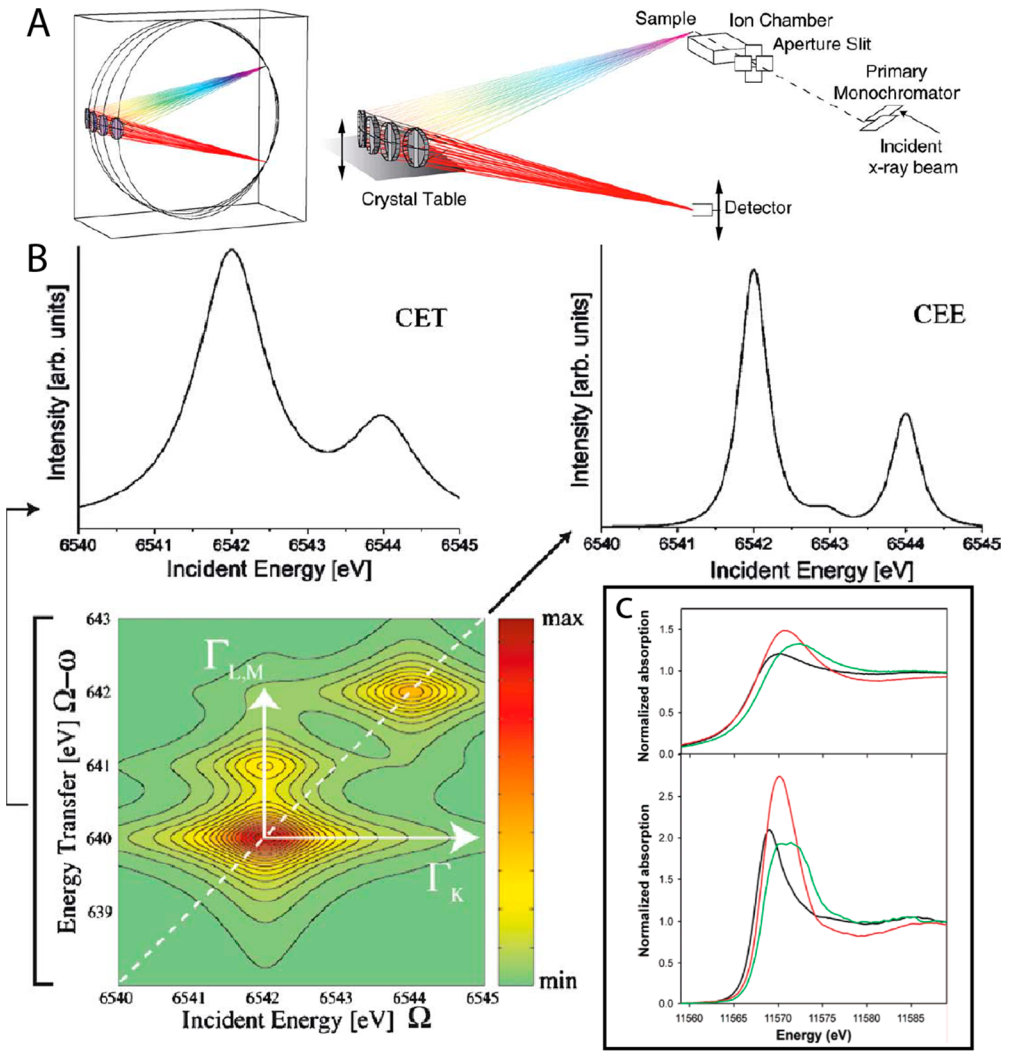

Figure 71. (A) Scheme of experimental setup for HERFD-XAS. The black circles and arrow mark the Rowland circles and its orientation. (B) Computed RIXS plane, highlighting the difference between CET, integrated along energy transfer and plotted as a function of incident energy, and CEE, diagonal cut containing the resonant peak (white dashed line in 2D RIXS pattern) and plotted as a function of incident energy. Γ_k and $\Gamma_{l,m}$ refer to the lifetime broadening of the K orbit and L, M orbit. (C) Comparison of conventional total fluorescence detection (top) and HERFD-XAS (bottom) at the Pt L_3-edge on Pt nanoparticles in three different atmospheres: He (black), He + O_2 (red), and 1% CO/He (green). Panel A is reprinted with permission from ref 995. Copyright 2014 Royal Society of Chemistry. Panel B is reprinted with permission from ref 996. Copyright 2005 Elsevier. Panel C is reprinted with permission from ref 1009. Copyright 2006 American Chemical Society.

8.1.2. High-Energy Resolution Fluorescence Detection (HERFD) XAS. Although XANES is extremely useful for measuring electronic structures, fundamental physics—specifically, the lifetime of the core-hole—limits the energy resolution of XANES.[993] A core-hole is generated when an atom transitions to an excited state by absorbing an X-ray. The core-hole is subsequently annihilated when the atom relaxes as an electron from a higher state fills in the core-hole. This process leads to a finite lifetime of core-holes (Δt) and causes the energy broadening Γ in XANES, based on the energy−time uncertainty principle $\Gamma = \hbar/\Delta t$. Generally, the effect of lifetime broadening on XANES spectra behaves like a convolution with a Gaussian/Lorentz function with a finite width Γ and thus reduces the peak intensity and broadens the line width of features, such as pre-edge peaks, making it difficult to quantify such structural information. Since the finite lifetime of a core-hole is intrinsic to X-ray absorption, the broadening is present no matter whether in transmission mode or total fluorescence detection mode.

The pioneering work[994] by Eisenberger et al. demonstrated that using fluorescence XAS and collecting fluorescence within only a narrow energy range near the resonance energy (such as Kα) can significantly reduce the lifetime broadening. The method is now called high-energy resolution fluorescence detection of XAS (HERFD-XAS). In practice, this method is realized by replacing a conventional solid-state fluorescence detector (e.g., Vortex), which has a typical energy resolution of more than 150 eV, with a single-crystal analyzer to achieve an energy resolution on the order of 1 eV. The throughput and energy resolution are optimized using several spherically bent crystals near backscattering in the Rowland circle geometry. A schematic of the experimental setup is shown in Figure 71A.[995] Using this high-resolution analyzer, HERFD-XAS effectively reduces the core-hole broadening to less than 2 eV. The reduction of lifetime broadening in HERFD-XAS can be understood using a simple model provided by Glatzel et al.[996] Briefly, this model calculates the fluorescence caused by an electronic transition between two states—a core-hole state

https://doi.org/10.1021/acs.chemrev.1c00331
Chem. Rev. XXXX, XXX, XXX−XXX

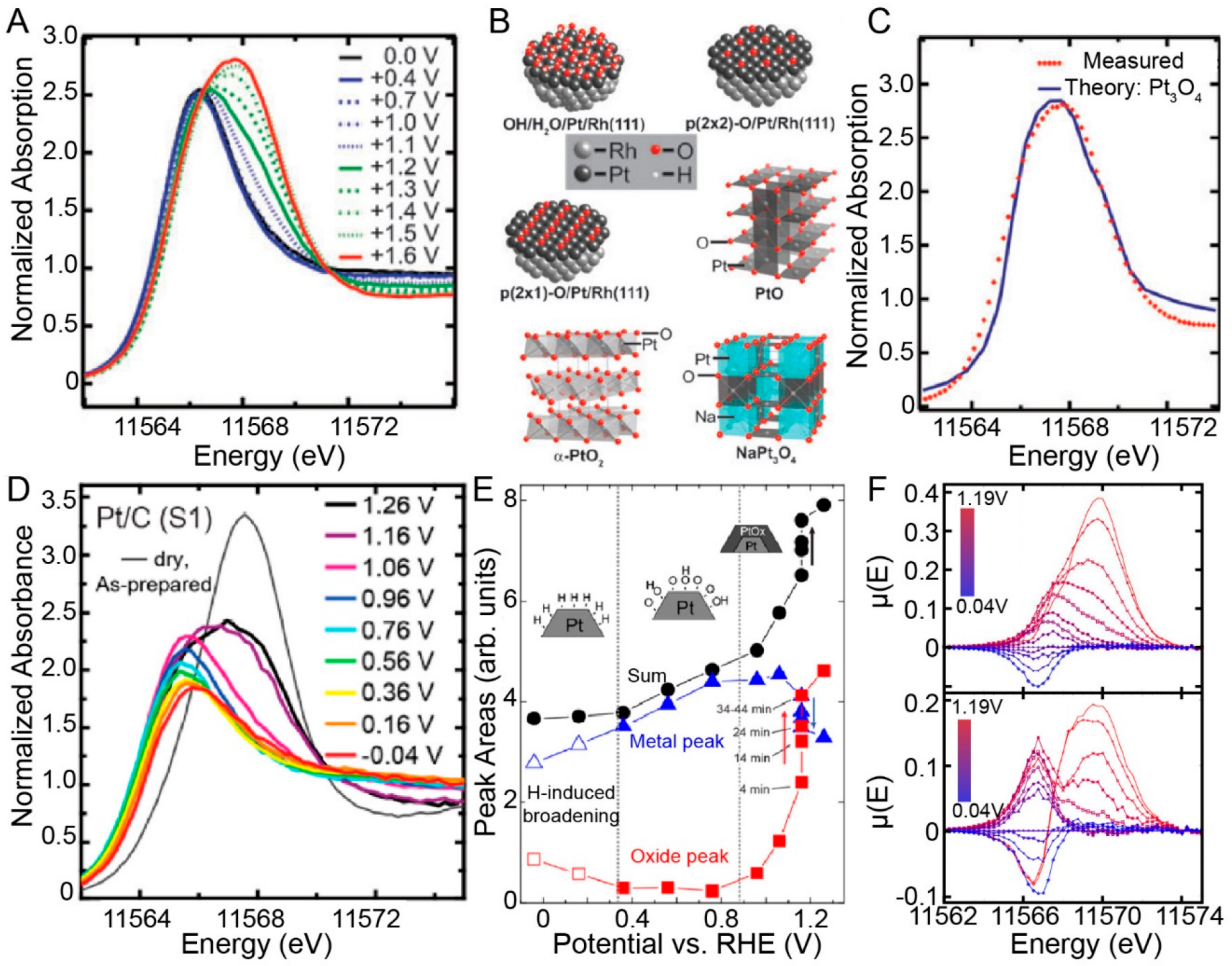

Figure 72. (A) HERFD-XAS of the Pt L_3-edge for Pt/Rh(111) in 0.01 M $HClO_4$ as a function of potential. (B) Structure of Pt/Rh(111) for simulating HERFD-XAS using FEFF software. (C) Comparison between simulated Pt_3O_4 XANES and the experimental profile at 1.6 V. (D) HERFD-XAS of the Pt L_3-edge for a Pt nanoparticle on glassy carbon in 0.1 M $HClO_4$ as a function of potential. (E) Best fitted peak intensity for the metallic Pt and Pt oxide from HERFD-XAS as a function of potential. (F) *In situ* $\Delta\mu$ XANES for Pt in 1 M KOH flowing with N_2 (top) and O_2 (bottom). Panels A–C are reprinted with permission from ref 1011. Copyright 2011 Royal Society of Chemistry. Panels D and E are reprinted with permission from ref 1012. Copyright 2012 American Chemical Society. Panel F is reprinted with permission from ref 1013. Copyright 2019 MDPI.

with shorter lifetime (Γ_k, K-shell) and a higher-level hole state with longer lifetime (such as Γ_l, L-shell, data adopted from Mn)—and plots the fluorescence as a function of the energy (Ω) of the incident X-ray and the net energy transfer ($\Omega-\omega$), where ω is the energy of the emitted photon. Elastic scattering corresponds to $\omega = 0$. As shown in Figure 71B, the horizontal and vertical broadening of the fluorescence is solely caused by the lifetime of the core state (Γ_k) and of the higher state (Γ_l), respectively. Using this calculated 2D-RIXS spectrum, we can understand why constant emission energy (CEE) spectra produce sharper features.

In CET (constant energy transfer), the measured signal is obtained by plotting as a function of the incident energy. When the detector has broad energy resolution (>150 eV), the measured signal is obtained by integrating over ω and is the conventional XAS result. In contrast, in CEE, a line profile is selected along the diagonal direction ($y = x$ + constant), so that the fluorescence energy is a constant ω = constant, which is the HERFD-XAS case. When comparing the signal between CET (conventional) and CEE (HERFD), CEE clearly produces a much higher signal contrast. de Groot et al. provide a convenient equation to estimate the effective lifetime broadening (Γ_{eff}) in HERFD-XAS, through $\left(\frac{1}{\Gamma_{eff}}\right)^2 \approx \left(\frac{1}{\Gamma_k}\right)^2 + \left(\frac{1}{\Gamma_l}\right)^2$.[997] Thus, by selecting the fluorescence line from the transition between the higher orbit and core orbit, the effective lifetime will increase towards that of the higher orbit. Clearly, HERFD-XAS filters away a large portion of the fluorescence photons and thus has an overall lower signal. This inefficiency of HERFD-XAS is clearly a drawback when studying systems with weak or time-resolved signals such as studies of catalysis under *operando*/*in situ* conditions. However, due to the continuous upgrades of synchrotron X-ray facilities worldwide, there is a rapidly increasing number of experiments deploying HERFD-XAS for mechanistic studies of catalysis.[998−1008]

Because of the critical role of Pt in understanding alkaline electrocatalysis, this section selects recent work applying HERFD-XAS to Pt and Pt-related catalysts in different forms, including nanoparticle, monolayer, and single-atom catalysts. For Pt, XANES of the L_3-edge is of strong interest, since it contains information on electrons excited from the 2p states to unoccupied 5d states and thus probes the structure and occupancy of the 5d states. Specifically, in the XANES region, there is an intense peak near the rising absorption edge,

https://doi.org/10.1021/acs.chemrev.1c00331
Chem. Rev. XXXX, XXX, XXX−XXX

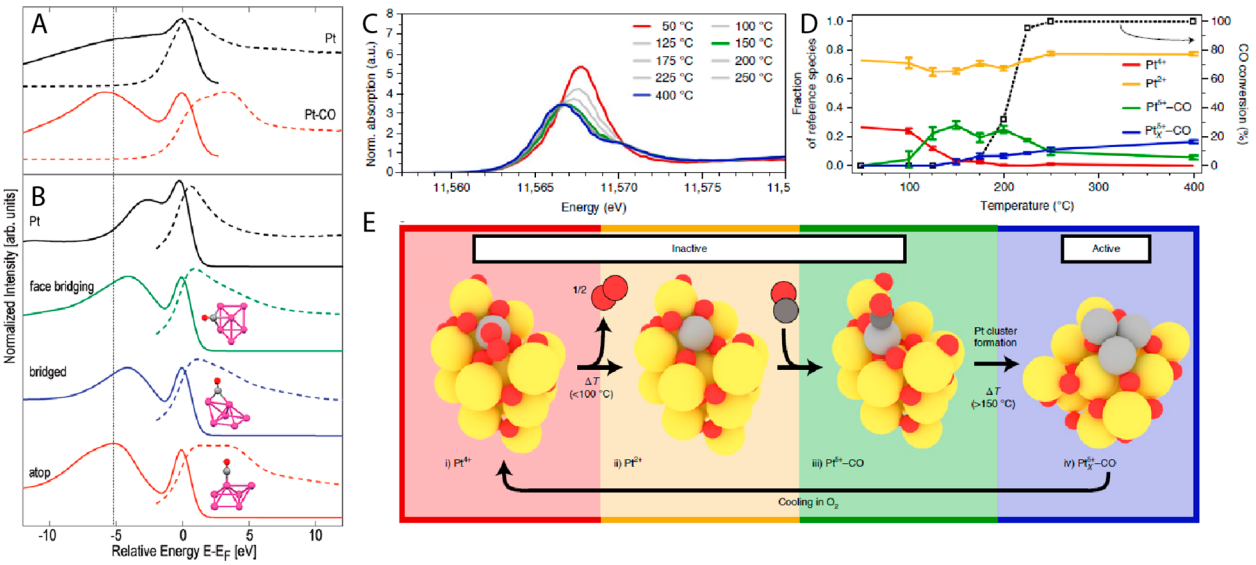

Figure 73. (A) Experimental RIXS (solid line) and HERFD-XAS (dashed line) of the Pt L_3-edge. (B) Calculated RIXS and XAS pattern for the cluster of Pt_6 without CO and with coordinated CO at three different sites: face-bridging, bridged, and atop. (C) *In situ* HERFD-XAS of the Pt L_3-edge in the reaction environment (1000 ppm of CO, 10% O_2 in He) at different temperatures. (D) Catalytic activity for CO oxidation and fraction of different Pt species. (E) Scheme for the reversible formation of the catalytically active Pt cluster (grey, Pt; yellow, Ce; red, O; dark grey, C). Panels A and B are reprinted with permission from ref 1014. Copyright 2010 American Chemical Society. Panels C–E are reprinted with permission from ref 1015. Copyright 2020 Springer Nature.

called the *white-line*. In Pt, the intensity and position of the white-line is associated with the electron transition from $2p_{3/2}$ to 5d orbitals. Any changes in the 5d states, such as rehybridization, bonding with absorbates, and charge transfer, which potentially influence catalytic performance, are reflected by changes in the white-line. HERFD-XAS is very well-suited for quantitatively characterizing these changes in the white-line. Figure 71C compares profiles of the Pt L_3 white-line measured with (top) conventional total fluorescence detection and (bottom) HERFD mode. In HERFD mode, the intensity of the white-line is significantly enhanced, and the peak width is narrower resulting in a much improved contrast.[1009,1010]

Friebel et al. applied *in situ* grazing incidence HERFD-XAS to a monolayer of Pt deposited on Rh(111) in 0.01 M $HClO_4$ and captured the formation of Pt oxides above 1.0 V vs RHE (Figure 72A).[1011] The grazing incidence X-ray geometry enhances the surface sensitivity of the measurement. In their studies, they observed that when the potential is between 0 and 1.0 V, there is no significant evolution. However, when the potential is increased from 1.0 to 1.6 V, a larger and continuous change occurs. The white-line intensity increases, and the peak shifts to higher energy. The XANES profiles of a series of Pt oxides (α-PtO_2, PtO, $NaPt_3O_4$, and Pt_3O_4) are simulated and shown in Figure 72B. Only Pt_3O_4 reasonably reproduces the HERFD-XAS measured at 1.6 V (Figure 72C). Thus, they infer that, in Pt monolayers, Pt oxidizes into square planar PtO_4 units, similar to Pt_3O_4, at high potential. Merte et al. observed a similar behavior in Pt NPs (1.2 nm) on glassy carbon in a 0.1 M $HClO_4$ solution (Figure 72D).[1012] They observed a continuous evolution of the white-line when the potential was held at 1.16 V for 44 min, suggesting that the Pt NPs are gradually oxidized from their outer surface. To characterize these *in situ* XANES profiles, they used two asymmetric modified Gaussian–Lorentzian functions to fit the profiles and calculated the relative portions between metallic Pt and Pt oxide, as shown in Figure 72E. The final structure of oxidized NPs was found to contain 25–50% metallic Pt. Based on the evolution of fitting parameters with potential, it is convenient to divide the potential range into three sections: hydrogen chemisorption (0–0.3 V), oxygen chemisorption (0.3–0.96 V), and Pt oxide formation (>0.96 V). Kusano et al. conducted similar experiments on 2–4 nm Pt NPs in alkaline media and observed that the evolution of the XANES profiles also depended on whether N_2 or O_2 was flowing.[1013] They used the change of the XANES signal $\Delta\mu$ to characterize the change of HERFD-XAS. This method first selects the XANES profile at 0.34 V as a standard and plots the deviation of XANES from the standard, denoted as $\Delta\mu$, at other potentials (Figure 72F). Based on this analysis, they proposed the formation of superoxide anions absorbed on the Pt surface when flowing O_2 in the solution from 0.34 to 0.74 V, which is consistent with previous *in situ* vibrational spectroscopic studies (Figure 15B).

Another group of *in situ* HERFD-XAS experiments on Pt focus on surface absorption/oxidation in gaseous environments, such as H_2, CO, H_2O, and O_2.[1009,1010,1014−1017] For example, Safonova et al. characterized the structure of CO absorbed on Pt monolayers on Al substrates.[1009] A clear difference in both the intensity and the peak position of the white-line was observed in three gas environments: He, He with a trace of O_2, and He with 1% CO. Later, Glatzel et al. investigated the adsorption of CO on Pt NPs, using the combination of RIXS and HERFD-XAS.[1014] They integrated the 2D RIXS pattern along the incident energy and plotted integrated RIXS as a function of energy transfer, together with the XANES relative to the Fermi level (Figure 73A). In both studies, through the simulation of three different structures of CO on the Pt_6 cluster—face bridging, bridged, and atop (Figure 73B)—they confirmed that only the atop configuration of CO–Pt agrees with the experimental result of both RIXS and XANES. Cui et al.[1010] investigated the surface oxidation of Pt NPs in an oxygen environment. They used linear combination fitting in the XANES region to calculate the equivalent oxidation rate and observed that the oxidation rate

https://doi.org/10.1021/acs.chemrev.1c00331
Chem. Rev. XXXX, XXX, XXX−XXX

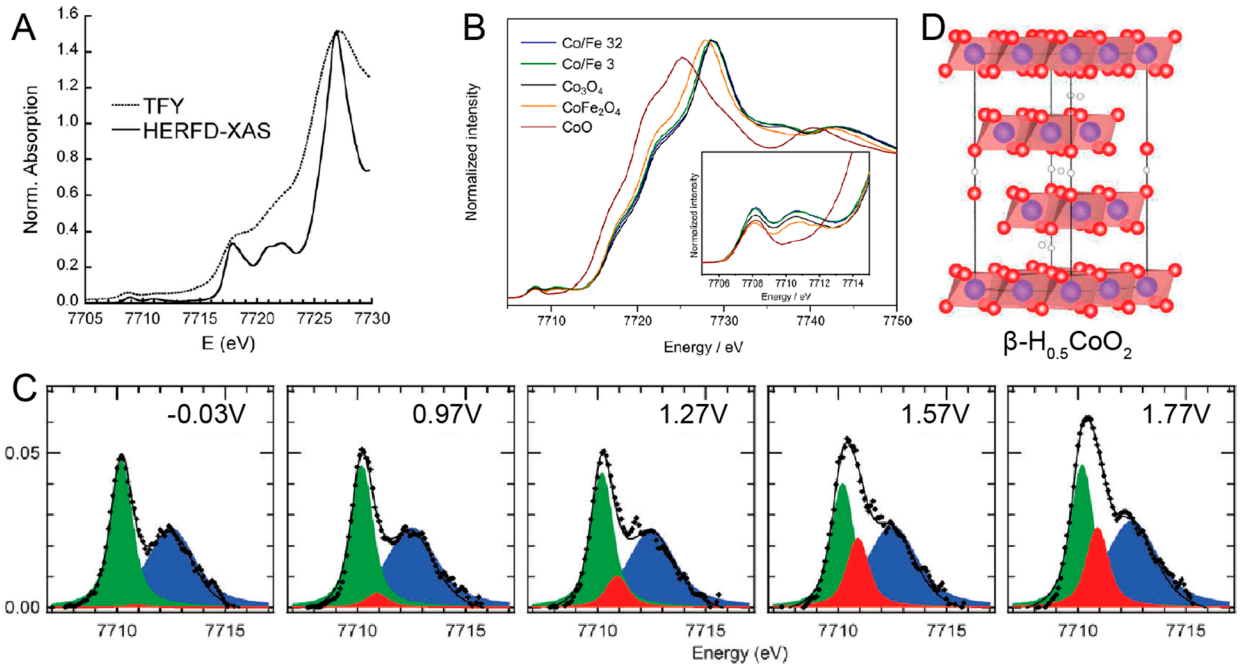

Figure 74. (A) Comparison between conventional total fluorescence detection (dashed line) and HERFD-XAS (solid line). (B) HERFD-XAS of a Co/Fe oxide nanowire with different ratios of Co and Fe, $CoFe_2O_4$, CoO, and Co_3O_4. (C) *In situ* HERFD-XAS pre-edge peaks of the Co K-edge. Solid black line: summed fittings from three pseudo-Voigt profiles (green, blue, and red). Green and blue peaks are observed in the prepeak profile in CoOOH. (D) Optimized structure of β-$H_{0.5}CoO_2$. Panel A is reprinted with permission from ref 1019. Copyright 2010 American Physical Society. Panel B is reprinted with permission from ref 1020. Copyright 2020 American Chemical Society. Panels C and D are reprinted with permission from ref 1021. Copyright 2013 Royal Society of Chemistry.

in a gaseous environment containing both H_2O and O_2 is higher than in an environment that only contains H_2O or O_2, indicating a cooperative behavior between O_2 and H_2O. Recently, Maurer et al. applied HERFD-XAS, accompanied with *in situ* infrared spectroscopy, on the single-atom catalytic system Pt on CeO_2 and observed its change in electronic structures when contacting O_2 and CO.[1015] Figure 73C shows the *in situ* XANES profiles in 1000 ppm of CO and 10% O_2 in He as a function of temperature. The white-line continuously decreased in intensity, and the position shifted towards lower energy as the temperature increased from 50 to 150 °C. Based on linear combination fitting using reference materials, the fractions of different species, such as Pt^{4+} and Pt^{2+}, in the catalyst were calculated (Figure 73D), leading to a scheme for the formation of an active catalyst for CO conversion (Figure 73E). During the initial heating, surface-adsorbed O on single-atom Pt starts to be desorbed (<50 °C) and replaced by CO (50−100 °C). From 100 to 150 °C, Pt^{2+} is converted to Pt $^{\delta+}$−CO. Above 150 °C, the Pt atoms migrate from 4-fold hollow sites to form small Pt clusters, which corresponds to the onset of catalytic activation for CO oxidation. However, in another study, an Ir single-atom catalyst on $MgAl_2O_4$ was reported to be active for CO oxidation at similar temperatures while maintaining the single-atom configuration. Through *in situ* HERFD-XAS, it was shown that the single-atom Ir adsorbs CO as a ligand and forms an Ir(CO) complex under reaction conditions.[1018]

HERFD-XAS is especially powerful in detecting weak signals, such as pre-edge peaks, in XANES regions which contain information about coordination symmetry, spin, and ligand bonding. Figure 74A compares the Co K-edge in $LiCoO_2$ under conventional total fluorescence yield detection (TFY, dash line) and under the HERFD-XAS (solid line).[1019] In HERFD-XAS, the different pre-edge peaks are resolved. Budiyanto et al. studied Co_3O_4 oxide nanowires as catalysts for the OER and found that, by adding Fe, the overpotential for OER decreased.[1020] With HERFD-XAS at the Co K-edge, they observed an increase in the pre-edge feature intensity, suggesting that Fe incorporation increases the distortion around Co and tetrahedral Co sites (Figure 74B). Friebel et al. reported the *in situ* HERFD-XAS studies on the OER of electrodeposited Co on Au(111) (Figure 74C).[1021] The initial prepeak features at −0.03 V resemble the structure of CoOOH. With an increase in the potential from 0.97 to 1.77 V, an additional pre-edge peak feature appears and is confirmed to be a nonstoichiometric $HxCoO_2$ phase (Figure 74D).

8.1.3. Crystal Truncation Rod (CTR) Measurements. X-ray diffraction/crystallography (XRD) is an ideal tool for characterizing the crystal structure of catalysts under *in situ* and/or *operando* conditions. However, conventional crystallography measures the average bulk structure and is insensitive to the surface/interface structure that is critical for electrocatalysis. A straightforward strategy to enhance the surface sensitivity is to set the angle of incidence below the critical angle for total external reflection (TER). The evanescent wave of the TER doubles the electric field at the surface enhancing the sensitivity and has a finite extinction length which significantly suppresses the scattering from the bulk. Since the critical angle for total external reflection is ≤0.1°, experiments utilizing this strategy are called *grazing incidence diffraction*. TER is also frequently adopted in X-ray spectroscopy experiments to enhance surface sensitivity. Here, we focus on another strategy for surface crystallography: *crystal truncation rods* (CTRs).

https://doi.org/10.1021/acs.chemrev.1c00331
Chem. Rev. XXXX, XXX, XXX−XXX

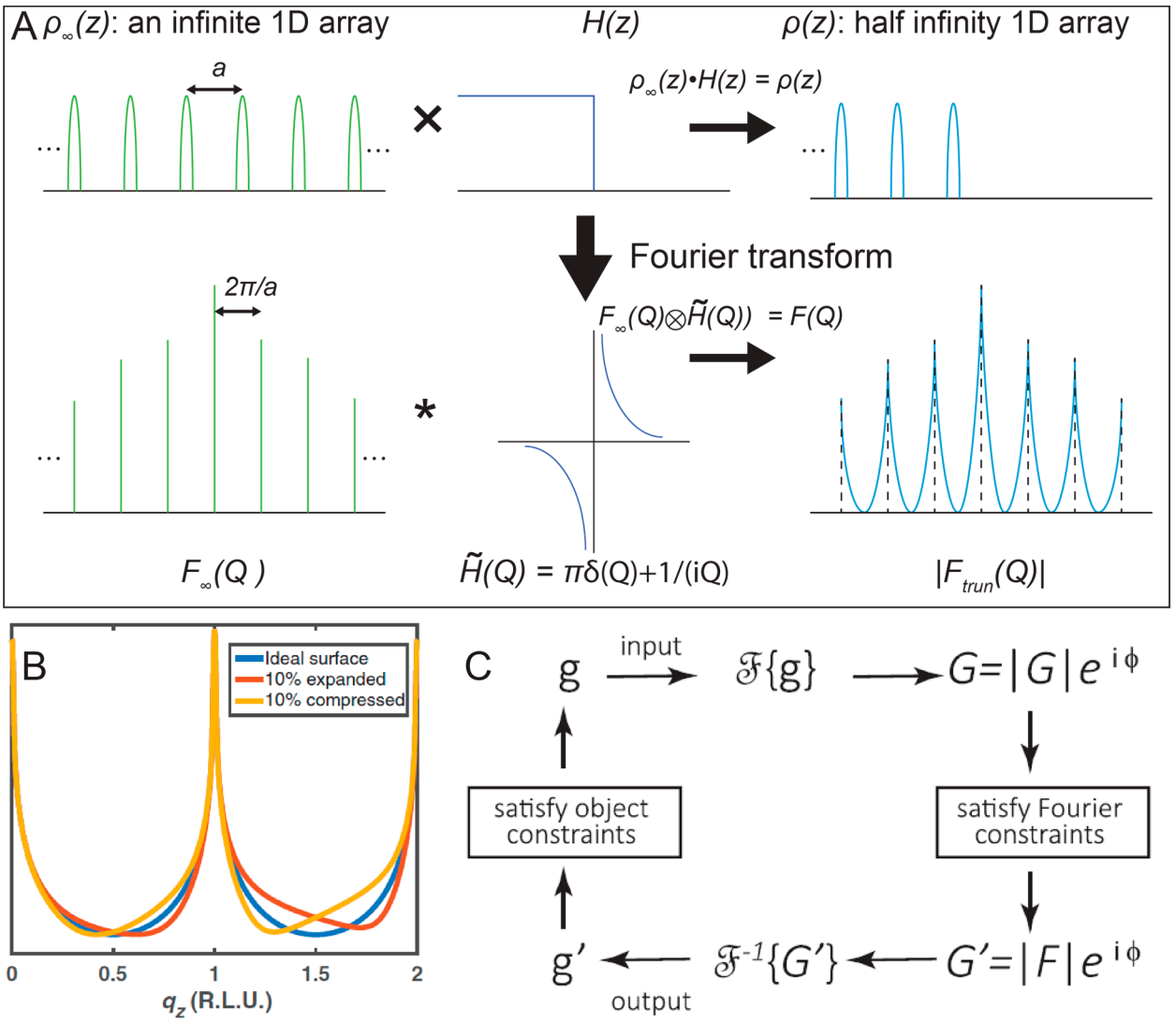

Figure 75. (A) Electron density and form factor for a truncated, semi-infinite, 1D periodic array of atoms. (B) Changes in the CTR profile for a surface with uniform relaxation along the z direction. (c) Scheme of the general concept of the direct method. Panel A is reprinted with permission from ref 1025. Copyright 2020 Wiley. Panel B is reprinted with permission from ref 1027. Copyright 1978 The Optical Society.

CTRs can be understood using a simple single-crystal diffraction model. For an infinite crystal (in practice, the crystal only needs to be larger than the coherence length of the X-ray), the scattering pattern consists of a three-dimensional periodic array of sharp diffraction peaks known as Bragg peaks. When the crystal is truncated to generate a flat surface, the diffraction peaks spread along the surface normal direction, turning into "rods". These "rods" of scattering are the CTRs.[1022,1023] In X-ray diffraction, the *form factor* (F) is used to express the scattering amplitude of a material.[1024] Formally, F is the Fourier transform of the number density of electrons, $\rho(r)$.

$$F(\vec{q}) \equiv \int \mathrm{d}^3\vec{r}\ \rho(\vec{r})\mathrm{e}^{\mathrm{i}\vec{q}\cdot r} \tag{22}$$

$$I(\vec{q}) \propto |F(\vec{q})|^2 \tag{23}$$

where $I(q)$ is the diffracted intensity. To illustrate the origin of CTRs, we calculate the form factor $F_\infty(q)$ of a one-dimensional, infinite, periodic array of "atoms" with period a. The situation is shown schematically in Figure 75A, where the one-dimensional electron density, $\rho_\infty(z)$, is plotted as function of position. Fourier transforming, we obtain the form factor, $F_\infty(q)$, which is given by a series of periodic array (spacing $2\pi/a$) of delta-function (Bragg) peaks. The details of the atomic charge distribution are mapped onto the amplitude of the Bragg peaks. This is conventional bulk crystallography. To create a "surface", we multiply $\rho_\infty(z)$ by a step function, $H(z)$.

$$\rho(z) = \rho_\infty(z)\, H(z) \tag{24}$$

Multiplication in real space becomes a convolution in reciprocal space; therefore

$$F = F_\infty \otimes \tilde{H} \tag{25}$$

where $H(Q)$ is the Fourier transform of $H(z)$. As shown in Figure 75A, the convolution imprints the surface structure onto each Bragg peak.

If the surface is not ideally truncated, we can simply add the scattering amplitude of the actual surface to the scattering amplitude of the ideally truncated surface and then calculate the intensity. In this way, adlayers, surface reconstructions, and roughness can all be handled. Figure 75B uses this technique to calculate the changes to the CTR if the height of the first

https://doi.org/10.1021/acs.chemrev.1c00331
Chem. Rev. XXXX, XXX, XXX−XXX

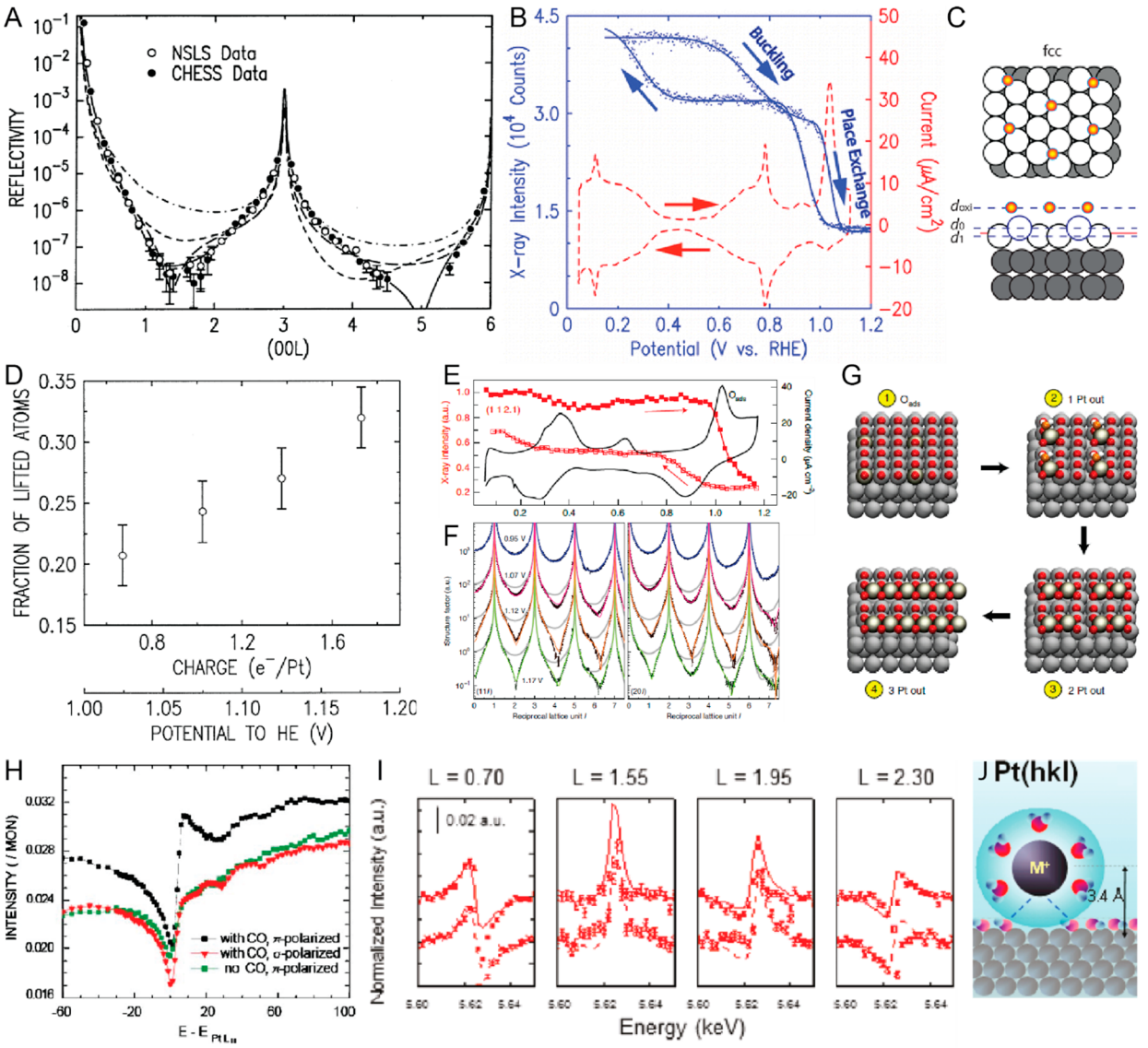

Figure 76. (A) Specular CTR on Pt(111) in 0.1 M $HClO_4$ at 1.175 V vs RHE. Three models are compared: ideal Pt bulklike surface (dot-dashed), buckled 1st Pt layer (long-dashed), ClO_4^- adsorbed surface (short-dashed), and place exchanged surface (solid). (B) Cyclic voltammogram of Pt(111) in 0.1 M $HClO_4$ (red dashed) and CTR intensity at (0 0 4.5) as a function of potential (blue dots) with a fitted profile using two-step error functions (blue solid). (C) Scheme of Pt(111) surface at potentials between 0.6 and 0.95 V. (D) Fraction of lifted Pt atoms at potentials between 1.0 and 1.2 V. (E) Cyclic voltammogram of Pt(100) in 0.1 M $HClO_4$ and CTR intensity at (1 1 2.1). (F) (11L) and (20L) CTRs on Pt(100) at different potentials. (G) Scheme of the main steps of place exchange and dissolution on Pt(100). (H) Energy scans through the Pt L-edge at anti-Bragg position on Pt(111) with and without CO adsorption. (I) Energy scans at different L values of CTR measured on Pt(111) at 0.85 and 0.25 V. (J) Scheme of partially hydrated cation adsorbed on a Pt surface. Panels A, D, and H are reprinted with permission from refs 1034, 1040. Copyright 2002, 2006 Elsevier. Panels B, C, I, and J are reprinted with permission from refs 1036, 1041. Copyright 2016, 2011 American Chemical Society. Panels E–G are reprinted with permission from ref 1039. Copyright 2020 Springer Nature.

atomic layer is increased or decreased by 10% of the layer spacing.[1025] The CTRs are clearly sensitive to displacements that are a small fraction of a lattice spacing.

One challenge is the quality of the surface. A successful CTR experiment requires a high-quality single crystal with an atomically flat surface/interface (roughness within a few nm). As the surface roughness increases, the CTR signal decreases.[1026] This explains the observation that many experiments without high-quality surfaces do not observe CTRs. Away from the Bragg peaks, the intensity of the CTRs is several orders of magnitude lower than the intensity of the Bragg peaks. Thus, CTR experiments require high-flux sources such as a synchrotron. However, with sufficiently good samples and a synchrotron, a variety of CTR experiments are straightforward. For example, one can use the grazing incidence diffraction and rotate the in-plane orientation of the sample to measure multiple (off-specular) CTRs. Alternatively, one can scan along the specular direction, similar to X-ray reflectivity measurements.

After data collection, the second challenge in CTR experiments is the data analysis. Though it is easy to calculate the CTR from a well-defined structural model, the reverse operation is not straightforward. The challenge arises from the fact that the phase information for the form factor is lost during the X-ray detection. To determine the structure, a common method is structure refinement through least-squares

https://doi.org/10.1021/acs.chemrev.1c00331
Chem. Rev. XXXX, XXX, XXX−XXX

fitting. Firstly, a starting structural model is proposed. Then, selected structural parameters such as atomic position, occupancy, and Debye−Waller factor are relaxed to minimize the square error. By relaxing the structural parameters via iteration, a good fit can eventually be achieved. Clearly, this method depends heavily on a good starting model. Complex structures usually require an increased number of relaxed parameters, leading to a higher risk of overinterpreting the experimental data. Although this procedure will give the parameter set which best describes the data, the experimenter must determine if the model has physical significance.

Another group of methods is based on iterative phase retrieval algorithms, known as direct methods. In contrast to structural refinement, direct methods do not rely on a good starting model. Instead, they extract the phase information from a known model (which could even be random) and use the extracted phase as the lost phase of the form factor from the experiment. This artificial form factor is then inverse Fourier transformed to obtain a three-dimensional electron density. This electron density is filtered with real-space constraints, such as removal of negative electron density. The filtered electron density is then Fourier transformed again to obtain a new form factor, from which the phase information is fed back to the next iteration. Through iteration, the algorithm finally reaches a structural model that is compatible with all real-space constrains and the measured $|F|$.[1028] The process is schematically illustrated in Figure 75C.[1027] Several variants of direct methods have been developed. Three well-known examples are coherent Bragg rod analysis (COBRA),[1029] difference map using the constraints of atomicity and film shift (DCAF),[1030] and the phase and amplitude recovery and diffraction image generation method (PARADIGM).[1031]

Although these methods provide a precise model that agrees with the measured CTR profiles, the model is not guaranteed to yield the lowest free-energy state. Recently, Plaza et al. proposed an algorithm that combines structural refinement with *ab initio* calculation.[1032] They adopted the joint density-functional theory (JDFT) approach, which can simulate the interfaces between crystals and electrolytes, to guide the model refinement. A modified R factor was proposed as the goodness of fit measure: $R^2 = \chi^2 + \frac{1}{2}\gamma \sum_{i=1} (\zeta_i - z_i)^2$. The modified R factor contains two parts: (1) χ^2, which depends on the difference between the model and measured CTR intensity, and (2) $\sum_{i=1}(\zeta_i - z_i)^2$, which depends on the deviations between the atomic positions predicted by the model (ζ_i) and the JDFT minimum energy position z_i to include non-equilibrium processes and disorder. The variable γ determines the relative weight between CTR and JDFT.

CTR measurements have become a critically important tool for studying single-crystal electrodes to characterize surface/interface reconstruction and ionic adsorption.[1033,1034] In 1994, You et al. reported a series of *in situ* CTR measurements of the Pt(111) surface in acidic media (Figure 76A)[1034,1035] and observed changes in the CTR profiles as a function of potential. Above 1.2 V vs RHE, the intensity of the CTR irreversibly decreased, indicating irreversible surface roughening. At potentials between 0.9 and 1.2 V, the structural changes were reversible, as shown in Figure 76B.[1036] From the figure, changes in the CTR become severe above 1.0 V yet are still reversible. Following this work, many CTR experiments on single-crystal Pt electrodes have been conducted, showing that the reversible change of the CTR on Pt(111) is caused by deformation in the first atomic Pt layer.[1035,1037] Between 0.6 and 0.95 V, a small portion of the Pt atoms in the first layer are slightly buckled upwards relative to their original sites and thus do not dramatically affect the CTR (Figure 76C). Between 1.0 and 1.2 V, which is termed the place-exchange region, a larger number of Pt atoms in the first layer lift away from the surface to form a partially occupied layer (Figure 76D). After removing the potential, these Pt atoms move downward and return to their original sites. A competing explanation for the structural changes between 0.6 and 0.95 V is that the surface of Pt is completely covered by a monolayer of an oxygen species.[1038] This disagreement illustrates the fact that CTRs are sensitive to the electron density and are not element-specific. Therefore, CTRs cannot distinguish between O and partially occupied Pt layers with a similar electron distribution. Additionally, it has been reported that the structural changes on a Pt(100) surface are completely irreversible, unlike the reversible structural changes on Pt(111) (Figure 76E,F). As shown by a recent *in situ* CTR study,[1039] the irreversible structural changes are well-described by a more complex Pt extraction process (Figure 76G). After Pt atoms are extracted from the (100) surface, they move to the neighboring sites and coordinate with four adsorbed O atoms, finally forming a stripelike surface. This stripelike surface is likely to create unstable surface atoms that can be dissolved in the following oxidation, making this process irreversible.

The surface structure of Pt can also be influenced by the type of cation in the electrolyte.[1042,1043] A recent report by Kumeda et al. showed that the addition of hydrophobic cations to the electrolyte enhances ORR activity.[1044] The CTR was adapted to characterize the interphase structure of Pt(111) in 0.1 M $HClO_4$ containing 10^{-5} M hydrophobic tetra-*n*-hexylammonium cations. At low potential (0.5 V vs RHE), the addition of hydrophobic cations does not influence the intensity of the CTR. However, when the potential reaches 0.9 V, the influence of hydrophobic cations is clear. Based on this interpretation of the CTR data, the authors claim that the hydrophobic cations destabilize the surface oxygen species, decreasing the coverage of adsorbed OH, and thus promoting the access of oxygen molecules to the surface of Pt. Pt-based catalysts and other classical metal electrodes have been investigated using CTR as well.[1045−1049] For example, Stamenkovic et al. adopted CTRs to study the surface structure of highly ORR-active $Pt_3Ni(111)$ which shows a Pt-rich first atomic layer and a Ni-rich second atomic layer.[1050] Besides metals, CTR measurements have been applied to single-crystal oxide electrodes.[1051−1055,439] An example is $RuO_2(110)$ for its promising OER activity. On the $RuO_2(110)$ surface, it was found that certain CTRs (such as the 10L CTR) have less contribution from Ru in the sublayers, due to their atomic position, and thus respond stronger to changes in the surface oxygen positions. By measuring CTRs at different potentials, a clear structural evolution of the surface oxygen species on RuO_2 was proposed. For more details on these topics, the reader is referred to other literature.[439,441,442,1056]

8.1.4. Resonant Surface Scattering. Resonant scattering originates from the scattering where the energy of the incident X-ray is near the absorption edge of selected elements. This energy not only triggers strong X-ray absorption and emission but also produces anomalous scattering which is an elementally sensitive signal. Moreover, it has been demonstrated that,

https://doi.org/10.1021/acs.chemrev.1c00331
Chem. Rev. XXXX, XXX, XXX−XXX

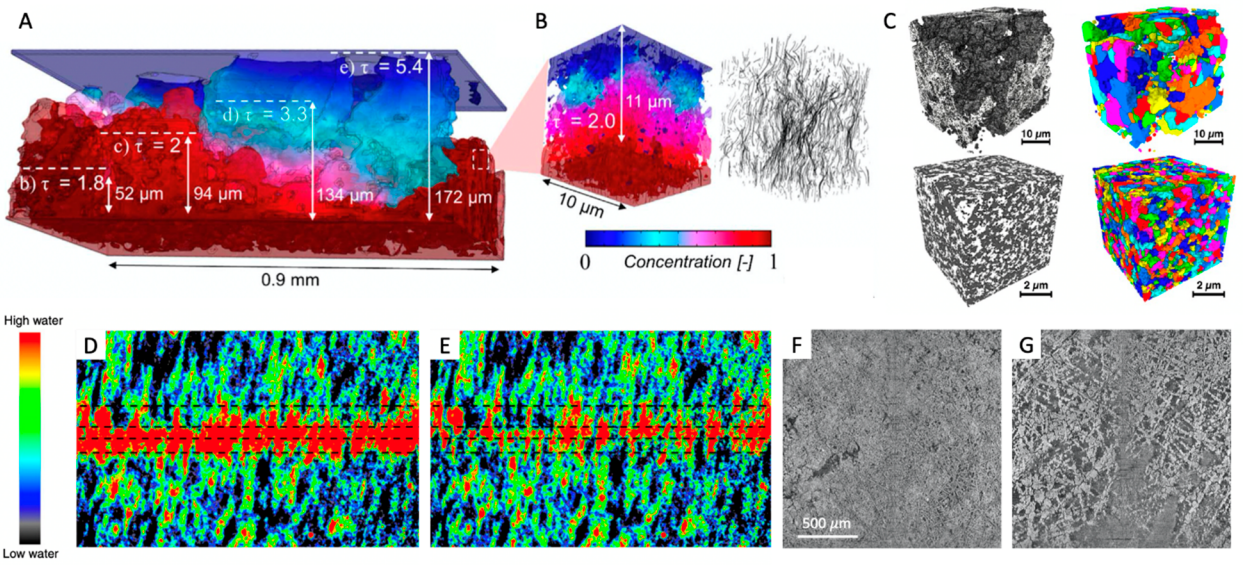

Figure 77. (A) Micro-CT reconstruction showing calculated tortuosity as a function of sample thickness (shown in subdivisions). (B) Mesoscale tortuosity obtained with nano-CT. (C) 3D rendering of the nano-CT image of the PGM-free electrode in (top-left) large FOV and (bottom-left) high resolution. (top-right and bottom-right) Respective images after segmentation and morphological separation with color labeling. *Operando* neutron imaging with (D) full humidity and (E) reduced dew point. The hydrated thickness of the AEM was 50 μm, and the layers of the sample from top to bottom separated by dashed lines were the anode GDL, anode CL, membrane, cathode CL, and cathode GDL. AEMFC micro-CT images of the longitudinal sections of (F) anode and (G) cathode GDEs with added PTFE. Panels A and B are reprinted with permission from ref 1064. Copyright 2017 Elsevier. Panel C is reprinted with permission from ref 1065. Copyright 2016 American Chemical Society. Panels D–G are reprinted with permission from ref 904. Copyright 2020 Springer Nature.

because of the anisotropic environment at the surface/interface, resonant scattering signal along the CTR is strongly influenced by the polarization of the X-ray beam (parallel or perpendicular to the surface).[1040,1057] Thus, this technique merges with CTR measurements for high spatial resolution and X-ray spectroscopy for element-specificity on the surface. A convenient strategy is to measure the CTR intensity at an anti-Bragg position (middle position between two Bragg peaks), where the signal is most sensitive to the surface layer, and scan the incident X-ray energy through the absorption edge. Changes in valence and atomic structure of the surface elements can be detected. Figure 76H shows the energy scan through the Pt L-edge on Pt(111) with and without CO adsorption. A clear signal difference, due to CO adsorption, appears when using π-polarized X-ray (normal to the surface).[1040,1057,1058] In some systems, the surface-adsorbed ions form ordered adlayers on the electrode surface, such as Br^- on Cu(001). Resonant surface scattering can be conducted at the edge energies of Br and Cu separately to clearly identify the interface structure.[1057] Strmcnik et al. investigated the surface structure of Pt(111) in 0.1 M KOH with 1 mM Ba^{2+} in solution.[1041] Combining CTR measurements and the energy scan at the Ba L_2-edge at different locations on the CTRs (Figure 76I), they could precisely detect the position of Ba^{2+} on top of the Pt(111) surface, out of other elements in the solution, such as K^+. Through the experiment, they found that the height of Ba^{2+} was similar to the hydrated radius of the cation in the solution, instead of only the ionic radius (Figure 76J). Although CTR is extremely powerful for revealing key mechanisms in alkaline fuel cell studies, such as surface reconstruction and adsorption, it is worth mentioning that CTR is based on the principle of X-ray scattering, which is closely related to the electron distribution. Thus, CTR signals are more sensitive to the position of heavier elements in the system, making it challenging to identify the structure of lighter elements in the presence of heavy ones, such as the structure of hydroxyl species adsorbed on the Pt surface.

8.1.5. Transmission X-ray Microscopy (TXM). In full-field transmission X-ray microscopy (TXM) techniques, the image of the sample is projected onto an area detector. An objective lens, often a Fresnel zone plate, is placed between the sample and the detector to focus the transmitted X-rays through the sample, which are then converted to visible photons by the scintillator crystal or detected directly with a pixelated X-ray detector.[1059,1060] With synchrotron radiation, the spatial resolution achieved is several tens of nanometers for hard X-rays[1061] and under 15 nm for soft X-rays.[1062] One key advantage of full-field methods is the relatively short data acquisition time because the entire field of view (FOV) is imaged at once, instead of imaging pixel by pixel as with scanning methods. Additionally, the spatial resolution of full-field TXM is dependent on the objective lens rather than on the spot size on the sample.

Another closely related technique is X-ray computed tomography (CT), which relies on taking full-field images from different angles by rotating the sample along an axis perpendicular to the incident beam. A tomographic reconstruction algorithm[1063] is then applied to the 2D images in order to numerically reconstruct the 3D morphology of the sample. Synchrotron light sources allow for tunable X-ray energies, and with the addition of other detectors, tomographic imaging can be done in conjunction with absorption or fluorescence studies.[1061] In one study, Atanassov et al. used both micro- and nano-CT to characterize the transport-dependent morphology of PGM-free electrocatalysts for the ORR.[1064] The Fe-based catalyst was fabricated into an MEA, and electrochemical testing showed a larger resistance to

https://doi.org/10.1021/acs.chemrev.1c00331
Chem. Rev. XXXX, XXX, XXX−XXX

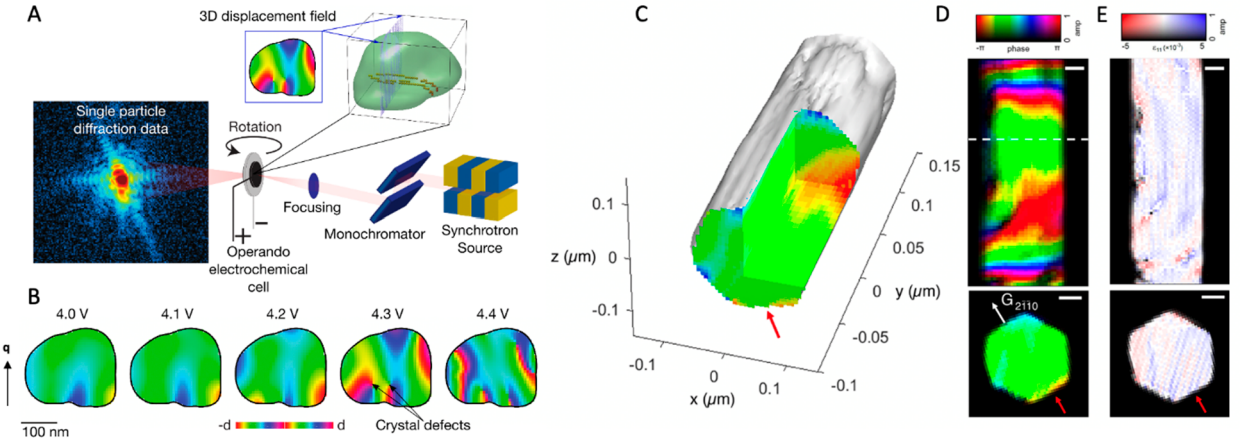

Figure 78. (A) *Operando* imaging of the 3D displacement field using Bragg CDI, allowing a tracking of the evolution of a single nanoparticle during electrochemical charging. (B) Displacement field along a plane through the nanoparticle during charging (the plane is shown in panel A). The voltage vs Li^+ is indicated at the top. Two edge dislocations are identified as singularities of the displacement field and are indicated at 4.3 V vs Li^+. Cut through the (C, a) 3D strain field in a GaInAs nanowire and (C, b) 2D cuts taken from this volume. The cross-section cut was taken from the marked line (dashed white line). The scale bar is 50 nm. Panels A and B are reprinted with permission from ref 1073. Copyright 2018 The Authors, Springer Nature. Panels C−E are reprinted with permission from ref 1077. Copyright 2018 American Chemical Society.

electron and proton transport in devices containing the PGM-free catalyst as compared to PGM-based electrodes. As such, the structure of the gas diffusion electrode was imaged at different length scales with CT in order to correlate the morphology to observed transport properties. Figure 77A shows the micro-CT reconstruction of the structure and tortuosity (parameter relating porosity to effective transport coefficient) as a function of sample thickness. Micro-CT images were taken at 24 keV and 100 ms exposure time. A scintillator with 5× magnification lenses and a camera (resulting in 1.33 μm pixels and 3.3 mm horizontal FOV) detected the scattering signal. A portion of the CL was reconstructed from nano-CT (Figure 77B) images taken at 8 keV and 1 s exposure time per projection. A Fresnel zone plate (60 nm outermost zone width) was used to focus the beam, and the FOV was 80 μm. The calculated tortuosity values from these measurements demonstrated that the high tortuosity (indicating reduced transport) occurred in aggregates at the microscale, rather than in smaller catalyst layer structures.

While synchrotron light sources offer a high degree of experimental flexibility, nano-CT imaging can also be done with a lab source. Litster, Zelenay, and coworkers conducted nano-CT imaging of a catalyst-coated membrane made with Fe−N−C catalysts, prepared from cyanamide−polyaniline−iron precursors, at two different resolution levels.[1065] Figure 77C shows the 3D reconstruction of nano-CT images taken with the larger FOV (top left) and at high resolution (bottom left) using Zernike phase contrast scans. Solid domains were identified by separation based on concave interfaces and labeled by color for regions of interest in the large FOV (Figure 77C, top right) and high-resolution (Figure 77C, bottom right) nano-CT images. As synchrotron beamline compatible customized cells are being developed, *in situ* and *operando* studies will become more prevalent. For example, in the Fischer−Tropsch-to-Olefins synthesis field, Gonzalez-Jimenez et al. combined TXM (spatial resolution of 30 nm) with XANES to image the changes in structure and chemical composition of a 20 μm catalyst particle in a customized *in situ* reactor.[1066] Changes in the morphology of the active phase over time, as synthesis gas (H_2/CO) was converted into hydrocarbon chains, were observed at working conditions of 350 °C and 10 bar.

One of the challenges associated with developing AEMFCs is understanding and mitigating cell degradation mechanisms over extended-duration cell operation. In particular, it has been shown that oscillations in cell water distribution in the electrodes can lead to flooding and ionomer degradation.[918] Zenyuk, Mustain, and coworkers used *operando* X-ray computed microtomography with a voxel resolution of 1.3 μm to study the water dynamics and changes in the morphology of PtRu/C anode and Pt/C cathode catalyst layers in AEMFCs under various operating conditions.[904] *Operando* neutron imaging was also conducted to directly visualize liquid water in the cells under different dew point conditions (Figure 77D,E). Figure 77D shows flooding inside the cell at full humidity, and Figure 77E shows drying out at a reduced dew point. Preliminary studies also suggested that cell longevity depended on operating at high reacting gas dew points to mitigate cell flooding. The AEMFC structure was then modified by integrating new gas diffusion electrodes with hydrophobic polytetrafluoroethylene (PTFE) (8 wt % in the catalyst layer and 20 wt % in the gas diffusion layer). Figure 77F,G shows the X-ray computed microtomography images of the new AEMFC anode and cathode, respectively, at 0.1 V in 100% RH under H_2/O_2 reacting gases fed to the cell at 200 sccm. The MEA achieved a peak power density of 2.35 W/cm^2 under H_2/O_2 and 1.06 W/cm^2 under H_2/CO_2-free air. Notably, the addition of PTFE to the electrodes enabled the AEMFC to stably operate for over 1000 h at 600 mA/cm^2 with less than 5% loss in cell voltage. This study highlights the importance of developing *operando* imaging methods in driving the design of new energy materials.

Some potential drawbacks to full-field imaging methods utilizing intense X-ray sources are radiation damage and low spatial resolution of XRF or Auger electrons.[1067] With synchrotron light sources and advanced X-ray focusing optics, fast scanning probe techniques such as scanning transmission X-ray microscopy (STXM) require lower dwell time per scan (although more overhead for motor movement) and can employ multiple detectors such as transmission, fluorescence,

https://doi.org/10.1021/acs.chemrev.1c00331
Chem. Rev. XXXX, XXX, XXX−XXX

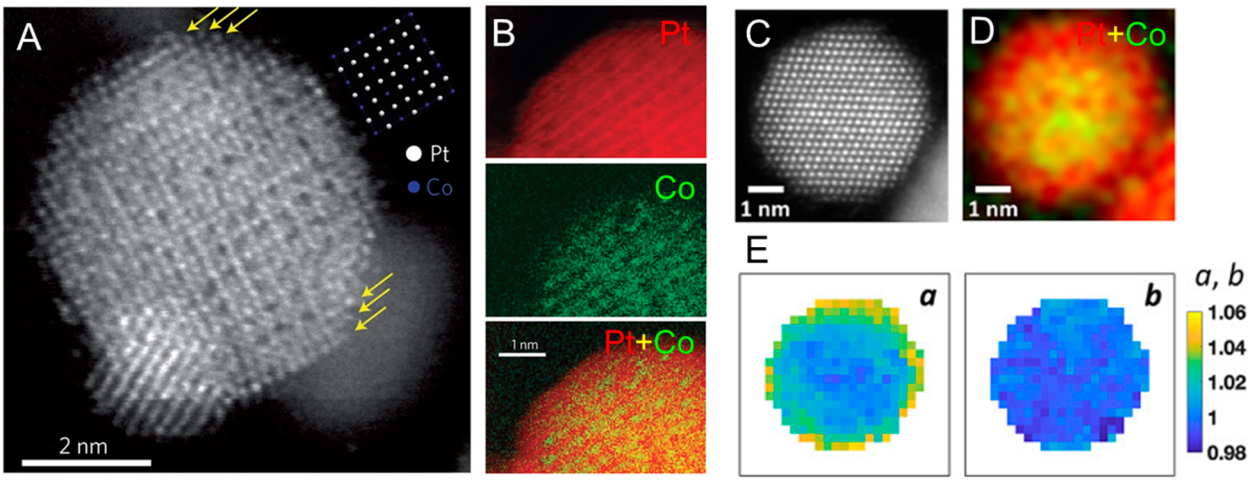

Figure 79. (A) Atomic-resolution ADF-STEM image of Pt_3Co ordered intermetallic with yellow arrows indicating the Pt-rich shell. A smaller particle (lower left) overlaps the larger particle in projection. The inset shows the projected unit cell along the [001] axis. (B) STEM-EELS maps of Pt, Co, and the composite of Pt vs Co of Pt_3Co/C after 5000 potential cycles. (C, D) Atomic-scale STEM image and EELS map of one Pt_3Co particle on the [110] zone axis. (E) Strain mapping of the Pt_3Co particle in panel C with sub-nanometer resolution and sub-picometer precision based on an exit wave power-cepstrum (EWPC) transform of scanning nanobeam electron diffraction acquired in 4D-STEM data sets. Subpanels a and b are the semimajor and semiminor axes of the strain ellipse construction. Panels A and B are reprinted with permission from ref 1081. Copyright 2013 The Authors, Springer Nature. Panels C−E are reprinted with permission from ref 1083. Copyright 2020 The Authors, Microscopy Society of America.

and diffraction, simultaneously.[1059,1068] In STXM, X-rays are focused by a zone plate to a spot (micron or tens of nanometers) on the sample, which is two-dimensionally raster-scanned in the focal plane. STXM with chemical compositional information is the X-ray analogue to STEM/EELS, but with less radiation damage, allowing *operando* techniques.[1069]

8.1.6. *Operando* Nanoscale X-ray Coherent Diffractive Imaging of Crystal Defects. X-ray beams at third- and fourth-generation synchrotron radiation sources display a high degree of transverse coherence, a useful property that enables imaging without lenses.[1070] X-ray Bragg coherent diffractive imaging (CDI) is a lensless X-ray imaging technique, in which a coherent X-ray beam illuminates a nanocrystal, and the resulting diffraction pattern of a Bragg peak is collected on an X-ray-sensitive area detector (Figure 78A). A 3D reciprocal space map of the Bragg peak is obtained by taking diffraction images while tilting the nanocrystal by a fraction of a degree around the Bragg peak.[1070] The dimensions of the crystal must be sufficiently smaller than the transverse coherence length of the beam so that scattering from all parts of the sample coherently contributes to the diffraction pattern, and the detector must be placed far enough from the sample to resolve the fringes around the Bragg peak.[1071] An iterative phase retrieval algorithm[1072] is used to transform the data into the 3D real-space displacement distribution along the direction of the scattering vector. In addition to the high coherence of the X-ray beam, the high brightness of undulator-based "third-generation" synchrotron sources allows for faster imaging, enabling *operando* studies of systems during evolution.

The benefit of using Bragg imaging is its ability to identify crystal defects,[1073,1074] which are expected to play a key role in catalytic reactions. Singer et al. used *operando* Bragg CDI to image dislocation nucleation in high-capacity lithium-rich layered oxide (LRLO) cathode nanoparticles during the lithium extraction process (charging) of a lithium-ion battery.[1073] Figure 78B shows the changes in displacement field (top) at different voltages vs Li^+ during charging in a planar cut of a single nanoparticle. The onset of dislocation nucleation in the bulk of the nanoparticle was identified at a voltage of 4.3 V vs Li^+ by singularities in the reconstructed displacement field. The ability to image dislocations and strain fields nondestructively under operating conditions offers a versatile alternative to traditional nanoscale characterization techniques such as transmission electron microscopy and enables further study of structure−property relations in novel materials for electrocatalysis in alkaline media.

In cases where the sample dimensions are unsuitable for Bragg CDI or where extended imaging is desirable, X-ray scanning probe techniques such as scanning nanodiffraction or Bragg ptychography may be considered. X-ray optics are used to focus the incoming X-ray beam, which is raster-scanned over an area of the sample.[1068] Typically, 2D diffraction images are recorded at each point in the 2D plane of the scan, creating a 4D X-ray data set, which is similar to the 4D-STEM discussed later in Figure 79. In nanodiffraction, the 4D data is analyzed directly in a way similar to dark-field imaging, and the heterogeneous strain distribution is measured.[1075] Similar to CDI, Bragg ptychography uses the coherence of the X-ray beam to resolve sample features smaller than the spot size, and knowledge of the probe from the 4D data set can be used to obtain amplitude and phase maps with an iterative phase retrieval algorithm.[1076] Hill et al. implemented a variation of this technique, which was named multiangle Bragg projection ptychography (maBPP), combined with coarser-scanning Bragg nanodiffraction to image a single $In_{0.86}Ga_{0.14}As$ nanowire across length scales from nanometers to microns.[1077] Figure 78C shows the 3D strain distribution imaged using Bragg ptychography on the $2\bar{1}10$ peak. The 2D cross-sections show the lattice displacement (Figure 78D) and strain distribution (Figure 78E) along the scattering vector. Thus far, *in situ* Bragg ptychography studies of electrocatalytic systems are not yet prevalent, but the capability of imaging local strain states will prove invaluable in future investigations.

https://doi.org/10.1021/acs.chemrev.1c00331
Chem. Rev. XXXX, XXX, XXX−XXX

8.2. Scanning/Transmission Electron Microscopy (S/TEM)

The aforementioned *operando* X-ray methods provide structural and spectroscopic information on large ensembles of bulk or nanoparticle electrocatalysts at a macroscopic level. Compared to high-energy X-rays that can penetrate electrocatalyst samples with μm-to-mm thickness, electron beams are most useful for analyzing samples thinner than 1 μm. When high-energy X-rays and electrons are employed, it is critical to minimize the beam damage in order to probe the dynamic structural/compositional changes without beam-induced artifacts. While X-rays interact more weakly with the catalyst materials, they interact more weakly for both useful imaging events and harmful damaging events. What matters for imaging is the ratio: X-rays produce a level of beam damage (inelastic scattering events) per useful elastic scattering event, which is one or two orders of magnitude higher than that for electrons across all wavelengths and energies.[1078] This becomes a pronounced challenge at high spatial resolution, where the imaging resolution is dose-limited by counting statistics. Therefore, X-rays and electrons can serve as complementary techniques to resolve the reaction dynamics of electrocatalysts across multiple length scales.

The development and application of aberration-corrected scanning/transmission electron microscopes (S/TEM), equipped with electron energy loss spectroscopy (EELS) and energy-dispersive X-ray spectroscopy (EDX), offer invaluable complementary insights for establishing structure/composition−reactivity/durability correlations of electrocatalysts at a microscopic level. STEM with EELS and EDX can provide sub-Ångström spatial resolution with a tremendous amount of morphological/compositional information and the electronic structure of electrocatalysts. STEM-based characterizations have emerged as an indispensable tool for advancing our understanding of fuel cell electrocatalysts and their dynamic evolution during electrochemical reactions at the nm and atomic scales. In this section, we will review STEM studies of nanoparticle electrocatalysts and emphasize the correlations between catalyst activity and microstructures.

While TEM has been instrumental in the development of solid-state electrocatalysts, conventional TEM operates under high vacuum conditions ($\sim 10^{-10}$ bar) and is incompatible to study materials in liquids and/or gases. Recent advances in TEM instrumentation and microchips, with thin, but robust, electron-transparent windows, have enabled *operando*/*in situ* electrochemical liquid-cell STEM (EC-STEM) with nm- and even atomic-scale spatial resolution in realistic electrolytes under operating conditions. Here, we will introduce the recent progress as well as challenges of *operando*/*in situ* STEM for directly visualizing (electro)chemical reactions at electrode/electrolyte interfaces. In addition, we will discuss the applications of cryogenic TEM (cryo-TEM) for the reliable characterization of beam-sensitive soft materials such as alkaline membranes and ionomers.

8.2.1. *Ex Situ* Atomic-Scale STEM Studies of Electrocatalysts. The use of S/TEM and EELS/EDX can provide valuable insights for these structural descriptors and advance our understanding of structure−activity relationships of a broad range of electrocatalysts and supports, as previous discussed in sections 3−5. For a comprehensive review on *ex situ* STEM studies of electrocatalysts, interested readers are referred to a recent review by the authors.[18] The high spatial resolution of STEM poses an intrinsic limitation on a robust statistical analysis of inhomogeneous nanoparticle electrocatalysts, making it challenging to perform a rigorous comparison of changes at the same location before and after electrochemical reactions. The application of identical location TEM (IL-TEM) enables the probing of the identical regions of electrocatalysts and provides a direct and unambiguous tracking of the sequential changes of NPs before, during, and after the tests.[1079,1080] As a class of important supplementary methods to understand electrocatalysts, IL-TEM techniques offer a promising bridge between conventional *ex situ* TEM and challenging *in situ* TEM experiments. Besides regular 2D STEM imaging, 3D STEM tomography, through acquiring a series of 2D images over a wide tilt range and post-reconstruction, enables the direct visualization of the 3D structure and accurate quantitative analysis of both active nanoparticles and porous carbon supports (Figure 29). Here, we will use the example of Pt−Co electrocatalysts for the ORR to highlight the unique capability of STEM imaging and EELS spectroscopy.

After over a decade of development, Pt−Co intermetallic nanoparticles have emerged as one of the most active and efficient ORR electrocatalysts in PEMFCs.[17,1081] Pt−Co, with different compositions and structures, are nowadays manufactured at scale for practical PEMFC engines in fuel cell electric vehicles (FCEVs). We have used high-angle annular dark-field (HAADF)-STEM to directly visualize the atomic structure of Pt_3Co ordered intermetallic NPs, and Figure 79A shows one Pt_3Co NP on the [001] zone axis.[1081] Since the intensity of an ADF STEM image scales with the atomic number ($I \propto Z^{1.7}$), heavier elements exhibit a brighter intensity than lighter elements, which provides an opportunity to directly distinguish/identify different elements in multimetallic alloys or oxides. In this case, Pt atomic columns, at the corners, appear much brighter than Co atomic columns at the centers, which is fully consistent with the simulated image contrast on the same zone axis (Figure 79A, inset). In comparison, conventional bright-field (BF) TEM or STEM imaging is based on the phase contrast of electrons and is more sensitive to light elements such as C and O, although the image contrast in BF mode is subjected to complications arising from sample thickness variations, tilting, and/or the level of defocusing. For the physical principles of S/TEM imaging and EELS, interested readers are referred to an earlier review.[1082] The periodic bright and dark contrast in the STEM image suggests an ordered Pt_3Co intermetallic, rather than disordered, alloy. The elemental compositions of Pt_3Co/C were investigated with STEM-EELS (Figure 79B). The EELS composite map shows a Pt_3Co core (yellow) surrounded by a 2−3 atomic-layer pure Pt shell, which is present in the as-synthesized NPs and is still well-preserved after 5000 potential cycles in acid. The Pt-rich shell can also be directly visualized in the atomic-scale STEM image as indicated by the yellow arrows in Figure 79A. The identified ordered intermetallic core, surrounded by a 2−3 atomic-layer-thick Pt-rich shell, suggests that the active Pt shell on the Pt_3Co core has a lattice contraction caused by the incorporation of smaller Co atoms into the Pt lattice. Such strain engineering is widely believed to weaken the oxygen binding energy of Pt to an optimal level, which may be responsible for the 2−3-fold increase in ORR activity, relative to random Pt_3Co alloys. At the same time, the ordered Pt_3Co intermetallic core provides a more stable structure, relative to the disordered Pt_3Co alloy, which leads to a significantly enhanced durability.

https://doi.org/10.1021/acs.chemrev.1c00331
Chem. Rev. XXXX, XXX, XXX−XXX

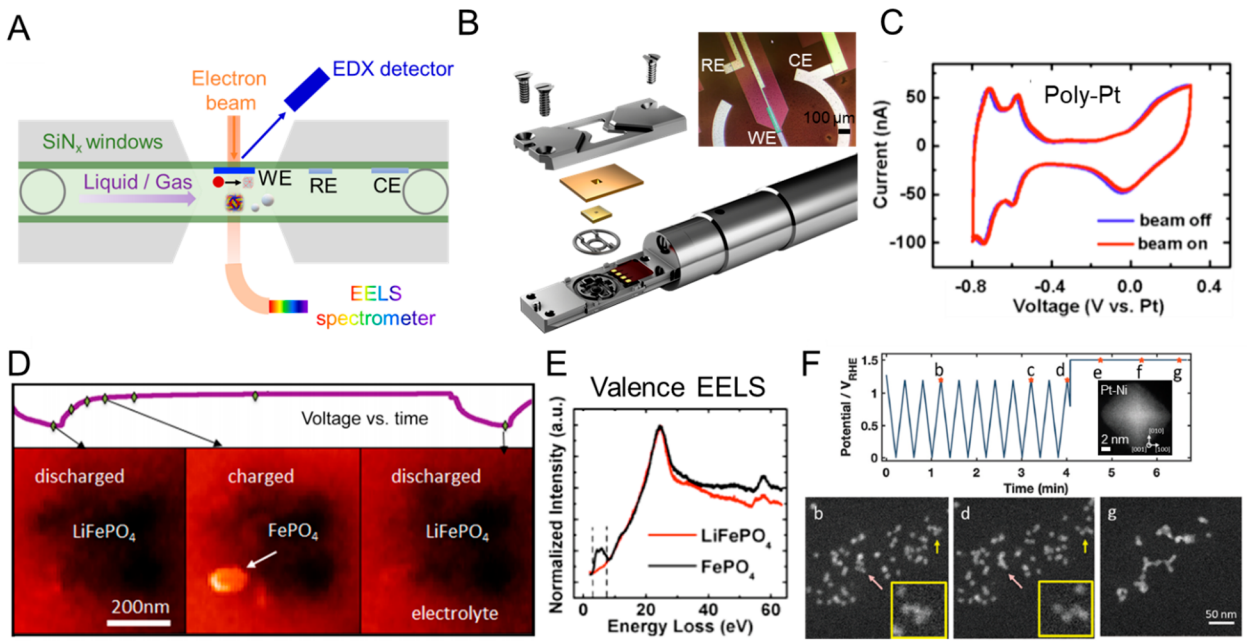

Figure 80. *In situ* electrochemical liquid-cell S/TEM studies. (A) Cross-sectional schematic of an *in situ* electrochemical TEM holder with SiN_x windows encapsulating a fluid layer. The working electrode (WE) is made of carbon while the reference and counter electrodes (RE, CE) are made of Pt. (B) Schematic of the layered structure of a Protochips Poseidon liquid-cell holder. Inset: optical image of the three-electrode microchip loaded with Pt/C nanoparticles. (C) CV profiles of polycrystalline Pt films in acidic media when the electron beam is on and off. (D) *In situ* discharging/charging processes of the $LiFePO_4$ cathode in 0.5 M Li_2SO_4 solution as shown in the 5 eV spectroscopic EF-TEM images. (E) Valence EELS of dry $LiFePO_4$ and the delithiated counterpart $FePO_4$, showing a distinct peak for $LiFePO_4$ but not for $FePO_4$. (F) *In situ* HAADF-STEM imaging of a Pt−Ni catalyst during electrochemical potential cycling between 0.0 and +1.2 V vs RHE for 20 cycles at 100 mV/s in 0.1 M $HClO_4$, followed by a step into high potential. Subpanels b−d correspond to the points in the upper panel. Insets in subpanels b−d show enlarged fractions of particles aligning on their facets. In panel B, the schematic (excluding the inset) is reprinted with permission. Copyright Protochips Inc. Panels C−E are reprinted with permission from ref 1094. Copyright 2014 The Authors, American Chemical Society. Panel F is reprinted with permission from ref 686. Copyright 2019 The Authors, Royal Society of Chemistry.

In an effort to directly visualize and reliably quantify the local strain of individual catalyst NPs, Padgett et al. developed an exit-wave power-cepstrum (EWPC) transform to analyze scanning nanobeam electron diffraction (NBED) based on 4D-STEM data sets acquired with a fast pixelated detector.[1083] Figure 79C exhibits a ∼5 nm Pt−Co NP after long-term durability tests in PEMFCs, which is oriented on the [110] zone axis. EELS composite maps of Pt vs Co exhibited a well-defined ∼1 nm thick Pt shell (red) surrounding a Pt−Co core (yellow) (Figure 79D). An EWPC transform of the NBED of this particle was visualized with the semimajor (a) and semiminor (b) axes of a strain ellipse, which approximately correspond to the radial and tangential strain of a nearly spherical core−shell geometry. The strain maps in Figure 79E clearly show a ∼5% radial expansion and ∼2% tangential compression of the Pt shell, providing clear evidence of a surface lattice contraction for the Pt_3Co@Pt core−shell structure. Moreover, the EWPC analysis can analyze randomly oriented NPs and is robust to sample mistilts commonly encountered in STEM imaging of nanoparticle electrocatalysts. We anticipate that strain mapping with the EWPC transform will be one practical way to analyze hundreds of heterogeneous catalyst NPs to build up reliable statistics.

Pt_3Co ordered intermetallic NPs are prepared through high-temperature thermal annealing of disordered Pt_3Co alloy NPs. To understand the order−disorder phase transition, we employed *in situ* synchrotron-based XRD to quantify the degree of ordering at various annealing conditions (annealing temperature, time, and cooling rate).[1084] Pt_3Co/C could achieve an optimal ∼30% of ordered intermetallic phase after annealing at 750 °C for 2 h in a forming gas environment. *In situ* heating STEM was further used to directly visualize the morphological changes and the formation of both fully and partially ordered NPs at the atomic scale. In general, a higher degree of ordering leads to more active and durable electrocatalysts. Annealed Pt_3Co/C with an optimal degree of ordering exhibited significantly enhanced durability (5% performance loss after 30 000 cycles), relative to disordered Pt_3Co alloy (14% loss) in practical MEA measurements.

In summary, it has been demonstrated that STEM can provide morphological, compositional, and structural information of nanoscale electrocatalysts at the atomic scale. *Ex situ* STEM provides a baseline understanding of catalyst NPs and necessary guidance for *operando*/*in situ* TEM to resolve complex electrochemical reaction dynamics.

8.2.2. *Operando*/*in Situ* Electrochemical Liquid-Cell STEM. Numerous renewable energy technologies involve electro(chemical) processes at solid/liquid interfaces, in general, and the electrode−electrolyte, in particular. Electrocatalytic reactions at solid/liquid interfaces are often accompanied by potential-dependent morphological, compositional, and structural changes of the catalysts during operation, which, in turn, play an important role in the electrocatalyst's activity, selectivity, and durability. With differential pumping apertures around the specimen area, gas pressures of a few mbar can be achieved using dedicated environmental TEMs.[1085−1087] Recent advances in TEM instrumentation and microchips, with thin, but robust, electron-transparent

https://doi.org/10.1021/acs.chemrev.1c00331
Chem. Rev. XXXX, XXX, XXX−XXX

windows, have enabled *in situ/operando* liquid/gas-phase S/TEM with nm- and even atomic-scale spatial resolution under realistic reaction conditions. *In situ* liquid-cell TEM (LC-TEM) can shed light on the fundamental understanding of electrocatalytic processes and catalyst degradation mechanisms under native environments without the need for drying samples. Given strong beam−sample interactions in liquids, it is necessary to minimize the beam effect on the (electro)chemical reactions, to optimize spatial and temporal resolution in liquid-cell TEM.[1088,1089]

The electrochemical liquid-cell TEM work was pioneered by Ross et al. who employed a homemade liquid cell with a two-electrode system to perform TEM studies of Cu electrodeposition.[1090] Recently, *in situ* liquid-cell S/TEM has been used to investigate the durability of nanoparticle fuel cell catalysts during potential cycles,[686,1091−1093] discharge/charge mechanisms of electrode materials in lithium-ion batteries,[1094−1098] and structural evolution of Cu-based catalysts during the electrochemical reduction of CO_2.[1099,1100] Liquid-cell TEM has been widely used to study beam-induced growth and corrosion of Pt-, Pd-, or Au-based NPs.[1101−1103] However, it should be noted that the electron beam has served as an active reactant to grow or corrode nanoparticles and has made the reaction mechanisms significantly different from regular (electro)chemical processes. Liquid-cell TEM has also been broadly applied to the observation of growth and movement of soft materials, such as polymers, MOFs, and proteins.[1104,1105] Biological samples and many energy materials, such as polymer membranes/ionomers in fuel cells and sulfur cathodes in Li−S batteries, among others, share similar beam-sensitive characteristics, especially when immersed in liquid electrolytes.[1078,1106,1107] Thus, the liquid-cell TEM studies of electrocatalysts can benefit tremendously from the extensive liquid-cell and cryogenic TEM studies of biological samples over the past several decades.[1078] For a comprehensive review of all of those active areas, interested readers are referred to other earlier reviews.[1108−1110] Although liquid-cell TEM has been extensively employed to study chemical phenomena, very few studies have demonstrated reliable electrochemical results in liquid-cell TEM, which can be faithfully compared to standard electrochemical measurements. Here, we place particular emphasis on *in situ* liquid-cell TEM studies to reliably quantify electrochemical processes and discuss the major challenges facing rigorous electrochemical measurements in liquid-cell TEM.

Figure 80A illustrates a typical *in situ* electrochemical liquid-cell STEM (EC-STEM) with a three-electrode microchip, an EELS spectrometer, and an EDX detector for chemical analysis. The electrochemical chip is composed of two electron-transparent SiN_x windows, each with a thickness of ∼50 nm, which are able to seal a sub-μm liquid pocket, withstand the UHV environment inside the TEM chamber, and enable a microfluidic flow to constantly supply fresh electrolyte. Figure 80B shows the layered structure of a liquid-cell TEM holder (Protochips Inc.), and the inset shows an optical image of the electrochemical chip. The three-electrode configuration follows the design rules of working, reference, and counter electrodes (WE, RE, and CE) in a standard electrochemical measurement. The CE has a large surface area, relative to the WE, to enable a rapid polarization while the RE serves as a stable reference point for measuring and controlling the potential of the WE. The distance between the RE and WE is adjusted in order to minimize the IR drop in a thin electrolyte layer. In most studies, both the RE and CE are made of Pt for its chemical stability while the WE is made of carbon to enable the electron beam to image interesting metal or metal oxide particles with minimal background scattering. In order to show that the customized microchip is capable of yielding well-established electrochemical results, Holtz performed CVs of a Pt film in acidic electrolyte (∼500 nm thick).[1094] Figure 80C exhibits the characteristic behavior of poly-Pt with hydrogen adsorption/desorption peaks and the broad Pt oxidation/reduction peaks. Negligible changes in CV profiles were detected when the electron beam was turned on, indicating minimal beam-induced damage on the electrochemical measurement, since the CV measurement is extremely sensitive to trace levels of contaminants or changes on the surface or in solution at the submonolayer level. Further thinning the electrolyte to ∼150 nm caused significant ohmic drops in the CV measurements,[1094] indicating an inherent compromise between the optimal spatial resolution and the quantitative electrochemistry. This compromise in spatial resolution presents a great challenge for EELS or EDX analysis, which demands thin liquids to minimize background signals. Therefore, it is highly recommended to obtain the well-established CV profiles of Pt before exploring unknown electrochemical reactions in liquid-cell TEM. Recently, Mayrhofer et al. reported that the CV of Pt could be severely interrupted by electrolyte decomposition and Pt redeposition at large beam doses.[1110] Unocic et al. showed that it is important to have a well-defined electrode geometry and microfluidic conditions and to ensure that the WE is thin (<50 nm) and highly conductive to enable a uniform current density distribution for quantitative electrochemical measurements.[1111−1113] The potentials in Figure 80C are presented against a Pt pseudo-RE, which relies on the metastable redox couple of PtO_x/Pt. Given that the position of the characteristic Pt{110} is often located at ∼0.1 V vs RHE in 0.1 M $HClO_4$, it was estimated that the potential difference between the Pt pseudo-RE and SHE is ∼0.8 V so that researchers in the electrochemistry community can be easily "calibrated" to the commonly used RHE scale. In practice, we notice a potential drift of ∼50 mV during extended CV potential cycles, which comes from an intrinsic limitation of the chip design in which all three electrodes are immersed in the same electrolyte. The potential of a Pt RE can drift when the CV measurements change the electrolyte composition, and the current at the CE produces trace amounts of soluble hydrogen or oxygen gas, which can diffuse to the RE and alter the nature of the Pt RE to, for instance, Pt−H/Pt (i.e., forming a Pt RHE). Thus, the lower/upper limits of the CV should be constantly monitored and carefully adjusted, to avoid undesirable hydrogen or oxygen evolution reactions. An active area under investigation is the search for more stable REs to replace the Pt pseudo-RE.

With a rigorous electrochemical analysis established, Holtz et al. then introduced a liquid-cell TEM study tracking the delithiation/lithiation dynamics of $LiFePO_4$, an important cathode material in Li-ion batteries (Figure 80D).[1094] In addition to the morphological information provided by S/TEM imaging in liquids, EELS was employed in this study since EDX is not suitable for light elements like lithium. Core-loss EELS is widely employed to provide a chemical analysis in which the electron beam excites a core electron to unoccupied orbitals above the Fermi level. In comparison, valence EELS (below 50 eV) is suited to provide electronic structure information by studying the electron interacting with outer-

https://doi.org/10.1021/acs.chemrev.1c00331
Chem. Rev. XXXX, XXX, XXX−XXX

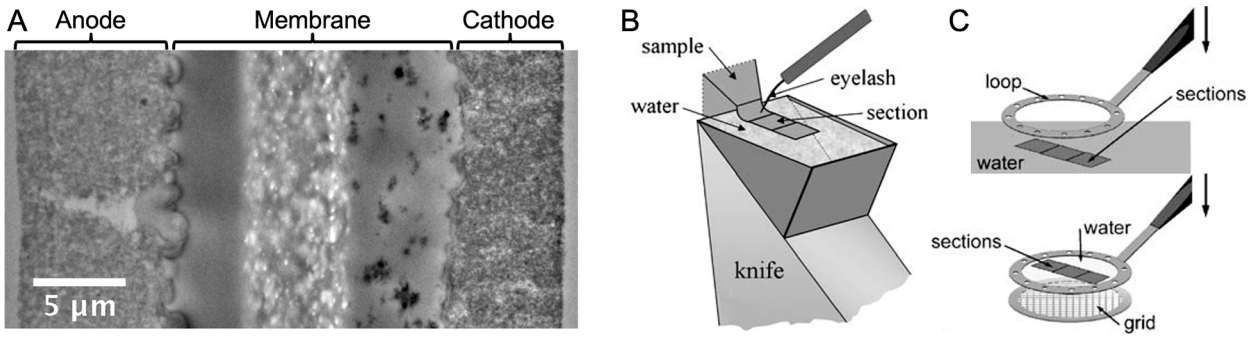

Figure 81. Ultramicrotomy of MEA cross-sections for TEM imaging. (A) Cross-section of an MEA prepared by ultramicrotomy and imaged in TEM. (B) Schematic of the ultramicrotomy sectioning process. The specimen is sliced by the diamond knife edge, and the slices are collected in water. When sectioning is performed at cryogenic temperatures, a mixture of dimethyl sulfoxide (DMSO) and water can be used to prevent the water from freezing. (C) The thin sections are collected from the water or DMSO/water mixture and placed on a TEM grid for subsequent imaging. Panel A is reprinted with permission from ref 1119. Copyright by The Authors. Panels B and C are reprinted with permission from ref 1118. Copyright 2008 Springer.

shell valence electrons, which surveys the same electronic levels as ultraviolet−visible (UV−vis) spectroscopy. Core-loss EELS suffers from multiple scattering and can be overwhelmed by the plasma peak of the liquid when the liquid thickness is more than 2−3 mean free paths (200−300 nm), making it practically inaccessible in electrochemical liquid-cell TEM with a ∼500 nm thick liquid layer. In contrast, the valence EELS can tolerate liquids up to 6−7 mean free paths (600−700 nm) given its large scattering cross-sections and low background from the liquid plasmon peak. For an in-depth discussion of EELS in liquids, interested readers are referred to the report by Holtz et al.[1092] The valence EELS of delithiated $FePO_4$ in Figure 80E shows a sharp feature at ∼5 eV, which is not present in the lithiated $LiFePO_4$. This peak enables a quick spectroscopic mapping of the depth of lithiation with energy-filtered TEM (EF-TEM) imaging. UV−vis, together with DFT calculations, assigned a unique feature at ∼6 eV to $LiSO_4^-$, which can be used to track the dynamic concentration gradient of the Li_2SO_4 electrolyte upon discharge/charge processes. EF-TEM images with a window of 2.5−7.5 eV can monitor the dynamic lithium distribution in both the electrode and electrolyte. As shown in Figure 80D (lower middle), during the charging process, a bright NP was detected in the 5 eV EF-TEM image at a safe dose rate of ∼500 e/(nm^2 s), corresponding to a delithiated $FePO_4$ NP. The 5 eV EF-TEM image in the solution region also showed brighter intensity after the charging process, corresponding to the formation $LiSO_4^-$. During the discharging process (Figure 80D, lower right), the bright particles disappeared, indicating the formation of $LiFePO_4$, and the surrounding solution also showed lower intensity due to the depletion of $LiSO_4^-$. $LiFePO_4$ NPs exhibited great structural inhomogeneity, and two competing lithiation mechanisms, core−shell and anisotropic growth, could occur in parallel. This study represents a general approach to employ *in situ* electrochemical liquid-cell S/TEM and EELS to perform rigorous electrochemical measurements and track dynamics of charge/ion transfer kinetics at electrode/electrolyte interfaces.

In situ electrochemical liquid-cell TEM has provided important guidance for how to improve the stability of fuel cell electrocatalysts under electrochemical conditions. Figure 80F shows an *in situ* liquid-cell TEM study of the activation and degradation processes of octahedrally shaped Pt−Ni alloys, a family of highly active ORR electrocatalysts in acidic media.[686] The structural stability of both the catalysts and carbon supports can face significant challenges at high oxidizing potentials, which can occur in the startup/shutdown conditions in MEAs, reaching potentials as high as ∼1.6 V vs RHE due to the existence of a H_2/air interface at the anode side. Figure 80F shows the time-resolved morphological changes of the octahedral Pt−Ni NPs (∼8 nm) as a function of potential cycles. Only mild particle coalescence and aggregation were observed (panels b and d) during potential cycles between 0.05 and 1.2 V vs RHE. An aggressive potential hold at 1.4 V for several minutes caused severe particle motion and aggregation (panel g), which is likely due to the oxidation and corrosion of carbon, inducing the detachment of particles from the weakly bound carbon supports. The shape-controlled NPs, including those in the present study, have weak catalyst−support interactions, when compared to the strong catalyst−support interactions arising from widely used impregnation methods, since those NPs are often loaded on carbon supports after their synthesis, rather than being directly grown onto supports. In our previous *in situ* liquid-cell STEM study of Pt−Co NPs on carbon supports synthesized by impregnation methods, only mild particle coalescence was observed, despite significant carbon corrosion at high oxidizing potentials.[1093] Similarly, mild catalyst coalescence and carbon corrosion were reported in Pt−Fe alloys prepared by impregnation methods.[1114] Those *in situ* liquid-cell TEM studies offer an important lesson about reducing the surface mobility of catalyst nanoparticles by enhancing particle−support interactions. Inspired by those *in situ* liquid-cell TEM studies, several strategies have been proposed to mitigate these issues, such as enhancing the chemical interactions by doping carbon with foreign elements (e.g., N)[659] and designing porous carbon structures for confining particle motion and increasing the contact area for nanoparticles. Designing corrosion-resistant support materials to replace carbon and oxidation-resistant catalysts, as discussed in section 5, will be critical to developing electrocatalysts for long-term fuel cell operation.

In summary, *in situ* electrochemical liquid-cell TEM is a fasting-growing technique that is providing unprecedented time-resolved information on dynamic changes in morphology, structure, and composition of electrocatalysts under reaction conditions. STEM, equipped with a large-solid-angle EDX detector, enables nm-scale elemental mapping in 100−500 nm thick electrolytes due to the high penetration depth of X-

https://doi.org/10.1021/acs.chemrev.1c00331
Chem. Rev. XXXX, XXX, XXX−XXX

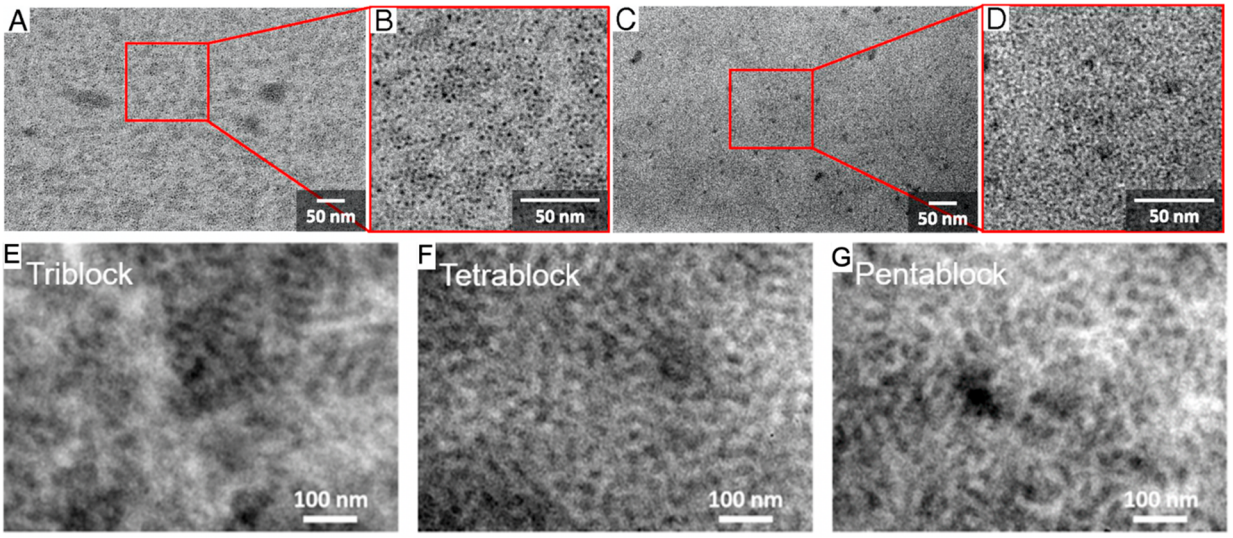

Figure 82. Top: TEM images of a diblock copolymer membrane (A, B) and a random copolymer membrane (C, D). The TEM images reveal microphase separation in the less conductive block copolymer and an amorphous organization in the random copolymer. Contrast between hydrophobic and hydrophilic domains is achieved by exchanging the membrane counteranions with iodide ions. Bottom: Cryo-TEM images of a series of polynorbornene block copolymer membranes ranging from triblock to pentablock display clear contrast variations due to microphase separation. The use of bromide as the counteranion in the membrane synthesis allows for imaging without the risk of artifacts caused by staining. Panels A−D are reprinted with permission from ref 744. Copyright 2019 The Authors, National Academy of Sciences. Panels E−G are reprinted with permission from ref 1121. Copyright 2021 The Authors, American Chemical Society.

rays.[1115] It can be particularly powerful for resolving the structural evolution of multimetallic heterogeneous electrocatalysts during (electro)chemical processes. Liquid-cell TEM will continue to enable us to advance new frontiers in electrochemistry, such as reaction kinetics at elevated temperatures.[1116] Further developments on liquid-cell TEM will continue to improve the spatiotemporal resolution for tracking fast reaction kinetics using newly developed electron detectors with fast readout and enhanced electron sensitivity for low-dose STEM.[1117]

8.2.3. Cryogenic TEM (Cryo-TEM). Cryo-TEM has played a major role in the characterization of the nanoscale morphology of AEMs as well as of the membrane−-catalyst interface. The use of cryogenic temperatures in the imaging of soft specimens is advantageous as it allows for preservation of their internal structure. The analysis of AEMs and MEAs requires a view of cross-sections of these bulk materials. Such cross-sections can be prepared for TEM imaging with the use of cryo-ultramicrotomy. Ultramicrotomy involves the slicing of samples using a diamond knife and results in thin cross-sections of the bulk material (Figure 81).[1118,1119] Combining ultramicrotomy with cryogenic temperatures allows an application of this type of sectioning to soft materials while preserving their internal organization.

Compared to the electrocatalysts discussed in section 8.2, soft materials, including polymer membranes and ionomers, pose additional challenges for high-resolution characterization by TEM or STEM. These materials are highly radiation-sensitive, and imaging contrast is low. Contrast enhancement for TEM studies of membranes is often achieved via heavy-element stains or ion exchange. Although these methods have allowed characterization of ionic domains in membranes, it is important to note that the use of such methods also leaves room for artifacts caused by incomplete or nonspecific staining or swelling behavior resulting from ion exchange.[1120] Nevertheless, identification of the hydrophobic and hydrophilic domains in membranes by TEM has highlighted the role of microphase separation in conductivity in both PEMs and AEMs.[744,1120] In the AEM study, Coates, Muller, and coworkers achieved sufficient TEM contrast to image microphase separation by exchanging the membrane's counteranions with heavier iodide ions.[744] The results displayed in the top panel in Figure 82 include TEM images revealing the nanoscale morphology of block copolymer AEMs. Figure 82A,B demonstrates the internal structure of a diblock copolymer membrane in comparison to a random copolymer membrane shown in Figure 82C,D. Both membranes were synthesized via the ring-opening metathesis polymerization (ROMP) method and comprise polyethylene backbones with alkaline-stable imidazolium cations. TEM images show distinct domain ordering, suggesting that a homogeneous microstructure allows for more continuous hydroxide transport and increased membrane conductivity. For membranes that contain heavier counterions, the inherent contrast may be sufficient to directly image their organization without the use of stains or ion exchange. Figure 82E−G shows cryo-TEM images of a series of polynorbornene multiblock copolymers with a bromide counteranion.[1121]

Radiation damage of soft materials is a major hurdle for high-resolution characterization by TEM. Cryogenic cooling of the sample inside the microscope reduces ionization damage and enables the use of additional techniques for probing the internal organization of AEMs. For example, methods such as cryoelectron tomography (CET) have given insight into the 3D structure of the hydrophilic−hydrophobic microphase separation. Allen et al. used CET to image the 3D structure of microphase domains in hydrated Nafion, revealing an interconnected channel-type network and domain spacings on the order of 5 nm.[1120] Combining cryogenic temperatures with methods such as electron spectroscopy and 4D-STEM also presents new opportunities in the characterization of AEMFC materials. EELS, in conjunction with cryo-STEM

https://doi.org/10.1021/acs.chemrev.1c00331
Chem. Rev. XXXX, XXX, XXX−XXX

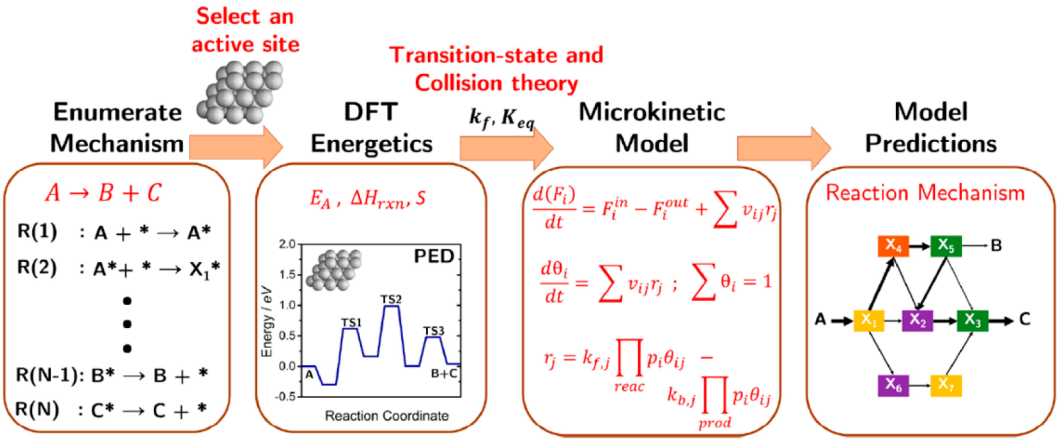

Figure 83. Schematic of a procedure to construct a DFT-based mean-field microkinetic model. Reprinted with permission from ref 55. Copyright 2020 The Authors, American Chemical Society.

imaging, may be used to study the elemental distribution of ionomers in the catalyst layer of the MEAs. Mapping the ionomer at micron length scales has been achieved using EDX at room temperature.[1122,1123] In order to achieve nm-scale mapping of the radiation-sensitive ionomer, however, cryogenic cooling may be necessary. 4D-STEM, previously used to study crystalline materials,[1083,1124,1125] can provide insight into the organization of crystalline domains within polymer membranes and their effects on the membrane's mechanical properties, conductivity, and durability. Cryo-TEM methods have led to significant advances in understanding the internal morphology of fuel cell materials, and we expect advances in imaging methods to further develop this understanding.

8.3. Summary

In this section, we reviewed the structural characterization techniques using X-rays and electrons as probes, which are suitable for mechanistic studies of alkaline fuel cells. We illustrated how catalytic studies have benefited from a wide variety of *operando*/*in situ* X-ray techniques: X-ray spectroscopy (XAS and HERFD-XAS), X-ray diffraction (CTR measurement and resonant surface scattering), and X-ray imaging (TXM, CT, and coherent imaging techniques). XAS has been used extensively to study the reaction mechanisms in electrocatalysis, providing information on the oxidation state, electronic structure, and coordination environment of metal centers of catalysts during catalytic reactions. We have also provided guidelines for designing electrochemical cells for *operando* XAS experiments and reviewed recent progresses achieved using *operando* XAS for understanding catalytic mechanisms of binary and ternary catalysts. To achieve a finer energy resolution in XAS, the HERFD-XAS technique was developed, making it possible to calculate the detailed electronic and geometric structures around the metal centers of catalysts from the XANES region. For X-ray diffraction, we focused on the CTR measurements, which are used to precisely determine the structure of the surface/interface of single crystals. This technique is frequently applied in mechanistic studies of single-crystal electrodes, revealing their surface reconstructions and surface adsorption under catalytic conditions. CTR measurements can be combined with resonant scattering to produce element-sensitive measurements at the surface of the catalyst. Thirdly, we discussed the application of X-ray imaging techniques in catalyst studies. With full-field TXM, it is straightforward to visualize the morphological evolution of catalysts, and it can be used to reconstruct the three-dimensional morphology in CT. By combining imaging techniques with X-ray spectroscopy (X-ray absorption or fluorescence), one can capture the evolution in both morphology and chemical composition during the catalytic reaction. With highly coherent X-ray beams available in 3rd and 4th generation synchrotrons, coherent imaging techniques, such as CDI and ptychography, have been developed, which are extremely useful in revealing more detailed structural information, such as crystal defects and heterogeneous strain distribution.

We then reviewed recent progress on *ex situ* atomic-scale STEM, *operando*/*in situ* electrochemical liquid-cell STEM (EC-STEM), and cryo-TEM. STEM can provide morphological, compositional, and structural information of nanoscale electrocatalysts at the atomic scale. *Ex situ* STEM provides a baseline understanding of catalyst nanoparticles and valuable guidance for *operando*/*in situ* EC-STEM to resolve complex electrochemical reaction dynamics. *Operando*/*in situ* electrochemical liquid-cell TEM reveals unprecedented information about dynamic structural evolution of electrocatalysts under electrochemical conditions. Insights gained from EC-STEM can advance the design of electrocatalysts with tunable activity, selectivity, and durability. Cryo-TEM is well-positioned to enable the study of beam-sensitive materials, such as alkaline membranes and ionomers, and can often benefit from liquid-cell TEM studies which have a similar requirement to minimize beam-induced effects/damage on samples in liquid.

In summary, high-energy X-rays can penetrate electrocatalyst samples with μm-to-mm thickness while electron beams are most useful for analyzing samples thinner than 1 μm. X-rays and electrons can serve as complementary techniques to resolve the reaction dynamics of electrocatalysts across multiple length scales.

9. THEORY

First-principles, *ab initio* theory provides much needed information for understanding and, ultimately, optimizing the key microscopic processes which underlie the operations of alkaline-based energy systems. In addition to insights regarding electron charge-transfer processes (section 2.1) and such processes when coupled to proton transfer (section 2.2), *ab initio* theory is a powerful tool providing insight into the theory of surface catalysis generally (section 9.1). Additionally, *ab*

https://doi.org/10.1021/acs.chemrev.1c00331
Chem. Rev. XXXX, XXX, XXX−XXX

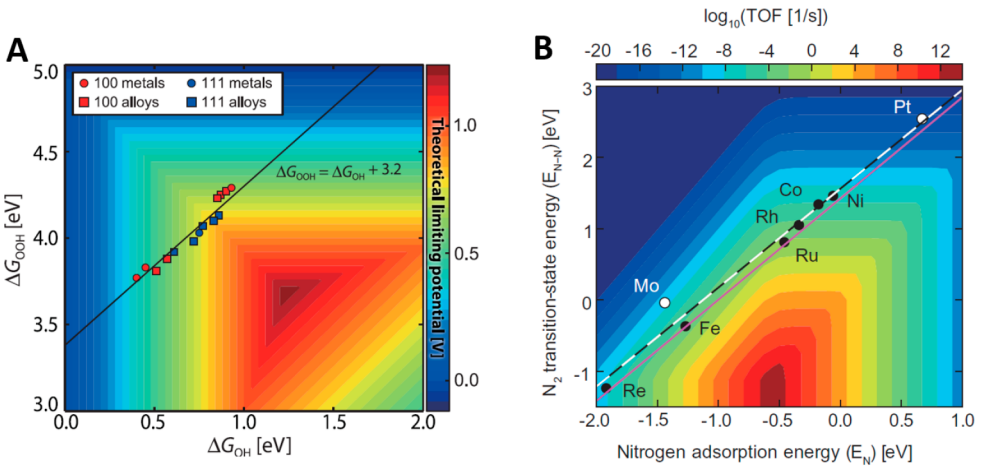

Figure 84. (A) Theoretical limiting potential for the oxygen reduction reaction (ORR) in an acidic environment as a function of two key reactivity descriptors: the Gibbs free energy of adsorption for OH and OOH. The black line indicates the scaling relation correlating the two reactivity descriptors. (B) Volcano plot for vapor-phase ammonia synthesis (TOF stands for turnover frequency) on stepped transition metal surfaces as a function of nitrogen adsorption energy (E_N) and transition state energy for N_2. The dashed black−white line indicates the scaling relation correlating the two quantities. Panel A is reprinted with permission from ref 52. Copyright 2017 American Association for the Advancement of Science. Panel B is reprinted with permission from ref 53. Copyright 2015 Oxford University Press.

initio theory can be used to understand the transport of hydroxide in liquid water (section 9.2) and the impact of electrochemical environments including the roles of the electrode potential, the formation of the electrochemical double layer, and the formation and structure of solid−liquid interfaces (section 9.3), as well as the stability of membrane polymers in alkaline environments (section 9.4).

9.1. *Ab Initio* Theory of Surface Catalysis

Electronic-structure methods are powerful tools for elucidating reaction mechanisms, activity, and selectivity trends among electrocatalysts and ultimately for unravelling the nature of the catalytic active site under realistic electrochemical conditions. In this section, we will review some of the fundamental principles governing surface catalysis, by showing how first-principles-derived quantities can be used to comprehend complex phenomena occurring at electrocatalytic interfaces and to guide the synthesis of improved electrocatalysts.

The importance of micro-kinetic models (MKMs) in the context of electrochemical processes has been discussed in section 2.1. A general stepwise procedure to build coverage-cognizant MKMs has been recently described by Bhandari et al.[55,1126] Briefly, the procedure schematically illustrated in Figure 83 always starts by enumerating the hypothesized elementary steps in the reaction mechanism. By performing density-functional theory (DFT) calculations or by using other electronic-structure methods, the binding energies of reaction intermediates and transition-state energies of elementary steps are calculated on a hypothesized model structure of the active site. Then, a system of differential-algebraic equations is built within the mean-field approximation, using DFT-derived parameters for kinetics (activation energies and pre-exponential factors) and thermochemistry. By solving this model, it is possible to obtain reaction rates (or current densities), selectivity, apparent activation energy barriers, reaction orders, and rate-/selectivity-determining steps. The first step of the procedure is the most computationally expensive. An accurate estimate of the computational time required for state-of-the-art energy minimization and geometry optimization of surface reaction intermediates should take into account many factors, as it depends on the method employed to solve the electronic-structure problem. Roughly, DFT methods scale as $O(n^3)$, where n is the number of electrons treated explicitly. Generally, even a simple electrocatalytic reaction mechanism, such as the ORR, presents at least four surface reaction intermediates, and under realistic reaction conditions, the surface is partially covered by several reaction species. Therefore, performing detailed DFT calculations for all intermediates and elementary steps in order to construct MKMs, able to rationalize trends among different electrocatalysts and active site models, becomes a computationally prohibitive task. For this reason, descriptor-based approaches, based on the use of easily computable quantities that are able to describe reactivity, have seen increased utilization over the past 15 years. The binding energy of key surface reaction intermediates is typically used as a reactivity descriptor.

The work of Abild-Pedersen et al.[1127] was the first to define a "linear-scaling relationship" between the binding energy of a hydrogen-containing intermediate, adsorbed on close-packed and stepped transition metal surfaces, and the binding energy of the atom through which the intermediate binds to the surface. For example, the binding energy of CH_x (with x = 0, 1, 2, 3) on different transition metal surfaces, with the same geometry, scales linearly with the binding energy of C on the same surfaces, with the scaling constant depending on the value of x. Therefore, leveraging linear-scaling relationships, it is possible to efficiently estimate the binding energy of reaction intermediates by calculating the binding energy of much simpler and less computationally expensive adsorbed species. Similar to these linear-scaling relationships, Brønsted−Evans−Polanyi (BEP)[1128,1129] correlations connect energies of minima in an elementary reaction step with energies of maxima (i.e., transition states) in the same step. One such BEP correlation suggests that the transition state energy for O_2 dissociation on close-packed transition metal surfaces traces the final state energy of the dissociation event (atomic O).[1130] In other words, the more exothermic a reaction step is, the lower its transition state energy. Naturally, the combined use of scaling and BEP correlations substantially decreases the computational cost required for rationalizing trends in (electro)catalyst

https://doi.org/10.1021/acs.chemrev.1c00331
Chem. Rev. XXXX, XXX, XXX−XXX

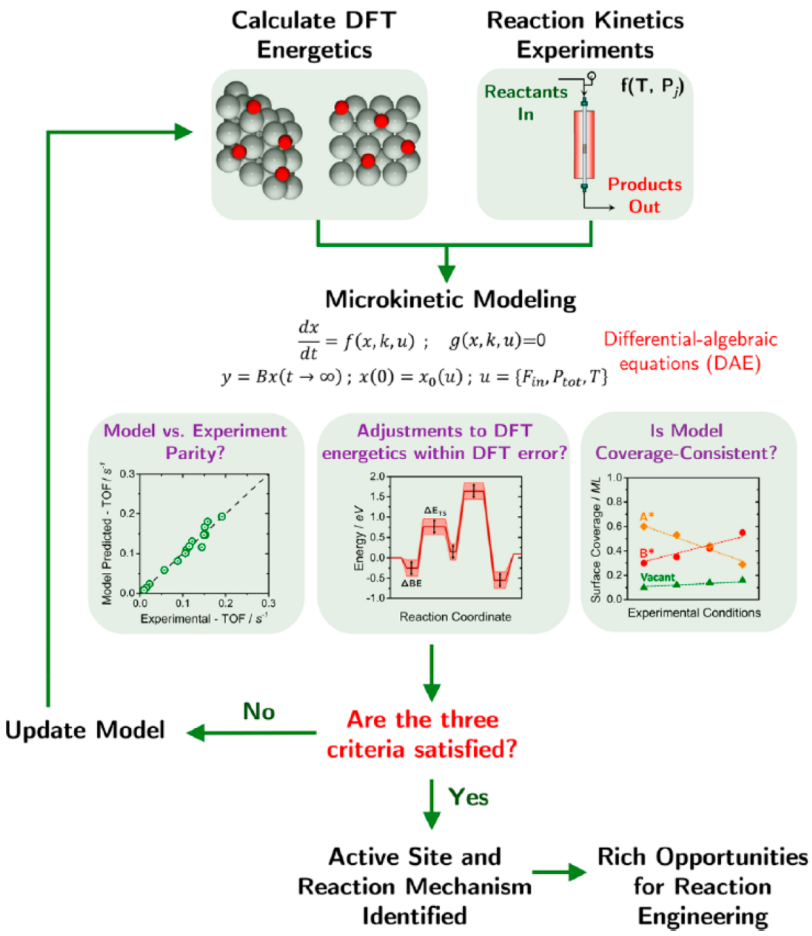

Figure 85. Algorithmic scheme for elucidating the nature and decoration of the catalytic active site and the reaction mechanism through the formulation of mean-field MKMs, and by using DFT-derived energetics. Reprinted with permission from ref 55. Copyright 2020 The Authors, American Chemical Society.

activity and selectivity. As a result, numerous examples of applying this methodology to vapor-phase heterogeneous catalysis,[1131−1136] electrocatalysis,[52,72,1137−1141] and more recently molecular catalysis,[1142−1144] have been reported in the literature.

While linear-scaling and BEP correlations provide the foundations for modern computational (electro)catalyst discovery, the existence of these correlations limits the degrees of freedom for designing catalytically active sites with improved performance. For example, Figure 84A presents a DFT-derived theoretical limiting potential plot for the ORR, i.e., the maximum potential at which all of the reaction steps are energetically downhill, while Figure 84B shows an activity plot for the nitrogen reduction reaction (NRR). Because of the linear scaling relations existing between reaction intermediate binding energies (OH*, O*, and OOH*) or between binding energies and transition state energies for the NRR, the data points corresponding to a specific class of catalytic active site models all lie on a scaling relation line. Therefore, scaling relations restrict the area that it is possible to span on volcano activity plots, oftentimes making it impossible to come up with materials that are much closer to the volcano's peak for activity or selectivity. For this reason, several strategies have been proposed to "break" scaling relations, such as the use of atomically dispersed materials,[1145−1147] near surface alloys,[1148−1150] and bifunctional catalysts.[1151−1156] We direct the reader to other studies for further details on strategies to escape linear-scaling relationships.[28,53,1157,1158]

Among the fundamental handles used to design improved electrocatalytic active sites, here, we single out strain and ligand effects. Surface compressive or tensile strain can be applied by interfacing materials with different lattice constants, as is the case encountered in core−shell nanoparticles.[1159−1161] Mavrikakis et al. were the first to rationalize the effect of strain on the reactivity of surfaces.[1162] Usually, the binding energy of surface intermediates becomes more negative (stronger binding) with the application of tensile strain on surfaces, whereas compressive strain tends to destabilize surface species. While this property helps in the design of improved (electro)catalysts,[568] often times it is not possible to escape scaling relations by simply modifying strain: unless the catalytically active site is modified (e.g., through reconstructions), it is not possible to (de)stabilize only one surface reaction intermediate without (de)stabilizing all of the others in a proportional way. However, recent studies have demonstrated that, under particular applied strain conditions, it is possible to independently change the binding energy of surface intermediates adsorbed on different surface sites, hence breaking scaling relationships.[1163,1164] For example, Khorshidi et al.[1163] employed a mechanics-based eigenstress model to rationalize how single adsorbates, adsorbed on different sites of a given surface, can exhibit directionally opposite responses to biaxial strain. Taking the example of CH_2 adsorbed on bridge

https://doi.org/10.1021/acs.chemrev.1c00331
Chem. Rev. XXXX, XXX, XXX−XXX

and 4-fold hollow sites of Cu(110), the authors demonstrated the opposite dependence of the CH_2 binding energy on strain for these two sites. Therefore, it could be possible to reverse the order of stability of a given adsorbate on these two surface adsorption sites through strain-engineering. Similarly, recent theories suggest that, by oscillating the binding energy of surface reaction intermediates, for example, by using piezoelectric materials continuously changing the applied strain on the surface, it is possible to considerably enhance catalytic performance.[1165] The "ligand effect" in bimetallic catalysis[1166,1167] reflects the strength of the interaction between the top metal layer in the catalyst and the metal layer right below. Depending on the identity of the two metals, the bond strength between them and the associated electronic interactions can vary dramatically, thereby leading to a concomitant change in surface binding properties. The presence of the ligand effect oftentimes gives rise to unexpected catalytic properties, even exceeding the limit of scaling relations. Near-surface alloys (NSAs) are a typical example of that. Indeed, Greeley and Mavrikakis demonstrated that, similarly to Au and Cu, specific NSAs bind atomic hydrogen weakly and yet dissociate H_2 much easier than noble metals. This property offers clear advantages for improved anode catalysts for application in low-temperature fuel cells.[1148,1168]

9.1.1. Combined Theory and Experiments for Elucidating the Nature of the Active Site: MKMs. A collection of important studies reporting DFT-derived MKMs in the context of electrochemical processes in alkaline and acidic environments are provided in section 2.1. Although providing useful qualitative trends, MKMs constructed from DFT-derived quantities without proper calibration against experimental measurements cannot be used to obtain quantitative information on reaction rates, apparent activation energies, and reaction orders. The lack of quantitative agreement with experiments can originate from multiple sources, including an incorrect description of the active site and the intrinsic errors associated with DFT-derived energetics. For example, for room-temperature processes, a difference of 0.06 eV in calculated energies translates to an order of magnitude difference in rate constants. Therefore, it is necessary to apply a systematic and consistent procedure in order to derive meaningful information from MKMs. An iterative procedure used to construct MKMs yielding quantitative agreement with reaction kinetics experiments after a proper parameter adjustment is described in Figure 85. Simultaneously, this procedure yields improved information pertaining to the nature and decoration of the active site by key reactive intermediates.

Three main criteria are evaluated to assess the quality of the MKM predictions: (i) accuracy of the model in the reproduction of experimental data; (ii) magnitude of parameter adjustments required to achieve quantitative agreement with reaction kinetics experiments; and (iii) coverage self-consistency. Briefly, in order to satisfy the first condition, the MKM should be able to predict, with quantitative accuracy, reaction orders, rates, and apparent activation energies obtained from experiments under various conditions and in the presence of various amounts of cofed species. Importantly, the quantitative prediction of experimental quantities alone is not enough to assess the predictive power of the MKMs. Indeed, finding the solutions to the system of differential equations is a stiff nonlinear optimization problem that could lead to different equally correct quantitative solutions. It is therefore necessary to evaluate, among the possible solutions, the one that is obtained with minimal parameter adjustments. The process of determining the magnitude of these parameter adjustments and which of the DFT-derived quantities contribute the most to the discrepancy between simulated and experimental results is known as *parameter estimation*.[1169] Acceptable parameter adjustments are in the range 0.1−0.2 eV. Usually, adjustments larger than 0.2 eV are indicative of an incorrect description of the model used for the catalytically active site, or an inaccuracy in the choice of the exchange-correlation functional employed for DFT calculations. Finally, coverage self-consistency is essential: the surface coverage of key reactive intermediates predicted by the MKMs should be in agreement with the respective coverage employed in the DFT models used to derive the energetics implemented in the MKMs. Coverage-cognizant MKMs were recently demonstrated to be necessary to achieve quantitative agreement with experimental vapor-phase reaction kinetics and electrocatalytic measurements.[1126,1141] If one or more of criteria i−iii are not satisfied, the MKM is revised by changing either the catalyst model [e.g., by considering the (100) facet instead of the (111) facet] or the coverage of spectator species. More technical details on the development and utilization of MKMs can be found in more specialized reviews.[28,55,56]

9.2. *Ab Initio* Theory of Aqueous Hydroxide

In this section, we provide a brief review of the *ab initio* theory of the aqueous hydroxide ion. We begin with *ab initio* studies of bulk liquid water under ambient conditions (section 9.2.1) and a description of the typical methodologies used for simulating proton-transfer processes in aqueous H_3O^+/OH^- solutions (section 9.2.2). This is followed by a more detailed discussion of the proton-transfer mechanisms in aqueous H_3O^+ and OH^- solutions, including the presolvation concept (section 9.2.3), concerted proton transfer promoted by water wire compression (section 9.2.4), and the more recent discovery regarding the differential distribution of concerted proton-transfer processes between aqueous H_3O^+ and OH^- (section 9.2.5). This section concludes with a discussion of recent *ab initio* studies of aqueous OH^- diffusion through AEMs as well as a brief summary and future outlook (section 9.2.6).

9.2.1. *Ab Initio* Studies of Liquid Water. Water, in its liquid form, is arguably the most important molecule for human civilization. Theoretical modeling of liquid water is an extensive field that goes far beyond *ab initio* simulations, and a proper coverage of *ab initio* simulations of liquid water alone could easily fill a review article. As such, our intention here is to provide a brief (and surely incomplete) survey of the *ab initio* theory of liquid water to motivate our (more complete) discussion of the *ab initio* study of aqueous solutions containing the fundamental H_3O^+ and OH^- ions—the diffusion of which plays a key role in fuel cell applications.

Ever since the first *ab initio* molecular dynamics (AIMD)[1170,1171] simulation of liquid water in 1993 by Laasonen, Sprik, Parrinello, and Car,[1172] there have been many first-principles simulations of liquid water performed using DFT[1173,1174] within the generalized gradient approximation (GGA), e.g., BLYP[1175,1176] and PBE.[1177] The AIMD approach generates the nuclear potential energy surface "on-the-fly" from the electronic ground state without empirical

https://doi.org/10.1021/acs.chemrev.1c00331
Chem. Rev. XXXX, XXX, XXX−XXX

input, and is therefore suitable for predicting the structure and dynamics of a targeted system as well as its electronic and dielectric properties in a reactive fashion (i.e., in conjunction with the breaking and forming of chemical bonds).[1170,1171] However, the accuracy of DFT-based AIMD simulations is determined by the underlying approximation to the exchange-correlation energy. For the electrons, GGA-DFT suffers from several limitations, namely, the presence of self-interaction error (SIE)[1178,1179] and the lack of long-range van der Waals (vdW)/dispersion interactions,[1180−1183] both of which lead to errors when describing the structural and dynamical properties of liquid water systems.[1184−1216] To combat the deleterious effects of SIE, hybrid-GGA functionals, which are substantially more computationally expensive than GGAs, were first employed by Hutter,[1195] Galli,[1207] and Gygi[1208] in the study of bulk liquid water. To accurately describe the long-range vd*W*/*d*ispersion interactions, both GGA and hybrid-GGA functionals can be outfitted with a number of different vdW/dispersion correction schemes.[1180−1183] Using this approach, DiStasio et al.[1214] then studied the individual and collective effects that originate from treating both of these improvements at the dispersion-corrected hybrid-GGA level, pushing us closer to an accurate and reliable first-principles description of the microscopic structure of ambient liquid water. More recently, the strongly constrained and appropriately normed (SCAN) meta-GGA functional proposed by Sun, Ruzsinszky, and Perdew[1217] has emerged as a more computationally affordable higher-rung alternative to GGA-DFT. As such, this approach has already been used to model the structures (and relative stabilities) of the ice phases by Sun et al.[1218] and the structure and diffusion of liquid water by Chen et al.,[1216] Zheng et al.,[1219] and Wiktor et al.,[1220] as well as compute the sum frequency generation (SFG) spectrum of interfacial water on an anatase TiO_2 surface by Selloni and coworkers.[1221] Carnevale, Borguet, and coworkers[1222] also demonstrated that SCAN estimates the pK_a value of water to within 1.0 unit lower than the experimental assignment.

In addition to providing a detailed description of the electronic structure, *ab initio* modeling of liquid water also faces challenges due to the quantum mechanical nature of the nuclei (particularly for light atoms such as H). To account for these nuclear quantum effects (NQEs), the discretized Feynman path-integral (PI) scheme[1223,1224] has been integrated with AIMD by Marx, Tuckerman, Klein, and Parrinello.[1225,1226] For a detailed review of NQEs in aqueous systems, we point the interested reader to the recent review by Ceriotti, Markland, and coworkers.[1227]

9.2.2. Simulating Proton Transfer Processes in Aqueous H_3O^+/OH^- Solutions. While the *ab initio* simulation of liquid water remains a challenging and active field of research, essentially all water molecules under ambient bulk conditions remain intact. This is due to the fact that autoionization is an extremely rare process, which was studied in detail by Geissler, Chandler, and coworkers[1228] via the combined use of Car−Parrinello AIMD and transition path sampling techniques.[1229] As such, several simple yet accurate empirical force fields, including (but not limited to) SPC/E,[1230] TIP4P/2005,[1231] and MB-Pol,[1232] have been constructed to study bulk liquid water. However, the simulation of aqueous H_3O^+ and/or OH^- solutions—both of which involve a reactive (bond-breaking/bond-forming) proton-transfer process between H_3O^+ (or OH^-) and the surrounding solvent H_2O molecules—pose a significant challenge for such conventional force-field-based approaches and therefore require more sophisticated reactive force fields (which allow for bond-breaking and bond-forming processes, see refs 1233−1236) or a fully *ab initio* treatment via AIMD simulations.

This proton-transfer process was hypothesized by von Grotthuss 200 years ago (see ref 1237 for an interesting historical review), yet the microscopic details underlying the proton-transfer mechanism remained largely unknown until the mid-1990s. During that time, Tuckerman, Laasonen, Sprik, and Parrinello performed the first AIMD simulations on aqueous H_3O^+ and OH^-.[1238−1240] Based on these simulations, they provided a microscopic picture of the Grotthuss mechanism, in which the proton-transfer process happens on the ps time scale—orders of magnitude more frequently than the autoionization process in ambient liquid water.[1228] In conjunction with these AIMD simulations, Vuilleumier and Borgis,[1241] Sagnella and Tuckerman,[1242] and Schmitt and Voth[1243] demonstrated that *ab initio*-derived empirical valence bond (EVB) approaches can also be a viable tool to study the proton-transfer process in aqueous H_3O^+ and OH^- solutions (particularly for extended length and time scales not easily accessible by AIMD); see ref 1244 for a detailed review.

9.2.3. Proton Transfer Mechanisms in Aqueous H_3O^+/OH^- Solutions. In the Grotthuss mechanism, H_3O^+ and OH^- are regarded as topological defects in the tetrahedral hydrogen bond (HB) network of H_2O molecules that can migrate via proton transfer through a connecting HB molecular wire. Such structural diffusion can therefore be significantly faster than vehicular/Stokes diffusion, an argument advanced by von Grotthuss to (qualitatively) explain the anomalously high mobility of H_3O^+ and OH^- in aqueous solutions.[1245,1246]

Based on AIMD simulations, Tuckerman, Marx, and Parrinello provided key atomistic insights into the Grotthuss mechanism by introducing the concept of *presolvation* leading up to proton-transfer processes in aqueous H_3O^+/OH^- solutions.[1247,1248] This presolvation concept states that successful structural migration events require a proton acceptor (i.e., H_2O in acid; OH^- in base) to exhibit the local solvation structure corresponding to the product of the proton-transfer process (i.e., H_3O^+ in acid; H_2O in base). For instance, the structural diffusion of H_3O^+ under acidic conditions (Figure 86A−C) is characterized by transitions between the presolvated Eigen complex, i.e., $[H_3O^+\cdot(H_2O)_3]$ (Figure 86A,C) and the Zundel complex, i.e., $[H_2O\cdots H\cdots OH_2]^+$ (Figure 86B). During this process, the local solvation structure of the acceptor H_2O (i.e., the water molecule directly to the right of the H_3O^+ in Figure 86A) must fluctuate to recover the solvation structure of the product H_3O^+ (as shown in Figure 86C) to allow structural diffusion to effectively proceed to the Zundel complex (Figure 86B) and finally to the product of the proton-transfer process (Figure 86C).

The mechanism for proton transfer in aqueous H_3O^+ reached a consensus earlier than that in aqueous OH^-, which was settled after a longer scientific debate.[1246] In short, the discussion surrounding aqueous OH^- mainly focused on the following three potential mechanisms for proton transfer: (i) the mirror image scenario, (ii) the static hypercoordination scenario, and (iii) the dynamic hypercoordination scenario.

The mirror image scenario (which dates back to the 1950s, i.e., well before the invention of the Car−Parrinello AIMD approach[1170]) assumes that the proton-transfer mechanism in aqueous OH^- can be inferred from that of aqueous H_3O^+ by

https://doi.org/10.1021/acs.chemrev.1c00331
Chem. Rev. XXXX, XXX, XXX−XXX

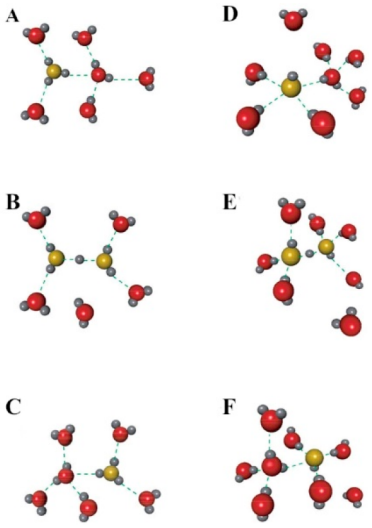

Figure 86. Graphical depiction of the proton-transfer mechanism in aqueous H_3O^+ (A–C) and OH^- (D–F). Atoms are labeled based on their species [H, white; O (solvent water), red; and O (involved in structural diffusion), yellow]. Reprinted with permission from ref 1247. Copyright 2002 Springer Nature.

assuming that OH^- is a proton hole (i.e., the mirror image of the solvated proton, H_3O^+). However, this mirror image argument cannot explain the significantly lower (by around a factor of 2) diffusivity of OH^- under ambient conditions.[1249−1251] With the aid of AIMD simulations, the asymmetry between aqueous H_3O^+ and OH^- was attributed to a rather stable hypercoordinated solvation structure surrounding the OH^- ion (Figure 86D,F) that was not present in aqueous H_3O^+.[1238−1240,1252,1253] Such asymmetry (which was recently attributed to differences in the amphiphilicity of the aqueous H_3O^+ and OH^- ions[1254]) further invalidates the assumption of the mirror image scenario.

The debate as to whether the hypercoordination of OH^- is static or dynamic was also largely settled with the combined use of the presolvation concept and AIMD simulations.[1238−1240,1246,1247] Since the hypercoordinated OH^- solvation structure is topologically distinct from the tetrahedral solvation structure[1255] surrounding a bulk water molecule (i.e., the product of the proton transfer to a OH^- ion), the presolvation concept requires thermal and/or quantum fluctuations to transform the hypercoordinated solvation structure (Figure 86D,F) to the tetrahedral solvation structure (i.e., corresponding to the OH^- on the left in Figure 86E).[1247] After the proton transfer, the water molecules surrounding the product OH^- relax back to the hypercoordinated solvation structure (Figure 86F), thereby completing the proton-transfer mechanism in aqueous OH^-. As such, the static hypercoordination scenario—in which the hypercoordinated solvation structure is too stable to fluctuate—is incompatible with structural/Grotthuss diffusion of OH^- (via the presolvation requirements) and suggests that OH^- would be essentially limited to vehicular/Stokes diffusion only.[1246] As such, the debate surrounding the proton-transfer mechanism in aqueous OH^- settled on the dynamic hypercoordination scenario, in which the diffusion of OH^- is characterized by a combination of vehicular and structural diffusion. In this picture, the solvation structure surrounding the OH^- ion fluctuates between a hypercoordinated or "resting" state (in which the ion primarily undergoes vehicular diffusion) and a presolvated or "active" state (in which the ion primarily undergoes structural diffusion).[1246,1247]

As mentioned above, nuclear quantum fluctuations are non-negligible in aqueous H_3O^+ and OH^- solutions due to the presence of light atoms such as H. In these cases, Marx and coworkers employed PI-AIMD simulations to demonstrate that NQEs (such as tunneling and zero-point motion) generally increase the fluxionality of proton-centered aqueous complexes and can therefore have a substantial influence on the free-energy profile of the proton-transfer process.[1246,1256,1257] However, NQEs do not qualitatively change the underlying structural diffusion mechanism described above.[1246]

9.2.4. Concerted Proton Transfer Processes: Water Wire Compression. While the dynamic hypercoordination scenario already sketches out the microscopic picture of the OH^- diffusion mechanism in an aqueous environment, Hassanali and coworkers[1258,1259] provided new insight into this mechanism. Using AIMD simulations, they observed that multiple proton-transfer processes tend to occur in correlated bursts (or jumps) over short windows of time separated by

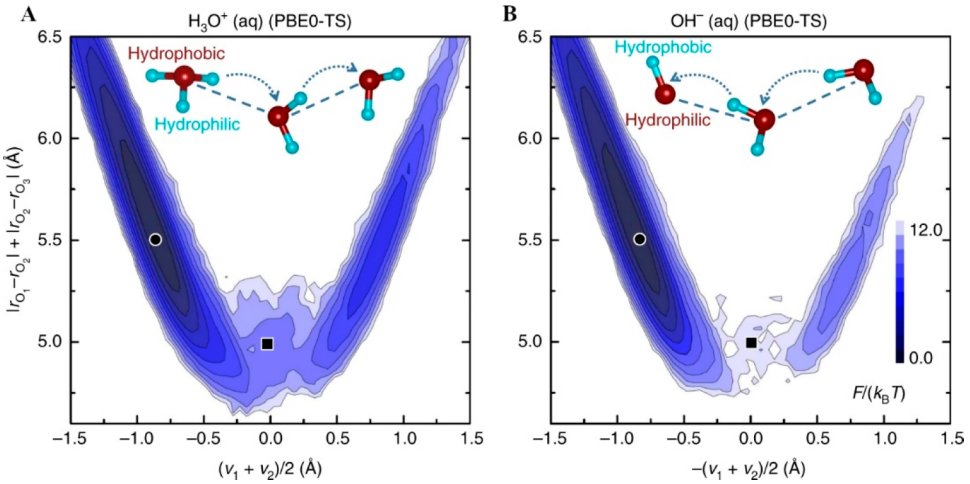

Figure 87. Free-energy profile for water wire compression and double proton jumps with the PBE0-TS[1263−1266] functional for aqueous H_3O^+ (A) and aqueous OH^- (B). Reprinted with permission from ref 1254. Copyright 2018 The Authors, Springer Nature.

https://doi.org/10.1021/acs.chemrev.1c00331
Chem. Rev. XXXX, XXX, XXX−XXX

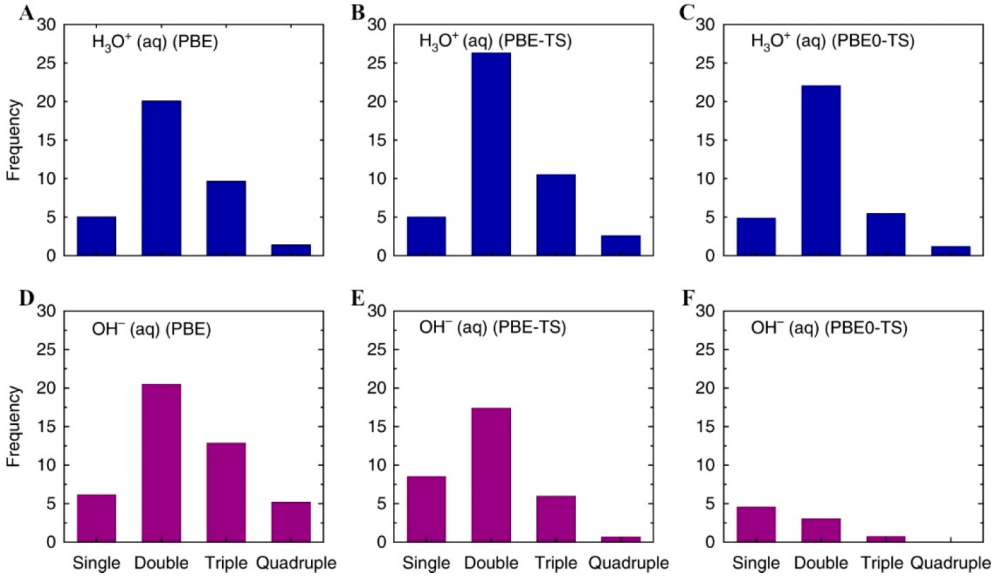

Figure 88. Frequency of proton-transfer events with three different exchange-correlation functionals: PBE (A, D), PBE-TS (B, E), and PBE0-TS (C, F) for aqueous H_3O^+ (top, blue) and OH^- (bottom, purple). Reprinted with permission from ref 1254. Copyright 2018 Macmillan Publishers Limited, part of Springer Nature.

longer periods where structural diffusion is inactive. Such correlated multiple proton-transfer events are promoted by collective compressions in the network of water molecules connected to the topological defect (H_3O^+ or OH^-) via HBs, i.e., water wire compression.[1259]

For a double proton-transfer event (in which the proton is transferred over two water molecules), the effect of water wire compression can be visualized using a two-dimensional collective variable (Figure 87).[1254,1259] In this case, the first dimension is defined as $|\mathbf{r}_{O1} - \mathbf{r}_{O2}| + |\mathbf{r}_{O2} - \mathbf{r}_{O3}|$ using the position vectors of the three consecutive oxygen atoms (O_1, O_2, O_3) involved in the double proton-transfer event; as such, this dimension measures the extent of the water wire compression. The second dimension is defined as $(\nu_1 + \nu_2)/2$ for H_3O^+ or $-(\nu_1 + \nu_2)/2$ for OH^-, where $\nu_1 = |\mathbf{r}_{O1} - \mathbf{r}_{H1}| - |\mathbf{r}_{H1} - \mathbf{r}_{O2}|$ is the coordinate for the first proton (H_1) transferred between O_1 and O_2, and $\nu_2 = |\mathbf{r}_{O2} - \mathbf{r}_{H2}| - |\mathbf{r}_{H2} - \mathbf{r}_{O3}|$ is the coordinate for the second proton (H_2) transferred between O_2 and O_3. Successful completion of the double proton-transfer process would therefore correspond to $\nu_1 + \nu_2 > 0$ for H_3O^+ or $-(\nu_1 + \nu_2) > 0$ for OH^-, which corresponds to the right-hand side of Figure 87A,B.[1254,1259] Using these collective variables, the free-energy barriers associated with double (and higher) proton-transfer events promoted by water wire compression in aqueous H_3O^+ and OH^- solutions can be computed based on AIMD trajectories.

9.2.5. Why Does OH^- Diffuse Slower than H_3O^+? Climbing the DFT Hierarchy. In the aforementioned AIMD simulations of aqueous H_3O^+ and OH^-, GGA-DFT has been employed to model exchange-correlation effects. However, as discussed in section 9.2.1, GGA-DFT is known to suffer from several theoretical limitations (i.e., SIE[1178,1179] and the lack of long-range vdW/dispersion interactions[1180−1183]) which lead to errors when describing the structural and dynamical properties of aqueous systems.[1184−1216] As such, it is not clear how the molecular-level details regarding the proton-transfer mechanism in aqueous H_3O^+ and OH^- obtained at the GGA-DFT level would change if revisited using more sophisticated dispersion-inclusive hybrid DFT functionals, which are known to provide a more accurate and reliable description of the microscopic structure of liquid water.[1207,1208,1214] To answer this question, Wu, Car, and coworkers[1254] applied a linear-scaling exact exchange algorithm[1214,1260−1262] that enables large-scale AIMD simulations of condensed-phase systems to study the proton-transfer process in aqueous H_3O^+ and OH^- at the dispersion-corrected hybrid DFT (i.e., PBE0-TS[1263−1266]) level.

In doing so, this work identified a key qualitative difference in the proton transport mechanisms in aqueous H_3O^+ and OH^- solutions, namely, that Grotthuss migration of H_3O^+ primarily occurs via multiple concerted jumps (Figure 88C), while structural diffusion of OH^- tends to be much more sequential in nature (Figure 88F). Interestingly, such differential behavior was not observed when using conventional GGA-DFT (i.e., PBE;[1177] see Figure 88A,D) nor dispersion-corrected GGA-DFT (i.e., PBE-TS;[1177,1265,1266] see Figure 88B,E) and was attributed to the simultaneously improved description of both HB interactions as well as intermolecular vdW/dispersion forces at the dispersion-corrected hybrid DFT level. Here, an improved description of the long-range vdW/dispersion interactions allows for tighter water wire compression, which promotes multiple concerted jumps during the proton-transfer process. Taken on its own, this effect would increase the rate of structural diffusion for both H_3O^+ and OH^-. However, such long-range vdW/dispersion interactions also further stabilize the hypercoordinated (resting) solvation structure surrounding the OH^- ion and therefore lead to an overall slower diffusion rate in aqueous OH^- solutions. Mitigation of SIE reduces the HB strength,[1207,1208,1214] which reduces the overall tetrahedrality of each water molecule and further softens the liquid water structure. In addition, the amphiphilic propensity of the solvated OH^- ion is also enhanced, which increases the attraction between OH^- and the surrounding water molecules and hence the relative stability/lifetime of the hypercoordinated (resting) solvation structure.[1254] In this regard, the predicted potlike solvation structure surrounding OH^- also agrees better with the neutron-scattering assignment by Soper and coworkers.[1267]

https://doi.org/10.1021/acs.chemrev.1c00331
Chem. Rev. XXXX, XXX, XXX−XXX

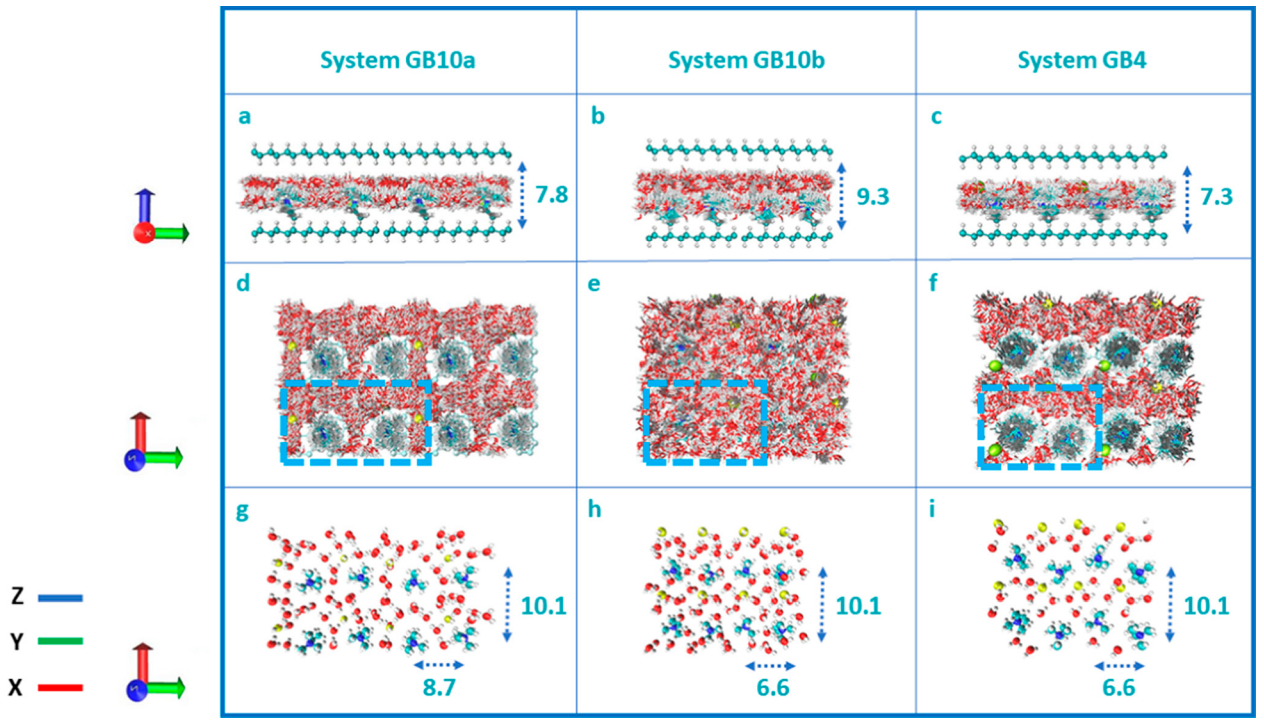

Figure 89. Atomistic graphane bilayer used in *ab initio* modeling of OH^- diffusion through AEM channels. Atoms/molecules are labeled based on their species [C, green; N, blue; O (solvent water), red; H, white; O (in OH^-), yellow]. Reprinted with permission from ref 1274. Copyright 2019 American Chemical Society.

When taken together, the net effect of using dispersion-inclusive hybrid DFT modifies the structural diffusion mechanism of OH^- from occurring primarily through multiple concerted jumps to occurring primarily through sequential proton transfers (while leaving the physical picture of diffusion in aqueous H_3O^+ qualitatively intact). As such, this work builds upon the seminal concepts of presolvation, dynamic hypercoordination, and water wire compression to provide an even more refined understanding of why OH^- diffuses slower than H_3O^+.

9.2.6. *Ab Initio* Modeling of Aqueous OH^- through AEMs. Over the past few years, AIMD simulations have also been increasingly used to study OH^- transport through AEMs. While an atomistic-level characterization of the surfaces and channels in a given membrane still remains an open challenge to date, several theoretical studies have shed light on the mesoscale structure of specific AEMs. For instance, Paddison and coworkers[1268] have used mesoscale dissipative particle dynamics (DPD) simulations[1269] to study how membrane morphology depends on hydration level. In doing so, this work identified that the AEM morphology can transform between perforated lamellae (low hydration), perfect lamellae (intermediate hydration), and disordered bicontinuous domains (high hydration). Similar coarse-grained simulations have also been used to study OH^- diffusion through AEM membranes by Zhuang,[375,376] Paddison,[1270,1271] Lee,[1272,1273] and their respective coworkers. While such coarse-grained studies are unable to describe structural (Grotthuss) OH^- diffusion, they can be used to probe the interior structure of the AEM as well as estimate the length and time scales associated with confined OH^- transport.

Motivated by some of these mesoscale simulations, Zelovich et al.[1274] then proposed the use of tetramethylammonium (TMA) cations tethered to nanoconfined structures as models for an *ab initio* study of OH^- diffusion through AEM channels. In particular, this work considered two types of confinement models to mimic the diverse interior AEM environment: (i) channel confinement via TMA-tethered carbon nanotubes and (ii) interfacial confinement via TMA-tethered graphane bilayers (GB). Using several different GB-based AEM models (Figure 89), they performed AIMD simulations of OH^- diffusion at various different (low) hydration levels, observing that OH^- transport changes from a mixture of structural (Grotthuss) and vehicular (Stokes) diffusion to exclusively vehicular diffusion and, finally, to nondiffusive behavior as the surrounding water density was decreased.[1275] Recently, Zelovich and Tuckerman[1276] also performed AIMD simulations using these GB-based AEM models at high hydration levels, showing how different water layers can either promote or suppress OH^- diffusion. While such pioneering studies have provided us with the first fully *ab initio* look into model AEM channels, direct *ab initio* simulation of aqueous OH^- diffusion through an AEM over experimentally relevant length and time scales remains a grand challenge to date. While such length and time scales remain largely inaccessible using DFT-based AIMD approaches, we expect that emerging machine-learning-based *ab initio* techniques[1277−1287] will provide us with a viable route forward.

9.3. *Ab Initio* Theory of Electrochemical Environments

As touched upon in section 9.1, first-principles, *ab initio* theory enables, in principle, the direct calculation of electrocatalytic reactions, including reaction rates and thermodynamically stable phases. To be complete for alkaline environments, such predictions require the computation of the free energies of *fluid-immersed* solid surfaces and reactants, with stable phases determined as those with the lowest free energy and with reaction rates computed using transition state theory.[1288,1289]

https://doi.org/10.1021/acs.chemrev.1c00331
Chem. Rev. XXXX, XXX, XXX−XXX

Rate calculations can be further extended to complex multistep reactions by computing the reaction rate for the individual steps and then solving the resulting reaction network. *Ab initio* electrochemical calculations, however, are particularly challenging because of the potential impacts of all relevant aspects of the system, including the fluid environment, the ions in the fluid, the electrode, the adsorbates on the electrode, and the potential of the electrode.

First-principles electrochemical methods typically group the above aspects into "solid" and "fluid" components of the calculation and then link these components through an interaction term,[1290,1291] (Figure 90A). The "solid component" (red shaded regions, Figure 90) generally consists of the electrode, the adsorbates, and the electrode potential, which is linked directly to the free charge in the form of electrons which can enter or leave the electrode through an external circuit. First-principles calculations generally handle these components through standard DFT calculations.[1292−1296] In contrast, a wide range of theoretical descriptions are available for the "fluid component" consisting of the fluid itself and any included ions (blue shaded regions, Figure 90). Fluid component descriptions span a range from simplistic continuum models to sophisticated classical density-functional theories (section 9.3.2), with a parallel set of descriptions for the ions in the fluid, ranging from linearized continuum Debye−Hückle screening to, again, classical density-functional theories (section 9.3.3). When combined with the "fluid component", the "solid component" must be able to balance the charge in the fluid so as to maintain charge neutrality. Moreover, it is important to include the effects of changing electrode potential on the electrode charge and other key quantities of interest, such as the energies of transition states and the resulting reaction rates (section 9.3.4). A number of researchers have successfully included all of these effects in electrochemical calculations (section 9.3.4).

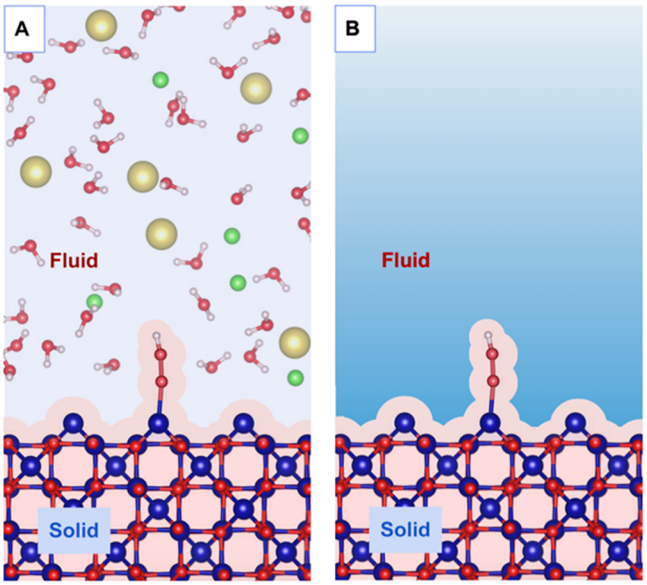

Figure 90. *Ab initio* description of solvated systems in electrochemical environments using (A) explicit and (B) implicit methods: the illustration shows a $Co_3O_4(100)$ surface with an *OOH adsorbate in an aqueous solution with sodium and chloride ions, with atoms represented as spheres (red = oxygen, blue = cobalt, white = hydrogen, yellow = chlorine, green = sodium), and the electrode charge as e^-'s, with the "solid component" in red and the "fluid component" in blue. Implicit methods (B) replace the atomistic description of the fluid from Panel A with a continuum description.

9.3.1. Fluids. Accurate predictions in the electrochemical setting require a detailed description of the fluid environment, especially when the structure of the electrochemical double layer plays an important role. The most direct approach to inclusion of the fluid environment is through explicit AIMD, which has been covered in section 9.2 and a number of review articles.[1297] While the most accurate, AIMD is very computationally demanding because it requires the *ab initio* treatment of large numbers of fluid molecules (Figure 90A), which is compounded by the need to repeat such very demanding calculations tens of thousands of times to provide adequate statistical sampling to obtain meaningful results.[1298] The demanding nature of this approach limits the practicality of its application, particularly for systems involving complex surface reactions and for computational surveys that would explore large numbers of possible catalysts and reactants.

There are several methods available that maintain accuracy while allowing for the study of a broader range of systems. The first such method applies a detailed, explicit electronic representation for those parts of the system that absolutely require an *ab initio* description, while representing the fluid molecules using a more approximate molecular mechanics approach. The fluid and the key components of the system are then coupled using the quantum mechanics/molecular mechanics (QM/MM) method.[1299] Although this approach removes much of the computational cost by eliminating a full, *ab initio* calculation of the molecules in the fluid, the QM/MM method still requires large numbers of demanding *ab initio* quantum mechanical calculations for the key components of the system in order to provide sufficient statistics.[1300] Another intermediate approach is to treat all components of the system *ab initio*, but to include only the key components and a limited number of layers of surrounding fluid molecules.[1301,1302] A primary pitfall of this approach is that actual electrochemical systems have characteristically long ionic screening lengths, for example, 30 Å at 0.1 M ionic strength, that extend far beyond tractable numbers of explicit layers, so that this scheme cannot include essential long-range screening effects. Finally, even with a limited number of fluid layers, such calculations, once again, can be impractical because of the extensive sampling and thus lengthy computation needed to compute meaningful averages and free energies.[1300]

An alternative set of approaches, which are much more computationally tractable, represent the system−solvent interaction as the dielectric response of a continuum medium surrounding the system (blue shaded region, Figure 90B).[1303−1306] Such polarizable continuum model (PCM) theories exploit the fact that the dielectric response of the fluid is the main contributor to the free energy of solvation[1307] and thereby eliminate the large numbers of explicit electrolyte molecules otherwise needed to capture fluid effects. Moreover, these approaches save significant computational cost by accounting directly for the dielectric response without the need for statistical sampling. Within these approaches, the fluid−system interaction occurs at an interface (curve separating red and blue regions in Figure 90B). Some approaches determine this interface using van der Waals spheres centered at solute atom positions.[1303] An alternate approach, the isodensity method, defines the interface as an isosurface of a particular value of the electronic density, which

https://doi.org/10.1021/acs.chemrev.1c00331
Chem. Rev. XXXX, XXX, XXX−XXX

has the advantages of significantly simplifying the thermodynamic average force on the atoms and of providing an electron-density-based description of the interface which works well within the density-functional theory framework.[1308−1312] Once the spatial dependence of the dielectric constant is determined, PCM approaches then use a variety of methods to solve for the corresponding bound charges, including both a direct solution of the Poisson−Boltzmann equation using spectral methods[1308,1309] and also a direct solution for the charges at the vacuum−dielectric interface.[1313] Finally, PCMs generally also include secondary interactions with solutes, such as cavity-formation free energies, dispersion interactions, and short-range steric repulsion.[1303]

Traditionally PCMs represent the effects of the fluid environment with a linear dielectric response[1314] and do not account for the details of the liquid shell structure. Nonlinear effects can be quite important, particularly when dealing with highly polar solutes or polar surfaces.[1315] Such effects can be modeled through inclusion of a layer of lower dielectric constant at the interface to represent dielectric saturation[1303] or through direct solution of nonlinear dielectric equations obtained through representing the electrolyte environment as a continuous field of interacting dipoles.[1315] PCM methods suffer from a major disadvantage: because they begin by replacing the fluid with a continuum, these methods provide no information about solvation shell structure or liquid layering above a surface. Without such effects, these approaches give an oversimplified description of the electrochemical double layer that resembles the Gouy−Chapman model[1316] but without the important subtleties of the refinements by Stern[1317] and Grahame.[1318] Some progress has been made in refining PCMs to improve the description of the electrochemical double layer;[1319] however, the direct replacement of the molecular fluid with a continuum limits the development of systematic approaches to improve PCMs.[1301]

To allow for the development of systematically improvable approaches, joint density-functional theory (JDFT) incorporates the molecular structure rigorously and, in principle, exactly, by joining a standard electronic density-functional theory calculation for the explicit system with a classical density-functional theory (CDFT) for the liquid.[1300,1309] Such CDFTs, in principle, give an exact description of the thermodynamics of a classical molecular fluid system including all molecular-scale effects.[1320−1322] The CDFTs, by building upon the free energy of the noninteracting molecular gas, give first-principles access to effects including steric repulsion, shell structure,[1323] layering above a surface,[1324,1325] and linear and nonlinear dielectric and ionic screening.[1326] By combining such CDFT descriptions with electronic structure calculations, JDFT provides a very economical, yet accurate, method for incorporating into *ab initio* calculations fluid effects which are essential to the description of electrochemical environments.[1298]

9.3.2. Ions. Ions are an essential component of the electrolyte and must be considered when representing electrochemical environments. In particular, ions play a critical role in maintaining charge neutrality in the presence of a charged electrode. Moreover, without the inclusion of the compensating effects of ions at some level, there is no way to place electrode potentials extracted from *ab initio* calculations on an absolute electrochemical scale.[1300]

The simplest attempts to represent the compensating ionic charge in DFT calculations have been to smear the total charges from the ions into a uniform distribution spread evenly through space,[1302] even throughout the region of the solid electrode. This approach however, is unrealistic and leads to electrostatic potentials in the fluid that do not converge at large distances from the surface and to unrealistically large differential capacitances for the electrochemical interface.[1300] Other methods represent the compensating ions as a charged sheet at a fixed distance from the electrode.[1327,1328] However, the placement of this sheet is relatively arbitrary and can have a nonphysical impact on the potential.[1300] More recently, others have modelled the electrolyte using a layer of explicit hydrogen atoms, which then separate into a solvated proton layer and an electronic charge deposited onto the electrode.[1329] This allows for an electrode−electrolyte double layer while keeping the unit cell neutral.[35,1330,1331] However, this approach again amounts to modelling the ions as a layer of charge, in this case protons, and the locations for the H atom inclusion are again arbitrary.

There are more sophisticated approaches to the compensating ionic charge. These approaches consider an *a posteriori* continuum model which incorporates the fluid dielectric response and Debye screening by solving *ab initio* calculations with modified Poisson−Boltzmann equations.[1308,1330,1332,1333] Poisson−Boltzmann-like equations do not include important nonlocal and nonlinear features.[11] However, nonlinear saturation effects have an important role in electrochemical systems, particularly near the liquid−solid interface, and must be represented accurately to obtain reliable *ab initio* results.[1298]

Even in its nonlinear forms, the Poisson−Boltzmann equation fails to account for physically relevant phenomena such as nonlinear capacitance effects due to ion adsorption, the nonlocality of the dielectric response of the fluid, and the surface tension associated with formation of the liquid−solid interface.[1315] Poisson−Boltzmann approaches, without significant augmentation, thus give poor representations of differential electrochemical capacitance.[1298] The most physically representative, if challenging, approach to describe screening from ions in the fluid at an electrode interface is to use a CDFT.[1334] Variations of this approach have been used in joint calculations with a DFT description of the electrode to produce a realistic description of the electrochemical interface.[1319]

9.3.3. Electrode Charge. As described above in section 9.3.2, a proper description of the ionic component of the fluid ensures charge compensation between the fluid and solid components and the establishment of a standard reference for the electrostatic potential. There are two theoretical approaches for handling charged electrodes. The first approach sets the net charge of the electrode by fixing the total number of electrons N in the solid component of the calculation and relaxes the solid component together with the fluid component to find the final configuration of minimum free energy. To extract the electrode potential from within this approach, one converts the chemical potential for electrons (μ), which many works refer to loosely as the "Fermi level", to a standard electrochemical scale as described below. This approach has the advantage that working with a fixed number of electrons and reporting the electron chemical potential, μ, are supported by all standard electronic structure packages.[1291,1335,1336]

The second approach for dealing with charged electrodes sets the electrode potential by fixing the electron chemical potential μ for the calculation, while allowing electrons to enter or leave the electrode so as to minimize the combined free

https://doi.org/10.1021/acs.chemrev.1c00331
Chem. Rev. XXXX, XXX, XXX−XXX

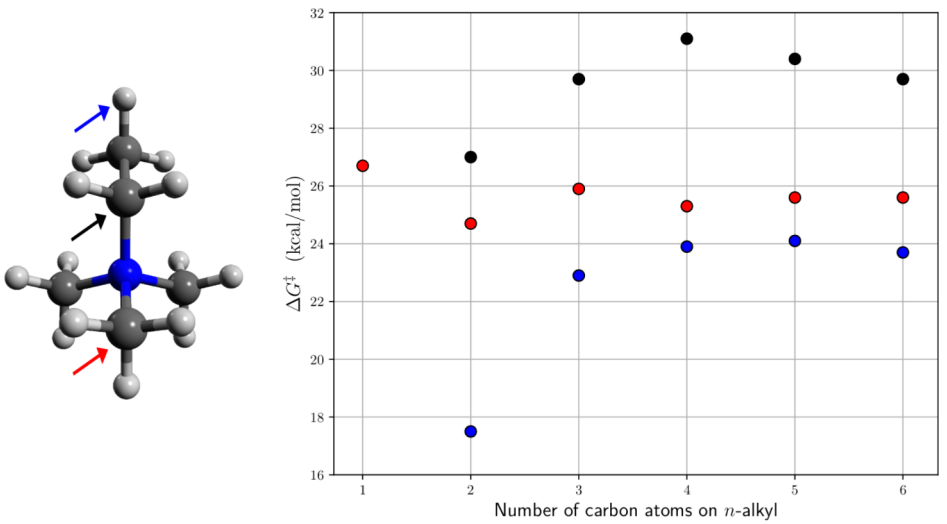

Figure 91. Free-energy barriers ($\Delta G^{\ddagger}$ in kcal/mol) for Hofmann elimination (blue), S_N2 on the *trans-*/*anti*-methyl group (red), and S_N2 on *n*-alkyl group (black) as a function of the *n*-alkyl carbon chain length in *n*-alkyltrimethylammonium cations. Reprinted with permission from ref 763. Copyright 2012 The Authors, American Chemical Society.

energy of the solid and fluid components.[1337] This approach then determines the total charge by computing the resulting total number of electrons in the solid using the standard Fermi function:

$$N = \sum_i f(E_i) = \frac{1}{\exp((E_i - \mu)/k_B T) + 1} \quad (26)$$

where the sum is over each electronic energy state i in the electrode, E_i gives the energy of the corresponding state, T is the temperature of the system, and k_B is Boltzmann's constant. The variable charge on the electrode makes this approach particularly susceptible to charge sloshing, a numerical issue where electrons flow back and forth into and out of the electrode. Fortunately, specialized numerical approaches have been developed which resolve this issue.[1337]

Relating results from either of the above two approaches to physical measurements requires conversion of the μ to an electrode potential E on a standard electrochemical potential scale. The relation $\mu - \mu_0 = -eE$ accomplishes this conversion, where e is the fundamental charge in SI units, and μ_0 represents the electron chemical potential corresponding to a standard reference potential such as the SHE.[1338]

The fixed charge and fixed potential approaches allow the calculation of a number of electrochemically measurable quantities. Within the fixed charge approach, the potential of zero charge (pzc) can be calculated quite simply by setting the number of electrons to make the electrode neutrally charged.[1300,1338] The ability to perform this calculation highlights a key advantage of the *ab initio* framework: experimentally, one can only directly measure the potential of zero *total* charge (pztc), which includes the effects of surface contamination, whereas the *ab initio* approach gives the potential of zero *free* charge (pzfc) directly. Under the fixed potential approach, on the other hand, one can compute the impact of electrode potential on any electrochemical process of interest, for example, effects of electrode potential on surface diffusion barriers that have been observed in experiments.[1339] Finally, both approaches are capable of determining the charge vs potential curve for an electrochemical system, from which the differential capacitance can be extracted directly.

9.3.4. Applications. A full treatment of electrochemical systems requires the use of the above techniques within a unified framework, and there have been numerous studies and reviews regarding the use of *ab initio* techniques to investigate electrolysis and surface reactivity while including effects from the electrochemical environment.[1340−1344] Such studies generally fall into two broad categories, equilibrium studies and kinetic studies.

In terms of equilibria, aqueous redox potentials of organic molecules have been computed with good agreement with experiment (0.1−0.4 eV, mean unsigned error) using PCMs and computing energy differences of different charge states of the species.[1345,1346] Also, underpotential deposition has been studied *ab initio* using used JDFT with a continuum fluid model.[1337] This study showed that chloride desorption is responsible for a voltammetric peak formerly believed to be from formation of a partial copper monolayer.[1337] *Ab initio* calculations have also been used to determine the lowest free-energy surface phases of electrocatalysts as a function of pH and potential in order to predict Pourbaix diagrams.[1347,1348] Finally, PCM techniques have been combined with DFT techniques to study equilibrium systems involving ionic liquids.[1349−1351]

In terms of kinetic studies, the dissociation of water at a silicon carbide surface has been studied using *ab initio* MD, with the interesting result that the dissociation of water molecules in the liquid phase is unexpectedly similar to the dissociation found in the gas phase.[1352] Additionally, the stability and surface diffusion of lithium−electrolyte interfaces have been studied to understand dendrite formation in lithium batteries.[1353] As a final example, *ab initio* MD calculations have been employed to study the electrochemical double layer at the rutile (110) surface.[1032,1354]

9.4. *Ab Initio* Modeling of Membrane Degradation

Ab initio modeling studies have also been used to aid in the search for alkaline-stable cationic functional groups to incorporate into AEMs. Such studies generally employ DFT to predict the stability of candidate cationic groups in alkaline conditions in a variety of ways, including calculating the pK_a of acidic hydrogens on the cation,[1355] the lowest unoccupied

https://doi.org/10.1021/acs.chemrev.1c00331
Chem. Rev. XXXX, XXX, XXX−XXX

molecular orbital (LUMO) energy[1356] of the cation, as well as the free-energy barriers ($\Delta G^{\ddagger}$) of potential degradation pathways according to classical transition state theory (TST). The benefits of performing such computational studies are numerous. For one, these studies can provide a detailed understanding of the reaction mechanisms underlying the degradation process (e.g., identification of the rate-limiting step in complex multistep reactions), thereby providing valuable insights into how the stability of these cations can be improved. Secondly, such studies can be used to investigate how substituent effects can modify the stability of cationic groups and can therefore be used in conjunction with (or in place of) experimental stability studies, which can be time-consuming (i.e., ∼30 days) to perform.[745] In addition, computational investigations can be used to elucidate potential degradation mechanisms in cases where it is difficult to detect and/or distinguish the degradation products experimentally.

9.4.1. *Ab Initio* Modeling of Tetraalkylammonium Cationic Groups. Computationally speaking, tetraalkylammonium cations are probably the most thoroughly studied class of cations for use in AEMs.[747,748,763,818,1357−1359] Such cations can react irreversibly with OH^-, primarily via Hofmann (E2) elimination or S_N2 reactions (Scheme 3).[763,1357,1358] However, these quaternary ammoniums are generally quite stable due to the high $\Delta G^{\ddagger}$ to such reactions.[1357] In a systematic study conducted by Pivovar and coworkers,[763] $\Delta G^{\ddagger}$ values for a number of potential degradation pathways were computed for a series of *n*-alkyltrimethylammonium cations using DFT in conjunction with an implicit solvation model. As depicted in Figure 91, Hofmann elimination tends to be the degradation pathway with the lowest $\Delta G^{\ddagger}$ value when compared to the competing S_N2 pathways. This suggests that the stability of such tetraalkylammonium cations can be improved by removing the β-hydrogens, which can be achieved by methylating the β-position.[763] Similarly, the viability of the Hofmann elimination pathway can also be reduced through the introduction of steric interference and/or geometric constraints that hinder the β-hydrogen from accessing the antiperiplanar position (with respect to the nitrogen atom) that is required for Hofmann elimination to proceed.[747,748,763,818] An example of such hindered Hofmann elimination is seen in the piperidinium and spirocyclic quaternary ammonium cations, which have been shown to be quite stable[748,818,1359] as the TS for ring-opening Hofmann elimination reactions requires high-energy bond lengths and angles.[747,748,818,1359] As such, many recent research efforts have focused on incorporating such cationic groups into AEMs (*vide infra*).

It has also been shown via H−D exchange experiments that OH^- can abstract α-hydrogens; however, this reaction tends to be highly reversible, and *ab initio* calculations have shown that the resulting ylide intermediate is unstable.[763,1357,1358] In order to proceed from the ylide intermediate towards a degradation product, first-principles calculations have also shown that the only viable pathway proceeds through the same TS structure as that found in the corresponding S_N2 attack; hence, the ylide and S_N2 pathways are experimentally indistinguishable.[1357] One notable exception is benzyltrimethylammonium, where it has been suggested that the ylide could undergo a Stevens or Sommelet−Hauser rearrangement to further degrade into benzylamine or phenethylamine derivatives.[1358,1360] Recently, it has also been argued that degradation preceding ylide formation might be possible through a more complicated mechanism involving multiple OH^- ions.[1361]

9.4.2. *Ab Initio* Modeling of Imidazolium Cationic Groups. Imidazolium cations are another promising candidate for use in AEMs. Both experimental and theoretical studies have shown that the primary degradation pathway for simple imidazolium cations is via nucleophilic addition−elimination at the C2 carbon atom.[1362−1365] The free-energy diagram for this degradation pathway was also studied by Pivovar and coworkers[1362] and is depicted for 1,3-dimethylimidazolium in Figure 92. Here, a rather intuitive design principle that can be

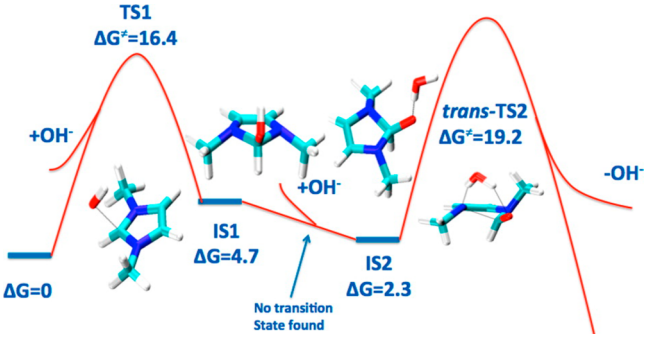

Figure 92. Free-energy diagram (ΔG in kcal/mol) for the addition−elimination pathway of OH^- with the 1,3-dimethylimidazolium cation. Depicted is the low-energy mechanism involving two OH^- ions. Reprinted with permission from ref 1362. Copyright 2014 The Authors, American Chemical Society.

obtained from these calculations is that introducing a bulky substituent at the C2-position should improve stability by sterically blocking the initial OH^- attack site.[1362−1366] However, it has also been computationally shown that the rate-limiting step in the degradation of 1,3-dimethylimidazolium is the subsequent ring-opening at the C2-position, which suggests that introducing substituents that also sterically interfere with the ring-opening TS structure might be an even better route towards improved imidazolium cation stability.[1362,1363] In lieu of performing a series of detailed TS searches, the susceptibility of imidazolium cations to OH^- attack at the C2-position has also been rationalized in terms of the LUMO energy of the cation, which can be increased via the introduction of an electron-donating substituent. This suggests that adding electron-donating substituents anywhere on the imidazolium ring can increase alkaline stability.[758,767,1364−1366] It has also been argued that the barrier associated with the ring-opening step depends on the OH^- concentration, in which the ring opening proceeds through a more facile mechanism involving multiple OH^- ions at high OH^- concentrations.[1363]

9.4.3. *Ab Initio* Modeling of Other Cationic Groups. Quaternary phosphonium cations also show great promise for use in AEMs. For such cations, one of the primary degradation pathways proceeds via OH^- directly attacking the central phosphorus atom; as such, the introduction of substituents can be used to stabilize these cations through electronic or steric effects.[775] In a combined experimental and theoretical study by Yan and coworkers,[775] these two effects were quantified in a semiempirical relationship based on the Taft equation: $\Delta G^{\ddagger} = a\delta + bE_s + c$, where δ is the polar substituent constant, E_s is the steric substituent constant, and a, b, and c are linear fitting parameters. In this equation, $\Delta G^{\ddagger}$ was obtained using *ab initio*

https://doi.org/10.1021/acs.chemrev.1c00331
Chem. Rev. XXXX, XXX, XXX−XXX

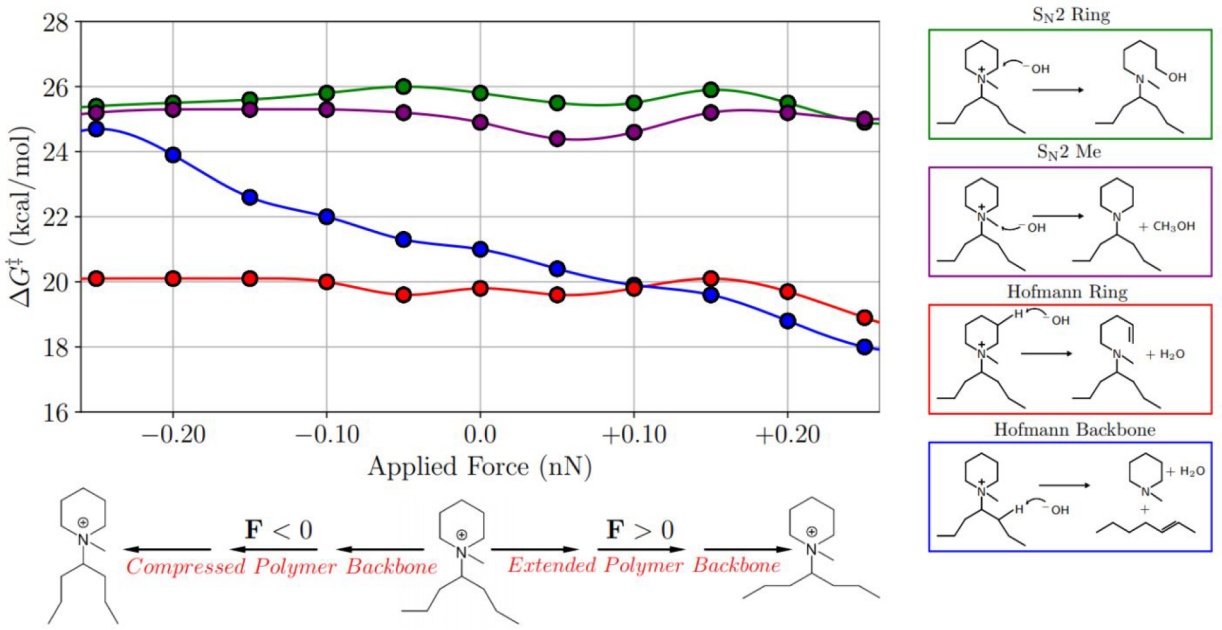

Figure 93. Free-energy barriers ($\Delta G^{\ddagger}$ in kcal/mol) for a series of degradation pathways in model-PEPM (see insets) as a function of an applied force (**F** in nN) to the distance between backbone γ-carbons. All barrier heights were computed using dispersion-inclusive hybrid DFT and the PCM implicit solvent model. Reprinted with permission from ref 818. Copyright 2021 The Authors, Royal Society of Chemistry.

calculations, and δ was obtained from ^{31}P NMR chemical shifts, which are a good measure of electron-donating effects; E_s was determined by computing the ΔG value between *ortho* and *para* substitutions, in which the substituents only cause steric effects when placed in the *ortho* position.[775] Although simple, this formula allows for a rapid screening of many potential quaternary phosphonium cations without the need for experimental degradation studies.

A number of other cationic groups have also been explored computationally for use in AEMs. One such cation is benzyltrimethylammonium, which has been shown to degrade primarily via S_N2 attack at the benzylic carbon.[1367,1368] Here, the introduction of electron-donating groups can stabilize the cation, although the associated $\Delta\Delta G^{\ddagger}$ value is a modest 1.6 kcal/mol, even in the most dramatic case studied (i.e., substitution of $-N(CH_3)_2$ at the 3- and 5-positions of the aromatic ring).[1367,1368] A somewhat similar case is the phenyltrimethylammonium cation, which degrades via nucleophilic attack on the methyl groups. In this case, electron-donating $-N(CH_3)_2$ moieties can improve the stability considerably, i.e., by up to 3.7 kcal/mol for triply $-N(CH_3)_2$-substituted phenyltrimethylammonium.[1369] Another set of cations that have been computationally investigated are the substituted guanidinium cations,[1370] which primarily degrade via direct attack by OH^- on the central carbon, which is followed by an intramolecular deprotonation of the attached $-OH$ to form tetramethylurea. At high OH^- concentrations, a second OH^- can cause this deprotonation, making the second degradation step much more facile.[1370] In this case, substituents are generally too far from the attacking position to introduce steric hindrance. Instead, substituent effects on guanidinium stability are generally rationalized based on changes to the LUMO of the cation, where electron-donating substituents can be used to increase the LUMO energy and stabilize the cationic species.[1370,1371]

9.4.4. *Ab Initio* Modeling of Backbone Degradation. *Ab initio* modeling has also been used to investigate how properties of the polymer membrane affect the degradation of cationic functional groups. One such property is water content, where one often finds that OH^- ions in dry conditions tend to be poorly solvated and thus more reactive. Computationally speaking, a simple and approximate way to account for such dry conditions involves decreasing the dielectric constant used in the implicit model for the solvent (i.e., the PCM).[1372−1375] As one might expect, it has been shown that decreasing the dielectric constant can significantly decrease the $\Delta G^{\ddagger}$ for degradation via OH^- attack.[1357,1363] In some AEMs, the polymer backbone itself is also vulnerable to OH^- attack. In benzyltrimethylammonium-functionalized polyaromatics, for example, it has been shown that the primary source of degradation in some poly(arylene ether) backbones occurs via S_NAr attack.[1376] Here, eliminating electron-withdrawing groups from the polymer backbone, or replacing the polymer backbone with poly(phenylene), greatly improves the stability of such membranes.[1376,1377]

In a recent experimental and theoretical study by DiStasio, Knowles, Coates, and coworkers,[818] *ab initio* methods were also used to investigate how local backbone morphology affected the stability of piperidinium-functionalized polyethylene membranes.[818] In this study, the external forces explicitly included (EFEI) approach[1378] was used to add a small external force that either stretched or compressed the backbone in a model polyethylene system to mimic the ensemble of backbone conformations in an AEM environment. Figure 93 shows the $\Delta G^{\ddagger}$ values for each of the considered degradation pathways as a function of the local backbone morphology. In this study, Hofmann elimination on the model polyethylene backbone was shown to occur much more readily if the backbone was in an extended conformation. Similarly, Hofmann elimination could be significantly hindered for compressed backbone conformations, with the difference between such extreme cases corresponding to changes in the reaction rate constant by up to 4 orders of magnitude.[818] In direct contrast, the barrier heights for the other degradation

https://doi.org/10.1021/acs.chemrev.1c00331
Chem. Rev. XXXX, XXX, XXX−XXX

pathways remained largely unchanged by the local backbone morphology.

9.5. Summary

In section 9.1, we discussed some of the principles governing surface catalysis, such as linear scaling and Brønsted−Evans−Polanyi correlations. Starting from these principles, we then surveyed several strategies used to tune the (electro)catalytic activity of materials, such as the strain and ligand effects, including new aspects of theoretical surface catalysis aimed at surpassing the intrinsic limits imposed by linear correlations. Furthermore, we provided extensive details on state-of-the-art computational techniques that can be used to unravel the nature of (electro)catalyst active sites under realistic reaction conditions. Among these, we showed that MKMs, informed with DFT-derived quantities, are particularly powerful for developing a fundamental understanding of reaction mechanisms, both in vapor-phase catalysis and electrocatalysis. In this context, we emphasized the importance of constructing MKMs that are not only in quantitative agreement with experiments but also "coverage-cognizant".

Next, in section 9.2, we turned to ion transport in alkaline electrochemical systems and reviewed the *ab initio* study of aqueous hydroxide through powerful, albeit brute-force, approaches of treating large numbers of water molecules and hydroxide ions directly *ab initio*. With almost three decades of research since the first AIMD simulations of liquid water, several major breakthroughs have been made towards an accurate and comprehensive microscopic understanding of the two-century-old structural/Grotthuss mechanism for H_3O^+ and OH^- diffusion in bulk aqueous environments. These breakthroughs include the following: (i) establishment of the presolvation concept, (ii) identification of a dynamic hypercoordinated solvation structure surrounding the OH^- ion, (iii) discovery of multiple concerted proton-transfer events promoted by water wire compression, and (iv) refinement of the qualitative distinction between Grotthuss diffusion in aqueous OH^- (primarily sequential single jumps) and aqueous H_3O^+ (primarily multiple concerted jumps) using more sophisticated dispersion-corrected hybrid DFT-based AIMD simulations. While there are still open questions regarding the diffusion of H_3O^+ and OH^- in bulk aqueous solutions, *ab initio* simulations of OH^- at interfaces and in confined environments have started to increase our understanding of OH^- diffusion through AEMs in fuel cell applications and beyond. Such simulations are particularly challenging as they simultaneously require an accurate and reliable description of the bond-breaking and bond-forming events underlying structural diffusion in aqueous OH^- as well as sampling extended length and time scales that are currently inaccessible using *ab initio* methods except for some carefully tailored models.[1379,1380] Here, we expect that emerging machine-learning-based *ab initio* simulation techniques[1277−1287] will play a key role and pave the way towards simulating and understanding these challenging systems with unprecedented accuracy and reliability.

We then reviewed in section 9.3 general methods for the first-principles treatment of the effects of electrochemical environments without the need for a brute-force treatment of large numbers of environment molecules. Varied approaches exist to include the key effects of an electrochemical setting, applicable at a spectrum of scales and detail. Advances including polarizable continuum methods (PCMs) and *ab initio* classical density-functional theory (CDFT) aim to balance speed and accuracy of the analysis of solvated systems by abrogating the need for an explicit treatment and thermodynamic sampling of large numbers of liquid molecules. We then discussed how, to be truly informative, such descriptions must also account for compensating ionic charges, particularly when dealing with electrodes with an applied potential. We then described how *ab initio* calculations of applied potentials can be carried out through either a fixed charge or a fixed potential approach. Finally, we emphasized how a full *ab initio* treatment of electrochemical systems requires the use of the above techniques within a unified framework and that joint density-functional theory (JDFT) provides such a framework and captures the inherently challenging nonlinear and long-range response of the fluid to the electrode. This subsection then closed with a review of examples of numerous studies which have utilized such techniques to comprehensively investigate solvation kinetics, behavior at interfaces, and conditions on surfaces.

Finally, in section 9.4, we describe how *ab initio* modeling has been employed to study the degradation of cationic functional groups in AEMs, with the most common approaches involving the identification of potential degradation pathways (for a given candidate cation) using DFT and an implicit solvation model (such as PCMs). Since low free-energy barrier heights typically correspond to facile degradation pathways, such theoretical efforts have also been used to predict which cationic functional groups will be stable in AEMs. In doing so, these efforts have provided valuable insights into the degradation process (i.e., the role of local polymer backbone morphology on degradation) and how one might improve AEM stability (i.e., substituent effects and cation functional group choice). To date, such studies have been in good agreement with experimental stability trends for various cation classes (e.g., tetraalkylammonium, imidazolium, phosphonium, and guanidinium) and have therefore shown great promise for future computational screening studies in this area.

10. CONCLUSIONS AND PERSPECTIVE

In summary, the past decade has resulted in tremendous progress in understanding electrocatalysis in alkaline media and tackling significant challenges in alkaline-based energy technologies. The cost advantages of alkaline fuel cell technologies benefit from the use of nonprecious electrocatalysts for the ORR while it also faces the challenge of a slower HOR, relative to PEMFCs. Theoretical methods, such as DFT and MD simulations, have provided critical insights into the thermodynamic and kinetic aspects of hydrogen and oxygen electrocatalysis and, in particular, the PCET processes with water as the proton donor in alkaline media. Based on extensive electrochemical measurements, the RDSs of the HOR were proposed to be, on one hand, the H_2 adsorption step (Tafel or Heyrovsky step) in acidic media and, on the other hand, its oxidation of adsorbed H (Volmer step) in alkaline media. Various HOR/HER activity descriptors have been proposed to explain the HOR/HER activity in alkaline media. Despite its initial success, H-binding energy is an oversimplified descriptor without considering the local environment of adsorbed H_2O, OH, and alkali cations. The oxophilic effect involving OH adsorption was proposed to explain the significantly enhanced HER activity of $Ni(OH)_2$-modified Pt, and electronic effects have been used to rationalize the outstanding HOR performance of PtRu, relative

https://doi.org/10.1021/acs.chemrev.1c00331
Chem. Rev. XXXX, XXX, XXX−XXX

to Pt. In contrast to those conventional thermodynamic perspectives, the interfacial water structure provides a critical complementary picture of the local environment and is inherently a potential-dependent kinetic property. During the HER, the interfacial water network on Pt is much more rigid in alkaline media than in acidic media since the applied potential is far more negative than the pzfc, leading to a more sluggish HER in alkaline media. The addition of $Ni(OH)_2$ induces a more disordered water structure and thus faster HER kinetics. Nonspecific adsorbed alkali cations are likely to interact with adsorbed H and OH species and strongly modulate the interfacial water structure. Those fundamental studies provide necessary guidance for designing low-Pt and non-PGM HOR electrocatalysts.

Pt single crystals with tunable stepped structures offer a well-defined model system to integrate electrochemical, *operando* spectroscopic and theoretical studies to interrogate ORR mechanisms, which feature the key intermediate species of HO_2 in acid and O_2^- in base along with other O-containing adsorbed species. Kinetic studies of Pt-based RDE measurements suggested a possible $C_sE_1CE_3$ mechanism, involving a fast surface chemical reaction preceding a fast irreversible electron transfer process as the RDSs, which are followed by another chemical reaction and a second multistep $3e^-$ charge-transfer processes. The fundamental difference between the acidic and alkaline ORR on stepped Pt surfaces originates from the potential-dependent interfacial water structures. In particular, given the relative positions of applied potentials vs the pzfc, adsorbed H_2O molecules on charged Pt surfaces exhibit an H-up and H-down configuration in acid and base, respectively. This fundamental difference of the interfacial water structure was used to explain important experimental observations: a higher step density of Pt single crystals leads to a higher ORR activity in acid while Pt(111) exhibits the highest ORR activity, relative to all stepped Pt surfaces, in base. The interfacial water structures were quantified by pzfc/pztc, measured by molecular/ionic probes such as CO, N_2O, and $S_2O_8^{2-}$, and pme, measured by a laser-induced temperature-jumped method.

The newly emerged non-precious-metal and oxide electrocatalysts show great potential in providing a comparable ORR activity to Pt at a much lower cost. Inspired by Pt single crystals, atomically flat oxide thin films were designed to provide precise control of the surface/subsurface compositions and structures to advance our understanding of structure–activity/stability correlations in alkaline media. Several activity descriptors were proposed to rationalize the structure–activity/stability correlations, including e_g electron, metal–oxygen covalency, and oxygen vacancy, among others. In contrast to Pt, metal oxides likely involve the participation of lattice oxygen during the ORR process. It is worthwhile to highlight the fast-developing nonprecious ORR electrocatalysts, such as 3d transition metal oxides (spinel, perovskites, etc.), conductive nitrides/oxynitrides, and atomically dispersed M–N–C. In particular, Co–Mn spinels achieved a performance comparable to that of Pt/C in MEAs and catalyzed the ORR through a synergistic mechanism in which Mn prefers to bind O_2 while Co activates coadsorbed H_2O, which is fundamentally different from the conventional wisdom of ORR mechanisms of Pt-based alloys based on lattice strain and electronic effects. The development of nonprecious ORR electrocatalysts has been the main driving force to achieve comparable AEMFC performances to PEMFCs yet with a significantly lower catalyst cost.

Catalyst supports, although often overlooked, provide necessary electron and mass transport pathways and large-surface-area porous architectures for a high dispersion of catalyst nanoparticles and are corrosion-resistive to maintain their structural integrity during fuel cell operation. Recent developments of noncarbon supports offer additional strategies to modulate the support–catalyst interaction to enhance catalyst activity and, more importantly, to significantly improve catalyst stability.

The recent progress in highly conductive and durable alkaline membranes and ionomers has enabled AEMFCs to achieve an equal or higher power density when compared to PEMFCs. Among the various organic cation moieties discussed herein, piperidinium has attracted an increasing amount of attention for its structural stability and ease of incorporation into polymers, some of which can sustain stable MEA operation over hundreds of hours. Among the polymer backbones discussed, polyethylene and poly(norbornene)s are attractive AEM candidates for their mechanical strength, alkaline stability, and reduced adsorption on metal electrocatalysts, relative to polyarylenes. Ultimately, a balance of ionic content, water uptake, mechanical durability, synthetic feasibility, and catalyst interactions needs to be considered in the design of novel AEMs.

Traditionally, most electrocatalyst development pauses after preliminary activity and stability are demonstrated in half-cell RDE measurements, and most AEM evaluation is constrained to soaking in hydroxide solution. Those divided individual evaluations, despite being useful for high-throughput material screening, provide very limited guidance when translating into realistic fuel cell performance. In this Review, we hope to bridge the gap between catalyst and membrane communities by encouraging more research resources to be devoted to full-cell MEA measurements. Standard MEA fabrication and testing protocols are illustrated to offer an opportunity to faithfully deconvolute scientific progress from device engineering optimization, especially for those newly designed nonprecious oxygen cathodes and hydrogen anodes. The effects of CO_2 in air have received special attention in attempts to tackle the challenges of MEA operation in realistic air. The mass transport of ionic and gas reactants/products still needs to be optimized to accommodate the catalyst kinetics driven at large current densities. With continuous advances in alkaline fuel cell technologies, it is foreseeable to achieve DOE AEMFC MEA milestones of performance $\geq$600 mW/cm^2 with long-term durability under H_2/air in PGM-free MEA by 2030.[874]

In this Review, we present novel *operando*/*in situ* X-ray and STEM characterizations to probe the structural and compositional changes at electrode–electrolyte interfaces, which offer a rare opportunity to monitor an operating electrocatalyst under real-time fuel cell operation conditions. Additionally, cryo-TEM is well-positioned to study the catalyst/ionomer/membrane interfaces with minimal beam damage. Finally, we introduced the recent development of *ab initio* theory, which offers a direct and accurate description of reaction mechanisms in electrochemical environments, such as surface electrocatalysis, PCET, and ion transport in electrolytes and the degradation of polymer membranes. Combining *operando* methods with a theoretical simulation on well-defined catalyst and membrane model systems offers the potential to identify

https://doi.org/10.1021/acs.chemrev.1c00331
Chem. Rev. XXXX, XXX, XXX–XXX

specific reaction pathways that dictate reaction kinetics and selectivity.

In the future, we hope that this Review can guide the community to focus on the scientific understanding of electrocatalysis in alkaline media and alkaline membrane-based energy technologies. We highlight three major challenges facing this fast-growing field.

(1) What factors govern electrocatalysis in alkaline media?
- What are the analogues of quantum confinement in (alkaline) electrocatalysis, including electronic and lattice strain effects, and how can we accurately predict and control them?
- How does PCET (proton-coupled electron transfer) involving the OH^- ion and other molecules prevalent at pH 14 affect the conversion and transport (especially ionic and electronic) of energy?
- What chemical and physical effects do supports exert on electrocatalysts in alkaline media, and how are they reflected in catalyst structure, activity, stability, and selectivity?

(2) How do we understand and control transport in alkaline media?
- How does the architecture of catalysts, supports, and polymer electrolytes control the transport of reactants and products in alkaline electrochemical systems?
- How do we describe the effects of interfacial water activity?
- Can we control/design hydrophobic/hydrophilic interactions to optimize interfacial water management and ionic transport?

(3) What makes energy materials durable in alkaline media?
- Can we understand fundamental degradation mechanisms in alkaline media during transport of OH^-?
- How do the OH^- ions and other species present in alkaline environments affect the stability and structure of polymer membranes at multiple length scales?
- Can we design and synthesize electrolytes with high hydroxide conductivity yet maintain their chemical durability, mechanical strength, water uptake/management, and polymer−electrocatalyst interface stability under operating conditions?

The strategies of investigating hydrogen and oxygen electrocatalysis mechanisms and establishing structure−activity/stability correlations, described herein, are valuable not only for alkaline fuel cells and water electrolyzers but also for many other emerging alkaline-based energy technologies, such as CO_2 and N_2 reduction. The AEMs developed for alkaline hydrogen fuel cells are also suitable for a broad range of fuel cells with easily accessible C-based and N-based fuels such as methanol, ethanol, hydrazine, and ammonia. We anticipate that the continuous developments in electrocatalyst/supports and membrane/ionomers, guided by *operando* methods and theoretical simulation, will lead to groundbreaking advances in addressing fundamental questions for electrocatalysis in alkaline media and achieving affordable alkaline-based renewable energy technologies at a large scale.

AUTHOR INFORMATION

Corresponding Author

Héctor D. Abruna − *Department of Chemistry and Chemical Biology, Cornell University, Ithaca, New York 14853, United States; Center for Alkaline Based Energy Solutions (CABES), Cornell University, Ithaca, New York 14853, United States;* orcid.org/0000-0002-3948-356X; Email: hda1@cornell.edu

Authors

Yao Yang − *Department of Chemistry and Chemical Biology, Cornell University, Ithaca, New York 14853, United States;* orcid.org/0000-0003-0321-3792

Cheyenne R. Peltier − *Department of Chemistry and Chemical Biology, Cornell University, Ithaca, New York 14853, United States;* orcid.org/0000-0003-4654-2051

Rui Zeng − *Department of Chemistry and Chemical Biology, Cornell University, Ithaca, New York 14853, United States;* orcid.org/0000-0002-7577-767X

Roberto Schimmenti − *Department of Chemical and Biological Engineering, University of Wisconsin−Madison, Madison, Wisconsin 53706, United States;* orcid.org/0000-0003-1129-2988

Qihao Li − *College of Chemistry and Molecular Sciences, Wuhan University, Wuhan 430072, China*

Xin Huang − *School of Applied and Engineering Physics, Cornell University, Ithaca, New York 14853, United States;* orcid.org/0000-0001-5404-4437

Zhifei Yan − *Department of Chemistry, University of Pennsylvania, Philadelphia, Pennsylvania 19104, United States*

Georgia Potsi − *Department of Materials Science and Engineering, Cornell University, Ithaca, New York 14853, United States;* orcid.org/0000-0001-5121-0866

Ryan Selhorst − *Department of Chemistry, Carnegie Mellon University, Pittsburgh, Pennsylvania 15213, United States*

Xinyao Lu − *Department of Chemistry and Chemical Biology, Cornell University, Ithaca, New York 14853, United States;* orcid.org/0000-0002-2649-5721

Weixuan Xu − *Department of Chemistry and Chemical Biology, Cornell University, Ithaca, New York 14853, United States*

Mariel Tader − *Department of Physics, Cornell University, Ithaca, New York 14853, United States*

Alexander V. Soudackov − *Department of Chemistry, Yale University, New Haven, Connecticut 06520, United States;* orcid.org/0000-0001-9581-8494

Hanguang Zhang − *Materials Physics and Applications Division, Los Alamos National Laboratory, Los Alamos, New Mexico 87545, United States*

Mihail Krumov − *Department of Chemistry and Chemical Biology, Cornell University, Ithaca, New York 14853, United States*

Ellen Murray − *Department of Chemical and Biological Engineering, University of Wisconsin−Madison, Madison, Wisconsin 53706, United States*

Pengtao Xu − *Department of Materials Science and Engineering, Cornell University, Ithaca, New York 14853, United States;* orcid.org/0000-0002-4470-446X

Jeremy Hitt − *Department of Chemistry, University of Pennsylvania, Philadelphia, Pennsylvania 19104, United States*

https://doi.org/10.1021/acs.chemrev.1c00331
Chem. Rev. XXXX, XXX, XXX−XXX

Linxi Xu − *Department of Chemistry, University of Pennsylvania, Philadelphia, Pennsylvania 19104, United States*
Hsin-Yu Ko − *Department of Chemistry and Chemical Biology, Cornell University, Ithaca, New York 14853, United States;* orcid.org/0000-0003-1619-6514
Brian G. Ernst − *Department of Chemistry and Chemical Biology, Cornell University, Ithaca, New York 14853, United States;* orcid.org/0000-0002-7900-9360
Colin Bundschu − *Department of Physics, Cornell University, Ithaca, New York 14853, United States*
Aileen Luo − *Department of Materials Science and Engineering, Cornell University, Ithaca, New York 14853, United States*
Danielle Markovich − *School of Applied and Engineering Physics, Cornell University, Ithaca, New York 14853, United States*
Meixue Hu − *College of Chemistry and Molecular Sciences, Wuhan University, Wuhan 430072, China*
Cheng He − *Chemical and Materials Science Center, National Renewable Energy Laboratory, Golden, Colorado 80401, United States;* orcid.org/0000-0002-6236-4761
Hongsen Wang − *Department of Chemistry and Chemical Biology, Cornell University, Ithaca, New York 14853, United States;* orcid.org/0000-0001-7926-2895
Jiye Fang − *Department of Chemistry, State University of New York at Binghamton, Binghamton, New York 13902, United States*
Robert A. DiStasio, Jr. − *Department of Chemistry and Chemical Biology, Cornell University, Ithaca, New York 14853, United States;* orcid.org/0000-0003-2732-194X
Lena F. Kourkoutis − *School of Applied and Engineering Physics and Kavli Institute at Cornell for Nanoscale Science, Cornell University, Ithaca, New York 14853, United States;* orcid.org/0000-0002-1303-1362
Andrej Singer − *Department of Materials Science and Engineering, Cornell University, Ithaca, New York 14853, United States;* orcid.org/0000-0002-2965-9242
Kevin J. T. Noonan − *Department of Chemistry, Carnegie Mellon University, Pittsburgh, Pennsylvania 15213, United States;* orcid.org/0000-0003-4061-7593
Li Xiao − *College of Chemistry and Molecular Sciences, Wuhan University, Wuhan 430072, China;* orcid.org/0000-0002-6416-3138
Lin Zhuang − *College of Chemistry and Molecular Sciences, Wuhan University, Wuhan 430072, China;* orcid.org/0000-0002-5642-6735
Bryan S. Pivovar − *Chemical and Materials Science Center, National Renewable Energy Laboratory, Golden, Colorado 80401, United States*
Piotr Zelenay − *Materials Physics and Applications Division, Los Alamos National Laboratory, Los Alamos, New Mexico 87545, United States;* orcid.org/0000-0002-8962-9520
Enrique Herrero − *Instituto de Electroquímica, Universidad de Alicante, Alicante E-03080, Spain;* orcid.org/0000-0002-4509-9716
Juan M. Feliu − *Instituto de Electroquímica, Universidad de Alicante, Alicante E-03080, Spain;* orcid.org/0000-0003-4751-3279
Jin Suntivich − *Department of Materials Science and Engineering and Kavli Institute at Cornell for Nanoscale Science, Cornell University, Ithaca, New York 14853, United States;* orcid.org/0000-0002-3427-4363
Emmanuel P. Giannelis − *Department of Materials Science and Engineering, Cornell University, Ithaca, New York 14853, United States*
Sharon Hammes-Schiffer − *Department of Chemistry, Yale University, New Haven, Connecticut 06520, United States;* orcid.org/0000-0002-3782-6995
Tomás Arias − *Department of Physics, Cornell University, Ithaca, New York 14853, United States*
Manos Mavrikakis − *Department of Chemical and Biological Engineering, University of Wisconsin−Madison, Madison, Wisconsin 53706, United States;* orcid.org/0000-0002-5293-5356
Thomas E. Mallouk − *Department of Chemistry, University of Pennsylvania, Philadelphia, Pennsylvania 19104, United States;* orcid.org/0000-0003-4599-4208
Joel D. Brock − *School of Applied and Engineering Physics, Cornell University, Ithaca, New York 14853, United States*
David A. Muller − *School of Applied and Engineering Physics and Kavli Institute at Cornell for Nanoscale Science, Cornell University, Ithaca, New York 14853, United States;* orcid.org/0000-0003-4129-0473
Francis J. DiSalvo − *Department of Chemistry and Chemical Biology, Cornell University, Ithaca, New York 14853, United States*
Geoffrey W. Coates − *Department of Chemistry and Chemical Biology, Cornell University, Ithaca, New York 14853, United States;* orcid.org/0000-0002-3400-2552

Complete contact information is available at: https://pubs.acs.org/10.1021/acs.chemrev.1c00331

Notes

The authors declare no competing financial interest.

Biographies

Yao Yang received his B.S. in Chemistry at Wuhan University (2015), Ph.D. in Chemistry at Cornell University (2021), and Miller Postdoctoral Fellowship at UC Berkeley (2021−2024). He focuses on the design and synthesis of nonprecious ORR electrocatalysts and the use and development of *operando* electrochemical liquid-cell STEM and synchrotron-based X-ray methods for an atomic-scale mechanistic understanding of interfacial electrocatalysis.

Cheyenne R. Peltier received her B.S. in Chemistry from Stanford University in 2018. She is currently a Ph.D. candidate in the Coates Group at Cornell University. Her research focuses on the design and synthesis of alkaline-stable polymer electrolytes.

Rui Zeng obtained his B.S. in Materials Physics from Wuhan University in 2015. Rui is currently pursuing a Ph.D. at Cornell University in the Abruna group. His main research interests include developing nonprecious electrocatalysts for alkaline fuel cells and employing differential electrochemical mass spectrometry for energy-related applications.

Roberto Schimmenti is a postdoctoral researcher at the University of Wisconsin—Madison. He received his Ph.D. in Materials Science from the University of Catania (Italy) in 2017 and his M.Sc. in Chemistry from the University of Palermo (Italy) in 2013. His research focuses on the elucidation of reaction mechanism and electrocatalysts dissolution processes under reaction conditions, through the use of electronic-structure methods.

Qihao Li received his B.S. in Chemistry from Wuhan University (2016). He is now pursuing a Ph.D. in Lin Zhuang's group. His research mainly focuses on alkaline electrolyte membrane fuel cell

https://doi.org/10.1021/acs.chemrev.1c00331
Chem. Rev. XXXX, XXX, XXX−XXX

device techniques and the development of nonprecious catalysts, including non-PGM HOR and ORR catalysts.

Xin Huang received his Ph.D. from the School of Applied & Engineering Physics at Cornell University in 2017. He is currently a postdoctoral associate in Cornell High Energy Synchrotron Source, working on *in situ/operando* X-ray studies in energy-related electrochemical systems and self-assembly of shaped nanocrystals.

Zhifei Yan received his B.S. in Chemistry from the China University of Geosciences (2015) and his Ph.D. in Chemistry from the University of Pennsylvania (2021). His research focuses on the ion management and mass transport in various electrochemical energy conversion systems.

Georgia Potsi is a postdoctoral associate at Cornell University. She owns a double Ph.D. in Materials Science from the University of Groningen (The Netherlands) and University of Ioannina (Greece) awarded in 2016. Her research focuses on the synthesis and characterization of carbon allotropes and 2D inorganic materials.

Ryan Selhorst is currently a Senior Research Scientist at Ecolectro Inc. He obtained an M.S. and Ph.D. in Polymer Science and Engineering from the University of Massachusetts Amherst and a Postdoctoral Research position at Carnegie Mellon University in Professor Kevin Noonan's lab working on the synthesis of novel materials for AEMs.

Xinyao Lu received her B.S. in Chemistry at Nanjing University in 2016. She then joined Prof. Héctor D. Abruna's group as a Ph.D. student at Cornell University. Her research focuses on the development and characterization of electrocatalysts and polymer electrolyte materials for AEMFCs.

Weixuan Xu received her B.S. at Nanjing University in 2018. She is currently a Ph.D. candidate at Cornell University under the supervision of Prof. Héctor Abruna. Her main research interest focuses on the synthesis of MOF-derived electrocatalysts for the oxygen reduction reaction (ORR) in alkaline fuel cells.

Mariel Tader received her BS in Mathematics and Physics at Case Western Reserve University in 2016. She is currently a Ph.D. candidate in Physics in the Arias group at Cornell University. Her research focuses on theory for membranes and catalysis in alkaline fuel cells using joint density-functional theory (JDFT) methods.

Alexander V. Soudackov received his M.S. in Chemistry from the Lomonosov Moscow State University and his Ph.D. in Physics and Mathematics from Karpov Institute of Physical Chemistry in Moscow, Russia. He is currently a research scientist in the Hammes-Schiffer group at Yale University.

Hanguang Zhang completed his Ph.D. in Chemical Engineering from the State University of New York at Buffalo (2019). He has been a postdoctoral researcher at Los Alamos National Laboratory since 2019. His current research focuses on the development of platinum group metal-free catalysts for electrocatalysis and fuel cells.

Mihail Krumov received his B.S. (2018) in Chemical Engineering at University of Illinois Urbana—Champaign. He is now pursuing a Ph.D. in the Abruna group at Cornell University. His research focuses on the use of scanning electrochemical microscopy for elucidating fundamental mechanisms in energy applications.

Ellen Murray received her B.S. in Chemical Engineering and B.S. in Biochemistry from the Colorado School of Mines in 2014. In 2020, she received her PhD in Chemical Engineering from the University of Wisconsin—Madison under the supervision of Prof. Manos Mavrikakis. Her research interests focus on electrocatalysis and electronic materials.

Pengtao Xu received his Ph.D. in Chemistry from The Pennsylvania State University (2018). He is currently a postdoctoral researcher at Cornell University. His research focuses on the development of novel spectroscopic techniques to characterize electrochemical interfaces and elucidate electrocatalytic reaction mechanisms.

Jeremy Hitt received a B.S. in Chemistry with an additional major in Physics and minor in Mathematics from The University of Alabama in 2017. He is currently pursuing a Ph.D. in Chemistry at the University of Pennsylvania under the supervision of Prof. Thomas E. Mallouk where his work is centered around electrocatalysis in fuel cells and carbon dioxide reduction.

Linxi Xu received her B.S. in Chemistry and Computer Science from Wofford College in 2018. She is a third-year graduate student in the Mallouk group at the University of Pennsylvania. She studies electrocatalysis, especially the electrocatalysts for the oxygen reduction reaction in alkaline fuel cells.

Hsin-Yu Ko is a Postdoctoral Researcher in the DiStasio Group at Cornell University. He completed his Ph.D. in Theoretical Chemistry (2019) with Roberto Car at Princeton University. His research interests include developing algorithms for *ab initio* simulations of condensed-phase systems.

Brian G. Ernst grew up in Walnutport Pennsylvania. He received his B.S. in Chemistry from The Pennsylvania State University in 2016. He is currently a Ph.D. student at Cornell University in the DiStasio group studying the theory and applications of density-functional theory.

Colin Bundschu obtained his B.S. in Computer Science from Harvey Mudd College and his M.S. in Applied Physics from Cornell University. He is currently pursuing a Ph.D. in Applied Physics in the Arias Group at Cornell University. His research focuses on developing *ab initio* methods for calculating electrochemical reaction pathways.

Aileen Luo received her B.S. in Materials Science and Engineering from UC Berkeley in 2019. She is currently pursuing her Ph.D. at Cornell University, and her research focuses on synchrotron-based X-ray characterization techniques. She is interested in energy materials and condensed matter systems.

Danielle Markovich received her B.S. in Engineering Physics at the University of Illinois at Urbana—Champaign (2019) and is pursuing a Ph.D. in Applied Physics at Cornell University. Her research involves the development of electron microscopy methods with a focus on studying energy materials.

Meixue Hu obtained her B.S. in Chemistry from Wuhan University (2017). She is now a Ph.D. candidate in the Lin Zhuang group. Her research focuses on designing alkaline polymer electrolytes (both membrane and ionomer) to achieve high-performance and proper water management for alkaline electrolyte membrane fuel cells.

Cheng He completed his Ph.D. in Chemical Engineering from Washington University in St. Louis under Prof. Vijay Ramani in 2019. He is currently a postdoctoral researcher in National Renewable Energy Laboratory. He is now working on high-performance alkaline fuel cell electrode design and diagnostics.

Hongsen Wang received his Ph.D. in Physical Chemistry from Beijing Normal University in 2001. He is now a senior research associate in Prof. Abruna's group at Cornell University. His research mainly focuses on developing alkaline fuel cell catalysts and employing DEMS, FTIR, DFT, and KMC simulations for mechanistic studies of energy-related electrocatalysis.

Jiye Fang is Professor of Chemistry and Materials Science & Engineering at State University of New York at Binghamton. His

https://doi.org/10.1021/acs.chemrev.1c00331
Chem. Rev. XXXX, XXX, XXX−XXX

current research interests include the synthesis of shape-controlled nanocrystals, self-assembly and superstructure, lattice strain study on noble-metal-based nanocrystals, and advanced catalysts for fuel cell applications in acidic and alkaline media.

Robert A. DiStasio Jr. is an Assistant Professor of Chemistry and Chemical Biology at Cornell University. An active contributor to the Q-Chem and Quantum ESPRESSO software packages, DiStasio focuses on the development, implementation, and application of novel methodologies that extend the frontiers of electronic structure theory in condensed-phase environments.

Lena F. Kourkoutis is an Associate Professor of Applied and Engineering Physics at Cornell University and the co-director of the Platform for the Accelerated Realization, Analysis, and Discovery of Interface Materials (PARADIM). Her group focuses on the development of novel cryogenic electron microscopy approaches to probe interface processes in materials and devices.

Andrej Singer is an Assistant Professor in the department of Materials Science and Engineering at Cornell University. His research focuses on using coherent X-ray scattering techniques at synchrotrons and free-electron lasers to study nonequilibrium phenomena in a wide range of materials, spanning from quantum materials to applied energy materials in *operando* devices.

Kevin J. T. Noonan is a Canadian-born chemist who completed his Ph.D. and postdoc work at UBC and Cornell. He joined the Department of Chemistry at Carnegie Mellon in 2011 where he is currently an Associate Professor. His research interests are broadly centered around designing new molecules and polymers.

Li Xiao received her B.S. and Ph.D. from Wuhan University in Chemistry in 2005 and 2010, followed by one year visiting in Prof. Abruna's lab at Cornell University. She is now an associate professor in electrochemistry at College of Chemistry and Molecular Science at Wuhan University. Her research focuses on fundamental studies and mechanistic insights of electrode polyelectrolyte interfaces, specifically for energy conversion reactions.

Lin Zhuang is the Chuan-Sin Cha Professor in Electrochemistry at College of Chemistry and Molecular Sciences, Wuhan University. His research has been focused on electrocatalysis and hydrogen energy technology, including fuel cells, water electrolysis, and CO_2 conversion.

Bryan S. Pivovar is a Senior Research Fellow at the National Renewable Energy Laboratory where he oversees electrolysis and fuel cell R&D. He has been a pioneer and has served leadership roles in several technical areas related to fuel cell and electrolysis technology including subfreezing effects, alkaline membranes, extended surface electrocatalysis, and H_2@Scale.

Piotr Zelenay is Professor of Chemistry, Fellow of the Electrochemical Society, and Laboratory Fellow at Los Alamos National Laboratory. He is an expert in electrocatalysis and electrochemical energy conversion, including polymer electrolyte fuel cells. The primary focus of his internationally acclaimed research has been in recent years on platinum-group-metal-free electrocatalysts for the oxygen reduction reaction.

Enrique Herrero is Professor of Physical Chemistry at the University of Alicante, Spain. His research focuses on understanding the mechanism of reactions involved in fuel cells using well defined surfaces and the effect of the surface structure and interfacial properties in the reactivity.

Juan M. Feliu is Professor of Physical Chemistry at the University of Alicante. His research aims to establish relationships between surface structure and composition of metallic electrodes and its reactivity. He received the B.E. Conway Award (2008), the C.N. Reilley Award (2017), the A. Arevalo SIBAE Price (2018), and the ISE Gold Medal (2018) and is Editor-in-Chief of *Journal of Electroanalytical Chemistry* since 2015.

Jin Suntivich is an associate professor of Materials Science and Engineering at Cornell University. He received his B.S. in Materials Science and Engineering and B.A. in Integrated Science from Northwestern University and his Sc.D. in Materials Science and Engineering from Massachusetts Institute of Technology. Prior to Cornell, he was a postdoctoral fellow at Harvard University. His research focuses on electrochemical interfaces and materials for energy and sustainability.

Emmanuel P. Giannelis is the Walter R. Read Professor of Engineering and the Vice President for Research and Innovation at Cornell. His recent research has focused on Nanomaterials for Energy. He is a Fellow of the American Chemical Society, and he is a member of the European Academy of Sciences.

Sharon Hammes-Schiffer received her B.A. in Chemistry from Princeton University in 1988 and her Ph.D. in Chemistry from Stanford University in 1993, followed by two years at AT&T Bell Laboratories. She was the Clare Boothe Luce Assistant Professor at the University of Notre Dame from 1995−2000, the Eberly Professor of Biotechnology at Pennsylvania State University until 2012, and the Swanlund Professor of Chemistry at the University of Illinois at Urbana—Champaign. Since 2018, she has been the John Gamble Kirkwood Professor of Chemistry at Yale University.

Tomás Arias obtained his S.B. and Ph.D. from MIT and is currently Professor of Physics at Cornell University. He has published ∼80 scientific articles on novel methods for first-principles calculations to address complex condensed-matter phenomena, with a recent focus on joint density-functional theory (JDFT) descriptions of electrochemical environments.

Manos Mavrikakis is the Paul A. Elfers Professor of Chemical Engineering at the University of Wisconsin—Madison. His research interests include first-principles and microkinetic modeling of heterogeneous catalysis and electrocatalysis. He received the 2014 R. H. Wilhelm Award in Chemical Reaction Engineering (AIChE) and the 2019 Gabor A. Somorjai Award for Creative Research in Catalysis (ACS) and served as Editor-in-Chief of *Surface Science* between 2012 and 2020.

Thomas E. Mallouk is the Vagelos Professor in Energy Research in the Department of Chemistry at the University of Pennsylvania. His research focuses on the synthesis of inorganic materials and their application to solar and electrochemical energy conversion, surface chemistry and electrocatalysis, nano- and microrobotics, and low-dimensional physical phenomena.

Joel D. Brock is the Given Foundation Professor of Engineering in the School of Applied & Engineering Physics at Cornell University and is the Director of the Cornell High Energy Synchrotron Source (CHESS). He applies synchrotron-based X-ray scattering to materials research and develops new synchrotron-based X-ray tools and techniques.

David A. Muller is the Samuel B. Eckert Professor of Engineering in the School of Applied and Engineering Physics at Cornell University and co-director of the Kavli Institute for Nanoscale Science at Cornell. His research interests include new electron microscopy methods for the atomic-scale control and characterization of matter for applications in energy storage and conversion.

https://doi.org/10.1021/acs.chemrev.1c00331
Chem. Rev. XXXX, XXX, XXX−XXX

Francis J. DiSalvo is the John A. Newman Professor of Physical Science at Cornell University since 1996. He was elected to the National Academy of Sciences in 1991. His group synthesizes, characterizes, and tests nanoscale materials, including solid state oxides, nitrides, or intermetallic compounds, for possible applications to renewable energy systems, such as catalysts or catalyst supports for fuel cells or electrodes for batteries.

Geoffrey W. Coates was born in Evansville, IN. He received his B.A. in Chemistry from Wabash College in 1989 and Ph.D. from Stanford University in 1994. After being an NSF Postdoctoral Fellow at the California Institute of Technology, he joined the faculty at Cornell University in 1997. Research in the Coates group focuses on the preparation of new polymer architectures.

Héctor D. Abruna was born and raised in Puerto Rico. He received a B.S. in Chemistry from Rensselaer Polytechnic Institute in 1975 and a Ph.D. in 1980 from the University of North Carolina at Chapel Hill. From 1980 to 1981 he was a Post-Doctoral Associate with A.J. Bard at the University of Texas at Austin. After a brief stay at the University of Puerto Rico, he joined Cornell in 1983 and was Chairman of the Department of Chemistry and Chemical Biology from 2004 to 2008. He considers his students and Post-Docs as his most important achievements and contributions.

ACKNOWLEDGMENTS

This work was supported by the Center for Alkaline-Based Energy Solutions, an Energy Frontier Research Center program supported by the U.S. Department of Energy, under Grant DE-SC0019445. This work acknowledges the long-term support of TEM facilities at the Cornell Center for Materials Research (CCMR) which are supported through the National Science Foundation Materials Research Science and Engineering Center (NSF MRSEC) program (DMR1719875), and Cornell high-energy synchrotron sources (CHESS), which is supported by the National Science Foundation under Award DMR-1332208. We thank Alexandra Macbeth in the Coates group at Cornell University for intellectual discussion and comments on the manuscript.

ABBREVIATIONS

AAEMFC = alkaline anion exchange membrane fuel cell
ADT = accelerated durability testing
AEM = anion exchange membrane
AEMFC = anion exchange membrane fuel cell
AFC = alkaline fuel cell
AFM = atomic force microscopy
AIMD = *ab initio* molecular dynamics
ALD = atomic layer deposition
AM = alkali metals
APE = alkaline polymer electrolyte
APEFC = alkaline polymer electrolyte fuel cell
AP-XPS = ambient pressure X-ray photoelectron spectroscopy
ATR-FTIR = attenuated total reflection Fourier-transform infrared spectroscopy
BEP = Brønsted−Evans−Polanyi
BET = Brunauer−Emmett−Teller
BF = bright-field
BMOF = bimetallic organic framework
BTMA = benzyltrimethylammonium
CO_2 = O_2 solubility
CB = carbon black
CCM = catalyst-coated membrane
CDFT = classical density-functional theory
CDI = coherent diffractive imaging
CE = counter electrode
CEE = constant emission energy
CET = constant energy transfer
CHE = computational hydrogen electrode
CL = catalyst layer
CNF = carbon nanofiber
CNT = carbon nanotube
COBRA = coherent Bragg rod analysis
COE = cyclooctene
CP = chronopotentiometry
Cryo-TEM = cryogenic transmission electron microscopy
CT = computed tomography
CTR = crystal truncation rod
CV = cyclic voltammetry
CVD = chemical vapor deposition
CWDOS = cumulative weighted densities of states
CyMe = cyclohexylmethyl phosphonium
DABCO = 1,4-diazabicyclo[2.2.2]octane
DCAF = difference map using the constraints of atomicity and film shift
DEMS = differential electrochemical mass spectrometry
DFT = density-functional theory
DISP = disproportionation
DMA = dynamic mechanical analysis
DMP = dimethylpiperidinium
DOE = Department of Energy
DPD = dissipative particle dynamics
dq = degree of quaternization
DSC = differential scanning calorimetry
DWNT = double-wall carbon nanotube
E_F = Fermi level
e_g = electron occupancy
E_{onset} = onset potential
ECSA = electrochemical surface area
EC-STEM = electrochemical liquid-cell scanning transmission electron microscopy
EC-XPS = electrochemical X-ray photoelectron spectroscopy
EDL = electrochemical double layer
EDX = energy-dispersive X-ray spectroscopy
EELS = electron energy loss spectroscopy
EFEI = external forces explicitly included
EF-TEM = energy-filtered transmission electron microscopy
EIS = electrochemical impedance spectroscopy
ELNES = energy-loss near-edge structure
equiv = equivalent
EQCM = electrochemical quartz crystal microbalance
ETFE = poly(ethylene-*co*-tetrafluoroethylene)
EV = electric vehicle
EVB = empirical valence bond
EWPC = exit-wave power-cepstrum
EXAFS = extended X-ray absorption fine structure
fcc = face centered cubic
FCEV = fuel cell electric vehicle
FED = free-energy diagram
FEP = fluorinated ethylene-propylene
Fe-TPPCN = nitrile-functionalized Fe-porphyrin derivative
Fe-TTP = Fe meso-tetraphenylporphyrine chloride
FLN = poly(fluorene)
FOV = field of view
FTIR = Fourier-transform infrared spectroscopy

https://doi.org/10.1021/acs.chemrev.1c00331
Chem. Rev. XXXX, XXX, XXX−XXX

GC−MS = gas chromatography−mass spectrometry
GDE = gas diffusion electrode
GDL = gas diffusion layer
GGA = generalized gradient approximation
GISAXS = grazing incident small-angle X-ray scattering
GNP = graphene nanoplate
GO = graphene oxide
H_{opd} = overpotential deposited hydrogen
H_{upd} = hydrogen underpotential deposition
HAADF-STEM = high-angle annular dark-field scanning transmission electron microscopy
HAP = hydroxyapatite
HB = hydrogen bond
HBE = hydrogen binding energy
HB-PVBC = hyperbranched poly(vinylbenzyl chloride)
hcp = hexagonal closest packed
HDPE = high-density polyethylene
HEMFC = hydroxide exchange membrane fuel cell
HER = hydrogen evolution reaction
HERFD = high-energy resolution fluorescence detection
HERFD-XAS = high-energy resolution fluorescence detection X-ray absorption spectroscopy
HOMO = highest occupied molecular orbital
HOPG = highly oriented pyrolytic graphite
HOR = hydrogen oxidation reaction
HSAB = hard−soft/acid−base
HSC = high-surface-area carbon
i_0 = exchange current
i_k = kinetic current
I_{lim} = diffusion-limited current
ICP-MS = inductively coupled mass spectroscopy
IEC = ion exchange capacity
IL-TEM = identical location transmission electron microscopy
IPA = isopropyl alcohol
IPN = interpenetrating poly network
IPrMe = isopropyl methyl phosphonium
IRRAS = infrared reflection absorption spectroscopy
ITC = isothermal titration calorimetry
ITO = indium tin oxide
j_k = kinetic current density
j_{lim} = diffusion-limited current density
j_m = measured current density
j_p = peak current density
JDFT = joint density-functional theory
k° = reaction rate constant
KB = Ketjen Black
KIE = kinetic isotope effect
KMC = kinetic Monte Carlo
LC-TEM = liquid-cell transmission electron microscopy
LDPE = low-density polyethylene
LEED = later low-energy electron diffraction
LRLO = lithium-rich layered oxide
LSM = layered synthetic microstructure
LSV = linear sweep voltammetry
LUMO = lowest unoccupied molecular orbital
MA = mass-specific activity
maBPP = multiangle Bragg projection ptychography
MBE = molecular beam epitaxy
MD = molecular dynamics
MEA = membrane electrode assembly
MKM = microkinetic model
MOF = metal−organic framework
M−N−C = metal-containing N-doped carbon
MPB = modified Poisson−Boltzmann
MW = molecular weight
MWCNT = multiwall carbon nanotube
NBED = nanobeam electron diffraction
N−C = nitrogen-doped carbon
N−C−CoO_x = nitrogen-doped carbon−CoO_x
NP = nanoparticle
NQE = nuclear quantum effect
NRR = nitrogen reduction reaction
NSA = near-surface alloys
NSTF = nanostructured thin film
NW = nanowire
OCP = open circuit potential
OCV = open circuit voltage
OER = oxygen evolution reaction
ORR = oxygen reduction reaction
PA = poly(aromatics) or poly(arylene)
PAE = poly(arylene ether)
PAES = poly(arylene ether sulfone)
PAN = polyacrylonitrile
PARADIGM = phase and amplitude recovery and diffraction image generation method
PBI = poly(benzimidazole)
PBP = poly(biphenylene)
PCET = proton-coupled electron transfer
PCM = polarizable continuum model
PDS = peroxodisulfate, $S_2O_8^{2-}$
PE = polyethylene
PED = pulse electrodeposition
PEG = poly(ethylene glycol)
PEMFC = proton exchange membrane fuel cell
PEPM = piperidinium-functionalized polyethylene membranes
PGM = precious group metal
pH_{pzc} = pH of zero change
PLD = pulsed laser deposition
pme = potential of maximum entropy
PNB = polynorbornene
PP = polyphenylene
PPD = peak power density
PPF = postpolymerization functionalization
PPy = polypyrrole
PS = polystyrene
PTFE = polytetrafluoroethylene
PTP = poly(terphenylene)
PVA = poly(vinyl alcohol)
pzc = potential of zero charge
pzfc = potential of zero free charge
pztc = potential of zero total charge
QA = quaternary ammonium
QAPPT = poly(*p*-terphenyl-piperidinium)
QAPS = quaternary ammonium-functionalized poly(arylene ether sulfone)
QMMD = quantum mechanics molecular dynamics
QM/MM = quantum mechanics/molecular mechanics
R_{ct} = charge-transfer resistance
RCP = region of constant potential
RDE = rotating disk electrode
RDeE = reversible deuterium electrode
RDS = rate-determining step
RE = reference electrode
rGO = reduced graphene oxide

https://doi.org/10.1021/acs.chemrev.1c00331
Chem. Rev. XXXX, XXX, XXX−XXX

RH = relative humidity
RHE = reversible hydrogen electrode
RIXS = resonant inelastic X-ray scattering
ROMP = ring-opening metathesis polymerization
RPD = reaction phase diagram
rPNB = ring-opening metathesis polymerization polynorbornene
RRDE = rotating ring disk electrode
SA = surface-specific activity
SANS = small-angle neutron scattering
SAXS = small-angle X-ray scattering
sccm = standard cubic centimeters per min
SEBS = poly(styrene-ethylene-*co*-butylene-styrene)
SECM = scanning electrochemical microscopy
SEIRAS = surface-enhanced infrared spectrometry
SERS = surface-enhanced Raman spectroscopy
SFG = sum frequency generation
SHE = standard hydrogen electrode
SHG = second harmonic generation
SHINERS = shell-isolated nanoparticles-enhanced Raman spectroscopy
SIE = self-interaction error
SMSI = strong metal−support interaction
SP = spirocyclic piperidinium
STEM = scanning transmission electron microscopy
STM = scanning tunneling microscopy
STXM = scanning transmission X-ray microscopy
SWCNT = single-wall carbon nanotube
T_c = crystallization temperature
T_g = glass transition temperature
T_m = melting transition temperature
$t_{1/2}$ = half-life time
TEM = transmission electron microscopy
TER = total external reflection
TFY = total fluorescence yield
TGA = thermogravimetric analysis
T-jump = temperature-jump
TMA = trimethylammonium or tetramethylammonium
TMAOH = trimethylammonium hydroxide
TMHDA = *N*,*N*,*N*,*N*-tetramethylhexamethylenediamine
TMO = transition metal oxide
TOF = turnover frequency
TPB = triple phase boundary
TXM = transmission X-ray microscopy
TS = transition state
TST = transition sate theory
UHV = ultrahigh vacuum
UME = ultra-microelectrode
UPD = underpotential deposition
UV−vis = ultraviolet−visible
va = vinyl addition polymerization
vaPNB = vinyl addition polymerization polynorbornene
vdW = van der Waals
v/v = volume/volume
WAXS = wide-angle X-ray scattering
WC = tungsten carbide
WE = working electrode
wt % = weight percent
WU = water uptake
XANES = X-ray absorption near-edge structure
XAS = X-ray absorption spectrometry
XL = cross-link
XPS = X-ray photoelectron spectroscopy
XRD = X-ray diffraction
XRF = X-ray fluorescence
XSW = X-ray standing wave
ZIF = zeolitic imidazolate framework
ΔG = Gibbs free energy
ΔS° = standard entropy change
ΔH° = standard enthalpy change
ΔG° = standard Gibbs free-energy change
ΔG^f = formal molar Gibbs free energy
ΔG_O = adsorption energy of oxygen

REFERENCES

(1) Abruña, H. D. Energy in the Age of Sustainability. *J. Chem. Educ.* **2013**, *90*, 1411−1413.
(2) Pivovar, B. Catalysts for Fuel Cell Transportation and Hydrogen Related Uses. *Nat. Catal.* **2019**, *2*, 562−565.
(3) Debe, M. Electrocatalyst Approaches and Challenges for Automotive Fuel Cells. *Nature* **2012**, *486*, 43−51.
(4) Pivovar, B.; Rustagi, N.; Satyapal, S. Hydrogen at Scale (H_2@ Scale) Key to a Clean, Economic, and Sustainable Energy System. *Electrochem. Soc. Interface* **2018**, *27*, 47−52.
(5) Schiller, M. Hydrogen Energy Storage: The Holy Grail for Renewable Energy Grid Integration. *Fuel Cells Bulletin* **2013**, *2013*, 12−15.
(6) Borup, R.; et al. Scientific Aspects of Polymer Electrolyte Fuel Cell Durability and Degradation. *Chem. Rev.* **2007**, *107*, 3904−3951.
(7) Gasteiger, H. A.; Kocha, S. S.; Somali, B.; Wagner, F. T. Activity Benchmarks and Requirements for Pt, Pt-alloy, and non-Pt Oxygen Reduction Catalysts for PEMFCs. *Appl. Catal., B* **2005**, *56*, 9−35.
(8) Shao, M.; Chao, Q.; Dodelet, J.-P.; Chenitz, R. Recent Advances in Electrocatalysts for Oxygen Reduction Reaction. *Chem. Rev.* **2016**, *116*, 3594−3657.
(9) Papageorgopoulos, D. *Annual Merit Review and Peer Evaluation Meeting in Fuel Cells Program Area*; U.S. Department of Energy: Washington, DC, 2019.
(10) Ge, X.; Sumboja, A.; Wuu, D.; An, T.; Li, B.; Goh, F. W. T.; Hor, T. S. A.; Zong, Y.; Liu, Z. Oxygen Reduction in Alkaline Media: From Mechanisms to Recent Advances of Catalysts. *ACS Catal.* **2015**, *5*, 4643−4667.
(11) Zhao, Q.; Yan, Z.; Chen, C.; Chen, J. Spinels: Controlled Preparation, Oxygen Reduction/Evolution Reaction Application, and Beyond. *Chem. Rev.* **2017**, *117*, 10121−10211.
(12) Varcoe, J. R.; Slade, R. C. T. An Electron-Beam-Grafted ETFE Alkaline Anion-Exchange Membrane in Metal-Cation-Free Solid-State Alkaline Fuel Cells. *Electrochem. Commun.* **2006**, *8*, 839−843.
(13) Lu, S.; Pan, J.; Huang, A.; Zhuang, L.; Lu, J. Alkaline Polymer Electrolyte Fuel Cells Completely Free from Noble Metal Catalysts. *Proc. Natl. Acad. Sci. U. S. A.* **2008**, *105*, 20611−20614.
(14) Varcoe, J. R.; Atanassov, P.; Dekel, D. R.; Herring, A. M.; Hickner, M. A.; Kohl, P. A.; Kucernak, A. R.; Mustain, W. E.; Nijmeijer, K.; Scott, K.; Xu, T.; Zhuang, L. Anion-Exchange Membranes in Electrochemical Energy Systems. *Energy Environ. Sci.* **2014**, *7*, 3135−3191.
(15) Gottesfeld, S.; Dekel, D. R.; Page, M.; Bae, C.; Yan, Y.; Zelenay, P.; Kim, Y. S. Anion Exchange Membrane Fuel Cells: Current Status and Remaining Challenges. *J. Power Sources* **2018**, *375*, 170−184.
(16) Wang, Y.; Yang, Y.; Jia, S.; Wang, X.; Lyu, K.; Peng, Y.; Zheng, H.; Wei, X.; Ren, H.; Xiao, L.; Wang, J.; Muller, D. A.; Abruna, H. D.; Hwang, B. J.; Lu, J.; Zhuang, L. Synergistic Mn-Co Catalyst Outperforms Pt on High-Rate Oxygen Reduction Reaction for Alkaline Polymer Electrolyte Fuel Cells. *Nat. Commun.* **2019**, *10*, 1506.
(17) Davydova, E. S.; Mukerjee, S.; Jaouen, F.; Dekel, D. R. Electrocatalysts for HOR in Alkaline Media. *ACS Catal.* **2018**, *8*, 6665−6690.
(18) Yang, Y.; Xiong, Y.; Zeng, R.; Lu, X.; Krumov, M.; Huang, X.; Xu, W.; Wang, H.; DiSalvo, F. J.; Brock, J. D.; Muller, D. A.; Abruna,

https://doi.org/10.1021/acs.chemrev.1c00331
Chem. Rev. XXXX, XXX, XXX−XXX

H. D. Operando Methods in Electrocatalysis. *ACS Catal.* **2021**, *11*, 1136−1178.
(19) Trasatti, S. Work Function, Electronegativity, and Electrochemical Behaviour of Metals: III. Electrolytic Hydrogen Evolution in Acid Solutions. *J. Electroanal. Chem. Interfacial Electrochem.* **1972**, *39*, 163−184.
(20) Nørskov, J. K.; Bligaard, T.; Logadottir, A.; Kitchin, J. R.; Chen, J. G.; Pandelov, S.; Stimming, U. Trends in the Exchange Current for Hydrogen Evolution. *J. Electrochem. Soc.* **2005**, *152*, J23−J26.
(21) Sheng, W.; Myint, M.; Chen, J. G.; Yan, Y. Correlating the Hydrogen Evolution Reaction Activity in Alkaline Electrolytes with the Hydrogen Binding Energy on Monometallic Surfaces. *Energy Environ. Sci.* **2013**, *6*, 1509−1512.
(22) Durst, J.; Siebel, A.; Simon, C.; Hasché, F.; Herranz, J.; Gasteiger, H. A. New Insights into the Electrochemical Hydrogen Oxidation and Evolution Reaction Mechanism. *Energy Environ. Sci.* **2014**, *7*, 2255−2260.
(23) Sheng, W.; Zhuang, Z.; Gao, M.; Zheng, J.; Chen, J. G.; Yan, Y. Correlating Hydrogen Oxidation and Evolution Activity on Platinum at Different PH with Measured Hydrogen Binding Energy. *Nat. Commun.* **2015**, *6*, 5848.
(24) Subbaraman, R.; Tripkovic, D.; Strmcnik, D.; Chang, K. C.; Uchimura, M.; Paulikas, A. P.; Stamenkovic, V.; Markovic, N. M. Enhancing Hydrogen Evolution Activity in Water Splitting by Tailoring Li+-Ni(OH)2-Pt Interfaces. *Science* **2011**, *334*, 1256−1260.
(25) Strmcnik, D.; Uchimura, M.; Wang, C.; Subbaraman, R.; Danilovic, N.; van der Vliet, D.; Paulikas, A. P.; Stamenkovic, V. R.; Markovic, N. M. Improving the Hydrogen Oxidation Reaction Rate by Promotion of Hydroxyl Adsorption. *Nat. Chem.* **2013**, *5*, 300−306.
(26) Ledezma-Yanez, I.; Wallace, W. D. Z.; Sebastián-Pascual, P.; Climent, V.; Feliu, J. M.; Koper, M. T. M. Interfacial Water Reorganization as a PH-Dependent Descriptor of the Hydrogen Evolution Rate on Platinum Electrodes. *Nat. Energy* **2017**, *2*, 17031.
(27) Ryu, J.; Surendranath, Y. Tracking Electrical Fields at the Pt/H_2O Interface during Hydrogen Catalysis. *J. Am. Chem. Soc.* **2019**, *141*, 15524−15531.
(28) Chen, B. W. J.; Xu, L.; Mavrikakis, M. Computational Methods in Heterogeneous Catalysis. *Chem. Rev.* **2021**, *121*, 1007.
(29) Marshall, A. T. Using Microkinetic Models to Understand Electrocatalytic Reactions. *Curr. Opin. Electrochem.* **2018**, *7*, 75−80.
(30) Intikhab, S.; Snyder, J. D.; Tang, M. H. Adsorbed Hydroxide Does Not Participate in the Volmer Step of Alkaline Hydrogen Electrocatalysis. *ACS Catal.* **2017**, *7*, 8314−8319.
(31) Rebollar, L.; Intikhab, S.; Snyder, J. D.; Tang, M. H. Determining the Viability of Hydroxide-Mediated Bifunctional HER/HOR Mechanisms through Single-Crystal Voltammetry and Microkinetic Modeling. *J. Electrochem. Soc.* **2018**, *165*, J3209−J3221.
(32) Lamoureux, P. S.; Singh, A. R.; Chan, K. PH Effects on Hydrogen Evolution and Oxidation over Pt(111): Insights from First-Principles. *ACS Catal.* **2019**, *9*, 6194−6201.
(33) Liu, L.; Liu, Y.; Liu, C. Enhancing the Understanding of Hydrogen Evolution and Oxidation Reactions on Pt(111) through Ab Initio Simulation of Electrode/Electrolyte Kinetics. *J. Am. Chem. Soc.* **2020**, *142*, 4985−4989.
(34) McCrum, I. T.; Koper, M. T. M. The Role of Adsorbed Hydroxide in Hydrogen Evolution Reaction Kinetics on Modified Platinum. *Nat. Energy* **2020**, *5*, 891−899.
(35) Nørskov, J. K.; Rossmeisl, J.; Logadottir, A.; Lindqvist, L.; Kitchin, J. R.; Bligaard, T.; Jónsson, H. Origin of the Overpotential for Oxygen Reduction at a Fuel-Cell Cathode. *J. Phys. Chem. B* **2004**, *108*, 17886−17892.
(36) Chatenet, M.; Genies-Bultel, L.; Aurousseau, M.; Durand, R.; Andolfatto, F. Oxygen Reduction on Silver Catalysts in Solutions Containing Various Concentrations of Sodium Hydroxide - Comparison with Platinum. *J. Appl. Electrochem.* **2002**, *32*, 1131−1140.
(37) Hoogers, G.; Thompsett, D. Catalysis in Proton Exchange Membrane Fuel Cell Technology. *CaTTech (Amst.)* **1999**, *3*, 106−124.
(38) Koper, M. T. M. Theory of Multiple Proton-Electron Transfer Reactions and Its Implications for Electrocatalysis. *Chem. Sci.* **2013**, *4*, 2710−2723.
(39) Li, M. F.; Liao, L. W.; Yuan, D. F.; Mei, D.; Chen, Y.-X. pH Effect on Oxygen Reduction Reaction at Pt(111) Electrode. *Electrochim. Acta* **2013**, *110*, 780−789.
(40) Štrbac, S.; AdŠić, R. R. The Influence of pH on Reaction Pathways for O2 Reduction on the Au(100) Face. *Electrochim. Acta* **1996**, *41*, 2903−2908.
(41) Mei, D.; He, Z. D.; Zheng, Y. L.; Jiang, D. C.; Chen, Y.-X. Mechanistic and Kinetic Implications on the ORR on a Au(100) Electrode: pH, Temperature and H-D Kinetic Isotope Effects. *Phys. Chem. Chem. Phys.* **2014**, *16*, 13762−13773.
(42) Blizanac, B. B.; Ross, P. N.; Markovic, N. M. Oxygen Electroreduction on Ag(111): The pH Effect. *Electrochim. Acta* **2007**, *52*, 2264−2271.
(43) Van Velzen, C. J.; Sluyters-Rehbach, M.; Remijnse, A. G.; Brug, G. J.; Sluyters, J. H. The Electrochemical Reduction of Oxygen to Hydrogen Peroxide at the Dropping Mercury Electrode: Part I. Its Kinetics at 605 pH<12.5. *J. Electroanal. Chem. Interfacial Electrochem.* **1982**, *134*, 87−100.
(44) Koper, M. T. M. Volcano Activity Relationships for Proton-Coupled Electron Transfer Reactions in Electrocatalysis. *Top. Catal.* **2015**, *58*, 1153−1158.
(45) Quaino, P.; Luque, N. B.; Nazmutdinov, R.; Santos, E.; Schmickler, W. Why Is Gold Such a Good Catalyst for Oxygen Reduction in Alkaline Media? *Angew. Chem., Int. Ed.* **2012**, *51*, 12997−13000.
(46) Staszak-Jirkovský, J.; Subbaraman, R.; Strmcnik, D.; Harrison, K. L.; Diesendruck, C. E.; Assary, R.; Frank, O.; Kobr, L.; Wiberg, G. K. H.; Genorio, B.; Connell, J. G.; Lopes, P. P.; Stamenkovic, V. R.; Curtiss, L.; Moore, J. S.; Zavadil, K. R.; Markovic, N. M. Water as a Promoter and Catalyst for Dioxygen Electrochemistry in Aqueous and Organic Media. *ACS Catal.* **2015**, *5*, 6600−6607.
(47) Stamenkovic, V. R.; Strmcnik, D.; Lopes, P. P.; Markovic, N. M. Energy and Fuels from Electrochemical Interfaces. *Nat. Mater.* **2017**, *16*, 57−69.
(48) Li, X.; Wang, H.; Cui, Z.; Li, Y.; Xin, S.; Zhou, J.; Long, Y.; Jin, C.; Goodenough, J. B. Exceptional Oxygen Evolution Reactivities on $CaCoO_3$ and $SrCoO_3$. *Sci. Adv.* **2019**, *5*, No. eaav6262.
(49) Liu, H.; Yu, J.; Sunarso, J.; Zhou, C.; Liu, B.; Shen, Y.; Zhou, W.; Shao, Z. Mixed Protonic-Electronic Conducting Perovskite Oxide as a Robust Oxygen Evolution Reaction Catalyst. *Electrochim. Acta* **2018**, *282*, 324−330.
(50) Grimaud, A.; Diaz-Morales, O.; Han, B.; Hong, W. T.; Lee, Y.-L.; Giordano, L.; Stoerzinger, K. A.; Koper, M. T. M.; Shao-Horn, Y. Activating Lattice Oxygen Redox Reactions in Metal Oxides to Catalyse Oxygen Evolution. *Nat. Chem.* **2017**, *9*, 457−465.
(51) Han, B.; Grimaud, A.; Giordano, L.; Hong, W. T.; Diaz-Morales, O.; Yueh-Lin, L.; Hwang, J.; Charles, N.; Stoerzinger, K. A.; Yang, W.; Koper, M. T. M.; Shao-Horn, Y. Iron-Based Perovskites for Catalyzing Oxygen Evolution Reaction. *J. Phys. Chem. C* **2018**, *122*, 8445−8454.
(52) Seh, Z. W.; Kibsgaard, J.; Dickens, C. F.; Chorkendorff, I.; Nørskov, J. K.; Jaramillo, T. F. Combining Theory and Experiment in Electrocatalysis: Insights into Materials Design. *Science* **2017**, *355*, No. eaad4998.
(53) Vojvodic, A.; Nørskov, J. K. New Design Paradigm for Heterogeneous Catalysts. *National Science Review* **2015**, *2*, 140−143.
(54) Dumesic, J. A.; Rudd, D. F.; Aparicio, L. M.; Rekoske, J. E.; Trevino, A. A. *The Microkinetics of Heterogeneous Catalysis*; American Chemical Society: Washington, DC, 1993.
(55) Bhandari, S.; Rangarajan, S.; Mavrikakis, M. Combining Computational Modeling with Reaction Kinetics Experiments for Elucidating the In Situ Nature of the Active Site in Catalysis. *Acc. Chem. Res.* **2020**, *53*, 1893−1904.
(56) Motagamwala, A. H.; Dumesic, J. A. Microkinetic Modeling: A Tool for Rational Catalyst Design. *Chem. Rev.* **2021**, *121*, 1049−1076.

https://doi.org/10.1021/acs.chemrev.1c00331
Chem. Rev. XXXX, XXX, XXX−XXX

(57) Motagamwala, A. H.; Ball, M. R.; Dumesic, J. A. Microkinetic Analysis and Scaling Relations for Catalyst Design. *Annu. Rev. Chem. Biomol. Eng.* **2018**, *9*, 413−450.
(58) Chan, K.; Nørskov, J. K. Potential Dependence of Electrochemical Barriers from Ab Initio Calculations. *J. Phys. Chem. Lett.* **2016**, *7*, 1686−1690.
(59) Ikeshoji, T.; Otani, M. Toward Full Simulation of the Electrochemical Oxygen Reduction Reaction on Pt Using First-Principles and Kinetic Calculations. *Phys. Chem. Chem. Phys.* **2017**, *19*, 4447−4453.
(60) Herron, J. A.; Morikawa, Y.; Mavrikakis, M. Ab Initio Molecular Dynamics of Solvation Effects on Reactivity at Electrified Interfaces. *Proc. Natl. Acad. Sci. U. S. A.* **2016**, *113*, E4937−E4945.
(61) Chan, K.; Nørskov, J. K. Electrochemical Barriers Made Simple. *J. Phys. Chem. Lett.* **2015**, *6*, 2663−2668.
(62) Tripković, V.; Skúlason, E.; Siahrostami, S.; Nørskov, J. K.; Rossmeisl, J. The Oxygen Reduction Reaction Mechanism on Pt(111) from Density Functional Theory Calculations. *Electrochim. Acta* **2010**, *55*, 7975−7981.
(63) Hansen, H. A.; Viswanathan, V.; Nørskov, J. K. Unifying Kinetic and Thermodynamic Analysis of 2 e- and 4 e- Reduction of Oxygen on Metal Surfaces. *J. Phys. Chem. C* **2014**, *118*, 6706−6718.
(64) Markovic, N.; Gasteiger, H.; Ross, P. N. Kinetics of Oxygen Reduction on Pt(hkl) Electrodes: Implications for the Crystallite Size Effect with Supported Pt Electrocatalysts. *J. Electrochem. Soc.* **1997**, *144*, 1591−1597.
(65) Stamenkovic, V. R.; Fowler, B.; Mun, B. S.; Wang, G.; Ross, P. N.; Lucas, C. A.; Marković, N. M. Improved Oxygen Reduction Activity on $Pt_3Ni(111)$ via Increased Surface Site Availability. *Science* **2007**, *315*, 493−497.
(66) Shao, M. H.; Huang, T.; Liu, P.; Zhang, J.; Sasaki, K.; Vukmirovic, M. B.; Adzic, R. R. Palladium Monolayer and Palladium Alloy Electrocatalysts for Oxygen Reduction. *Langmuir* **2006**, *22*, 10409−10415.
(67) Stephens, I. E. L.; Bondarenko, A. S.; Perez-Alonso, F. J.; Calle-Vallejo, F.; Bech, L.; Johansson, T. P.; Jepsen, A. K.; Frydendal, R.; Knudsen, B. P.; Rossmeisl, J.; Chorkendorff, I. Tuning the Activity of Pt(111) for Oxygen Electroreduction by Subsurface Alloying. *J. Am. Chem. Soc.* **2011**, *133*, 5485−5491.
(68) Campbell, C. T. The Degree of Rate Control: A Powerful Tool for Catalysis Research. *ACS Catal.* **2017**, *7*, 2770−2779.
(69) Stegelmann, C.; Andreasen, A.; Campbell, C. T. Degree of Rate Control: How Much the Energies of Intermediates and Transition States Control Rates. *J. Am. Chem. Soc.* **2009**, *131*, 8077−8082.
(70) Exner, K. S.; Over, H. Kinetics of Electrocatalytic Reactions from First-Principles: A Critical Comparison with the Ab Initio Thermodynamics Approach. *Acc. Chem. Res.* **2017**, *50*, 1240−1247.
(71) Tripkovic, V.; Vegge, T. Potential- and Rate-Determining Step for Oxygen Reduction on Pt(111). *J. Phys. Chem. C* **2017**, *121*, 26785−26793.
(72) Rebarchik, M.; Bhandari, S.; Kropp, T.; Mavrikakis, M. How Noninnocent Spectator Species Improve the Oxygen Reduction Activity of Single-Atom Catalysts: Microkinetic Models from First-Principles Calculations. *ACS Catal.* **2020**, *10*, 9129−9135.
(73) Guo, C.; Fu, X.; Xiao, J. Theoretical Insights on the Synergy and Competition between Thermochemical and Electrochemical Steps in Oxygen Electroreduction. *J. Phys. Chem. C* **2020**, *124*, 25796−25804.
(74) Liu, S.; White, M. G.; Liu, P. Oxygen Reduction Reaction on Ag(111) in Alkaline Solution: A Combined Density Functional Theory and Kinetic Monte Carlo Study. *ChemCatChem* **2018**, *10*, 540−549.
(75) Lu, F.; Zhang, Y.; Liu, S.; Lu, D.; Su, D.; Liu, M.; Zhang, Y.; Liu, P.; Wang, J. X.; Adzic, R. R.; Gang, O. Surface Proton Transfer Promotes Four-Electron Oxygen Reduction on Gold Nanocrystal Surfaces in Alkaline Solution. *J. Am. Chem. Soc.* **2017**, *139*, 7310−7317.
(76) Liu, S.; White, M. G.; Liu, P. Mechanism of Oxygen Reduction Reaction on Pt(111) in Alkaline Solution: Importance of Chemisorbed Water on Surface. *J. Phys. Chem. C* **2016**, *120*, 15288−15298.
(77) Duan, Z.; Henkelman, G. Theoretical Resolution of the Exceptional Oxygen Reduction Activity of Au(100) in Alkaline Media. *ACS Catal.* **2019**, *9*, 5567−5573.
(78) Kelly, S. R.; Kirk, C.; Chan, K.; Nørskov, J. K. Electric Field Effects in Oxygen Reduction Kinetics: Rationalizing pH Dependence at the Pt(111), Au(111), and Au(100) Electrodes. *J. Phys. Chem. C* **2020**, *124*, 14581−14591.
(79) Ignaczak, A.; Nazmutdinov, R.; Goduljan, A.; Moreira de Campos Pinto, L.; Juarez, F.; Quaino, P.; Santos, E.; Schmickler, W. A Scenario for Oxygen Reduction in Alkaline Media. *Nano Energy* **2016**, *26*, 558−564.
(80) Ignaczak, A.; Santos, E.; Schmickler, W. Oxygen Reduction Reaction on Gold in Alkaline Solutions - The Inner or Outer Sphere Mechanisms in the Light of Recent Achievements. *Curr. Opin. Electrochem.* **2019**, *14*, 180−185.
(81) Goduljan, A.; de Campos Pinto, L. M.; Juarez, F.; Santos, E.; Schmickler, W. Oxygen Reduction on Ag(100) in Alkaline Solutions-A Theoretical Study. *ChemPhysChem* **2016**, *17*, 500−505.
(82) Schmidt, T. J.; Ross, P. N.; Markovic, N. M. Temperature Dependent Surface Electrochemistry on Pt Single Crystals in Alkaline Electrolytes: Part 2. The Hydrogen Evolution/Oxidation Reaction. *J. Electroanal. Chem.* **2002**, *524-525*, 252−260.
(83) Sheng, W.; Gasteiger, H. A.; Shao-Horn, Y. Hydrogen Oxidation and Evolution Reaction Kinetics on Platinum: Acid vs Alkaline Electrolytes. *J. Electrochem. Soc.* **2010**, *157*, B1529−B1536.
(84) Stephens, I. E. L.; Bondarenko, A. S.; Grønbjerg, U.; Rossmeisl, J.; Chorkendorff, I. Understanding the Electrocatalysis of Oxygen Reduction on Platinum and Its Alloys. *Energy Environ. Sci.* **2012**, *5*, 6744−6762.
(85) Dogonadze, R. R.; Kuznetsov, A. M.; Levich, V. G. Quantum Theory of Hydrogen Overvoltage. *Russ. J. Electrochem.* **1967**, *3*, 739−742.
(86) Dogonadze, R. R.; Kuznetsov, A. M.; Levich, V. G. Theory of Hydrogen-Ion Discharge on Metals: Case of High Overvoltages. *Electrochim. Acta* **1968**, *13*, 1025−1044.
(87) McIntyre, J. D. E.; Salomon, M. Kinetic Isotope Effects in the Hydrogen Electrode Reaction. *J. Phys. Chem.* **1968**, *72*, 2431−2434.
(88) Dogonadze, R. R.; Kuznetsov, A. M.; Vorotyntsev, M. A. The Kinetics of the Adiabatic and Nonadiabatic Reactions at the Metal and Semiconductor Electrodes. *Croat. Chim. Acta* **1972**, *44*, 257−273.
(89) Krishtalik, L. I. Proton Transfer in Electrode Reactions - Experimental Test of Two Theoretical Models. *Faraday Discuss. Chem. Soc.* **1982**, *74*, 205−213.
(90) Koper, M. T. M.; Schmickler, W. A Kramers Reaction Rate Theory for Electrochemical Ion Transfer Reactions. *Chem. Phys.* **1996**, *211*, 123−133.
(91) Schmickler, W. *Interfacial Electrochemistry*; Oxford University Press: New York, 1996.
(92) Zhang, T.; Anderson, A. B. Hydrogen Oxidation and Evolution on Platinum Electrodes in Base: Theoretical Study. *J. Phys. Chem. C* **2007**, *111*, 8644−8648.
(93) Wilhelm, F.; Schmickler, W.; Nazmutdinov, R. R.; Spohr, E. A Model for Proton Transfer to Metal Electrodes. *J. Phys. Chem. C* **2008**, *112*, 10814−10826.
(94) Santos, E.; Lundin, A.; Pötting, K.; Quaino, P.; Schmickler, W. Model for the Electrocatalysis of Hydrogen Evolution. *Phys. Rev. B: Condens. Matter Mater. Phys.* **2009**, *79*, 235436.
(95) Skúlason, E.; Tripkovic, V.; Björketun, M. E.; Gudmundsdóttir, S.; Karlberg, G.; Rossmeisl, J.; Bligaard, T.; Jónsson, H.; Nørskov, J. K. Modeling the Electrochemical Hydrogen Oxidation and Evolution Reactions on the Basis of Density Functional Theory Calculations. *J. Phys. Chem. C* **2010**, *114*, 18182−18197.
(96) Wilhelm, F.; Schmickler, W.; Nazmutdinov, R.; Spohr, E. Modeling Proton Transfer to Charged Silver Electrodes. *Electrochim. Acta* **2011**, *56*, 10632−10644.

https://doi.org/10.1021/acs.chemrev.1c00331
Chem. Rev. XXXX, XXX, XXX−XXX

(97) Quaino, P.; Santos, E.; Soldano, G.; Schmickler, W. Recent Progress in Hydrogen Electrocatalysis. *Adv. Phys. Chem.* **2011**, *2011*, 1−14.
(98) Santos, E.; Quaino, P.; Schmickler, W. Theory of Electrocatalysis: Hydrogen Evolution and More. *Phys. Chem. Chem. Phys.* **2012**, *14*, 11224−11233.
(99) Goldsmith, Z. K.; Lam, Y. C.; Soudackov, A. V.; Hammes-Schiffer, S. Proton Discharge on a Gold Electrode from Triethylammonium in Acetonitrile: Theoretical Modeling of Potential-Dependent Kinetic Isotope Effects. *J. Am. Chem. Soc.* **2019**, *141*, 1084−1090.
(100) Lam, Y. C.; Soudackov, A. V.; Goldsmith, Z. K.; Hammes-Schiffer, S. Theory of Proton Discharge on Metal Electrodes: Electronically Adiabatic Model. *J. Phys. Chem. C* **2019**, *123*, 12335−12345.
(101) Lam, Y. C.; Soudackov, A. V.; Hammes-Schiffer, S. Kinetics of Proton Discharge on Metal Electrodes: Effects of Vibrational Nonadiabaticity and Solvent Dynamics. *J. Phys. Chem. Lett.* **2019**, *10*, 5312−5317.
(102) Lam, Y.-C.; Soudackov, A. V.; Hammes-Schiffer, S. Theory of Electrochemical Proton-Coupled Electron Transfer in Diabatic Vibronic Representation: Application to Proton Discharge on Metal Electrodes in Alkaline Solution. *J. Phys. Chem. C* **2020**, *124*, 27309−27322.
(103) Kucernak, A. R.; Zalitis, C. General Models for the Electrochemical Hydrogen Oxidation and Hydrogen Evolution Reactions: Theoretical Derivation and Experimental Results under near Mass-Transport Free Conditions. *J. Phys. Chem. C* **2016**, *120*, 10721−10745.
(104) McCrum, I. T.; Janik, M. J. pH and Alkali Cation Effects on the Pt Cyclic Voltammogram Explained Using Density Functional Theory. *J. Phys. Chem. C* **2016**, *120*, 457−471.
(105) Jia, Q.; Liu, E.; Jiao, L.; Li, J.; Mukerjee, S. Current Understandings of the Sluggish Kinetics of the Hydrogen Evolution and Oxidation Reactions in Base. *Curr. Opin. Electrochem.* **2018**, *12*, 209−217.
(106) Zhang, Y.; Lei, H.; Duan, D.; Villota, E.; Liu, C.; Ruan, R. New Insight into the Mechanism of the Hydrogen Evolution Reaction on MoP(001) from First Principles. *ACS Appl. Mater. Interfaces* **2018**, *10*, 20429−20439.
(107) Huang, J.; Li, P.; Chen, S. Quantitative Understanding of the Sluggish Kinetics of Hydrogen Reactions in Alkaline Media Based on a Microscopic Hamiltonian Model for the Volmer Step. *J. Phys. Chem. C* **2019**, *123*, 17325−17334.
(108) Zhao, L.; Liu, H.; Liu, Y.; Han, X.; Xu, J.; Xing, W.; Guo, W. Mechanistic Insights into the Hydrogen Oxidation Reaction on Ptni Alloys in Alkaline Media: A First-Principles Investigation. *ACS Appl. Mater. Interfaces* **2020**, *12*, 40248−40260.
(109) Cross, R. W.; Dzade, N. Y. First-Principles Mechanistic Insights into the Hydrogen Evolution Reaction on Ni_2P Electrocatalyst in Alkaline Medium. *Catalysts* **2020**, *10*, 307.
(110) Huang, J.; et al. Boosting Hydrogen Transfer During Volmer Reaction at Oxides/Metal Nanocomposites for Efficient Alkaline Hydrogen Evolution. *ACS Energy Lett.* **2019**, *4*, 3002−3010.
(111) Liu, E. S.; Li, J. K.; Jiao, L.; Doan, H. T. T.; Liu, Z. Y.; Zhao, Z. P.; Huang, Y.; Abraham, K. M.; Mukerjee, S.; Jia, Q. Y. Unifying the Hydrogen Evolution and Oxidation Reactions Kinetics in Base by Identifying the Catalytic Roles of Hydroxyl-Water-Cation Adducts. *J. Am. Chem. Soc.* **2019**, *141*, 3232−3239.
(112) Li, J.; Ghoshal, S.; Bates, M. K.; Miller, T. E.; Davies, V.; Stavitski, E.; Attenkofer, K.; Mukerjee, S.; Ma, Z. F.; Jia, Q. Experimental Proof of the Bifunctional Mechanism for the Hydrogen Oxidation in Alkaline Media. *Angew. Chem., Int. Ed.* **2017**, *56*, 15594−15598.
(113) Chen, X. T.; McCrum, I. T.; Schwarz, K. A.; Janik, M. J.; Koper, M. T. M. Co-Adsorption of Cations as the Cause of the Apparent Ph Dependence of Hydrogen Adsorption on a Stepped Platinum Single-Crystal Electrode. *Angew. Chem., Int. Ed.* **2017**, *56*, 15025−15029.
(114) Strmcnik, D.; Lopes, P. P.; Genorio, B.; Stamenkovic, V. R.; Markovic, N. M. Design Principles for Hydrogen Evolution Reaction Catalyst Materials. *Nano Energy* **2016**, *29*, 29−36.
(115) Chen, A.; Lipkowski, J. Electrochemical and Spectroscopic Studies of Hydroxide Adsorption at the Au(111) Electrode. *J. Phys. Chem. B* **1999**, *103*, 682−691.
(116) Luo, Y.; Li, X.; Cai, X.; Zou, X.; Kang, F.; Cheng, H.-M.; Liu, B. Two-Dimensional MoS_2 Confined $Co(OH)_2$ Electrocatalysts for Hydrogen Evolution in Alkaline Electrolytes. *ACS Nano* **2018**, *12*, 4565−4573.
(117) Xu, Z.; Li, W.; Yan, Y.; Wang, H.; Zhu, H.; Zhao, M.; Yan, S.; Zou, Z. In-Situ Formed Hydroxide Accelerating Water Dissociation Kinetics on Co 3 N for Hydrogen Production in Alkaline Solution. *ACS Appl. Mater. Interfaces* **2018**, *10*, 22102−22109.
(118) Zhong, H.-F.; Yin, H.; Zhang, D.-X.; Gan, L.-Y.; Wang, P. Intrinsically Synergistic Active Centers Coupled with Surface Metal Doping to Facilitate Alkaline Hydrogen Evolution Reaction. *J. Phys. Chem. C* **2019**, *123*, 24220−24224.
(119) Venkataraman, C.; Soudackov, A. V.; Hammes-Schiffer, S. Theoretical Formulation of Nonadiabatic Electrochemical Proton-Coupled Electron Transfer at Metal-Solution Interfaces. *J. Phys. Chem. C* **2008**, *112*, 12386−12397.
(120) Navrotskaya, I.; Soudackov, A. V.; Hammes-Schiffer, S. Model System-Bath Hamiltonian and Nonadiabatic Rate Constants for Proton-Coupled Electron Transfer at Electrode-Solution Interfaces. *J. Chem. Phys.* **2008**, *128*, 244712.
(121) Hammes-Schiffer, S.; Soudackov, A. V. Proton-Coupled Electron Transfer in Solution, Proteins, and Electrochemistry. *J. Phys. Chem. B* **2008**, *112*, 14108−14123.
(122) Soudackov, A.; Hammes-Schiffer, S. Derivation of Rate Expressions for Nonadiabatic Proton-Coupled Electron Transfer Reactions in Solution. *J. Chem. Phys.* **2000**, *113*, 2385−2396.
(123) Zusman, L. D. Outer-Sphere Electron Transfer Reactions at an Electrode. *Chem. Phys.* **1987**, *112*, 53−59.
(124) Zusman, L. D. Outer-Sphere Electron Transfer in Polar Solvents. *Chem. Phys.* **1980**, *49*, 295−304.
(125) Smith, B. B.; Hynes, J. T. Electronic Friction and Electron Transfer Rates at Metallic Electrodes. *J. Chem. Phys.* **1993**, *99*, 6517−6530.
(126) Sakaushi, K. Quantum Proton Tunneling in Multi-Electron/-Proton Transfer Electrode Processes. *Faraday Discuss.* **2020**, *221*, 428−448.
(127) Sakaushi, K. Observation of Kinetic Isotope Effect in Electrocatalysis with Fully Deuterated Ultrapure Electrolytes. *J. Electroanal. Chem.* **2019**, *849*, 113372.
(128) Vielstich, W., Lamm, A., Gasteiger, H. A., Yokokawa, H., Eds. *Handbook of Fuel Cells - Fundamentals, Technology and Applications*; John Wiley & Sons, Ltd: Chichester, UK, 2010.
(129) Durst, J.; Simon, C.; Siebel, A.; Rheinländer, P. J.; Schuler, T.; Hanzlik, M.; Herranz, J.; Hasché, F.; Gasteiger, H. A. (Invited) Hydrogen Oxidation and Evolution Reaction (HOR/HER) on Pt Electrodes in Acid vs Alkaline Electrolytes: Mechanism, Activity and Particle Size Effects. *ECS Trans.* **2014**, *64*, 1069−1080.
(130) Marković, N. M.; Grgur, B. N.; Ross, P. N. Temperature-Dependent Hydrogen Electrochemistry on Platinum Low-Index Single-Crystal Surfaces in Acid Solutions. *J. Phys. Chem. B* **1997**, *101*, 5405−5413.
(131) Shinagawa, T.; Garcia-Esparza, A. T.; Takanabe, K. Insight on Tafel Slopes from a Microkinetic Analysis of Aqueous Electrocatalysis for Energy Conversion. *Sci. Rep.* **2015**, *5*, 13801.
(132) Durst, J.; Simon, C.; Hasché, F.; Gasteiger, H. A. Hydrogen Oxidation and Evolution Reaction Kinetics on Carbon Supported Pt, Ir, Rh, and Pd Electrocatalysts in Acidic Media. *J. Electrochem. Soc.* **2015**, *162*, F190−F203.
(133) Chen, S.; Kucernak, A. Electrocatalysis under Conditions of High Mass Transport: Investigation of Hydrogen Oxidation on Single Submicron Pt Particles Supported on Carbon. *J. Phys. Chem. B* **2004**, *108*, 13984−13994.

https://doi.org/10.1021/acs.chemrev.1c00331
Chem. Rev. XXXX, XXX, XXX−XXX

(134) Wang, J. X.; Springer, T. E.; Adzic, R. R. Dual-Pathway Kinetic Equation for the Hydrogen Oxidation Reaction on Pt Electrodes. *J. Electrochem. Soc.* **2006**, *153*, A1732−A1740.
(135) Zoski, C. G. Scanning Electrochemical Microscopy: Investigation of Hydrogen Oxidation at Polycrystalline Noble Metal Electrodes. *J. Phys. Chem. B* **2003**, *107*, 6401−6405.
(136) Neyerlin, K. C.; Gu, W.; Jorne, J.; Gasteiger, H. A. Study of the Exchange Current Density for the Hydrogen Oxidation and Evolution Reactions. *J. Electrochem. Soc.* **2007**, *154*, B631−B635.
(137) Sun, Y.; Lu, J.; Zhuang, L. Rational Determination of Exchange Current Density for Hydrogen Electrode Reactions at Carbon-Supported Pt Catalysts. *Electrochim. Acta* **2010**, *55*, 844−850.
(138) Zalitis, C. M.; Kramer, D.; Kucernak, A. R. Electrocatalytic Performance of Fuel Cell Reactions at Low Catalyst Loading and High Mass Transport. *Phys. Chem. Chem. Phys.* **2013**, *15*, 4329−4340.
(139) Markovića, N. M.; Sarraf, S. T.; Gasteiger, H. A.; Ross, P. N. Hydrogen Electrochemistry on Platinum Low-Index Single-Crystal Surfaces in Alkaline Solution. *J. Chem. Soc., Faraday Trans.* **1996**, *92*, 3719−3725.
(140) Rheinländer, P. J.; Herranz, J.; Durst, J.; Gasteiger, H. A. Kinetics of the Hydrogen Oxidation/Evolution Reaction on Polycrystalline Platinum in Alkaline Electrolyte Reaction Order with Respect to Hydrogen Pressure. *J. Electrochem. Soc.* **2014**, *161*, F1448−F1457.
(141) Ertl, G., Knözinger, H., Schüth, F., Weitkamp, J., Eds. *Handbook of Heterogeneous Catalysis*, 2nd ed.; Wiley-VCH Verlag GmbH: Weinheim, Germany, 2008; Vol. *1*.
(142) Conway, B. E.; Tilak, B. V. Interfacial Processes Involving Electrocatalytic Evolution and Oxidation of H_2, and the Role of Chemisorbed H. *Electrochim. Acta* **2002**, *47*, 3571−3594.
(143) Sibert, E.; Faure, R.; Durand, R. High Frequency Impedance Measurements on Pt(111) in Sulphuric and Perchloric Acids. *J. Electroanal. Chem.* **2001**, *515*, 71−81.
(144) Łósiewicz, B.; Jurczakowski, R.; Lasia, A. Kinetics of Hydrogen Underpotential Deposition at Polycrystalline Platinum in Acidic Solutions. *Electrochim. Acta* **2012**, *80*, 292−301.
(145) Bagotzky, V. S.; Osetrova, N. V. Investigations of Hydrogen Ionization on Platinum with the Help of Micro-Electrodes. *J. Electroanal. Chem. Interfacial Electrochem.* **1973**, *43*, 233−249.
(146) Tarasevich, M. R.; Korchagin, O. V. Electrocatalysis and pH (a Review). *Russ. J. Electrochem.* **2013**, *49*, 600−618.
(147) Appleby, A. J. Electrocatalysis and Fuel Cells. *Catal. Rev.: Sci. Eng.* **1971**, *4*, 221−244.
(148) Zheng, J.; Sheng, W.; Zhuang, Z.; Xu, B.; Yan, Y. Universal Dependence of Hydrogen Oxidation and Evolution Reaction Activity of Platinum-Group Metals on pH and Hydrogen Binding Energy. *Sci. Adv.* **2016**, *2*, No. e1501602.
(149) Herranz, J.; Durst, J.; Fabbri, E.; Patru, A.; Cheng, X.; Permyakova, A. A.; Schmidt, T. J. Interfacial Effects on the Catalysis of the Hydrogen Evolution, Oxygen Evolution and CO_2-Reduction Reactions for (Co-)Electrolyzer Development. *Nano Energy* **2016**, *29*, 4−28.
(150) Zheng, J.; Nash, J.; Xu, B.; Yan, Y. Perspective—Towards Establishing Apparent Hydrogen Binding Energy as the Descriptor for Hydrogen Oxidation/Evolution Reactions. *J. Electrochem. Soc.* **2018**, *165*, H27−H29.
(151) Cheng, T.; Wang, L.; Merinov, B. V.; Goddard, W. A. Explanation of Dramatic PH-Dependence of Hydrogen Binding on Noble Metal Electrode: Greatly Weakened Water Adsorption at High PH. *J. Am. Chem. Soc.* **2018**, *140*, 7787−7790.
(152) Kim, J.; Kim, H.; Lee, W. J.; Ruqia, B.; Baik, H.; Oh, H. S.; Paek, S. M.; Lim, H. K.; Choi, C. H.; Choi, S. Il Theoretical and Experimental Understanding of Hydrogen Evolution Reaction Kinetics in Alkaline Electrolytes with Pt-Based Core-Shell Nanocrystals. *J. Am. Chem. Soc.* **2019**, *141*, 18256−18263.
(153) Van Der Niet, M. J. T. C.; Garcia-Araez, N.; Hernández, J.; Feliu, J. M.; Koper, M. T. M. Water Dissociation on Well-Defined Platinum Surfaces: The Electrochemical Perspective. *Catal. Today* **2013**, *202*, 105−113.
(154) Strmcnik, D.; Tripkovic, D.; van der Vliet, D.; Stamenkovic, V.; Marković, N. M. Adsorption of Hydrogen on Pt(1 1 1) and Pt(1 0 0) Surfaces and Its Role in the HOR. *Electrochem. Commun.* **2008**, *10*, 1602−1605.
(155) Marković, N. M.; Ross, P. N. Surface Science Studies of Model Fuel Cell Electrocatalysts. *Surf. Sci. Rep.* **2002**, *45*, 117−229.
(156) Tadjeddine, A.; Peremans, A. Vibrational Spectroscopy of the Electrochemical Interface by Visible Infrared Sum Frequency Generation. *J. Electroanal. Chem.* **1996**, *409*, 115−121.
(157) Kunimatsu, K.; Senzaki, T.; Tsushima, M.; Osawa, M. A Combined Surface-Enhanced Infrared and Electrochemical Kinetics Study of Hydrogen Adsorption and Evolution on a Pt Electrode. *Chem. Phys. Lett.* **2005**, *401*, 451−454.
(158) Kunimatsu, K.; Uchida, H.; Osawa, M.; Watanabe, M. In Situ Infrared Spectroscopic and Electrochemical Study of Hydrogen Electro-Oxidation on Pt Electrode in Sulfuric Acid. *J. Electroanal. Chem.* **2006**, *587*, 299−307.
(159) Zhu, S.; Qin, X.; Yao, Y.; Shao, M. pH-Dependent Hydrogen and Water Binding Energies on Platinum Surfaces as Directly Probed through Surface-Enhanced Infrared Absorption Spectroscopy. *J. Am. Chem. Soc.* **2020**, *142*, 8748−8754.
(160) Wang, J. X.; Springer, T. E.; Liu, P.; Shao, M.; Adzic, R. R. Hydrogen Oxidation Reaction on Pt in Acidic Media: Adsorption Isotherm and Activation Free Energies. *J. Phys. Chem. C* **2007**, *111*, 12425−12433.
(161) Cai, Y.; Anderson, A. B. The Reversible Hydrogen Electrode: Potential-Dependent Activation Energies over Platinum from Quantum Theory. *J. Phys. Chem. B* **2004**, *108*, 9829−9833.
(162) Lindgren, P.; Kastlunger, G.; Peterson, A. A. A Challenge to the G ∼0 Interpretation of Hydrogen Evolution. *ACS Catal.* **2020**, *10*, 121−128.
(163) Zhang, Q.; Liu, Y.; Chen, S. A DFT Calculation Study on the Temperature-Dependent Hydrogen Electrocatalysis on Pt(111) Surface. *J. Electroanal. Chem.* **2013**, *688*, 158−164.
(164) Ramaswamy, N.; Ghoshal, S.; Bates, M. K.; Jia, Q.; Li, J.; Mukerjee, S. Hydrogen Oxidation Reaction in Alkaline Media: Relationship between Electrocatalysis and Electrochemical Double-Layer Structure. *Nano Energy* **2017**, *41*, 765−771.
(165) Weber, D. J.; Janssen, M.; Oezaslan, M. Effect of Monovalent Cations on the HOR/HER Activity for Pt in Alkaline Environment. *J. Electrochem. Soc.* **2019**, *166*, F66−F73.
(166) Osawa, M.; Tsushima, M.; Mogami, H.; Samjeské, G.; Yamakata, A. Structure of Water at the Electrified Platinum-Water Interface: A Study by Surface-Enhanced Infrared Absorption Spectroscopy. *J. Phys. Chem. C* **2008**, *112*, 4248−4256.
(167) Sebastián-Pascual, P.; Sarabia, F.; Climent, V.; Feliu, J. M.; Escudero-Escribano, M. Elucidating the Structure of the Cu-Alkaline Electrochemical Interface with the Laser-Induced Temperature Jump Method. *J. Phys. Chem. C* **2020**, *124*, 23253−23259.
(168) Sarabia, F. J.; Sebastián-Pascual, P.; Koper, M. T. M.; Climent, V.; Feliu, J. M. Effect of the Interfacial Water Structure on the Hydrogen Evolution Reaction on Pt(111) Modified with Different Nickel Hydroxide Coverages in Alkaline Media. *ACS Appl. Mater. Interfaces* **2019**, *11*, 613−623.
(169) Intikhab, S.; Rebollar, L.; Fu, X.; Yue, Q.; Li, Y.; Kang, Y.; Tang, M. H.; Snyder, J. D. Exploiting Dynamic Water Structure and Structural Sensitivity for Nanoscale Electrocatalyst Design. *Nano Energy* **2019**, *64*, 103963.
(170) Yang, X.; Nash, J.; Oliveira, N.; Yan, Y.; Xu, B. Understanding the pH Dependence of Underpotential Deposited Hydrogen on Platinum. *Angew. Chem., Int. Ed.* **2019**, *58*, 17718−17723.
(171) Hu, J.; Kuttiyiel, K. A.; Sasaki, K.; Zhang, C.; Adzic, R. R. Determination of Hydrogen Oxidation Reaction Mechanism Based on Pt-H Ad Energetics in Alkaline Electrolyte. *J. Electrochem. Soc.* **2018**, *165*, J3355−J3362.
(172) Rebollar, L.; Intikhab, S.; Snyder, J. D.; Tang, M. H. Kinetic Isotope Effects Quantify pH-Sensitive Water Dynamics at the Pt Electrode Interface. *J. Phys. Chem. Lett.* **2020**, *11*, 2308−2313.

https://doi.org/10.1021/acs.chemrev.1c00331
Chem. Rev. XXXX, XXX, XXX−XXX

(173) Rossmeisl, J.; Chan, K.; Skúlason, E.; Björketun, M. E.; Tripkovic, V. On the pH Dependence of Electrochemical Proton Transfer Barriers. *Catal. Today* **2016**, *262*, 36−40.
(174) Corn, R. M.; Higgins, D. A. Optical Second Harmonic Generation as a Probe of Surface Chemistry. *Chem. Rev.* **1994**, *94*, 107−125.
(175) Feng, Z.; Li, L.; Zheng, X.; Li, J.; Yang, N.; Ding, W.; Wei, Z. Role of Hydroxyl Species in Hydrogen Oxidation Reaction: A DFT Study. *J. Phys. Chem. C* **2019**, *123*, 23931−23939.
(176) Briega-Martos, V.; Ferre-Vilaplana, A.; Herrero, E.; Feliu, J. M. Why the Activity of the Hydrogen Oxidation Reaction on Platinum Decreases as pH Increases. *Electrochim. Acta* **2020**, *354*, 136620.
(177) Watanabe, M.; Motoo, S. Electrocatalysis by Ad-Atoms. Part II. Enhancement of the Oxidation of Methanol on Platinum by Ruthenium Ad-Atoms. *J. Electroanal. Chem. Interfacial Electrochem.* **1975**, *60*, 267−273.
(178) Koper, M. T. M. Hydrogen Electrocatalysis: A Basic Solution. *Nat. Chem.* **2013**, *5*, 255−256.
(179) Shen, L.-f.; Lu, B.-a.; Qu, X.-m.; Ye, J.; Zhang, J.; Yin, S.; Wu, Q.; Wang, R.; Shen, S.; Sheng, T.; Jiang, Y.; Sun, S. Does the Oxophilic Effect Serve the Same Role for Hydrogen Evolution/Oxidation Reaction in Alkaline Media? *Nano Energy* **2019**, *62*, 601−609.
(180) Lu, S.; Zhuang, Z. Investigating the Influences of the Adsorbed Species on Catalytic Activity for Hydrogen Oxidation Reaction in Alkaline Electrolyte. *J. Am. Chem. Soc.* **2017**, *139*, 5156−5163.
(181) Strmcnik, D.; Kodama, K.; Van Der Vliet, D.; Greeley, J.; Stamenkovic, V. R.; Marković, N. M. The Role of Non-Covalent Interactions in Electrocatalytic Fuel-Cell Reactions on Platinum. *Nat. Chem.* **2009**, *1*, 466−472.
(182) Wang, Y.-H.; Wang, X.-T.; Ze, H.; Zhang, X.-G.; Radjenovic, P. M.; Zhang, Y.-J.; Dong, J.-C.; Tian, Z.-Q.; Li, J.-F. Spectroscopic Verification of Adsorbed Hydroxyl Intermediate in the Bifunctional Mechanism of Hydrogen Oxidation Reaction. *Angew. Chem. Int. Ed.* **2021**, *60*, 5708−5711.
(183) Wang, Y.; Wang, G.; Li, G.; Huang, B.; Pan, J.; Liu, Q.; Han, J.; Xiao, L.; Lu, J.; Zhuang, L. Pt-Ru Catalyzed Hydrogen Oxidation in Alkaline Media: Oxophilic Effect or Electronic Effect? *Energy Environ. Sci.* **2015**, *8*, 177−181.
(184) Schwämmlein, J. N.; Stühmeier, B. M.; Wagenbauer, K.; Dietz, H.; Tileli, V.; Gasteiger, H. A.; El-Sayed, H. A. Origin of Superior HOR/HER Activity of Bimetallic Pt-Ru Catalysts in Alkaline Media Identified via Ru@Pt Core-Shell Nanoparticles. *J. Electrochem. Soc.* **2018**, *165*, H229−H239.
(185) Schwammlein, J. N.; El-Sayed, H. A.; Stuhmeier, B. M.; Wagenbauer, K. F.; Dietz, H.; Gasteiger, H. A. Origin of Superior Activity of Ru@Pt Core-Shell Nanoparticles towards Hydrogen Oxidation in Alkaline Media. *ECS Trans.* **2016**, *75*, 971−982.
(186) Liu, W.; Lyu, K.; Xiao, L.; Lu, J.; Zhuang, L. Hydrogen Oxidation Reaction on Modified Platinum Model Electrodes in Alkaline Media. *Electrochim. Acta* **2019**, *327*, 135016.
(187) Li, Q.; Peng, H.; Wang, Y.; Xiao, L.; Lu, J.; Zhuang, L. The Comparability of Pt to Pt-Ru in Catalyzing the Hydrogen Oxidation Reaction for Alkaline Polymer Electrolyte Fuel Cells Operated at 80 °C. *Angew. Chem., Int. Ed.* **2019**, *58*, 1442−1446.
(188) Wang, H.; Abruna, H. D. Designing Synergistic Electrocatalysts for H_2 Oxidation and Evolution Reactions in Alkaline Media. *J. Phys. Chem. C* **2021**, *125*, 7188−7203.
(189) Wang, G.; Li, W.; Wu, N.; Huang, B.; Xiao, L.; Lu, J.; Zhuang, L. Unraveling the Composition-Activity Relationship of Pt-Ru Binary Alloy for Hydrogen Oxidation Reaction in Alkaline Media. *J. Power Sources* **2019**, *412*, 282−286.
(190) Cong, Y.; Chai, C.; Zhao, X.; Yi, B.; Song, Y. $Pt_{0.25}Ru_{0.75}$/N-C as Highly Active and Durable Electrocatalysts toward Alkaline Hydrogen Oxidation Reaction. *Adv. Mater. Interfaces* **2020**, *7*, 2000310.
(191) Wang, L.; Mahoney, E. G.; Zhao, S.; Yang, B.; Chen, J. G. Low Loadings of Platinum on Transition Metal Carbides for Hydrogen Oxidation and Evolution Reactions in Alkaline Electrolytes. *Chem. Commun.* **2016**, *52*, 3697−3700.
(192) Elbert, K.; Hu, J.; Ma, Z.; Zhang, Y.; Chen, G.; An, W.; Liu, P.; Isaacs, H. S.; Adzic, R. R.; Wang, J. X. Elucidating Hydrogen Oxidation/Evolution Kinetics in Base and Acid by Enhanced Activities at the Optimized Pt Shell Thickness on the Ru Core. *ACS Catal.* **2015**, *5*, 6764−6772.
(193) St. John, S.; Atkinson, R. W.; Unocic, K. A.; Unocic, R. R.; Zawodzinski, T. A.; Papandrew, A. B. Platinum and Palladium Overlayers Dramatically Enhance the Activity of Ruthenium Nanotubes for Alkaline Hydrogen Oxidation. *ACS Catal.* **2015**, *5*, 7015−7023.
(194) Scofield, M. E.; Zhou, Y.; Yue, S.; Wang, L.; Su, D.; Tong, X.; Vukmirovic, M. B.; Adzic, R. R.; Wong, S. S. Role of Chemical Composition in the Enhanced Catalytic Activity of Pt-Based Alloyed Ultrathin Nanowires for the Hydrogen Oxidation Reaction under Alkaline Conditions. *ACS Catal.* **2016**, *6*, 3895−3908.
(195) Okubo, K.; Ohyama, J.; Satsuma, A. Surface Modification of Pt Nanoparticles with Other Metals Boosting the Alkaline Hydrogen Oxidation Reaction. *Chem. Commun.* **2019**, *55*, 3101−3104.
(196) Alia, S. M.; Pivovar, B. S.; Yan, Y. Platinum-Coated Copper Nanowires with High Activity for Hydrogen Oxidation Reaction in Base. *J. Am. Chem. Soc.* **2013**, *135*, 13473−13478.
(197) Xiao, W.; Lei, W.; Wang, J.; Gao, G.; Zhao, T.; Cordeiro, M. A. L.; Lin, R.; Gong, M.; Guo, X.; Stavitski, E.; Xin, H. L.; Zhu, Y.; Wang, D. Tuning the Electrocatalytic Activity of Pt by Structurally Ordered PdFe/C for the Hydrogen Oxidation Reaction in Alkaline Media. *J. Mater. Chem. A* **2018**, *6*, 11346−11352.
(198) Zhao, T.; Hu, Y.; Gong, M.; Lin, R.; Deng, S.; Lu, Y.; Liu, X.; Chen, Y.; Shen, T.; Hu, Y.; Han, L.; Xin, H.; Chen, S.; Wang, D. Electronic Structure and Oxophilicity Optimization of Mono-Layer Pt for Efficient Electrocatalysis. *Nano Energy* **2020**, *74*, 104877.
(199) Zhao, T.; Wang, G.; Gong, M.; Xiao, D.; Chen, Y.; Shen, T.; Lu, Y.; Zhang, J.; Xin, H.; Li, Q.; Wang, D. Self-Optimized Ligand Effect in $L1_2$-PtPdFe Intermetallic for Efficient and Stable Alkaline Hydrogen Oxidation Reaction. *ACS Catal.* **2020**, *10*, 15207−15216.
(200) Henning, S.; Herranz, J.; Gasteiger, H. A. Bulk-Palladium and Palladium-on-Gold Electrocatalysts for the Oxidation of Hydrogen in Alkaline Electrolyte. *J. Electrochem. Soc.* **2015**, *162*, F178−F189.
(201) Zheng, J.; Zhou, S.; Gu, S.; Xu, B.; Yan, Y. Size-Dependent Hydrogen Oxidation and Evolution Activities on Supported Palladium Nanoparticles in Acid and Base. *J. Electrochem. Soc.* **2016**, *163*, F499−F506.
(202) Jervis, R.; Mansor, N.; Gibbs, C.; Murray, C. A.; Tang, C. C.; Shearing, P. R.; Brett, D. J. L. Hydrogen Oxidation on PdIr/C Catalysts in Alkaline Media. *J. Electrochem. Soc.* **2014**, *161*, F458−F463.
(203) Cong, Y.; McCrum, I. T.; Gao, X.; Lv, Y.; Miao, S.; Shao, Z.; Yi, B.; Yu, H.; Janik, M. J.; Song, Y. Uniform $Pd_{0.33}Ir_{0.67}$ Nanoparticles Supported on Nitrogen-Doped Carbon with Remarkable Activity toward the Alkaline Hydrogen Oxidation Reaction. *J. Mater. Chem. A* **2019**, *7*, 3161−3169.
(204) Qin, X.; Zhang, L.; Xu, G. L.; Zhu, S.; Wang, Q.; Gu, M.; Zhang, X.; Sun, C.; Balbuena, P. B.; Amine, K.; Shao, M. The Role of Ru in Improving the Activity of Pd toward Hydrogen Evolution and Oxidation Reactions in Alkaline Solutions. *ACS Catal.* **2019**, *9*, 9614−9621.
(205) Qiu, Y.; Xin, L.; Li, Y.; McCrum, I. T.; Guo, F.; Ma, T.; Ren, Y.; Liu, Q.; Zhou, L.; Gu, S.; Janik, M. J.; Li, W. BCC-Phased PdCu Alloy as a Highly Active Electrocatalyst for Hydrogen Oxidation in Alkaline Electrolytes. *J. Am. Chem. Soc.* **2018**, *140*, 16580−16588.
(206) Bakos, I.; Paszternák, A.; Zitoun, D. Pd/Ni Synergestic Activity for Hydrogen Oxidation Reaction in Alkaline Conditions. *Electrochim. Acta* **2015**, *176*, 1074−1082.
(207) Alia, S. M.; Yan, Y. Palladium Coated Copper Nanowires as a Hydrogen Oxidation Electrocatalyst in Base. *J. Electrochem. Soc.* **2015**, *162*, F849−F853.
(208) Arulrajan, A. C.; Subramanian, P.; Singh, R. K.; Schechter, A. Pd-Decorated Tungsten as Pt-Free Bimetallic Catalysts for Hydrogen

https://doi.org/10.1021/acs.chemrev.1c00331
Chem. Rev. XXXX, XXX, XXX−XXX

Oxidation Reaction in Alkaline Electrolyte. *Isr. J. Chem.* **2020**, *60*, 563−569.
(209) Miller, H. A.; Lavacchi, A.; Vizza, F.; Marelli, M.; Di Benedetto, F.; D'Acapito, F.; Paska, Y.; Page, M.; Dekel, D. R. A Pd/C-CeO_2 Anode Catalyst for High-Performance Platinum-Free Anion Exchange Membrane Fuel Cells. *Angew. Chem., Int. Ed.* **2016**, *55*, 6004−6007.
(210) Miller, H. A.; Vizza, F.; Marelli, M.; Zadick, A.; Dubau, L.; Chatenet, M.; Geiger, S.; Cherevko, S.; Doan, H.; Pavlicek, R. K.; Mukerjee, S.; Dekel, D. R. Highly Active Nanostructured Palladium-Ceria Electrocatalysts for the Hydrogen Oxidation Reaction in Alkaline Medium. *Nano Energy* **2017**, *33*, 293−305.
(211) Yu, H.; Davydova, E. S.; Ash, U.; Miller, H. A.; Bonville, L.; Dekel, D. R.; Maric, R. Palladium-Ceria Nanocatalyst for Hydrogen Oxidation in Alkaline Media: Optimization of the Pd-CeO_2 Interface. *Nano Energy* **2019**, *57*, 820−826.
(212) Speck, F. D.; Ali, F. S. M.; Paul, M. T. Y.; Singh, R. K.; Böhm, T.; Hofer, A.; Kasian, O.; Thiele, S.; Bachmann, J.; Dekel, D. R.; Kallio, T.; Cherevko, S. Improved Hydrogen Oxidation Reaction Activity and Stability of Buried Metal-Oxide Electrocatalyst Interfaces. *Chem. Mater.* **2020**, *32*, 7716−7724.
(213) Ohyama, J.; Sato, T.; Yamamoto, Y.; Arai, S.; Satsuma, A. Size Specifically High Activity of Ru Nanoparticles for Hydrogen Oxidation Reaction in Alkaline Electrolyte. *J. Am. Chem. Soc.* **2013**, *135*, 8016−8021.
(214) Zhao, T.; Xiao, D.; Chen, Y.; Tang, X.; Gong, M.; Deng, S.; Liu, X.; Ma, J.; Zhao, X.; Wang, D. Boosting Alkaline Hydrogen Electrooxidation on an Unconventional fcc-Ru Polycrystal. *J. Energy Chem.* **2021**, *61*, 15.
(215) Zhao, Y.; Wang, X.; Cheng, G.; Luo, W. Phosphorus-Induced Activation of Ruthenium for Boosting Hydrogen Oxidation and Evolution Electrocatalysis. *ACS Catal.* **2020**, *10*, 11751−11757.
(216) Zeng, L.; Peng, H.; Liu, W.; Yin, J.; Xiao, L.; Lu, J.; Zhuang, L. Extraordinary Activity of Mesoporous Carbon Supported Ru toward the Hydrogen Oxidation Reaction in Alkaline Media. *J. Power Sources* **2020**, *461*, 228147.
(217) Ohyama, J.; Kumada, D.; Satsuma, A. Improved Hydrogen Oxidation Reaction under Alkaline Conditions by Ruthenium-Iridium Alloyed Nanoparticles. *J. Mater. Chem. A* **2016**, *4*, 15980−15985.
(218) Ishikawa, K.; Ohyama, J.; Okubo, K.; Murata, K.; Satsuma, A. Enhancement of Alkaline Hydrogen Oxidation Reaction of Ru-Ir Alloy Nanoparticles through Bifunctional Mechanism on Ru-Ir Pair Site. *ACS Appl. Mater. Interfaces* **2020**, *12*, 22771−22777.
(219) Qin, B.; Yu, H.; Gao, X.; Yao, D.; Sun, X.; Song, W.; Yi, B.; Shao, Z. Ultrathin IrRu Nanowire Networks with High Performance and Durability for the Hydrogen Oxidation Reaction in Alkaline Anion Exchange Membrane Fuel Cells. *J. Mater. Chem. A* **2018**, *6*, 20374−20382.
(220) Wang, H.; Yang, Y.; Disalvo, F. J.; Abruna, H. D. Multifunctional Electrocatalysts: Ru-M (M = Co, Ni, Fe) for Alkaline Fuel Cells and Electrolyzers. *ACS Catal.* **2020**, *10*, 4608−4616.
(221) Xue, Y.; Shi, L.; Liu, X.; Fang, J.; Wang, X.; Setzler, B. P.; Zhu, W.; Yan, Y.; Zhuang, Z. A Highly-Active, Stable and Low-Cost Platinum-Free Anode Catalyst Based on RuNi for Hydroxide Exchange Membrane Fuel Cells. *Nat. Commun.* **2020**, *11*, 5651.
(222) Zhou, Y.; Xie, Z.; Jiang, J.; Wang, J.; Song, X.; He, Q.; Ding, W.; Wei, Z. Lattice-Confined Ru Clusters with High CO Tolerance and Activity for the Hydrogen Oxidation Reaction. *Nat. Catal.* **2020**, *3*, 454−462.
(223) Zheng, J.; Zhuang, Z.; Xu, B.; Yan, Y. Correlating Hydrogen Oxidation/Evolution Reaction Activity with the Minority Weak Hydrogen-Binding Sites on Ir/C Catalysts. *ACS Catal.* **2015**, *5*, 4449−4455.
(224) Wang, H.; Abruna, H. D. IrPdRu/C as H_2 Oxidation Catalysts for Alkaline Fuel Cells. *J. Am. Chem. Soc.* **2017**, *139*, 6807−6810.
(225) Qin, B.; Yu, H.; Jia, J.; Jun, C.; Gao, X.; Yao, D.; Sun, X.; Song, W.; Yi. A novel IrNi@PdIr/C core-shell electrocatalyst with enhanced activity and durability for the hydrogen oxidation reaction in alkaline anion exchange membrane fuel cells. *Nanoscale* **2018**, *10*, 4872−4881.
(226) Zhang, W.; Li, L.; Ding, W.; Chen, S.; Wang, H.; Wei, Z. A Solvent Evaporation plus Hydrogen Reduction Method to Synthesize IrNi/C Catalysts for Hydrogen Oxidation. *J. Mater. Chem. A* **2014**, *2*, 10098−10103.
(227) Liao, J.; Ding, W.; Tao, S.; Nie, Y.; Li, W.; Wu, G.; Chen, S.; Li, L.; Wei, Z. Carbon Supported IrM (M = Fe, Ni, Co) Alloy Nanoparticles for the Catalysis of Hydrogen Oxidation in Acidic and Alkaline Medium. *Chin. J. Catal.* **2016**, *37*, 1142−1148.
(228) Jiang, J.; Liao, J.; Tao, S.; Najam, T.; Ding, W.; Wang, H.; Wei, Z. Modulation of Iridium-Based Catalyst by a Trace of Transition Metals for Hydrogen Oxidation/Evolution Reaction in Alkaline. *Electrochim. Acta* **2020**, *333*, 135444.
(229) Fu, L.; Li, Y.; Yao, N.; Yang, F.; Cheng, G.; Luo, W. IrMo Nanocatalysts for Efficient Alkaline Hydrogen Electrocatalysis. *ACS Catal.* **2020**, *10*, 7322−7327.
(230) Wang, H.; Abruna, H. D. Rh and Rh Alloy Nanoparticles as Highly Active H_2 Oxidation Catalysts for Alkaline Fuel Cells. *ACS Catal.* **2019**, *9*, 5057−5062.
(231) Yang, F.; Bao, X.; Gong, D.; Su, L.; Cheng, G.; Chen, S.; Luo, W. Rhodium Phosphide: A New Type of Hydrogen Oxidation Reaction Catalyst with Non-Linear Correlated Catalytic Response to pH. *ChemElectroChem* **2019**, *6*, 1990−1995.
(232) Ramaswamy, N.; Mukerjee, S. Alkaline Anion-Exchange Membrane Fuel Cells: Challenges in Electrocatalysis and Interfacial Charge Transfer. *Chem. Rev.* **2019**, *119*, 11945−11979.
(233) Oshchepkov, A. G.; Braesch, G.; Bonnefont, A.; Savinova, E. R.; Chatenet, M. Recent Advances in the Understanding of Nickel-Based Catalysts for the Oxidation of Hydrogen-Containing Fuels in Alkaline Media. *ACS Catal.* **2020**, *10*, 7043−7068.
(234) Oshchepkov, A. G.; Bonnefont, A.; Saveleva, V. A.; Papaefthimiou, V.; Zafeiratos, S.; Pronkin, S. N.; Parmon, V. N.; Savinova, E. R. Exploring the Influence of the Nickel Oxide Species on the Kinetics of Hydrogen Electrode Reactions in Alkaline Media. *Top. Catal.* **2016**, *59*, 1319−1331.
(235) Oshchepkov, A. G.; Bonnefont, A.; Parmon, V. N.; Savinova, E. R. On the Effect of Temperature and Surface Oxidation on the Kinetics of Hydrogen Electrode Reactions on Nickel in Alkaline Media. *Electrochim. Acta* **2018**, *269*, 111−118.
(236) Oshchepkov, A. G.; Bonnefont, A.; Savinova, E. R. On the Influence of the Extent of Oxidation on the Kinetics of the Hydrogen Electrode Reactions on Polycrystalline Nickel. *Electrocatalysis* **2020**, *11*, 133−142.
(237) Pan, Y.; Hu, G.; Lu, J.; Xiao, L.; Zhuang, L. Ni$(OH)_2$-Ni/C for Hydrogen Oxidation Reaction in Alkaline Media. *J. Energy Chem.* **2019**, *29*, 111−115.
(238) Oshchepkov, A. G.; Bonnefont, A.; Pronkin, S. N.; Cherstiouk, O. V.; Ulhaq-Bouillet, C.; Papaefthimiou, V.; Parmon, V. N.; Savinova, E. R. Nanostructured Nickel Nanoparticles Supported on Vulcan Carbon as a Highly Active Catalyst for the Hydrogen Oxidation Reaction in Alkaline Media. *J. Power Sources* **2018**, *402*, 447−452.
(239) Simonov, P. A.; Cherstiouk, O. V.; Kuznetsov, A. N.; Zaikovskii, V. I.; Kardash, T. Y.; Oshchepkov, A. G.; Bonnefont, A.; Savinova, E. R. Highly Active Carbon-Supported Ni Catalyst Prepared by Nitrate Decomposition with a Sacrificial Agent for the Hydrogen Oxidation Reaction in Alkaline Medium. *J. Electroanal. Chem.* **2019**, *852*, 113551.
(240) Ni, W.; Wang, T.; Schouwink, P. A.; Chuang, Y.; Chen, H. M.; Hu, X. Efficient Hydrogen Oxidation Catalyzed by Strain-Engineered Nickel Nanoparticles. *Angew. Chem., Int. Ed.* **2020**, *59*, 10797−10801.
(241) Yang, Y.; Sun, X.; Han, G.; Liu, X.; Zhang, X.; Sun, Y.; Zhang, M.; Cao, Z.; Sun, Y. Enhanced Electrocatalytic Hydrogen Oxidation on Ni/NiO/C Derived from a Nickel-Based Metal-Organic Framework. *Angew. Chem., Int. Ed.* **2019**, *58*, 10644−10649.
(242) Zhuang, Z.; Giles, S. A.; Zheng, J.; Jenness, G. R.; Caratzoulas, S.; Vlachos, D. G.; Yan, Y. Nickel Supported on Nitrogen-Doped Carbon Nanotubes as Hydrogen Oxidation Reaction Catalyst in Alkaline Electrolyte. *Nat. Commun.* **2016**, *7*, 10141.

https://doi.org/10.1021/acs.chemrev.1c00331
Chem. Rev. XXXX, XXX, XXX−XXX

(243) Yang, F.; Bao, X.; Zhao, Y.; Wang, X.; Cheng, G.; Luo, W. Enhanced HOR Catalytic Activity of PGM-Free Catalysts in Alkaline Media: The Electronic Effect Induced by Different Heteroatom Doped Carbon Supports. *J. Mater. Chem. A* **2019**, *7*, 10936−10941.
(244) Song, F.; Li, W.; Yang, J.; Han, G.; Liao, P.; Sun, Y. Interfacing Nickel Nitride and Nickel Boosts Both Electrocatalytic Hydrogen Evolution and Oxidation Reactions. *Nat. Commun.* **2018**, *9*, 4531.
(245) Ni, W.; Krammer, A.; Hsu, C.; Chen, H. M.; Schüler, A.; Hu, X. Ni_3N as an Active Hydrogen Oxidation Reaction Catalyst in Alkaline Medium. *Angew. Chem., Int. Ed.* **2019**, *58*, 7445−7449.
(246) Wang, T.; Wang, M.; Yang, H.; Xu, M.; Zuo, C.; Feng, K.; Xie, M.; Deng, J.; Zhong, J.; Zhou, W.; Cheng, T.; Li, Y. Weakening Hydrogen Adsorption on Nickel via Interstitial Nitrogen Doping Promotes Bifunctional Hydrogen Electrocatalysis in Alkaline Solution. *Energy Environ. Sci.* **2019**, *12*, 3522−3529.
(247) Yang, F.; Han, P.; Yao, N.; Cheng, G.; Chen, S.; Luo, W. Inter-Regulated d-Band Centers of the Ni_3B/Ni Heterostructure for Boosting Hydrogen Electrooxidation in Alkaline Media. *Chem. Sci.* **2020**, *11*, 12118−12123.
(248) Oshchepkov, A. G.; Simonov, P. A.; Cherstiouk, O. V.; Nazmutdinov, R. R.; Glukhov, D. V.; Zaikovskii, V. I.; Kardash, T. Y.; Kvon, R. I.; Bonnefont, A.; Simonov, A. N.; Parmon, V. N.; Savinova, E. R. On the Effect of Cu on the Activity of Carbon Supported Ni Nanoparticles for Hydrogen Electrode Reactions in Alkaline Medium. *Top. Catal.* **2015**, *58*, 1181−1192.
(249) Cherstiouk, O. V.; Simonov, P. A.; Oshchepkov, A. G.; Zaikovskii, V. I.; Kardash, T. Y.; Bonnefont, A.; Parmon, V. N.; Savinova, E. R. Electrocatalysis of the Hydrogen Oxidation Reaction on Carbon-Supported Bimetallic NiCu Particles Prepared by an Improved Wet Chemical Synthesis. *J. Electroanal. Chem.* **2016**, *783*, 146−151.
(250) Roy, A.; Talarposhti, M. R.; Normile, S. J.; Zenyuk, I. V.; De Andrade, V.; Artyushkova, K.; Serov, A.; Atanassov, P. Nickel-Copper Supported on a Carbon Black Hydrogen Oxidation Catalyst Integrated into an Anion-Exchange Membrane Fuel Cell. *Sustain. Energy Fuels* **2018**, *2*, 2268−2275.
(251) Wang, G.; Li, W.; Huang, B.; Xiao, L.; Lu, J.; Zhuang, L. Exploring the Composition-Activity Relation of Ni-Cu Binary Alloy Electrocatalysts for Hydrogen Oxidation Reaction in Alkaline Media. *ACS Appl. Energy Mater.* **2019**, *2*, 3160−3165.
(252) Salmazo, D.; Juarez, M. F.; Oshchepkov, A. G.; Cherstiouk, O. V.; Bonnefont, A.; Shermukhamedov, S. A.; Nazmutdinov, R. R.; Schmickler, W.; Savinova, E. R. On the Feasibility of Bifunctional Hydrogen Oxidation on Ni and NiCu Surfaces. *Electrochim. Acta* **2019**, *305*, 452−458.
(253) Wei, C.; Sun, Y.; Scherer, G. G.; Fisher, A. C.; Sherburne, M.; Ager, J. W.; Xu, Z. J. Surface Composition Dependent Ligand Effect in Tuning the Activity of Nickel-Copper Bimetallic Electrocatalysts toward Hydrogen Evolution in Alkaline. *J. Am. Chem. Soc.* **2020**, *142*, 7765−7775.
(254) Sheng, W.; Bivens, A. P.; Myint, M.; Zhuang, Z.; Forest, R. V.; Fang, Q.; Chen, J. G.; Yan, Y. Non-Precious Metal Electrocatalysts with High Activity for Hydrogen Oxidation Reaction in Alkaline Electrolytes. *Energy Environ. Sci.* **2014**, *7*, 1719−1724.
(255) Kabir, S.; Lemire, K.; Artyushkova, K.; Roy, A.; Odgaard, M.; Schlueter, D.; Oshchepkov, A.; Bonnefont, A.; Savinova, E.; Sabarirajan, D. C.; Mandal, P.; Crumlin, E. J.; Zenyuk, I. V.; Atanassov, P.; Serov, A. Platinum Group Metal-Free NiMo Hydrogen Oxidation Catalysts: High Performance and Durability in Alkaline Exchange Membrane Fuel Cells. *J. Mater. Chem. A* **2017**, *5*, 24433−24443.
(256) Wang, M.; Yang, H.; Shi, J.; Chen, Y.; Zhou, Y.; Wang, L.; Di, S.; Zhao, X.; Zhong, J.; Cheng, T.; Zhou, W.; Li, Y. Alloying Nickel with Molybdenum Significantly Accelerates Alkaline Hydrogen Electrocatalysis. *Angew. Chem., Int. Ed.* **2021**, *60*, 5771−5777.
(257) Duan, Y.; Yu, Z. Y.; Yang, L.; Zheng, L. R.; Zhang, C. T.; Yang, X. T.; Gao, F. Y.; Zhang, X. L.; Yu, X.; Liu, R.; Ding, H. H.; Gu, C.; Zheng, X. S.; Shi, L.; Jiang, J.; Zhu, J. F.; Gao, M. R.; Yu, S. H. Bimetallic Nickel-Molybdenum/Tungsten Nanoalloys for High-Efficiency Hydrogen Oxidation Catalysis in Alkaline Electrolytes. *Nat. Commun.* **2020**, *11*, 4789.
(258) Yang, F.; Bao, X.; Li, P.; Wang, X.; Cheng, G.; Chen, S.; Luo, W. Boosting Hydrogen Oxidation Activity of Ni in Alkaline Media through Oxygen-Vacancy-Rich CeO_2/Ni Heterostructures. *Angew. Chem., Int. Ed.* **2019**, *58*, 14179−14183.
(259) Gao, L.; Wang, Y.; Li, H.; Li, Q.; Ta, N.; Zhuang, L.; Fu, Q.; Bao, X. A Nickel Nanocatalyst within a H-BN Shell for Enhanced Hydrogen Oxidation Reactions. *Chem. Sci.* **2017**, *8*, 5728−5734.
(260) Davydova, E. S.; Speck, F. D.; Paul, M. T. Y.; Dekel, D. R.; Cherevko, S. Stability Limits of Ni-Based Hydrogen Oxidation Electrocatalysts for Anion Exchange Membrane Fuel Cells. *ACS Catal.* **2019**, *9*, 6837−6845.
(261) Hu, Q.; Li, G.; Pan, J.; Tan, L.; Lu, J.; Zhuang, L. Alkaline Polymer Electrolyte Fuel Cell with Ni-Based Anode and Co-Based Cathode. *Int. J. Hydrogen Energy* **2013**, *38*, 16264−16268.
(262) Gao, Y.; Peng, H.; Wang, Y.; Wang, G.; Xiao, L.; Lu, J.; Zhuang, L. Improving the Antioxidation Capability of the Ni Catalyst by Carbon Shell Coating for Alkaline Hydrogen Oxidation Reaction. *ACS Appl. Mater. Interfaces* **2020**, *12*, 31575−31581.
(263) Gao, Y.; Yang, Y.; Murray, E.; Schimmenti, R.; Peng, H.; Wang, Y.; Wang, G.; DiSalvo, F. J.; Muller, D. A.; Mavrikakis, M.; Xiao, L.; Abruna, H. D.; Zhuang, L. A Completely Precious-Metal-Free Alkaline Fuel Cell with Enhanced Performance Using a Carbon-Coated Nickel Anode. **2021***Proc. Natl. Acad. Sci. U. S. A*, Accepted.
(264) Gómez-Marín, A.M.; Rizo, R.; Feliu, J. M. Oxygen Reduction Reaction at Pt Single Crystals: A Critical Review. *Catal. Sci. Technol.* **2014**, *4*, 1685−1698.
(265) Gómez-Marín, A.M.; Feliu, J. M. Oxygen Reduction at Platinum Electrodes: The Interplay between Surface and Surrounding Properties. *Curr. Opin. Electrochem.* **2018**, *9*, 166−172.
(266) Markovic, N. M.; Gasteiger, H. A.; Ross, P. N. Oxygen Reduction on Platinum Low-Index Single-Crystal Surfaces in Alkaline Solution: Rotating Ring Disk Pt(hkl) Studies. *J. Phys. Chem.* **1996**, *100*, 6715−6721.
(267) Clavilier, J.; Faure, R.; Guinet, G.; Durand, R. Preparation of monocrystalline Pt microelectrodes and electrochemical study of the plane surfaces cut in the direction of the {111} and {110} planes. *J. Electroanal. Chem. Interfacial Electrochem.* **1980**, *107*, 205−209.
(268) Orts, J. M.; Gomez, R.; Feliu, J. M.; Aldaz, A.; Clavilier, J. Potentiostatic Charge Displacement by Exchanging Adsorbed Species On Pt(111) Electrodes-Acidic Electrolytes With Specific Anion Adsorption. *Electrochim. Acta* **1994**, *39*, 1519−1524.
(269) Climent, V.; Feliu, J. M. Thirty-Year of Platinum Single Crystal Electrochemistry. *J. Solid State Electrochem.* **2011**, *15*, 1297−1315.
(270) Markovic, N. M.; Adzic, R. R.; Cahan, B. D.; Yeager, E. B. Structural Effects in Electrocatalysis: Oxygen Reduction on Platinum Low Index Single-Crystal Surfaces in Perchloric Acid Solutions. *J. Electroanal. Chem.* **1994**, *377*, 249−259.
(271) Damjanovic, A.; Genshaw, M. A.; Bockris, J. O. The Role of Hydrogen Peroxide in the Reduction of Oxygen at Platinum Electrodes. *J. Phys. Chem.* **1966**, *70*, 3761−3762.
(272) Damjanovic, A.; Genshaw, M. A.; Bockris, J. O. The Mechanism of Oxygen Reduction at Platinum in Alkaline Solutions with Special Reference to H_2O_2. *J. Electrochem. Soc.* **1967**, *114*, 1107−1112.
(273) Paulus, U.; Schmidt, T.; Gasteiger, H.; Behm, R. Oxygen Reduction on a High-Surface Area Pt/Vulcan Carbon Catalyst: A Thin-Film Rotating Ring-Disk Electrode Study. *J. Electroanal. Chem.* **2001**, *495*, 134−145.
(274) Zhang, Y.; Parrondo, J.; Sankarasubramanian, S.; Ramani, V. Detection of Reactive Oxygen Species in Anion Exchange Membrane Fuel Cells using In Situ Fluorescence Spectroscopy. *ChemSusChem* **2017**, *10*, 3056−3062.
(275) Kim, Y.; Moh, L. C. H.; Swager, T. Anion Exchange Membrane: Enhancement by Addition of Unfunctionalized Triptycene Poly(Ether Sulfones). *ACS Appl. Mater. Interfaces* **2017**, *9*, 42409−42414.

https://doi.org/10.1021/acs.chemrev.1c00331
Chem. Rev. XXXX, XXX, XXX−XXX

(276) Gómez-Marín, A.M.; Feliu, J. M.; Ticianelli, E. Oxygen Reduction on Platinum Surfaces in Acid Media: Experimental Evidence of a CECE/DISP Initial Reaction Path. *ACS Catal.* **2019**, *9*, 2238−2251.
(277) Gómez-Marín, A.M.; Feliu, J. M.; Ticianelli, E. Reaction Mechanism for Oxygen Reduction on Platinum: Existence of a Fast Initial Chemical Step and a Soluble Species Different from H_2O_2. *ACS Catal.* **2018**, *8*, 7931−7943.
(278) Briega-Martos, V.; Herrero, E.; Feliu, J. M. Effect of pH and Water Structure on the Oxygen Reduction Reaction on Platinum Electrodes. *Electrochim. Acta* **2017**, *241*, 497−509.
(279) Staszak-Jirkovsky, J.; Jirkovsky, J.; Ahlberg, E.; Panas, I.; Schiffrin, D. J. The Bifurcation Point of the Oxygen Reduction Reaction on Au-Pd Nanoalloys. *Faraday Discuss.* **2016**, *188*, 257−278.
(280) Liu, S.; White, M. G.; Liu, P. Mechanism of Oxygen Reduction Reaction on Pt(111) in Alkaline Solution: Importance of Chemisorbed Water on Surface. *J. Phys. Chem. C* **2016**, *120*, 15288−15298.
(281) Tse, E. M.; Barile, C. J.; Kirchschlager, N. A.; Gewargis, J.; Zimmerman, S. C.; Hosseini, A.; Gewirth, A. A. Proton Transfer Dynamics Control the Mechanism of O_2 Reduction by a Non-Precious Metal Electrocatalyst. *Nat. Mater.* **2016**, *15*, 754−759.
(282) Bielski, B. Reevaluation of the Spectral and Kinetic Properties of HO_2 And O_2^- Free Radicals. *Photochem. Photobiol.* **1978**, *28*, 645−649.
(283) Chen, W.; Xu, M.-L.; Li, M.-F.; Wei, Z.; Cai, J.; Chen, Y.-X. Quantifying intrinsic kinetics of electrochemical reaction controlled by mass transfer of multiple species under rotating disk electrode configuration. *J. Electronanal. Chem.* **2020**, *872*, 114042.
(284) Langer, J.; et al. Present and Future of Surface-Enhanced Raman Scattering. *ACS Nano* **2020**, *14*, 28−117.
(285) Kukunuri, S.; Noguchi, H. In Situ Spectroscopy Study of Oxygen Reduction Reaction Intermediates at the Pt/Acid Interface: Surface-Enhanced Infrared Absorbance Spectroscopy. *J. Phys. Chem. C* **2020**, *124*, 7267−7273.
(286) Dong, J.; Zhang, X.-G.; Briega-Martos, V.; Jin, X.; Yang, J.; Chen, S.; Yang, Z.-L.; Wu, D.-Y.; Feliu, J. M.; Williams, C. T.; Tian, Z.-Q.; Li, J.-F. In situ Raman Spectroscopic Evidence for Oxygen Reduction Reaction Intermediates at Platinum Single-Crystal Surfaces. *Nat. Energy.* **2019**, *4*, 60−67.
(287) Dong, J.-C.; Min, S.; Briega-Martos, V.; Li, L.; Le, J.-B.; Radjenovc, R.; Zhou, X.-S.; Feliu, J. M.; Tian, Z.-Q.; Li, J.-F. Direct In Situ Raman Spectroscopic Evidence of Oxygen Reduction Reaction Intermediates at High-Index Pt(hkl) Surfaces. *J. Am. Chem. Soc.* **2020**, *142*, 715−719.
(288) Wang, Y.-H.; Le, J.-B.; Li, W.-Q.; Wei, J.; Radjenovic, P. M.; Zhang, H.; Zhou, X.-S.; Cheng, J.; Tian, Z.-Q.; Li, J.-F. In situ Spectroscopic Insight into the Origin of the Enhanced Performance of Bimetallic Nanocatalysts towards the Oxygen Reduction Reaction (ORR). *Angew. Chem., Int. Ed.* **2019**, *58*, 16062−16066.
(289) Shao, M. H.; Liu, P.; Adzic, R. R. Superoxide Anion is the Intermediate in the Oxygen Reduction Reaction on Platinum Electrodes. *J. Am. Chem. Soc.* **2006**, *128*, 7408−7409.
(290) Briega-Martos, V.; Cheuquepán, W.; Feliu, J. M. Detection of Superoxide Anion Oxygen Reduction Reaction Intermediate on Pt(111) by Infrared Reflection Absorption Spectroscopy in Neutral pH Conditions. *J. Phys. Chem. Lett.* **2021**, *12*, 1588−1592.
(291) Ohta, N.; Nomura, K.; Yagi, I. Adsorption and Electroreduction of Oxygen on Gold in Acidic Media: In Situ Spectroscopic Identification of Adsorbed Molecular Oxygen and Hydrogen Superoxide. *J. Phys. Chem. C* **2012**, *116*, 14390−14400.
(292) Li, X.; Gewirth, A. A. Oxygen Electroreduction through a Superoxide Intermediate on Bi-Modified Au Surfaces. *J. Am. Chem. Soc.* **2005**, *127*, 5252−5260.
(293) Kunimatsu, K.; Yoda, T.; Tryk, D. A.; Uchida, H.; Watanabe, M. In Situ ATR-FTIR Study of Oxygen Reduction at the Pt/Nafion Interface. *Phys. Chem. Chem. Phys.* **2010**, *12*, 621−629.
(294) Gómez-Marín, A. M.; Berna, A.; Feliu, J. M. Spectroelectrochemical Studies of the Pt(111)/Nafion Interface Cast Electrode. *J. Phys. Chem. C* **2010**, *114*, 20130−20140.
(295) Omura, J.; Yano, H.; Watanabe, M.; Uchida, H. Electrochemical Quartz Crystal Microbalance Analysis of the Oxygen Reduction Reaction on Pt-Based Electrodes. Part 1: Effect of Adsorbed Anions on the Oxygen Reduction Activities of Pt in HF, $HClO_4$, and H_2SO_4 Solutions. *Langmuir* **2011**, *27*, 6464−6470.
(296) Wakisaka, M.; Suzuki, H.; Mitsui, S.; Uchida, H.; Watanabe, M. Identification and Quantification of Oxygen Species Adsorbed on Pt(111) Single-Crystal and Polycrystalline Pt Electrodes by Photoelectron Spectroscopy. *Langmuir* **2009**, *25*, 1897−1900.
(297) Wakisaka, M.; Suzuki, H.; Mitsui, S.; Uchida, H.; Watanabe, M. Increased Oxygen Coverage at Pt-Fe Alloy Cathode for the Enhanced Oxygen Reduction Reaction Studied by EC-XPS. *J. Phys. Chem. C* **2008**, *112*, 2750−2755.
(298) Briega-Martos, V.; Herrero, E.; Feliu, J. M. The Inhibition of Hydrogen Peroxide Reduction at Low Potentials on Pt(111): Hydrogen Adsorption or Interfacial Charge? *Electrochem. Commun.* **2017**, *85*, 32−35.
(299) Damjanovic, A.; Brusic, V. Electrode Kinetics of Oxygen Reduction on Oxide-Free Platinum Electrodes. *Electrochim. Acta* **1967**, *12*, 615−628.
(300) Sepa, D. B.; Voinovic, M.V; Damjanovic, A. Reaction Intermediates as a Controlling Factor in the Kinetics and Mechanism of Oxygen Reduction at Platinum Electrodes. *Electrochim. Acta* **1981**, *26*, 781−793.
(301) Gómez-Marín, A. M.; Feliu, J. M. New Insights into the Oxygen Reduction Reaction Mechanism on Pt (111): A Detailed Electrochemical Study. *ChemSusChem* **2013**, *6*, 1091−1100.
(302) Perry, S. C.; Denuault, G. Transient Study of the Oxygen Reduction Reaction on Reduced Pt and Pt Alloys Microelectrodes: Evidence for the Reduction of Pre-Adsorbed Oxygen Species Linked to Dissolved Oxygen. *Phys. Chem. Chem. Phys.* **2015**, *17*, 30005−30012.
(303) Gomez-Marín, A. M.; Rizo, R.; Feliu, J. M. Some Reflections on the Understanding of the Oxygen Reduction Reaction at Pt(111). *Beilstein J. Nanotechnol.* **2013**, *4*, 956−967.
(304) Amatore, C.; Gareil, M.; Savéant, J.-M. Homogeneous vs. Heterogeneous Electron Transfer in Electrochemical Reactions: Application to the Electrohydrogenation of Anthracene and Related Reactions. *J. Electroanal. Chem. Interfacial Electrochem.* **1983**, *147*, 1−38.
(305) Berna, A.; Climent, V.; Feliu, J. M. New Understanding of the Nature of OH Adsorption on Pt(111) Electrodes. *Electrochem. Commun.* **2007**, *9*, 2789−2794.
(306) Gómez-Marín, A. M.; Clavilier, J.; Feliu, J. M. Sequential Pt(111) Oxide Formation in Perchloric Acid: An Electrochemical Study of Surface Species Inter-Conversion. *J. Electroanal. Chem.* **2013**, *688*, 360−370.
(307) Gómez-Marín, A. M.; Feliu, J. M. Oxide Growth Dynamics at Pt(1 1 1) in Absence of Specific Adsorption: A Mechanistic Study. *Electrochim. Acta* **2013**, *104*, 367−377.
(308) Kuzume, A.; Herrero, E.; Feliu, J. M. Oxygen Reduction on Stepped Platinum Surfaces in Acidic Media. *J. Electroanal. Chem.* **2007**, *599*, 333−343.
(309) Rizo, R.; Herrero, E.; Feliu, J. M. Oxygen Reduction Reaction on Stepped Platinum Surfaces in Alkaline Media. *Phys. Chem. Chem. Phys.* **2013**, *15*, 15416−15425.
(310) Markovic, N. M.; Gasteiger, H. A.; Ross, P. N. Kinetics of Oxygen Reduction on Pt(hkl) Electrodes: Implications for the Crystallite Size Effect with supported Pt Electrocatalysts. *J. Electrochem. Soc.* **1997**, *144*, 1591−1597.
(311) Aaronson, B. D. B.; Chen, C.-H.; Li, H.; Koper, M. T. M.; Lai, S. C. S.; Unwin, P. R. Pseudo-Single-Crystal Electrochemistry on Polycrystalline Electrodes: Visualizing Activity at Grains and Grain Boundaries on Platinum for the Fe^{2+}/Fe^{3+} Redox Reaction. *J. Am. Chem. Soc.* **2013**, *135*, 3873−3880.

https://doi.org/10.1021/acs.chemrev.1c00331
Chem. Rev. XXXX, XXX, XXX−XXX

(312) Tian, N.; Zhou, Z.-Y.; Sun, S.-G.; Ding, Y.; Wang, Z. L. Synthesis of Tetrahexahedral Platinum Nanocrystals with High-Index Facets and High Electro-Oxidation Activity. *Science* **2007**, *316*, 732−735.
(313) Yu, T.; Kim, D. Y.; Zhang, H.; Xia, Y. Platinum Concave Nanocubes with High-Index Facets and Their Enhanced Activity for Oxygen Reduction Reaction. *Angew. Chem., Int. Ed.* **2011**, *50*, 2773−2777.
(314) Chen, C.; Kang, Y.; Huo, Z.; Zhu, Z.; Huang, W.; Xin, H. L.; Snyder, J. D.; Li, D.; Herron, J. A.; Mavrikakis, M.; Chi, M.; More, K. L.; Li, Y.; Markovic, N. M.; Somorjai, G. A.; Yang, P.; Stamenkovic, V. R. Highly Crystalline Multimetallic Nanoframes with Three-Dimensional Electrocatalytic Surfaces. *Science* **2014**, *343*, 1339−1343.
(315) Calle-Vallejo, F.; Pohl, M. D.; Reinisch, D.; Loffreda, D.; Sautet, P.; Bandarenka, A. S. Why Conclusions from Platinum Model Surfaces do not Necessarily Lead to Enhanced Nanoparticle Catalysts for the Oxygen Reduction Reaction. *Chem. Sci.* **2017**, *8*, 2283−2289.
(316) Jinnouchi, R.; Kodama, K.; Nagoya, A.; Morimoto, Y. Simulated Volcano Plot of Oxygen Reduction Reaction on Stepped Pt Surfaces. *Electrochim. Acta* **2017**, *230*, 470−478.
(317) Gómez-Marín, A. M. A.; Feliu, J. M. Role of Oxygen-Containing Species at Pt(111) on the Oxygen Reduction Reaction in Acid Media. *J. Solid State Electrochem.* **2015**, *19*, 2831−2841.
(318) Jinnouchi, R.; Kodama, K.; Morimoto, Y. DFT Calculations on H, OH and O Adsorbate Formations on Pt(111) and Pt(332) Electrodes. *Electrochem. Acta* **2014**, *716*, 31−44.
(319) Martínez-Hincapié, R.; Berná, H. A.; Rodes, B. A.; Climent, V.; Feliu, J. M. Surface Acid-Base Properties of Anion-Adsorbed Species at Pt(111) Electrode Surfaces in Contact with CO_2-Containing Perchloric Acid Solutions. *J. Phys. Chem. C* **2016**, *120*, 16191−16199.
(320) Strmcnik, D.; Kodama, K.; van der Vliet, D.; Greeley, J.; Stamenkovic, V. R.; Markvoic, N. M. The Role of Non-Covalent interactions in Electrocatalytic Fuel-Cell Reactions on Platinum. *Nat. Chem.* **2009**, *1*, 466−472.
(321) Stoffelsma, C.; Rodriguez, P.; Garcia, G.; Garcia-Araez, N.; Strmcnik, D.; Markovic, N. M.; Koper, M. T. M. Promotion of the Oxidation of Carbon Monoxide at Stepped Platinum Single-Crystal Electrodes in Alkaline Media by Lithium and Beryllium Cations. *J. Am. Chem. Soc.* **2010**, *132*, 16127−16133.
(322) Markovic, N. M.; Gasteiger, H. A.; Ross, P. N. Oxygen Reduction on Platinum Low-Index Single-Crystal Surfaces in Sulfuric Acid Solution: Rotating Ring-Pt(hkl) Disk Studies. *J. Phys. Chem.* **1995**, *99*, 3411−3415.
(323) Garcia-Araez, N.; Climent, V.; Feliu, J. M. Temperature Effects on Platinum Single-Crystal Electrodes. *Russ. J. Electrochem.* **2012**, *48*, 271−280.
(324) Gómez, R.; Orts, J. M.; Ä Lvarez-Ruiz, B. A.; Feliu, J. M. Effect of Temperature on Hydrogen Adsorption on Pt(111), Pt(110), and Pt(100) Electrodes in 0.1 M $HClO_4$. *J. Phys. Chem. B* **2004**, *108*, 228−238.
(325) Climent, V.; Gómez, R.; Orts, J. M.; Feliu, J. M. Thermodynamic Analysis of the Temperature Dependence of OH Adsorption on Pt(111) and Pt(100) Electrodes in Acidic Media in the Absence of Specific Anion Adsorption. *J. Phys. Chem. B* **2006**, *110*, 11344−11351.
(326) Herrero, E.; Alvarez, B.; Feliu, J. M.; Blais, S.; Radovic-Hrapovic, Z.; Jerkiewicz, G. Temperature Dependence of the CO Ads Oxidation Process on Pt(1 1 1), Pt(1 0 0), and Pt(1 1 0) Electrodes. *J. Electroanal. Chem.* **2004**, *567*, 139−149.
(327) Carrasco, J.; Hodgson, A.; Michaelides, A. A Molecular Perspective of Water at Metal Interfaces. *Nat. Mater.* **2012**, *11*, 667−674.
(328) Wernet, P.; Nordlund, D.; Bergmann, U.; Cavalleri, M.; Odelius, M.; Ogasawara, H.; Naslund, L. Å.; Hirsch, T. K.; Ojamae, L.; Glatzel, P.; Pettersson, L. G. M.; Nilsson, A. The Structure of the First Coordination Shell in Liquid Water. *Science* **2004**, *304*, 995−999.
(329) Björneholm, O.; Hansen, M. H.; Hodgson, A.; Liu, L.-M.; Limmer, D. T.; Michaelides, A.; Pedevilla, P.; Rossmeisl, J.; Shen, H.; Tocci, G.; Tyrode, E.; Walz, M.-M.; Werner, J.; Bluhm, H. Water at Interfaces. *Chem. Rev.* **2016**, *116*, 7698−7726.
(330) Nilsson, A.; Pettersson, L. G. M. Perspective on the Structure of Liquid Water. *Chem. Phys.* **2011**, *389*, 1−34.
(331) Doering, D. L.; Madey, T. E. The Adsorption of Water on Clean and Oxygen-Dosed Ru(001). *Surf. Sci.* **1982**, *123*, 305−337.
(332) Feibelman, P. J. Partial Dissociation of Water on Ru(0001). *Science* **2002**, *295*, 99−102.
(333) Tatarkhanov, M.; Fomin, E.; Salmeron, M.; Andersson, K.; Ogasawara, H.; Pettersson, L. G. M.; Nilsson, A.; Cerdá, J. I. The Structure of Mixed Monolayer Films on Ru(0001). *J. Chem. Phys.* **2008**, *129*, 154109.
(334) Carrasco, J.; Michaelides, A.; Forster, M.; Haq, S.; Raval, R.; Hodgson, A. A One-Dimensional Ice Structure Built from Pentagons. *Nat. Mater.* **2009**, *8*, 427−431.
(335) Nie, S.; Feibelman, P. J.; Bartelt, N. C.; Thurmer, K. Pentagons and Heptagons in the First Water Layer on Pt(111). *Phys. Rev. Lett.* **2010**, *105*, 026102.
(336) Schiros, T.; Naslund, L. A.; Andersson, K.; Gyllenpalm, J.; Karberg, G. S.; Odelius, M.; Ogasawara, H.; Pettersson, L. G. M.; Nilsson, A. Structure and Bonding of the Water-Hydroxyl Mixed Phase on Pt(111). *J. Phys. Chem. C* **2007**, *111*, 15003−15012.
(337) Schiros, T.; Ogasawara, H.; Naslund, L. A.; Andersson, K.; Ren, J.; Meng, Sh; Karberg, G. S.; Odelius, M.; Nilsson, A.; Pettersson, L. G. M. Cooperativity in Surface Bonding and Hydrogen Bonding of Water and Hydroxyl at Metal Surfaces. *J. Phys. Chem. C* **2010**, *114*, 10240−10248.
(338) Abruna, H.; Bommarito, G.; Acevedo, D. The Study of Solid/Liquid Interfaces with X-ray Standing Waves. *Science* **1990**, *250*, 69−74.
(339) Wang, J.; Ocko, B. M.; Davenport, A. J.; Isaacs, H. S. In Situ X-ray-Diffraction and -Reflectivity Studies of the Au(111)/Electrolyte Interface: Reconstruction and Anion Adsorption. *Phys. Rev. B: Condens. Matter Mater. Phys.* **1992**, *46*, 10321.
(340) Toney, M. F.; Howard, J. N.; Richer, J.; Borges, G. L.; Gordon, J. G.; Melroy, O. R.; Wiesler, D. G.; Yee, D.; Sorensen, L. B. Voltage-Dependent Ordering of Water Molecules at an Eelectrode-Electrolyte Interface. *Nature* **1994**, *368*, 444−446.
(341) Li, C.-Y.; Le, J.-B.; Wang, Y.-H.; Chen, S.; Yang, Z.-L.; Li, J.-F.; Cheng, J.; Tian, Z.-Q. In Situ Probing Electrified Interfacial Water Structures at Atomically Flat Surfaces. *Nat. Mater.* **2019**, *18*, 697−701.
(342) Fang, Y.; Ding, S.; Zhang, M.; Steinmann, S. N.; Hu, R.; Mao, B.; Feliu, J. M.; Tian, Z. Revisiting the Atomistic Structures at the Interface of Au(111) Electrode-Sulfuric Acid Solution. *J. Am. Chem. Soc.* **2020**, *142*, 9439−9446.
(343) Velasco-Velez, J.-J.; Wu, C.; Pascal, T. A.; Wan, L. F.; Guo, J.; Prendergast, D.; Salmeron, M. The Structure of Interfacial Water on Gold Electrodes Studied by X-Ray Absorption Spectroscopy. *Science* **2014**, *346*, 831−834.
(344) Wu, C.; Pascal, T. A.; Baskin, A.; Wang, H.; Fang, H.-T.; Liu, Y.-S.; Lu, Y.-H.; Guo, J.; Prendergast, D.; Salmeron, M. Molecular-Scale Structure of Electrode-Electrolyte Interfaces: The Case of Platinum in Aqueous Sulfuric Acid. *J. Am. Chem. Soc.* **2018**, *140*, 16237−16244.
(345) Kolb, M. J.; Farber, R. G.; Derouin, J.; Badan, C.; Calle-Vallejo, F.; Juurlink, L. B. F.; Killelea, D. R.; Koper, M. T. M. Double-Stranded Water on Stepped Platinum Surfaces. *Phys. Rev. Lett.* **2016**, *116*, 136101.
(346) Osawa, M.; Tsushima, M.; Mogami, H.; Samjeské, G.; Yamakata, A. Structure of Water at the Electrified Platinum-Water Interface: A Study by Surface-Enhanced Infrared Absorption Spectroscopy. *J. Phys. Chem. C* **2008**, *112*, 4248−4256.
(347) Ataka, K.-I.; Yotsuyanagi, T.; Osawa, M. Potential-Dependent Reorientation of Water Molecules at an Electrode/Electrolyte Interface Studied by Surface-Enhanced Infrared Absorption Spectroscopy. *J. Phys. Chem.* **1996**, *100*, 10664−10672.

https://doi.org/10.1021/acs.chemrev.1c00331
Chem. Rev. XXXX, XXX, XXX−XXX

(348) Favaro, M.; Jeong, B.; Ross, P. N.; Yano, J.; Hussain, Z.; Liu, Z.; Crumlin, E. J. Unravelling the Electrochemical Double Layer by Direct Probing of the Solid/Liquid Interface. *Nat. Commun.* **2016**, *7*, 12695.
(349) Magnussen, O. M.; Groß, A. Toward an Atomic-Scale Understanding of Electrochemical Interface Structure and Dynamics. *J. Am. Chem. Soc.* **2019**, *141*, 4777−4790.
(350) Frumkin, A. N.; Petrii, O. A. Potential of Zero Toal and Zero Free Charge of Platinum Group Metals. *Electrochim. Acta* **1975**, *20*, 347−359.
(351) Climent, V.; Garcia-Araez, N.; Herrero, E.; Feliu, J. M. Potential of Zero Total Charge of Platinum Single Crystals: A Local Approach to Stepped Surfaces Vicinal to Pt(111). *Russ. J. Electrochem.* **2006**, *42*, 1145−1160.
(352) Damaskin, B. B.; Petrii, O. A. Historical Development of Theories of the Electrochemical Double Layer. *J. Solid State Electrochem.* **2011**, *15*, 1317−1334.
(353) Rizo, R.; Sitta, E.; Herrero, E.; Climent, V.; Feliu, J. M. Towards the Understanding of the Interfacial pH Scale at Pt(111) Electrodes. *Electrochim. Acta* **2015**, *162*, 138−145.
(354) Climent, V.; Attard, G. A.; Feliu, J. M. Potential of Zero Charge of Platinum Stepped Surfaces: A Combined Approach of CO Charge Displacement and N_2O Reduction. *J. Electroanal. Chem.* **2002**, *532*, 67−74.
(355) Attard, G. A.; Hazzazi, O.; Wells, P. B.; Climent, V.; Herrero, E.; Feliu, J. M. On the Global and Local Values of the Potential of Zero Total Charge at Well-Defined Platinum Surfaces: Stepped and Adatom Modified Surfaces. *J. Electroanal. Chem.* **2004**, *568*, 329−342.
(356) Climent, V.; Macia, M. D.; Herrero, E.; Feliu, J. M.; Petrii, O. A. Peroxodisulphate Reduction as a Novel Probe for the Study of Platinum Single Crystal/Solution Interphases. *J. Eelectroanal. Chem.* **2008**, *612*, 269−276.
(357) Martínez-Hincapié, R.; Climent, V.; Feliu, J. M. Peroxodisulfate Reduction as a Probe to Interfacial Charge. *Electrochem. Commun.* **2018**, *88*, 43−46.
(358) Martínez-Hincapié, R.; Climent, V.; Feliu, J. M. New Probes to Surface Free Charge at Electrochemical Interfaces with Platinum Electrodes. *Curr. Opin. Electrochem.* **2019**, *14*, 16−22.
(359) Martínez-Hincapié, R.; Climent, V.; Feliu, J. M. Investigation of the Interfacial Properties of Platinum Stepped Surfaces Using Peroxodisulfate Reduction as a Local Probe. *Electrochim. Acta* **2019**, *307*, 553−563.
(360) Gómez, R.; Climent, V.; Feliu, J. M.; Weaver, M. J. Dependence of the Potential of Zero Charge of Stepped Platinum (111) Electrodes on the Oriented Step-Edge Density: Electrochemical Implications and Comparison with Work Function Behavior. *J. Phys. Chem. B* **2000**, *104*, 597−605.
(361) Chen, Q.-S.; Solla-Gullón, J.; Sun, S.-G.; Feliu, J. M. The Potential of Zero Total Charge of Pt Nanoparticles and Polycrystalline Electrodes with Different Surface Structure: The Role of Anion Adsorption In Fundamental Electrocatalysis. *Electrochim. Acta* **2010**, *55*, 7982.
(362) Mayrhofer, K. J. J.; Blizanac, B. B.; Arenz, M.; Stamenkovic, V. R.; Ross, P. N.; Markovic, N. M. The Impact of Geometric and Surface Electronic Properties of Pt-Catalysts on the Particle Size Effect in Electrocatalysis. *J. Phys. Chem. B* **2005**, *109*, 14433−14440.
(363) Benderskii, V.-A.; Velichko, G. I. Temperture Jump in Electric Doublelayer Study Part 1. Method of Measurements. *J. Electroanal. Chem. Interfacial Electrochem.* **1982**, *140*, 1−22.
(364) Garcia-Araez, N.; Climent, V.; Feliu, J. M. Evidence of Water Reorientation on Model Electrocatalytic Surfaces from Nanosecond-Laser-Pulsed Experiments. *J. Am. Chem. Soc.* **2008**, *130*, 3824−3833.
(365) Climent, V.; Coles, B. A.; Compton, R. G. Laser-Induced Potential Transients on a Au(111) Single-Crystal Electrode. Determination of the Potential of Maximum Entropy of Double-Layer Formation. *J. Phys. Chem. B* **2002**, *106*, 5258−5265.
(366) Climent, V.; Coles, B. A.; Compton, R. G. Coulostatic Potential Transients Induced by Laser Heating of a Pt(111) Single-Crystal Electrode in Aqueous Acid Solutions. Rate of Hydrogen Adsorption and Potential of Maximum Entropy. *J. Phys. Chem. B* **2002**, *106*, 5988−5996.
(367) Garcia-Araez, N.; Climent, V.; Feliu, J. M. Potential-Dependent Water Orientation on Pt(111), Pt(100), and Pt(110), As Inferred from Laser-Pulsed Experiments. Electrostatic and Chemical Effects. *J. Phys. Chem. C* **2009**, *113*, 9290−9304.
(368) García-Aráez, N.; Climent, V.; Feliu, J. M. Potential-Dependent Water Orientation on Pt(1 1 1) Stepped Surfaces from Laser-Pulsed Experiments. *Electrochim. Acta* **2009**, *54*, 966−977.
(369) Sebastián, P.; Martínez-Hincapié, R.; Climent, V.; Feliu, J. M. Study of the Pt (111) | Electrolyte Interface in the Region Close to Neutral pH Solutions by the Laser Induced Temperature Jump Technique. *Electrochim. Acta* **2017**, *228*, 667−676.
(370) Rotermund, H. H.; Jakubith, S.; Kubala, S.; von-Oertzen, A.; Ertl, G. Investigation of Surfaces by Scanning Photoemission Microscopy. *J. Electron Spectrosc. Relat. Phenom.* **1990**, *52*, 811−819.
(371) Sarabia, F.; Sebastian, P.; Climent, V.; Feliu, J. M. New Insights into the Pt(hkl)-Alkaline Solution Interphases from the Laser-Induced Temperature Jump Method. *J. Electroanal. Chem.* **2020**, *872*, 114068.
(372) Sibert, E.; Faure, R.; Durand, R. High Frequency Impedance Measurements on Pt(111) in Sulphuric and Perchloric Acids. *J. Electroanal. Chem.* **2001**, *515*, 71−81.
(373) Morin, S.; Dumont, H.; Conway, B. E. Evaluation of the Effect of Two-Dimensional Geometry of Pt Single-Crystal Faces on the Kinetics of UPD of H Using Impedance Spectroscopy. *J. Electroanal. Chem.* **1996**, *412*, 39−52.
(374) Schouten, K. J. P.; van der Niet, M. J. T. C.; Koper, M. T. M. Impedance Spectroscopy of H and OH Adsorption on Stepped Single-Crystal Platinum Electrodes in Alkaline and Acidic Media. *Phys. Chem. Chem. Phys.* **2010**, *12*, 15217−15224.
(375) Pan, J.; Chen, C.; Zhuang, L.; Lu, J. Designing Advanced Alkaline Polymer Electrolytes for Fuel Cell Applications. *Acc. Chem. Res.* **2012**, *45*, 473−481.
(376) Pan, J.; Chen, C.; Li, Y.; Wang, L.; Tan, L.; Li, G.; Tang, X.; Xiao, L.; Lu, J.; Zhuang, L. Constructing Ionic Highway in Alkaline Polymer Electrolytes. *Energy Environ. Sci.* **2014**, *7*, 354−360.
(377) Xiao, L.; Zhang, S.; Pan, J.; Yang, C.; He, M.; Zhuang, L.; Lu, J. First Implementation of Alkaline Polymer Electrolyte Water Electrolysis Working Only with Pure Water. *Energy Environ. Sci.* **2012**, *5*, 7869−7871.
(378) Yin, Z.; Peng, H.; Wei, X.; Zhou, H.; Gong, J.; Huai, M.; Xiao, L.; Wang, G.; Lu, J.; Zhuang, L. An Alkaline Polymer Electrolyte CO_2 Electrolyzer Operated with Pure Water. *Energy Environ. Sci.* **2019**, *12*, 2455−2462.
(379) Hong, W. T.; Risch, M.; Stoerzinger, K. A.; Grimaud, A.; Suntivich, J.; Shao-Horn, Y. Toward the Rational Design of Non-Precious Transition Metal Oxides for Oxygen Electrocatalysts. *Energy Environ. Sci.* **2015**, *8*, 1404−1427.
(380) Goodenough, J. B.; Manoharan, R.; Paranthaman, M. Surface Protonation and Electrochemical Activity of Oxides in Aqueous Solution. *J. Am. Chem. Soc.* **1990**, *112*, 2076−2082.
(381) Bockris, J. O.; Otagawa, T. The Electrocatalysis of Oxygen Evolution on Perovskites. *J. Electrochem. Soc.* **1984**, *131*, 290−302.
(382) Noh, J.; Schwarz, J. A. Estimation of The Point of Zero Charge of Simple Oxides by Mass Titration. *J. Colloid Interface Sci.* **1989**, *130*, 157−164.
(383) Kosmulski, M. pH-Dependent Surface Charging and Points of Zero Charge. IV. Update and New Approach. *J. Colloid Interface Sci.* **2009**, *337*, 439−448.
(384) Wohlfahrt-Mehrens, M.; Heitbaum, J. Oxygen Evolution on Ru and RuO_2 Electrodes Studied Using Isotope Labelling and On-line Mass Spectrometry. *J. Electroanal. Chem. Interfacial Electrochem.* **1987**, *237*, 251−260.
(385) Fierro, S.; Nagel, T.; Baltruschat, H.; Comninellis, C. Invesitigation of the Oxygen Evolution Reaction on Ti/IrO_2 Electrodes Using Isotope Labelling and On-line Mass Spectrometry. *Electrochem. Commun.* **2007**, *9*, 1969−1974.

https://doi.org/10.1021/acs.chemrev.1c00331
Chem. Rev. XXXX, XXX, XXX−XXX

(386) Amin, H. M. A.; Baltruschat, H. How many surface atoms in Co_3O_4 take part in Oxygen Evoltion? Isotope Labelling Together with Differential Electrochemcial Mass Spectrometry. *Phys. Chem. Chem. Phys.* **2017**, *19*, 25527−25536.
(387) Baltruschat, H. Differential Electrochemical Mass Spectrometry. *J. Am. Soc. Mass Spectrom.* **2004**, *15*, 1693−1706.
(388) Oberacher, H.; Pitterl, F.; Erb, R.; Plattner, S. Mass Spectrometric Methods for Monitoring Redox Processes in Electrochemical Cells. *Mass Spectrom. Rev.* **2015**, *34*, 64−92.
(389) Wang, H.; Rus, E.; Abruna, H. D. New Double-Band-Electrode Channel Flow Differential Electrochemical Mass Spectrometry Cell: Application for Detecting Product Formation during Methanol Electrooxidation. *Anal. Chem.* **2010**, *82*, 4319−4324.
(390) Wang, H.; Alden, L. R.; Abruna, H. D. Methanol Electrooxidation on PtRu Bulk Alloys and Carbon-Supported PtRu Nanoparticle Catalysts: A Quantitative DEMS Study. *Langmuir* **2009**, *25*, 7725−7735.
(391) Zeng, R.; Yang, Y.; Shen, T.; Wang, H.; Xiong, Y.; Zhu, J.; Wang, D.; Abruňa, H. D. Methanol Oxidation Using Ternary Ordered Intermetallic Electrocatalysts: A DEMS Study. *ACS Catal.* **2020**, *10*, 770−776.
(392) Meadowcroft, D. B. Low-Cost Oxygen Electrode Material. *Nature* **1970**, *226*, 847−848.
(393) Trasatti, S. Electrocatalysis by Oxides - Attempt at a Unifying Approach. *J. Electroanal. Chem. Interfacial Electrochem.* **1980**, *111*, 125−131.
(394) Matsumoto, Y.; Sato, E. Electrocatalytic Properties of Transition Metal Oxides for Oxygen Evolution Reaction. *Mater. Chem. Phys.* **1986**, *14*, 397−426.
(395) Bockris, J. O.; Otagawa, T. Mechanism of Oxygen Evolution on Perovskites. *J. Phys. Chem.* **1983**, *87*, 2960−2971.
(396) Matsumoto, Y.; Yoneyama, H.; Tamura, H. Catalytic Activity for Electrochemical Reduction of Oxygen of Lanthanum Nickel Oxide and Related Oxides. *J. Electroanal. Chem. Interfacial Electrochem.* **1977**, *79*, 319−326.
(397) Matsumoto, Y.; Manabe, H.; Sato, E. Oxygen Evolution on $La_{1-x}Sr_xCoO_3$ in Alkaline Solutions. *J. Electrochem. Soc.* **1980**, *127*, 811−814.
(398) Matsumoto, Y.; Sato, E. Oxygen Evolution on $Lal_{1-x}Sr_xMnO_3$ in Alkaline Solutions. *Electrochim. Acta* **1979**, *24*, 421−423.
(399) Inai, M.; Iwakura, C.; Tamura, H. A Consideration of The Activation Energy for the Chlorine Evolution Reaction on RuO_2 and IrO_2 Electrodes. *Electrochim. Acta* **1979**, *24*, 993−996.
(400) Suntivich, J.; Gasteiger, H. A.; Yabuuchi, N.; Nakanishi, H.; Goodenough, J.; Shao-Horn, Y. Design Principles for Oxygen-Reduction Activity on Perovskite Oxide Catalysts for Fuel Cells and Metal-Air Batteries. *Nat. Chem.* **2011**, *3*, 546−550.
(401) Suntivich, J.; Gasteiger, H. A.; Goodenough, J.; Shao-Horn, Y. A Perovskite Oxide Optimized for Oxygen Evolution Catalysis from Molecular Orbital Principles. *Science* **2011**, *334*, 1383−1385.
(402) Hwang, J.; Rao, R. R.; Giordano, L.; Katayama, Y.; Yu, Y.; Shao-Horn, Y. Perovskites in Catalysis and Electrocatalysis. *Science* **2017**, *358*, 751−756.
(403) Stoerzinger, K. A.; Reisch, M.; Han, B.; Shao-Horn, Y. Recent Insights into Manganese Oxides in Catalyzing Oxygen Reduction Kinetics. *ACS Catal.* **2015**, *5*, 6021−6031.
(404) Dowden, D. A. Crystal and Ligand Field Models of Solid Catalysts. *Catal. Rev.: Sci. Eng.* **1972**, *5*, 1−32.
(405) Gray, H. B.; Beach, N. A. The Electronic Structures of Octahedral Metal Complexes. I. Metal Hexacarbonyls and Hexacyanides. *J. Am. Chem. Soc.* **1963**, *85*, 2922−2927.
(406) Wei, C.; Feng, Z.; Scherer, G. G.; Barber, J.; Shao-Horn, Y.; Xu, Z. J. Cations in Octahedral Sites: A Descriptor for Oxygen Electrocatalysis on Transition-Metal Spinels. *Adv. Mater.* **2017**, *29*, 1606800.
(407) Muller, D. A.; Kourkoutis, L. F.; Murfitt, M.; Song, J. H.; Hwang, H. Y.; Silcox, J.; Delby, N.; Krivanek, O. L. Atomic-Scale Chemical Imaging of Composition and Bonding by Aberration-Corrected Microscopy. *Science* **2008**, *319*, 1073−1076.
(408) Mefford, J. T.; Rong, X.; Abakumov, A. M.; Hardin, W. G.; Dai, S.; Kolpak, A. M.; Johnston, K. P.; Stevenson, K. J. Water Electrolysis on $La_{1-x}Sr_xCoO_{3-\delta}$ Perovskite Electrocatalysts. *Nat. Commun.* **2016**, *7*, 11053.
(409) Duan, Y.; Sun, S.; Xi, S.; Ren, X.; Zhou, Y.; Zhang, G.; Yang, H.; Du, Y.; Xu, Z. J. Tailoring the Co 3d-O 2p Covalency in $LaCoO_3$ by Fe Substitution to Promote Oxygen Evolution Reaction. *Chem. Mater.* **2017**, *29*, 10534−10541.
(410) Grimaud, A.; May, K. J.; Carlton, C. E.; Lee, Y.-L.; Risch, M.; Hong, W. T.; Zhou, J.; Shao-Horn, Y. Double Perovskites as a Family of Highly Active Catalysts for Oxygen Evolution in Alkaline Solution. *Nat. Commun.* **2013**, *4*, 2439.
(411) Conder, K.; Pomjakushina, E.; Soldatov, A.; Mitberg, E. Oxygen Content Determination in Perovskite-Type Cobaltates. *Mater. Res. Bull.* **2005**, *40*, 257−263.
(412) Karppinen, M.; Matvejeff, M.; Salomaki, K.; Yamauchi, H. Oxygen Content Analysis of Functional Perovskite-Derived Cobalt Oxides. *J. Mater. Chem.* **2002**, *12*, 1761−1764.
(413) Wolcyrz, M.; Horyn, R.; Bouree, F.; Bukowska, E. Structural Defects in $LaMnO_3$ Phase Studied by Neutron Diffraction. *J. Alloys Compd.* **2003**, *353*, 170−174.
(414) Zhu, Y.; Zhou, W.; Yu, J.; Chen, Y.; Liu, M.; Shao, Z. Enhancing Electrocatalytic Activity of Perovskite Oxides by Tuning Cation Deficiency for Oxygen Reduction and Evolution Reactions. *Chem. Mater.* **2016**, *28*, 1691−1697.
(415) Mefford, J. T.; Kurilovich, A. A.; Saunders, J.; Hardin, W. G.; Abakumov, A. M.; Forslund, R. P.; Bonnefont, A.; Dai, S.; Johnston, K. P.; Stevenson, K. J. Decoupling the roles of carbon and metal oxides on the electrocatalytic reduction of oxygen on $La_{1-x}Sr_xCoO_{3-\delta}$ Perovskite Composite Electrodes. *Phys. Chem. Chem. Phys.* **2019**, *21*, 3327−3338.
(416) Fabbri, E.; Mohamed, R.; Levecque, P.; Conrad, O.; Kotz, R.; Schmidt, T. J. Composite Electrode Boosts the Activity of Ba0.5Sr0.5Co0.8Fe0.2O3−δ Perovskite and Carbon Toward Oxygen Reduction in Alkaline Media. *ACS Catal.* **2014**, *4*, 1061−1070.
(417) Frydendal, R.; Paoli, E. A.; Knudsen, B. P.; Wickman, B.; Malacrida, P.; Stephens, I. E. L.; Chorkendorff, I. Benchmarking the Stability of Oxygen Evolution Reaction Catalysts: The Importance of Monitoring Mass Losses. *ChemElectroChem* **2014**, *1*, 2075−2081.
(418) Chang, S. H.; Danilovic, N.; Chang, K.-C.; Subbaraman, R.; Paulikas, A. P.; Fong, D. D.; Highland, M. J.; Baldo, P. M.; Stamenkovic, V.; Freeland, J. W.; Eastman, J. A.; Markovic, N. M. Functional Links between Stability and Reactivity of Strontium Ruthenate Single Crystals During Oxygen Evolution. *Nat. Commun.* **2014**, *5*, 4191.
(419) Karlsson, G. Reduction of Oxygen on $LaNiO_3$ in Alkaline Solution. *J. Power Sources* **1983**, *10*, 319−331.
(420) Matsumoto, Y.; Yoneyama, H.; Tamura, H. Influence of Preparation Condition on Catalytic Activity for Oxygen Reduction of Lanthanum Nickel Oxide and Related Oxides. *J. Electroanal. Chem. Interfacial Electrochem.* **1977**, *83*, 167−176.
(421) Matsumoto, Y.; Yoneyama, H.; Tamura, H. The Mechanism of Oxygen Reduction at a $LaNiO_3$ Electrode. *Bull. Chem. Soc. Jpn.* **1978**, *51*, 1927−1930.
(422) Bursell, M.; Pirjamali, M.; Kiros, Y. $La_{0.6}Ca_{0.4}CoO_3$, $La_{0.1}Ca_{0.9}MnO_3$ and $LaNiO_3$ as Bifunctional Oxygen Electrodes. *Electrochim. Acta* **2002**, *47*, 1651−1660.
(423) Eom, C. J.; Kuo, D.-Y.; Adamo, C.; Moon, E. J.; May, S. J.; Crumlin, E. J.; Schlom, D. G.; Suntivich, J. Tailoring Manganese Oxide with Atomic Precision to Increase Surface Site Availability for Oxygen Reduction Catalysis. *Nat. Commun.* **2018**, *9*, 4034.
(424) Suntivich, J.; Gasteiger, H. A.; Yabuuchi, N.; Shao-Horn, Y. Electrocatalytic Measurement Methodology of Oxide Catalysts Using a Thin-Film Rotating Disk Electrode. *J. Electrochem. Soc.* **2010**, *157*, B1263−B1268.
(425) Stoerzinger, K.; Lu, W.; Li, C.; Ariando Venkatesan, T.; Shao-Horn, Y. Highly Active Epitaxial $La_{(1-x)}Sr_xMnO_3$ Surfaces for the Oxygen Reduction Reaction: Role of Charge Transfer. *J. Phys. Chem. Lett.* **2015**, *6*, 1435−1440.

https://doi.org/10.1021/acs.chemrev.1c00331
Chem. Rev. XXXX, XXX, XXX−XXX

(426) Stoerzinger, K.; Hong, W. T.; Wang, X. R.; Rao, R. R.; Subramanyam, S. B.; Li, C.; Ariando Venkatesan, T.; Liu, Q.; Crumlin, E. J.; Varanasi, K. K.; Shao-Horn, Y. Decreasing the Hydroxylation Affinity of $La_{1-x}Sr_xMnO_3$ Perovskites to Promote Oxygen Reduction Electrocatalysis. *Chem. Mater.* **2017**, *29*, 9990−9997.
(427) Komo, M.; Hagiwara, A.; Taminato, S.; Hirayama, M.; Kanno, R. Oxygen Evolution and Reduction Reactions on $La_{0.8}Sr_{0.2}CoO_3$ (001), (110), and (111) Surfaces in an Alkaline Solution. *Electrochemistry* **2012**, *80*, 834−838.
(428) Stoerzinger, K. A.; Choi, W. S.; Jeen, H.; Lee, H. N.; Shao-Horn, Y. Role of Strain and Conductivity in Oxygen Electrocatalysis on $LaCoO_3$ Thin Films. *J. Phys. Chem. Lett.* **2015**, *6*, 487−492.
(429) Kuo, D.-Y.; Eom, C. J.; Kawasaki, J. K.; Petretto, G.; Nelson, J. N.; Hautier, G.; Crumlin, E. J.; Shen, K. M.; Schlom, D. G.; Suntivich, J. Influence of Strain on the Surface-Oxygen Interaction and the Oxygen Evolution Reaction of $SrIrO_3$. *J. Phys. Chem. C* **2018**, *122*, 4359−4364.
(430) Monkman, E. J.; Adamo, C.; Mundy, J. A.; Shai, D. E.; Harter, J. W.; Shen, D.; Burganov, B.; Muller, D. A.; Schlom, D. G.; Shen, K. M. Quantum Many-Body Interactions in Digital Oxide Superlattices. *Nat. Mater.* **2012**, *11*, 855−859.
(431) Kuo, D.-Y.; Paik, H.; Kloppenburg, J.; Shen, K. M.; Schlom, D. G.; Hautier, G.; Suntivich, J. Measurements of Oxygen Electroadsorption Energies and Oxygen Evolution Reaction on RuO_2(110): A Discussion of the Sabatier Principle and Its Role in Electrocatalysis. *J. Am. Chem. Soc.* **2018**, *140*, 17597−17605.
(432) Hu, B.; Kuo, D.-Y.; Paik, H.; Schlom, D. G.; Suntivich, J. Enthalpy and Entropy of Oxygen Electroadsorption on RuO_2(110) in Alkaline Media. *J. Chem. Phys.* **2020**, *152*, 094704.
(433) Kuo, D.-Y.; Kawasaki, J. K.; Nelson, J. N.; Kloppenburg, J.; Hautier, G.; Shen, K. M.; Schlom, D. G.; Suntivich, J. Influence of Surface Adsorption on the Oxygen Evolution Reaction on IrO_2 (110). *J. Am. Chem. Soc.* **2017**, *139*, 3473−3479.
(434) Cheng, L.; Fenter, P.; Nagy, K. L.; Schlegel, M. L.; Sturchio, N. C. Molecular-Scale Density Oscillations in Water Adjacent to a Mica Surface. *Phys. Rev. Lett.* **2001**, *87*, 156103.
(435) Kendelewicz, T.; Kaya, S.; Newberg, J. T.; Bluhm, H.; Mulakaluri, N.; Moritz, W.; Scheffler, M.; Nilsson, A.; Pentcheva, R.; Brown, G. E. X-ray Photoemission and Density Functional Theory Study of the Interaction of Water Vapor with the Fe_3O_4(001) Surface at Near-Ambient Conditions. *J. Phys. Chem. C* **2013**, *117*, 2719−2733.
(436) Yamamoto, S.; et al. Water Adsorption on α-Fe_2O_3(0001) at near Ambient Conditions. *J. Phys. Chem. C* **2010**, *114*, 2256−2266.
(437) Kim, Y. D.; Seitsonen Wendt, S.; Wang, J.; Fan, C.; Jacobi, K.; Over, H.; Ertl, G. Characterization of Various Oxygen Species on an Oxide Surface: RuO_2(110). *J. Phys. Chem. B* **2001**, *105*, 3752−3758.
(438) Lin, W. F.; Zei, M. S.; Kim, Y. D.; Over, H.; Ertl, G. Electrochemical versus Gas-Phase Oxidation of Ru Single-Crystal Surfaces. *J. Phys. Chem. B* **2000**, *104*, 6040−6048.
(439) Chu, Y. S.; Lister, T. E.; Cullen, W. G.; You, H.; Nagy, Z. Commensurate Water Monolayer at the RuO_2(110)/Water Interfaces. *Phys. Rev. Lett.* **2001**, *86*, 3364−3367.
(440) Lister, T. E.; Chu, Y. S.; Cullen, W. G.; You, H.; Yonco, R. M.; Mitchell, J. F.; Nagy, Z. Electrochemical and X-ray Scattering Study of Well Defined RuO_2 Single Crystal Surfaces. *J. Electroanal. Chem.* **2002**, *524*, 201−218.
(441) Rao, R. R.; Kolb, M. J.; Halck, N. B.; Pedersen, A. F.; Mehta, A.; You, H.; Stoerzinger, K. A.; Feng, Z.; Hansen, H. A.; Zhou, H.; Giordano, L.; Rossmeisl, J.; Vegge, T.; Chorkendorff, I.; Stephens, I. E. L.; Shao-Horn, Y. Towards Identifying the Active Sites on RuO_2 (110) in Catalyzing Oxygen Evolution. *Energy Environ. Sci.* **2017**, *10*, 2626−2637.
(442) Rao, R. R.; Kolb, M. J.; Giordano, L.; Pedersen, A. F.; Katayama, Y.; Hwang, J.; Mehta, A.; You, H.; Lunger, J. R.; Zhou, H.; Halck, N. B.; Vegge, T.; Chorkendorff, I.; Stephens, I. E. L.; Shao-Horn, Y. *Operando* Identification of Site-Dependent Water Oxidation Activity on Ruthenium Dioxide Single-Crystal Surfaces. *Nat. Catal.* **2020**, *3*, 516−525.
(443) Stoerzinger, K. A.; Diaz-Morales, O.; Kolb, M.; Rao, R. R.; Frydendal, R.; Qiao, L.; Wang, X. R.; Halck, N. B.; Rossmeisl, J.; Hansen, H. A.; Vegge, T.; Stephens, I. E. L.; Koper, M. T. M.; Shao-Horn, Y. Orientation-Dependent Oxygen Evolution on RuO_2 without Lattice Exchange. *ACS Energy Lett.* **2017**, *2*, 876−881.
(444) Paoli, E. A.; Masini, F.; Frydendal, R.; Deiana, D.; Schlaup, C.; Malizia, M.; Hansen, T. W.; Horch, S.; Sephens, I. E. L.; Chorkendorff, I. Oxygen Evolution on Well-Characterized Mass Selected Ru and RuO_2 Nanoparticles. *Chem. Sci.* **2015**, *6*, 190−196.
(445) Abruna, H. D.; Bommarito, G. M.; Yee, H. S. X-ray Standing Waves and Surface EXAFS Studies of Electrochemical Interfaces. *Acc. Chem. Res.* **1995**, *28*, 273−279.
(446) Abruna, H. D.; White, J. H.; Albarelli, M. J.; Bommarito, G. M.; Bedzyk, M. J.; McMillan, M. Is There Any Beam Yet? Uses of Synchrotron Radiation in the in Situ Study of Electrochemical Interfaces. *J. Phys. Chem.* **1988**, *92*, 7045−7052.
(447) Nemsak, S.; Shavorshiky, A.; Karslioglu, O.; Zegkinoglou, I.; Rattanachata, A.; Conlon, C. S.; Keqi, A.; Greene, P. K.; Burks, E. C.; Salmssi, F.; Gullikson, E. M.; Yang, S.-H.; Liu, K.; Bluhm, H.; Fadley, C. S. Concentration and Chemical-State Profiles at Heterogeneous Interfaces with Sub-Nm Accuracy from Standing-Wave Ambient-Pressure Photoemission. *Nat. Commun.* **2014**, *5*, 5441.
(448) Hartman, T.; Wondergem, C. S.; Kumar, N.; van den Berg, A.; Weckhuysen, B. M. Surface- and Tip-Enhanced Raman Spectroscopy in Catalysis. *J. Phys. Chem. Lett.* **2016**, *7*, 1570−1584.
(449) Yang, C.; Woll, C. IR Spectroscopy Applied to Metal Oxide Surfaces: Adsorbate vibrations and Beyond. *Adv. Phys.* **2017**, *2*, 373−408.
(450) Chan, H.; Takoudis, C. G.; Weaver, M. J. High-Pressure Oxidation of Ruthenium as Probed by Surface-Enhanced Raman and X-Ray Photoelectron Spectroscopies. *J. Catal.* **1997**, *172*, 336−345.
(451) Mo, Y.; Cai, W.; Dong, J.; Carey, P. R.; Scherson, D. A. *In Situ* Surface Enhanced Raman Scattering of Ruthenium Dioxide Films in Acid Electrolytes. *Electrochem. Solid-State Lett.* **2001**, *4*, E37−E38.
(452) Yeo, B. S.; Bell, A. T. Enhanced Activity of Gold-Supported Cobalt Oxide for the Electrochemical Evolution of Oxygen. *J. Am. Chem. Soc.* **2011**, *133*, 5587−5593.
(453) Louie, M. W.; Bell, A. T. An Investigation of Thin-Film Ni-Fe Oxide Catalysts for the Electrochemical Evolution of Oxygen. *J. Am. Chem. Soc.* **2013**, *135*, 12329−12337.
(454) Ling, X. Y.; Yan, R.; Lo, S.; Hoang, D. T.; Liu, C.; Fardy, M. A.; Khan, S. B.; Asiri, A. M.; Bawaked, S. M.; Yang, P. Alumina-Coated Ag Nanocrystal Monolayers as Surface Enhanced Raman Spectroscopy Platforms for the Direct Spectroscopic Detection of Water Splitting Reaction Intermediates. *Nano Res.* **2014**, *7*, 132−143.
(455) Liang, Y.; Li, Y.; Wang, H.; Zhou, J.; Wang, J.; Regier, T.; Dai, H. Co_3O_4 Nanocrystals on Graphene as a Synergistic Catalyst for Oxygen Reduction Reaction. *Nat. Mater.* **2011**, *10*, 780−786.
(456) Liang, Y.; Wang, H.; Zhou, J.; Li, Y.; Wang, J.; Regier, T.; Dai, H. Covalent Hybrid of Spinel Manganese-Cobalt Oxide and Graphene as Advanced Oxygen Reduction Electrocatalysts. *J. Am. Chem. Soc.* **2012**, *134*, 3517−3523.
(457) Restovic, A.; Ríos, E.; Barbato, S.; Ortiz, J.; Gautier, J. Oxygen Reduction in Alkaline Medium at Thin $Mn_xCo_{3-x}O_4$ ($0 \leq x \leq 1$) Spinel Films Prepared by Spray Pyrolysis. Effect of Oxide Cation Composition on the Reaction Kinetics. *J. Electroanal. Chem.* **2002**, *522*, 141−151.
(458) Meng, Y.; Song, W.; Huang, H.; Ren, Z.; Chen, S.; Suib, S. Structure-Property Relationship of Bifunctional MnO_2 Nanostructures: Highly Efficient, Ultra-Stable Electrochemical Water Oxidation and Oxygen Reduction Reaction Catalysts Identified in Alkaline Media. *J. Am. Chem. Soc.* **2014**, *136*, 11452−11464.
(459) Wang, H.; Liu, R.; Li, Y.; Lu, X.; Wang, Q.; Zhao, S.; Yuan, K.; Cui, Z.; Li, X.; Xin, S.; Zhang, R.; Lei, M.; Lin, Z. Durable and Efficient Hollow Porous Oxide Spinel Microspheres for Oxygen Reduction. *Joule* **2018**, *2*, 337−348.
(460) Li, C.; Han, X.; Cheng, F.; Hu, Y.; Chen, C.; Chen, J. Phase and Composition Controllable Synthesis of Cobalt Manganese Spinel

https://doi.org/10.1021/acs.chemrev.1c00331
Chem. Rev. XXXX, XXX, XXX−XXX

Nanoparticles towards Efficient Oxygen Electrocatalysis. *Nat. Commun.* **2015**, *6*, 7345.
(461) Cheng, F.; Shen, J.; Peng, B.; Pan, Y.; Tao, Z.; Chen, J. Rapid Room-Temperature Synthesis of Nanocrystalline Spinels as Oxygen Reduction and Evolution Electrocatalysts. *Nat. Chem.* **2011**, *3*, 79−84.
(462) Ni, Y.; Lin, L.; Shang, Y.; Luo, L.; Wang, L.; Lu, Y.; Li, Y.; Yan, Z.; Zhang, K.; Cheng, F.; Chen, J. Regulating Electrocatalytic Oxygen Reduction Activity of a Metal Coordination Polymer via d-π Conjugation. *Angew. Chem., Int. Ed.* **2021**, *60*, 16937−16941.
(463) Cheng, F.; Su, Y.; Liang, J.; Tao, Z.; Chen, J. MnO_2-Based Nanostructures as Catalysts for Electrochemical Oxygen Reduction in Alkaline Media. *Chem. Mater.* **2010**, *22* (3), 898−905.
(464) Du, J.; Chen, C.; Cheng, F.; Chen, J. Rapid Synthesis and Efficient Electrocatalytic Oxygen Reduction/Evolution Reaction of $CoMn_2O_4$ Nanodots Supported on Graphene. *Inorg. Chem.* **2015**, *54*, 5467−5474.
(465) Xiong, Y.; Yang, Y.; DiSalvo, F. J.; Abruna, H. D. Metal-Organic-Framework-Derived Co-Fe Bimetallic Oxygen Reduction Electrocatalyst for Alkaline Fuel Cells. *J. Am. Chem. Soc.* **2019**, *141*, 10744−10750.
(466) Yang, Y.; Xiong, Y.; Holtz, M. E.; Feng, X.; Zeng, R.; Chen, G.; DiSalvo, F. J.; Muller, H. D.; Abruna, H. D. Octahedral Spinel Electrocatalysts for Alkaline Fuel Cells. *Proc. Natl. Acad. Sci. U. S. A.* **2019**, *116*, 24425−24432.
(467) Williams, D. B.; Carter, C. B. *Transmission Electron Microscopy: A Textbook for Materials Science*, 2nd ed.; Springer: New York, 2009; p 741.
(468) Garvie, L. A. J.; Craven, A. J. High-resolution Parallel Electron Energy-loss Spectroscopy of Mn $L_{2,3}$-Edges in Inorganic Manganese Compounds. *Phys. Chem. Miner.* **1994**, *21*, 191−206.
(469) Yang, Y.; Wang, Y.; Xiong, Y.; Huang, X.; Shen, L.; Huang, R.; Wang, H.; Pastore, J. P.; Yu, S. H.; Xiao, L.; Brock, J. D.; Zhuang, L.; Abruna, H. D. *In Situ* X-Ray Absorption Spectroscopy of a Synergistic Co-Mn Oxide Catalyst for the Oxygen Reduction Reaction. *J. Am. Chem. Soc.* **2019**, *141*, 1463−1466.
(470) Xiong, Y.; Yang, Y.; Feng, X.; DiSalvo, F. J.; Abruna, H. D. A Strategy for Increasing the Efficiency of the Oxygen Reduction Reaction in Mn-Doped Cobalt Ferrites. *J. Am. Chem. Soc.* **2019**, *141*, 4412−4421.
(471) Wu, J.; Zhang, J.; Peng, Z.; Yang, S.; Wagner, F. T.; Yang, H. Truncated Octahedral Pt_3Ni Oxygen Reduction Reaction Electrocatalysts. *J. Am. Chem. Soc.* **2010**, *132*, 4984−4985.
(472) Gan, L.; Cui, C.; Heggen, M.; Dionigi, F.; Rudi, S.; Strasser, P. Element-Specific Anisotropic Growth of Shaped Platinum Alloy Nanocrystals. *Science* **2014**, *346*, 1502−1506.
(473) Kongkanand, A.; Mathias, M. The Priority and Challenge of High-Power Performance of Low-Platinum Proton-Exchange Membrane Fuel Cells. *J. Phys. Chem. Lett.* **2016**, *7*, 1127−1137.
(474) Huang, Y.; Zhang, J.; Kongkanand, A.; Wagner, F. T.; Li, J.; Jorne, J. Transient Platinum Oxide Formation and Oxygen Reduction on Carbon-Supported Platinum and Platinum-Alloy Electrocatalysts. *J. Electrochem. Soc.* **2014**, *161*, F10−F15.
(475) Wakabayashi, R.; Paik, H.; Murphy, M. J.; Schlom, D. G.; Brutzam, M.; Uecker, R.; van Dover, B.; DiSalvo, F. J.; Abruna, H. D. Rotating Disk Electrode Voltammetry of Thin Films of Novel Oxide Materials. *J. Electrochem. Soc.* **2017**, *164*, H1154−H1160.
(476) Yang, Y.; Zeng, R.; Xiong, Y.; DiSalvo, F. J.; Abruna, H. D. Rock-Salt-Type $MnCo_2O_3$/C as Efficient Oxygen Reduction Electrocatalysts for Alkaline Fuel Cells. *Chem. Mater.* **2019**, *31*, 9331−9337.
(477) Yang, Y.; Zeng, R.; Xiong, Y.; DiSalvo, F. J.; Abruna, H. D. Cobalt-Based Nitride-Core Oxide-Shell Oxygen Reduction Electrocatalysts. *J. Am. Chem. Soc.* **2019**, *141*, 19241−19245.
(478) Luo, J.; Tian, X.; Zeng, J.; Li, Y.; Song, H.; Liao, S. Limitations and Improvement Strategies for Early-Transition-Metal Nitrides as Competitive Catalysts toward the Oxygen Reduction Reaction. *ACS Catal.* **2016**, *6*, 6165−6174.
(479) Miura, A.; Rosero-Navarro, C.; Masubuchi, Y.; Higuchi, M.; Kikkawa, S.; Tadanaga, K. Nitrogen-Rich Manganese Oxynitrides with Enhanced Catalytic Activity in the Oxygen Reduction Reaction. *Angew. Chem., Int. Ed.* **2016**, *55*, 7963−7967.
(480) Varga, T.; Vásárhelyi, L.; Ballai, G.; Haspel, H.; Oszkó, A.; Kukovecz, A.; Kónya, Z. Noble-Metal-Free Iron Nitride/Nitrogen-Doped Graphene Composite for the Oxygen Reduction Reaction. *ACS Omega* **2019**, *4*, 130−139.
(481) Chen, P.; Xu, K.; Fang, Z.; Tong, Y.; Wu, J.; Lu, X.; Peng, X.; Ding, H.; Wu, C.; Xie, Y. Metallic Co_4N Porous Nanowire Arrays Activated by Surface Oxidation as Electrocatalysts for the Oxygen Evolution Reaction. *Angew. Chem., Int. Ed.* **2015**, *54*, 14710−14714.
(482) Tian, X.; Luo, J.; Nan, H.; Fu, Z.; Zeng, J.; Liao, S. Binary Transition Metal Nitrides with Enhanced Activity and Durability for the Oxygen Reduction Reaction. *J. Mater. Chem. A* **2015**, *3*, 16801−16809.
(483) Zhang, H.; Liu, M.; Cheng, W.; Li, Y.; Zhou, W.; Su, H.; Zhao, X.; Yao, P.; Liu, Q. Metallic Ni_3/N Quantum Dots as a Synergistic Promoter for NiO Nanosheet toward Efficient Oxygen Reduction Electrocatalysis. *J. Phys. Chem. C* **2019**, *123*, 8633−8639.
(484) Wu, H.; Chen, W. Copper Nitride Nanocubes: Size-Controlled Synthesis and Application as Cathode Catalyst in Alkaline Fuel Cells. *J. Am. Chem. Soc.* **2011**, *133*, 15236−15239.
(485) Chen, P.; Xu, K.; Fang, Z.; Tong, Y.; Li, X.; Tao, S.; Fang, Z.; Chu, W.; Wu, X.; Wu, C.; Wu, J.; Lu, X.; Peng, X.; Ding, H.; Wu, C. Cobalt Nitrides as a Class of Metallic Electrocatalysts for the Oxygen Evolution Reaction. *Inorg. Chem. Front.* **2016**, *3*, 236−242.
(486) Zhang, Y.; Ouyang, B.; Xu, J.; Jia, G.; Chen, S.; Rawat, R. S.; Fan, H. J. Rapid Synthesis of Cobalt Nitride Nanowires: Highly Efficient and Low-Cost Catalysts for Oxygen Evolution. *Angew. Chem., Int. Ed.* **2016**, *55*, 8670−8674.
(487) Zhu, X.; Jin, T.; Tian, C.; Lu, C.; Liu, X.; Zeng, M.; Zhuang, X.; Yang, S.; He, L.; Liu, H.; Dai, S. In Situ Coupling Strategy for the Preparation of FeCo Alloys and Co_4N Hybrid for Highly Efficient Oxygen Evolution. *Adv. Mater.* **2017**, *29*, 1704091.
(488) Meng, F.; Zhong, H.; Bao, D.; Yan, J.; Zhang, X. In Situ Coupling of Strung Co_4N and Intertwined N-C Fibers toward Free-Standing Bifunctional Cathode for Robust, Efficient, and Flexible Zn-Air Batteries. *J. Am. Chem. Soc.* **2016**, *138*, 10226−10231.
(489) Yoon, K. R.; Shin, K.; Park, J.; Cho, S. H.; Kim, C.; Jung, J. W.; Cheong, J. Y.; Byon, H. R.; Lee, H. M.; Kim, I. D. Brush-Like Cobalt Nitride Anchored Carbon Nanofiber Membrane: Current Collector-Catalyst Integrated Cathode for Long Cycle Li-O_2 Batteries. *ACS Nano* **2018**, *12*, 128−139.
(490) Davis, R. E.; Horvath, G. L.; Tobias, C. W. The Solubility and Diffusion Coefficient of Oxygen in Potassium Hydroxide Solutions. *Electrochim. Acta* **1967**, *12*, 287−297.
(491) Zeng, R.; Yang, Y.; DiSalvo, F. J.; Abruna, H. D. Nonprecious Transition MetalNitrides as Oxygen Reduction Electrocatalysts for Alkaline Fuel Cells. *Sci. Adv.* **2022**, *8*, DOI: 10.1126/sciadv.abj1584
(492) Yu, Y.; Li, H.; Yuan, X.-Z.; Wang, G.; Pan, W. A Review on Performance Degradation of Proton Exchange Membrane Fuel Cells during Startup and Shutdown Processes: Causes, Consequences, and Mitigation Strategies. *J. Power Sources* **2012**, *205*, 10−23.
(493) Jasinski, R. A New Fuel Cell Cathode Catalyst. *Nature* **1964**, *201*, 1212−1213.
(494) Jahnke, H.; Schönborn, M.; Zimmermann, G. In *Physical and Chemical Applications of Dyestuffs*; Springer, 1976.
(495) Peng, H.; Liu, F.; Liu, X.; Liao, S.; You, C.; Tian, X.; Nan, H.; Luo, F.; Song, H.; Fu, Z.; Huang, P. Effect of Transition Metals on the Structure and Performance of the Doped Carbon Catalysts Derived from Polyaniline and Melamine for ORR Application. *ACS Catal.* **2014**, *4*, 3797−3805.
(496) Yang, Z.; Chen, B.; Chen, W.; Qu, Y.; Zhou, F.; Zhao, C.; Xu, Q.; Zhang, Q.; Duan, X.; Wu, Y. Directly Transforming Copper (I) Oxide Bulk into Isolated Single-Atom Copper Sites Catalyst through Gas-Transport Approach. *Nat. Commun.* **2019**, *10*, 3734.
(497) Li, J.; Chen, M.; Cullen, D. A.; Hwang, S.; Wang, M.; Li, B.; Liu, K.; Karakalos, S.; Lucero, M.; Zhang, H.; Lei, C.; Xu, H.; Sterbinsky, G. E.; Feng, Z.; Su, D.; More, K. L.; Wang, G.; Wang, Z.; Wu, G. Atomically Dispersed Manganese Catalysts for Oxygen

https://doi.org/10.1021/acs.chemrev.1c00331
Chem. Rev. XXXX, XXX, XXX−XXX

Reduction in Proton-Exchange Membrane Fuel Cells. *Nat. Catal.* **2018**, *1*, 935−945.
(498) Choi, C. H.; Lim, H.-K.; Chung, M. W.; Chon, G.; Ranjbar Sahraie, N.; Altin, A.; Sougrati, M.-T.; Stievano, L.; Oh, H. S.; Park, E. S.; Luo, F.; Strasser, P.; Dražić, G.; Mayrhofer, K. J. J.; Kim, H.; Jaouen, F. The Achilles' Heel of Iron-Based Catalysts During Oxygen Reduction in an Acidic Medium. *Energy Environ. Sci.* **2018**, *11*, 3176−3182.
(499) Bashyam, R.; Zelenay, P. A Class of Non-Precious Metal Composite Catalysts for Fuel Cells. *Nature* **2006**, *443*, 63−66.
(500) Lefevre, M.; Proietti, E.; Jaouen, F.; Dodelet, J.-P. Iron-Based Catalysts with Improved Oxygen Reduction Activity in Polymer Electrolyte Fuel Cells. *Science* **2009**, *324*, 71−74.
(501) Wu, G.; More, K. L.; Johnston, C. M.; Zelenay, P. High-Performance Electrocatalysts for Oxygen Reduction Derived from Polyaniline, Iron, and Cobalt. *Science* **2011**, *332*, 443−447.
(502) Chung, H. T.; Cullen, D. A.; Higgins, D.; Sneed, B. T.; Holby, E. F.; More, K. L.; Zelenay, P. Direct Atomic-Level Insight into the Active Sites of a High-Performance Pgm-Free ORR Catalyst. *Science* **2017**, *357*, 479−484.
(503) Proietti, E.; Jaouen, F.; Lefevre, M.; Larouche, N.; Tian, J.; Herranz, J.; Dodelet, J.-P. Iron-Based Cathode Catalyst with Enhanced Power Density in Polymer Electrolyte Membrane Fuel Cells. *Nat. Commun.* **2011**, *2*, 416.
(504) Kramm, U. I.; Herranz, J.; Larouche, N.; Arruda, T. M.; Lefevre, M.; Jaouen, F.; Bogdanoff, P.; Fiechter, S.; Abs-Wurmbach, I.; Mukerjee, S.; Dodelet, J.-P. Structure of the Catalytic Sites in Fe/N/C-Catalysts for O_2-Reduction in Pem Fuel Cells. *Phys. Chem. Chem. Phys.* **2012**, *14*, 11673−11688.
(505) Mineva, T.; Matanovic, I.; Atanassov, P.; Sougrati, M.-T.; Stievano, L.; Clémancey, M.; Kochem, A.; Latour, J.-M.; Jaouen, F. Understanding Active Sites in Pyrolyzed Fe-N-C Catalysts for Fuel Cell Cathodes by Bridging Density Functional Theory Calculations and ^{57}Fe Mössbauer Spectroscopy. *ACS Catal.* **2019**, *9*, 9359−9371.
(506) Li, J.; Chen, S.; Yang, N.; Deng, M.; Ibraheem, S.; Deng, J.; Li, J.; Li, L.; Wei, Z. Ultrahigh-Loading Zinc Single-Atom Catalyst for Highly Efficient Oxygen Reduction in Both Acidic and Alkaline Media. *Angew. Chem., Int. Ed.* **2019**, *58*, 7035−7039.
(507) Thompson, S. T.; Wilson, A. R.; Zelenay, P.; Myers, D. J.; More, K. L.; Neyerlin, K. C.; Papageorgopoulos, D. Electrocat: DOE's Approach to Pgm-Free Catalyst and Electrode R&D. *Solid State Ionics* **2018**, *319*, 68−76.
(508) Ma, S.; Goenaga, G. A.; Call, A. V.; Liu, D. J. Cobalt Imidazolate Framework as Precursor for Oxygen Reduction Reaction Electrocatalysts. *Chem. - Eur. J.* **2011**, *17*, 2063−2067.
(509) Shen, H.; Gracia-Espino, E.; Ma, J.; Tang, H.; Mamat, X.; Wagberg, T.; Hu, G.; Guo, S. Atomically FeN_2 Moieties Dispersed on Mesoporous Carbon: A New Atomic Catalyst for Efficient Oxygen Reduction Catalysis. *Nano Energy* **2017**, *35*, 9−16.
(510) Li, Y.; Liu, X.; Zheng, L.; Shang, J.; Wan, X.; Hu, R.; Guo, X.; Hong, S.; Shui, J. Preparation of Fe-N-C Catalysts with FeN_x (x = 1, 3, 4) Active Sites and Comparison of Their Activities for the Oxygen Reduction Reaction and Performances in Proton Exchange Membrane Fuel Cells. *J. Mater. Chem. A* **2019**, *7*, 26147−26153.
(511) Zhao, Y.-M.; Zhang, P.-C.; Xu, C.; Zhou, X.-Y.; Liao, L.-M.; Wei, P.-J.; Liu, E.; Chen, H.; He, Q.; Liu, J.-G. Design and Preparation of Fe-N_5 Catalytic Sites in Single-Atom Catalysts for Enhancing the Oxygen Reduction Reaction in Fuel Cells. *ACS Appl. Mater. Interfaces* **2020**, *12*, 17334−17342.
(512) Jia, Q.; Ramaswamy, N.; Hafiz, H.; Tylus, U.; Strickland, K.; Wu, G.; Barbiellini, B.; Bansil, A.; Holby, E. F.; Zelenay, P.; Mukerjee, S. Experimental Observation of Redox-Induced Fe-N Switching Behavior as a Determinant Role for Oxygen Reduction Activity. *ACS Nano* **2015**, *9*, 12496−12505.
(513) Zitolo, A.; Goellner, V.; Armel, V.; Sougrati, M.-T.; Mineva, T.; Stievano, L.; Fonda, E.; Jaouen, F. Identification of Catalytic Sites for Oxygen Reduction in Iron- and Nitrogen-Doped Graphene materials. *Nat. Mater.* **2015**, *14*, 937−942.
(514) Zitolo, A.; Ranjbar-Sahraie, N.; Mineva, T.; Li, J.; Jia, Q.; Stamatin, S.; Harrington, G. F.; Lyth, S. M.; Krtil, P.; Mukerjee, S. Identification of Catalytic Sites in Cobalt-Nitrogen-Carbon Materials for the Oxygen Reduction Reaction. *Nat. Commun.* **2017**, *8*, 957.
(515) Marshall-Roth, T.; Libretto, N. J.; Wrobel, A. T.; Anderton, K. J.; Pegis, M. L.; Ricke, N. D.; Voorhis, T. V.; Miller, J. T.; Surendranath, Y. A Pyridinic Fe-N_4 Macrocycle Models the Active Sites in Fe/N-Doped Carbon Electrocatalysts. *Nat. Commun.* **2020**, *11*, 5283.
(516) Guo, D.; Shibuya, R.; Akiba, C.; Saji, S.; Kondo, T.; Nakamura, J. Active Sites of Nitrogen-Doped Carbon Materials for Oxygen Reduction Reaction Clarified Using Model Catalysts. *Science* **2016**, *351*, 361−365.
(517) Liu, X.; Dai, L. Carbon-Based Metal-Free Catalysts. *Nat. Rev. Mater.* **2016**, *1*, 16064.
(518) Sebastián, D.; Nieto-Monge, M.; Pérez-Rodríguez, S.; Pastor, E.; Lázaro, M. Nitrogen Doped Ordered Mesoporous Carbon as Support of PtRu Nanoparticles for Methanol Electro-Oxidation. *Energies* **2018**, *11*, 831.
(519) Masa, J.; Zhao, A.; Xia, W.; Sun, Z.; Mei, B.; Muhler, M.; Schuhmann, W. Trace Metal Residues Promote the Activity of Supposedly Metal-Free Nitrogen-Modified Carbon Catalysts for the Oxygen Reduction Reaction. *Electrochem. Commun.* **2013**, *34*, 113−116.
(520) Wang, L.; Ambrosi, A.; Pumera, M. Metal-Free" Catalytic Oxygen Reduction Reaction on Heteroatom-Doped Graphene Is Caused by Trace Metal Impurities. *Angew. Chem.* **2013**, *125*, 14063−14066.
(521) Masa, J.; Xia, W.; Muhler, M.; Schuhmann, W. On the Role of Metals in Nitrogen-Doped Carbon Electrocatalysts for Oxygen Reduction. *Angew. Chem., Int. Ed.* **2015**, *54*, 10102−10120.
(522) Rao, C. V.; Cabrera, C. R.; Ishikawa, Y. In Search of the Active Site in Nitrogen-Doped Carbon Nanotube Electrodes for the Oxygen Reduction Reaction. *J. Phys. Chem. Lett.* **2010**, *1*, 2622−2627.
(523) Chen, Z.; Higgins, D.; Tao, H.; Hsu, R. S.; Chen, Z. Highly Active Nitrogen-Doped Carbon Nanotubes for Oxygen Reduction Reaction in Fuel Cell Applications. *J. Phys. Chem. C* **2009**, *113*, 21008−21013.
(524) Tang, Y.; Burkert, S. C.; Zhao, Y.; Saidi, W. A.; Star, A. The Effect of Metal Catalyst on the Electrocatalytic Activity of Nitrogen-Doped Carbon Nanotubes. *J. Phys. Chem. C* **2013**, *117*, 25213−25221.
(525) Jurkschat, K.; Ji, X.; Crossley, A.; Compton, R. G.; Banks, C. E. Super-Washing Does Not Leave Single Walled Carbon Nanotubes Iron-Free. *Analyst* **2007**, *132*, 21−23.
(526) Pumera, M. Carbon Nanotubes Contain Residual Metal Catalyst Nanoparticles Even after Washing with Nitric Acid at Elevated Temperature Because These Metal Nanoparticles Are Sheathed by Several Graphene Sheets. *Langmuir* **2007**, *23*, 6453−6458.
(527) Jaouen, F.; Lefevre, M.; Dodelet, J.-P.; Cai, M. Heat-Treated Fe/N/C Catalysts for O_2 Electroreduction: Are Active Sites Hosted in Micropores? *J. Phys. Chem. B* **2006**, *110*, 5553−5558.
(528) Malko, D.; Kucernak, A.; Lopes, T. In Situ Electrochemical Quantification of Active Sites in Fe-N/C Non-Precious Metal Catalysts. *Nat. Commun.* **2016**, *7*, 13285.
(529) Ramaswamy, N.; Mukerjee, S. Fundamental Mechanistic Understanding of Electrocatalysis of Oxygen Reduction on Pt and Non-Pt Surfaces: Acid Versus Alkaline Media. *Adv. Phys. Chem.* **2012**, *2012*, 491604.
(530) Rojas-Carbonell, S.; Artyushkova, K.; Serov, A.; Santoro, C.; Matanovic, I.; Atanassov, P. Effect of Ph on the Activity of Platinum Group Metal-Free Catalysts in Oxygen Reduction Reaction. *ACS Catal.* **2018**, *8*, 3041−3053.
(531) Bagotzky, V.; Tarasevich, M.; Radyushkina, K.; Levina, O.; Andrusyova, S. Electrocatalysis of the Oxygen Reduction Process on Metal Chelates in Acid Electrolyte. *J. Power Sources* **1978**, *2*, 233−240.

https://doi.org/10.1021/acs.chemrev.1c00331
Chem. Rev. XXXX, XXX, XXX−XXX

(532) Gupta, S.; Tryk, D.; Bae, I.; Aldred, W.; Yeager, E. Heat-Treated Polyacrylonitrile-Based Catalysts for Oxygen Electroreduction. *J. Appl. Electrochem.* **1989**, *19*, 19−27.
(533) Li, X.; Liu, G.; Popov, B. N. Activity and Stability of Non-Precious Metal Catalysts for Oxygen Reduction in Acid and Alkaline Electrolytes. *J. Power Sources* **2010**, *195*, 6373−6378.
(534) Yang, L.; Cheng, D.; Xu, H.; Zeng, X.; Wan, X.; Shui, J.; Xiang, Z.; Cao, D. Unveiling the High-Activity Origin of Single-Atom Iron Catalysts for Oxygen Reduction Reaction. *Proc. Natl. Acad. Sci. U. S. A.* **2018**, *115*, 6626−6631.
(535) Yi, J.-D.; Xu, R.; Wu, Q.; Zhang, T.; Zang, K.-T.; Luo, J.; Liang, Y.-L.; Huang, Y.-B.; Cao, R. Atomically Dispersed Iron-Nitrogen Active Sites within Porphyrinic Triazine-Based Frameworks for Oxygen Reduction Reaction in Both Alkaline and Acidic Media. *ACS Energy Lett.* **2018**, *3*, 883−889.
(536) Zhang, H.; Hwang, S.; Wang, M.; Feng, Z.; Karakalos, S.; Luo, L.; Qiao, Z.; Xie, X.; Wang, C.; Su, D. Single Atomic Iron Catalysts for Oxygen Reduction in Acidic Media: Particle Size Control and Thermal Activation. *J. Am. Chem. Soc.* **2017**, *139*, 14143−14149.
(537) Furukawa, H.; Cordova, K. E.; O'Keeffe, M.; Yaghi, O. M. The Chemistry and Applications of Metal-Organic Frameworks. *Science* **2013**, *341*, 1230444.
(538) Park, K. S.; Ni, Z.; Coté, A. P.; Choi, J. Y.; Huang, R.; Uribe-Romo, F. J.; Chae, H. K.; O'Keeffe, M.; Yaghi, O. M. Exceptional Chemical and Thermal Stability of Zeolitic Imidazolate Frameworks. *Proc. Natl. Acad. Sci. U. S. A.* **2006**, *103*, 10186−10191.
(539) Zhao, D.; Shui, J. L.; Grabstanowicz, L. R.; Chen, C.; Commet, S. M.; Xu, T.; Lu, J.; Liu, D. J. Highly Efficient Non-Precious Metal Electrocatalysts Prepared from One-Pot Synthesized Zeolitic Imidazolate Frameworks. *Adv. Mater.* **2014**, *26*, 1093−1097.
(540) Zhang, L.; Su, Z.; Jiang, F.; Yang, L.; Qian, J.; Zhou, Y.; Li, W.; Hong, M. Highly Graphitized Nitrogen-Doped Porous Carbon Nanopolyhedra Derived from ZIF-8 Nanocrystals as Efficient Electrocatalysts for Oxygen Reduction Reactions. *Nanoscale* **2014**, *6*, 6590−6602.
(541) Strickland, K.; Miner, E.; Jia, Q.; Tylus, U.; Ramaswamy, N.; Liang, W.; Sougrati, M.-T.; Jaouen, F.; Mukerjee, S. Highly Active Oxygen Reduction Non-Platinum Group Metal Electrocatalyst without Direct Metal-Nitrogen Coordination. *Nat. Commun.* **2015**, *6*, 7343.
(542) Tang, J.; Salunkhe, R. R.; Liu, J.; Torad, N. L.; Imura, M.; Furukawa, S.; Yamauchi, Y. Thermal Conversion of Core-Shell Metal-Organic Frameworks: A New Method for Selectively Functionalized Nanoporous Hybrid Carbon. *J. Am. Chem. Soc.* **2015**, *137*, 1572−1580.
(543) Zhang, H.; Chung, H. T.; Cullen, D. A.; Wagner, S.; Kramm, U. I.; More, K. L.; Zelenay, P.; Wu, G. High-Performance Fuel Cell Cathodes Exclusively Containing Atomically Dispersed Iron Active Sites. *Energy Environ. Sci.* **2019**, *12*, 2548−2558.
(544) Chen, Y.; Ji, S.; Wang, Y.; Dong, J.; Chen, W.; Li, Z.; Shen, R.; Zheng, L.; Zhuang, Z.; Wang, D. Isolated Single Iron Atoms Anchored on N-Doped Porous Carbon as an Efficient Electrocatalyst for the Oxygen Reduction Reaction. *Angew. Chem.* **2017**, *129*, 7041−7045.
(545) Wang, X. X.; Cullen, D. A.; Pan, Y. T.; Hwang, S.; Wang, M.; Feng, Z.; Wang, J.; Engelhard, M. H.; Zhang, H.; He, Y. Nitrogen-Coordinated Single Cobalt Atom Catalysts for Oxygen Reduction in Proton Exchange Membrane Fuel Cells. *Adv. Mater.* **2018**, *30*, 1706758.
(546) Liu, S.; Li, Z.; Wang, C.; Tao, W.; Huang, M.; Zuo, M.; Yang, Y.; Yang, K.; Zhang, L.; Chen, S. Turning Main-Group Element Magnesium into a Highly Active Electrocatalyst for Oxygen Reduction Reaction. *Nat. Commun.* **2020**, *11*, 938.
(547) Chen, Y.; Gao, R.; Ji, S.; Li, H.; Tang, K.; Jiang, P.; Hu, H.; Zhang, Z.; Hao, H.; Qu, Q. Atomic-Level Modulation of Electronic Density at Cobalt Single-Atom Sites Derived from Metal-Organic Frameworks: Enhanced Oxygen Reduction Performance. *Angew. Chem., Int. Ed.* **2021**, *60*, 3212−3221.
(548) Hou, C. C.; Zou, L.; Sun, L.; Zhang, K.; Liu, Z.; Li, Y.; Li, C.; Zou, R.; Yu, J.; Xu, Q. Single-Atom Iron Catalysts on Overhang-Eave Carbon Cages for High-Performance Oxygen Reduction Reaction. *Angew. Chem.* **2020**, *132*, 7454−7459.
(549) Jiao, L.; Wan, G.; Zhang, R.; Zhou, H.; Yu, S. H.; Jiang, H. L. From Metal-Organic Frameworks to Single-Atom Fe Implanted N-Doped Porous Carbons: Efficient Oxygen Reduction in Both Alkaline and Acidic Media. *Angew. Chem., Int. Ed.* **2018**, *57*, 8525−8529.
(550) Wang, X.; Zhang, H.; Lin, H.; Gupta, S.; Wang, C.; Tao, Z.; Fu, H.; Wang, T.; Zheng, J.; Wu, G. Directly Converting Fe-Doped Metal-Organic Frameworks into Highly Active and Stable Fe-N-C Catalysts for Oxygen Reduction in Acid. *Nano Energy* **2016**, *25*, 110−119.
(551) Chung, H. T.; Won, J. H.; Zelenay, P. Active and Stable Carbon Nanotube/Nanoparticle Composite Electrocatalyst for Oxygen Reduction. *Nat. Commun.* **2013**, *4*, 1922.
(552) Guan, B. Y.; Lu, Y.; Wang, Y.; Wu, M.; Lou, X. W. Porous Iron-Cobalt Alloy/Nitrogen-Doped Carbon Cages Synthesized via Pyrolysis of Complex Metal-Organic Framework Hybrids for Oxygen Reduction. *Adv. Funct. Mater.* **2018**, *28*, 1706738.
(553) Ren, H.; Wang, Y.; Yang, Y.; Tang, X.; Peng, Y.; Peng, H.; Xiao, L.; Lu, J.; Abruna, H. D.; Zhuang, L. Fe/N/C Nanotubes with Atomic Fe Sites: A Highly Active Cathode Catalyst for Alkaline Polymer Electrolyte Fuel Cells. *ACS Catal.* **2017**, *7*, 6485−6492.
(554) Chen, Y. Z.; Wang, C.; Wu, Z. Y.; Xiong, Y.; Xu, Q.; Yu, S. H.; Jiang, H. L. From Bimetallic Metal-Organic Framework to Porous Carbon: High Surface Area and Multicomponent Active Dopants for Excellent Electrocatalysis. *Adv. Mater.* **2015**, *27*, 5010−5016.
(555) Santori, P. G.; Speck, F. D.; Cherevko, S.; Firouzjaie, H. A.; Peng, X.; Mustain, W. E.; Jaouen, F. High Performance Fenc and Mn-Oxide/FeNC Layers for Aemfc Cathodes. *J. Electrochem. Soc.* **2020**, *167*, 134505.
(556) Xiong, Y.; Xiao, L.; Yang, Y.; DiSalvo, F. J.; Abruna, H. D. High-Loading Intermetallic Pt_3Co/C Core-Shell Nanoparticles as Enhanced Activity Electrocatalysts toward the Oxygen Reduction Reaction (ORR). *Chem. Mater.* **2018**, *30*, 1532−1539.
(557) Zhu, J.; Yang, Y.; Chen, L.; Xiao, W.; Liu, H.; Abruna, H. D.; Wang, D. Copper-Induced Formation of Structurally Ordered Pt-Fe-Cu Ternary Intermetallic Electrocatalysts with Tunable Phase Structure and Improved Stability. *Chem. Mater.* **2018**, *30*, 5987−5995.
(558) Xie, Y.; Yang, Y.; Muller, D. A.; Abruna, H. D.; Dimitrov, N.; Fang, J. Enhanced ORR Kinetics on Au-Doped Pt-Cu Porous Films in Alkaline Media. *ACS Catal.* **2020**, *10*, 9967−9976.
(559) Lima, F.; Zhang, J.; Shao, M.; Sasaki, K.; Vukmirovic, M.; Ticianelli, E.; Adzic, R. Catalytic Activity-d-Band Center Correlation for the O_2 Reduction Reaction on Platinum in Alkaline Solutions. *J. Phys. Chem. C* **2007**, *111*, 404−410.
(560) Hoshi, N.; Nakamura, M.; Maki, N. Yamaguchi, Structural Effects on Voltammograms of the Low Index Planes of Palladium and Pd(S)-[n(100)×(111)] Surfaces in Alkaline Solution. *J. Electroanal. Chem.* **2008**, *624*, 134−138.
(561) Erikson, H.; Sarapuu, A.; Alexeyeva, N.; Tammeveski, K.; Solla-Gullon, J.; Feliu, J. M. Electrochemical Reduction of Oxygen on Palladium Nanocubes in Acid and Alkaline Solutions. *Electrochim. Acta* **2012**, *59*, 329−335.
(562) Lusi, M.; Erikson, H.; Sarapuu, A.; Tammeveski, K.; Solla-Gullon, J.; Feliu, J. M. Oxygen Reduction Reaction on Carbon-Supported Palladium Nanocubes in Alkaline Media. *Electrochem. Commun.* **2016**, *64*, 9−13.
(563) Strbac, S.; Adzic, R. R. The Influence of pH on Reaction Pathways for O_2 Reduction on the Au(100) Face. *Electrochim. Acta* **1996**, *41*, 2903−2908.
(564) Prieto, A.; Hernandez, J.; Herrero, E.; Feliu, J. M. The Role of Anions in Oxygen Reduction in Neutral and Basic Media on Gold Single-Crystal Electrodes. *J. Solid State Electrochem.* **2003**, *7*, 599−606.
(565) Yang, Y.; Chen, G.; Villarino, A. M.; Disalvo, F. J.; van Dover, R. B.; Abruna, H. D. Combinatorial Studies of Palladium-Based Oxygen Reduction Electrocatalysts for Alkaline Fuel Cells. *J. Am. Chem. Soc.* **2020**, *142*, 3980−3988.

https://doi.org/10.1021/acs.chemrev.1c00331
Chem. Rev. XXXX, XXX, XXX−XXX

(566) Yang, Y.; Xiao, W.; Feng, X.; Xiong, Y.; Gong, M.; Shen, T.; Lu, Y.; Abruna, H. D.; Wang, D. Golden Palladium Zinc Ordered Intermetallics as Oxygen Reduction Electrocatalysts. *ACS Nano* **2019**, *13*, 5968−5974.
(567) Omasta, T. J.; Peng, X.; Miller, H. A.; Vizza, F.; Wang, L.; Varcoe, J. R.; Dekel, D.; Mustain, W. E. Beyond 1.0W cm^{-2} Performance without Platinum: The Beginning of a New Era in Anion Exchange Membrane Fuel Cells. *J. Electrochem. Soc.* **2018**, *165*, J3039−J3044.
(568) Zhang, J.; Vukmirovic, M.; Xu, Y.; Mavrikakis, M.; Adzic, R. R. Controlling the Catalytic of Platinum-Monolayer Electrocatalysts for Oxygen Reduction with Different Substrates. *Angew. Chem., Int. Ed.* **2005**, *44*, 2132−2135.
(569) Zhang, J.; Mo, Y.; Vukmirovic, M. B.; Klie, R.; Sasaki, K.; Adzic, R. R. Platinum Monolayer Electrocatalysts for O_2 Reduction: Pt Monolayer on Pd(111) and on Carbon-Supported Pd Nanoparticles. *J. Phys. Chem. B* **2004**, *108*, 10955−10964.
(570) Kongkanand, A.; Subramanian, N. P.; Yu, Y.; Liu, Z.; Igarashi, H.; Muller, D. A. Achieving High-Power PEM Fuel Cell Performance with an Ultralow-Pt-Content Core-Shell Catalyst. *ACS Catal.* **2016**, *6*, 1578−1583.
(571) Wang, G.; Guan, J.; Xiao, L.; Huang, B.; Wu, N.; Lu, J.; Zhuang, L. Pd Skin on AuCu Intermetallic Nanoparticles: A highly Active Electrocatalyst for Oxygen Reduction Reaction in Alkaline Media. *Nano Energy* **2016**, *29*, 268−274.
(572) Wang, G.; Huang, B.; Xiao, L.; Ren, Z.; Chen, H.; Wang, D.; Abruna, H. D.; Lu, J.; Zhuang, L. Pt Skin on AuCu Intermetallic Nanoparticles: A highly Active Electrocatalyst for Oxygen Reduction Reaction in Alkaline Media. *J. Am. Chem. Soc.* **2014**, *136*, 9643−9649.
(573) Lu, X.; Ahmadi, M.; DiSalvo, F. J.; Abruna, H. D. Enhancing the Electrocatalytic Activity of Pd/M (M = Ni, Mn) Nanoparticles for the Oxygen Reduction Reaction in Alkaline Media through Electrochemical Dealloying. *ACS Catal.* **2020**, *10*, 5891−5898.
(574) Beermann, V.; Gocyla, M.; Willinger, E.; Rudi, S.; Heggen, M.; Dunin-Borkowski, R. E.; Willinger, M.-G.; Strasser, P. Rh-Doped Pt-Ni Octahedral Nanoparticles: Understanding the Correlation between Elemental Distribution, Oxygen Reduction Reaction, and Shape Stability. *Nano Lett.* **2016**, *16*, 1719−1725.
(575) Xu, Y.; Chen, Y.; Xu, G.; Zhang, X.; Chen, Z.; Li, J.; Huang, L.; Amine, K.; Sun, S.-G. RuO_2 Nanoparticles Supported on MnO_2 Nanorods as High Efficient Bifunctional Electrocatalyst of Lithium-Oxygen Battery. *Nano Energy* **2016**, *28*, 63−70.
(576) Wang, H.; Abruna, H. D. Single-Phase $Ru_{1-x-y}Mn_xCo_yO_2$ Nanoparticles as Highly Effective Oxygen Reduction Electrocatalysts in Alkaline Media with Enhanced Stability and Fuel-Tolerance. *Appl. Catal., B* **2020**, *277*, 119149.
(577) Wang, L.; Brink, J. J.; Varcoe, J. R. The First Anion-Exchange Membrane Fuel Cell to Exceed 1 W cm^{-2} at 70° C with a Non-Pt-Group (O_2) Cathode. *Chem. Commun.* **2017**, *53*, 11771−11773.
(578) Slanac, D.; Hardin, W. G.; Johnston, K. P.; Stevenson, K. J. Atomic Ensemble and Electronic Effects in Ag-Rich AgPd Nanoalloy Catalysts for Oxygen Reduction in Alkaline Media. *J. Am. Chem. Soc.* **2012**, *134*, 9812−9819.
(579) Amin, H. M. A.; Bondue, C. J.; Eswara, S.; Kaiser, U.; Baltruschat, H. A Carbon-Free Ag-Co_3O_4 Composite as a Bifunctional Catalyst for Oxygen Reduction and Evolution: Spectroscopic, Microscopic and Electrochemical Characterization. *Electrocatalysis* **2017**, *8*, 540−553.
(580) Wang, Y.; Lu, X.; Liu, Y.; Deng, Y. Silver Supported on Co_3O_4 Modified Carbon as Electrocatalyst for Oxygen Reduction Reaction in Alkaline Media. *Electrochem. Commun.* **2013**, *31*, 108−111.
(581) Meier, J. C.; Galeano, C.; Katsounaros, I.; Witte, J.; Bongard, H. J.; Topalov, A. A.; Baldizzone, C.; Mezzavilla, S.; Schuth, F.; Mayrhofer, K. J. Design Criteria for Stable Pt/C Fuel Cell Catalysts. *Beilstein J. Nanotechnol.* **2014**, *5*, 44−67.
(582) Zelenay, P.; Myers, D. *Hydrogen and Fuel Cells Program 2020 Annual Progress Report*; ElectroCat (Electrocatalysis Consortium); Washington, DC, 2020.
(583) Ejikeme, P. M.; Makgopa, K.; Ozoemena, K. I. Effects of Catalyst-Support Materials on the Performance of Fuel Cells. In *Nanomaterials for Fuel Cell Catalysis*; K. Ozoemena, S. C., Ed.; Springer International Publishing: Cham, 2016; pp 517−550.
(584) Antolini, E. Carbon Supports for Low-Temperature Fuel Cell Catalysts. *Appl. Catal., B* **2009**, *88*, 1−24.
(585) Samad, S.; Loh, K. S.; Wong, W. Y.; Lee, T. K.; Sunarso, J.; Chong, S. T.; Wan Daud, W. R. Carbon and Non-Carbon Support Materials for Platinum-Based Catalysts in Fuel Cells. *Int. J. Hydrogen Energy* **2018**, *43*, 7823−7854.
(586) Zhou, X.; Qiao, J.; Yang, L.; Zhang, J. A Review of Graphene-Based Nanostructural Materials for Both Catalyst Supports and Metal-Free Catalysts in PEM Fuel Cell Oxygen Reduction Reactions. *Adv. Energy Mater.* **2014**, *4*, 1301523.
(587) Kordesch, K.; Marko, A. Selektive Sauerstoffbestimmung in Kleinen Gasmengen - (Ein Neues Direkt Anzeigendes Gerät.). *Microchim. Acta* **1951**, *36-37*, 420−424.
(588) Kordesch, K. V. 25 Years of Fuel Cell Development (1951-1976). *J. Electrochem. Soc.* **1978**, *125*, 77C−91C.
(589) Kordesch, K. V. Characterization of Hydrogen (Carbon) Electrodes for Fuel Cells. *Electrochim. Acta* **1971**, *16*, 597−602.
(590) Trogadas, P.; Fuller, T. F.; Strasser, P. Carbon as Catalyst and Support for Electrochemical Energy Conversion. *Carbon* **2014**, *75*, 5−42.
(591) Dicks, A. L. The Role of Carbon in Fuel Cells. *J. Power Sources* **2006**, *156*, 128−141.
(592) Wang, D. W.; Su, D. Heterogeneous Nanocarbon Materials for Oxygen Reduction Reaction. *Energy Environ. Sci.* **2014**, *7*, 576−591.
(593) Donnet, J.-B.; Wang, T. K. Surface Microstructure of Carbon Black: Advances in Characterization by Scanning Tunneling Microscopy. *Macromol. Symp.* **1996**, *108*, 97−109.
(594) Pantea, D.; Darmstadt, H.; Kaliaguine, S.; Roy, C. Electrical Conductivity of Conductive Carbon Blacks: Influence of Surface Chemistry and Topology. *Appl. Surf. Sci.* **2003**, *217*, 181−193.
(595) Yaldagard, M.; Jahanshahi, M.; Seghatoleslami, N. Carbonaceous Nanostructured Support Materials for Low Temperature Fuel Cell Electrocatalysts—A Review. *World J. Nano Sci. Eng.* **2013**, *3*, 121−153.
(596) Fang, B.; Kim, J. H.; Kim, M. S.; Yu, J. S. Hierarchical Nanostructured Carbons with Meso-Macroporosity: Design, Characterization, and Applications. *Acc. Chem. Res.* **2013**, *46*, 1397−1406.
(597) Serp, P.; Corrias, M.; Kalck, P. Carbon Nanotubes and Nanofibers in Catalysis. *Appl. Catal., A* **2003**, *253*, 337−358.
(598) Sebastián, D.; Calderón, J. C.; González-Expósito, J. A.; Pastor, E.; Martínez-Huerta, M. V.; Suelves, I.; Moliner, R.; Lázaro, M. J. Influence of Carbon Nanofiber Properties as Electrocatalyst Support on the Electrochemical Performance for PEM Fuel Cells. *Int. J. Hydrogen Energy* **2010**, *35*, 9934−9942.
(599) Sur, U. K. Graphene: A Rising Star on the Horizon of Materials Science. *Int. J. Electrochem.* **2012**, *2012*, 1−12.
(600) Surprise Gwebu, S.; N. Nomngongo, P.; W. Maxakato, N. Platinum-Based Carbon Nanodots Nanocatalysts for Direct Alcohol Fuel Cells. In *Nanocatalysts*; Nomngongo, P. N., Ed.; IntechOpen: Rijeka, 2019; Ch. 2.
(601) Karousis, N.; Suarez-Martinez, I.; Ewels, C. P.; Tagmatarchis, N. Structure, Properties, Functionalization, and Applications of Carbon Nanohorns. *Chem. Rev.* **2016**, *116*, 4850−4883.
(602) Hiralal, P.; Wang, H.; Unalan, H. E.; Liu, Y.; Rouvala, M.; Wei, D.; Andrew, P.; Amaratunga, G. A. J. Enhanced Supercapacitors from Hierarchical Carbon Nanotube and Nanohorn Architectures. *J. Mater. Chem.* **2011**, *21*, 17810−17815.
(603) Suda, Y.; Shimizu, Y.; Ozaki, M.; Tanoue, H.; Takikawa, H.; Ue, H.; Shimizu, K.; Umeda, Y. Electrochemical Properties of Fuel Cell Catalysts Loaded on Carbon Nanomaterials with Different Geometries. *Mater. Today Commun.* **2015**, *3*, 96−103.
(604) Jafri, R. I.; Rajalakshmi, N.; Ramaprabhu, S. Nitrogen-Doped Multi-Walled Carbon Nanocoils as Catalyst Support for Oxygen

https://doi.org/10.1021/acs.chemrev.1c00331
Chem. Rev. XXXX, XXX, XXX−XXX

Reduction Reaction in Proton Exchange Membrane Fuel Cell. *J. Power Sources* **2010**, *195*, 8080−8083.
(605) Che, G.; Lakshmi, B. B.; Martin, C. R.; Fisher, E. R. Metal-Nanocluster-Filled Carbon Nanotubes: Catalytic Properties and Possible Applications in Electrochemical Energy Storage and Production. *Langmuir* **1999**, *15*, 750−758.
(606) Che, G.; Lakshmi, B. B.; Martin, C. R.; Fisher, E. R.; Ruoff, R. S. Chemical Vapor Deposition Based Synthesis of Carbon Nanotubes and Nanofibers Using a Template Method. *Chem. Mater.* **1998**, *10*, 260−267.
(607) Antolini, E. Graphene as a New Carbon Support for Low-Temperature Fuel Cell Catalysts. *Appl. Catal., B* **2012**, *123-124*, 52−68.
(608) He, Y.; Liu, S.; Priest, C.; Shi, Q.; Wu, G. Atomically Dispersed Metal-Nitrogen-Carbon Catalysts for Fuel Cells: Advances in Catalyst Design, Electrode Performance, and Durability Improvement. *Chem. Soc. Rev.* **2020**, *49*, 3484−3524.
(609) Chai, G. S.; Shin, I. S.; Yu, J. S. Synthesis of Ordered, Uniform, Macroporous Carbons with Mesoporous Walls Templated by Aggregates of Polystyrene Spheres and Silica Particles for Use as Catalyst Supports in Direct Methanol Fuel Cells. *Adv. Mater.* **2004**, *16*, 2057−2061.
(610) Joo, S. H.; Choi, S. J.; Oh, I.; Kwak, J.; Liu, Z.; Terasaki, O.; Ryoo, R. Ordered Nanoporous Arrays of Carbon Supporting High Dispersions of Platinum Nanoparticles. *Nature* **2001**, *412*, 169−172.
(611) Tan, Y.; Xu, C.; Chen, G.; Fang, X.; Zheng, N.; Xie, Q. Facile Synthesis of Manganese-Oxide-Containing Mesoporous Nitrogen-Doped Carbon for Efficient Oxygen Reduction. *Adv. Funct. Mater.* **2012**, *22*, 4584−4591.
(612) Estevez, L.; Dua, R.; Bhandari, N.; Ramanujapuram, A.; Wang, P.; Giannelis, E. P. A Facile Approach for the Synthesis of Monolithic Hierarchical Porous Carbons-High Performance Materials for Amine Based CO_2 Capture and Supercapacitor Electrode. *Energy Environ. Sci.* **2013**, *6*, 1785−1790.
(613) Shen, M.; Ruan, C.; Chen, Y.; Jiang, C.; Ai, K.; Lu, L. Covalent Entrapment of Cobalt-Iron Sulfides in N-Doped Mesoporous Carbon: Extraordinary Bifunctional Electrocatalysts for Oxygen Reduction and Evolution Reactions. *ACS Appl. Mater. Interfaces* **2015**, *7*, 1207−1218.
(614) Tan, H.; Li, Y.; Jiang, X.; Tang, J.; Wang, Z.; Qian, H.; Mei, P.; Malgras, V.; Bando, Y.; Yamauchi, Y. Perfectly Ordered Mesoporous Iron-Nitrogen Doped Carbon as Highly Efficient Catalyst for Oxygen Reduction Reaction in Both Alkaline and Acidic Electrolytes. *Nano Energy* **2017**, *36*, 286−294.
(615) Zhang, Y.; Liu, Y.; Liu, W.; Li, X.; Mao, L. Synthesis of Honeycomb-like Mesoporous Nitrogen-Doped Carbon Nanospheres as Pt Catalyst Supports for Methanol Oxidation in Alkaline Media. *Appl. Surf. Sci.* **2017**, *407*, 64−71.
(616) Farzaneh, A.; Saghatoleslami, N.; Goharshadi, E. K.; Gharibi, H.; Ahmadzadeh, H. 3-D Mesoporous Nitrogen-Doped Reduced Graphene Oxide as an Efficient Metal-Free Electrocatalyst for Oxygen Reduction Reaction in Alkaline Fuel Cells: Role of π and Lone Pair Electrons. *Electrochim. Acta* **2016**, *222*, 608−618.
(617) Shui, J.; Chen, C.; Grabstanowicz, L.; Zhao, D.; Liu, D.-J. Highly Efficient Nonprecious Metal Catalyst Prepared with Metal-Organic Framework in a Continuous Carbon Nanofibrous Network. *Proc. Natl. Acad. Sci. U. S. A.* **2015**, *112*, 10629.
(618) Lee, K.; Zhang, J.; Wang, H.; Wilkinson, D. P. Progress in the Synthesis of Carbon Nanotube- And Nanofiber-Supported Pt Electrocatalysts for PEM Fuel Cell Catalysis. *J. Appl. Electrochem.* **2006**, *36*, 507−522.
(619) Fang, B.; Kim, M. S.; Kim, J. H.; Song, M. Y.; Wang, Y. J.; Wang, H.; Wilkinson, D. P.; Yu, J. S. High Pt Loading on Functionalized Multiwall Carbon Nanotubes as a Highly Efficient Cathode Electrocatalyst for Proton Exchange Membrane Fuel Cells. *J. Mater. Chem.* **2011**, *21*, 8066−8073.
(620) Yang, D. S.; Chaudhari, S.; Rajesh, K. P.; Yu, J. S. Preparation of Nitrogen-Doped Porous Carbon Nanofibers and the Effect of Porosity, Electrical Conductivity, and Nitrogen Content on Their Oxygen Reduction Performance. *ChemCatChem* **2014**, *6*, 1236−1244.
(621) Miao, M. Electrical Conductivity of Pure Carbon Nanotube Yarns. *Carbon* **2011**, *49*, 3755−3761.
(622) Qiao, M.; Titirici, M. M. Engineering the Interface of Carbon Electrocatalysts at the Triple Point for Enhanced Oxygen Reduction Reaction. *Chem. - Eur. J.* **2018**, *24*, 18374−18384.
(623) Tang, C.; Zhang, Q. Nanocarbon for Oxygen Reduction Electrocatalysis: Dopants, Edges, and Defects. *Adv. Mater.* **2017**, *29*, 1604103.
(624) Yan, D.; Li, Y.; Huo, J.; Chen, R.; Dai, L.; Wang, S. Defect Chemistry of Nonprecious-Metal Electrocatalysts for Oxygen Reactions. *Adv. Mater.* **2017**, *29*, 1606459.
(625) Jiang, Y.; Yang, L.; Sun, T.; Zhao, J.; Lyu, Z.; Zhuo, O.; Wang, X.; Wu, Q.; Ma, J.; Hu, Z. Significant Contribution of Intrinsic Carbon Defects to Oxygen Reduction Activity. *ACS Catal.* **2015**, *5*, 6707−6712.
(626) Li, Q.; Zhang, S.; Dai, L.; Li, L. S. Nitrogen-Doped Colloidal Graphene Quantum Dots and Their Size-Dependent Electrocatalytic Activity for the Oxygen Reduction Reaction. *J. Am. Chem. Soc.* **2012**, *134*, 18932−18935.
(627) Qiu, M.; Zhang, B.; Wu, H.; Cao, L.; He, X.; Li, Y.; Li, J.; Xu, M.; Jiang, Z. Preparation of Anion Exchange Membrane with Enhanced Conductivity and Alkaline Stability by Incorporating Ionic Liquid Modified Carbon Nanotubes. *J. Membr. Sci.* **2019**, *573*, 1−10.
(628) Shao, Y.; Liu, J.; Wang, Y.; Lin, Y. Novel Catalyst Support Materials for PEM Fuel Cells: Current Status and Future Prospects. *J. Mater. Chem.* **2009**, *19*, 46−59.
(629) Iglesias, D.; Giuliani, A.; Melchionna, M.; Marchesan, S.; Criado, A.; Nasi, L.; Bevilacqua, M.; Tavagnacco, C.; Vizza, F.; Prato, M.; Fornasiero, P. N-Doped Graphitized Carbon Nanohorns as a Forefront Electrocatalyst in Highly Selective O_2 Reduction to H_2O_2. *Chem.* **2018**, *4*, 106−123.
(630) Burchardt, T.; Gouérec, P.; Sanchez-Cortezon, E.; Karichev, Z.; Miners, J. H. Alkaline Fuel Cells: Contemporary Advancement and Limitations. *Fuel* **2002**, *81*, 2151−2155.
(631) Gouérec, P.; Poletto, L.; Denizot, J.; Sanchez-Cortezon, E.; Miners, J. H. The Evolution of the Performance of Alkaline Fuel Cells with Circulating Electrolyte. *J. Power Sources* **2004**, *129*, 193−204.
(632) Zadick, A.; Dubau, L.; Sergent, N.; Berthomé, G.; Chatenet, M. Huge Instability of Pt/C Catalysts in Alkaline Medium. *ACS Catal.* **2015**, *5*, 4819−4824.
(633) Borup, R.; Meyers, J.; Pivovar, B.; Kim, Y. S.; Mukundan, R.; Garland, N.; Myers, D.; Wilson, M.; Garzon, F.; Wood, D.; Zelenay, P.; More, K.; Stroh, K.; Zawodzinski, T.; Boncella, J.; McGrath, J. E.; Inaba, M.; Miyatake, K.; Hori, M.; Ota, K.; Ogumi, Z.; Miyata, S.; Nishikata, A.; Siroma, Z.; Uchimoto, Y.; Yasuda, K.; Kimijima, K.; Iwashita, N. Scientific Aspects of Polymer Electrolyte Fuel Cell Durability and Degradation. *Chem. Rev.* **2007**, *107*, 3904−3951.
(634) Dubau, L.; Castanheira, L.; Maillard, F.; Chatenet, M.; Lottin, O.; Maranzana, G.; Dillet, J.; Lamibrac, A.; Perrin, J.-C.; Moukheiber, E.; ElKaddouri, A.; De Moor, G.; Bas, C.; Flandin, L.; Caqué, N. A Review of PEM Fuel Cell Durability: Materials Degradation, Local Heterogeneities of Aging and Possible Mitigation Strategies. *Wiley Interdiscip. Rev.: Energy Environ.* **2014**, *3*, 540−560.
(635) Su-Il, P.; Eung-Jo, L.; Tae-Young, K.; Seo-Jae, L.; Young-Gyoon, R.; Chang-Soo, K. Role of Surface Oxides in Corrosion of Carbon Black in Phosphoric Acid Solution at Elevated Temperature. *Carbon* **1994**, *32*, 155−159.
(636) Du, L.; Shao, Y.; Sun, J.; Yin, G.; Liu, J.; Wang, Y. Advanced Catalyst Supports for PEM Fuel Cell Cathodes. *Nano Energy* **2016**, *29*, 314−322.
(637) Tomantschger, K.; Findlay, R.; Hanson, M.; Kordesch, K.; Srinivasan, S. Degradation Modes of Alkaline Fuel Cells and Their Components. *J. Power Sources* **1992**, *39*, 21−41.
(638) Lafforgue, C.; Zadick, A.; Dubau, L.; Maillard, F.; Chatenet, M. Selected Review of the Degradation of Pt and Pd-Based Carbon-

https://doi.org/10.1021/acs.chemrev.1c00331
Chem. Rev. XXXX, XXX, XXX−XXX

Supported Electrocatalysts for Alkaline Fuel Cells: Towards Mechanisms of Degradation. *Fuel Cells* **2018**, *18*, 229−238.
(639) Lafforgue, C.; Maillard, F.; Martin, V.; Dubau, L.; Chatenet, M. Degradation of Carbon-Supported Platinum-Group-Metal Electrocatalysts in Alkaline Media Studied by in Situ Fourier Transform Infrared Spectroscopy and Identical-Location Transmission Electron Microscopy. *ACS Catal.* **2019**, *9*, 5613−5622.
(640) Kabir, S.; Zadick, A.; Atanassov, P.; Dubau, L.; Chatenet, M. Stability of Carbon-Supported Palladium Nanoparticles in Alkaline Media: A Case Study of Graphitized and More Amorphous Supports. *Electrochem. Commun.* **2017**, *78*, 33−37.
(641) Park, J. H.; Hwang, S.-M.; Park, G.-G.; Park, S.-H.; Park, E.-D.; Yim, S.-D. Variations in Performance-Degradation Behavior of Pt/CNF and Pt/C MEAs for the Same Degree of Carbon Corrosion. *Electrochim. Acta* **2018**, *260*, 674−683.
(642) Padgett, E.; Yarlagadda, V.; Holtz, M. E.; Ko, M.; Levin, B. D. A.; Kukreja, R. S.; Ziegelbauer, J. M.; Andrews, R. N.; Ilavsky, J.; Kongkanand, A.; Muller, D. A. Mitigation of PEM Fuel Cell Catalyst Degradation with Porous Carbon Supports. *J. Electrochem. Soc.* **2019**, *166*, F198−F207.
(643) McBreen, J.; Olender, H.; Srinivasan, S.; Kordesch, K. V. Carbon Supports for Phosphoric Acid Fuel Cell Electrocatalysts: Alternative Materials and Methods of Evaluation. *J. Appl. Electrochem.* **1981**, *11*, 787−796.
(644) Kim, J. H.; Cheon, J. Y.; Shin, T. J.; Park, J. Y.; Joo, S. H. Effect of Surface Oxygen Functionalization of Carbon Support on the Activity and Durability of Pt/C Catalysts for the Oxygen Reduction Reaction. *Carbon* **2016**, *101*, 449−457.
(645) Zheng, H. T.; Li, Y.; Chen, S.; Shen, P. K. Effect of Support on the Activity of Pd Electrocatalyst for Ethanol Oxidation. *J. Power Sources* **2006**, *163*, 371−375.
(646) Liu, Z.; Lin, X.; Lee, J. Y.; Zhang, W.; Han, M.; Gan, L. M. Preparation and Characterization of Platinum-Based Electrocatalysts on Multiwalled Carbon Nanotubes for Proton Exchange Membrane Fuel Cells. *Langmuir* **2002**, *18*, 4054−4060.
(647) Molina-García, M. A.; Rees, N. V. Effect of Catalyst Carbon Supports on the Oxygen Reduction Reaction in Alkaline Media: A Comparative Study. *RSC Adv.* **2016**, *6*, 94669−94681.
(648) Jalan, I.; Vinod, M. Method for Producing Highly Dispersed Catalytic Platinum. US Patent US4136059A, 1979.
(649) Watanabe, M.; Tryk, D. A. The Role of Carbon Blacks as Catalyst Supports and Structural Elements in Polymer Electrolyte Fuel Cells. In *Nanocarbons for Energy Conversion: Supramolecular Approaches*; Springer International Publishing: Cham, 2019; pp 81−118.
(650) Kim, J.; Lee, S. W.; Carlton, C.; Shao-Horn, Y. Pt-Covered Multiwall Carbon Nanotubes for Oxygen Reduction in Fuel Cell Applications. *J. Phys. Chem. Lett.* **2011**, *2*, 1332−1336.
(651) Saha, M. S.; Li, R.; Sun, X. High Loading and Monodispersed Pt Nanoparticles on Multiwalled Carbon Nanotubes for High Performance Proton Exchange Membrane Fuel Cells. *J. Power Sources* **2008**, *177*, 314−322.
(652) Qi, J.; Benipal, N.; Liang, C.; Li, W. PdAg/CNT Catalyzed Alcohol Oxidation Reaction for High-Performance Anion Exchange Membrane Direct Alcohol Fuel Cell (Alcohol=methanol, Ethanol, Ethylene Glycol and Glycerol). *Appl. Catal., B* **2016**, *199*, 494−503.
(653) Miller, T. S.; Sansuk, S.; E, S. P.; Lai, S. C. S.; Macpherson, J. V.; Unwin, P. R. Pt Nanoparticle Modified Single Walled Carbon Nanotube Network Electrodes for Electrocatalysis: Control of the Specific Surface Area Over Three Orders of Magnitude. *Catal. Today* **2015**, *244*, 136−145.
(654) Esmaeilifar, A.; Rowshanzamir, S.; Eikani, M. H.; Ghazanfari, E. Synthesis Methods of Low-Pt-Loading Electrocatalysts for Proton Exchange Membrane Fuel Cell Systems. *Energy* **2010**, *35*, 3941−3957.
(655) Hierso, J.-C.; Feurer, R.; Kalck, P. Platinum and Palladium Films Obtained by Low-Temperature MOCVD for the Formation of Small Particles on Divided Supports as Catalytic Materials. *Chem. Mater.* **2000**, *12*, 390−399.
(656) Sherrell, P. C.; Zhang, W.; Zhao, J.; Wallace, G. G.; Chen, J.; Minett, A. I. Microwave Decoration of Pt Nanoparticles on Entangled 3D Carbon Nanotube Architectures as PEM Fuel Cell Cathode. *ChemSusChem* **2012**, *5*, 1233−1240.
(657) Higgins, D.; Zamani, P.; Yu, A.; Chen, Z. The Application of Graphene and Its Composites in Oxygen Reduction Electrocatalysis: A Perspective and Review of Recent Progress. *Energy Environ. Sci.* **2016**, *9*, 357−390.
(658) Huang, H.; Chen, H.; Sun, D.; Wang, X. Graphene Nanoplate-Pt Composite as a High Performance Electrocatalyst for Direct Methanol Fuel Cells. *J. Power Sources* **2012**, *204*, 46−52.
(659) Xiong, Y.; Yang, Y.; DiSalvo, F. J.; Abruna, H. D. Synergistic Bimetallic Metallic Organic Framework-Derived Pt-Co Oxygen Reduction Electrocatalysts. *ACS Nano* **2020**, *14*, 13069−13080.
(660) Padgett, E.; Andrejevic, N.; Liu, Z.; Kongkanand, A.; Gu, W.; Moriyama, K.; Jiang, Y.; Kumaraguru, S.; Moylan, T. E.; Kukreja, R.; Muller, D. A. Editors' Choice—Connecting Fuel Cell Catalyst Nanostructure and Accessibility Using Quantitative Cryo-STEM Tomography. *J. Electrochem. Soc.* **2018**, *165*, F173−F180.
(661) Xu, C.; Cheng, L.; Shen, P.; Liu, Y. Methanol and Ethanol Electrooxidation on Pt and Pd Supported on Carbon Microspheres in Alkaline Media. *Electrochem. Commun.* **2007**, *9*, 997−1001.
(662) Chen, X.-m.; Lin, Z.-j.; Jia, T.-t.; Cai, Z.-m.; Huang, X.-l.; Jiang, Y.-q.; Chen, X.; Chen, G.-n. A Facile Synthesis of Palladium Nanoparticles Supported on Functional Carbon Nanotubes and Its Novel Catalysis for Ethanol Electrooxidation. *Anal. Chim. Acta* **2009**, *650*, 54−58.
(663) Habibi, B.; Mohammadyari, S. Facile Synthesis of Pd Nanoparticles on Nano Carbon Supports and Their Application as an Electrocatalyst for Oxidation of Ethanol in Alkaline Media: The Effect of Support. *Int. J. Hydrogen Energy* **2015**, *40*, 10833−10846.
(664) Morozan, A.; Donck, S.; Artero, V.; Gravel, E.; Doris, E. Carbon Nanotubes-Gold Nanohybrid as Potent Electrocatalyst for Oxygen Reduction in Alkaline Media. *Nanoscale* **2015**, *7*, 17274−17277.
(665) Lim, E. J.; Choi, S. M.; Seo, M. H.; Kim, Y.; Lee, S.; Kim, W. B. Highly Dispersed Ag Nanoparticles on Nanosheets of Reduced Graphene Oxide for Oxygen Reduction Reaction in Alkaline Media. *Electrochem. Commun.* **2013**, *28*, 100−103.
(666) Gong, K.; Yu, P.; Su, L.; Xiong, S.; Mao, L. Polymer-Assisted Synthesis of Manganese Dioxide/Carbon Nanotube Nanocomposite with Excellent Electrocatalytic Activity toward Reduction of Oxygen. *J. Phys. Chem. C* **2007**, *111*, 1882−1887.
(667) Al-Hakemy, A. Z.; Nassr, A. B. A. A.; Naggar, A. H.; Elnouby, M. S.; Soliman, H. M. A. E. F.; Taher, M. A. Electrodeposited Cobalt Oxide Nanoparticles Modified Carbon Nanotubes as a Non-Precious Catalyst Electrode for Oxygen Reduction Reaction. *J. Appl. Electrochem.* **2017**, *47*, 183−195.
(668) Zhao, Y.; Zhan, L.; Tian, J.; Nie, S.; Ning, Z. MnO_2 Modified Multi-Walled Carbon Nanotubes Supported Pd Nanoparticles for Methanol Electro-Oxidation in Alkaline Media. *Int. J. Hydrogen Energy* **2010**, *35*, 10522−10526.
(669) Liu, X.; Hu, W. Iron Oxide/Oxyhydroxide Decorated Graphene Oxides for Oxygen Reduction Reaction Catalysis: A Comparison Study. *RSC Adv.* **2016**, *6*, 29848−29854.
(670) Dai, L.; Xue, Y.; Qu, L.; Choi, H. J.; Baek, J. B. Metal-Free Catalysts for Oxygen Reduction Reaction. *Chem. Rev.* **2015**, *115*, 4823−4892.
(671) Ratso, S.; Kruusenberg, I.; Joost, U.; Saar, R.; Tammeveski, K. Enhanced Oxygen Reduction Reaction Activity of Nitrogen-Doped Graphene/Multi-Walled Carbon Nanotube Catalysts in Alkaline Media. *Int. J. Hydrogen Energy* **2016**, *41*, 22510−22519.
(672) Liu, Q.; Zhang, H.; Zhong, H.; Zhang, S.; Chen, S. N-Doped Graphene/Carbon Composite as Non-Precious Metal Electrocatalyst for Oxygen Reduction Reaction. *Electrochim. Acta* **2012**, *81*, 313−320.
(673) Sheng, Z. H.; Shao, L.; Chen, J. J.; Bao, W. J.; Wang, F. B.; Xia, X. H. Catalyst-Free Synthesis of Nitrogen-Doped Graphene via Thermal Annealing Graphite Oxide with Melamine and Its Excellent Electrocatalysis. *ACS Nano* **2011**, *5*, 4350−4358.

https://doi.org/10.1021/acs.chemrev.1c00331
Chem. Rev. XXXX, XXX, XXX−XXX

(674) Chen, Z.; Chen, Z.; Higgins, D. Nitrogen Doped Carbon Nanotubes and Their Impact on the Oxygen Reduction Reaction in Fuel Cells. *Carbon* **2010**, *48*, 3057−3065.
(675) Vikkisk, M.; Kruusenberg, I.; Ratso, S.; Joost, U.; Shulga, E.; Kink, I.; Rauwel, P.; Tammeveski, K. Enhanced Electrocatalytic Activity of Nitrogen doped Multi-Walled Carbon Nanotubes towards the Oxygen Reduction Reaction in Alkaline Media. *RSC Adv.* **2015**, *5*, 59495−59505.
(676) Unni, S. M.; Bhange, S. N.; Illathvalappil, R.; Mutneja, N.; Patil, K. R.; Kurungot, S. Nitrogen-Induced Surface Area and Conductivity Modulation of Carbon Nanohorn and Its Function as an Efficient Metal-Free Oxygen Reduction Electrocatalyst for Anion-Exchange Membrane Fuel Cells. *Small* **2015**, *11*, 352−362.
(677) Lai, L.; Potts, J. R.; Zhan, D.; Wang, L.; Poh, C. K.; Tang, C.; Gong, H.; Shen, Z.; Lin, J.; Ruoff, R. S. Exploration of the Active Center Structure of Nitrogen-Doped Graphene-Based Catalysts for Oxygen Reduction Reaction. *Energy Environ. Sci.* **2012**, *5*, 7936−7942.
(678) Ning, X.; Li, Y.; Ming, J.; Wang, Q.; Wang, H.; Cao, Y.; Peng, F.; Yang, Y.; Yu, H. Electronic Synergism of Pyridinic- and Graphitic-Nitrogen on N-Doped Carbons for the Oxygen Reduction Reaction. *Chem. Sci.* **2019**, *10*, 1589−1596.
(679) Li, W.; Yang, D.; Chen, H.; Gao, Y.; Li, H. Sulfur-Doped Carbon Nanotubes as Catalysts for the Oxygen Reduction Reaction in Alkaline Medium. *Electrochim. Acta* **2015**, *165*, 191−197.
(680) Liu, Z.; Peng, F.; Wang, H.; Yu, H.; Tan, J.; Zhu, L. Novel Phosphorus-Doped Multiwalled Nanotubes with High Electrocatalytic Activity for O_2 Reduction in Alkaline Medium. *Catal. Commun.* **2011**, *16*, 35−38.
(681) Liu, Z. W.; Peng, F.; Wang, H. J.; Yu, H.; Zheng, W. X.; Yang, J. Phosphorus-Doped Graphite Layers with High Electrocatalytic Activity for the O_2 Reduction in an Alkaline Medium. *Angew. Chem., Int. Ed.* **2011**, *50*, 3257−3261.
(682) Lu, B.-A.; Shen, L.-F.; Liu, J.; Zhang, Q.; Wan, L.-Y.; Morris, D. J.; Wang, R.-X.; Zhou, Z.-Y.; Li, G.; Sheng, T.; Gu, L.; Zhang, P.; Tian, N.; Sun, S.-G. Structurally Disordered Phosphorus-Doped Pt as a Highly Active Electrocatalyst for an Oxygen Reduction Reaction. *ACS Catal.* **2021**, *11*, 355−363.
(683) Yang, L.; Jiang, S.; Zhao, Y.; Zhu, L.; Chen, S.; Wang, X.; Wu, Q.; Ma, J.; Ma, Y.; Hu, Z. Boron-Doped Carbon Nanotubes as Metal-Free Electrocatalysts for the Oxygen Reduction Reaction. *Angew. Chem., Int. Ed.* **2011**, *50*, 7132−7135.
(684) Cherevko, S. Stability and Dissolution of Electrocatalysts: Building the Bridge Between Model and "Real World" Systems. *Curr. Opin. Electrochem.* **2018**, *8*, 118−125.
(685) Schlögl, K.; Mayrhofer, K. J. J.; Hanzlik, M.; Arenz, M. Identical-Location TEM Investigations of Pt/C Electrocatalyst Degradation at Elevated Temperatures. *J. Electroanal. Chem.* **2011**, *662*, 355−360.
(686) Beermann, V.; Holtz, M. E.; Padgett, E.; de Araujo, J. F.; Muller, D. A.; Strasser, P. Real-Time Imaging of Activation and Degradation of Carbon Supported Octahedral Pt-Ni Alloy Fuel Cell Catalysts at the Nanoscale Using in Situ Electrochemical Liquid Cell STEM. *Energy Environ. Sci.* **2019**, *12*, 2476−2485.
(687) Liu, S.; Xu, W.; Niu, Y.; Zhang, B.; Zheng, L.; Liu, W.; Li, L.; Wang, J. Ultrastable Au Nanoparticles on Titania through an Encapsulation Strategy under Oxidative Atmosphere. *Nat. Commun.* **2019**, *10*, 5790.
(688) Hayek, K.; Kramer, R.; Paál, Z. Metal-Support Boundary Sites in Catalysis. *Appl. Catal., A* **1997**, *162*, 1−15.
(689) Horsley, J. A. A Molecular Orbital Study of Strong Metal-Support Interaction between Platinum and Titanium Dioxide. *J. Am. Chem. Soc.* **1979**, *101*, 2870−2874.
(690) Neophytides, S. G.; Zafeiratos, S.; Papakonstantinou, G. D.; Jaksic, J. M.; Paloukis, F. E.; Jaksic, M. M. Extended Brewer Hypo-Hyper-d-Interionic Bonding Theory II. Strong Metal-Support Interaction Grafting of Composite Electrocatalysts. *Int. J. Hydrogen Energy* **2005**, *30*, 393−410.
(691) Strayer, M. E.; Senftle, T. P.; Winterstein, J. P.; Vargas-Barbosa, N. M.; Sharma, R.; Rioux, R. M.; Janik, M. J.; Mallouk, T. E. Charge Transfer Stabilization of Late Transition Metal Oxide Nanoparticles on a Layered Niobate Support. *J. Am. Chem. Soc.* **2015**, *137*, 16216−16224.
(692) Tauster, S. J. Strong Metal-Support Interactions. *Acc. Chem. Res.* **1987**, *20*, 389−394.
(693) Wang, Y.-J.; Wilkinson, D. P.; Zhang, J. Noncarbon Support Materials for Polymer Electrolyte Membrane Fuel Cell Electrocatalysts. *Chem. Rev.* **2011**, *111*, 7625−7651.
(694) Sharma, S.; Pollet, B. G. Support Materials for PEMFC and DMFC Electrocatalysts—A Review. *J. Power Sources* **2012**, *208*, 96−119.
(695) Zhang, Z.; Liu, J.; Gu, J.; Su, L.; Cheng, L. An Overview of Metal Oxide Materials as Electrocatalysts and Supports for Polymer Electrolyte Fuel Cells. *Energy Environ. Sci.* **2014**, *7*, 2535−2558.
(696) Huang, D.; Zhang, B.; Bai, J.; Zhang, Y.; Wittstock, G.; Wang, M.; Shen, Y. Pt Catalyst Supported within TiO_2 Mesoporous Films for Oxygen Reduction Reaction. *Electrochim. Acta* **2014**, *130*, 97−103.
(697) Huang, S.-Y.; Ganesan, P.; Popov, B. N. Electrocatalytic Activity and Stability of Titania-Supported Platinum-Palladium Electrocatalysts for Polymer Electrolyte Membrane Fuel Cell. *ACS Catal.* **2012**, *2*, 825−831.
(698) Huang, S.-Y.; Ganesan, P.; Park, S.; Popov, B. N. Development of a Titanium Dioxide-Supported Platinum Catalyst with Ultrahigh Stability for Polymer Electrolyte Membrane Fuel Cell Applications. *J. Am. Chem. Soc.* **2009**, *131*, 13898−13899.
(699) Nguyen, S. T.; Lee, J.-M.; Yang, Y.; Wang, X. Excellent Durability of Substoichiometric Titanium Oxide as a Catalyst Support for Pd in Alkaline Direct Ethanol Fuel Cells. *Ind. Eng. Chem. Res.* **2012**, *51*, 9966−9972.
(700) Bauer, A.; Lee, K.; Song, C.; Xie, Y.; Zhang, J.; Hui, R. Pt Nanoparticles Deposited on TiO_2 Based Nanofibers: Electrochemical Stability and Oxygen Reduction Activity. *J. Power Sources* **2010**, *195*, 3105−3110.
(701) Jukk, K.; Kongi, N.; Tarre, A.; Rosental, A.; Treshchalov, A. B.; Kozlova, J.; Ritslaid, P.; Matisen, L.; Sammelselg, V.; Tammeveski, K. Electrochemical Oxygen Reduction Behaviour of Platinum Nanoparticles Supported on Multi-Walled Carbon Nanotube/Titanium Dioxide Composites. *J. Electroanal. Chem.* **2014**, *735*, 68−76.
(702) Chen, G.; Bare, S. R.; Mallouk, T. E. Development of Supported Bifunctional Electrocatalysts for Unitized Regenerative Fuel Cells. *J. Electrochem. Soc.* **2002**, *149*, A1092−A1099.
(703) Waraksa, C. C.; Chen, G.; Macdonald, D. D.; Mallouk, T. E. EIS Studies of Porous Oxygen Electrodes with Discrete Particles: II. Transmission Line Modeling. *J. Electrochem. Soc.* **2003**, *150* (9), E429.
(704) Eder, D.; Kramer, R. Stoichiometry of "Titanium Suboxide" Part 2. Electric Properties. *Phys. Chem. Chem. Phys.* **2003**, *5*, 1314−1319.
(705) Estudillo-Wong, L. A.; Ramos-Sanchez, G.; Calvillo, L.; Granozzi, G.; Alonso-Vante, N. Support Interaction Effect of Platinum Nanoparticles on Non-, Y-, Ce-Doped Anatase and Its Implication on the ORR in Acid and Alkaline Media. *ChemElectroChem* **2017**, *4*, 3264−3275.
(706) Bauer, A.; Chevallier, L.; Hui, R.; Cavaliere, S.; Zhang, J.; Jones, D.; Roziere, J. Synthesis and Characterization of Nb-TiO_2 Mesoporous Microsphere and Nanofiber Supported Pt Catalysts for High Temperature PEM Fuel Cells. *Electrochim. Acta* **2012**, *77*, 1−7.
(707) Siracusano, S.; Stassi, A.; Modica, E.; Baglio, V.; Arico, A. S. Preparation and Characterisation of Ti Oxide Based Catalyst Supports for Low Temperature Fuel Cells. *Int. J. Hydrogen Energy* **2013**, *38*, 11600−11608.
(708) Elezovic, N. R.; Babic, B. M.; Radmilovic, V. R.; Vracar, Lj M.; Krstajic, N. V. Nb-TiO_2 Supported Platinum Nanocatalyst for Oxygen Reduction Reaction in Alkaline Solutions. *Electrochim. Acta* **2011**, *56*, 9020−9026.
(709) Chen, G.; Waraksa, C. C.; Cho, H.; Macdonald, D. D.; Mallouka, T. E. EIS Studies of Porous Oxygen Electrodes with Discrete Particles: I. Impedance of Oxide Catalyst Supports. *J. Electrochem. Soc.* **2003**, *150*, E423−E428.

https://doi.org/10.1021/acs.chemrev.1c00331
Chem. Rev. XXXX, XXX, XXX−XXX

(710) Dang, T. M. D.; Nguyen, T. M. H.; Nguyen, H. P. The Preparation of Nano-Gold Catalyst Supported on Iron Doped Titanium Oxide. *Adv. Nat. Sci.: Nanosci. Nanotechnol.* **2010**, *1*, 025011.
(711) Ho, V. T. T.; Pan, C.-J.; Rick, J.; Su, W.-N.; Hwang, B.-J. Nanostructured $Ti_{0.7}Mo_{0.3}O_2$ Support Enhances Electron Transfer to Pt: High-Performance Catalyst for Oxygen Reduction Reaction. *J. Am. Chem. Soc.* **2011**, *133*, 11716−11724.
(712) Park, K.-W.; Seol, K.-S. Nb-TiO_2 Supported Pt Cathode Catalyst for Polymer Electrolyte Membrane Fuel Cells. *Electrochem. Commun.* **2007**, *9*, 2256−2260.
(713) Parrondo, J.; Han, T.; Niangar, E.; Wang, C.; Dale, N.; Adjemian, K.; Ramani, V. Platinum Supported on Titanium-Ruthenium Oxide Is a Remarkably Stable Electrocatayst for Hydrogen Fuel Cell Vehicles. *Proc. Natl. Acad. Sci. U. S. A.* **2014**, *111*, 45−50.
(714) Elezovic, N. R.; Radmilovic, V. R.; Kovac, J.; Babic, B. M.; Gaijic-Krstajic, L. M.; Krstajic, N. V. Pt Nanoparticles on Tin Oxide Based Support as a Beneficial Catalyst for Oxygen Reduction in Alkaline Solutions. *RSC Adv.* **2015**, *5*, 15923−15929.
(715) Lee, S. H.; Lim, E. J.; Jo, Y.-R.; Kim, B.-J.; Kim, W. B. Directly Grown and Square-Patterned Arrays of Metal Oxide Nanowires for High-Performance Catalyst Support Platforms. *ACS Appl. Mater. Interfaces* **2014**, *6*, 20634−20642.
(716) Zhao, S.; Wangstrom, A. E.; Liu, Y.; Rigdon, W. A.; Mustain, W. E. Stability and Activity of Pt/ITO Electrocatalyst for Oxygen Reduction Reaction in Alkaline Media. *Electrochim. Acta* **2015**, *157*, 175−182.
(717) Lim, C.; Alavijeh, A. S.; Lauritzen, M.; Kolodziej, J.; Knights, S.; Kjeang, E. Fuel Cell Durability Enhancement with Cerium Oxide under Combined Chemical and Mechanical Membrane Degradation. *ECS Electrochem. Lett.* **2015**, *4*, F29−F31.
(718) Liu, Y.; Liu, C.; Yu, X.; Osgood, H.; Wu, G. CeO_2 -Modified α-MoO_3 Nanorods as a Synergistic Support for Pt Nanoparticles with Enhanced CO_{ads} Tolerance during Methanol Oxidation. *Phys. Chem. Chem. Phys.* **2017**, *19*, 330−339.
(719) Ntais, S.; Serov, A.; Andersen, N. I.; Roy, A. J.; Cossar, E.; Allagui, A.; Lu, Z.; Cui, X.; Baranova, E. A.; Atanassov, P. Promotion of Ammonia Electrooxidation on Pt Nanoparticles by Nickel Oxide Support. *Electrochim. Acta* **2016**, *222*, 1455−1463.
(720) Thotiyl, M. M. O.; Ravikumar, T.; Sampath, S. Platinum Particles Supported on Titanium Nitride: An Efficient Electrode Material for the Oxidation of Methanol in Alkaline Media. *J. Mater. Chem.* **2010**, *20*, 10643−10651.
(721) Roca-Ayats, M.; García, G.; Galante, J. L.; Pena, M. A.; Martínez-Huerta, M. V. TiC, TiCN, and TiN Supported Pt Electrocatalysts for CO and Methanol Oxidation in Acidic and Alkaline Media. *J. Phys. Chem. C* **2013**, *117*, 20769−20777.
(722) Liu, G.; Li, J.; Fu, J.; Jiang, G.; Lui, G.; Luo, D.; Deng, Y.-P.; Zhang, J.; Cano, Z. P.; Yu, A.; Su, D.; Bai, Z.; Yang, L.; Chen, Z. An Oxygen-Vacancy-Rich Semiconductor-Supported Bifunctional Catalyst for Efficient and Stable Zinc-Air Batteries. *Adv. Mater.* **2019**, *31*, 1806761.
(723) Cui, Z.; Burns, R. G.; DiSalvo, F. J. Mesoporous $Ti_{0.5}Nb_{0.5}N$ Ternary Nitride as a Novel Noncarbon Support for Oxygen Reduction Reaction in Acid and Alkaline Electrolytes. *Chem. Mater.* **2013**, *25*, 3782−3784.
(724) Tian, X.; Luo, J.; Nan, H.; Zou, H.; Chen, R.; Shu, T.; Li, X.; Li, Y.; Song, H.; Liao, S.; Adzic, R. R. Transition Metal Nitride Coated with Atomic Layers of Pt as a Low-Cost, Highly Stable Electrocatalyst for the Oxygen Reduction Reaction. *J. Am. Chem. Soc.* **2016**, *138* (5), 1575−1583.
(725) Xiao, Y.; Zhan, G.; Fu, Z.; Pan, Z.; Xiao, C.; Wu, S.; Chen, C.; Hu, G.; Wei, Z. Titanium Cobalt Nitride Supported Platinum Catalyst with High Activity and Stability for Oxygen Reduction Reaction. *J. Power Sources* **2015**, *284*, 296−304.
(726) Yang, M.; Guarecuco, R.; DiSalvo, F. J. Mesoporous Chromium Nitride as High-Performance Catalyst Support for Methanol Electrooxidation. *Chem. Mater.* **2013**, *25*, 1783−1787.
(727) Hamo, E. R.; Singh, R. K.; Douglin, J. C.; Chen, S.; Hassine, M. B.; Carbo-Argibay, E.; Lu, S.; Wang, H.; Ferreira, P. J.; Rosen, B. A.; Dekel, D. R. Carbide-Supported PtRu Catalysts for Hydrogen Oxidation Reaction in Alkaline Electrolyte. *ACS Catal.* **2021**, *11*, 932−947.
(728) Weidman, M. C.; Esposito, D. V.; Hsu, Y.-C.; Chen, J. G. Comparison of Electrochemical Stability of Transition Metal Carbides (WC, W_2C, Mo_2C) over a Wide pH Range. *J. Power Sources* **2012**, *202*, 11−17.
(729) Sohn, Y.; Jung, J. Y.; Kim, P. Facile Synthesis of Tungsten Carbide-Carbon Composites for Oxygen Reduction Reaction. *Korean J. Chem. Eng.* **2017**, *34*, 2162−2168.
(730) Zhang, X.-Y.; Guo, B.-Y.; Li, F.-T.; Dong, B.; Zhang, J.-Q.; Ma, X.; Xie, J.-Y.; Yang, M.; Chai, Y.-M.; Liu, C.-G. In Situ Electro-Oxidation Modulation of $Ru(OH)_x$/Ag Supported on Nickel Foam for Efficient Hydrogen Evolution Reaction in Alkaline Media. *Int. J. Hydrogen Energy* **2019**, *44*, 21683−21691.
(731) Zhao, J.; Shao, M.; Yan, D.; Zhang, S.; Lu, Z.; Li, Z.; Cao, X.; Wang, B.; Wei, M.; Evans, D. G.; Duan, X. A Hierarchical Heterostructure Based on Pd Nanoparticles/Layered Double Hydroxide Nanowalls for Enhanced Ethanol Electrooxidation. *J. Mater. Chem. A* **2013**, *1*, 5840−5846.
(732) Cui, Q.; Chao, S.; Bai, Z.; Yan, H.; Wang, K.; Yang, L. Based on a New Support for Synthesis of Highly Efficient Palladium/Hydroxyapatite Catalyst for Ethanol Electrooxidation. *Electrochim. Acta* **2014**, *132*, 31−36.
(733) Uppuluri, R.; Gupta, A. S.; Rosas, A. S.; Mallouk, T. E. Soft Chemistry of Ion-Exchangeable Layered Metal Oxides. *Chem. Soc. Rev.* **2018**, *47*, 2401−2430.
(734) Maurya, S.; Shin, S.-H.; Kim, Y.; Moon, S.-H. A Review on Recent Developments of Anion Exchange Membranes for Fuel Cells and Redox Flow Batteries. *RSC Adv.* **2015**, *5*, 37206−37230.
(735) Hagesteijn, K. F. L.; Jiang, S.; Ladewig, B. P. A Review of the Synthesis and Characterization of Anion Exchange Membranes. *J. Mater. Sci.* **2018**, *53*, 11131−11150.
(736) Wang, Y.-J.; Qiao, J.; Baker, R.; Zhang, J. Alkaline Polymer Electrolyte Membranes for Fuel Cell Applications. *Chem. Soc. Rev.* **2013**, *42*, 5768−5787.
(737) Arges, C. G.; Zhang, L. Anion Exchange Membranes' Evolution toward High Hydroxide Ion Conductivity and Alkaline Resiliency. *ACS Appl. Energy Mater.* **2018**, *1*, 2991−3012.
(738) Vijayakumar, V.; Nam, S. Y. Recent Advancements in Applications of Alkaline Anion Exchange Membranes for Polymer Electrolyte Fuel Cells. *J. Ind. Eng. Chem.* **2019**, *70*, 70−86.
(739) Chen, N.; Lee, Y. M. Anion Exchange Polyelectrolytes for Membranes and Ionomers. *Prog. Polym. Sci.* **2021**, *113*, 101345.
(740) You, W.; Noonan, K. J. T.; Coates, G. W. Alkaline-Stable Anion Exchange Membranes: A Review of Synthetic Approaches. *Prog. Polym. Sci.* **2020**, *100*, 101177.
(741) Fan, J.; Willdorf-Cohen, S.; Schibli, E. M.; Paula, Z.; Li, W.; Skalski, T. J. G.; Sergeenko, A. T.; Hohenadel, A.; Frisken, B. J.; Magliocca, E.; Mustain, W. E.; Diesendruck, C. E.; Dekel, D. R.; Holdcroft, S. Poly(bis-arylimidazoliums) Possessing High Hydroxide Ion Exchange Capacity and High Alkaline Stability. *Nat. Commun.* **2019**, *10*, 2306.
(742) Fan, J.; Wright, A. G.; Britton, B.; Weissbach, T.; Skalski, T. J. G.; Ward, J.; Peckham, T. J.; Holdcroft, S. Cationic Polyelectrolytes, Stable in 10 M KOH_{aq} at 100 °C. *ACS Macro Lett.* **2017**, *6*, 1089−1093.
(743) Noonan, K. J. T.; Hugar, K. M.; Kostalik, H. A.; Lobkovsky, E. B.; Abruna, H. D.; Coates, G. W. Phosphonium-Functionalized Polyethylene: A New Class of Base-Stable Alkaline Anion Exchange Membranes. *J. Am. Chem. Soc.* **2012**, *134*, 18161−18164.
(744) You, W.; Padgett, E.; MacMillan, S. N.; Muller, D. A.; Coates, G. W. Highly Conductive and Chemically Stable Alkaline Anion Exchange Membranes via ROMP of Trans-Cyclooctene Derivatives. *Proc. Natl. Acad. Sci. U. S. A.* **2019**, *116*, 9729−9734.

https://doi.org/10.1021/acs.chemrev.1c00331
Chem. Rev. XXXX, XXX, XXX−XXX

(745) Hugar, K. M.; You, W.; Coates, G. W. Protocol for the Quantitative Assessment of Organic Cation Stability for Polymer Electrolytes. *ACS Energy Lett.* **2019**, *4*, 1681−1686.
(746) Mohanty, A. D.; Bae, C. Mechanistic Analysis of Ammonium Cation Stability for Alkaline Exchange Membrane Fuel Cells. *J. Mater. Chem. A* **2014**, *2*, 17314−17320.
(747) You, W.; Hugar, K. M.; Selhorst, R. C.; Treichel, M.; Peltier, C. R.; Noonan, K. J. T.; Coates, G. W. Degradation of Organic Cations under Alkaline Conditions. *J. Org. Chem.* **2021**, *86*, 254−263.
(748) Marino, M. G.; Kreuer, K. D. Alkaline Stability of Quaternary Ammonium Cations for alkaline fuel cell membranes and ionic liquids. *ChemSusChem* **2015**, *8*, 513−523.
(749) Sturgeon, M. R.; Macomber, C. S.; Engtrakul, C.; Long, H.; Pivovar, B. S. Hydroxide based Benzyltrimethylammonium Degradation: Quantification of Rates and Degradation Technique Development. *J. Electrochem. Soc.* **2015**, *162*, F366−F372.
(750) Hugar, K. M.; Kostalik, H. A.; Coates, G. W. Imidazolium Cations with Exceptional Alkaline Stability: A Systematic Study of Structure-Stability Relationships. *J. Am. Chem. Soc.* **2015**, *137*, 8730−8737.
(751) Pellerite, M. J.; Kaplun, M. M.; Webb, R. J. Characterizing Cation Chemistry for Anion Exchange Membranes—A Product Study of Benzylimidazolium Salt Decompositions in Base. *J. Org. Chem.* **2019**, *84*, 15486−15497.
(752) Olsson, J. S.; Pham, T. H.; Jannasch, P. Functionalizing Polystyrene with N-Alicyclic Piperidine-Based Cations via Friedel-Crafts Alkylation for Highly Alkali-Stable Anion-Exchange Membranes. *Macromolecules* **2020**, *53*, 4722−4732.
(753) Pham, T. H.; Olsson, J. S.; Jannasch, P. Effects of the N-alicyclic Cation and Backbone Structures on the Performance of Poly(terphenyl)-based Hydroxide Exchange Membranes. *J. Mater. Chem. A* **2019**, *7*, 15895−15906.
(754) Pham, T. H.; Olsson, J. S.; Jannasch, P. Poly(arylene alkylene)s with Pendant N-spirocyclic Quaternary Ammonium Cations for Anion Exchange Membranes. *J. Mater. Chem. A* **2018**, *6*, 16537−16547.
(755) Dang, H.-S.; Jannasch, P. A Comparative Study of Anion-Exchange Membranes Tethered with Different Hetero-Cycloaliphatic Quaternary Ammonium Hydroxides. *J. Mater. Chem. A* **2017**, *5*, 21965−21978.
(756) Sun, Z.; Pan, J.; Guo, J.; Yan, F. The Alkaline Stability of Anion Exchange Membrane for Fuel Cell Applications: The Effects of Alkaline Media. *Adv. Sci.* **2018**, *5*, 1800065.
(757) Yang, C.; Wang, S.; Ma, W.; Jiang, L.; Sun, G. Comparison of Alkaline Stability of Quaternary Ammonium- and 1,2-Methylimidazolium-based Alkaline Anion Exchange Membranes. *J. Membr. Sci.* **2015**, *487*, 12−18.
(758) Gu, F.; Dong, H.; Li, Y.; Si, Z.; Yan, F. Highly Stable N3-Substituted Imidazolium-Based Alkaline Anion Exchange Membranes: Experimental Studies and Theoretical Calculations. *Macromolecules* **2014**, *47*, 208−216.
(759) Zhang, B.; Kaspar, R. B.; Gu, S.; Wang, J.; Zhuang, Z.; Yan, Y. A New Alkali-Stable Phosphonium Cation Based on Fundamental Understanding of Degradation Mechanisms. *ChemSusChem* **2016**, *9*, 2374−2379.
(760) Nunez, S. A.; Capparelli, C.; Hickner, M. A. N-Alkyl Interstitial Spacers and Terminal Pendants Influence the Alkaline Stability of Tetraalkylammonium Cations for Anion Exchange Membrane Fuel Cells. *Chem. Mater.* **2016**, *28*, 2589−2598.
(761) Price, S. C.; Williams, K. S.; Beyer, F. L. Relationships between Structure and Alkaline Stability of Imidazolium Cations for Fuel Cell Membrane Applications. *ACS Macro Lett.* **2014**, *3*, 160−165.
(762) Jeon, J. Y.; Park, S.; Han, J.; Maurya, S.; Mohanty, A. D.; Tian, D.; Saikia, N.; Hickner, M. A.; Ryu, C. Y.; Tuckerman, M. E.; Paddison, S. J.; Kim, Y. S.; Bae, C. Synthesis of Aromatic Anion Exchange Membranes by Friedel-Crafts Bromoalkylation and Cross-Linking of Polystyrene Block Copolymers. *Macromolecules* **2019**, *52*, 2139−2147.
(763) Long, H.; Kim, K.; Pivovar, B. S. Hydroxide Degradation Pathways for Substituted Trimethylammonium Cations: A DFT Study. *J. Phys. Chem. C* **2012**, *116*, 9419−9426.
(764) Olsson, J. S.; Pham, T. H.; Jannasch, P. Poly(N, N-diallylazacycloalkane)s for Anion-Exchange Membranes Functionalized with N-Spirocyclic Quaternary Ammonium Cations. *Macromolecules* **2017**, *50*, 2784−2793.
(765) Wang, X.; Sheng, W.; Shen, Y.; Liu, L.; Dai, S.; Li, N. N-cyclic Quaternary Ammonium-Functionalized Anion Exchange Membrane with Improved Alkaline Stability Enabled by Aryl-Ether Free Polymer Backbones for Alkaline Fuel Cells. *J. Membr. Sci.* **2019**, *587*, 117135.
(766) Wang, J.; Gu, S.; Kaspar, R. B.; Zhang, B.; Yan, Y. Stabilizing the Imidazolium Cation in Hydroxide-Exchange Membranes for Fuel Cells. *ChemSusChem* **2013**, *6*, 2079−2082.
(767) Lin, B.; Dong, H.; Li, Y.; Si, Z.; Gu, F.; Yan, F. Alkaline Stable C2-Substituted Imidazolium-Based Anion-Exchange Membranes. *Chem. Mater.* **2013**, *25*, 1858−1867.
(768) Meek, K. M.; Nykaza, J. R.; Elabd, Y. A. Alkaline Chemical Stability and Ion Transport in Polymerized Ionic Liquids with Various Backbones and Cations. *Macromolecules* **2016**, *49*, 3382−3394.
(769) Si, Z.; Qiu, L.; Dong, H.; Gu, F.; Li, Y.; Yan, F. Effects of Substituents and Substitution Positions on Alkaline Stability of Imidazolium Cations and Their Corresponding Anion-Exchange Membranes. *ACS Appl. Mater. Interfaces* **2014**, *6*, 4346−4355.
(770) Yang, Y.; Wang, J.; Zheng, J.; Li, S.; Zhang, S. A Stable Anion Exchange Membrane based on Imidazolium Salt for Alkaline Fuel Cell. *J. Membr. Sci.* **2014**, *467*, 48−55.
(771) Meek, K. M.; Elabd, Y. A. Alkaline Chemical Stability of Polymerized Ionic Liquids with Various Cations. *Macromolecules* **2015**, *48*, 7071−7084.
(772) You, W.; Hugar, K. M.; Coates, G. W. Synthesis of Alkaline Anion Exchange Membranes with Chemically Stable Imidazolium Cations: Unexpected Cross-Linked Macrocycles from Ring-Fused ROMP Monomers. *Macromolecules* **2018**, *51*, 3212−3218.
(773) Weissbach, T.; Wright, A. G.; Peckham, T. J.; Sadeghi Alavijeh, A.; Pan, V.; Kjeang, E.; Holdcroft, S. Simultaneous, Synergistic Control of Ion Exchange Capacity and Cross-Linking of Sterically-Protected Poly(benzimidazolium)s. *Chem. Mater.* **2016**, *28*, 8060−8070.
(774) Wright, A. G.; Weissbach, T.; Holdcroft, S. Poly(phenylene) and m-Terphenyl as Powerful Protecting Groups for the Preparation of Stable Organic Hydroxides. *Angew. Chem., Int. Ed.* **2016**, *55*, 4818−4821.
(775) Zhang, B.; Long, H.; Kaspar, R. B.; Wang, J.; Gu, S.; Zhuang, Z.; Pivovar, B.; Yan, Y. Relating Alkaline Stability to the Structure of Quaternary Phosphonium Cations. *RSC Adv.* **2018**, *8*, 26640−26645.
(776) Womble, C. T.; Kang, J.; Hugar, K. M.; Coates, G. W.; Bernhard, S.; Noonan, K. J. T. Rapid Analysis of Tetrakis-(dialkylamino)phosphonium Stability in Alkaline Media. *Organometallics* **2017**, *36*, 4038−4046.
(777) Treichel, M.; Tyler Womble, C.; Selhorst, R.; Gaitor, J.; Pathiranage, T. M. S. K.; Kowalewski, T.; Noonan, K. J. T. Exploring the Effects of Bulky Cations Tethered to Semicrystalline Polymers: The Case of Tetraaminophosphoniums with Ring-Opened Polynorbornenes. *Macromolecules* **2020**, *53*, 8509−8518.
(778) Mohanty, A. D.; Tignor, S. E.; Krause, J. A.; Choe, Y.-K.; Bae, C. Systematic Alkaline Stability Study of Polymer Backbones for Anion Exchange Membrane Applications. *Macromolecules* **2016**, *49*, 3361−3372.
(779) Yang, K.; Chu, X.; Zhang, X.; Li, X.; Zheng, J.; Li, S.; Li, N.; Sherazi, T. A.; Zhang, S. The Effect of Polymer Backbones and Cation Functional Groups on Properties of Anion Exchange Membranes for Fuel Cells. *J. Membr. Sci.* **2020**, *603*, 118025.
(780) Nunez, S. A.; Hickner, M. A. Quantitative 1H NMR Analysis of Chemical Stabilities in Anion-Exchange Membranes. *ACS Macro Lett.* **2013**, *2*, 49−52.
(781) Okuzono, T.; Kobayashi, M.; Doi, M. Final Shape of a Drying Thin Film. *Phys. Rev. E* **2009**, *80*, 021603.

https://doi.org/10.1021/acs.chemrev.1c00331
Chem. Rev. XXXX, XXX, XXX−XXX

(782) Chen, W.; Mandal, M.; Huang, G.; Wu, X.; He, G.; Kohl, P. A. Highly Conducting Anion-Exchange Membranes Based on Cross-Linked Poly(norbornene): Ring Opening Metathesis Polymerization. *ACS Appl. Energy Mater.* **2019**, *2*, 2458−2468.
(783) Mandal, M.; Huang, G.; Kohl, P. A. Highly Conductive Anion-Exchange Membranes Based on Cross-Linked Poly-(norbornene): Vinyl Addition Polymerization. *ACS Appl. Energy Mater.* **2019**, *2*, 2447−2457.
(784) Robertson, N. J.; Kostalik, H. A.; Clark, T. J.; Mutolo, P. F.; AbruňA, H. C. D.; Coates, G. W. Tunable High Performance Cross-Linked Alkaline Anion Exchange Membranes for Fuel Cell Applications. *J. Am. Chem. Soc.* **2010**, *132*, 3400−3404.
(785) Clark, T. J.; Robertson, N. J.; Kostalik, H. A. T.; Lobkovsky, E. B.; Mutolo, P. F.; Abruna, H. D.; Coates, G. W. A Ring-Opening Metathesis Polymerization Route to Alkaline Anion Exchange Membranes: Development of Hydroxide-Conducting Thin Films from an Ammonium-Functionalized Monomer. *J. Am. Chem. Soc.* **2009**, *131*, 12888−12889.
(786) Wei, X.-F.; Linde, E.; Hedenqvist, M. S. Plasticiser Loss from Plastic or Rubber Products through Diffusion and Evaporation. *NPJ. Mater. Degrad.* **2019**, *3*, 18.
(787) Mandal, M.; Huang, G.; Kohl, P. A. Anionic Multiblock Copolymer Membrane based on Vinyl Addition Polymerization of Norbornenes: Applications in Anion-Exchange Membrane Fuel Cells. *J. Membr. Sci.* **2019**, *570-571*, 394−402.
(788) Xu, F.; Su, Y.; Lin, B. Progress of Alkaline Anion Exchange Membranes for Fuel Cells: The Effects of Micro-Phase Separation. *Front. Mater.* **2020**, *7*, 4.
(789) Lee, W.-H.; Park, E. J.; Han, J.; Shin, D. W.; Kim, Y. S.; Bae, C. Poly(terphenylene) Anion Exchange Membranes: The Effect of Backbone Structure on Morphology and Membrane Property. *ACS Macro Lett.* **2017**, *6*, 566−570.
(790) Lee, W.-H.; Kim, Y.; Bae, C. Robust Hydroxide Ion Conducting Poly(biphenyl alkylene)s for Alkaline Fuel Cell Membranes. *ACS Macro Lett.* **2015**, *4*, 814−818.
(791) Olsson, J. S.; Pham, T. H.; Jannasch, P. Poly(arylene piperidinium) Hydroxide Ion Exchange Membranes: Synthesis, Alkaline Stability, and Conductivity. *Adv. Funct. Mater.* **2018**, *28*, 1702758.
(792) Peng, H.; Li, Q.; Hu, M.; Xiao, L.; Lu, J.; Zhuang, L. Alkaline Polymer Electrolyte Fuel Cells Stably Working at 80 °C. *J. Power Sources* **2018**, *390*, 165−167.
(793) Wang, J.; Zhao, Y.; Setzler, B. P.; Rojas-Carbonell, S.; Ben Yehuda, C.; Amel, A.; Page, M.; Wang, L.; Hu, K.; Shi, L.; Gottesfeld, S.; Xu, B.; Yan, Y. Poly(aryl piperidinium) Membranes and Ionomers for Hydroxide Exchange Membrane Fuel Cells. *Nat. Energy* **2019**, *4*, 392−398.
(794) Zhu, H.; Li, Y.; Chen, N.; Lu, C.; Long, C.; Li, Z.; Liu, Q. Controllable Physical-Crosslinking Poly(arylene 6-azaspiro[5.5] undecanium) for Long-Lifetime Anion Exchange Membrane Applications. *J. Membr. Sci.* **2019**, *590*, 117307.
(795) Mayadevi, T. S.; Sung, S.; Varghese, L.; Kim, T.-H. Poly(*meta*/*para*-Terphenylene-Methyl Piperdinium)-Based Anion Exchange Membranes: The Effect of Backbone Structure in AEMFC Application. *Membranes* **2020**, *10*, 329.
(796) Wright, A. G.; Holdcroft, S. Hydroxide-Stable Ionenes. *ACS Macro Lett.* **2014**, *3*, 444−447.
(797) Lin, B.; Xu, F.; Su, Y.; Han, J.; Zhu, Z.; Chu, F.; Ren, Y.; Zhu, L.; Ding, J. Ether-Free Polybenzimidazole Bearing Pendant Imidazolium Groups for Alkaline Anion Exchange Membrane Fuel Cells Application. *ACS Appl. Energy Mater.* **2020**, *3*, 1089−1098.
(798) Maurya, S.; Lee, A. S.; Li, D.; Park, E. J.; Leonard, D. P.; Noh, S.; Bae, C.; Kim, Y. S. On the Origin of Permanent Performance Loss of Anion Exchange Membrane Fuel Cells: Electrochemical Oxidation of Phenyl Group. *J. Power Sources* **2019**, *436*, 226866.
(799) Wang, C.; Lin, B.; Qiao, G.; Wang, L.; Zhu, L.; Chu, F.; Feng, T.; Yuan, N.; Ding, J. Polybenzimidazole/ionic Liquid Functionalized Graphene Oxide Nanocomposite Membrane for Alkaline Anion Exchange Membrane Fuel Cells. *Mater. Lett.* **2016**, *173*, 219−222.
(800) Chen, N.; Zhu, H.; Chu, Y.; Li, R.; Liu, Y.; Wang, F. Cobaltocenium-Containing Polybenzimidazole Polymers for Alkaline Anion Exchange Membrane Applications. *Polym. Chem.* **2017**, *8*, 1381−1392.
(801) Maurya, S.; Noh, S.; Matanovic, I.; Park, E. J.; Narvaez Villarrubia, C.; Martinez, U.; Han, J.; Bae, C.; Kim, Y. S. Rational Design of Polyaromatic Ionomers for Alkaline Membrane Fuel Cells with >1 W cm^{-2} Power Density. *Energy Environ. Sci.* **2018**, *11*, 3283−3291.
(802) Lee, W.-H.; Mohanty, A. D.; Bae, C. Fluorene-Based Hydroxide Ion Conducting Polymers for Chemically Stable Anion Exchange Membrane Fuel Cells. *ACS Macro Lett.* **2015**, *4*, 453−457.
(803) Miyanishi, S.; Yamaguchi, T. Highly Conductive Mechanically Robust High M_w Polyfluorene Anion Exchange Membrane for Alkaline Fuel Cell and Water Electrolysis Application. *Polym. Chem.* **2020**, *11*, 3812−3820.
(804) Ono, H.; Kimura, T.; Takano, A.; Asazawa, K.; Miyake, J.; Inukai, J.; Miyatake, K. Robust Anion Conductive Polymers Containing Perfluoroalkylene and Pendant Ammonium Groups for High Performance Fuel Cells. *J. Mater. Chem. A* **2017**, *5*, 24804−24812.
(805) Miyanishi, S.; Yamaguchi, T. Highly Durable Spirobifluorene-based Aromatic Anion Conducting Polymer for a Solid Ionomer of Alkaline Fuel Cells and Water Electrolysis Cells. *J. Mater. Chem. A* **2019**, *7*, 2219−2224.
(806) Maurya, S.; Fujimoto, C. H.; Hibbs, M. R.; Narvaez Villarrubia, C.; Kim, Y. S. Toward Improved Alkaline Membrane Fuel Cell Performance Using Quaternized Aryl-Ether Free Polyaromatics. *Chem. Mater.* **2018**, *30*, 2188−2192.
(807) Zeng, L.; He, Q.; Liao, Y.; Kuang, S.; Wang, J.; Ding, W.; Liao, Q.; Wei, Z. Anion Exchange Membrane Based on Interpenetrating Polymer Network with Ultrahigh Ion Conductivity and Excellent Stability for Alkaline Fuel Cell. *Research (Wash D C).* **2020**, *2020*, 4794706.
(808) Ge, Q.; Liu, Y.; Yang, Z.; Wu, B.; Hu, M.; Liu, X.; Hou, J.; Xu, T. Hyper-Branched Anion Exchange Membranes with High Conductivity and Chemical Stability. *Chem. Commun.* **2016**, *52*, 10141−10143.
(809) Ge, Q.; Liang, X.; Ding, L.; Hou, J.; Miao, J.; Wu, B.; Yang, Z.; Xu, T. Guiding the Self-Assembly of Hyperbranched Anion Exchange Membranes Utilized in Alkaline Fuel Cells. *J. Membr. Sci.* **2019**, *573*, 595−601.
(810) Mohanty, A. D.; Ryu, C. Y.; Kim, Y. S.; Bae, C. Stable Elastomeric Anion Exchange Membranes Based on Quaternary Ammonium-Tethered Polystyrene-b-poly(ethylene-co-butylene)-b-polystyrene Triblock Copolymers. *Macromolecules* **2015**, *48*, 7085−7095.
(811) Yang, C.; Wang, S.; Ma, W.; Zhao, S.; Xu, Z.; Sun, G. Highly Stable Poly(ethylene glycol)-Grafted Alkaline Anion Exchange Membranes. *J. Mater. Chem. A* **2016**, *4*, 3886−3892.
(812) Ertem, S. P.; Caire, B. R.; Tsai, T.-H.; Zeng, D.; Vandiver, M. A.; Kusoglu, A.; Seifert, S.; Hayward, R. C.; Weber, A. Z.; Herring, A. M.; Coughlin, E. B.; Liberatore, M. W. Ion Transport Properties of Mechanically Stable Symmetric ABCBA Pentablock Copolymers with Quaternary Ammonium Functionalized Midblock. *J. Polym. Sci., Part B: Polym. Phys.* **2017**, *55*, 612−622.
(813) Zhu, L.; Yu, X.; Peng, X.; Zimudzi, T. J.; Saikia, N.; Kwasny, M. T.; Song, S.; Kushner, D. I.; Fu, Z.; Tew, G. N.; Mustain, W. E.; Yandrasits, M. A.; Hickner, M. A. Poly(olefin)-Based Anion Exchange Membranes Prepared Using Ziegler-Natta Polymerization. *Macromolecules* **2019**, *52*, 4030−4041.
(814) Zhu, L.; Peng, X.; Shang, S. L.; Kwasny, M. T.; Zimudzi, T. J.; Yu, X.; Saikia, N.; Pan, J.; Liu, Z. K.; Tew, G. N.; Mustain, W. E.; Yandrasits, M.; Hickner, M. A. High Performance Anion Exchange Membrane Fuel Cells Enabled by Fluoropoly(olefin) Membranes. *Adv. Funct. Mater.* **2019**, *29*, 1902059.
(815) Zhang, M.; Liu, J.; Wang, Y.; An, L.; Guiver, M. D.; Li, N. Highly Stable Anion Exchange Membranes Based on Quaternized Polypropylene. *J. Mater. Chem. A* **2015**, *3*, 12284−12296.

https://doi.org/10.1021/acs.chemrev.1c00331
Chem. Rev. XXXX, XXX, XXX−XXX

(816) Zhang, M.; Shan, C.; Liu, L.; Liao, J.; Chen, Q.; Zhu, M.; Wang, Y.; An, L.; Li, N. Facilitating Anion Transport in Polyolefin-Based Anion Exchange Membranes via Bulky Side Chains. *ACS Appl. Mater. Interfaces* **2016**, *8*, 23321−23330.
(817) Zhu, T.; Xu, S.; Rahman, A.; Dogdibegovic, E.; Yang, P.; Pageni, P.; Kabir, M. P.; Zhou, X.-D.; Tang, C. Cationic Metallo-Polyelectrolytes for Robust Alkaline Anion-Exchange Membranes. *Angew. Chem., Int. Ed.* **2018**, *57*, 2388−2392.
(818) You, W.; Ganley, J. M.; Ernst, B. G.; Peltier, C. R.; Ko, H.-Y.; DiStasio, R. A.; Knowles, R. R.; Coates, G. W. Expeditious Synthesis of Aromatic-Free Piperidinium-Functionalized Polyethylene as Alkaline Anion Exchange Membranes. *Chem. Sci.* **2021**, *12* (11), 3898−3910.
(819) Wang, L.; Peng, X.; Mustain, W. E.; Varcoe, J. R. Radiation-Grafted Anion-Exchange Membranes: the Switch from Low- to High-Density Polyethylene Leads to Remarkably Enhanced Fuel Cell Performance. *Energy Environ. Sci.* **2019**, *12*, 1575−1579.
(820) Wang, L.; Magliocca, E.; Cunningham, E. L.; Mustain, W. E.; Poynton, S. D.; Escudero-Cid, R.; Nasef, M. M.; Ponce-González, J.; Bance-Souahli, R.; Slade, R. C. T.; Whelligan, D. K.; Varcoe, J. R. An Optimised Synthesis of High Performance Radiation-Grafted Anion-Exchange Membranes. *Green Chem.* **2017**, *19*, 831−843.
(821) Ponce-González, J.; Ouachan, I.; Varcoe, J. R.; Whelligan, D. K. Radiation-Induced Grafting of a Butyl-Spacer Styrenic Monomer onto ETFE: the Synthesis of the Most Alkali Stable Radiation-Grafted Anion-Exchange Membrane to Date. *J. Mater. Chem. A* **2018**, *6*, 823−827.
(822) Zhao, Y.; Yoshimura, K.; Mahmoud, A. M. A.; Yu, H.-C.; Okushima, S.; Hiroki, A.; Kishiyama, Y.; Shishitani, H.; Yamaguchi, S.; Tanaka, H.; Noda, Y.; Koizumi, S.; Radulescu, A.; Maekawa, Y. A Long Side Chain Imidazolium-Based Graft-Type Anion-Exchange Membrane: Novel Electrolyte and Alkaline-Durable Properties and Structural Elucidation Using SANS Contrast Variation. *Soft Matter* **2020**, *16*, 8128−8143.
(823) Li, Y.; Liu, Y.; Savage, A. M.; Beyer, F. L.; Seifert, S.; Herring, A. M.; Knauss, D. M. Polyethylene-Based Block Copolymers for Anion Exchange Membranes. *Macromolecules* **2015**, *48*, 6523−6533.
(824) Buggy, N. C.; Du, Y.; Kuo, M.-C.; Ahrens, K. A.; Wilkinson, J. S.; Seifert, S.; Coughlin, E. B.; Herring, A. M. A Polyethylene-Based Triblock Copolymer Anion Exchange Membrane with High Conductivity and Practical Mechanical Properties. *ACS Appl. Polym. Mater.* **2020**, *2*, 1294−1303.
(825) Kim, D.-G.; Bell, A.; Register, R. A. Living Vinyl Addition Polymerization of Substituted Norbornenes by a t-Bu_3P-Ligated Methylpalladium Complex. *ACS Macro Lett.* **2015**, *4*, 327−330.
(826) Tsai, S. D.; Register, R. A. Endo/Exo Reactivity Ratios in Living Vinyl Addition Polymerization of Substituted Norbornenes. *Macromol. Chem. Phys.* **2018**, *219*, 1800059.
(827) Yamashita, M.; Takamiya, I.; Jin, K.; Nozaki, K. Syntheses and Structures of Bulky Monophosphine-Ligated Methylpalladium Complexes: Application to Homo- and Copolymerization of Norbornene and/or Methoxycarbonylnorbornene. *Organometallics* **2006**, *25*, 4588−4595.
(828) Bermeshev, M. V.; Bulgakov, B. A.; Genaev, A. M.; Kostina, J. V.; Bondarenko, G. N.; Finkelshtein, E. S. Cationic Polymerization of Norbornene Derivatives in the Presence of Boranes. *Macromolecules* **2014**, *47*, 5470−5483.
(829) Wang, C.; Mo, B.; He, Z.; Shao, Q.; Pan, D.; Wujick, E.; Guo, J.; Xie, X.; Xie, X.; Guo, Z. Crosslinked Norbornene Copolymer Anion Exchange Membrane for Fuel Cells. *J. Membr. Sci.* **2018**, *556*, 118−125.
(830) Price, S. C.; Ren, X.; Savage, A. M.; Beyer, F. L. Synthesis and Characterization of Anion-Exchange Membranes Based on Hydrogenated Poly(norbornene). *Polym. Chem.* **2017**, *8*, 5708−5717.
(831) He, X.; Cheng, C.; Huang, S.; Zhang, F.; Duan, Y.; Zhu, C.; Guo, Y.; Wang, K.; Chen, D. Alkaline Anion Exchange Membranes with Imidazolium-Terminated Flexible Side-Chain Cross-Linked Topological Structure Based on ROMP-Type Norbornene Copolymers. *Polymer* **2020**, *195*, 122412.
(832) Kwasny, M. T.; Zhu, L.; Hickner, M. A.; Tew, G. N. Thermodynamics of Counterion Release Is Critical for Anion Exchange Membrane Conductivity. *J. Am. Chem. Soc.* **2018**, *140*, 7961−7969.
(833) Ziv, N.; Dekel, D. R. A Practical Method for Measuring the True Hydroxide Conductivity of Anion Exchange Membranes. *Electrochem. Commun.* **2018**, *88*, 109−113.
(834) Holtz, M. E.; Yu, Y.; Rivera, J.; Abruna, H. D.; Muller, D. A. In Situ TEM for Quantitative Electrochemistry of Energy Systems. *Microsc. Microanal.* **2015**, *21*, 1509−1510.
(835) Suzuki, S.; Muroyama, H.; Matsui, T.; Eguchi, K. Influence of CO_2 Dissolution into Anion Exchange Membrane on Fuel Cell Performance. *Electrochim. Acta* **2013**, *88*, 552−558.
(836) Kiss, A. M.; Myles, T. D.; Grew, K. N.; Peracchio, A. A.; Nelson, G. J.; Chiu, W. K. S. Carbonate and Bicarbonate Ion Transport in Alkaline Anion Exchange Membranes. *J. Electrochem. Soc.* **2013**, *160*, F994−F999.
(837) Bharath, V. J.; Jervis, J. R.; Bailey, J. J.; Engebretsen, E.; Neville, T. P.; Millichamp, J.; Mason, T.; Shearing, P. R.; Brown, R. J. C.; Manos, G.; Brett, D. J. L. Effect of Humidity on the Interaction of CO_2 with Alkaline Anion Exchange Membranes Probed Using the Quartz Crystal Microbalance. *Int. J. Hydrogen Energy* **2017**, *42*, 24301−24307.
(838) Fukuta, K.; Inoue, H.; Watanabe, S.; Yanagi, H. In-Situ Observation of CO_2 through the Self-Purging in Alkaline Membrane Fuel Cell (AMFC). *ECS Trans.* **2009**, *19*, 23−27.
(839) John, J.; Hugar, K. M.; Rivera-Meléndez, J.; Kostalik, H. A.; Rus, E. D.; Wang, H.; Coates, G. W.; Abruna, H. D. An Electrochemical Quartz Crystal Microbalance Study of a Prospective Alkaline Anion Exchange Membrane Material for Fuel Cells: Anion Exchange Dynamics and Membrane Swelling. *J. Am. Chem. Soc.* **2014**, *136*, 5309−5322.
(840) Yanagi, H.; Fukuta, K. Anion Exchange Membrane and Ionomer for Alkaline Membrane Fuel Cells (AMFCs). *ECS Trans.* **2009**, *16*, 257−262.
(841) Krewer, U.; Weinzierl, C.; Ziv, N.; Dekel, D. R. Impact of Carbonation Processes in Anion Exchange Membrane Fuel Cells. *Electrochim. Acta* **2018**, *263*, 433−446.
(842) Yarlagadda, V.; Carpenter, M. K.; Moylan, T. E.; Kukreja, R. S.; Koestner, R.; Gu, W.; Thompson, L.; Kongkanand, A. Boosting Fuel Cell Performance with Accessible Carbon Mesopores. *ACS Energy Lett.* **2018**, *3*, 618−621.
(843) Ott, S.; Orfanidi, A.; Schmies, H.; Anke, B.; Nong, H. N.; Hübner, J.; Gernert, U.; Gliech, M.; Lerch, M.; Strasser, P. Ionomer Distribution Control in Porous Carbon-Supported Catalyst Layers for High-Power and Low Pt-Loaded Proton Exchange Membrane Fuel Cells. *Nat. Mater.* **2020**, *19*, 77−85.
(844) Ahn, C.; Ahn, J.; Kang, S. Y.; Kim, O.; Lee, D. W.; Lee, J. H.; Shim, J. G.; Lee, C. H.; Cho, Y.; Sung, Y. Enhancement of Service Life of Polymer Electrolyte Fuel Cells through Application of Nano-dispersed Ionomer. *Sci. Adv.* **2020**, *6*, No. eaaw0870.
(845) Li, D.; Chung, H. T.; Maurya, S.; Matanovic, I.; Kim, Y. S. Impact of Ionomer Adsorption on Alkaline Hydrogen Oxidation Activity and Fuel Cell Performance. *Curr. Opin. Electrochem.* **2018**, *12*, 189−195.
(846) Chung, H. T.; Martinez, U.; Matanovic, I.; Kim, Y. S. Cation-Hydroxide-Water Coadsorption Inhibits the Alkaline Hydrogen Oxidation Reaction. *J. Phys. Chem. Lett.* **2016**, *7*, 4464−4469.
(847) Matanovic, I.; Maurya, S.; Park, E. J.; Jeon, J. Y.; Bae, C.; Kim, Y. S. Adsorption of Polyaromatic Backbone Impacts the Performance of Anion Exchange Membrane Fuel Cells. *Chem. Mater.* **2019**, *31*, 4195−4204.
(848) Park, H. J.; Chu, X.; Kim, S. P.; Choi, D.; Jung, J. W.; Woo, J.; Baek, S. Y.; Yoo, S. J.; Chung, Y. C.; Seong, J. G.; Lee, S. Y.; Li, N.; Lee, Y. M. Effect of N-Cyclic Cationic Groups in Poly(Phenylene Oxide)-Based Catalyst Ionomer Membranes for Anion Exchange Membrane Fuel Cells. *J. Membr. Sci.* **2020**, *608*, 118183.
(849) Park, E. J.; Maurya, S.; Lee, A. S.; Leonard, D. P.; Li, D.; Yeob, J. J.; Bae, C.; Kim, Y. S. How Does a Small Structural Change of

https://doi.org/10.1021/acs.chemrev.1c00331
Chem. Rev. XXXX, XXX, XXX−XXX

Anode Ionomer Make a Big Difference in Alkaline Membrane Fuel Cell Performance? *J. Mater. Chem. A* **2019**, *7*, 25040−25046.
(850) Carlson, A.; Eriksson, B.; Olsson, J. S.; Lindbergh, G.; Lagergren, C.; Jannasch, P.; Wreland Lindström, R. Fuel Cell Evaluation of Anion Exchange Membranes Based on Poly(Phenylene Oxide) with Different Cationic Group Placement. *Sustain. Energy Fuels* **2020**, *4*, 2274−2283.
(851) Huang, G.; Mandal, M.; Peng, X.; Yang-Neyerlin, A. C.; Pivovar, B. S.; Mustain, W. E.; Kohl, P. A. Composite Poly-(Norbornene) Anion Conducting Membranes for Achieving Durability, Water Management and High Power (3.4 W/cm^2) in Hydrogen/Oxygen Alkaline Fuel Cells. *J. Electrochem. Soc.* **2019**, *166*, F637−F644.
(852) Hu, M.; Li, Q.; Wang, G.; Lu, J.; Zhuang, L.; Xiao, L. Using Operando Method to Quantify Water Transport and Achieve 3.4 W/cm^2 Performance in Alkaline Polymer Electrolyte Fuel Cells. **2021**, submitted.
(853) Ul Hassan, N.; Mandal, M.; Huang, G.; Firouzjaie, H. A.; Kohl, P. A.; Mustain, W. E. Achieving Hig-Performance and 2000 h Stability in Anion Exchange Membrane Fuel Cells by Manipulating Ionomer Properties and Electrode Optimization. *Adv. Energy Mater.* **2020**, *10*, 2001986.
(854) Zheng, Y.; Omasta, T. J.; Peng, X.; Wang, L.; Varcoe, J. R.; Pivovar, B. S.; Mustain, W. E. Quantifying and Elucidating the Effect of CO_2 on the Thermodynamics, Kinetics and Charge Transport of AEMFCs. *Energy Environ. Sci.* **2019**, *12*, 2806−2819.
(855) Wang, Y.; Li, L.; Hu, L.; Zhuang, L.; Lu, J.; Xu, B. A Feasibility Analysis for Alkaline Membrane Direct Methanol Fuel Cell: Thermodynamic Disadvantages Versus Kinetic Advantages. *Electrochem. Commun.* **2003**, *5*, 662−666.
(856) Varcoe, J. R.; Slade, R. C. T. Prospects for Alkaline Anion-Exchange Membranes in Low Temperature Fuel Cells. *Fuel Cells* **2005**, *5*, 187−200.
(857) Gu, S.; Cai, R.; Luo, T.; Jensen, K.; Contreras, C.; Yan, Y. Quaternary Phosphonium-Based Polymers as Hydroxide Exchange Membranes. *ChemSusChem* **2010**, *3*, 555−558.
(858) Pan, J.; Lu, S.; Li, Y.; Huang, A.; Zhuang, L.; Lu, J. High-Performance Alkaline Polymer Electrolyte for Fuel Cell Applications. *Adv. Funct. Mater.* **2010**, *20*, 312−319.
(859) Zhao, Y.; Yu, H.; Yang, D.; Li, J.; Shao, Z.; Yi, B. High-Performance Alkaline Fuel Cells Using Crosslinked Composite Anion Exchange Membrane. *J. Power Sources* **2013**, *221*, 247−251.
(860) Li, G.; Pan, J.; Han, J.; Chen, C.; Lu, J.; Zhuang, L. Ultrathin Composite Membrane of Alkaline Polymer Electrolyte for Fuel Cell Applications. *J. Mater. Chem. A* **2013**, *1*, 12497−12502.
(861) Wang, Y.; Wang, G.; Li, G.; Huang, B.; Pan, J.; Liu, Q.; Han, J.; Xiao, L.; Lu, J.; Zhuang, L. Pt-Ru Catalyzed Hydrogen Oxidation in Alkaline Media: Oxophilic Effect or Electronic Effect? *Energy Environ. Sci.* **2015**, *8*, 177−181.
(862) Li, Q.; Peng, H.; Wang, Y.; Xiao, L.; Lu, J.; Zhuang, L. The Comparability of Pt to Pt-Ru in Catalyzing the Hydrogen Oxidation Reaction for Alkaline Polymer Electrolyte Fuel Cells Operated at 80 °C. *Angew. Chem., Int. Ed.* **2019**, *58*, 1442−1446.
(863) Wang, L.; Bellini, M.; Miller, H. A.; Varcoe, J. R. A High Conductivity Ultrathin Anion-Exchange Membrane with 500+ h Alkali Stability for Use in Alkaline Membrane Fuel Cells That Can Achieve 2 W cm^{-2} at 80 °C. *J. Mater. Chem. A* **2018**, *6*, 15404−15412.
(864) Wang, T.; Shi, L.; Wang, J.; Zhao, Y.; Setzler, B. P.; Rojas-Carbonell, S.; Yan, Y. High-Performance Hydroxide Exchange Membrane Fuel Cells through Optimization of Relative Humidity, Backpressure and Catalyst Selection. *J. Electrochem. Soc.* **2019**, *166*, F3305−F3310.
(865) Omasta, T. J.; Park, A.; LaManna, J. M.; Zhang, Y.; Peng, X.; Wang, L.; Jacobson, D. L.; Varcoe, J. R.; Hussey, D. S.; Pivovar, B.; Mustain, W. E. Beyond Catalysis and Membranes: Visualizing and Solving the Challenge of Electrode Water Accumulation and Flooding in AEMFCs. *Energy Environ. Sci.* **2018**, *11*, 551−558.
(866) Mandal, M.; Huang, G.; Hassan, N. U.; Peng, X.; Gu, T.; Brooks-Starks, A. H.; Bahar, B.; Mustain, W. E.; Kohl, P. A. The Importance of Water Transport in High Conductivity and High-Power Alkaline Fuel Cells. *J. Electrochem. Soc.* **2020**, *167*, 054501.
(867) Hu, M.; Li, Q.; Peng, H.; Ma, H.; Xiao, L.; Wang, G.; Lu, J.; Zhuang, L. Alkaline Polymer Electrolyte Fuel Cells without Anode Humidification and H_2 Emission. *J. Power Sources* **2020**, *472*, 228471.
(868) Mustain, W. E. Understanding How High-Performance Anion Exchange Membrane Fuel Cells Were Achieved: Component, Interfacial, and Cell-Level Factors. *Curr. Opin. Electrochem.* **2018**, *12*, 233−239.
(869) Lee, Y. M.; Chen, N.; Hu, C.; Wang, H. H.; Kim, S. P.; Kim, H. M.; Lee, W. H.; Bae, J. Y.; Park, J. H. Poly(Alkyl-Terphenyl Piperidinium) Ionomers and Membranes with Outstanding Alkaline Membrane Fuel Cell Performance of 2.58 W cm^{-2}. *Angew. Chem., Int. Ed.* **2021**, *60*, 7710−7718.
(870) Peng, X.; Omasta, T. J.; Magliocca, E.; Wang, L.; Varcoe, J. R.; Mustain, W. E. Nitrogen-Doped Carbon-Coox Nanohybrids: A Precious Metal Free Cathode That Exceeds 1.0 W cm^{-2} Peak Power and 100 h Life in Anion-Exchange Membrane Fuel Cells. *Angew. Chem., Int. Ed.* **2019**, *58*, 1046−1051.
(871) Yang, Y.; Peng, H.; Xiong, Y.; Li, Q.; Lu, J.; Xiao, L.; DiSalvo, F. J.; Zhuang, L.; Abruna, H. D. High-Loading Composition-Tolerant Co-Mn Spinel Oxides with Performance Beyond 1 W/cm^2 in Alkaline Polymer Electrolyte Fuel Cells. *ACS Energy Lett.* **2019**, *4*, 1251−1257.
(872) Peng, X.; Kashyap, V.; Ng, B.; Kurungot, S.; Wang, L.; Varcoe, J.; Mustain, W. High-Performing PGM-Free AEMFC Cathodes from Carbon-Supported Cobalt Ferrite Nanoparticles. *Catalysts* **2019**, *9*, 264.
(873) *Fuel Cell Technical Team Roadmap: United States Driving Research and Innovation for Vehicle Efficiency and Energy sustainability (U.S. DRIVE)*; U.S. Department of Energy, 2017. https://www.energy.gov/sites/prod/files/2017/11/f46/FCTT_Roadmap_Nov_2017_FINAL.pdf.
(874) Thompson, S. T.; Peterson, D.; Ho, D.; Papageorgopoulos, D. Perspective—The Next Decade of AEMFCs: Near-Term Targets to Accelerate Applied R&D. *J. Electrochem. Soc.* **2020**, *167*, 084514.
(875) Song, F.; Li, W.; Yang, J.; Han, G.; Yan, T.; Liu, X.; Rao, Y.; Liao, P.; Cao, Z.; Sun, Y. Interfacial Sites between Cobalt Nitride and Cobalt Act as Bifunctional Catalysts for Hydrogen Electrochemistry. *ACS Energy Lett.* **2019**, *4*, 1594−1601.
(876) Tang, M. H.; Hahn, C.; Klobuchar, A. J.; Ng, J. W.; Wellendorff, J.; Bligaard, T.; Jaramillo, T. F. Nickel-Silver Alloy Electrocatalysts for Hydrogen Evolution and Oxidation in an Alkaline Electrolyte. *Phys. Chem. Chem. Phys.* **2014**, *16*, 19250−19257.
(877) Leonard, D. P.; Maurya, S.; Park, E. J.; Delfin Manriquez, L.; Noh, S.; Wang, X.; Bae, C.; Baca, E. D.; Fujimoto, C.; Kim, Y. S. Asymmetric Electrode Ionomer for Low Relative Humidity Operation of Anion Exchange Membrane Fuel Cells. *J. Mater. Chem. A* **2020**, *8*, 14135−14144.
(878) Miller, H. A.; Pagliaro, M. V.; Bellini, M.; Bartoli, F.; Wang, L.; Salam, I.; Varcoe, J. R.; Vizza, F. Integration of a Pd-CeO_2/C Anode with Pt and Pt-Free Cathode Catalysts in High Power Density Anion Exchange Membrane Fuel Cells. *ACS Appl. Energy Mater.* **2020**, *3*, 10209−10214.
(879) Zheng, Y.; Huang, G.; Wang, L.; Varcoe, J. R.; Kohl, P. A.; Mustain, W. E. Effect of Reacting Gas Flowrates and Hydration on the Carbonation of Anion Exchange Membrane Fuel Cells in the Presence of CO_2. *J. Power Sources* **2020**, *467*, 228350.
(880) Matsui, Y.; Saito, M.; Tasaka, A.; Inaba, M. Influence of Carbon Dioxide on the Performance of Anion-Exchange Membrane Fuel Cells. *ECS Trans.* **2009**, *25*, 105−110.
(881) Inaba, M.; Matsui, Y.; Saito, M.; Tasaka, A.; Fukuta, K.; Watanabe, S.; Yanagi, H. J. E. Effects of Carbon Dioxide on the Performance of Anion-Exchange Membrane Fuel Cells. *Electrochemistry* **2011**, *79*, 322−325.
(882) Zeng, R.; Poynton, S. D.; Kizewski, J. P.; Slade, R. C. T.; Varcoe, J. R. A Novel Reference Electrode for Application in Alkaline Polymer Electrolyte Membrane Fuel Cells. *Electrochem. Commun.* **2010**, *12*, 823−825.

https://doi.org/10.1021/acs.chemrev.1c00331
Chem. Rev. XXXX, XXX, XXX−XXX

(883) Svensson, A. M.; Nisancioglu, K. Interpretation of Measured Polarization Resistance at a Solid Electrode/Electrolyte Interface. *J. Electrochem. Soc.* **1999**, *146*, 1840−1846.
(884) Adler, S.; Henderson, B.; Wilson, M.; Taylor, D.; Richards, R. Reference Electrode Placement and Seals in Electrochemical Oxygen Generators. *Solid State Ionics* **2000**, *134*, 35−42.
(885) Chan, S.; Chen, X.; Khor, K. Reliability and Accuracy of Measured Overpotential in a Three-Electrode Fuel Cell System. *J. Appl. Electrochem.* **2001**, *31*, 1163−1170.
(886) Adler, S. B. Reference Electrode Placement in Thin Solid Electrolytes. *J. Electrochem. Soc.* **2002**, *149*, E166−E172.
(887) He, W.; Van Nguyen, T. Edge Effects on Reference Electrode Measurements in PEM Fuel Cells. *J. Electrochem. Soc.* **2004**, *151*, A185−A195.
(888) Li, G.; Pickup, P. G. Measurement of Single Electrode Potentials and Impedances in Hydrogen and Direct Methanol Pem Fuel Cells. *Electrochim. Acta* **2004**, *49*, 4119−4126.
(889) Liu, Z.; Wainright, J. S.; Huang, W.; Savinell, R. F. Positioning the Reference Electrode in Proton Exchange Membrane Fuel Cells : Calculations of Primary and Secondary Current Distribution. *Electrochim. Acta* **2004**, *49*, 923−935.
(890) Donnan, F. G. Theory of Membrane Equilibria and Membrane Potentials in the Presence of Non-Dialysing Electrolytes. A Contribution to Physical-Chemical Physiology. *J. Membr. Sci.* **1995**, *100*, 45−55.
(891) Li, Q.; Wang, Y.; Ma, H.; Xiao, L.; Wang, G.; Lu, J.; Jun-Tao Zhuang, L. A Model for the Anodic Carbonization of Alkaline Polymer Electrolyte Fuel Cells. *J. Electrochem.* **2020**, *26*, 731−739.
(892) Goeppert, A.; Czaun, M.; May, R. B.; Prakash, G. K. S.; Olah, G. A.; Narayanan, S. R. Carbon Dioxide Capture from the Air Using a Polyamine Based Regenerable Solid Adsorbent. *J. Am. Chem. Soc.* **2011**, *133*, 20164−20167.
(893) Matz, S.; Setzler, B. P.; Weiss, C. M.; Shi, L.; Gottesfeld, S.; Yan, Y. Demonstration of Electrochemically-Driven CO_2 Separation Using Hydroxide Exchange Membranes. *J. Electrochem. Soc.* **2021**, *168*, 014501.
(894) Wang, Y.; Ruiz Diaz, D. F.; Chen, K. S.; Wang, Z.; Adroher, X. C. Materials, Technological Status, and Fundamentals of PEM Fuel Cells - A Review. *Mater. Today* **2020**, *32*, 178−203.
(895) Chen, Z. Water Balancing. *Nat. Energy* **2020**, *5*, 12−13.
(896) Marino, M. G.; Melchior, J. P.; Wohlfarth, A.; Kreuer, K. D. Hydroxide, Halide and Water Transport in a Model Anion Exchange Membrane. *J. Membr. Sci.* **2014**, *464*, 61−71.
(897) Varcoe, J. R. Investigations of the Ex Situ Ionic Conductivities At 30 Degrees C of Metal-Cation-Free Quaternary Ammonium Alkaline Anion-Exchange Membranes in Static Atmospheres of Different Relative Humidities. *Phys. Chem. Chem. Phys.* **2007**, *9*, 1479−1486.
(898) Machado, B. S.; Chakraborty, N.; Das, P. K. Influences of Flow Direction, Temperature and Relative Humidity on the Performance of a Representative Anion Exchange Membrane Fuel Cell: A Computational Analysis. *Int. J. Hydrogen Energy* **2017**, *42*, 6310−6323.
(899) Gao, X.; Yu, H.; Qin, B.; Jia, J.; Hao, J.; Xie, F.; Shao, Z. Enhanced Water Transport in AEMs Based on Poly(Styrene-Ethylene-Butylene-Styrene) Triblock Copolymer for High Fuel Cell Performance. *Polym. Chem.* **2019**, *10*, 1894−1903.
(900) Truong, V. M.; Duong, N. B.; Wang, C. L.; Yang, H. Effects of Cell Temperature and Reactant Humidification on Anion Exchange Membrane Fuel Cells. *Materials* **2019**, *12*, 2048.
(901) Lal, S.; Lamibrac, A.; Eller, J.; Büchi, F. N. Determination of Water Evaporation Rates in Gas Diffusion Layers of Fuel Cells. *J. Electrochem. Soc.* **2018**, *165*, F652−F661.
(902) Saebea, D.; Chaiburi, C.; Authayanun, S. Model Based Evaluation of Alkaline Anion Exchange Membrane Fuel Cells with Water Management. *Chem. Eng. J.* **2019**, *374*, 721−729.
(903) Huo, S.; Zhou, J.; Wang, T.; Chen, R.; Jiao, K. Experimental and Analytical Analysis of Polarization and Water Transport Behaviors of Hydrogen Alkaline Membrane Fuel Cell. *J. Power Sources* **2018**, *382*, 1−12.
(904) Peng, X.; Kulkarni, D.; Huang, Y.; Omasta, T. J.; Ng, B.; Zheng, Y.; Wang, L.; LaManna, J. M.; Hussey, D. S.; Varcoe, J. R.; Zenyuk, I. V.; Mustain, W. E. Using Operando Techniques to Understand and Design High Performance and Stable Alkaline Membrane Fuel Cells. *Nat. Commun.* **2020**, *11*, 3561.
(905) Shiau, H.-S.; Zenyuk, I. V.; Weber, A. Z. Elucidating Performance Limitations in Alkaline-Exchange- Membrane Fuel Cells. *J. Electrochem. Soc.* **2017**, *164*, E3583−E3591.
(906) Jang, S.; Her, M.; Kim, S.; Jang, J. H.; Chae, J. E.; Choi, J.; Choi, M.; Kim, S. M.; Kim, H. J.; Cho, Y. H.; Sung, Y. E.; Yoo, S. J. Membrane/Electrode Interface Design for Effective Water Management in Alkaline Membrane Fuel Cells. *ACS Appl. Mater. Interfaces* **2019**, *11*, 34805−34811.
(907) Luo, X.; Wright, A.; Weissbach, T.; Holdcroft, S. Water Permeation through Anion Exchange Membranes. *J. Power Sources* **2018**, *375*, 442−451.
(908) Paul, D. K.; Karan, K.; Docoslis, A.; Giorgi, J. B.; Pearce, J. Characteristics of Self-Assembled Ultrathin Nafion Films. *Macromolecules* **2013**, *46*, 3461−3475.
(909) Kusoglu, A.; Dursch, T. J.; Weber, A. Z. Nanostructure/Swelling Relationships of Bulk and Thin-Film PFSA Ionomers. *Adv. Funct. Mater.* **2016**, *26*, 4961−4975.
(910) Divekar, A. G.; Buggy, N. C.; Dudenas, P. J.; Kusoglu, A.; Seifert, S.; Pivovar, B. S.; Herring, A. M. Thin Film Morphological Characteristics of a Perfluorinated Anion Exchange Membrane. *ECS Trans.* **2019**, *92*, 715−722.
(911) Huo, S.; Park, J. W.; He, P.; Wang, D.; Jiao, K. Analytical Modeling of Liquid Saturation Jump Effect for Hydrogen Alkaline Anion Exchange Membrane Fuel Cell. *Int. J. Heat Mass Transfer* **2017**, *112*, 891−902.
(912) Shao, Y.; Yin, G.; Gao, Y. Understanding and Approaches for the Durability Issues of Pt-Based Catalysts for PEM Fuel Cell. *J. Power Sources* **2007**, *171*, 558−566.
(913) Macauley, N.; Papadias, D. D.; Fairweather, J.; Spernjak, D.; Langlois, D.; Ahluwalia, R.; More, K. L.; Mukundan, R.; Borup, R. L. Carbon Corrosion in PEM Fuel Cells and the Development of Accelerated Stress Tests. *J. Electrochem. Soc.* **2018**, *165*, F3148−F3160.
(914) He, C.; Sankarasubramanian, S.; Matanovic, I.; Atanassov, P.; Ramani, V. Understanding the Oxygen Reduction Reaction Activity and Oxidative Stability of Pt Supported on Nb-Doped TiO_2. *ChemSusChem* **2019**, *12*, 3468−3480.
(915) Lo, C.-P.; Wang, G.; Kumar, A.; Ramani, V. TiO_2-RuO_2 Electrocatalyst Supports Exhibit Exceptional Electrochemical Stability. *Appl. Catal., B* **2013**, *140-141*, 133−140.
(916) Gao, X.; He, L.; Yu, H.; Xie, F.; Yang, Y.; Shao, Z. The Non-Precious Metal ORR Catalysts for the Anion Exchange Membrane Fuel Cells Application: A Numerical Simulation and Experimental Study. *Int. J. Hydrogen Energy* **2020**, *45*, 23353−23367.
(917) Holdcroft, S. Fuel Cell Catalyst Layers: A Polymer Science Perspective. *Chem. Mater.* **2014**, *26*, 381−393.
(918) Dekel, D. R.; Amar, M.; Willdorf, S.; Kosa, M.; Dhara, S.; Diesendruck, C. E. Effect of Water on the Stability of Quaternary Ammonium Groups for Anion Exchange Membrane Fuel Cell Applications. *Chem. Mater.* **2017**, *29*, 4425−4431.
(919) Dekel, D. R.; Willdorf, S.; Ash, U.; Amar, M.; Pusara, S.; Dhara, S.; Srebnik, S.; Diesendruck, C. E. The Critical Relation between Chemical Stability of Cations and Water in Anion Exchange Membrane Fuel Cells Environment. *J. Power Sources* **2018**, *375*, 351−360.
(920) Omasta, T. J.; Wang, L.; Peng, X.; Lewis, C. A.; Varcoe, J. R.; Mustain, W. E. Importance of Balancing Membrane and Electrode Water in Anion Exchange Membrane Fuel Cells. *J. Power Sources* **2018**, *375*, 205−213.
(921) Willdorf-Cohen, S.; Mondal, A. N.; Dekel, D. R.; Diesendruck, C. E. Chemical Stability of Poly(Phenylene Oxide)-Based Ionomers

https://doi.org/10.1021/acs.chemrev.1c00331
Chem. Rev. XXXX, XXX, XXX−XXX

in an Anion Exchange-Membrane Fuel Cell Environment. *J. Mater. Chem. A* **2018**, *6*, 22234−22239.
(922) Müller, J.; Zhegur, A.; Krewer, U.; Varcoe, J. R.; Dekel, D. R. Practical Ex-Situ Technique to Measure the Chemical Stability of Anion-Exchange Membranes under Conditions Simulating the Fuel Cell Environment. *ACS Mater. Lett.* **2020**, *2*, 168−173.
(923) Bharath, V. J.; Jervis, R.; Millichamp, J.; Neville, T. P.; Mason, T.; Tjaden, B.; Shearing, P. R.; Brown, R. J. C.; Manos, G.; Brett, D. J. L. Alkaline Anion Exchange Membrane Degradation as a Function of Humidity Measured Using the Quartz Crystal Microbalance. *Int. J. Hydrogen Energy* **2017**, *42*, 6243−6249.
(924) Yassin, K.; Rasin, I. G.; Brandon, S.; Dekel, D. R. Quantifying the Critical Effect of Water Diffusivity in Anion Exchange Membranes for Fuel Cell Applications. *J. Membr. Sci.* **2020**, *608*, 118206.
(925) Veh, P.; Britton, B.; Holdcroft, S.; Zengerle, R.; Vierrath, S.; Breitwieser, M. Improving the Water Management in Anion-Exchange Membrane Fuel Cells via Ultra-Thin, Directly Deposited Solid Polymer Electrolyte. *RSC Adv.* **2020**, *10*, 8645−8652.
(926) Kaspar, R. B.; Letterio, M. P.; Wittkopf, J. A.; Gong, K.; Gu, S.; Yan, Y. Manipulating Water in High-Performance Hydroxide Exchange Membrane Fuel Cells through Asymmetric Humidification and Wetproofing. *J. Electrochem. Soc.* **2015**, *162*, F483−F488.
(927) Huo, S.; Deng, H.; Chang, Y.; Jiao, K. Water Management in Alkaline Anion Exchange Membrane Fuel Cell Anode. *Int. J. Hydrogen Energy* **2012**, *37*, 18389−18402.
(928) Li, Y. S.; Zhao, T. S.; Yang, W. W. Measurements of Water Uptake and Transport Properties in Anion-Exchange Membranes. *Int. J. Hydrogen Energy* **2010**, *35*, 5656−5665.
(929) Barnes, A. M.; Liu, B.; Buratto, S. K. Humidity-Dependent Surface Structure and Hydroxide Conductance of a Model Quaternary Ammonium Anion Exchange Membrane. *Langmuir* **2019**, *35*, 14188−14193.
(930) Luo, X.; Rojas-Carbonell, S.; Yan, Y.; Kusoglu, A. Structure-Transport Relationships of Poly(Aryl Piperidinium) Anion-Exchange Membranes: Eeffect of Anions and Hydration. *J. Membr. Sci.* **2020**, *598*, 117680.
(931) Kimura, T.; Kawamoto, T.; Aoki, M.; Mizusawa, T.; Yamada, N. L.; Miyatake, K.; Inukai, J. Sublayered Thin Films of Hydrated Anion Exchange Ionomer for Fuel Cells Formed on SiO_2 and Pt Substrates Analyzed by Neutron Reflectometry under Controlled Temperature and Humidity Conditions. *Langmuir* **2020**, *36*, 4955−4963.
(932) Nonoyama, N.; Okazaki, S.; Weber, A. Z.; Ikogi, Y.; Yoshida, T. Analysis of Oxygen-Transport Diffusion Resistance in Proton-Exchange-Membrane Fuel Cells. *J. Electrochem. Soc.* **2011**, *158*, B416−B423.
(933) Debe, M. K.; Schmoeckel, A. K.; Vernstrom, G. D.; Atanasoski, R. High Voltage Stability of Nanostructured Thin Film Catalysts for PEM Fuel Cells. *J. Power Sources* **2006**, *161*, 1002−1011.
(934) Kusoglu, A.; Kushner, D.; Paul, D. K.; Karan, K.; Hickner, M. A.; Weber, A. Z. Impact of Substrate and Processing on Confinement of Nafion Thin Films. *Adv. Funct. Mater.* **2014**, *24*, 4763−4774.
(935) Weber, A. Z.; Kusoglu, A. Unexplained Transport Resistances for Low-Loaded Fuel-Cell Catalyst Layers. *J. Mater. Chem. A* **2014**, *2*, 17207−17211.
(936) Paul, D. K.; Fraser, A.; Karan, K. Towards the Understanding of Proton Conduction Mechanism in PEMFC Catalyst Layer: Conductivity of Adsorbed Nafion Films. *Electrochem. Commun.* **2011**, *13*, 774−777.
(937) Morawietz, T.; Handl, M.; Oldani, C.; Friedrich, K. A.; Hiesgen, R. Quantitative in Situ Analysis of Ionomer Structure in Fuel Cell Catalytic Layers. *ACS Appl. Mater. Interfaces* **2016**, *8*, 27044−27054.
(938) Ignaszak, A.; Ye, S.; Gyenge, E. A Study of the Catalytic Interface for O_2 Electroreduction on Pt: The Interaction between Carbon Support Meso/Microstructure and Ionomer (Nafion) Distribution. *J. Phys. Chem. C* **2009**, *113*, 298−307.
(939) Sambandam, S.; Parrondo, J.; Ramani, V. Estimation of Electrode Ionomer Oxygen Permeability and Ionomer-Phase Oxygen Transport Resistance in Polymer Electrolyte Fuel Cells. *Phys. Chem. Chem. Phys.* **2013**, *15*, 14994−15002.
(940) Ayad, A.; Bouet, J.; Fauvarque, J. F. Comparative Study of Protonic Conducting Polymers Incorporated in the Oxygen Electrode of the PEMFC. *J. Power Sources* **2005**, *149*, 66−71.
(941) García de Arquer, F. P.; Dinh, C.-T.; Ozden, A.; Wicks, J.; McCallum, C.; Kirmani, A. R.; Nam, D.-H.; Gabardo, C.; Seifitokaldani, A.; Wang, X.; Li, Y. C.; Li, F.; Edwards, J.; Richter, L. J.; Thorpe, S. J.; Sinton, D.; Sargent, E. H. CO_2 Electrolysis to Multicarbon Products at Activities Greater than 1 A cm^{-2}. *Science* **2020**, *367*, 661−666.
(942) Wang, G.; Osmieri, L.; Star, A. G.; Pfeilsticker, J.; Neyerlin, K. C. Elucidating the Role of Ionomer in the Performance of Platinum Group Metal-Free Catalyst Layer via in Situ Electrochemical Diagnostics. *J. Electrochem. Soc.* **2020**, *167*, 044519.
(943) Moore, M.; Wardlaw, P.; Dobson, P.; Boisvert, J. J.; Putz, A.; Spiteri, R. J.; Secanell, M. Understanding the Effect of Kinetic and Mass Transport Processes in Cathode Agglomerates. *J. Electrochem. Soc.* **2014**, *161*, E3125−E3137.
(944) Epting, W. K.; Litster, S. Effects of an Agglomerate Size Distribution on the PEFC Agglomerate Model. *Int. J. Hydrogen Energy* **2012**, *37*, 8505−8511.
(945) Greszler, T. A.; Caulk, D.; Sinha, P. The Impact of Platinum Loading on Oxygen Transport Resistance. *J. Electrochem. Soc.* **2012**, *159*, F831−F840.
(946) Owejan, J. P.; Owejan, J. E.; Gu, W. Impact of Platinum Loading and Catalyst Layer Structure on PEMFC Performance. *J. Electrochem. Soc.* **2013**, *160*, F824−F833.
(947) Suzuki, T.; Kudo, K.; Morimoto, Y. Model for Investigation of Oxygen Transport Limitation in a Polymer Electrolyte Fuel Cell. *J. Power Sources* **2013**, *222*, 379−389.
(948) Yoon, W.; Weber, A. Z. Modeling Low-Platinum-Loading Effects in Fuel-Cell Catalyst Layers. *J. Electrochem. Soc.* **2011**, *158*, B1007−B1018.
(949) Park, Y.-C.; Kakinuma, K.; Uchida, H.; Watanabe, M.; Uchida, M. Effects of Short-Side-Chain Perfluorosulfonic Acid Ionomers as Binders on the Performance of Low Pt Loading Fuel Cell Cathodes. *J. Power Sources* **2015**, *275*, 384−391.
(950) Soboleva, T.; Malek, K.; Xie, Z.; Navessin, T.; Holdcroft, S. PEMFC Catalyst Layers: The Role of Micropores and Mesopores on Water Sorption and Fuel Cell Activity. *ACS Appl. Mater. Interfaces* **2011**, *3*, 1827−1837.
(951) Soboleva, T.; Zhao, X.; Malek, K.; Xie, Z.; Navessin, T.; Holdcroft, S. On the Micro-, Meso-, and Macroporous Structures of Polymer Electrolyte Membrane Fuel Cell Catalyst Layers. *ACS Appl. Mater. Interfaces* **2010**, *2*, 375−384.
(952) Huang, J.; Li, Z.; Zhang, J. Review of Characterization and Modeling of Polymer Electrolyte Fuel Cell Catalyst Layer: The Blessing and Curse of Ionomer. *Front. Energy* **2017**, *11*, 334−364.
(953) Chan, K.; Eikerling, M. A Pore-Scale Model of Oxygen Reduction in Ionomer-Free Catalyst Layers of PEFCs. *J. Electrochem. Soc.* **2011**, *158*, B18−B28.
(954) Orfanidi, A.; Rheinländer, P. J.; Schulte, N.; Gasteiger, H. A. Ink Solvent Dependence of the Ionomer Distribution in the Catalyst Layer of a PEMFC. *J. Electrochem. Soc.* **2018**, *165*, F1254−F1263.
(955) Yang, T.-H.; Yoon, Y.-G.; Park, G.-G.; Lee, W.-Y.; Kim, C.-S. Fabrication of a Thin Catalyst Layer Using Organic Solvents. *J. Power Sources* **2004**, *127*, 230−233.
(956) Doo, G.; Lee, J. H.; Yuk, S.; Choi, S.; Lee, D.-H.; Lee, D. W.; Kim, H. G.; Kwon, S. H.; Lee, S. G.; Kim, H.-T. Tuning the Ionomer Distribution in the Fuel Cell Catalyst Layer with Scaling the Ionomer Aggregate Size in Dispersion. *ACS Appl. Mater. Interfaces* **2018**, *10*, 17835−17841.
(957) Malek, K.; Mashio, T.; Eikerling, M. Microstructure of Catalyst Layers in PEM Fuel Cells Redefined: A Computational Approach. *Electrocatalysis* **2011**, *2*, 141−157.
(958) He, Q.; Suraweera, N. S.; Joy, D. C.; Keffer, D. J. Structure of the Ionomer Film in Catalyst Layers of Proton Exchange Membrane Fuel Cells. *J. Phys. Chem. C* **2013**, *117*, 25305−25316.

https://doi.org/10.1021/acs.chemrev.1c00331
Chem. Rev. XXXX, XXX, XXX−XXX

(959) Zhao, Z.; Hossain, M. D.; Xu, C.; Lu, Z.; Liu, Y.-S.; Hsieh, S.-H.; Lee, I.; Gao, W.; Yang, J.; Merinov, B. V.; Xue, W.; Liu, Z.; Zhou, J.; Luo, Z.; Pan, X.; Zaera, F.; Guo, J.; Duan, X.; Goddard, W. A.; Huang, Y. Tailoring a Three-Phase Microenvironment for High-Performance Oxygen Reduction Reaction in Proton Exchange Membrane Fuel Cells. *Matter* **2020**, *3*, 1774−1790.
(960) Orfanidi, A.; Madkikar, P.; El-Sayed, H. A.; Harzer, G. S.; Kratky, T.; Gasteiger, H. A. The Key to High Performance Low Pt Loaded Electrodes. *J. Electrochem. Soc.* **2017**, *164*, F418−F426.
(961) Wang, Q.; Eikerling, M.; Song, D.; Liu, Z. Structure and Performance of Different Types of Agglomerates in Cathode Catalyst Layers of PEM Fuel Cells. *J. Electroanal. Chem.* **2004**, *573*, 61−69.
(962) Broka, K.; Ekdunge, P. Modelling the PEM Fuel Cell Cathode. *J. Appl. Electrochem.* **1997**, *27*, 281−289.
(963) Weber, A. Z.; Newman, J. Modeling Transport in Polymer-Electrolyte Fuel Cells. *Chem. Rev.* **2004**, *104*, 4679−4726.
(964) Inoue, G.; Ohnishi, T.; So, M.; Park, K.; Ono, M.; Tsuge, Y. Simulation of Carbon Black Aggregate and Evaluation of Ionomer Structure on Carbon in Catalyst Layer of Polymer Electrolyte Fuel Cell. *J. Power Sources* **2019**, *439*, 227060.
(965) So, M.; Park, K.; Tsuge, Y.; Inoue, G. A Particle Based Ionomer Attachment Model for a Fuel Cell Catalyst Layer. *J. Electrochem. Soc.* **2020**, *167*, 013544.
(966) Cetinbas, F. C.; Ahluwalia, R. K.; Kariuki, N. N.; Andrade, V. D.; Myers, D. J. Effects of Porous Carbon Morphology, Agglomerate Structure and Relative Humidity on Local Oxygen Transport Resistance. *J. Electrochem. Soc.* **2020**, *167*, 013508.
(967) Secanell, M.; Karan, K.; Suleman, A.; Djilali, N. Multi-Variable Optimization of PEMFC Cathodes Using an Agglomerate Model. *Electrochim. Acta* **2007**, *52*, 6318−6337.
(968) Sun, W.; Peppley, B. A.; Karan, K. An Improved Two-Dimensional Agglomerate Cathode Model to Study the Influence of Catalyst Layer Structural Parameters. *Electrochim. Acta* **2005**, *50*, 3359−3374.
(969) Zhang, J.; Yang, W.; Xu, L.; Wang, Y. Simulation of the Catalyst Layer in PEMFC Based on a Novel Two-Phase Lattice Model. *Electrochim. Acta* **2011**, *56*, 6912−6918.
(970) Song, D.; Wang, Q.; Liu, Z.; Eikerling, M.; Xie, Z.; Navessin, T.; Holdcroft, S. A Method for Optimizing Distributions of Nafion and Pt in Cathode Catalyst Layers of PEM Fuel Cells. *Electrochim. Acta* **2005**, *50*, 3347−3358.
(971) Weckhuysen, B. M. Snapshots of a Working Catalyst: Possibilities and Limitations of *In Situ* Spectroscopy in the Field of Heterogeneous Catalysis. *Chem. Commun.* **2002**, 97−110.
(972) Baňares, M. A. Operando Methodology: Combination of In Situ Spectroscopy and Simultaneous Activity Measurements under Catalytic Reaction Conditions. *Catal. Today* **2005**, *100*, 71−77.
(973) Bone, S. E.; Steinruck, H.-G.; Toney, M. F. Advanced Characterization in Clean Water Technologies. *Joule* **2020**, *4*, 1637−1659.
(974) Weker, J. N.; Toney, M. F. Emerging In Situ and Operando Nanoscale X-Ray Imaging Techniques for Energy Storage Materials. *Adv. Funct. Mater.* **2015**, *25*, 1622−1637.
(975) Russell, A. E.; Rose, A. X-ray Absorption Spectroscopy of Low Temperature Fuel Cell Catalysts. *Chem. Rev.* **2004**, *104*, 4613−4635.
(976) Gorlin, Y.; Lassalle-Kaiser, B.; Benck, J. D.; Gul, S.; Webb, S. M.; Yachandra, V. K.; Yano, J.; Jaramillo, T. F. In Situ X-ray Absorption Spectroscopy Investigation of a Bifunctional Manganese Oxide Catalyst with High Activity for Electrochemical Water Oxidation and Oxygen Reduction. *J. Am. Chem. Soc.* **2013**, *135*, 8525−8534.
(977) Wiltshire, R. J. K.; King, C. R.; Ross, A.; Wells, P. P.; Hogarth, M. P.; Thompsett, D.; Russell, A. E. A PEM Fuel Cell for in situ XAS Studies. *Electrochim. Acta* **2005**, *50*, 5208−5217.
(978) Imai, H.; Izumi, K.; Matsumoto, M.; Kubo, Y.; Kato, K.; Imai, Y. In Situ and Real-Time Monitoring of Oxide Growth in a Few Monolayers at Surfaces of Platinum Nanoparticles in Aqueous Media. *J. Am. Chem. Soc.* **2009**, *131*, 6293−6300.
(979) Erickson, E. M.; Thorum, M. S.; Vasić, R.; Marinković, N. S.; Frenkel, A. I.; Gewirth, A. A.; Nuzzo, R. G. In Situ Electrochemical X-ray Absorption Spectroscopy of Oxygen Reduction Electrocatalysis with High Oxygen Flux. *J. Am. Chem. Soc.* **2012**, *134*, 197−200.
(980) Casalongue, H. S.; Kaya, S.; Viswanathan, V.; Miller, D. J.; Friebel, D.; Hansen, H. A.; Nørskov, J. K.; Nilsson, A.; Ogasawara, H. Direct Observation of the Oxygenated Species during Oxygen Reduction on a Platinum Fuel Cell Cathode. *Nat. Commun.* **2013**, *4*, 2817.
(981) Becknell, N.; Kang, Y.; Chen, C.; Resasco, J.; Kornienko, N.; Guo, J.; Marković, N. M.; Somorjai, G. A.; Stamenković, V. R.; Yang, P. Atomic Structure of Pt_3Ni Nanoframe Electrocatalysts by In Situ X-ray Absorption Spectroscopy. *J. Am. Chem. Soc.* **2015**, *137*, 15817−15824.
(982) Sasaki, K.; Marinkovic, N.; Isaacs, H. S.; Adzic, R. R. Synchrotron-Based In Situ Characterization of Carbon-Supported Platinum and Platinum Monolayer Electrocatalysts. *ACS Catal.* **2016**, *6*, 69−76.
(983) Kanan, M. W.; Yano, J.; Surendranath, Y.; Dincă, M.; Yachandra, V. K.; Nocera, D. G. Structure and Valency of a Cobalt-Phosphate Water Oxidation Catalyst Determined by in Situ X-ray Spectroscopy. *J. Am. Chem. Soc.* **2010**, *132*, 13692−13701.
(984) Bates, M.; Jia, Q.; Doan, H.; Liang, W.; Mukerjee, S. Charge-Transfer Effects in Ni-Fe and Ni-Fe-Co Mixed-Metal Oxides for the Alkaline Oxygen Evolution Reaction. *ACS Catal.* **2016**, *6*, 155−161.
(985) Risch, M.; Stoerzinger, K. A.; Han, B.; Regier, T. Z.; Peak, D.; Sayed, Y.; Wei, C.; Xu, Z.; Shao-Horn, Y. Redox Processes of Manganese Oxide in Catalyzing Oxygen Evolution and Reduction: An in Situ Soft X-Ray Absorption Spectroscopy Study. *J. Phys. Chem. C* **2017**, *121*, 17682−17692.
(986) Weir, M. G.; Myers, V. S.; Frenkel, A. I.; Crooks, R. M. In situ X-ray Absorption Analysis of ∼1.8 nm Dendrimer-Encapsulated Pt Nanoparticles during Electrochemical CO Oxidation. *ChemPhysChem* **2010**, *11*, 2942−2950.
(987) Tylus, U.; Jia, Q.; Strickland, K.; Ramaswamy, N.; Serov, A.; Atanassov, P.; Mukerjee, S. Elucidating Oxygen Reduction Active Sites in Pyrolyzed Metal-Nitrogen Coordinated Non-Precious-Metal Electrocatalyst Systems. *J. Phys. Chem. C* **2014**, *118*, 8999−9008.
(988) Viswanathan, R.; Hou, G. Y.; Liu, R. X.; Bare, S. R.; Modica, F.; Mickelson, G.; Segre, C. U.; Leyarovska, N.; Smotkin, E. S. In-Situ XANES of Carbon-Supported Pt-Ru Anode Electrocatalyst for Reformate-Air Polymer Electrolyte Fuel Cells. *J. Phys. Chem. B* **2002**, *106*, 3458−3465.
(989) Mukerjee, S.; Srinivasan, S.; Soriaga, M. P.; McBreen, J. Role of Structural and Electronic Properties of Pt and Pt Alloys on Electrocatalysts of Oxygen Reduction. *J. Electrochem. Soc.* **1995**, *142*, 1409−1421.
(990) Roth, C.; Martz, N.; Buhrmester, T.; Scherer, J.; Fuess, H. In-Situ XAFS Fuel Cell Measurements of a Carbon-Supported Pt-Ru Anode Electrocatalyst in Hydrogen and Direct Methanol Operation. *Phys. Chem. Chem. Phys.* **2002**, *4*, 3555−3557.
(991) Ishiguro, N.; Kityalarn, S.; Sekizawa, O.; Uruga, T.; Sasabe, T.; Nagasawa, K.; Yokoyama, T.; Tada, M. Rate Enhancements in Structural Transformations of Pt-Co and Pt-Ni Bimetallic Cathode Catalysts in Polymer Electrolyte Fuel Cells Studied by in Situ Time-Resolved X-ray Absorption Fine Structure. *J. Phys. Chem. C* **2014**, *118*, 15874−15883.
(992) Higashi, K.; Samjeske, G.; Takao, S.; Kaneko, T.; Sekizawa, O.; Uruga, T.; Iwasawa, Y. The Relationship between the Active Pt Fraction in a PEFC Pt/C Catalyst and the ECSA and Mass Activity during Start-Up/Shut-Down Degradation by in Situ Time-Resolved XAFS Technique. *J. Phys. Chem. C* **2017**, *121*, 22164−22177.
(993) Timoshenko, J.; Roldan Cuenya, B. In Situ/Operando Electrocatalyst Characterization by X-Ray Absorption Spectroscopy. *Chem. Rev.* **2021**, *121*, 882−961.
(994) Eisenberger, P.; Platzman, P. M.; Winick, H. X-Ray Resonant Raman Scattering: Observation of Characteristic Radiation Narrower Than the Lifetime Width. *Phys. Rev. Lett.* **1976**, *36*, 623−626.

https://doi.org/10.1021/acs.chemrev.1c00331
Chem. Rev. XXXX, XXX, XXX−XXX

(995) Bauer, M. HERFD-XAX and Valence-to-Core-XES: New Tools to Push the Limits in Research with Hard X-Rays? *Phys. Chem. Chem. Phys.* **2014**, *16*, 13827−13837.
(996) Glatzel, P.; Bergmann, U. High Resolution 1s Core Hole X-Ray Spectroscopy in 3d Transition Metal Complexes—Electronic and Structural Information. *Coord. Chem. Rev.* **2005**, *249*, 65−95.
(997) de Groot, F. M. F.; Krisch, M. H.; Vogel, J. Spectral Sharpening of the Ptledges by High-Resolution X-Ray Emission. *Phys. Rev. B: Condens. Matter Mater. Phys.* **2002**, *66*, 195112.
(998) Bordiga, S.; Groppo, E.; Agostini, G.; van Bokhoven, J. A.; Lamberti, C. Reactivity of Surface Species in Heterogeneous Catalysts Probed by in Situ X-Ray Absorption Techniques. *Chem. Rev.* **2013**, *113*, 1736−1850.
(999) Friebel, D.; Ogasawara, H.; Nilsson, A. X-Ray Spectroscopy at Electro-Catalytic Interfaces. In *Surface and Interface Science*; Wiley-VCH: Weinheim, Germany, 2020; pp 733−772.
(1000) Burkhardt, L.; Holzwarth, M.; Plietker, B.; Bauer, M. Detection and Characterization of Hydride Ligands in Iron Complexes by High-Resolution Hard X-Ray Spectroscopy and Implications for Catalytic Processes. *Inorg. Chem.* **2017**, *56*, 13300−13310.
(1001) Friebel, D.; Louie, M. W.; Bajdich, M.; Sanwald, K. E.; Cai, Y.; Wise, A. M.; Cheng, M.-J.; Sokaras, D.; Weng, T.-C.; Alonso-Mori, R.; Davis, R. C.; Bargar, J. R.; Nørskov, J. K.; Nilsson, A.; Bell, A. T. Identification of Highly Active Fe Sites in (Ni, Fe)OOH for Electrocatalytic Water Splitting. *J. Am. Chem. Soc.* **2015**, *137*, 1305−1313.
(1002) Agote-Arán, M.; Lezcano-González, I.; Greenaway, A. G.; Hayama, S.; Díaz-Moreno, S.; Kroner, A. B.; Beale, A. M. Operando HERFD-XANES/XES Studies Reveal Differences in the Activity of Fe-Species in MFI and CHA Structures for the Standard Selective Catalytic Reduction of NO with NH_3. *Appl. Catal., A* **2019**, *570*, 283−291.
(1003) Günter, T.; Doronkin, D. E.; Boubnov, A.; Carvalho, H. W. P.; Casapu, M.; Grunwaldt, J. D. The SCR of NO_x with NH_3 Examined by Novel X-Ray Emission and X-Ray Absorption Methods. *Top. Catal.* **2016**, *59*, 866−874.
(1004) Sun, X.; Wang, R.; Ould-Chikh, S.; Osadchii, D.; Li, G.; Aguilar, A.; Hazemann, J.-L.; Kapteijn, F.; Gascon, J. Structure-Activity Relationships in Metal Organic Framework Derived Mesoporous Nitrogen-Doped Carbon Containing Atomically Dispersed Iron Sites for CO_2 Electrochemical Reduction. *J. Catal.* **2019**, *378*, 320−330.
(1005) Beheshti Askari, A.; al Samarai, M.; Hiraoka, N.; Ishii, H.; Tillmann, L.; Muhler, M.; DeBeer, S. In Situ X-Ray Emission and High-Resolution X-Ray Absorption Spectroscopy Applied to Ni-Based Bimetallic Dry Methane Reforming Catalysts. *Nanoscale* **2020**, *12*, 15185−15192.
(1006) Günter, T.; Carvalho, H. W. P.; Doronkin, D. E.; Sheppard, T.; Glatzel, P.; Atkins, A. J.; Rudolph, J.; Jacob, C. R.; Casapu, M.; Grunwaldt, J.-D. Structural Snapshots of the SCR Reaction Mechanism on Cu-SSZ-13. *Chem. Commun.* **2015**, *51*, 9227−9230.
(1007) Li, L.; Yang, J.; Ali-Löytty, H.; Weng, T.-C.; Toma, F. M.; Sokaras, D.; Sharp, I. D.; Nilsson, A. Operando Observation of Chemical Transformations of Iridium Oxide During Photoelectrochemical Water Oxidation. *ACS Appl. Energy Mater.* **2019**, *2*, 1371−1379.
(1008) Gao, D.; Sinev, I.; Scholten, F.; Arán-Ais, R. M.; Divins, N. J.; Kvashnina, K.; Timoshenko, J.; Roldan Cuenya, B. Selective CO_2 Electroreduction to Ethylene and Multicarbon Alcohols via Electrolyte-Driven Nanostructuring. *Angew. Chem., Int. Ed.* **2019**, *58*, 17047−17053.
(1009) Safonova, O. V.; Tromp, M.; van Bokhoven, J. A.; de Groot, F. M. F.; Evans, J.; Glatzel, P. Identification of CO Adsorption Sites in Supported Pt Catalysts Using High-Energy-Resolution Fluorescence Detection X-Ray Spectroscopy. *J. Phys. Chem. B* **2006**, *110*, 16162−16164.
(1010) Cui, Y.-T.; Harada, Y.; Niwa, H.; Hatanaka, T.; Nakamura, N.; Ando, M.; Yoshida, T.; Ishii, K.; Matsumura, D.; Oji, H.; Ofuchi, H.; Oshima, M. Wetting Induced Oxidation of Pt-Based Nano Catalysts Revealed by in Situ High Energy Resolution X-Ray Absorption Spectroscopy. *Sci. Rep.* **2017**, *7*, 1482.
(1011) Friebel, D.; Miller, D. J.; O'Grady, C. P.; Anniyev, T.; Bargar, J.; Bergmann, U.; Ogasawara, H.; Wikfeldt, K. T.; Pettersson, L. G. M.; Nilsson, A. In Situ X-Ray Probing Reveals Fingerprints of Surface Platinum Oxide. *Phys. Chem. Chem. Phys.* **2011**, *13*, 262−266.
(1012) Merte, L. R.; Behafarid, F.; Miller, D. J.; Friebel, D.; Cho, S.; Mbuga, F.; Sokaras, D.; Alonso-Mori, R.; Weng, T.-C.; Nordlund, D.; Nilsson, A.; Roldan Cuenya, B. Electrochemical Oxidation of Size-Selected Pt Nanoparticles Studied Using in Situ High-Energy-Resolution X-Ray Absorption Spectroscopy. *ACS Catal.* **2012**, *2*, 2371−2376.
(1013) Kusano, S.; Matsumura, D.; Ishii, K.; Tanaka, H.; Mizuki, J. I. Electrochemical Adsorption on Pt Nanoparticles in Alkaline Solution Observed Using in Situ High Energy Resolution X-Ray Absorption Spectroscopy. *Nanomaterials* **2019**, *9*, 642.
(1014) Glatzel, P.; Singh, J.; Kvashnina, K. O.; van Bokhoven, J. A. In Situ Characterization of the 5d Density of States of Pt Nanoparticles Upon Adsorption of CO. *J. Am. Chem. Soc.* **2010**, *132*, 2555−2557.
(1015) Maurer, F.; Jelic, J.; Wang, J.; Gänzler, A.; Dolcet, P.; Wöll, C.; Wang, Y.; Studt, F.; Casapu, M.; Grunwaldt, J.-D. Tracking the Formation, Fate and Consequence for Catalytic Activity of Pt Single Sites on CeO_2. *Nat. Catal.* **2020**, *3*, 824−833.
(1016) Qureshi, M.; Garcia-Esparza, A. T.; Jeantelot, G.; Ould-Chikh, S.; Aguilar-Tapia, A.; Hazemann, J.-L.; Basset, J.-M.; Loffreda, D.; Le Bahers, T.; Takanabe, K. Catalytic Consequences of Ultrafine Pt Clusters Supported on $SrTiO_3$ for Photocatalytic Overall Water Splitting. *J. Catal.* **2019**, *376*, 180−190.
(1017) Piccolo, L.; Afanasiev, P.; Morfin, F.; Len, T.; Dessal, C.; Rousset, J. L.; Aouine, M.; Bourgain, F.; Aguilar-Tapia, A.; Proux, O.; Chen, Y.; Soler, L.; Llorca, J. Operando X-Ray Absorption Spectroscopy Investigation of Photocatalytic Hydrogen Evolution over Ultradispersed Pt/TiO_2 Catalysts. *ACS Catal.* **2020**, *10*, 12696−12705.
(1018) Lu, Y.; Wang, J.; Yu, L.; Kovarik, L.; Zhang, X.; Hoffman, A. S.; Gallo, A.; Bare, S. R.; Sokaras, D.; Kroll, T.; Dagle, V.; Xin, H.; Karim, A. M. Identification of the Active Complex for CO Oxidation over Single-Atom Ir-on-$MgAl_2O_4$ Catalysts. *Nat. Catal.* **2019**, *2*, 149−156.
(1019) Juhin, A.; de Groot, F.; Vankó, G.; Calandra, M.; Brouder, C. Angular Dependence of Core Hole Screening in $LiCoO_2$: A DFT+U Calculation of the Oxygen and Cobalt K-Edge X-Ray Absorption Spectra. *Phys. Rev. B: Condens. Matter Mater. Phys.* **2010**, *81*, 115115.
(1020) Budiyanto, E.; Yu, M.; Chen, M.; DeBeer, S.; Rüdiger, O.; Tüysüz, H. Tailoring Morphology and Electronic Structure of Cobalt Iron Oxide Nanowires for Electrochemical Oxygen Evolution Reaction. *ACS Appl. Energy Mater.* **2020**, *3*, 8583−8594.
(1021) Friebel, D.; Bajdich, M.; Yeo, B. S.; Louie, M. W.; Miller, D. J.; Sanchez Casalongue, H.; Mbuga, F.; Weng, T.-C.; Nordlund, D.; Sokaras, D.; Alonso-Mori, R.; Bell, A. T.; Nilsson, A. On the Chemical State of Co Oxide Electrocatalysts During Alkaline Water Splitting. *Phys. Chem. Chem. Phys.* **2013**, *15*, 17460−17467.
(1022) Robinson, I. K.; Tweet, D. J. Surface X-Ray Diffraction. *Rep. Prog. Phys.* **1992**, *55*, 599−651.
(1023) Renaud, G. Oxide Surfaces and Metal/Oxide Interfaces Studied by Grazing Incidence X-Ray Scattering. *Surf. Sci. Rep.* **1998**, *32*, 5−90.
(1024) Als-Nielsen, J.; McMorrow, D. *Elements of Modern X-Ray Physics*; John Wiley & Sons, Ltd: Chichester, UK, 2011.
(1025) Disa, A. S.; Walker, F. J.; Ahn, C. H. High-Resolution Crystal Truncation Rod Scattering: Application to Ultrathin Layers and Buried Interfaces. *Adv. Mater. Interfaces* **2020**, *7*, 1901772.
(1026) Robinson, I. K. Crystal Truncation Rods and Surface Roughness. *Phys. Rev. B: Condens. Matter Mater. Phys.* **1986**, *33*, 3830−3836.
(1027) Fienup, J. R. Reconstruction of an Object from the Modulus of Its Fourier Transform. *Opt. Lett.* **1978**, *3*, 27−29.

https://doi.org/10.1021/acs.chemrev.1c00331
Chem. Rev. XXXX, XXX, XXX−XXX

(1028) Saldin, D. K.; Harder, R. J.; Shneerson, V. L.; Moritz, W. Phase Retrieval Methods for Surface X-Ray Diffraction. *J. Phys.: Condens. Matter* **2001**, *13*, 10689−10707.
(1029) Yacoby, Y.; Pindak, R.; MacHarrie, R.; Pfeiffer, L.; Berman, L.; Clarke, R. Direct Structure Determination of Systems with Two-Dimensional Periodicity. *J. Phys.: Condens. Matter* **2000**, *12*, 3929−3938.
(1030) Björck, M.; Schlepütz, C. M.; Pauli, S. A.; Martoccia, D.; Herger, R.; Willmott, P. R. Atomic Imaging of Thin Films with Surface X-Ray Diffraction: Introducing DCAF. *J. Phys.: Condens. Matter* **2008**, *20*, 445006.
(1031) Fung, R.; Shneerson, V. L.; Lyman, P. F.; Parihar, S. S.; Johnson-Steigelman, H. T.; Saldin, D. K. Phase and Amplitude Recovery and Diffraction Image Generation Method: Structure of Sb/Au(110)-$\sqrt{3} \times \sqrt{3}$R54.7° from Surface X-Ray Diffraction. *Acta Crystallogr., Sect. A: Found. Crystallogr.* **2007**, *63*, 239−250.
(1032) Plaza, M.; Huang, X.; Ko, J. Y. P.; Shen, M.; Simpson, B. H.; Rodríguez-López, J.; Ritzert, N. L.; Letchworth-Weaver, K.; Gunceler, D.; Schlom, D. G.; Arias, T. A.; Brock, J. D.; Abruna, H. D. Structure of the Photo-Catalytically Active Surface of $SrTiO_3$. *J. Am. Chem. Soc.* **2016**, *138*, 7816−7819.
(1033) Harlow, G. S.; Lundgren, E.; Escudero-Escribano, M. Recent Advances in Surface X-Ray Diffraction and the Potential for Determining Structure-Sensitivity Relations in Single-Crystal Electrocatalysis. *Curr. Opin. Electrochem.* **2020**, *23*, 162−173.
(1034) Nagy, Z.; You, H. Applications of Surface X-Ray Scattering to Electrochemistry Problems. *Electrochim. Acta* **2002**, *47*, 3037−3055.
(1035) You, H.; Zurawski, D. J.; Nagy, Z.; Yonco, R. M. In-Situ X-Ray Reflectivity Study of Incipient Oxidation of Pt(111) Surface in Electrolyte Solutions. *J. Chem. Phys.* **1994**, *100*, 4699−4702.
(1036) Liu, Y.; Barbour, A.; Komanicky, V.; You, H. X-Ray Crystal Truncation Rod Studies of Surface Oxidation and Reduction on Pt(111). *J. Phys. Chem. C* **2016**, *120*, 16174−16178.
(1037) Drnec, J.; Ruge, M.; Reikowski, F.; Rahn, B.; Carla, F.; Felici, R.; Stettner, J.; Magnussen, O. M.; Harrington, D. A. Initial Stages of Pt(111) Electrooxidation: Dynamic and Structural Studies by Surface X-Ray Diffraction. *Electrochim. Acta* **2017**, *224*, 220−227.
(1038) Kondo, T.; Masuda, T.; Aoki, N.; Uosaki, K. Potential-Dependent Structures and Potential-Induced Structure Changes at Pt(111) Single-Crystal Electrode/Sulfuric and Perchloric Acid Interfaces in the Potential Region between Hydrogen Underpotential Deposition and Surface Oxide Formation by in Situ Surface X-Ray Scattering. *J. Phys. Chem. C* **2016**, *120*, 16118−16131.
(1039) Fuchs, T.; Drnec, J.; Calle-Vallejo, F.; Stubb, N.; Sandbeck, D. J. S.; Ruge, M.; Cherevko, S.; Harrington, D. A.; Magnussen, O. M. Structure Dependency of the Atomic-Scale Mechanisms of Platinum Electro-Oxidation and Dissolution. *Nat. Catal.* **2020**, *3*, 754−761.
(1040) Menzel, A.; Chang, K.-C.; Komanicky, V.; You, H.; Chu, Y. S.; Tolmachev, Y. V.; Rehr, J. J. Resonance Anomalous Surface X-Ray Scattering. *Radiat. Phys. Chem.* **2006**, *75*, 1651−1660.
(1041) Strmcnik, D.; van der Vliet, D. F.; Chang, K. C.; Komanicky, V.; Kodama, K.; You, H.; Stamenkovic, V. R.; Marković, N. M. Effects of Li^+, K^+, and Ba^{2+} Cations on the ORR at Model and High Surface Area Pt and Au Surfaces in Alkaline Solutions. *J. Phys. Chem. Lett.* **2011**, *2*, 2733−2736.
(1042) Nakamura, M.; Nakajima, Y.; Hoshi, N.; Tajiri, H.; Sakata, O. Effect of Non-Specifically Adsorbed Ions on the Surface Oxidation of Pt(111). *ChemPhysChem* **2013**, *14*, 2426−2431.
(1043) Liu, Y.; Kawaguchi, T.; Pierce, M. S.; Komanicky, V.; You, H. Layering and Ordering in Electrochemical Double Layers. *J. Phys. Chem. Lett.* **2018**, *9*, 1265−1271.
(1044) Kumeda, T.; Tajiri, H.; Sakata, O.; Hoshi, N.; Nakamura, M. Effect of Hydrophobic Cations on the Oxygen Reduction Reaction on Single-Crystal Platinum Electrodes. *Nat. Commun.* **2018**, *9*, 4378.
(1045) Lucas, C. A.; Thompson, P.; Gründer, Y.; Markovic, N. M. The Structure of the Electrochemical Double Layer: Ag(111) in Alkaline Electrolyte. *Electrochem. Commun.* **2011**, *13*, 1205−1208.
(1046) Lucas, C. A.; Maroun, F.; Sisson, N.; Thompson, P.; Gründer, Y.; Cortes, R.; Allongue, P. Film and Interface Atomic Structures of Electrodeposited Co/Au(111) Layers: An in Situ X-Ray Scattering Study as a Function of the Surface Chemistry and the Electrochemical Potential. *J. Phys. Chem. C* **2016**, *120*, 3360−3370.
(1047) Ocko, B. M.; Wang, J.; Davenport, A.; Isaacs, H. In Situx-Ray Reflectivity and Diffraction Studies of the Au(001) Reconstruction in an Electrochemical Cell. *Phys. Rev. Lett.* **1990**, *65*, 1466−1469.
(1048) Shipilin, M.; Gustafson, J.; Zhang, C.; Merte, L. R.; Stierle, A.; Hejral, U.; Ruett, U.; Gutowski, O.; Skoglundh, M.; Carlsson, P.-A.; Lundgren, E. Transient Structures of PdO during CO Oxidation over Pd(100). *J. Phys. Chem. C* **2015**, *119*, 15469−15476.
(1049) Gallagher, M. E.; Lucas, C. A.; Stamenković, V.; Marković, N. M.; Ross, P. N. Surface Structure and Relaxation at the Pt_3Sn(111)/Electrolyte Interface. *Surf. Sci.* **2003**, *544*, L729−L734.
(1050) Stamenkovic, V. R.; Fowler, B.; Mun, B. S.; Wang, G.; Ross, P. N.; Lucas, C. A.; Markovic, N. M. Improved Oxygen Reduction Activity on Pt_3Ni(111) via Increased Surface Site Availability. *Science* **2007**, *315*, 493−497.
(1051) Kawaguchi, T.; Rao, R. R.; Lunger, J. R.; Liu, Y.; Walko, D.; Karapetrova, E. A.; Komanicky, V.; Shao-Horn, Y.; You, H. Stern Layers on RuO_2 (100) and (110) in Electrolyte: Surface X-Ray Scattering Studies. *J. Electroanal. Chem.* **2020**, *875*, 114228.
(1052) Shirasawa, T.; Voegeli, W.; Arakawa, E.; Takahashi, T.; Matsushita, T. Structural Change of the Rutile-TiO_2(110) Surface During the Photoinduced Wettability Conversion. *J. Phys. Chem. C* **2016**, *120*, 29107−29115.
(1053) Treacy, J. P. W.; Hussain, H.; Torrelles, X.; Cabailh, G.; Bikondoa, O.; Nicklin, C.; Thornton, G.; Lindsay, R. Structure of a Superhydrophilic Surface: Wet Chemically Prepared Rutile-TiO_2(110)(1 × 1). *J. Phys. Chem. C* **2019**, *123*, 8463−8468.
(1054) McBriarty, M. E.; Stubbs, J. E.; Eng, P. J.; Rosso, K. M. Potential-Specific Structure at the Hematite-Electrolyte Interface. *Adv. Funct. Mater.* **2018**, *28*, 1705618.
(1055) McBriarty, M. E.; von Rudorff, G. F.; Stubbs, J. E.; Eng, P. J.; Blumberger, J.; Rosso, K. M. Dynamic Stabilization of Metal Oxide-Water Interfaces. *J. Am. Chem. Soc.* **2017**, *139*, 2581−2584.
(1056) Rao, R. R.; Kolb, M. J.; Hwang, J.; Pedersen, A. F.; Mehta, A.; You, H.; Stoerzinger, K. A.; Feng, Z.; Zhou, H.; Bluhm, H.; Giordano, L.; Stephens, I. E. L.; Shao-Horn, Y. Surface Orientation Dependent Water Dissociation on Rutile Ruthenium Dioxide. *J. Phys. Chem. C* **2018**, *122*, 17802−17811.
(1057) Gründer, Y.; Lucas, C. A. Probing the Charge Distribution at the Electrochemical Interface. *Phys. Chem. Chem. Phys.* **2017**, *19*, 8416−8422.
(1058) Menzel, A.; Tolmachev, Y. V.; Chang, K. C.; Komanicky, V.; Chu, Y. S.; Rehr, J. J.; You, H. Polarization-Dependent Resonant Anomalous Surface X-Ray Scattering of Co/Pt(111). *Europhys. Lett.* **2006**, *74*, 1032−1038.
(1059) Sakdinawat, A.; Attwood, D. Nano-scale X-Ray Imaging. *Nat. Photonics* **2010**, *4*, 840−848.
(1060) Niemann, B.; Rudolph, D.; Schmahl, G. X-Ray Microscopy with Synchrotron Radiation. *Appl. Opt.* **1976**, *15*, 1883−1884.
(1061) Liu, Y.; Andrews, J. C.; Meirer, F.; Mehta, A.; Gil, S. C.; Sciau, P.; Mester, Z.; Pianetta, P. Applications of Hard X-Ray Full-Field Transmission X-Ray Microscopy at SSRL. *AIP Conf. Proc.* **2010**, *1365*, 357−360.
(1062) Chao, W. L.; Harteneck, B. D.; Liddle, J.A.; Anderson, E. H.; Attwood, D. T. Soft X-Ray Microscopy at a Spatial Resolution Better Than 15nm. *Nature* **2005**, *435*, 1210−1213.
(1063) Chen, G. H.; Tang, J.; Leng, S. Prior Image Constrained Compressed Sensing (PICCS): A Method to Accurately Reconstruct Dynamic Ct Images from Highly Undersampled Projection Data Sets. *Med. Phys.* **2008**, *35*, 660−663.
(1064) Serov, A.; Shum, A. D.; Xiao, X.; De Andrade, V.; Artyushkova, K.; Zenyuk, I. V.; Atanassov, P. Nano-Structured Platinum Group Metal-Free Catalysts and Their Integration in Fuel Cell Electrode Architectures. *Appl. Catal., B* **2018**, *237*, 1139−1147.

https://doi.org/10.1021/acs.chemrev.1c00331
Chem. Rev. XXXX, XXX, XXX−XXX

(1065) Komini Babu, S.; Chung, H. T.; Zelenay, P.; Litster, S. Resolving Electrode Morphology's Impact on Platinum Group Metal-Free Cathode Performance Using Nano-CT of 3D Hierarchical Pore and Ionomer Distribution. *ACS Appl. Mater. Interfaces* **2016**, *8*, 32764−32777.
(1066) Gonzalez-Jimenez, I. D.; Cats, K.; Davidian, T.; Ruitenbeek, M.; Meirer, F.; Liu, Y.; Nelson, J.; Andrews, J. C.; Pianetta, P.; de Groot, F. M. F.; Weckhuysen, B. M. Hard X-Ray Nanotomography of Catalytic Solids at Work. *Angew. Chem., Int. Ed.* **2012**, *51*, 11986−11990.
(1067) Meirer, F.; Weckhuysen, B. M. Spatial and Temporal Exploration of Hetergeneous Catalysts with Synchrotron Radiation. *Nat. Rev. Mater.* **2018**, *3*, 324−340.
(1068) Lin, F.; Liu, Y.; Yu, X.; Cheng, L.; Singer, A.; Shpyrko, O. G.; Xin, H. L.; Tamura, N.; Tian, C.; Weng, T.-C.; Yang, X.-Q.; Meng, Y. S.; Nordlund, D.; Yang, W.; Doeff, M. M. Synchrotron X-Ray Analytical Techniques for Studying Materials Electrochemistry in Rechargeable Batteries. *Chem. Rev.* **2017**, *117*, 13123−13186.
(1069) Wu, J.; Zhu, X.; West, M. M.; Tyliszczak, T.; Shiu, H.-W.; Shapiro, D.; Berejnov, V.; Susac, D.; Stumper, J.; Hitchcock, A. P. High-Resolution Imaging of Polymer Electrolyte Membrane Fuel Cell Cathode Layers by Soft X-Ray Spectro-Ptychography. *J. Phys. Chem. C* **2018**, *122*, 11709−11719.
(1070) Chapman, H. N.; Nugent, K. A. Coherent Lensless X-Ray Imaging. *Nat. Photonics* **2010**, *4*, 833−839.
(1071) Robinson, I.; Harder, R. Coherent X-Ray Diffraction Imaging of Strain at the Nanoscale. *Nat. Mater.* **2009**, *8*, 291−298.
(1072) Fienup, J. R. Phase Retrieval Algorithms - a Comparison. *Appl. Opt.* **1982**, *21*, 2758−2769.
(1073) Singer, A.; Zhang, M.; Hy, S.; Cela, D.; Fang, C.; Wynn, T. A.; Qiu, B.; Xia, Y.; Liu, Z.; Ulvestad, A.; Hua, N.; Wingert, J.; Liu, H.; Sprung, M.; Zozulya, A. V.; Maxey, E.; Harder, R.; Meng, Y. S.; Shpyrko, O. G. Nucleation of Dislocations and Their Dynamics in Layered Oxide Cathode Materials During Battery Charging. *Nat. Energy.* **2018**, *3*, 641−647.
(1074) Clark, J. N.; Ihli, J.; Schenk, A. S.; Kim, Y.-Y.; Kulak, A. N.; Campbell, J. M.; Nisbet, G.; Meldrum, F. C.; Robinson, I. K. Three-Dimensional Imaging of Dislocation Propagation During Crystal Growth and Dissolution. *Nat. Mater.* **2015**, *14*, 780−784.
(1075) Singer, A.; Ramirez, J. G.; Valmianski, I.; Cela, D.; Hua, N.; Kukreja, R.; Wingert, J.; Kovalchuk, O.; Glownia, J. M.; Sikorski, M.; Chollet, M.; Holt, M.; Schuller, I. K.; Shpyrko, O.G. Nonequilibrium Phase Precursors during a Photoexcited Insulator-to-Metal Transition in V_2O_3. *Phys. Rev. Lett.* **2018**, *120*, 207601.
(1076) Faulkner, H. M. L.; Rodenburg, J. M. Movable Aperture Lensless Transmission Microscopy: A Novel Phase Retrieval Algorithm. *Phys. Rev. Lett.* **2004**, *93*, 023903.
(1077) Hill, M. O.; Calvo-Almazan, I.; Allain, M.; Holt, M. V.; Ulvestad, A.; Treu, J.; Koblmüller, G.; Huang, C.; Huang, X.; Yan, H.; Nazaretski, E.; Chu, Y. S.; Stephenson, G. B.; Chamard, V.; Lauhon, L. J.; Hruszkewycz, S. O. Measuring Three-Dimensional Strain and Structural Defects in a Single InGaAs Nanowire Using Coherent X-Ray Multiangle Bragg Projection Ptychography. *Nano Lett.* **2018**, *18*, 811−819.
(1078) Henderson, R. The Potential and Limitations of Neutrons, Electrons and X-rays for Atomic Resolution Microscopy of Unstained Biological Moleclues. *Q. Rev. Biophys.* **1995**, *28*, 171−193.
(1079) Arán-Ais, R. M.; Yu, Y.; Hovden, R.; Solla-Gullón, J.; Herrero, E.; Feliu, J. M.; Abruna, H. D. IL-TEM Imaging of Site-Selective Pt Nanocatalysts: Electrochemical Activation and Surface Disordering. *J. Am. Chem. Soc.* **2015**, *137*, 14992−14998.
(1080) Yu, Y.; Xin, H. L.; Hovden, R.; Wang, D.; Rus, E. D.; Mundy, J. A.; Muller, D. A.; Abruna, H. D. Three-Dimensional Tracking and Visualization of Hundreds of Pt-Co Fuel Cell Nanocatalysts During Electrochemical Aging. *Nano Lett.* **2012**, *12*, 4417−4423.
(1081) Wang, D.; Xin, H. L.; Hovden, R.; Wang, H.; Yu, Y.; Muller, D. A.; DiSalvo, F. J.; Abruna, H. D. Structurally Ordered Intermetallic Platinum-Cobalt Core-Shell Nanoparticles with Enhanced Activity and Stability as Oxygen Reduction Electrocatalysts. *Nat. Mater.* **2013**, *12*, 81−87.
(1082) Muller, D. A. Structure and Bonding at the Atomic Scale by Scanning Transmission Electron Microscopy. *Nat. Mater.* **2009**, *8*, 263−270.
(1083) Padgett, E.; Holtz, M. E.; Cueva, P.; Shao, Y.-T.; Langenberg, E.; Schlom, D. G.; Muller, D. G. The Exit-Wave Power-Cepstrum Transform for Scanning Nanobeam Electron Diffraction: Robust Strain Mapping at Subnanometer Resolution and Subpicometer Precision. *Ultramicroscopy* **2020**, *214*, 112994.
(1084) Xiong, Y.; Yang, Y.; Joress, H.; Padgett, E.; Gupta, U.; Yarlagadda, V.; Agyeman-Budu, D. N.; Huang, X.; Moylan, T. E.; Zeng, R.; Kongkanand, A.; Escobedo, F. A.; Brock, J. D.; DiSalvo, F. J.; Muller, D. A.; Abruna, H. D. Revealing the Atomic Ordering of Binary Intermetallics Using *in Situ* Heating Techniques at Multilength Scales. *Proc. Natl. Acad. Sci. U. S. A.* **2019**, *116*, 1974−1983.
(1085) Hashimoto, H.; Naiki, T.; Eto, T.; Fujiwara, K. High Temperature Gas Reaction Specimen Chamber for an Electron Microscope. *Jpn. J. Appl. Phys.* **1968**, *7*, 946−952.
(1086) Parsons, D. F. Structure of Wet Specimens in Electron Microscopy. *Science* **1974**, *186*, 407−414.
(1087) Boyes, E. D.; Gai, P. L. Environmental High Resolution Electron Microscopy and Applications to Chemical Science. *Ultramicroscopy* **1997**, *67*, 219−232.
(1088) Schneider, N. M.; Norton, M. M.; Mendel, B. J.; Grogan, J. M.; Ross, F. M.; Bau, H. H. Electron-Water Interactions and Implications for Liquid Cell Electron Microscopy. *J. Phys. Chem. C* **2014**, *118*, 22373−22382.
(1089) de Jonge, N.; Houben, L.; Dunin-Borkowski, R. E.; Ross, F. M. Resolution and Aberration Correction in Liquid Cell Transmission Electron Microscopy. *Nat. Rev. Mater.* **2019**, *4*, 61−78.
(1090) Williamson, M.; Tromp, R.; Vereecken, P.; Hull, R.; Ross, F. Dynamic Microscopy of Nanoscale Cluster Growth at the Solid-Liquid Interface. *Nat. Mater.* **2003**, *2*, 532−536.
(1091) Holtz, M. E.; Yu, Y.; Rivera, J.; Abruna, H. D.; Muller, D. A. *In Situ* TEM for Quantitative Electrochemistry of Energy Systems. *Microsc. Microanal.* **2015**, *21*, 1509−1510.
(1092) Holtz, M. E.; Yu, Y.; Gao, J.; Abruna, H. D.; Muller, D. A. *In Situ* Electron Energy-Loss Spectroscopy in Liquids. *Microsc. Microanal.* **2013**, *19*, 1027−1035.
(1093) Yu, Y.; Holtz, M. E.; Xin, H. L.; Wang, D.; Abruna, H. D.; Muller, D. A. Understanding Pt-Co Catalyst Degradation Mechanism: from Ex-situ to In-situ. *Microsc. Microanal.* **2013**, *19*, 1666−1667.
(1094) Holtz, M. E.; Yu, Y.; Gunceler, D.; Gao, J.; Sundararaman, R.; Schwarz, K. A.; Arias, T. A.; Abruna, H. D.; Muller, D. A. Nanoscale Imaging of Lithium Ion Distribution during In Situ Operation of Battery Electrode and Electrolyte. *Nano Lett.* **2014**, *14*, 1453−1459.
(1095) Sacci, R. L.; Black, J. M.; Balke, N.; Dudney, N. J.; More, K. L.; Unocic, R. R. Nanoscale Imaging of Fundamental Li Battery Chemistry: Solid-Electrolyte Interphase Formation and Preferential Growth of Lithium Metal Nanoclusters. *Nano Lett.* **2015**, *15*, 2011−2018.
(1096) Yang, C.; Han, J.; Liu, P.; Hou, C.; Huang, G.; Fujita, T.; Hirata, A.; Chen, M. Direct Observations of the Formation and Redox-Mediator-Assisted Decomposition of Li_2O_2 in a Liquid-Cell Li-O_2 Microbattery by Scanning Transmission Electron Microscopy. *Adv. Mater.* **2017**, *29*, 1702752.
(1097) Lutz, L.; Dachraoui, W.; Demortie, A.; Johnson, L. R.; Bruce, P. G.; Grimaud, A.; Tarascon, J.-M. Operando Monitoring of the Solution-Mediated Discharge and Charge Processes in a Na-O_2 Battery Using Liquid-Electrochemical Transmission Electron Microscopy. *Nano Lett.* **2018**, *18*, 1280−1289.
(1098) Huang, J. Y.; Zhong, L.; Wang, C. M.; Sullivan, J. P.; Xu, W.; Zhang, L. Q.; Mao, S. X.; Hudak, N. S.; Liu, X. H.; Subramanian, A.; Fan, H.; Qi, L.; Kushima, A.; Li, J. In Situ Observation of the Electrochemical Lithiation of a Single SnO_2 Nanowire Electrode. *Science* **2010**, *330*, 1515−1520.

https://doi.org/10.1021/acs.chemrev.1c00331
Chem. Rev. XXXX, XXX, XXX−XXX

(1099) Aran-Ais, R. M.; Rizo, R.; Grosse, P.; Algara-Siller, G.; Dembele, K.; Plodinec, M.; Lunkenbein, T.; Chee, S. W.; Cuenya, B. R. Imaging Electrochemically Synthesized Cu_2O Cubes and Their Morphological Evolution under Conditions Relevant To CO_2 Electroreduction. *Nat. Commun.* **2020**, *11*, 3489.
(1100) Li, Y.; Kim, D.; Louisia, S.; Xie, C.; Kong, Q.; Yu, S.; Lin, T.; Aloni, S.; Fakra, S.; Yang, P. Electrochemically Scrambled Nanocrystals are Catalytically Active for CO_2-To-Multicarbons. *Proc. Natl. Acad. Sci. U. S. A.* **2020**, *117*, 9194−9201.
(1101) Hermannsdorfer, J.; de Jonge, N.; Verch, A. Electron Beam Induced Chemistry of Gold Nanoparticles in Saline Solution. *Chem. Commun.* **2015**, *51*, 16393−16396.
(1102) Liao, H.-G.; Zherebetskyy, D.; Xin, H.; Czarnik, C.; Ercius, P.; Elmlund, H.; Pan, M.; Wang, L.-W.; Zheng, H. Facet Development during Platinum Nanocube Growth. *Science* **2014**, *345*, 916−919.
(1103) Hauwiller, M. R.; Ondry, J. C.; Chan, C. M.; Khandekar, P.; Yu, J.; Alivisatos, A. P. Gold Nanocrystal Etching as a Means of Probing the Dynamic Chemical Environment in Graphene Liquid Cell Electron Microscopy. *J. Am. Chem. Soc.* **2019**, *141*, 4428−4437.
(1104) Proetto, M. T.; Rush, A. M.; Chien, M.-P.; Baeza, P. A.; Patterson, J. P.; Thompson, M. P.; Olson, N. H.; Moore, C. E.; Rheingold, A. L.; Andolina, C. Dynamics of Soft Nanomaterials Captured by Transmission Electron Microscopy in Liquid Water. *J. Am. Chem. Soc.* **2014**, *136*, 1162−1165.
(1105) de Jonge, N.; Peckys, D. B.; Kremers, G. J.; Piston, D. W. Electron Microscopy of Whole Cells in Liquid with Nanometer Resolution. *Proc. Natl. Acad. Sci. U. S. A.* **2009**, *106*, 2159−2164.
(1106) Levin, B. D. A.; Zachman, M. J.; Werner, J. G.; Sahore, R.; Nguyen, K. X.; Han, Y.; Xie, B.; Ma, L.; Archer, L. A.; Giannelis, E. P.; Wiesner, U.; Kourkoutis, L. F.; Muller, D. A. Characterization of Sulfur and Nanostructured Sulfur Battery Cathodes in Electron Microscopy Without Sublimation Artifacts. *Microsc. Microanal.* **2017**, *23*, 155−162.
(1107) Yang, Y.; Levin, B. D.A; Zhang, N.; Abruna, H. D.; Muller, D. A. Cryo-STEM-EDX for Reliable Characterization of Sulfur Distribution and the Rational Design of Sulfur Hosts for Li-S Batteries. *Microsc. Microanal.* **2020**, *26*, 1654−1658.
(1108) Ross, F. M. *Liquid Cell Electron Microscopy*; Cambridge University Press: New York, 2017; p 210.
(1109) Ross, F. M. Opportunities and Challenges in Liquid Cell Electron Microscopy. *Science* **2015**, *350*, No. aaa9886.
(1110) Hodnik, N.; Dehm, G.; Mayrhofer, K. J. J. Importance and Challenges of Electrochemical in Situ Liquid Cell Electron Microscopy for Energy Conversion Research. *Acc. Chem. Res.* **2016**, *49*, 2015−2022.
(1111) Unocic, R.; Sacci, R. L.; Brown, G. M.; Veith, G. M.; Dudney, N. J.; More, K. M.; Walden II, F. S.; Gardiner, D. S.; Damiano, J.; Nackashi, D. P. Quantitative Electrochemical Measurements Using *In Situ* ec-S/TEM Devices. *Microsc. Microanal.* **2014**, *20*, 452−461.
(1112) Stricker, E. A.; Ke, X.; Wainright, J. S.; Unocic, R.; Savinell, R. F. Current Density Distribution in Electrochemical Cells with Small Cell Heights and Coplanar Thin Electrodes as Used in EC-S/TEM Cell Geometries. *J. Electrochem. Soc.* **2019**, *166*, H126−H134.
(1113) Schilling, S.; Janssen, A.; Zaluzec, N.; Burke, M. G. Practical Aspects of Electrochemical Corrosion Measurements During In Situ Analytical Transmission Electron Microscopy (TEM) of Austenitic Stainless Steel in Aqueous Media. *Microsc. Microanal.* **2017**, *23*, 741−750.
(1114) Zhu, G.-Z.; Prabhudev, S.; Yang, J.; Gabardo, C. M.; Botton, G. A.; Solemani, L. In Situ Liquid Cell TEM Study of Morphological Evolution and Degradation of Pt-Fe Nanocatalysts During Potential Cycling. *J. Phys. Chem. C* **2014**, *118*, 22111−22119.
(1115) Lewis, E.; Haigh, S. J.; Slater, T. J. A.; He, Z.; Kulzick, M. A.; Burke, M. G.; Zaluzec, N. J. Real-Time Imaging and Local Elemental Analysis of Nanostructures in Liquids. *Chem. Commun.* **2014**, *50*, 10019−10022.
(1116) Ross, F. M. Temperature Effects in Liquid-Cell Transmission Electron Microscopy. *Microsc. Microanal.* **2020**, *26*, 2566−2567.
(1117) Yang, Y.; Shao, Y.-T.; Lu, X.; Abruna, H.; Muller, D. Elucidating Cathodic Corrosion Mechanisms with Operando Elec trochemical Liquid-Cell STEM in Multiple Dimensions. *Microsc. Microanal.* **2021**, *27*, 238−240.
(1118) Michler, G. H. Preparation of Thin Sections: (Cryo)-Ultramicrotomy and (Cryo)Microtomy. In *Electron Microscopy of Polymers*; Springer Laboratory: Berlin, Heidelberg, 2008; Chapter 10, pp 199−217.
(1119) Padgett, E. *Guiding Development of Fuel Cell Catalysts with Statistically Robust Transmission Electron Microscopy*. PhD Thesis, Cornell University, 2019.
(1120) Allen, F. I.; Comolli, L. R.; Kusoglu, A.; Modestino, M. A.; Minor, A. M.; Weber, A. Z. Morphology of Hydrated As-Cast Nafion Revealed through Cryo Electron Tomography. *ACS Macro Lett.* **2015**, *4*, 1−5.
(1121) Selhorst, R.; Gaitor, J.; Lee, M.; Markovich, D.; Yu, Y.; Kowalewski, T.; Kourkoutis, L.; Hayward, R.; Noonan, K. Anion Transport in Vinyl Addition Polynorbornenes: Understanding the Impact of Multiblock Copolymers. *ACS Appl. Energy Mater.* **2021**, *4*, 10273.
(1122) Osmieri, L.; Ahluwalia, R. K.; Wang, X.; Chung, H. T.; Yin, X.; Kropf, A. J.; Park, J.; Cullen, D. A.; More, K. L.; Zelenay, P.; Myers, D. J.; Neyerlin, K. C. Elucidation of Fe-N-C Electrocatalyst Active Site Functionality via in-Situ X-Ray Absorption and Operando Determination of Oxygen Reduction Reaction Kinetics in a PEFC. *Appl. Catal., B* **2019**, *257*, 117929.
(1123) Liang, X.; Shehzad, M. A.; Zhu, Y.; Wang, L.; Ge, X.; Zhang, J.; Yang, Z.; Wu, L.; Varcoe, J. R.; Xu, T. Ionomer Cross-Linking Immobilization of Catalyst Nanoparticles for High Performance Alkaline Membrane Fuel Cells. *Chem. Mater.* **2019**, *31*, 7812−7820.
(1124) Ophus, C. Four-Dimensional Scanning Transmission Electron Microscopy (4D-STEM): From Scanning Nanodiffraction to Ptychography and Beyond. *Microsc. Microanal.* **2019**, *25*, 563−582.
(1125) Panova, O.; Ophus, C.; Takacs, C. J.; Bustillo, K. C.; Balhorn, L.; Salleo, A.; Balsara, N.; Minor, A. M. Diffraction Imaging of Nanocrystalline Structures in Organic Semiconductor Molecular Thin Films. *Nat. Mater.* **2019**, *18*, 860−865.
(1126) Bhandari, S.; Rangarajan, S.; Maravelias, C. T.; Dumesic, J. A.; Mavrikakis, M. Reaction Mechanism of Vapor-Phase Formic Acid Decomposition over Platinum Catalysts: DFT, Reaction Kinetics Experiments, and Microkinetic Modeling. *ACS Catal.* **2020**, *10*, 4112−4126.
(1127) Abild-Pedersen, F.; Greeley, J.; Studt, F.; Rossmeisl, J.; Munter, T. R.; Moses, P. G.; Skúlason, E.; Bligaard, T.; Nørskov, J. K. Scaling Properties of Adsorption Energies for Hydrogen-Containing Molecules on Transition-Metal Surfaces. *Phys. Rev. Lett.* **2007**, *99*, 016105.
(1128) Bronsted, J. N. Acid and Basic Catalysis. *Chem. Rev.* **1928**, *5*, 231−338.
(1129) Evans, M. G.; Polanyi, M. Inertia and Driving Force of Chemical Reactions. *Trans. Faraday Soc.* **1938**, *34*, 11−24.
(1130) Xu, Y.; Ruban, A. V.; Mavrikakis, M. Adsorption and Dissociation of O_2 on Pt-Co and Pt-Fe Alloys. *J. Am. Chem. Soc.* **2004**, *126*, 4717−4725.
(1131) Ferrin, P.; Simonetti, D.; Kandoi, S.; Kunkes, E.; Dumesic, J. A.; Nørskov, J. K.; Mavrikakis, M. Modeling Ethanol Decomposition on Transition Metals: A Combined Application of Scaling and Brønsted-Evans-Polanyi Relations. *J. Am. Chem. Soc.* **2009**, *131*, 5809−5815.
(1132) Zhu, J.; Getman, R. B. Reaction Pathways and Microkinetic Modeling of N-Butane Oxidation to 1-Butanol on Cu, Cu_3Pd, Pd, Ag_3Pd, and PdZn (111) Surfaces. *Ind. Eng. Chem. Res.* **2018**, *57*, 5580−5590.
(1133) Yoo, J. S.; Abild-Pedersen, F.; Nørskov, J. K.; Studt, F. Theoretical Analysis of Transition-Metal Catalysts for Formic Acid Decomposition. *ACS Catal.* **2014**, *4*, 1226−1233.
(1134) Medford, A. J.; Lausche, A. C.; Abild-Pedersen, F.; Temel, B.; Schjødt, N. C.; Nørskov, J. K.; Studt, F. Activity and Selectivity

https://doi.org/10.1021/acs.chemrev.1c00331
Chem. Rev. XXXX, XXX, XXX−XXX

Trends in Synthesis Gas Conversion to Higher Alcohols. *Top. Catal.* **2014**, *57*, 135−142.
(1135) Schimmenti, R.; Cortese, R.; Godina, L.; Prestianni, A.; Ferrante, F.; Duca, D.; Murzin, D. Yu A Combined Theoretical and Experimental Approach for Platinum Catalyzed 1,2-Propanediol Aqueous Phase Reforming. *J. Phys. Chem. C* **2017**, *121*, 14636−14648.
(1136) Medford, A. J.; Vojvodic, A.; Hummelshøj, J. S.; Voss, J.; Abild-Pedersen, F.; Studt, F.; Bligaard, T.; Nilsson, A.; Nørskov, J. K. From the Sabatier Principle to a Predictive Theory of Transition-Metal Heterogeneous Catalysis. *J. Catal.* **2015**, *328*, 36−42.
(1137) Elnabawy, A. O.; Herron, J. A.; Scaranto, J.; Mavrikakis, M. Structure Sensitivity of Formic Acid Electrooxidation on Transition Metal Surfaces: A First-Principles Study. *J. Electrochem. Soc.* **2018**, *165*, J3109−J3121.
(1138) Ferrin, P.; Mavrikakis, M. Structure Sensitivity of Methanol Electrooxidation on Transition Metals. *J. Am. Chem. Soc.* **2009**, *131*, 14381−14389.
(1139) Montoya, J. H.; Tsai, C.; Vojvodic, A.; Nørskov, J. K. The Challenge of Electrochemical Ammonia Synthesis: A New Perspective on the Role of Nitrogen Scaling Relations. *ChemSusChem* **2015**, *8*, 2180−2186.
(1140) Siahrostami, S.; Verdaguer-Casadevall, A.; Karamad, M.; Deiana, D.; Malacrida, P.; Wickman, B.; Escudero-Escribano, M.; Paoli, E. A.; Frydendal, R.; Hansen, T. W.; Chorkendorff, I.; Stephens, I. E. L.; Rossmeisl, J. Enabling Direct H_2O_2 Production through Rational Electrocatalyst Design. *Nat. Mater.* **2013**, *12*, 1137−1143.
(1141) Kropp, T.; Mavrikakis, M. Transition Metal Atoms Embedded in Graphene: How Nitrogen Doping Increases CO Oxidation Activity. *ACS Catal.* **2019**, *9*, 6864−6868.
(1142) Craig, M. J.; Coulter, G.; Dolan, E.; Soriano-López, J.; Mates-Torres, E.; Schmitt, W.; García-Melchor, M. Universal Scaling Relations for the Rational Design of Molecular Water Oxidation Catalysts with Near-Zero Overpotential. *Nat. Commun.* **2019**, *10*, 4993.
(1143) Xu, H.; Cheng, D.; Cao, D.; Zeng, X. C. A Universal Principle for a Rational Design of Single-Atom Electrocatalysts. *Nat. Catal.* **2018**, *1*, 339−348.
(1144) Busch, M.; Wodrich, M. D.; Corminboeuf, C. Linear Scaling Relationships and Volcano Plots in Homogeneous Catalysis - Revisiting the Suzuki Reaction. *Chem. Sci.* **2015**, *6*, 6754−6761.
(1145) Flytzani-Stephanopoulos, M.; Gates, B. C. Atomically Dispersed Supported Metal Catalysts. *Annu. Rev. Chem. Biomol. Eng.* **2012**, *3*, 545−574.
(1146) Wang, H.; Liu, J.-X.; Allard, L. F.; Lee, S.; Liu, J.; Li, H.; Wang, J.; Wang, J.; Oh, S. H.; Li, W.; Flytzani-Stephanopoulos, M.; Shen, M.; Goldsmith, B. R.; Yang, M. Surpassing the Single-Atom Catalytic Activity Limit through Paired Pt-O-Pt Ensemble Built from Isolated Pt_1 Atoms. *Nat. Commun.* **2019**, *10*, 3808.
(1147) Marcinkowski, M. D.; Darby, M. T.; Liu, J.; Wimble, J. M.; Lucci, F. R.; Lee, S.; Michaelides, A.; Flytzani-Stephanopoulos, M.; Stamatakis, M.; Sykes, E. C. H. Pt/Cu Single-Atom Alloys as Coke-Resistant Catalysts for Efficient C-H Activation. *Nat. Chem.* **2018**, *10*, 325−332.
(1148) Greeley, J.; Mavrikakis, M. Alloy Catalysts Designed from First Principles. *Nat. Mater.* **2004**, *3*, 810−815.
(1149) Greeley, J.; Mavrikakis, M. Near-Surface Alloys for Hydrogen Fuel Cell Applications. *Catal. Today* **2006**, *111*, 52−58.
(1150) Greeley, J.; Jaramillo, T. F.; Bonde, J.; Chorkendorff, I.; Nørskov, J. K. Computational High-Throughput Screening of Electrocatalytic Materials for Hydrogen Evolution. *Nat. Mater.* **2006**, *5*, 909−913.
(1151) Govindarajan, N.; García-Lastra, J. M.; Meijer, E. J.; Calle-Vallejo, F. Does the Breaking of Adsorption-Energy Scaling Relations Guarantee Enhanced Electrocatalysis? *Curr. Opin. Electrochem.* **2018**, *8*, 110−117.
(1152) Andersen, M.; Medford, A. J.; Nørskov, J. K.; Reuter, K. Scaling-Relation-Based Analysis of Bifunctional Catalysis: The Case for Homogeneous Bimetallic Alloys. *ACS Catal.* **2017**, *7*, 3960−3967.
(1153) Gono, P.; Pasquarello, A. Oxygen Evolution Reaction: Bifunctional Mechanism Breaking the Linear Scaling Relationship. *J. Chem. Phys.* **2020**, *152*, 104712.
(1154) Elumeeva, K.; Masa, J.; Tietz, F.; Yang, F.; Xia, W.; Muhler, M.; Schuhmann, W. A Simple Approach towards High-Performance Perovskite-Based Bifunctional Oxygen Electrocatalysts. *ChemElectroChem* **2016**, *3*, 138−143.
(1155) Retuerto, M.; Calle-Vallejo, F.; Pascual, L.; Lumbeeck, G.; Fernandez-Diaz, M. T.; Croft, M.; Gopalakrishnan, J.; Pena, M. A.; Hadermann, J.; Greenblatt, M.; Rojas, S. $La_{1.5}Sr_{0.5}NiMn_{0.5}Ru_{0.5}O_6$ Double Perovskite with Enhanced ORR/OER Bifunctional Catalytic Activity. *ACS Appl. Mater. Interfaces* **2019**, *11*, 21454−21464.
(1156) Back, S.; Kulkarni, A. R.; Siahrostami, S. Single Metal Atoms Anchored in Two-Dimensional Materials: Bifunctional Catalysts for Fuel Cell Applications. *ChemCatChem* **2018**, *10*, 3034−3039.
(1157) Huang, Z.-F.; Song, J.; Dou, S.; Li, X.; Wang, J.; Wang, X. Strategies to Break the Scaling Relation toward Enhanced Oxygen Electrocatalysis. *Matter* **2019**, *1*, 1494−1518.
(1158) Pérez-Ramírez, J.; López, N. Strategies to Break Linear Scaling Relationships. *Nat. Catal.* **2019**, *2*, 971−976.
(1159) Wang, X.; Choi, S.-I.; Roling, L. T.; Luo, M.; Ma, C.; Zhang, L.; Chi, M.; Liu, J.; Xie, Z.; Herron, J. A.; Mavrikakis, M.; Xia, Y. Palladium-Platinum Core-Shell Icosahedra with Substantially Enhanced Activity and Durability towards Oxygen Reduction. *Nat. Commun.* **2015**, *6*, 7594.
(1160) Xie, S.; Choi, S.-I.; Lu, N.; Roling, L. T.; Herron, J. A.; Zhang, L.; Park, J.; Wang, J.; Kim, M. J.; Xie, Z.; Mavrikakis, M.; Xia, Y. Atomic Layer-by-Layer Deposition of Pt on Pd Nanocubes for Catalysts with Enhanced Activity and Durability toward Oxygen Reduction. *Nano Lett.* **2014**, *14*, 3570−3576.
(1161) Xiong, Y.; Shan, H.; Zhou, Z.; Yan, Y.; Chen, W.; Yang, Y.; Liu, Y.; Tian, H.; Wu, J.; Zhang, H.; Yang, D. Tuning Surface Structure and Strain in Pd-Pt Core-Shell Nanocrystals for Enhanced Electrocatalytic Oxygen Reduction. *Small* **2017**, *13*, 1603423.
(1162) Mavrikakis, M.; Hammer, B.; Nørskov, J. K. Effect of Strain on the Reactivity of Metal Surfaces. *Phys. Rev. Lett.* **1998**, *81*, 2819−2822.
(1163) Khorshidi, A.; Violet, J.; Hashemi, J.; Peterson, A. A. How Strain Can Break the Scaling Relations of Catalysis. *Nat. Catal.* **2018**, *1*, 263−268.
(1164) Yan, K.; Maark, T. A.; Khorshidi, A.; Sethuraman, V. A.; Peterson, A. A.; Guduru, P. R. The Influence of Elastic Strain on Catalytic Activity in the Hydrogen Evolution Reaction. *Angew. Chem., Int. Ed.* **2016**, *55*, 6175−6181.
(1165) Shetty, M.; Walton, A.; Gathmann, S. R.; Ardagh, M. A.; Gopeesingh, J.; Resasco, J.; Birol, T.; Zhang, Q.; Tsapatsis, M.; Vlachos, D. G.; Christopher, P.; Frisbie, C. D.; Abdelrahman, O. A.; Dauenhauer, P. J. The Catalytic Mechanics of Dynamic Surfaces: Stimulating Methods for Promoting Catalytic Resonance. *ACS Catal.* **2020**, *10*, 12666−12695.
(1166) Bligaard, T.; Nørskov, J. K. Ligand Effects in Heterogeneous Catalysis and Electrochemistry. *Electrochim. Acta* **2007**, *52*, 5512−5516.
(1167) Kitchin, J. R.; Nørskov, J. K.; Barteau, M. A.; Chen, J. G. Role of Strain and Ligand Effects in the Modification of the Electronic and Chemical Properties of Bimetallic Surfaces. *Phys. Rev. Lett.* **2004**, *93*, 156801.
(1168) Greeley, J.; Nørskov, J. K.; Mavrikakis, M. Electronic Structure and Catalysis on Metal Surfaces. *Annu. Rev. Phys. Chem.* **2002**, *53*, 319−348.
(1169) Rangarajan, S.; Maravelias, C. T.; Mavrikakis, M. Sequential-Optimization-Based Framework for Robust Modeling and Design of Heterogeneous Catalytic Systems. *J. Phys. Chem. C* **2017**, *121*, 25847−25863.
(1170) Car, R.; Parrinello, M. Unified Approach for Molecular Dynamics and Density-Functional Theory. *Phys. Rev. Lett.* **1985**, *55*, 2471−2474.

https://doi.org/10.1021/acs.chemrev.1c00331
Chem. Rev. XXXX, XXX, XXX−XXX

(1171) Marx, D.; Hutter, J. *Ab Initio Molecular Dynamics: Basic Theory and Advanced Methods*; Cambridge University Press: Cambridge, 2009.
(1172) Laasonen, K.; Sprik, M.; Parrinello, M.; Car, R. Ab Initio" Liquid Water. *J. Chem. Phys.* **1993**, *99*, 9080−9089.
(1173) Hohenberg, P.; Kohn, W. Inhomogeneous Electron Gas. *Phys. Rev.* **1964**, *136*, B864−B871.
(1174) Kohn, W.; Sham, L. J. Self-Consistent Equations Including Exchange and Correlation Effects. *Phys. Rev.* **1965**, *140*, A1133−A1138.
(1175) Becke, A. D. Density-Functional Exchange-Energy Approximation with Correct Asymptotic Behavior. *Phys. Rev. A: At., Mol., Opt. Phys.* **1988**, *38*, 3098−3100.
(1176) Lee, C.; Yang, W.; Parr, R. G. Development of the Colle-Salvetti Correlation-Energy Formula into a Functional of the Electron Density. *Phys. Rev. B: Condens. Matter Mater. Phys.* **1988**, *37*, 785−789.
(1177) Perdew, J. P.; Burke, K.; Ernzerhof, M. Generalized Gradient Approximation Made Simple. *Phys. Rev. Lett.* **1996**, *77*, 3865−3868.
(1178) Perdew, J. P.; Zunger, A. Self-Interaction Correction to Density-Functional Approximations for Many-Electron Systems. *Phys. Rev. B: Condens. Matter Mater. Phys.* **1981**, *23*, 5048−5079.
(1179) Cohen, A. J.; Mori-Sánchez, P.; Yang, W. Insights into Current Limitations of Density Functional Theory. *Science* **2008**, *321*, 792−794.
(1180) Klimeš, J.; Michaelides, A. Perspective: Advances and Challenges in Treating van Der Waals Dispersion Forces in Density Functional Theory. *J. Chem. Phys.* **2012**, *137*, 120901.
(1181) Berland, K.; Cooper, V. R.; Lee, K.; Schröder, E.; Thonhauser, T.; Hyldgaard, P.; Lundqvist, B. I. van der Waals Forces in Density Functional Theory: A Review of the vdW-DF Method. *Rep. Prog. Phys.* **2015**, *78*, 066501.
(1182) Grimme, S.; Hansen, A.; Brandenburg, J. G.; Bannwarth, C. Dispersion-Corrected Mean-Field Electronic Structure Methods. *Chem. Rev.* **2016**, *116*, 5105−5154.
(1183) Hermann, J.; DiStasio, R. A., Jr; Tkatchenko, A. First-Principles Models for van der Waals Interactions in Molecules and Materials: Concepts, Theory, and Applications. *Chem. Rev.* **2017**, *117*, 4714−4758.
(1184) Asthagiri, D.; Pratt, L. R.; Kress, J. D. Free Energy of Liquid Water on the Basis of Quasichemical Theory and Ab Initio Molecular Dynamics. *Phys. Rev. E: Stat. Phys., Plasmas, Fluids, Relat. Interdiscip. Top.* **2003**, *68*, 041505.
(1185) Grossman, J. C.; Schwegler, E.; Draeger, E. W.; Gygi, F.; Galli, G. Towards an Assessment of the Accuracy of Density Functional Theory for First Principles Simulations of Water. *J. Chem. Phys.* **2004**, *120*, 300−311.
(1186) Fernández-Serra, M. V.; Artacho, E. Network Equilibration and First-Principles Liquid Water. *J. Chem. Phys.* **2004**, *121*, 11136−11144.
(1187) Kuo, I.-F. W.; Mundy, C. J.; McGrath, M. J.; Siepmann, J. I.; VandeVondele, J.; Sprik, M.; Hutter, J.; Chen, B.; Klein, M. L.; Mohamed, F.; et al. Liquid Water from First Principles: Investigation of Different Sampling Approaches. *J. Phys. Chem. B* **2004**, *108*, 12990−12998.
(1188) Schwegler, E.; Grossman, J. C.; Gygi, F.; Galli, G. Towards an Assessment of the Accuracy of Density Functional Theory for First Principles Simulations of Water. II. *J. Chem. Phys.* **2004**, *121*, 5400−5409.
(1189) VandeVondele, J.; Mohamed, F.; Krack, M.; Hutter, J.; Sprik, M.; Parrinello, M. The Influence of Temperature and Density Functional Models in Ab Initio Molecular Dynamics Simulation of Liquid Water. *J. Chem. Phys.* **2005**, *122*, 014515.
(1190) Fernández-Serra, M. V.; Ferlat, G.; Artacho, E. Two Exchange-Correlation Functionals Compared for First-Principles Liquid Water. *Mol. Simul.* **2005**, *31*, 361−366.
(1191) McGrath, M. J.; Siepmann, J. I.; Kuo, I.-F. W.; Mundy, C. J.; VandeVondele, J.; Hutter, J.; Mohamed, F.; Krack, M. Isobaric-Isothermal Monte Carlo Simulations from First Principles: Application to Liquid Water at Ambient Conditions. *ChemPhysChem* **2005**, *6*, 1894−1901.
(1192) Sit, P. H.-L.; Marzari, N. Static and Dynamical Properties of Heavy Water at Ambient Conditions from First-Principles Molecular Dynamics. *J. Chem. Phys.* **2005**, *122*, 204510.
(1193) Lee, H.-S.; Tuckerman, M. E. Structure of Liquid Water at Ambient Temperature from Ab Initio Molecular Dynamics Performed in the Complete Basis Set Limit. *J. Chem. Phys.* **2006**, *125*, 154507.
(1194) McGrath, M. J.; Siepmann, J. I.; Kuo, I.-F. W.; Mundy, C. J. Vapor-Liquid Equilibria of Water from First Principles: Comparison of Density Functionals and Basis Sets. *Mol. Phys.* **2006**, *104*, 3619−3626.
(1195) Todorova, T.; Seitsonen, A. P.; Hutter, J.; Kuo, I.-F. W.; Mundy, C. J. Molecular Dynamics Simulation of Liquid Water: Hybrid Density Functionals. *J. Phys. Chem. B* **2006**, *110*, 3685−3691.
(1196) Lee, H.-S.; Tuckerman, M. E. Dynamical Properties of Liquid Water from Ab Initio Molecular Dynamics Performed in the Complete Basis Set Limit. *J. Chem. Phys.* **2007**, *126*, 164501.
(1197) Guidon, M.; Schiffmann, F.; Hutter, J.; VandeVondele, J. Ab Initio Molecular Dynamics Using Hybrid Density Functionals. *J. Chem. Phys.* **2008**, *128*, 214104.
(1198) Kühne, T. D.; Krack, M.; Parrinello, M. Static and Dynamical Properties of Liquid Water from First Principles by a Novel Car-Parrinello-like Approach. *J. Chem. Theory Comput.* **2009**, *5*, 235−241.
(1199) Lin, I.-C.; Seitsonen, A. P.; Coutinho-Neto, M. D.; Tavernelli, I.; Rothlisberger, U. Importance of van Der Waals Interactions in Liquid Water. *J. Phys. Chem. B* **2009**, *113*, 1127−1131.
(1200) Mattsson, A. E.; Mattsson, T. R. AM05 Density Functional Applied to the Water Molecule, Dimer, and Bulk Liquid. *J. Chem. Theory Comput.* **2009**, *5*, 887−894.
(1201) Schmidt, J.; VandeVondele, J.; Kuo, I.-F. W.; Sebastiani, D.; Siepmann, J. I.; Hutter, J.; Mundy, C. J. Isobaric-Isothermal Molecular Dynamics Simulations Utilizing Density Functional Theory: An Assessment of the Structure and Density of Water at Near-Ambient Conditions. *J. Phys. Chem. B* **2009**, *113*, 11959−11964.
(1202) Yoo, S.; Zeng, X. C.; Xantheas, S. S. On the Phase Diagram of Water with Density Functional Theory Potentials: The Melting Temperature of Ice I_h with the Perdew-Burke-Ernzerhof and Becke-Lee-Yang-Parr Functionals. *J. Chem. Phys.* **2009**, *130*, 221102.
(1203) Jonchiere, R.; Seitsonen, A. P.; Ferlat, G.; Saitta, A. M.; Vuilleumier, R. van der Waals Effects in Ab Initio Water at Ambient and Supercritical Conditions. *J. Chem. Phys.* **2011**, *135*, 154503.
(1204) Møgelhøj, A.; Kelkkanen, A. K.; Wikfeldt, K. T.; Schiøtz, J.; Mortensen, J. J.; Pettersson, L. G. M.; Lundqvist, B. I.; Jacobsen, K. W.; Nilsson, A.; Nørskov, J. K. Ab Initio van der Waals Interactions in Simulations of Water Alter Structure from Mainly Tetrahedral to High-Density-Like. *J. Phys. Chem. B* **2011**, *115*, 14149−14160.
(1205) Wang, J.; Román-Pérez, G.; Soler, J. M.; Artacho, E.; Fernández-Serra, M.-V. Density, Structure, and Dynamics of Water: The Effect of van der Waals Interactions. *J. Chem. Phys.* **2011**, *134*, 024516.
(1206) Yoo, S.; Xantheas, S. S. Communication: The Effect of Dispersion Corrections on the Melting Temperature of Liquid Water. *J. Chem. Phys.* **2011**, *134*, 121105.
(1207) Zhang, C.; Donadio, D.; Gygi, F.; Galli, G. First Principles Simulations of the Infrared Spectrum of Liquid Water Using Hybrid Density Functionals. *J. Chem. Theory Comput.* **2011**, *7*, 1443−1449.
(1208) Zhang, C.; Wu, J.; Galli, G.; Gygi, F. Structural and Vibrational Properties of Liquid Water from van Der Waals Density Functionals. *J. Chem. Theory Comput.* **2011**, *7*, 3054−3061.
(1209) Lin, I.-C.; Seitsonen, A. P.; Tavernelli, I.; Rothlisberger, U. Structure and Dynamics of Liquid Water from Ab Initio Molecular Dynamics—Comparison of BLYP, PBE, and RevPBE Density Functionals with and without van der Waals Corrections. *J. Chem. Theory Comput.* **2012**, *8*, 3902−3910.
(1210) Ma, Z.; Zhang, Y.; Tuckerman, M. E. Ab Initio Molecular Dynamics Study of Water at Constant Pressure Using Converged Basis Sets and Empirical Dispersion Corrections. *J. Chem. Phys.* **2012**, *137*, 044506.

https://doi.org/10.1021/acs.chemrev.1c00331
Chem. Rev. XXXX, XXX, XXX−XXX

(1211) Alfe, D.; Bartók, A. P.; Csányi, G.; Gillan, M. J. Communication: Energy Benchmarking with Quantum Monte Carlo for Water Nano-Droplets and Bulk Liquid Water. *J. Chem. Phys.* **2013**, *138*, 221102.
(1212) Bartók, A. P.; Gillan, M. J.; Manby, F. R.; Csányi, G. Machine-Learning Approach for One- and Two-Body Corrections to Density Functional Theory: Applications to Molecular and Condensed Water. *Phys. Rev. B: Condens. Matter Mater. Phys.* **2013**, *88*, 054104.
(1213) Del Ben, M.; Schönherr, M.; Hutter, J.; VandeVondele, J. Bulk Liquid Water at Ambient Temperature and Pressure from MP2 Theory. *J. Phys. Chem. Lett.* **2013**, *4*, 3753−3759.
(1214) DiStasio, R. A., Jr; Santra, B.; Li, Z.; Wu, X.; Car, R. The Individual and Collective Effects of Exact Exchange and Dispersion Interactions on the Ab Initio Structure of Liquid Water. *J. Chem. Phys.* **2014**, *141*, 084502.
(1215) Gillan, M. J.; Alfe, D.; Michaelides, A. Perspective: How Good Is DFT for Water? *J. Chem. Phys.* **2016**, *144*, 130901.
(1216) Chen, M.; Ko, H.-Y.; Remsing, R. C.; Andrade, M. F. C.; Santra, B.; Sun, Z.; Selloni, A.; Car, R.; Klein, M. L.; Perdew, J. P.; et al. Ab Initio Theory and Modeling of Water. *Proc. Natl. Acad. Sci. U. S. A.* **2017**, *114*, 10846−10851.
(1217) Sun, J.; Ruzsinszky, A.; Perdew, J. P. Strongly Constrained and Appropriately Normed Semilocal Density Functional. *Phys. Rev. Lett.* **2015**, *115*, 036402.
(1218) Sun, J.; Remsing, R. C.; Zhang, Y.; Sun, Z.; Ruzsinszky, A.; Peng, H.; Yang, Z.; Paul, A.; Waghmare, U.; Wu, X.; et al. Accurate First-Principles Structures and Energies of Diversely Bonded Systems from an Efficient Density Functional. *Nat. Chem.* **2016**, *8*, 831−836.
(1219) Zheng, L.; Chen, M.; Sun, Z.; Ko, H.-Y.; Santra, B.; Dhuvad, P.; Wu, X. Structural, Electronic, and Dynamical Properties of Liquid Water by Ab Initio Molecular Dynamics Based on SCAN Functional within the Canonical Ensemble. *J. Chem. Phys.* **2018**, *148*, 164505.
(1220) Wiktor, J.; Ambrosio, F.; Pasquarello, A. Note: Assessment of the SCAN+rVV10 Functional for the Structure of Liquid Water. *J. Chem. Phys.* **2017**, *147*, 216101.
(1221) Calegari Andrade, M. F.; Ko, H.-Y.; Car, R.; Selloni, A. Structure, Polarization, and Sum Frequency Generation Spectrum of Interfacial Water on Anatase TiO_2. *J. Phys. Chem. Lett.* **2018**, *9*, 6716−6721.
(1222) Wang, R.; Carnevale, V.; Klein, M. L.; Borguet, E. First-Principles Calculation of Water PKa Using the Newly Developed SCAN Functional. *J. Phys. Chem. Lett.* **2020**, *11*, 54−59.
(1223) Fosdick, L. D. Numerical Estimation of the Partition Function in Quantum Statistics. *J. Math. Phys.* **1962**, *3*, 1251−1264.
(1224) Chandler, D.; Wolynes, P. G. Exploiting the Isomorphism between Quantum Theory and Classical Statistical Mechanics of Polyatomic Fluids. *J. Chem. Phys.* **1981**, *74*, 4078−4095.
(1225) Marx, D.; Parrinello, M. Ab Initio Path Integral Molecular Dynamics: Basic Ideas. *J. Chem. Phys.* **1996**, *104*, 4077−4082.
(1226) Tuckerman, M. E.; Marx, D.; Klein, M. L.; Parrinello, M. Efficient and General Algorithms for Path Integral Car-Parrinello Molecular Dynamics. *J. Chem. Phys.* **1996**, *104*, 5579−5588.
(1227) Ceriotti, M.; Fang, W.; Kusalik, P. G.; McKenzie, R. H.; Michaelides, A.; Morales, M. A.; Markland, T. E. Nuclear Quantum Effects in Water and Aqueous Systems: Experiment, Theory, and Current Challenges. *Chem. Rev.* **2016**, *116*, 7529−7550.
(1228) Geissler, P. L.; Dellago, C.; Chandler, D.; Hutter, J.; Parrinello, M. Autoionization in Liquid Water. *Science* **2001**, *291*, 2121−2124.
(1229) Bolhuis, P. G.; Chandler, D.; Dellago, C.; Geissler, P. L. TRANSITION PATH SAMPLING: Throwing Ropes Over Rough Mountain Passes, in the Dark. *Annu. Rev. Phys. Chem.* **2002**, *53*, 291−318.
(1230) Berendsen, H. J. C.; Grigera, J. R.; Straatsma, T. P. The Missing Term in Effective Pair Potentials. *J. Phys. Chem.* **1987**, *91*, 6269−6271.
(1231) Abascal, J. L. F.; Vega, C. A General Purpose Model for the Condensed Phases of Water: TIP4P/2005. *J. Chem. Phys.* **2005**, *123*, 234505.
(1232) Babin, V.; Leforestier, C.; Paesani, F. Development of a "First Principles" Water Potential with Flexible Monomers: Dimer Potential Energy Surface, VRT Spectrum, and Second Virial Coefficient. *J. Chem. Theory Comput.* **2013**, *9*, 5395−5403.
(1233) van Duin, A. C. T.; Dasgupta, S.; Lorant, F.; Goddard, W. A. ReaxFF: A Reactive Force Field for Hydrocarbons. *J. Phys. Chem. A* **2001**, *105*, 9396−9409.
(1234) Hartke, B.; Grimme, S. Reactive Force Fields Made Simple. *Phys. Chem. Chem. Phys.* **2015**, *17*, 16715−16718.
(1235) Guo, F.; Wen, Y.-S.; Feng, S.-Q.; Li, X.-D.; Li, H.-S.; Cui, S.-X.; Zhang, Z.-R.; Hu, H.-Q.; Zhang, G.-Q.; Cheng, X.-L. Intelligent-ReaxFF: Evaluating the Reactive Force Field Parameters with Machine Learning. *Comput. Mater. Sci.* **2020**, *172*, 109393.
(1236) Leven, I.; Hao, H.; Das, A. K.; Head-Gordon, T. A Reactive Force Field with Coarse-Grained Electrons for Liquid Water. *J. Phys. Chem. Lett.* **2020**, *11*, 9240−9247.
(1237) Marx, D. Proton Transfer 200 Years after von Grotthuss: Insights from Ab Initio Simulations. *ChemPhysChem* **2006**, *7*, 1848−1870.
(1238) Tuckerman, M. E.; Laasonen, K.; Sprik, M.; Parrinello, M. Ab Initio Simulations of Water and Water Ions. *J. Phys.: Condens. Matter* **1994**, *6*, A93−A100.
(1239) Tuckerman, M.; Laasonen, K.; Sprik, M.; Parrinello, M. Ab Initio Molecular Dynamics Simulation of the Solvation and Transport of Hydronium and Hydroxyl Ions in Water. *J. Chem. Phys.* **1995**, *103*, 150−161.
(1240) Tuckerman, M.; Laasonen, K.; Sprik, M.; Parrinello, M. Ab Initio Molecular Dynamics Simulation of the Solvation and Transport of H_3O^+ and OH^- Ions in Water. *J. Phys. Chem.* **1995**, *99*, 5749−5752.
(1241) Vuilleumier, R.; Borgis, D. Molecular Dynamics of an Excess Proton in Water Using a Non-Additive Valence Bond Force Field. *J. Mol. Struct.* **1997**, *436-437*, 555−565.
(1242) Sagnella, D. E.; Tuckerman, M. E. An Empirical Valence Bond Model for Proton Transfer in Water. *J. Chem. Phys.* **1998**, *108*, 2073−2083.
(1243) Schmitt, U. W.; Voth, G. A. Multistate Empirical Valence Bond Model for Proton Transport in Water. *J. Phys. Chem. B* **1998**, *102*, 5547−5551.
(1244) Voth, G. A. Computer Simulation of Proton Solvation and Transport in Aqueous and Biomolecular Systems. *Acc. Chem. Res.* **2006**, *39*, 143−150.
(1245) (a) de Grotthuss, C. J. T. *Ann. Chim. (Paris)*, 1806; Vol. *54*, p LVIII. English translation (note the three misprints in the name): (b) de Grotthius, C. L. T. *Philos. Mag. (London)* **1806**, *25*, 330. Original pamphlet (unpublished, 22 pages plus front page and one page with Figures I and II, no pagination): (c) C. J. T., de Grotthuss *MÉMOIRE SUR LA DÉCOMPOSITION DE L'EAU et des corps qu'elle tient en dissolution a l'aide the L'ÉLECTRICITÉ GALVANIQUE*; Rome, 1805.
(1246) Marx, D.; Chandra, A.; Tuckerman, M. E. Aqueous Basic Solutions: Hydroxide Solvation, Structural Diffusion, and Comparison to the Hydrated Proton. *Chem. Rev.* **2010**, *110*, 2174−2216.
(1247) Tuckerman, M. E.; Marx, D.; Parrinello, M. The Nature and Transport Mechanism of Hydrated Hydroxide Ions in Aqueous Solution. *Nature* **2002**, *417*, 925−929.
(1248) Ludwig, R. New Insight into the Transport Mechanism of Hydrated Hydroxide Ions in Water. *Angew. Chem., Int. Ed.* **2003**, *42*, 258−260.
(1249) Weingärtner, H.; Chatzidimttriou-Dreismann, C. A. Anomalous H^+ and D^+ Conductance in H_2O-D_2O Mixtures. *Nature* **1990**, *346*, 548−550.
(1250) Sluyters, J. H.; Sluyters-Rehbach, M. The Mechanism of the Hydrogen Ion Conduction in Liquid Light and Heavy Water Derived from the Temperature Dependence of Their Limiting Conductivities. *J. Phys. Chem. B* **2010**, *114*, 15582−15589.

https://doi.org/10.1021/acs.chemrev.1c00331
Chem. Rev. XXXX, XXX, XXX−XXX

(1251) Halle, B.; Karlström, G. Prototropic Charge Migration in Water. Part 2.—Interpretation of Nuclear Magnetic Resonance and Conductivity Data in Terms of Model Mechanisms. *J. Chem. Soc., Faraday Trans. 2* **1983**, *79*, 1047−1073.
(1252) Tuckerman, M. E.; Chandra, A.; Marx, D. Structure and Dynamics of OH^-(Aq). *Acc. Chem. Res.* **2006**, *39*, 151−158.
(1253) Chandra, A.; Tuckerman, M. E.; Marx, D. Connecting Solvation Shell Structure to Proton Transport Kinetics in Hydrogen−Bonded Networks via Population Correlation Functions. *Phys. Rev. Lett.* **2007**, *99*, 145901.
(1254) Chen, M.; Zheng, L.; Santra, B.; Ko, H.-Y.; DiStasio, R. A., Jr; Klein, M. L.; Car, R.; Wu, X. Hydroxide Diffuses Slower than Hydronium in Water Because Its Solvated Structure Inhibits Correlated Proton Transfer. *Nat. Chem.* **2018**, *10*, 413−419.
(1255) Marx, D. Throwing Tetrahedral Dice. *Science* **2004**, *303*, 634−636.
(1256) Marx, D.; Tuckerman, M. E.; Hutter, J.; Parrinello, M. The Nature of the Hydrated Excess Proton in Water. *Nature* **1999**, *397*, 601−604.
(1257) Hynes, J. T. The Protean Proton in Water. *Nature* **1999**, *397*, 565−567.
(1258) Hassanali, A.; Prakash, M. K.; Eshet, H.; Parrinello, M. On the Recombination of Hydronium and Hydroxide Ions in Water. *Proc. Natl. Acad. Sci. U. S. A.* **2011**, *108*, 20410−20415.
(1259) Hassanali, A.; Giberti, F.; Cuny, J.; Kühne, T. D.; Parrinello, M. Proton Transfer through the Water Gossamer. *Proc. Natl. Acad. Sci. U. S. A.* **2013**, *110*, 13723−13728.
(1260) Wu, X.; Selloni, A.; Car, R. Order-N Implementation of Exact Exchange in Extended Insulating Systems. *Phys. Rev. B: Condens. Matter Mater. Phys.* **2009**, *79*, 085102.
(1261) Ko, H.-Y.; Jia, J.; Santra, B.; Wu, X.; Car, R.; DiStasio, R. A., Jr Enabling Large-Scale Condensed-Phase Hybrid Density Functional Theory Based Ab Initio Molecular Dynamics. 1. Theory, Algorithm, and Performance. *J. Chem. Theory Comput.* **2020**, *16*, 3757−3785.
(1262) Ko, H.-Y.; Santra, B.; DiStasio, R. A., Jr. Enabling Large-Scale Condensed-Phase Hybrid Density Functional Theory Based Ab Initio Molecular Dynamics II: Extensions to the Isobaric-Isoenthalpic and Isobaric-Isothermal Ensembles.*J. Chem. Theory Comput.* **2021**, *17*, 77897813.
(1263) Perdew, J. P.; Ernzerhof, M.; Burke, K. Rationale for Mixing Exact Exchange with Density Functional Approximations. *J. Chem. Phys.* **1996**, *105*, 9982−9985.
(1264) Adamo, C.; Barone, V. Toward Reliable Density Functional Methods without Adjustable Parameters: The PBE0Model. *J. Chem. Phys.* **1999**, *110*, 6158−6170.
(1265) Tkatchenko, A.; Scheffler, M. Accurate Molecular van ver Waals Interactions from Ground-State Electron Density and Free-Atom Reference Data. *Phys. Rev. Lett.* **2009**, *102*, 073005.
(1266) Ferri, N.; DiStasio, R. A., Jr; Ambrosetti, A.; Car, R.; Tkatchenko, A. Electronic Properties of Molecules and Surfaces with a Self-Consistent Interatomic van der Waals Density Functional. *Phys. Rev. Lett.* **2015**, *114*, 176802.
(1267) Botti, A.; Bruni, F.; Imberti, S.; Ricci, M. A.; Soper, A. K. Solvation of Hydroxyl Ions in Water. *J. Chem. Phys.* **2003**, *119*, 5001−5004.
(1268) Sepehr, F.; Liu, H.; Luo, X.; Bae, C.; Tuckerman, M. E.; Hickner, M. A.; Paddison, S. J. Mesoscale Simulations of Anion Exchange Membranes Based on Quaternary Ammonium Tethered Triblock Copolymers. *Macromolecules* **2017**, *50*, 4397−4405.
(1269) Espanol, P.; Warren, P. Statistical Mechanics of Dissipative Particle Dynamics. *EPL* **1995**, *30*, 191−196.
(1270) Luo, X.; Paddison, S. J. DPD Simulations of Anion Exchange Membrane: The Effect of an Alkyl Spacer on the Hydrated Morphology. *Solid State Ionics* **2019**, *339*, 115012.
(1271) Luo, X.; Liu, H.; Bae, C.; Tuckerman, M. E.; Hickner, M. A.; Paddison, S. J. Mesoscale Simulations of Quaternary Ammonium-Tethered Triblock Copolymers: Effects of the Degree of Functionalization and Styrene Content. *J. Phys. Chem. C* **2020**, *124*, 16315−16323.
(1272) Lee, M.-T. Exploring Side-Chain Designs for Enhanced Ion Conductivity of Anion-Exchange Membranes by Mesoscale Simulations. *J. Phys. Chem. C* **2019**, *123*, 10802−10815.
(1273) Lee, M.-T. Designing Anion Exchange Membranes with Enhanced Hydroxide Ion Conductivity by Mesoscale Simulations. *J. Phys. Chem. C* **2020**, *124*, 4470−4482.
(1274) Zelovich, T.; Long, Z.; Hickner, M.; Paddison, S. J.; Bae, C.; Tuckerman, M. E. Ab Initio Molecular Dynamics Study of Hydroxide Diffusion Mechanisms in Nanoconfined Structural Mimics of Anion Exchange Membranes. *J. Phys. Chem. C* **2019**, *123*, 4638−4653.
(1275) Zelovich, T.; Vogt-Maranto, L.; Hickner, M. A.; Paddison, S. J.; Bae, C.; Dekel, D. R.; Tuckerman, M. E. Hydroxide Ion Diffusion in Anion-Exchange Membranes at Low Hydration: Insights from Ab Initio Molecular Dynamics. *Chem. Mater.* **2019**, *31*, 5778−5787.
(1276) Zelovich, T.; Tuckerman, M. E. Water Layering Affects Hydroxide Diffusion in Functionalized Nanoconfined Environments. *J. Phys. Chem. Lett.* **2020**, *11*, 5087−5091.
(1277) Behler, J.; Parrinello, M. Generalized Neural-Network Representation of High-Dimensional Potential-Energy Surfaces. *Phys. Rev. Lett.* **2007**, *98*, 146401.
(1278) Bartók, A. P.; Payne, M. C.; Kondor, R.; Csányi, G. Gaussian Approximation Potentials: The Accuracy of Quantum Mechanics, without the Electrons. *Phys. Rev. Lett.* **2010**, *104*, 136403.
(1279) Rupp, M.; Tkatchenko, A.; Müller, K.-R.; von Lilienfeld, O. A. Fast and Accurate Modeling of Molecular Atomization Energies with Machine Learning. *Phys. Rev. Lett.* **2012**, *108*, 058301.
(1280) Montavon, G.; Rupp, M.; Gobre, V.; Vazquez-Mayagoitia, A.; Hansen, K.; Tkatchenko, A.; Müller, K.-R.; Lilienfeld, O. A. v. Machine Learning of Molecular Electronic Properties in Chemical Compound Space. *New J. Phys.* **2013**, *15*, 095003.
(1281) Chmiela, S.; Tkatchenko, A.; Sauceda, H. E.; Poltavsky, I.; Schütt, K. T.; Müller, K.-R. Machine Learning of Accurate Energy-Conserving Molecular Force Fields. *Sci. Adv.* **2017**, *3*, No. e1603015.
(1282) Smith, J. S.; Isayev, O.; Roitberg, A. E. ANI-1: An Extensible Neural Network Potential with DFT Accuracy at Force Field Computational Cost. *Chem. Sci.* **2017**, *8*, 3192−3203.
(1283) Zhang, L.; Han, J.; Wang, H.; Car, R.; E, W. Deep Potential Molecular Dynamics: A Scalable Model with the Accuracy of Quantum Mechanics. *Phys. Rev. Lett.* **2018**, *120*, 143001.
(1284) Zhang, L.; Han, J.; Wang, H.; Saidi, W.; Car, R. E. W. End-to-End Symmetry Preserving Inter-Atomic Potential Energy Model for Finite and Extended Systems. In *Advances in Neural Information Processing Systems 31*; Bengio, S., Wallach, H., Larochelle, H., Grauman, K., Cesa-Bianchi, N., Garnett, R., Eds.; Curran Associates: Red Hook, 2018; pp 4436−4446.
(1285) Ko, H.-Y.; Zhang, L.; Santra, B.; Wang, H.; E, W.; DiStasio, R. A., Jr; Car, R. Isotope Effects in Liquid Water via Deep Potential Molecular Dynamics. *Mol. Phys.* **2019**, *117*, 3269−3281.
(1286) Zhang, L.; Lin, D.-Y.; Wang, H.; Car, R.; E, W. Active Learning of Uniformly Accurate Interatomic Potentials for Materials Simulation. *Phys. Rev. Materials* **2019**, *3*, 023804.
(1287) Calegari Andrade, M. F.; Ko, H.-Y.; Zhang, L.; Car, R.; Selloni, A. Free Energy of Proton Transfer at the Water-TiO_2 Interface from Ab Initio Deep Potential Molecular Dynamics. *Chem. Sci.* **2020**, *11*, 2335−2341.
(1288) Connors, K. *Chemical Kinetics: The Study of Reaction Rates in Solution*; Wiley-VCH Verlag GmbH: Weinheim, 1990.
(1289) Voth, G. A.; Chandler, D.; Miller, W. H. Rigorous Formulation of Quantum Transition State Theory and Its Dynamical Corrections. *J. Chem. Phys.* **1989**, *91*, 7749−7760.
(1290) Rapaport, D. C. *The Art of Molecular Dynamics Simulation*; Cambridge University Press: Cambridge, 2004.
(1291) Sundararaman, R.; Letchworth-Weaver, K.; Schwarz, K. A.; Gunceler, D.; Ozhabes, Y.; Arias, T. JDFTx: Software for Joint Density-Functional Theory. *SoftwareX* **2017**, *6*, 278−284.
(1292) Fiolhais, C.; Nogueira, F.; Marques, M. A. *A Primer in Density Functional Theory*; Springer-Verlag Berlin Heidelberg: Berlin, 2003; Vol. *620*.

https://doi.org/10.1021/acs.chemrev.1c00331
Chem. Rev. XXXX, XXX, XXX−XXX

(1293) Gross, E. K.; Dreizler, R. M. *Density Functional Theory*; Springer Science & Business Media: New York, 1995; Vol. 337.
(1294) Koch, W.; Holthausen, M. C. *A Chemist's Guide to Density Functional Theory*; John Wiley & Sons: Hoboken, 2015.
(1295) Sholl, D.; Steckel, J. A. *Density Functional Theory: A Practical Introduction*; John Wiley & Sons: Hoboken, 2011.
(1296) Ziegler, T. Approximate Density Functional Theory as a Practical Tool in Molecular Energetics and Dynamics. *Chem. Rev.* **1991**, *91*, 651−667.
(1297) Kamerlin, S. C.; Haranczyk, M.; Warshel, A. Progress in Ab Initio Qm/Mm Free-Energy Simulations of Electrostatic Energies in Proteins: Accelerated Qm/Mm Studies of pK_a, Redox Reactions and Solvation Free Energies. *J. Phys. Chem. B* **2009**, *113*, 1253−1272.
(1298) Letchworth Weaver, K. *Microscopically Detailed Joint Density-Functional Theory for the Electrode-Electrolyte Interface*; Cornell University: Ithaca, 2016.
(1299) Paquet, E.; Viktor, H. L. Computational Methods for Ab Initio Molecular Dynamics. *Adv. Chem.* **2018**, *2018*, 1−14.
(1300) Letchworth-Weaver, K.; Arias, T. Joint Density Functional Theory of the Electrode-Electrolyte Interface: Application to Fixed Electrode Potentials, Interfacial Capacitances, and Potentials of Zero Charge. *Phys. Rev. B: Condens. Matter Mater. Phys.* **2012**, *86*, 075140.
(1301) Taylor, C. D.; Wasileski, S. A.; Filhol, J.-S.; Neurock, M. First Principles Reaction Modeling of the Electrochemical Interface: Consideration and Calculation of a Tunable Surface Potential from Atomic and Electronic Structure. *Phys. Rev. B: Condens. Matter Mater. Phys.* **2006**, *73*, 165402.
(1302) Janik, M. J.; Taylor, C. D.; Neurock, M. First Principles Analysis of the Electrocatalytic Oxidation of Methanol and Carbon Monoxide. *Top. Catal.* **2007**, *46*, 306−319.
(1303) Tomasi, J.; Mennucci, B.; Cammi, R. Quantum Mechanical Continuum Solvation Models. *Chem. Rev.* **2005**, *105*, 2999−3094.
(1304) Tomasi, J.; Persico, M. Molecular Interactions in Solution: An Overview of Methods Based on Continuous Distributions of the Solvent. *Chem. Rev.* **1994**, *94*, 2027−2094.
(1305) Giesen, D. J.; Gu, M. Z.; Cramer, C. J.; Truhlar, D. G. A Universal Organic Solvation Model. *J. Org. Chem.* **1996**, *61*, 8720−8721.
(1306) Cramer, C. J.; Truhlar, D. G. A Universal Approach to Solvation Modeling. *Acc. Chem. Res.* **2008**, *41*, 760−768.
(1307) Gunceler, D. *Joint Density-Functional Theory for Energetics and Spectroscopy in Complex Aqueous and Nonaqueous Solvents*; Cornell University: Ithaca, 2016.
(1308) Fattebert, J.-L.; Gygi, F. Density Functional Theory for Efficient Ab Initio Molecular Dynamics Simulations in Solution. *J. Comput. Chem.* **2002**, *23*, 662−666.
(1309) Petrosyan, S.; Rigos, A.; Arias, T. Joint Density-Functional Theory: Ab Initio Study of Cr_2O_3 Surface Chemistry in Solution. *J. Phys. Chem. B* **2005**, *109*, 15436−15444.
(1310) Andreussi, O.; Dabo, I.; Marzari, N. Revised Self-Consistent Continuum Solvation in Electronic-Structure Calculations. *J. Chem. Phys.* **2012**, *136*, 064102.
(1311) Dupont, C.; Andreussi, O.; Marzari, N. Self-Consistent Continuum Solvation (SCCS): The Case of Charged Systems. *J. Chem. Phys.* **2013**, *139*, 214110.
(1312) Sundararaman, R.; Gunceler, D.; Arias, T. Weighted-Density Functionals for Cavity Formation and Dispersion Energies in Continuum Solvation Models. *J. Chem. Phys.* **2014**, *141*, 134105.
(1313) Vilkas, M. J.; Zhan, C.-G. An Efficient Implementation for Determining Volume Polarization in Self-Consistent Reaction Field Theory. *J. Chem. Phys.* **2008**, *129*, 194109.
(1314) Fattebert, J.-L.; Gygi, F. First-Principles Molecular Dynamics Simulations in a Continuum Solvent. *Int. J. Quantum Chem.* **2003**, *93*, 139−147.
(1315) Gunceler, D.; Letchworth-Weaver, K.; Sundararaman, R.; Schwarz, K. A.; Arias, T. The Importance of Nonlinear Fluid Response in Joint Density-Functional Theory Studies of Battery Systems. *Modell. Simul. Mater. Sci. Eng.* **2013**, *21*, 074005.
(1316) White, W. M. *Encyclopedia of Geochemistry: A Comprehensive Reference Source on the Chemistry of the Earth*; Springer: New York, 2018.
(1317) Stern, O. Zur Theorie Der Elektrolytischen Doppelschicht. *Z. Elektrochem. Angew. Phys. Chem.* **1924**, *30*, 508−516.
(1318) Grahame, D. C. Effects of Dielectric Saturation Upon the Diffuse Double Layer and the Free Energy of Hydration of Ions. *J. Chem. Phys.* **1950**, *18*, 903−909.
(1319) Sundararaman, R.; Letchworth-Weaver, K.; Schwarz, K. A. Improving Accuracy of Electrochemical Capacitance and Solvation Energetics in First-Principles Calculations. *J. Chem. Phys.* **2018**, *148*, 144105.
(1320) Percus, J. K. Approximation Methods in Classical Statistical Mechanics. *Phys. Rev. Lett.* **1962**, *8*, 462−463.
(1321) Ebner, C.; Saam, W. F.; Stroud, D. Density-Functional Theory of Simple Classical Fluids. I. Surfaces. *Phys. Rev. A: At., Mol., Opt. Phys.* **1976**, *14*, 2264−2273.
(1322) Evans, R.; Oettel, M.; Roth, R.; Kahl, G. New Developments in Classical Density Functional Theory. *J. Phys.: Condens. Matter* **2016**, *28*, 240401.
(1323) Sundararaman, R.; Arias, T. Efficient Classical Density-Functional Theories of Rigid-Molecular Fluids and a Simplified Free Energy Functional for Liquid Water. *Comput. Phys. Commun.* **2014**, *185*, 818−825.
(1324) Cook, S.; Letchworth-Weaver, K.; Tung, I.-C.; Andersen, T. K.; Hong, H.; Marks, L. D.; Fong, D. D. How Heteroepitaxy Occurs on Strontium Titanate. *Sci. Adv.* **2019**, *5*, No. eaav0764.
(1325) Wu, J.; Jiang, T.; Jiang, D.-E.; Jin, Z.; Henderson, D. A Classical Density Functional Theory for Interfacial Layering of Ionic Liquids. *Soft Matter* **2011**, *7*, 11222−11231.
(1326) Lischner, J.; Arias, T. Classical Density-Functional Theory of Inhomogeneous Water Including Explicit Molecular Structure and Nonlinear Dielectric Response. *J. Phys. Chem. B* **2010**, *114*, 1946−1953.
(1327) Ho, K.-M.; Harmon, B.; Liu, S. Surface-State Contribution to the Electroreflectance of Noble Metals. *Phys. Rev. Lett.* **1980**, *44*, 1531−1534.
(1328) Fu, C.; Ho, K. External-Charge-Induced Surface Reconstruction on Ag (110). *Phys. Rev. Lett.* **1989**, *63*, 1617−1620.
(1329) Maheshwari, S.; Li, Y.; Agrawal, N.; Janik, M. J. Density Functional Theory Models for Electrocatalytic Reactions. In *Advances in Catalysis*; Elsevier: Amsterdam, 2018; Vol. *63*, pp 117−167.
(1330) Otani, M.; Sugino, O. First-Principles Calculations of Charged Surfaces and Interfaces: A Plane-Wave Non-repeated Slab Approach. *Phys. Rev. B: Condens. Matter Mater. Phys.* **2006**, *73*, 115407.
(1331) Kulkarni, A.; Siahrostami, S.; Patel, A.; Nørskov, J. K. Understanding Catalytic Activity Trends in the Oxygen Reduction Reaction. *Chem. Rev.* **2018**, *118*, 2302−2312.
(1332) Jinnouchi, R.; Anderson, A. B. Electronic Structure Calculations of Liquid-Solid Interfaces: Combination of Density Functional Theory and Modified Poisson-Boltzmann Theory. *Phys. Rev. B: Condens. Matter Mater. Phys.* **2008**, *77*, 245417.
(1333) Dabo, I.; Cances, E.; Li, Y.; Marzari, N. Towards First-Principles Electrochemistry. *arXiv:0901.0096*, arXiv.org e-Print archive, 2008. https://arxiv.org/abs/0901.0096.
(1334) Jiang, J.; Cao, D.; Henderson, D.; Wu, J. A Contact-Corrected Density Functional Theory for Electrolytes at an Interface. *Phys. Chem. Chem. Phys.* **2014**, *16*, 3934−3938.
(1335) Kresse, G.; Hafner, J. Ab Initio Molecular Dynamics for Liquid Metals. *Phys. Rev. B: Condens. Matter Mater. Phys.* **1993**, *47*, 558−561.
(1336) Giannozzi, P.; et al. Advanced Capabilities for Materials Modelling with Quantum ESPRESSO. *J. Phys.: Condens. Matter* **2017**, *29*, 465901.
(1337) Sundararaman, R.; Goddard, W. A., III; Arias, T. A. Grand Canonical Electronic Density-Functional Theory: Algorithms and Applications to Electrochemistry. *J. Chem. Phys.* **2017**, *146*, 114104.

https://doi.org/10.1021/acs.chemrev.1c00331
Chem. Rev. XXXX, XXX, XXX−XXX

(1338) Tripkovic, V.; Björketun, M. E.; Skúlason, E.; Rossmeisl, J. Standard Hydrogen Electrode and Potential of Zero Charge in Density Functional Calculations. *Phys. Rev. B: Condens. Matter Mater. Phys.* **2011**, *84*, 115452.
(1339) Martin, H.; Carro, P.; Hernández Creus, A.; González, S.; Salvarezza, R. C.; Arvia, A. J. Growth Mode Transition Involving a Potential-Dependent Isotropic to Anisotropic Surface Atom Diffusion Change. Gold Electrodeposition on HOPG Followed by STM. *Langmuir* **1997**, *13*, 100−110.
(1340) Islam, M. S.; Fisher, C. A. Lithium and Sodium Battery Cathode Materials: Computational Insights into Voltage, Diffusion and Nanostructural Properties. *Chem. Soc. Rev.* **2014**, *43*, 185−204.
(1341) Hammer, B.; Nørskov, J. K. Theoretical Surface Science and Catalysiscalculations and Concepts. *Adv. Catal.* **2000**, *45*, 71−129.
(1342) Meng, Y. S.; Arroyo-de Dompablo, M. E. Recent Advances in First Principles Computational Research of Cathode Materials for Lithium-Ion Batteries. *Acc. Chem. Res.* **2013**, *46*, 1171−1180.
(1343) Nørskov, J. K.; Abild-Pedersen, F.; Studt, F.; Bligaard, T. Density Functional Theory in Surface Chemistry and Catalysis. *Proc. Natl. Acad. Sci. U. S. A.* **2011**, *108*, 937−943.
(1344) Ceder, G. Opportunities and Challenges for First-Principles Materials Design and Applications to Li Battery Materials. *MRS Bull.* **2010**, *35*, 693−701.
(1345) Isegawa, M.; Neese, F.; Pantazis, D. A. Ionization Energies and Aqueous Redox Potentials of Organic Molecules: Comparison of DFT, Correlated Ab Initio Theory and Pair Natural Orbital Approaches. *J. Chem. Theory Comput.* **2016**, *12*, 2272−2284.
(1346) Lim, H.-D.; Lee, B.; Zheng, Y.; Hong, J.; Kim, J.; Gwon, H.; Ko, Y.; Lee, M.; Cho, K.; Kang, K. Rational Design of Redox Mediators for Advanced Li-O_2 Batteries. *Nat. Energy* **2016**, *1*, 1−9.
(1347) Exner, K. S.; Anton, J.; Jacob, T.; Over, H. Chlorine Evolution Reaction on RuO_2 (110): Ab Initio Atomistic Thermodynamics Study-Pourbaix Diagrams. *Electrochim. Acta* **2014**, *120*, 460−466.
(1348) Zeng, Z.; Chan, M. K.; Zhao, Z.-J.; Kubal, J.; Fan, D.; Greeley, J. Towards First Principles-Based Prediction of Highly Accurate Electrochemical Pourbaix Diagrams. *J. Phys. Chem. C* **2015**, *119*, 18177−18187.
(1349) Choudhury, S.; Wei, S.; Ozhabes, Y.; Gunceler, D.; Zachman, M. J.; Tu, Z.; Shin, J. H.; Nath, P.; Agrawal, A.; Kourkoutis, L. F.; Arias, T. A.; Archer, L. A. Designing Solid-Liquid Interphases for Sodium Batteries. *Nat. Commun.* **2017**, *8*, 898.
(1350) Cossi, M.; Barone, V.; Cammi, R.; Tomasi, J. Ab Initio Study of Solvated Molecules: A New Implementation of the Polarizable Continuum Model. *Chem. Phys. Lett.* **1996**, *255*, 327−335.
(1351) Santiago, R. S.; Santos, G. R.; Aznar, M. UNIQUAC Correlation of Liquid-Liquid Equilibrium in Systems Involving Ionic Liquids: The DET-PCM Approach. *Fluid Phase Equilib.* **2009**, *278*, 54−61.
(1352) Cicero, G.; Grossman, J. C.; Catellani, A.; Galli, G. Water at a Hydrophilic Solid Surface Probed by Ab Initio Molecular Dynamics: Inhomogeneous Thin Layers of Dense Fluid. *J. Am. Chem. Soc.* **2005**, *127*, 6830−6835.
(1353) Ozhabes, Y.; Gunceler, D.; Arias, T. Stability and Surface Diffusion at Lithium-Electrolyte Interphases with Connections to Dendrite Suppression. *arXiv:1504.05799*, arXiv.org e-Print archive, 2015. https://arxiv.org/abs/1504.05799.
(1354) Předota, M.; Bandura, A.; Cummings, P.; Kubicki, J.; Wesolowski, D.; Chialvo, A.; Machesky, M. L. Electric Double Layer at the Rutile (110) Surface. 1. Structure of Surfaces and Interfacial Water from Molecular Dynamics by Use of Ab Initio Potentials. *J. Phys. Chem. B* **2004**, *108*, 12049−12060.
(1355) de Paul Nzuwah Nziko, V.; Shih, J.; Jansone-Popova, S.; Bryantsev, V. S. Quantum Chemical Prediction of pKa Values of Cationic Ion-Exchange Groups in Polymer Electrolyte membranes. *J. Phys. Chem. C* **2018**, *122*, 2490−2501.
(1356) Matsuyama, K.; Ohashi, H.; Miyanishi, S.; Ushiyama, H.; Yamaguchi, T. Quantum Chemical Approach for Highly Durable Anion Exchange Groups in Solid-State Alkaline Fuel Cells. *RSC Adv.* **2016**, *6*, 36269−36272.
(1357) Chempath, S.; Einsla, B. R.; Pratt, L. R.; Macomber, C. S.; Boncella, J. M.; Rau, J. A.; Pivovar, B. S. Mechanism of Tetraalkylammonium Headgroup Degradation in Alkaline Fuel Cell Membranes. *J. Phys. Chem. C* **2008**, *112*, 3179−3182.
(1358) Chempath, S.; Boncella, J. M.; Pratt, L. R.; Henson, N.; Pivovar, B. S. Density Functional Theory Study of Degradation Of Tetraalkylammonium Hydroxides. *J. Phys. Chem. C* **2010**, *114*, 11977−11983.
(1359) Gu, L.; Dong, H.; Sun, Z.; Li, Y.; Yan, F. Spirocyclic Quaternary Ammonium Cations for Alkaline Anion Exchange Membrane Applications: An Experimental and Theoretical Study. *RSC Adv.* **2016**, *6*, 94387−94398.
(1360) Espiritu, R.; Tan, J. L.; Lim, L. H.; Arco, S. Density Functional Theory Study on the Degradation of Fuel Cell Anion Exchange Membranes via Removal of Vinylbenzyl Quaternary Ammonium Head Group. *J. Phys. Org. Chem.* **2020**, *33*, No. e4049.
(1361) Zhang, W.; Dong, D.; Bedrov, D.; van Duin, A. C. Hydroxide Transport and Chemical Degradation in Anion Exchange Membranes: A Combined Reactive and Non-Reactive Molecular Simulation Study. *J. Mater. Chem. A* **2019**, *7*, 5442−5452.
(1362) Long, H.; Pivovar, B. Hydroxide Degradation Pathways for Imidazolium Cations: A DFT Study. *J. Phys. Chem. C* **2014**, *118*, 9880−9888.
(1363) Wang, W.; Wang, S.; Xie, X.; Lv, Y.; Ramani, V. K. Hydroxide-Ion Induced Degradation Pathway for Dimethylimidazolium Groups in Anion Exchange Membranes. *J. Membr. Sci.* **2014**, *462*, 112−118.
(1364) Wang, W.; Wang, S.; Xie, X.; Lv, Y.; Ramani, V. Density Functional Theory Study of Hydroxide-Ion Induced Degradation of Imidazolium Cations. *Int. J. Hydrogen Energy* **2014**, *39*, 14355−14361.
(1365) Tsuchitani, R.; Nakanishi, H.; Shishitani, H.; Yamaguchi, S.; Tanaka, H.; Kasai, H. A Theoretical Study of How C2-substitution Affects Alkaline Stability in Imidazolium-Based Anion Exchange Membranes. *Solid State Ionics* **2015**, *278*, 5−10.
(1366) Dong, H.; Gu, F.; Li, M.; Lin, B.; Si, Z.; Hou, T.; Yan, F.; Lee, S. T.; Li, Y. Improving the Alkaline Stability of Imidazolium Cations by Substitution. *ChemPhysChem* **2014**, *15*, 3006−3014.
(1367) Long, H.; Pivovar, B. S. Computational Modeling of Degradation of Substituted Benzyltrimethyl Ammonium. *ECS Trans.* **2014**, *64*, 1211−1219.
(1368) Long, H.; Pivovar, B. S. Hydroxide Degradation Pathways for Substituted Benzyltrimethyl Ammonium: A DFT Study. *ECS Electrochem. Lett.* **2015**, *4*, F13−F16.
(1369) Xiang, T.; Si, H. Theoretical study of the Degradation Mechanisms of Substituted Phenyltrimethylammonium Cations. *Comput. Theor. Chem.* **2015**, *1065*, 12−17.
(1370) Li, W.; Wang, S.; Zhang, X.; Wang, W.; Xie, X.; Pei, P. Degradation of Guanidinium-Functionalized Anion Exchange Membrane During Alkaline Environment. *Int. J. Hydrogen Energy* **2014**, *39*, 13710−13717.
(1371) Li, G.; Yang, G.; Cheng, J.; Zhang, F.; Hao, C. Hydroxide Degradation Pathways for Guanidimidazolium Cation: A Density Functional Theory Study. *J. Phys. Org. Chem.* **2018**, *31*, No. e3861.
(1372) Cances, E.; Mennucci, B.; Tomasi, J. A New Integral Equation Formalism for the Polarizable Continuum Model: Theoretical Background and Applications to Isotropic and Anisotropic Dielectrics. *J. Chem. Phys.* **1997**, *107*, 3032−3041.
(1373) Chipman, D. M. Reaction Field Treatment of Charge Penetration. *J. Chem. Phys.* **2000**, *112*, 5558−5565.
(1374) Cances, E.; Mennucci, B. The Escaped Charge Problem in Solvation Continuum Models. *J. Chem. Phys.* **2001**, *115*, 6130−6135.
(1375) Tomasi, J.; Mennucci, B.; Cammi, R. Quantum Mechanical Continuum Solvation Models. *Chem. Rev.* **2005**, *105*, 2999−3093.
(1376) Choe, Y.; Fujimoto, C.; Lee, K.; Dalton, L. T.; Ayers, K.; Henson, N. J.; Kim, Y. S. Alkaline Stability of Benzyl Trimethyl Ammonium Functionalized Polyaromatics: A Computational and Experimental Study. *Chem. Mater.* **2014**, *26*, 5675−5682.

https://doi.org/10.1021/acs.chemrev.1c00331
Chem. Rev. XXXX, XXX, XXX−XXX

(1377) Zhang, F.; Li, T.; Chen, W.; Yan, X.; Wu, X.; Jiang, X.; Zhang, Y.; Wang, X.; He, G. High-Performance Anion Exchange membranes With Para-Type cations On Electron-Withdrawing C═O Links Free Backbone. *Macromolecules* **2020**, *53*, 10988−10997.
(1378) Ribas-Arino, J.; Shiga, M.; Marx, D. Understanding Covalent Mechanochemistry. *Angew. Chem., Int. Ed.* **2009**, *48*, 4190−4193.
(1379) Chen, C.; Tse, Y.-L. S.; Lindberg, G. E.; Knight, C.; Voth, G. A. Hydroxide Solvation and Transport in Anion Exchange Membranes. *J. Am. Chem. Soc.* **2016**, *138*, 991−1000.
(1380) Tse, Y.-L. S.; Chen, C.; Lindberg, G. E.; Kumar, R.; Voth, G. A. Propensity of Hydrated Excess Protons and Hydroxide Anions for the Air-Water Interface. *J. Am. Chem. Soc.* **2015**, *137*, 12610−12616.

https://doi.org/10.1021/acs.chemrev.1c00331
Chem. Rev. XXXX, XXX, XXX−XXX